Real-Time Lattice Simulations of the Glasma Coupled to Fermions

Dissertation

zur Erlangung des Doktorgrades

der Naturwissenschaften

vorgelegt beim Fachbereich 13 Physik

der Johann Wolfgang Goethe-Universität

in Frankfurt am Main

von

Andreas Mario Halsch

aus Hünfeld, Deutschland

Frankfurt am Main 2023

D30

Vom Fachbereich 13 Physik der

Johann Wolfgang Goethe-Universität als Dissertation angenommen.

Dekan:	Prof. Dr. Roger Erb
Gutachter:	Prof. Dr. Owe Philipsen Prof. Dr. Carsten Greiner

Datum der Disputation: 26.01.2024

Contents

Deutsche Zusammenfassung

Das in der zweiten Hälfte des 20. Jahrhundert entwickelte *Standardmodell der Teilchenphysik* ist eine Quantenfeldtheorie zur mikroskopischen Beschreibung von drei der vier fundamentalen Kräfte der Natur, der elektromagnetischen, der schwachen und der starken Wechselwirkung. Die vorliegende Arbeit beschränkt sich auf die Untersuchung des Sektors der starken Wechselwirkung, der innerhalb des Standardmodells durch die *Quantenchromodynamik* (QCD) beschrieben wird. Die Konstituenten der Quantenchromodynamik sind Teilchen mit verschiedener Masse und elektrischer Ladung, die als *Quarks* bezeichnet werden. Sie besitzen einen Eigendrehimpuls (*Spin*) von 1/2 und zählen somit zur Klasse der Fermionen. Aufgrund ihrer Eigenschaften unterscheidet man sechs verschiedene Sorten, die man als Quarks von unterschiedlichem *flavor* (Geschmack) bezeichnet. Die Wechselwirkung zwischen den Quarks wird durch Teilchen von ganzzahligem Spin vermittelt, die man als *Gluonen* bezeichnet. Diese bosonischen *Austauschteilchen* tragen selbst keine Masse und können darüber hinaus mit sich selbst wechselwirken. Entscheidend ist, dass die Stärke der Wechselwirkung abhängig von der Energieskala des Systems ist, was sich im Phänomen der *laufenden Kopplung* manifestiert. Bei niederen bis mittleren Energien und Dichten sind Quarks und Gluonen stark gekoppelt und man beobachtet das Phänomen des *Confinement*. Im Gegensatz zu anderen fundamentalen Bausteinen von Materie, wie beispielsweise Elektronen, ist es bei diesen Energien nicht möglich Quarks und Gluonen zu isolieren. Sie treten ausschließlich in gebundenen Zuständen, sogenannten *Hadronen* von mindestens drei Quarks (*Baryonen*) oder einem Quark-Antiquark Paar (*Mesonen*) auf. Auf Grundlage dessen, ordnet man Quarks eine *Farbladung* („chromo“) zu, so dass Hadronen *farbneutrale* Zustände darstellen, die entweder durch additive Farbmischung dreier Farben (rgb-Modell) oder durch Kombination von Farbe und Antifarbe gebildet werden. Erst bei hohen Energien und Dichten, wird die Kopplung der starken Wechselwirkung geringer und geht im Grenzfall in eine freie Theorie von Quarks und Gluonen über (*asymptotische Freiheit*). Es kommt somit zu einem Phasenübergang, bei dem sich die gebundenen Zustände aus Quarks und Gluonen auflösen, einer *deconfinement transition*. Die Quantenchromodynamik stellt eine Eichtheorie dar und ist somit invariant unter lokalen, nicht-Abelschen $SU(3)$ Eichtransformationen. Hierbei wird die Dynamik der Gluonen im Rahmen einer $SU(3)$ *Yang-Mills Theorie* beschrieben und die Kopplung von Quarks und Gluonen erfolgt mithilfe der *kovarianten Ableitung*. Im Bereich der starken Kopplung lassen sich Berechnungen nicht mithilfe von *Störungstheorie* durchführen und es ist notwendig auf *nicht-pertubative* Methoden zurückzugreifen. Neben einer Vielzahl von effektiven Theorien ist hierbei vor allem das Konzept der *Gitterquantenchromodynamik* erfolgreich. Die zentral Idee der Gitter-QCD ist, die kontinuierliche Raumzeit durch ein diskretes Gitter, typischerweise mit isotropem Gitterabstand, zu ersetzen und die Theorie ohne Verletzung der Eichinvarianz zu diskretisieren. Die Berechnung von Observablen erfolgt dann beispielsweise durch das Bestimmen von *Korrelationsfunktionen*, die durch das numerische Lösen von *Pfadintegralen* ausgewertet werden können. Diese Berechnung hochdimensionaler Integrale erfolgt typischerweise mithilfe von *Monte-Carlo* Integration, bei der man einen Teil des Integranden der Korrelationsfunktion als ein Wahrscheinlichkeitsmaß auffasst, um den Wert des Pfadintegrals mithilfe von *importance*

sampling entlang einer *Markow-Kette*, statistisch zu approximieren. Bei diesem Verfahren, ist es typischerweise notwendig, die reale Zeit anhand einer *Wick-Rotation* auf die imaginäre Achse zu rotieren und somit eine *euklidische Zeit* zu erhalten. Gitter-QCD eignet sich somit besonders zur Berechnung statischer Größen wie bspw. den Hadronmassen, oder auch für eine Anwendung in der statistischen Physik wie beispielsweise für die Berechnung der Zustandsgleichung der QCD.
Durch den Wechsel zu euklidischer Zeit ist es nicht mehr direkt möglich zeitabhängige physikalische Größen, wie bspw. die Energiedichte und den Druck in einem Systems außerhalb des thermischen Gleichgewichts zu bestimmen. Im nicht-pertubativen Bereich ist somit eine alternative Beschreibung, z.B. anhand von *effektiven Modellen* erforderlich, welche die reelle, physikalische Zeit beibehalten. Eine Möglichkeit bietet hierbei eine *klassische Approximation* der Theorie, die erlaubt, Quanteneffekte in führender Ordnung zu vernachlässigen und die Dynamik des Systems anhand von Hamiltonschen Bewegungsgleichungen für klassische Felder zu entwickeln. Für die Validität einer klassischen Approximation ist es zunächst notwendig, dass die klassischen Feldmoden im infraroten Bereich (*IR-Skala*) gegenüber den Quantenkorrekturen im ultravioletten Bereich (*UV-Skala*) dominieren. Dies ist nur in einer bosonischen Theorie möglich, da das *Paulische Ausschlussprinzip* für Fermionen eine Überbesetzung (*overoccupation*) spezifischer Feldmoden verbietet. Somit kann ausschließlich der Yang-Mills Sektor der Quantenchromodynamik als klassisch approximiert werden. Darüber hinaus muss die Theorie hinreichend schwach gekoppelt sein, was im Falle der QCD nur nahe der asymptotischen Freiheit bei hohen Energien gewährleistet ist. Eine Diskretisierung auf dem Gitter bietet nun die Möglichkeit die Impulse der UV-Skala durch die *Gitterregulasisierung* abzuschneiden (Impuls-*Cutoff* des Gitters) und gleichzeitig die Eichinvarianz der Theorie bei der Diskretisierung zu gewährleisten. Es ist allerdings nicht mehr möglich in einer klassischen Approximation auf dem Gitter einen *Kontinuumslimes* durchzuführen, bei dem der Gitterabstand gegen Null läuft und man das Ergebnis des Kontinuums extrapoliert, da die klassische Theorie in diesem Grenzfall divergiert. In Analogie zur UV-Divergenz der klassischen Beschreibung der Schwarzkörperstrahlung, wird dieses Phänomen häufig als *Rayleigh-Jeans* Divergenz der klassischen Theorie bezeichnet. Als Konsequenz sind insbesondere die Observablen, die im Rahmen einer klassischen Approximation auf dem Gitter berechnet werden, abhängig vom Gitterabstand. Es ist allerdings möglich den Gitterabstand über ein Abgleichen (*matching*) der klassischen Theorie mit einer Kontinuumstheorie festzulegen.
Um einen Phasenübergang innerhalb der QCD von einem stark gekoppelten, hin zu einem schwach gekoppelten System (quasi-)freier Quarks und Gluonen zu untersuchen, benötigt man ein System mit hoher Energie und Dichte. Ein solches ist durch eine ultrarelativistische, hochenergetische Kollision schwerer Ionen gegeben, die sich gut experimentell untersuchen lässt. Derartige Kollisionen von typischerweise Blei- oder Goldkernen, werden unter anderem am *Relativistic Heavy Ion Collider* (RHIC) in Brookhaven (USA) oder auch am *Large Hadron Collider* (LHC) in Genf (Schweiz/Frankreich) untersucht. In naher Zukunft sollen diese Experimente noch um die *Facility for Antiproton and Ion Research* (FAIR) in Darmstadt (Deutschland) ergänzt werden. In den jeweiligen Experimenten werden die Ionen auf ein hohes Perzentil der Lichtgeschwindigkeit beschleunigt und anschließend möglichst zentral kollidiert. Aufgrund dessen wird ihre Struktur zerstört und das System bis auf die unterste Ebene der Elementarteilchen, sprich der Quarks und Gluonen zerlegt. Es ist somit davon auszugehen, dass es zu einem Phasenübergang kommt bei dem Quarks und Gluonen in der Frühphase der Kollision frei vorliegen. Aufgrund der Expansion des heißen Feuerballs aus Elementarteilchen nimmt die Energiedichte allerdings rapide ab und in Folge dessen formieren sich erneut Hadronen aus den freien Quarks und Gluonen, bis schließlich,

nach einer Lebenszeit von ca. 10 fm, das System in sich zusammenbricht (*freeze-out*). Auf der Grundlage der Experimente konnte gezeigt werden, dass sich das System bereits in der Frühphase der Kollision nach ungefähr ~ 1 fm gut mithilfe von Hydrodynamik beschreiben lässt. Demnach verhält sich das Medium aus freien Quarks und Gluonen ähnlich einer Flüssigkeit und wird als *Quark-Gluonen Plasma* (QGP) bezeichnet. Eine zentrale Frage der Frühphase einer Schwerionenkollision ist hierbei die Suche nach einem Thermalisierungsprozess in der QCD. Unmittelbar nach der Kollision der Ionen ist das System außerhalb des thermischen Gleichgewichtes, allerdings wird für die Beschreibung des QGP mithilfe von Hydrodynamik zumindest ein lokales thermisches Gleichgewicht (*local thermal equilibrium (LTE)*) benötigt. In dieser Arbeit wird dabei der für das Erreichen des LTE wichtige Teilaspekt der Isotropisierung des Druckes untersucht.
Den in dieser Arbeit durchgeführten Simulationen der Frühphase einer Schwerionenkollision, liegt ein effektives Modell zugrunde, das auf der Beobachtung basiert, dass die Gluonendichte der kollidierenden Nuklei bei einer bestimmten Impulsskala saturiert. Beschleunigt man die schweren Ionen auf hohe Geschwindigkeiten und lässt sie zentral kollidieren, so emittieren die hochenergetischen Gluonen der Nuklei kaskadenartig niederenergetische Gluonen (*BFKL-ladder*) durch *Bremsstrahlung*. Die Gluonendichte saturiert sobald der Wirkungsquerschnitt für die Rekombination von Gluonen und der Wirkungsquerschnitt für die Emission von Bremsstrahlung von gleicher Ordnung sind. Dieser Punkt ist durch eine spezifische Impulsskala bestimmt, die als *saturation scale* bezeichnet wird. Die effektive Beschreibung erfolgt nun anhand einer Separation der Energieskalen der unterschiedlichen Gluonen. Die hochenergetischen Gluonen der UV-Skala (sowie die Valenz- und Sea-Quarks) können während der Kollision als statisch betrachtet werden, da sie aufgrund der Lorentzschen Zeitdilatation für die Dauer der Kollision eingefroren sind (*frozen-in*). Diese agieren nun als statischer Hintergundstrom für die Dynamik der niederenergetischen Gluonen (IR-Skala), und deren Dynamik kann in führender Ordnung anhand der klassischen Bewegungsgleichungen beschrieben werden. Da Gluonen Farbladung tragen und die hochenergetischen Gluonen in einem System mit saturierter Gluonendichte (ähnlich einem Kondensat) die Dynamik der niederenergetischen Gluonen über einen statischen Farbstrom beeinflussen, wird diese effektive Theorie als Theorie des Farbglaskondensats (*Color-Glass Condensate*) bezeichnet.
In der vorliegenden Arbeit verwenden wir diese effektive Theorie für die Konstruktion der Eichfelder des Yang-Mills Sektors als Anfangsbedingung in einer Gittersimulation auf einem dreidimensionalen Gitter mit reeller Zeit. Das so generierte Ensemble aus klassischen $SU(3)$ Yang-Mills Feldern stellt einen Übergangszustand zwischen dem Color-Glass Condensate und dem Quark-Gluonen Plasma dar und wird als *Glasma* bezeichnet. Die Dynamik des Glasmas lässt sich nun in führender Ordnung anhand der klassischen Bewegungsgleichungen entwickeln. Das Glasma wird unter anderem von zwei zentralen Eigenschaften charakterisiert. Zum Einen, bildet das System auf der Grundlage des statischen Farbstroms hochenergetischer Gluonen longitudinale Röhren mit konstantem Farbfluss (*color-flux tubes*) aus. Entlang dieser Röhren ist das chromo-elektrische Feld des Systems konstant, während es in transversaler Richtung verschwindet. In einem naiven Bild, kann man das System somit als eine Art Plattenkondensator beschreiben, bei denen die statischen, hochenergetischen Gluonen die mit Farbladung geladenen Platten darstellen, zwischen denen sich ein chromo-elektrisches Feld ausbildet. Zum Zweiten weist der Druck des Systems anfänglich eine hohe Anisotropie auf. Eine explizite Rechnung ergibt, dass der Druck in longitudinaler Richtung dem transversalen Druck mit umgekehrtem Vorzeichen entspricht. Eine zentrale Frage bei klassischen Simulationen des Glasmas ist somit, inwiefern die Dynamik des Systems zu einer Isotropisierung des Druckes führt und ob sich das

System somit in Richtung eines lokalen thermischen Gleichgewichts entwickelt.
In der Literatur konnte bereits mithilfe von klassischen Simulationen von reiner Yang-Mills Theorie gezeigt werden, dass es zu keiner Druckisotropisierung kommt und stattdessen ein Zustand erreicht wird, bei denen die Gluonen (quasi-)wechselwirkungsfrei propagieren, das sogenannte *free-streaming limit*. Dies ist sogar der Fall, wenn man die Expansion des Systems vernachlässigt und in einer statischen Box simuliert. Grund hierfür ist, dass die Anfangsbedingungen invariant unter longitudinalen Lorentztransformation sind und die klassischen Bewegungsgleichungen diese Invarianz erhalten. Somit ist das System in einer statischen Box effektiv zweidimensional und insbesondere wird die Struktur der longitudinalen Röhren mit konstantem Farbfluss erhalten, so dass es zu keiner Druckisotropisierung kommt. In der statischen Box konnte allerdings gezeigt werden, dass ein explizites Brechen der longitudinalen Boostinvarianz dazu führt, dass sich die Röhren mit konstantem Farbfluss mit der Zeit auflösen und es zu einer Isotropisierung des Drucks kommt. Eine solche explizite Verletzung der Boostinvarianz ist motiviert durch Quantenfluktuationen und hat das Ausbilden einer Instabilität zur Folge, die als *chromo-Weibel-Instabilität* bezeichnet wird. Wird diese Instabilität durch die Quantenfluktuationen induziert, verbreitet sie sich über das komplette Gitter und führt dazu, dass in einer Kaskade hochenergetische Moden besetzt werden, was schließlich auch zu einer Isotropisierung des Druckes führt. In einer longitudinal expandierenden Box konnte eine ähnliche Instabilität identifiziert werden, allerdings verhindert die rapide Expansion ein Isotropisierung und das System fällt in das free-streaming limit.
Bisherige Simulationen des Glasmas berücksichtigen nur reine Yang-Mills Theorie und vernachlässigen somit den Einfluss von Fermionen auf das System. Fermionen können zum einen nach der Kollision der Ionen im Medium gefangen werden, viel eher aber durch Paarerzeugung beim Zerfall von Gluonen entstehen. Es ist zu erwarten, dass eine Kopplung der klassischen Eichfelder des Glasmas an Fermionen einen mindestens gleichwertigen Einfluss auf das System ausübt, wie Quantenkorrekturen in der Yang-Mills Theorie. Unter Berücksichtigung der Beobachtung, dass Quantenfluktuationen im Yang-Mills Sektor einen signifikanten Beitrag zur Dynamik des Glasmas liefern und den Druck des Systems entscheidend beeinflussen, wird in dieser Arbeit untersucht, inwiefern eine Wechselwirkung der klassischen Eichfelder mit Fermionen in einer statischen und einer longitudinal expandierenden Box das System beeinflussen. Hierzu wird der fermionische Sektor der QCD unter Verwendung der Vakuumlösung der Dirac Gleichung initialisiert und im ersten Zeitschritt der Simulation an den klassischen Yang-Mills Sektor gekoppelt. Wie eingangs beschrieben, verbietet das Paulische Ausschlussprinizip eine klassische Approximation der Fermionen und sie stellen somit eine Quelle für Quanteneffekte dar. Infolgedessen ist es notwendig eine effektive Approximation der QCD zu entwickeln, die es erlaubt auf einem dreidimensionalen Gitter mit reeller Zeit die Dynamik von klassischen Eichfeldern, gekoppelt an Fermionen zu beschreiben. Im vierten Kapitel dieser Arbeit präsentieren wir eine solche, semi-klassische Approximation der QCD. Auf der Grundlage dessen ist es anschließend möglich die Bewegungsgleichungen der klassischen Eichfelder und insbesondere des chromo-elektrischen Feldes zu bestimmen, in der die Fermionen in der Form eines Farbstroms eingehen, der durch eine Auswertung des *statistischen Propagators* bestimmt ist. In Verbindung mit dem Lösen der *Dirac Gleichung* für die Dynamik der Fermionen, ist es somit möglich alle Felder mithilfe einer *leap-frog* Methode zum numerischen Lösen von Differentialgleichungen in der Zeit zu entwickeln.
Im ersten Teil der Arbeit betrachten wir das System in einer statischen Box. Neben der Diskussion einer Renormierung der semi-klassischen Approximation, die eine korrekte Dynamik der Eich- und Fermionfelder in einer regularisierten Theorie auf dem Gitter gewährleistet, leiten wir Observablen her, die in der Simulation numerisch berechnet werden. Wir bestimmen hierbei

die Energiedichte des Systems, sowie den Druck anhand der Diagonalelemente des Energie-Impuls-Tensors der QCD. Darüber hinaus präsentieren wir eine eichinvariante Möglichkeit zur Auswertung der Besetzung der Energiemoden des Systems, basierend auf der Identifikation der Energiemoden mit den Moden der fouriertransformierten Energiedichte des Systems. Die Berechnung der fermionischen Observablen erfolgt mithilfe einer stochastischen Methode, bei der die Erwartungswerte der fermionischen Feldoperatoren durch Mittelwerte eines Ensembles *stochastischer Fermionen* approximiert werden. Da es wie eingangs beschrieben nicht möglich ist im Falle der semi-klassischen Approximation einen Kontinuumslimes durchzuführen, legen wir den Gitterabstand mithilfe eines Matching fest. Hierfür matchen wir die Energiedichte unseres Systems an die abgeschätzte Energiedichte der Frühphase in einer Schwerionenkollision, die mithilfe einer effektiven Kontinuumstheorie, ebenfalls basierend auf dem Phänomen der Gluonsaturierung (*saturation model*), bestimmt wurde.
In der statischen Box konnten wir mithilfe von Gittersimulationen der semi-klassischen Approximation der QCD zeigen, dass das System aus klassischen Yang-Mills Feldern des Glasmas, durch die Kopplung an Vakuum-Fermionen isotropisiert. Ähnlich der chromo-Weibel Instabilität in reiner Yang-Mills Theorie mit explizit gebrochener longitudinaler Boostinvarianz, führt die Wechselwirkung zwischen den Feldern zu einer Besetzung hochenergetischer Moden und ein Isotropisierungsprozess setzt ein. Die Besetzung der Moden erfolgt hierbei durch die Rückkopplung der Fermionen auf die Yang-Mills Felder und den damit verbundenen Energietransfer. Wir konnten entsprechend zeigen, dass ein Reduzieren der Kopplung den Prozess verlangsamt, wohingegen eine Verdopplung der Freiheitsgrade des fermionischen Sektors, durch die Hinzunahme eines weiteren Quarkflavor mit gleicher Masse (entartete Quarks), die Equilibrierung der Besetzung der Energiemoden, sowie die Isotropisierung beschleunigt. Darüber hinaus konnten wir zeigen, dass dieser Prozess im Wesentlichen unabhängig von der gewählten Masse der Quarks ist, wobei wir Massen von der Ordnung des strange-Quarks und der up/down-Quarks getestet haben. Insbesondere leichte Quarkmassen sind aufgrund der hohen Energie- und Impulsskala des Glasmas bereits nahe dem ultrarelativistischen Grenzfall masseloser Quarks zu verorten. Verbunden mit der Equilibrierung der Besetzung der Energiemoden des Systems, konnten wir ebenfalls beobachten, dass sich die für das Glasma charakteristische Struktur der Röhren mit konstantem Farbfluss, mit fortlaufender Zeit auflöst. Im Gegensatz zu reiner Yang-Mills Theorie mit explizit gebrochener Boostinvarianz geschieht dies nicht durch das Ausbilden räumlich begrenzter Filamente aufgrund einer chromo-Weibel Instabilität, die sich anschließend rapide auf das gesamte Gitter übertragen, sondern ist an jedem Gitterpunkt präsent. Abseits der beobachteten Isotropisierung ist jedoch zentral, dass die übermäßige Besetzung niederenergetischer Moden im Yang-Mills Sektor, die eine notwendige Bedingung für die Validität der klassischen Approximation der Eichfelder darstellt, aufgrund der Wechselwirkung mit den Fermionen im Laufe der Zeit abnimmt. Zu späten Simulationszeiten konkurriert somit die Druckisotropisierung mit der Klassizität des Systems und die Approximation verliert aller Voraussicht nach ihre Gültigkeit.
In einem zweiten Abschnitt wurde das Modell von der statischen auf eine longitudinal expandierende Box erweitert, welche besser die physikalische Realität einer Schwerionenkollision modelliert. Die Beschreibung eines derartigen Systems erfolgt mithilfe eines spezifischen Koordinatensystems, dass als *Milne-* oder Bjorken-Koordinaten bezeichnet wird und dem eine longitudinale Expansion geometrisch immanent ist (*comoving Koordinaten*). Infolge dessen war es notwendig die Bewegungsgleichungen der semi-klassischen Approximation, sowie die Observablen auf das neue Koordinatensystem anzupassen. Hierbei musste insbesondere die freie Dirac-Gleichung in Milne-Koordinaten gelöst werden, deren Vakuumlösung die Anfangsbedingung

für den Fermion Sektor bildet. Aufgrund der nichtlinearen Zeitabhängigkeit der freien Dirac-Gleichung in der expandierenden Box, war es hierbei notwendig eine Variante der *Besselschen Differenzialgleichung* zu lösen, um den Vakuumspinor zu konstruieren. Die Initialisierung des Yang-Mills Sektors erfolgte, wie zuvor in der statischen Box, mithilfe der effektiven Theorie des Farbglaskondensats. Ebenfalls in Analogie zur statischen Box, ist es möglich anschließend den Gitterabstand über ein Matching-Verfahren für die Energiedichte des Systems festzulegen.
Wir konnten durch die Simulation des expandierenden Systems zeigen, dass im Gegensatz zur statischen Box, keine Druckisotropisierung erfolgt. Zwar wird die anfängliche starke Anisotropie des Systems aufgelöst, allerdings fällt es anschließend in das free-streaming limit, charakterisiert durch einen Abfall der Energiedichte, der invers proportional zur Zeit ist, einen Abfall des longitudinalen Druckes auf Null, sowie ein Verhältnis von transversalem Druck zu Energiedichte von ein-halb. Wie in der statischen Box ist diese Beobachtung unabhängig von der gewählten Masse der Fermionen. Weiterhin ist im Vergleich zur statischen Box eine Besetzung hochenergetischer Moden durch den Energietransfer zwischen beiden Sektoren in der expandierenden Box deutlich reduziert. Grund hierfür ist zum einen die rapide longitudinale Expansion, die der Wechselwirkung entgegenwirkt und zum anderen die Tatsache, dass die Energiemoden des Systems durch die Expansion zusätzlich abgesenkt werden und somit neue niederenergetische Moden geschaffen werden. Der Einfluss der Schnelligkeit der Expansion ließ sich bestätigen, indem ein langsam expandierendes System aus klassischen Yang-Mills Feldern des Glasmas und Fermionen simuliert wurde, welches zwar keine deutliche Druckisotropisierung zeigt, allerdings nicht in das free-streaming limit fällt. Wir konnten darüber hinaus zeigen, dass die Effekte einer induzierten Instabilität durch das explizite Brechen der longitudinalen Boostinvarianz im Yang-Mills Sektor und eine Instabilität durch das koppeln an Fermionen kombinieren. Nichtsdestotrotz verhindert die longitudinale Expansion eine Isotropisierung des Druckes. Ein Herabsetzen der Kopplung zeigte wie erwartet, dass hochenergetische Moden noch langsamer besetzt werden. Ein Verdoppeln der Freiheitsgrade des Fermion Sektors, durch die Hinzunahme eines weiteren, entarteten Quark-flavors, zeigte hingegen nur marginale Effekte auf die Besetzung der Energiemoden. In beiden Fällen konnte keine Druckisotropie erreicht werden. Durch die langsamere Besetzung hochenergetischer Moden in der expandierenden Box ist allerdings davon auszugehen, dass im Gegenteil zur statischen Box, die klassische Approximation auf längeren Zeitskalen valide ist, da die Überbesetzung klassischer Feldmoden länger gewährleistet ist.
Zusammenfassend konnten wir in dieser Arbeit zeigen, dass Quanteneffekte eine entscheidende Rolle für die Evolution des Mediums in der Frühphase einer Schwerionenkollision, hin zu einem System im lokalen thermischen Gleichgewicht spielen. Wir konnten dabei zeigen, dass die Kopplung der klassischen Yang-Mills Felder an Fermionen einen ähnlichen Effekt auf die Dynamik des Systems hat wie ein explizites Brechen der longitudinalen Boostinvarianz im Yang-Mills Sektor. In einer expandierenden Box konnte allerdings keine Druckisotropie durch die betrachteten Quanteneffekte erreicht werden. Darüber hinaus konnten wir zeigen, dass das Isotropisieren des Druckes mit der Validität der klassischen Approximation konkurriert, was eine alternative Beschreibung des Systems zu späten Zeiten notwendig macht. Insbesondere können die Quanteneffekte des Yang-Mills Sektors nicht länger vernachlässigt werden, da die Überbesetzung klassischer Feldmoden nicht mehr gewährleistet ist und somit die Klassizität zusammenbricht. Infolge dessen ist zu späten Zeiten eine alternative Beschreibung des Systems notwendig, die auch ein Laufen der Kopplung berücksichtigen sollte.

Danksagung

An erster Stelle danke ich meinem Doktorvater Prof. Dr. Owe Philipsen, der mich von der Bachelor- zur Masterarbeit, bishin zur Doktorarbeit, über mein gesamtes Studium begleitet hat. Ich bedanke mich besonders für sein Vertrauen und die Möglichkeit einer Promotion. Die unzähligen gemeinsamen Diskussionen haben wesentlich zu dieser Arbeit beigetragen, und ich bedanke mich in besonderem Maße dafür, dass ich mit Fragen stets auf ihn zukommen konnte und immer Unterstützung erhalten habe. Auch die Möglichkeit zur Lehre beitragen zu können, hat mir stets besonderen Spaß bereitet, was insbesondere auch im Hinblick auf die Unmöglichkeit einer Präsenzlehre während einer globalen Pandemie eine spannende Herausforderung war.
Ein weiterer großer Dank gebührt Prof. Dr. Carsten Greiner, und dies nicht nur für seine Bereitschaft das Zweitgutachten für diese Arbeit anzufertigen, sondern insbesondere auch für seine vielen wertvollen Beiträge und hilfreichen Literaturhinweise zu allen Phasen dieser Arbeit. Auch die gelegentlichen gemeinsamen Mittagessen, zusammen mit seiner Arbeitsgruppe haben mir häufig viel Freude bereitet.
Ich bedanke mich herzlich bei Dr. Oscar Garcia-Montero, der mich inbesondere in der finalen Phase meiner Promotion im Rahmen unzähliger Diskussionen unterstützt hat. Insbesondere möchte ich mich hierbei für seine Beiträge zum 3. Kapitel bedanken, da er immer wieder zentrale Veröffentlichungen an mich herangetragen hat und unser Austausch entscheidend zu meinem Verständins der Frühphase einer Schwerionenkollision beigetragen hat.
Ein besonderer Dank gilt auch meinem Freund, Kommilitonen und Mitbewohner Jan Rais, mit dem ich nicht nur eine Leidenschaft für klassische Musik teile, sondern auch die Begeisterung für Physik. Sowohl die gemeinsamen Konzerte als auch sein Lektorat haben mit Sicherheit einen großen Anteil am Gelingen dieser Arbeit.
Ähnliches gilt auch für Reinhold Kaiser, der mich ebenfalls sowohl musikalisch, als auch fachlich während meiner Promotionszeit unterstützt hat. Darüber hinaus möchte ich mich bei allen aktuellen und ehemaligen Mitgliedern der Arbeitsgruppe von Prof. Dr. Owe Philipsen bedanken, die nicht nur in technischen und inhaltlichen Fragen immer unterstützend waren, sondern auch ein äußerst angenehmes Arbeitsumfeld geschaffen haben. Hierbei möchte ich noch einmal Dr. Björn Fröhlich Wagenbach herausstellen, dessen Projekt ich übernehmen und weiterführen durfte und der mich insbesondere in der Anfangszeit sehr unterstützt hat.
Ich möchte mich bei Dr. Kurt Herget bedanken, der die vorliegende Arbeit im Hinblick auf die Korrektheit der englischen Sprache lektoriert hat und sich dabei als Anglist auch durch den Wust an mathematischen Gleichungen kämpfen musste.
Nicht zuletzt möchte ich mich auch sehr bei allen meinen Freundinnen und Freunden bedanken, die mich insbesondere in arbeitsintensiven Phasen besonders unterstützt haben.
Abschließend, aber in ganz besonderem Maße bedanke ich mich bei meiner Familie und besonders bei meinen Eltern, Birgit und Harald, die mir, nicht zuletzt auch finanziell, ein Studium mit anschließender Promotion ermöglicht haben und stets eine große Unterstützung und Hilfe sind.

Introduction

The *Standard Model of Particle Physics* had its genesis in the 70s of the previous century, but it still provides a challenging area of research in the first quarter of the 21st century. In the standard model, the microscopic quantum dynamics of three of the four fundamental forces of nature, the electromagnetic interaction, the weak interaction and the strong interaction are combined. The quantum theory of the latter one is known as *Quantum Chromodynamics* (QCD) and will be the subject of interest in this thesis. Quantum Chromodynamics is constructed from $N_f = 6$ fermion fields of different mass, referred to as quarks. The interaction of these fermion fields is mediated by non-abelian $SU(3)$ massless bosons, called gluons, making QCD an $SU(3)$ gauge theory. At low and mid energies, QCD is dominated by a phenomenon referred to as *Color Confinement*. Due to color confinement, color-charged particles, as quarks and gluons, can not directly be observed and are always bound in color neutral states. Such states can be constructed from three quarks of different color, creating a half integer spin particle, referred to as *Baryon*, or from a quark and an anti-quark, creating an integer spin particle, referred to as *Meson*. Besides that, exotic states as *glueballs*, which are theoretical proclaimed particles constructed from gluons only (see [1] for a review), or particles constructed from more than three quarks, as for example *Tetra- or Penta-quark states* (see e.g. [2] for a review), are interesting objects of recent research.

One important consequence of the phenomenon of color confinement is, that QCD is strongly coupled below high energy scales („*infrared slavery*“). As a consequence, it is not possible to derive the hadron spectrum of QCD using perturbation theory, making non-perturbative methods necessary. One of the most successful non-perturbative approaches is *Lattice Quantum Chromodynamics*. The idea is to systematically discretize QCD on a four dimensional lattice, while preserving gauge invariance. Within this discretization, it is possible to derive quantities as hadron masses from correlation functions, by solving high dimensional path integrals numerically. In practice, this can be realized by making use of *Monte-Carlo methods* for numerical integration of highly dimensional integrals. The bulk of these methods is based on *importance sampling*, where a probability weight function is defined from the integrand of the path integral, making it possible to approximate the true value of the path integral from generating field configurations in a *Markov Chain*. As a consequence, controlling the numerical error and the systematic error of the lattice discretization are two of the most important challenges in lattice simulations, where the latter one can be taken care of by a systematic *continuum limit*, that removes the lattice cutoff dependence.

The evaluation of path integrals in Lattice Quantum Chromodynamics requires a *Wick rotation* of Minkowski time to imaginary, *euclidean time*. The euclidean formulation is of great use in spectroscopy, as well as in statistical quantum field theory (see e.g. [3] for a review of lattice QCD thermodynamics), making it possible to investigate the QCD equation of state [4], the *deconfinement transition* [5] or the *Chiral Phase Transition* [6]. All these studies have in common, that quantities of interest are not dependent on real-time, making a computation on an euclidean lattice possible.

On the experimental side, a successful setup to test QCD for a deconfinement transition is provided by (ultra-)relativistic *Heavy Ion Collisions*, where heavy nuclei, e.g. *Au*- or *Pb*-nuclei, are accelerated to very high velocities and collided at huge center-of-mass energies. The largest operating experiments nowadays are the *Relativistic Heavy Ion Collider* (RHIC) in Brookhaven (USA), reaching center of mass energies up to $\sqrt{s} \approx 200$ GeV and the *Large Hadron Collider* (LHC) in Geneva (Switzerland/France), reaching center of mass energies up to $\sqrt{s} \approx 5$ TeV [7]. In the nearer future, the *Facility for Antiproton and Ion Reserach* (FAIR), located close to Darmstadt (Germany) is expected to start operating [8]. Around the year 2000, it has prominently been argued in [9], that experimental evidence in heavy ion collisions at the LHC indicates a new state of matter, which is formed shortly after the collision. The collective flow of this new state of matter [10, 11], could be described well, by making use of hydrodynamics [12, 13] and it turned out to be in good agreement with theoretical predictions for the existence of a state of non-confined quarks and gluons, known as the *Quark-Gluon-Plasma* (QGP). For a review on the experimental evidence in heavy ion collisions for a formation of the QGP, see [14] and for a review on the applicability of hydrodynamics, see [15].
Besides the search for the phase transitions of strongly interacting matter, heavy ion collisions provide important insights into the non-equilibrium dynamics of QCD. With the confined heavy nuclei colliding at very high velocities in the experiment, the system is out-of-equilibrium right after the collision. On the other hand, the QGP itself is expected to be at least in local thermal equilibrium [16], arising the question for a thermalization process in highly energetic QCD. A first step towards an understanding of the very early phase in a heavy ion collision, has been presented in terms of an effective theory for QCD, based on the phenomenon of *gluon saturation* [17]. The saturated regime allows to identify a separation of scales for the gluonic degrees of freedom of the system, where the hard gluons (*Ultraviolet*-scale) are frozen in due to time dilation and form a background current for the soft gluons (*Infrared*-scale) that behave classical to leading order. A prominent theoretical description of such a system in $SU(3)$ Yang-Mills theory, has been presented by L.D. MacLerran and R. Venugopalan and became popular as the *MV-model* [18, 19, 20]. The model was later extended, putting the assumption of the separation of scales on a more solid basis and resulting in an effective theory, referred to as *Color-Glass Condensate* (CGC) [21, 22, 23, 24].
As stated already, an important property of this effective theory is the assumption, that the dynamical, soft gluons of the system are classical to leading order. As a consequence, it is necessary that the IR-modes of the fields are highly occupied. This requirement leads to three necessities, that a theory has to fulfill, for the existence of a classical limit: (1) the fields have to be bosonic in character, because the Pauli-exclusion principle for fermions naturally forbids large occupation numbers, (2) the fields of the theory have to be associated with stable particles, allowing the establishment of a classical configuration on macroscopic time-scales and (3) the theory must have a sensible non-interactive limit [25]. The first two properties are naturally provided by the Yang-Mills sector of QCD, but the latter one is only established in the deconfined phase of the theory, with the saturated regime in the CGC essentially providing the necessary condition of highly occupied IR-modes for the gauge fields $A \sim \mathcal{O}(1/\alpha_s)$, with α_s the strong coupling.
Classical approximations have already been successfully used to calculate the soliton pair creation in real scalar field theory by D. Yu. Grigoriev and V.A. Rubakov in 1988 [26]. Later, they have systematically been studied in a hot scalar field theory by G. Aarts and J. Smit [27], demonstrating that indeed the quantum theory is approximated at high energy and weak coupling. These studies could then be extended to nonequilibrium fields in [28, 29]. The

possibility of approximating a bosonic theory as classical within a specific regime, opened the perspective of calculating real-time observables on the lattice. Instead of solving path integrals on a euclidean lattice, it is possible to simulate the evolution of a classical system, by solving Hamilton equations of motion on a three dimensional lattice, keeping real-time [30]. The lattice hereby provides a nonperturbative regularization of the classical theory, removing the non-classical UV-degrees of freedom, while preserving exact gauge invariance. On the downside, a continuum limit is no longer possible in the classical lattice theory, because the theory is UV-divergent (*Rayleigh-Jeans divergent*). Nevertheless, classical lattice simulations have successfully been used to investigate the topology of Yang-Mills theories [31, 32], the chiral-magnetic effect [33, 34], solid state physics [35] and heavy quark thermalization in QCD [36].

Another prominent application, is a simulation of the early time dynamics in a heavy ion collision. The dynamical gauge fields of the Color-Glass Condensate effective theory form a pre-QGP, out-of-equilibrium state, referred to as the *Glasma* [37]. The dynamics of the Glasma has already been investigated in pure Yang-Mills theory, making use of real-time lattice techniques. The Glasma is expected to form after $t \approx 0.1$ fm[1] in a heavy ion collision and acts as a transitional state, until hydrodynamics is expected to become applicable, at a hydrodynamization time of $t \approx 1$ fm [38]. Classical simulations of the Glasma have successfully been used to investigate the gluon multiplicity [39, 40, 41, 42, 43] and the energy density of the Glasma [44, 45]. For a review on simulations of the Glasma see [46]. Additionally, the Glasma has been used as an initial state [47, 48, 49] for different theoretical approaches to describe the early dynamics of a heavy ion collision, using e.g. QCD kinetic theory [50] or hydrodynamic models [51, 52].

Besides an investigation of the intrinsic features of the Glasma, the search for a thermalization process is of particular interest. A first step towards thermalization in QCD has been made in perturbative QCD, with the discovery of *bottom up* thermalization [53] in *overoccupied* systems, where initially a large number of low energy degrees of freedom is occupied. Later, its relation to QCD plasma instabilities has been discussed in [54], that actually might prevent the mechanism [55]. With the Glasma beeing an overoccupied system, studies have been extended to the regime of gluon saturation in *weakly coupled* QCD [56, 57], resulting in the discovery of a *non-thermal fixed point*, where a self-similar scaling behavior of the phase-space density could be observed. This observation could be related to the appearance of an *energy cascade*, where energy is transported from low- to high-momentum excitations. It has been argued, that essentially this transport is necessary for a thermalization process to appear [58, 59].

Another success was the discovery of a similar cascade for the occupation of high energy modes, in real-time lattice simulations of the Glasma, in a static box [60]. It could later be traced back to the development of a *chromo-Weibel instability*, that is realized by explicitly *breaking longitudinal boost invariance* by hand, introducing a quantum fluctuation on the level of the initial conditions. Although a full equilibration process is out of reach in a real-time classical simulation, it was possible to show, that the pressure of this system reaches an *isotropy*, which is a necessary step towards (local) thermal equilibrium. An extension of the study to a longitudinally expanding box, lead to the discovery of a similar instability, but pressure isotropy could never be reached and is prevented by the expansion. On the opposite, the *free-streaming limit* is reached by the system, where the classical gluon fields evolve (quasi-)free [61, 62]. Recently, a systematic calculation of NLO corrections in the Yang-Mills sector has been performed [63, 64], as well as a finite thickness of the colliding nuclei [65, 66, 67] has been considered, that could both provide

[1] We use natural units in this work, setting $c = 1$.

a source for an explicit breaking of longitudinal boost invariance.
All these studies have in common, that they only deal with a pure Yang-Mills theory and neglect fermions. In a first approximation this is reasonable, because the regime of gluon saturation is essentially gluon dominated, as indicated from *Deep Inelastic Scattering* (DIS) experiments at the *Hadron-Elektron-Ring-Anlage* (HERA) [68]. Nevertheless, fermions are expected to be produced from gluon decay in the Glasma and a first step towards the calculation of quark production has been presented in [69, 70], where a back-coupling of the quarks onto gluons has been neglected. Adopting an idea, presented for the calculation of fermion production in QED [71], it is possible to derive a *semi-classical* approximation of QCD, where a back-coupling of fermions onto the classical Yang-Mills fields is included and fermions enter the equations of motion via a color current [72]. This approximation has already been used to study the quark production in a static system for Glasma-type initial conditions, initializing a system of overoccupied gluons [73]. Additionally, in [74] a first step towards a calculation of quark production in a longitudinally expanding setup has been made, presenting first results in [75] and comparing them to results from kinetic theory [76, 77, 78].
In this work, we want to study how a coupling of fermions to the classical Yang-Mills fields of the Glasma modifies the evolution of the system in both, a static and a longitudinally expanding system. In similarity to a breaking of longitudinal boost invariance from quantum fluctuations in the Yang-Mills sector, fermions could potentially provide a quantum source for the development of an instability as well, that drives the system towards pressure isotropy. To study this, we initialize the Yang-Mills fields by solving the Poisson equation of the CGC effective theory on the lattice, generating the Glasma and couple it to vacuum fermions at the first time-step. The system can now be evolved, by making use of the semi-classical approximation of QCD. We implement it on a three dimensional isotropic lattice, keeping real-time. Our main goal is to study the energy density, the occupation of energy modes and the pressure of the system, which can be measured from the diagonal components of the QCD energy-momentum tensor. We will use the energy density to set the scale in our system, by matching it to an estimate for the initial energy density in a heavy ion collision. Investigating the pressure now allows us, to search for a process of pressure isotropization, induced by the fermions.

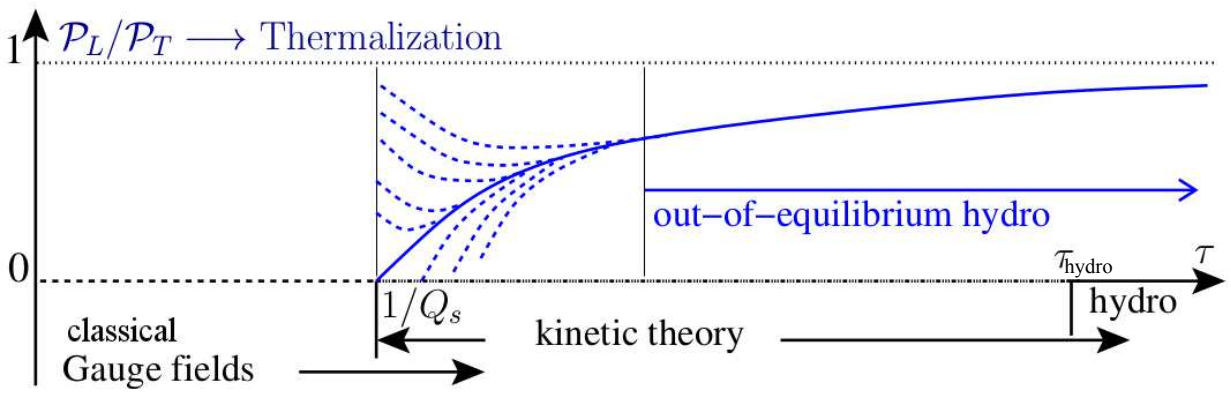

Figure 1: Illustration of the interplay of different theoretical approaches for the early time dynamics of a heavy ion collision. Illustration adapted from [79].

A description of an equilibration process within the (semi-)classical model is out of reach, because the validity of the model breaks down as soon as the overoccupation of soft bosonic field modes is diminished from the energy cascade. As a consequence, a complete description would

require a matching to either hydrodynamics or QCD kinetic theory (see figure 1). Kinetic theory has already been successfully used to study the equilibration of non-abelian pure Yang-Mills theory [57, 77, 80, 81, 82] and our work hereby provides information, how the initial state could be modified when including fermions already on the level of the Glasma. Studies of quark production and chemical equilibration within QCD kinetic theory have been presented in [83, 84, 85]. For a recent review on thermalization in QCD see [86].

This thesis is structured in the following way: In the first two chapters we briefly review continuum QCD and lattice QCD on a three dimensional lattice, with Minkowski time. In chapter 3 we introduce the effective theory of the Color Glass Condensate and the concept of gluon saturation. We present how to construct a lattice gauge link ensemble representing the Glasma state, that provides the initial condition for the Yang-Mills sector in our simulations. Furthermore, we discuss how the energy density of the early phase in a heavy ion collision, at the formation time of the Glasma $t \approx 0.1$ fm can be estimated. In a first part, we discuss how to simulate in a static box, introducing the evolution equations of the semi-classical model in chapter 4 and its renormalization in chapter 5. We continue by deriving the observables from the energy-momentum tensor of QCD in chapter 6. In chapter 7 we discuss the lattice implementation of the model and following that, we present a possibility to introduce a physical scale to our system, by matching the energy density in the simulation to an estimate of the energy density in the early phase of a heavy ion collision, fixing the lattice spacing a. We close the first part, by presenting the results of a simulation in the static box in chapter 8. The second part of this thesis extends the model to a longitudinally expanding system, starting with a discussion of the formalism in chapter 9. In the next chapter, we solve the free lattice Dirac equation in the expanding box, obtaining the vacuum solution of the spinor, that will be used as initial condition for the fermion sector in the simulation. In chapter 11 and chapter 12 the equations of motion and observables are extended to the longitudinally expanding system. Finally in chapter 13, the matching procedure for the energy density is repeated, to set the physical scale and the results for a simulation in an expanding box are presented. We close the thesis with a discussion of our results and future research perspectives.

1 Quantum Chromodynamics

Quantum Chromodynamics (QCD) is the quantum theory of strong interactions and its genesis began with the discovery of a variety of hadrons, starting in 1947 with the discovery of Kaons K in cosmic rays by George Rochester and Clifford Charles Butler [87] and was followed by the discovery of the Λ-Baryon in 1950 by V. D. Hopper and S. Biswas [88]. In the 60s and 70s, many more discoveries were made (e.g. the Ω baryon and the Ξ baryon, both in 1964, the J/Ψ meson in 1974), arriving at a situation that became famous as the *„particle zoo“*. The discovery of such a great amount of particles motivated a new theoretical description for strong interactions, first presented by Gell-Mann and Ne'eman, who ordered the hadrons into groups ($SU(3)$-multiplets), characterized by the particles properties and masses. This ordering became popular as the *„eightfold way“* [89, 90]. Later in 1964 Gell-Mann and Zweig proposed additional spin-1/2 particles of different *flavor* as constituents of these hadrons, called *quarks* [91, 92]. Due to the fermionic nature of the quarks, the discovery of the Δ^{++} resonance as a state constructed of three quarks of the same flavor (three up-quarks) and the same spin orientation (spin $+3/2$), marked a theoretical challenge, because such a state should be forbidden due to the Pauli exclusion principle. A solution for this problem was first proposed by Greenberg, Han and Nambu where they added an additional $SU(3)$ gauge degree of freedom to the quark model, that became later known as *color charge* [93, 94]. The idea of the model is, that hadronic states have to be color neutral, which can either be achieved by combining three quarks of different color or a quark with an anti-quark. The interaction of the quarks is mediated by $3^2 - 1$ vector bosons, which later became known as *gluons*. In 1973 Fritzsch, Leutwyler and Gell-Mann adopted the idea of color charge in the quark model and combined it with a theory for vector bosons [95], first discussed by Chan Ning Yang and Robert Mills (*Yang-Mills theory*) [96], to describe the dynamics of the gluons, finally specifying the model of Quantum Chromodynamics.

In this thesis, we will derive a semi-classical approximation of QCD, that will be applicable to simulate the early time dynamics of a heavy ion collision. In this chapter, we briefly review some aspects of the theory, presenting all equations that are necessary in later calculations and we clarify the notation and conventions used in this thesis.

1.1 The Action of Quantum Chromodynamics

As a quantum field theory, the theory of Quantum Chromodynamics can be formulated in terms of an action

$$S_{QCD} = \int \mathcal{L}_{QCD}\, d^4x, \tag{1.1}$$

where $\mathcal{L}_{QCD}$ is the corresponding Lagrange density of QCD

$$\mathcal{L}_{QCD} = -\frac{1}{4}F^{\mu\nu,a}F^a_{\mu\nu} + \sum_{f=1}^{N_f}\bar{\psi}^{(f)}(x)\Big(\mathrm{i}\gamma^\mu D_\mu - m^{(f)}\Big)\psi^{(f)}(x). \tag{1.2}$$

The QCD action and Lagrangian are invariant under Lorentz transformations. We denote Lorentz indices as greek indices and use the following signature for the Minkowski metric

$$\mathrm{diag}(\eta_{\mu\nu}) = (+,-,-,-), \tag{1.3}$$

where co- and contra-variant space-time vectors are represented as

$$x^\mu = \Big(x^0, x^i\Big) = \Big(t, \mathbf{x}\Big), \qquad x_\mu = \Big(x_0, x_i\Big) = \Big(t, -\mathbf{x}\Big). \tag{1.4}$$

The Lagrange density of QCD (eq. 1.2) can be divided into two parts, where the first part describes the dynamics of the fermion fields, referred to as fermion sector in this thesis

$$\mathcal{L}_f = \sum_{f=1}^{N_f}\bar{\psi}^{(f)}(x)\Big(\mathrm{i}\gamma^\mu D_\mu - m^{(f)}\Big)\psi^{(f)}(x), \tag{1.5}$$

and the second part the dynamics of the gauge fields, referred to as Yang-Mills sector

$$\mathcal{L}_{YM} = -\frac{1}{2}\mathrm{tr}F^{\mu\nu}F_{\mu\nu}. \tag{1.6}$$

The interaction of quarks and gluons is given from the covariant derivative D_μ[1]

$$D_\mu = \partial_\mu + \mathrm{i}gA_\mu(x), \tag{1.7}$$

with the coupling g.
The quarks are described in terms of Dirac spinors $\psi^{(f)}$, that are four dimensional vectors in Dirac space of spin-1/2, carrying an additional flavor index (f). The $N_f = 6$ different quark flavors have different masses $m^{(f)}$. We will restrict ourselves only to one fermion flavor of mass m, or to N_f degenerate quark flavors, with equal mass.

QCD is a gauge theory and the corresponding action (eq. 1.1) is invariant under local $SU(3)$ gauge transformations. The quarks hereby carry a color charge and transform within the fundamental representation of $SU(3)$

$$\psi^{(f)\prime} = U(x)\psi^{(f)} = e^{-\mathrm{i}\theta^a(x)T^a}\psi^{(f)}. \tag{1.8}$$

[1]The sign in front of the coupling g is a convention, where both $(+)$ and $(-)$ can be found in the literature.

The matrices T^a are the group generators of the $SU(3)$ Lie-group, with $a \in \{1, ..., 3^2 - 1\}$. The gluons are massless spin-1 vector bosons and transform as

$$A'_\mu(x) = U(x)A_\mu(x)U^{-1}(x) - \frac{\mathrm{i}}{g}U(x)\partial_\mu U^{-1}(x). \tag{1.9}$$

They are matrices in color-space and can be written as

$$A_\mu(x) = A^a_\mu(x)T^a. \tag{1.10}$$

The group generators of $SU(3)$ are given by the Gell-Mann matrices (eq. A.6) and satisfy the Lie algebra

$$\Big[T^a, T^b\Big] = \mathrm{i}f^{abc}T^c, \tag{1.11}$$

with f^{abc} the structure coefficients of the group (eq. A.5). The dynamics of the Yang-Mills fields of QCD is formulated in terms of the field strength tensor $F^{\mu\nu}$

$$\begin{aligned} F_{\mu\nu}(x) &= -\mathrm{i}\Big[D_\mu(x), D_\nu(x)\Big] \\ &= \partial_\mu A_\nu(x) - \partial_\nu A_\mu(x) + \mathrm{i}g\Big[A_\mu(x), A_\nu(x)\Big] \\ &= \partial_\mu A_\nu(x) - \partial_\nu A_\mu(x) - gf^{abc}T^a A^b_\mu(x)A^c_\nu(x). \end{aligned} \tag{1.12}$$

A gauge theory has some additional gauge degrees of freedom, requiring physical observables to be gauge invariant. This freedom of choosing a specific gauge allows us to isolate one gauge degree of freedom, choosing temporal (or Fock-Schwinger) gauge, setting

$$A_0 = 0. \tag{1.13}$$

With this choice of gauge, the gauge orbit is not yet completely fixed and one additional gauge degree of freedom remains. If not stated differently, we do not fix this additional degree of freedom, but if doing so, we make use of Coulomb gauge

$$\nabla\mathbf{A}(x) = 0. \tag{1.14}$$

1.1.1 Yang-Mills Theory

The Yang-Mills sector of QCD is of particular interest for the definition of the semi-classical model. As discussed in the introduction, a classical approximation is only possible for bosons, because it requires a large occupation of classical field modes, which is forbidden for fermions due to the Pauli exclusion principle. As a consequence, only the Yang-Mills sector of QCD can be approximated as classical. Choosing temporal gauge, the Lagrangian (eq. 1.6) reduces to

$$\mathcal{L}_{YM} = \mathrm{tr}\Big[F_{0i}F_{0i} - \sum_{i<j}F_{ij}F_{ij}\Big] = \mathrm{tr}\Big[F^2_{0i} - \sum_{i<j}F^2_{ij}\Big]. \tag{1.15}$$

It is possible to derive the corresponding Hamiltonian of pure Yang-Mills theory, by applying a Legendre transformation. The conjugate field is given as

$$\Pi^{\mu a}_A(x) = \frac{\partial\mathcal{L}_{YM}}{\partial\Big(\partial_0 A^a_\mu(x)\Big)} = -F^{0\mu,a}. \tag{1.16}$$

In analogy to Electrodynamics, we identify the conjugate field as the chromo-electric field

$$\Pi_A^{i,a}(x) = F_{0i}^a(x) := E_i^a(x) = \partial_0 A_i^a(x). \tag{1.17}$$

The Hamilton density of pure Yang-Mills theory is then given as

$$\begin{aligned}\mathcal{H}_{YM} =& \Pi_A^{\mu,a}(x)\partial_0 A_\mu^a(x) - \mathcal{L}_{YM} = E_i^a(x)\partial_0 A_i^a(x) - \mathcal{L}_{YM} \\ =& \mathrm{tr}\Big[E_i(x)E_i(x) + \sum_{i<j} F_{ij}(x)F_{ij}(x)\Big].\end{aligned} \tag{1.18}$$

The Yang-Mills Lagrangian can be expressed as a function of the chromo-electrical fields as well

$$\mathcal{L}_{YM} = \mathrm{tr}\Big[E_iE_i - \sum_{i<j} F_{ij}F_{ij}\Big]. \tag{1.19}$$

In a classical field theory, the dynamics of the system is governed by the classical equation of motion, derived from the Euler-Lagrange equation

$$\partial_\mu \frac{\partial \mathcal{L}_{YM}}{\partial\Big(\partial_\mu A_\nu^a\Big)} - \frac{\partial \mathcal{L}_{YM}}{\partial A_\nu^a} = 0, \tag{1.20}$$

leading to

$$\partial_\mu F^{\mu\nu,a} - g f^{abc} A_\mu^b F^{\mu\nu,c} = 0. \tag{1.21}$$

Setting $\nu = i$, it is possible to derive the equation of motion for the chromo-electric fields from (eq. 1.21)

$$\partial_t E_i^a(x) = \partial_j F^{ji,a}(x) - g f^{abc} A_j^b(x) F^{ji,c}(x). \tag{1.22}$$

1.1.2 The Hamiltonian of Quantum Chromodynamics

From the QCD Lagrangian (eq. 1.2), rewritten by making use of the chromo-electric fields (eq. 1.17)

$$\mathcal{L}_{QCD} = \mathcal{L}_{YM} + \mathcal{L}_f = \mathrm{tr}\Big[E_iE_i - \sum_{i<j} F_{ij}F_{ij}\Big] + \bar\psi(x)\Big(\mathrm{i}\gamma^\mu D_\mu - m\Big)\psi(x), \tag{1.23}$$

it is possible to derive the Hamiltonian, performing a Legendre transformation. We already presented this derivation for the Yang-Mills sector, arriving at (eq. 1.18). For the fermion sector, the conjugate field is given as

$$\Pi_f(x) = \frac{\partial \mathcal{L}_f}{\partial\Big(\partial_0\psi(x)\Big)} = \mathrm{i}\bar\psi(x)\gamma^0. \tag{1.24}$$

A Legendre transformation then leads to the Hamiltonian of the fermion sector of QCD (in temporal gauge)

$$\mathcal{H}_f = \Pi_f(x)\partial_0\psi(x) - \mathcal{L}_f = \bar\psi(x)\Big(-\mathrm{i}\gamma^i D_i + m\Big)\psi(x). \tag{1.25}$$

The total Hamiltonian is now given as the sum of (eq. 1.18) and (eq. 1.25)

$$\mathcal{H}_{QCD} = \mathcal{H}_f + \mathcal{H}_{YM} = \mathrm{tr}\Big[E_i(x)E_i(x) + \sum_{i<j} F_{ij}(x)F_{ij}(x)\Big] + \bar\psi(x)\Big(-\mathrm{i}\gamma^i D_i + m\Big)\psi(x). \tag{1.26}$$

1.2 Free Colored Fermions

The free theory of colored fermions is of particular interest for this thesis, because it will provide the initial condition for the fermion sector of QCD in the static box, in later simulations. It is given by setting $A_\mu = 0$ in the QCD Lagrangian (eq. 1.2)

$$\mathcal{L}_f = \bar{\psi}(x)\Big(\mathrm{i}\gamma^\mu\partial_\mu - m\Big)\psi(x), \tag{1.27}$$

where we consider only $N_f = 1$ fermion flavor.[2] It is straight forward to derive the corresponding equation of motion, making use of the Euler-Lagrange equation. The result is well known and referred to as the free Dirac equation

$$\Big(\mathrm{i}\gamma^\mu\partial_\mu - m\Big)\psi(x) = 0. \tag{1.28}$$

Its solution can be found from Fourier decomposing the spinor[3]

$$\psi(x) = \int \sum_{s=1}^{2}\sum_{c=1}^{3}\Big(a_{s,c}(\mathbf{p})u_s(\mathbf{p})\xi_c e^{-\mathrm{i}px} + b^\dagger_{s,c}(\mathbf{p})v_s(\mathbf{p})\xi_c e^{\mathrm{i}px}\Big)\frac{d^3p}{(2\pi)^3}, \tag{1.29}$$

where ξ_c is a (unit) vector in color space, but we will suppress its notation in most of the calculations.
To perform a canonical quantization, the Fourier coefficients $a_s(\mathbf{p})$ and $b^\dagger_s(\mathbf{p})$ are replaced by creation and annihilation operators, that satisfy an anti-commutation algebra

$$\{a_{s,c}(\mathbf{p}), a^\dagger_{s',c'}(\mathbf{k})\} = \{b_{s,c}(\mathbf{p}), b^\dagger_{s',c'}(\mathbf{k})\} = (2\pi)^3\delta_{ss'}\delta_{cc'}\delta(\mathbf{p}-\mathbf{k}), \tag{1.30}$$

with all other anti-commutators vanishing. As a consequence, the spinor ψ is an operator itself, satisfying an anti-commutation relation as well

$$\{\psi_\alpha(x), \bar{\psi}_\beta(y)\} = \gamma^0_{\alpha\beta}\delta(\mathbf{x}-\mathbf{y}), \tag{1.31}$$

evaluated at equal time $x_0 = y_0$.

The creation and annihilation operators act onto physical states, creating or annihilating a fermion. Letting an annihilation operator act onto the free vacuum state $|0\rangle$ leads to a zero contribution

$$a_s(\mathbf{p})\,|0\rangle = b_s(\mathbf{p})\,|0\rangle = 0, \qquad \langle 0|\,a^\dagger_s(\mathbf{p}) = \langle 0|\,b^\dagger_s(\mathbf{p}) = 0. \tag{1.32}$$

Physical observables are now given from calculating expectation values of operators, e.g. with respect to the vacuum state

$$\mathcal{O} = \langle 0|\,\hat{\mathcal{O}}\,|0\rangle\,. \tag{1.33}$$

In the free theory, these expectation values can easily be calculated by rewriting the operator $\hat{\mathcal{O}}$ in terms of creation and annihilation operators, with only specific combinations of creation

[2] We suppress the additional fundamental color index of the spinor fields in our notation.
[3] There can be found different normalizations of the basis spinors u/v in the literature, leading to different expressions for the Fourier decomposition of the spinor.

and annihilation operators contributing. It is therefore convenient to write the operator $\hat{\mathcal{O}}$ in a specific way, where all creation operators are written to the right and all annihilation operators are written to the left, referred to as *normal ordering*. Normal ordering is usually indicated by colons $:\hat{\mathcal{O}}:$ left and right of the operator.

The functions $u_s(\mathbf{p})$ and $v_s(\mathbf{p})$ are referred to as basis spinors and they are derived from the free Dirac equation in momentum space

$$\Big(\gamma^\mu p_\mu - m\Big)u_s(\mathbf{p}) = 0, \qquad \Big(\gamma^\mu p_\mu + m\Big)v_s(\mathbf{p}) = 0. \tag{1.34}$$

Their explicit solution is given as

$$u_s(\mathbf{p}) = N\begin{pmatrix}(\omega_\mathbf{p}+m)\varphi_s\\ \sigma^i p^i \varphi_s\end{pmatrix}, \qquad \varphi_0 = \begin{pmatrix}1\\0\end{pmatrix}, \quad \varphi_1 = \begin{pmatrix}0\\1\end{pmatrix}, \tag{1.35}$$

$$v_s(\mathbf{p}) = N\begin{pmatrix}\sigma^i p^i \chi_s\\ (\omega_\mathbf{p}+m)\chi_s\end{pmatrix}, \qquad \chi_0 = \begin{pmatrix}0\\1\end{pmatrix}, \quad \chi_1 = \begin{pmatrix}1\\0\end{pmatrix}, \tag{1.36}$$

with the Pauli matrices σ^i (eq. A.1) and a normalization $N = \frac{1}{\sqrt{2\omega_\mathbf{p}(\omega_\mathbf{p}+m)}}$, where $\omega_\mathbf{p} = \sqrt{\mathbf{p}^2+m^2}$ is the relativistic energy-momentum relation (free fermion dispersion relation).

The basis spinors fulfill a completeness relation

$$\sum_{s=1}^{2} u_{\alpha,s}(\mathbf{p})\bar{u}_{\beta,s}(\mathbf{p}) = \frac{1}{2\omega_\mathbf{p}}\Big(\gamma^\mu p_\mu + m\Big)_{\alpha\beta}, \tag{1.37}$$

$$\sum_{s=1}^{2} v_{\alpha,s}(\mathbf{p})\bar{v}_{\beta,s}(\mathbf{p}) = \frac{1}{2\omega_\mathbf{p}}\Big(\gamma^\mu p_\mu - m\Big)_{\alpha\beta}, \tag{1.38}$$

and they are ortho-normal

$$\bar{u}_r(\mathbf{p})u_s(\mathbf{p}) = \frac{m}{\omega_\mathbf{p}}\delta_{rs}, \qquad \bar{v}_r(\mathbf{p})v_s(\mathbf{p}) = -\frac{m}{\omega_\mathbf{p}}\delta_{rs}, \tag{1.39}$$

$$u_r^\dagger(\mathbf{p})u_s(\mathbf{p}) = \delta_{rs}, \qquad v_r^\dagger(\mathbf{p})v_s(\mathbf{p}) = -\delta_{rs}. \tag{1.40}$$

The evaluation of expectation values of creation and annihilation operators is modified when considering an ensemble of free fermions. Such an ensemble is describable in terms of statistical physics, where it is possible to associate a temperature T in equilibrium. In statistical quantum field theory [97] one derives the following relation for the expectation values of commutators of creation an annihilation operators, evaluated with respect to the statistical ensemble

$$\Big\langle\Big[\hat{a}_{s,c}(\mathbf{p}), a^\dagger_{s',c'}(\mathbf{k})\Big]\Big\rangle = (2\pi)^3\delta_{ss'}\delta_{cc'}\delta(\mathbf{p}-\mathbf{k})\Big(1-2n^s_+(\mathbf{p},T)\Big), \tag{1.41}$$

$$\Big\langle\Big[\hat{b}_{s,c}(\mathbf{p}), b^\dagger_{s',c'}(\mathbf{k})\Big]\Big\rangle = (2\pi)^3\delta_{ss'}\delta_{cc'}\delta(\mathbf{p}-\mathbf{k})\Big(1-2n^s_-(\mathbf{p},T)\Big), \tag{1.42}$$

where $n^s_\pm(\mathbf{p},T)$ denotes the occupation number. For a homogeneous distribution of temperature T, it is given by the Fermi-Dirac distribution

$$n_\pm(\mathbf{p},T) = \frac{1}{\exp\left(\frac{\omega_\mathbf{p}\pm\mu}{T}\right)+1}, \tag{1.43}$$

where μ denotes the chemical potential, that will be set to $\mu = 0$ in all considered cases.

1.2.1 The Statistical Fermion Propagator

An important quantity in statistical quantum field theory, that will be important in later calculations is the statistical fermion propagator, defined as

$$F_{\alpha\beta}(x,y) := \frac{1}{2}\Big\langle\Big[\psi_\alpha(x),\bar{\psi}_\beta(y)\Big]\Big\rangle. \tag{1.44}$$

With the propagator being defined as the expectation value of a commutator of spinor fields, it is connected to the occupation number, when taking the expectation value with respect to a statistical ensemble of fermions, as seen previously on the level of the creation and annihilation operators (eq. 1.41). Therefore it is referred to as statistical propagator. It is also possible to calculate the statistical propagator of free Dirac fermions, by evaluating the expectation value with respect to the vacuum state $|0\rangle$

$$F_{\alpha\beta}(x,y) = \frac{1}{2}\langle[\psi_\alpha(x),\bar{\psi}_\beta(y)]\rangle = \frac{1}{2}\int\sum_{s=1}^{2}\Big(u_\alpha^s(\mathbf{p})\bar{u}_\beta^s(\mathbf{p})e^{-\mathrm{i}p(x-y)} - v_\alpha^s(\mathbf{p})\bar{v}_\beta^s(\mathbf{p})e^{\mathrm{i}p(x-y)}\Big)\frac{d^3p}{(2\pi)^3}, \tag{1.45}$$

where we made use of (eq. 1.30) and (eq. 1.32). Performing the spin sums (eq. 1.37) we find

$$F_{\alpha\beta}(x,y) = \frac{1}{2}\int\frac{1}{2\omega_{\mathbf{p}}}\Big((\not{p}+m)_{\alpha\beta}e^{-\mathrm{i}p(x-y)} - (\not{p}-m)_{\alpha\beta}e^{\mathrm{i}p(x-y)}\Big)\frac{d^3p}{(2\pi)^3}. \tag{1.46}$$

At equal times $x_0 = y_0$ it is possible to simplify this result by exchanging $p \to -p$ in the second term, finally leading to

$$F_{\alpha\beta}^{ab}(x_0 = y_0,\mathbf{x},\mathbf{y}) = \delta^{ab}\int\frac{1}{2\omega_{\mathbf{p}}}\Big(p_i\gamma^i + m\Big)_{\alpha\beta}e^{\mathrm{i}\mathbf{p}(\mathbf{x}-\mathbf{y})}\frac{d^3p}{(2\pi)^3}. \tag{1.47}$$

1.2.2 Stochastic Low-Cost Fermions

Evaluating vacuum expectation values of fermion fields in a lattice simulation is a tedious exercise. Using numerical techniques as for example the mode function expansion method [98, 99, 100], often requires tremendous computational times, making it nearly impossible to access large lattices, because the number of numerical operations rises significantly with the number of lattice points. To reduce the computational cost, Borsanyi and Hindmarsh proposed an alternative method to calculate vacuum expectation values of fermion fields, replacing the vacuum expectation value by a stochastic ensemble average with respect to a finite ensemble N_{ens} of so called *gendered fermion fields* $\psi_G(x)$ [101]. In the following, this method will be presented in the continuum formulation.

To construct a suitable ensemble of stochastic fermion fields, a first step is to replace the creation and annihilation operators in the solution of the free Dirac equation (eq. 1.29) by complex numbers $\xi(\mathbf{p})$ and $\eta(\mathbf{p})$. These complex numbers have to be drawn from a Gaussian distribution in such a way, that taking the ensemble average recreates the familiar algebra of canonical quantization (eq. 1.30).
One can show, that this is only possible by introducing two kinds of fermion fields, called gendered fermion fields ψ_G. As a consequence, stochastic fermion fields can either be male ψ_M or female ψ_F

$$\psi_{M/F}(x) = \frac{1}{\sqrt{2}}\int\sum_{s=1}^{2}\Big(\xi_s(\mathbf{p})u_s(\mathbf{p})e^{-\mathrm{i}px} \pm \eta_s(\mathbf{p})v_s(\mathbf{p})e^{\mathrm{i}px}\Big)\frac{d^3p}{(2\pi)^3}. \tag{1.48}$$

The only difference between these two fermion fields is the sign in front of the second term and an additional factor of $\frac{1}{\sqrt{2}}$ has been introduced to obtain the correct normalization of the spinors, when taking the ensemble average.
To reproduce the algebra (eq. 1.30), the complex numbers $\xi(\mathbf{p})$ and $\eta(\mathbf{p})$ are sampled according to

$$\begin{aligned}\langle \xi_s(\mathbf{p})\xi_r^\star(\mathbf{k})\rangle_{N_{ens}} &= (2\pi)^3\delta_{sr}\delta(\mathbf{p}-\mathbf{k}) \\ \langle \eta_s(\mathbf{p})\eta_r^\star(\mathbf{k})\rangle_{N_{ens}} &= (2\pi)^3\delta_{sr}\delta(\mathbf{p}-\mathbf{k}).\end{aligned} \tag{1.49}$$

In case of a statistical ensemble of stochastic fermions of temperature T (eq. 1.49) is modified to

$$\begin{aligned}\langle \xi_s(\mathbf{p})\xi_r^\star(\mathbf{k})\rangle_{N_{ens}} &= (2\pi)^3\delta_{sr}\delta(\mathbf{p}-\mathbf{k})\Big((1-2n_F(\mathbf{p})\Big), \\ \langle \eta_s(\mathbf{p})\eta_r^\star(\mathbf{k})\rangle_{N_{ens}} &= (2\pi)^3\delta_{sr}\delta(\mathbf{p}-\mathbf{k})\Big((1-2n_F(\mathbf{p})\Big),\end{aligned} \tag{1.50}$$

with $n_F(\mathbf{p})$ the Fermi-Dirac distribution (eq. 1.43), where we assumed no spin polarisation and a vanishing chemical potential $\mu = 0$.

Having defined stochastic fermions, it is now possible to calculate the statistical propagator, making use of an ensemble average of these fermion fields

$$F_{\alpha\beta}(x,y) := \frac{1}{2}\left\langle[\psi_\alpha(x),\bar{\psi}_\beta(y)]\right\rangle = \langle\psi_\alpha^M(x)\bar{\psi}_\beta^F(y)\rangle_{N_{ens}} = \langle\psi_\alpha^F(x)\bar{\psi}_\beta^M(y)\rangle_{N_{ens}}. \tag{1.51}$$

Because physical observables should not depend on the ensemble size N_{ens} one has to choose an appropriate ensemble in a simulation.

The validity of (eq. 1.51) can be checked for free vacuum fermions, by explicitly inserting the Fourier representation of the stochastic spinors (eq. 1.48)

$$\begin{aligned}F_{\alpha\beta}(x,y) &= \left\langle\psi_\alpha^{M/F}(x)\bar{\psi}_\beta^{F/M}(y)\right\rangle_{N_{ens}} \\ &= \frac{1}{2}\int\int\sum_{s,r=1}^{2}\Big(\langle\xi_s(\mathbf{p})\xi_r^\star(\mathbf{k})\rangle_{N_{ens}}\,u_\alpha^s(\mathbf{p})\bar{u}_\beta^r(\mathbf{k})e^{-\mathrm{i}(px-ky)} \mp \langle\xi_s(\mathbf{p})\eta_r^\star(\mathbf{k})\rangle_{N_{ens}}\,u_\alpha^s(\mathbf{p})\bar{v}_\beta^r(\mathbf{k})e^{-\mathrm{i}(px+ky)} \\ &\quad \pm\Big\langle\eta_s(\mathbf{p})\xi_r^\star(\mathbf{k})\Big\rangle_{N_{ens}}v_\alpha^s(\mathbf{p})\bar{u}_\beta^r(\mathbf{k})e^{\mathrm{i}(px+ky)} - \langle\eta_s(\mathbf{p})\eta_r^\star(\mathbf{k})\rangle_{N_{ens}}\,v_\alpha^s(\mathbf{p})\bar{v}_\beta^r(\mathbf{k})e^{\mathrm{i}(px-ky)}\Big)\frac{d^3pd^3k}{(2\pi)^6} \\ &= \frac{1}{2}\int\sum_{s=1}^{2}\Big(u_\alpha^s(\mathbf{p})\bar{u}_\beta^s(\mathbf{p})e^{-\mathrm{i}p(x-y)} - v_\alpha^s(\mathbf{p})\bar{v}_\beta^s(\mathbf{p})e^{\mathrm{i}p(x-y)}\Big)\frac{d^3p}{(2\pi)^3},\end{aligned} \tag{1.52}$$

where we used (eq. 1.49), reproducing the familiar result (eq. 1.45).

In the simulation, the statistical propagator will be evaluated, by performing an additional gender average, because both combinations of genders should lead to the same result

$$F_{\alpha\beta}(x,y) = \frac{1}{2}\Big(\langle\psi_\alpha^M(x)\bar{\psi}_\beta^F(y)\rangle_{N_{ens}} + \langle\psi_\alpha^F(x)\bar{\psi}_\beta^M(y)\rangle_{N_{ens}}\Big). \tag{1.53}$$

2

Quantum Chromodynamics on the Lattice

In this chapter the quantum theory of strong interactions will be discretized and put on a lattice. In the majority of the literature, see e.g. [102, 103], this is done after performing a Wick rotation in time, leading to the euclidean formulation of QCD. This approach has been very successful to compute time independent observables as e.g. hadron masses, making use of Monte Carlo techniques to solve the euclidean path integrals. On the downside, it is no longer possible to derive time dependent observables within this approach, without a challenging analytical continuation to Minkowski time. Since we are particularly interested in time dependent observables, we keep real-time and do not consider an isotropic four dimensional lattice, but a three dimensional, spacial lattice. The lattice extent is notated as $N_x \times N_y \times N_z$, with isotropic lattice spacing a. Nevertheless, we will see later, that the solution of the equations of motion of the semi-classical approximation in a simulation, requires an additional discretization of time. We will discuss this discretization in detail in (chapter 7).

2.1 Lattice Yang-Mills Theory

Before turning to full QCD, let us start with pure Yang-Mills theory, neglecting the fermion sector of the QCD Lagrangian (eq. 1.2) for a second. When discretizing the theory, the continuum gauge fields A_μ are replaced by lattice gauge links U_μ, living on the edges of the lattice and *linking* the nearest neighbor lattice points. A visualization can be found in (figure 2.1). Their connection to the continuum fields is given as[1]

$$U_i(x) = e^{igaA_i(x)} = e^{igaA_i^a(x)T^a}. \tag{2.1}$$

A gauge link $U_i(x)$ connects the nearest neighbor lattice points x and $x + a\hat{i}$, but we will usually suppress the additional factor of the lattice spacing a, when writing a shift to the nearest neighbor lattice point in direction $\hat{i}$. Due to the linearity in a and g of the definition of U_i, it is convenient to introduce a dimensionless lattice field [102], by rescaling

$$\bar{A}_i(x) = agA_i(x). \tag{2.2}$$

[1] We will only discuss the spacial links in the following, because all temporal gauge links are set to $U_0 = 1$, due to the choice of temporal gauge $A_t = 0$.

In the following we will indicate dimensionless lattice objects by an additional bar over the quantity.

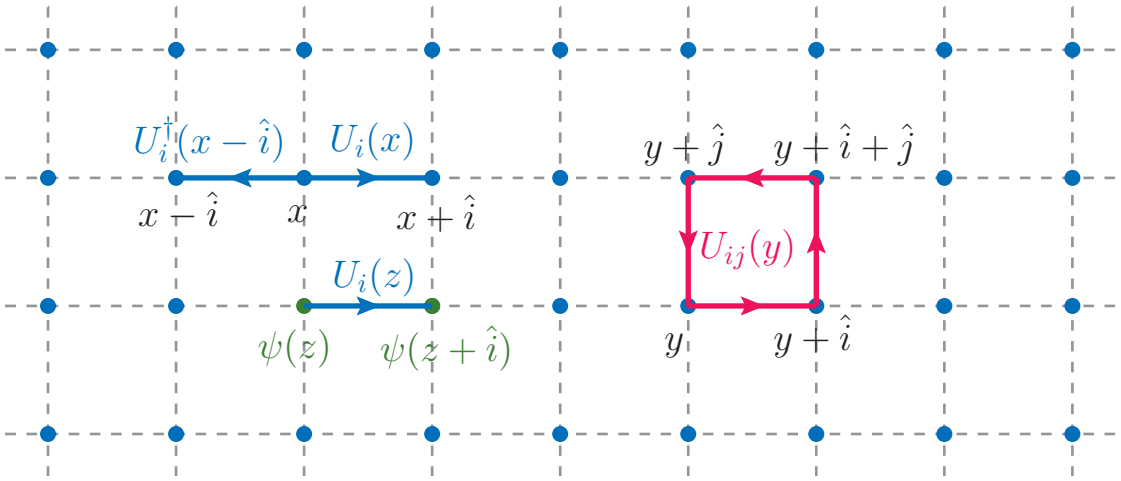

Figure 2.1: Visualization of the gauge links, the plaquette and the nearest neighbor interaction of fermion fields on the lattice.

The gauge links are an infinite series in the gauge fields A_μ, where higher order terms are suppressed by powers of the lattice spacing $\mathcal{O}(a)$

$$U_i(x) = 1 + \mathrm{i}gaA_i(x) + \mathcal{O}(a^2). \tag{2.3}$$

They transform in the following way under local gauge transformations $\Omega(x) \in SU(3)$

$$U_i(x) \quad \rightarrow \quad U_i'(x) = \Omega(x)U_i(x)\Omega^\dagger(x+\hat{i}). \tag{2.4}$$

For the discretization of a Yang-Mills theory, one requires a lattice Lagrangian that is invariant under local gauge transformations. Such a Lagrangian can be constructed from the lattice plaquette, which is given as a closed loop of four nearest neighbor gauge links (see figure 2.1)

$$U_{ij}(x) = U_i(x)U_j(x+\hat{i})U_i^\dagger(x+\hat{j})U_j^\dagger(x). \tag{2.5}$$

The conjugate lattice links are explicitly given as

$$U_j^\dagger(x) = U_{-j}(x+\hat{j}) = e^{-\mathrm{i}gaA_j(x)}. \tag{2.6}$$

It is immediately clear, by making use of (eq. 2.4), that the trace of the lattice plaquette (eq. 2.5) is a gauge invariant object.

The plaquette is connected to the field strength tensor of Yang-Mills theory

$$U_{ij}(x) = e^{\mathrm{i}a^2gF_{ij}(x)+\mathcal{O}(a^3)}. \tag{2.7}$$

Using this connection, one easily shows that

$$\begin{aligned} \mathrm{Retr}\Big[1 - U_{ij}(x)\Big] &= \mathrm{Retr}\Big[1 - \exp\Big(\mathrm{i}ga^2F_{ij}(x) + \mathcal{O}(a^3)\Big)\Big] \\ &= \frac{1}{2}g^2a^4\mathrm{tr}\Big[F_{ij}(x)F_{ij}(x)\Big] + \mathcal{O}(a^2). \end{aligned} \tag{2.8}$$

Using this result we can now rewrite the Lagrangian of Yang-Mills theory (eq. 1.19) on the lattice

$$\mathcal{L}_{YM} = \frac{1}{g^2 a^4}\mathrm{Retr}\Big[\bar{E}_i\bar{E}_i - 2\sum_{i<j}\Big(1 - U_{ij}\Big)\Big], \tag{2.9}$$

where we introduced the dimensionless lattice version of the chromo-electric field

$$\bar{E}_i(x) = ga^2 E_i(x). \tag{2.10}$$

The corresponding lattice Yang-Mills Hamiltonian is now obtained from a Legendre transformation

$$\mathcal{H}_{YM} = \frac{1}{g^2 a^4}\mathrm{Retr}\Big[\bar{E}_i\bar{E}_i + 2\sum_{i<j}\Big(1 - U_{ij}\Big)\Big]. \tag{2.11}$$

The dynamics of the classical Yang-Mills theory on the lattice is governed by the lattice Yang-Mills equation, hereby the equation of motion of the chromo-electric fields can be derived from a Hamilton equation

$$\partial_t E_i^a(x) = -\frac{\partial \mathcal{H}_{YM}}{\partial A_i^a(x)}. \tag{2.12}$$

Making use of the lattice Yang-Mills Hamiltonian (eq. 2.11) and carrying out the derivatives leads to

$$\partial_t E_i^a(x) = \frac{2}{ga^3}\sum_{j\neq i}\mathrm{Imtr}\Big[T^a\Big(U_{ji}(x) + U_{-ji}(x)\Big)\Big]. \tag{2.13}$$

A detailed derivation of this equation can be found in (Appendix A.4). It is possible to explicitly show, that the continuum result of the equation of motion for the chromo-electric field in pure Yang-Mills theory (eq. 1.22), is reproduced in the continuum limit $a \to 0$

$$\begin{aligned} ga^3\partial_t E_i^a(x) =& 2\sum_{j\neq i}\mathrm{Imtr}\Big[T^a\Big(U_{ji}(x) + U_{-ji}(x)\Big)\Big] \\ =& ga^3\sum_{j\neq i}\Big[\partial_j F_{ji}^a - g f^{abc} A_j^b(x) F_{ji}^c(x)\Big] + \mathcal{O}(a^4). \end{aligned} \tag{2.14}$$

This derivation is motivated in (Appendix A.5).

2.2 Colored Fermions on a Minkowski Lattice

Having discussed Yang-Mills theory, let us now turn to the discretization of the fermion sector of QCD. In the previous section, we introduced the gauge link $U_i(x)$ as a gauge transporter between the nearest neighbor lattice points, living on the edges of the lattice. On the opposite, fermions are located on the lattice sites (see figure 2.1) and their interaction is mediated by the gauge fields, entering via the covariant derivative (eq. 1.7). On the lattice this interaction is realized by combinations of gauge links, that connect the fermion fields along the lattice, as depicted in (figure 2.1). As a consequence, we require the gauge links $U_i(x)$ to enter the lattice version of the covariant derivative. The discretized covariant derivate on the lattice is given as

$$D_i\psi(x) = \frac{1}{2a}\Big[U_i(x)\psi(x+\hat{i}) - U_i^\dagger(x-\hat{i})\psi(x-\hat{i})\Big]. \tag{2.15}$$

When expanding in terms of $\mathcal{O}(a)$, one reproduces the continuum covariant derivative in the limit $a \to 0$

$$\begin{aligned} D_i\psi(x) &= \frac{1}{2a}\Big[e^{\mathrm{i}agA_i(x)}\psi(x+\hat{i}) - e^{-\mathrm{i}agA_i(x)}\psi(x-\hat{i})\Big] \\ &= \frac{\psi(x+\hat{i})-\psi(x-\hat{i})}{2a} + \mathrm{i}g\frac{1}{2}\Big(A_i(x)\psi(x+\hat{i}) + A_i(x-\hat{i})\psi(x-\hat{i})\Big) + \mathcal{O}(a) \\ &\overset{a\to 0}{=} \partial_i\psi(x) + \mathrm{i}gA_i(x)\psi(x) = D_i\psi(x). \end{aligned} \tag{2.16}$$

We can now write a first Ansatz for the lattice Lagrangian of the fermion sector of QCD

$$\mathcal{L}_f = \mathrm{i}\bar{\psi}(x)\gamma^0\partial_t\psi(x) + \frac{\mathrm{i}}{2a}\Big[\bar{\psi}(x)\gamma^i U_i(x)\psi(x+\hat{i}) - \bar{\psi}(x)\gamma^i U_i^\dagger(x-\hat{i})\psi(x-\hat{i})\Big] - m\bar{\psi}(x)\psi(x). \tag{2.17}$$

This Lagrangian can also be written in a different form, introducing the (naive) lattice Dirac operator

$$\begin{aligned} \mathcal{L}_f = \bar{\psi}(x)D(x,y)\psi(y) = \bar{\psi}(x)\Big[&\mathrm{i}\gamma^0\delta(x^0-y^0)\partial_{y^0}\delta_{\mathbf{xy}} - m\delta_{\mathbf{xy}}\delta(x^0-y^0) \\ &+ \frac{\mathrm{i}}{2a}\Big(\gamma^i U_i(x)\delta_{\mathbf{x}+\hat{i},\mathbf{y}} - \gamma^i U_\mu^\dagger(x-\hat{i})\delta_{\mathbf{x}-\hat{i},\mathbf{y}}\Big)\delta(x^0-y^0)\Big]\psi(y). \end{aligned} \tag{2.18}$$

2.2.1 Free Colored Fermions on the Lattice

As already stated in context of the continuum, free fermions on the lattice will provide the initial condition for the fermion sector of the semi-classical approximation in the static box. On the lattice, the theory of free fermions is again obtained by setting $A_i = 0$, which corresponds to setting $U_i(x) = 1$ in the lattice Lagrangian (eq. 2.17)

$$\mathcal{L}_f^{free} = \mathrm{i}\bar{\psi}(x)\gamma^0\partial_t\psi(x) + \frac{\mathrm{i}}{2a}\Big[\bar{\psi}(x)\gamma^i\psi(x+\hat{i}) - \bar{\psi}(x)\gamma^i\psi(x-\hat{i})\Big] - m\bar{\psi}(x)\psi(x). \tag{2.19}$$

The (naive) lattice Dirac operator of free fermions is then given as

$$\begin{aligned} &\bar{\psi}(x)\Big(\mathrm{i}\gamma^0\delta(x^0-y^0)\partial_{y^0}\delta_{\mathbf{xy}} + \sum_{i=1}^{3}\frac{\mathrm{i}}{2a}\gamma^i\Big(\delta_{\mathbf{x}+\hat{i},\mathbf{y}} - \delta_{\mathbf{x}-\hat{i},\mathbf{y}}\Big)\delta(x^0-y^0) - m\delta_{\mathbf{xy}}\delta(x^0-y^0)\Big)\psi(y) \\ &= \bar{\psi}(x)D(x,y)\psi(y). \end{aligned} \tag{2.20}$$

It is possible to derive the real-time lattice propagator of a free Dirac field from inverting the free Dirac operator. The inversion is best done in momentum space

$$\tilde{D}^{-1}(p) = -\frac{\gamma^0 p_0 + \sum\limits_{i=1}^{3}\frac{1}{a}\gamma^i\sin\left(p_i a\right) - m}{p_0^2 + \sum\limits_{i,j=1}^{3}\frac{1}{a^2}\eta^{ij}\sin(p_i a)\sin(p_j a) - m^2}. \tag{2.21}$$

A detailed derivation can be found in (Appendix A.6). When taking the continuum $a \to 0$ and the massless limit $m \to 0$, we reproduce the free fermion propagator in momentum space

$$\tilde{D}^{-1}(p)\Big|_{m=0} \overset{a\to 0}{=} -\frac{\gamma^\mu p_\mu}{p^\mu p_\mu} = -\frac{\gamma^\mu p_\mu}{p^2}. \tag{2.22}$$

The physical pole of the continuum propagator in the massless limit is given at $p^2 = m^2 = 0$. On the opposite, for the lattice Dirac propagator in the massless limit (eq. 2.21), it is possible to identify the physical pole at $p^2 = 0$ as well, but there are additional unphysical poles at the edges of the Brioullin zone, for the momenta $p_i \in \left(-\frac{\pi}{a_\mu}, \frac{\pi}{a_\mu}\right]$, e.g. $p^\mu = \left(0, \frac{\pi}{a}, 0, 0\right)$. Counting all possible combinations of such four-momenta, this leads to a total number of

$$\sum_{i=1}^{3} \binom{3}{i} = 7 \tag{2.23}$$

unphysical poles for a spacial lattice with continuous Minkowski time. These additional poles are referred to as unphysical doubler modes and their appearance is known as the problem of *fermion doubling*. We emphasize, that although we discussed the appearance of unphysical doubler modes for a massless free theory, the doubling problem is a general problem of the fermion sector in lattice QCD. A solution of the doubling problem has first been proposed by Kenneth Wilson [104]. The idea is to remove the fermion doublers by including an additional term to the Dirac operator, which has the following form in momentum space

$$\tilde{D}_W(p) = -\sum_{i=1}^{3} \frac{r}{a}\Big[1 - \cos\left(ap_i\right)\Big]. \tag{2.24}$$

The parameter r is known as Wilson parameter and usually takes the value 1. One easily checks, that the Wilson term is vanishing at the physical pole $p_\mu = 0$ and physics is not affected. For the doubler momenta of the form π/a_μ, the Wilson term contributes to the Dirac operator with an additional factor of $2/a$. This contribution can be interpreted as an additional mass term for the doubler modes, completely decoupling them from the theory when taking the continuum limit $a \to 0$.

The full Dirac operator in momentum space, including the Wilson term (eq. 2.24) is now given as

$$\tilde{D}(p) = -\gamma^0 p_0 - \sum_{i=1}^{3} \frac{1}{a}\gamma^i \sin\left(p_i a\right) - m - \sum_{i=1}^{3} \frac{r}{a}\Big[1 - \cos\left(ap_i\right)\Big]. \tag{2.25}$$

The lattice fermion propagator thus takes the following form

$$\tilde{D}^{-1}(p)\Big|_{m=0} = -\frac{\gamma^0 p_0 + \sum\limits_{i=1}^{3} \frac{1}{a}\gamma^i \sin\left(ap_i\right) + \left(m + \sum\limits_{i=1}^{3} \frac{r}{a}\Big[1 - \cos\left(ap_i\right)\Big]\right)}{p_0^2 + \sum\limits_{i,j=1}^{3} \frac{1}{a^2}\eta^{ij} \sin\left(ap_i\right)\sin\left(ap_j\right) - \left(m + \sum\limits_{i=1}^{3} \frac{r}{a}\Big[1 - \cos\left(ap_i\right)\Big]\right)^2}. \tag{2.26}$$

From (eq. 2.26) we observe, that the Wilson term modifies the lattice dispersion relation of the fermions

$$\begin{aligned} 0 &= p_0^2 + \sum_{i,j=1}^{3} \frac{1}{a^2}\eta^{ij} \sin\left(ap_i\right)\sin\left(ap_j\right) - \left(m + \sum_{i=1}^{3} \frac{r}{a}\Big[1 - \cos\left(ap_i\right)\Big]\right)^2 \\ \Rightarrow \omega_{\mathbf{p}}^2 &= \frac{1}{a^2}\sum_{i=1}^{3} \sin^2(p^i a) + \left(m + \sum_{i=1}^{3} \frac{r}{a}\Big[1 - \cos\left(ap_i\right)\Big]\right)^2. \end{aligned} \tag{2.27}$$

This modification is essential for the dynamics of the fermion fields, also if the continuum limit has not been taken. As depicted in (figure 2.2), the naive lattice dispersion relation of

the fermion fields drops to zero at the edges of the Brioullin zone, which is contradicting the behavior of the continuum dispersion relation. The additional Wilson term „cures“ the false dynamics of the naive dispersion relation, although there is still a systematic error present when compared to the continuum dispersion relation. This systematic error can only be eliminated from systematically taking the continuum limit.

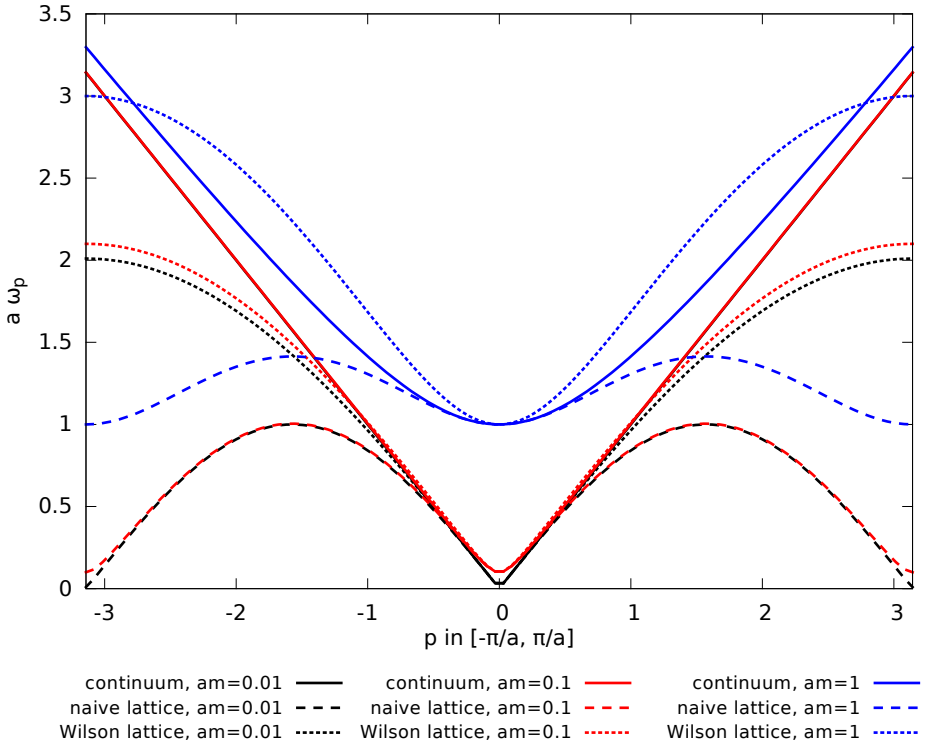

Figure 2.2: Comparison of the continuum, naive lattice and Wilson lattice dispersion relation for free fermions. All quantities have been rescaled in terms of the lattice spacing a and the momentum is fixed to the first Brioullin zone.

With the Wilson term contributing as a mass term for the unphysical doubler modes, the lightest doubler modes, which are associated to momenta of the form $p^\mu = (0, \pi/2, 0, 0)$, have a mass of $2/a$ (when setting $r = 1$). As a consequence, one has to assure, that there is a clear separation of mass scales between the physical mass m and the masses of the doubler modes. With a continuum limit not being possible in the semi-classical approximation, we are limited to a certain resolution in a. Measuring the fermion mass in orders of the lattice spacing $\bar{m} = am$, requires our choice of $\bar{m}$ to be at least one order of magnitude smaller than the mass of the lightest doubler modes, motivating the following upper limit for $\bar{m}$

$$\frac{\bar{m}_{max}}{a} = \frac{0.1}{a} < \frac{2}{a}. \tag{2.28}$$

When choosing a larger value for the fermion mass in lattice units, the dispersion relation is strongly affected, leading to an unphysical dynamics of the heavy fermion, as depicted in (figure 2.2) for a fermion mass of the order of the lattice spacing $m = \frac{1}{a}$. In position space, the Wilson term added to the Dirac operator takes the following form

$$D_W(x, y) = \sum_{i=1}^{3} \frac{r}{2a} \Big[\delta_{x+\hat{i},y} - 2\delta_{x,y} + \delta_{x-\hat{i},y} \Big]. \tag{2.29}$$

Letting it act on a spinor, it is possible to show that it can be written as a combination of a lattice forward and backward derivative

$$\begin{aligned}\sum_y D_W(x,y)\psi(y) &= \sum_{i=1}^{3}\frac{r}{2a}\Big[\psi(x+\hat{i})-2\psi(x)+\psi(x-\hat{i})\Big] \\ &= \sum_{i=1}^{3}\frac{ra}{2}\Delta_i^b\Delta_i^f\psi(x) := \frac{ra}{2}\Box_W^{free}\psi(x),\end{aligned} \tag{2.30}$$

where the lattice forward and backward derivative are defined as

$$\Delta_i^f\psi(x)=\frac{1}{a}\Big(\psi(x+\hat{i})-\psi(x)\Big), \qquad \Delta_i^b\psi(x)=\frac{1}{a}\Big(\psi(x)-\psi(x-\hat{i})\Big). \tag{2.31}$$

The full free Dirac operator in position space, including the Wilson term, now takes the following form

$$\begin{aligned}D(x,y) =& \mathrm{i}\gamma^0\delta(x^0-y^0)\partial_{y^0}\delta_{\mathbf{xy}} - \left(m+\sum_{i=1}^{3}\frac{r}{a}\right)\delta(x^0-y^0)\delta_{\mathbf{xy}} \\ &+\sum_{i=1}^{3}\frac{\mathrm{i}}{2a}\Big(\big(\gamma^i-\mathrm{i}r\big)\delta_{\mathbf{x}+\hat{i},\mathbf{y}}-\big(\gamma^i+\mathrm{i}r\big)\delta_{\mathbf{x}-\hat{i},\mathbf{y}}\Big)\delta(x^0-y^0).\end{aligned} \tag{2.32}$$

Having discussed the phenomenon of fermion doubling we are now able to formulate the physical version of the free Dirac Lagrangian on the lattice

$$\begin{aligned}\mathcal{L}_f^{free} =& \mathrm{i}\bar{\psi}(x)\gamma^0\partial_t\psi(x) - \left(m+\sum_{i=1}^{3}\frac{r}{a}\right)\bar{\psi}(x)\psi(x) \\ &+\frac{\mathrm{i}}{2a}\sum_{i=1}^{3}\Big[\bar{\psi}(x)\big(\gamma^i-\mathrm{i}r\big)\psi(x+\hat{i})-\bar{\psi}(x)\big(\gamma^i+\mathrm{i}r\big)\psi(x-\hat{i})\Big].\end{aligned} \tag{2.33}$$

From the Lagrangian, we can easily obtain the equation of motion of the fermion fields, namely the free Dirac equation on the lattice, making use of the Euler-Lagrange equation

$$\mathrm{i}\gamma^0\partial_t+\sum_{\mu=1}^{3}\frac{\mathrm{i}}{2a}\Big(\big(\gamma^i-\mathrm{i}r\big)\psi(x+\hat{i})-\big(\gamma^i+\mathrm{i}r\big)\psi(x-\hat{i})\Big)-\left(m+\frac{3r}{a}\right)\psi(x)=0. \tag{2.34}$$

From a Legendre transformation of (eq. 2.33), we find the lattice Hamiltonian of free Dirac fermions

$$\mathcal{H}_f=-\bar{\psi}(x)\left[\frac{\mathrm{i}}{2a}\sum_{i=1}^{3}\Big(\big(\gamma^i-\mathrm{i}r\big)\psi(x+\hat{i})-\big(\gamma^i+\mathrm{i}r\big)\psi(x-\hat{i})\Big)-\left(m-\frac{3r}{a}\right)\psi(x)\right]. \tag{2.35}$$

To initialize the fermion fields as free Dirac fermions in later simulations, we have to solve the free Dirac equation (eq. 2.34) on the lattice. In analogy to the continuum, we make the following ansatz

$$\psi_{\mathbf{p},s}(x)=u_s(\mathbf{p})e^{-\frac{\mathrm{i}}{a}s_0t+\mathrm{i}\mathbf{px}}. \tag{2.36}$$

Inserting this ansatz into (eq. 2.34), we find

$$\begin{aligned}0 =& \left[\gamma^0\frac{1}{a}s_0+\frac{\mathrm{i}}{2a}\gamma^i\underbrace{\left(e^{\mathrm{i}p^ia}-e^{-\mathrm{i}p^ia}\right)}_{=2\mathrm{i}\sin(p^ia)}-\frac{1}{a}\bar{m}-\frac{r}{2a}\sum_i\Big(2\underbrace{-e^{\mathrm{i}p^ia}-e^{-\mathrm{i}p^ia}}_{=-2\cos(p^ia)}\Big)\right]u_s(\mathbf{p})e^{-\frac{\mathrm{i}}{a}s_0t+\mathrm{i}\mathbf{px}} \\ =& \frac{1}{a}\left[\gamma^0s^0-\gamma^is^i-\mu\right]u_s(\mathbf{p})e^{-\frac{\mathrm{i}}{a}s_0t+\mathrm{i}\mathbf{px}}.\end{aligned} \tag{2.37}$$

We defined the (dimensionless) lattice momenta and the reduced lattice mass μ

$$s_i = \sin(p_i a), \qquad \mu = \bar{m} + r\sum_i \Big(1 - \cos(p_i a)\Big). \tag{2.38}$$

The equation is solved, for the lattice dispersion relation taking the following form

$$s_0^2 = \sum_{i=1}^{3} \sin^2(p^i a) + \left(\bar{m} + r\sum_{i=1}^{3}\Big[1 - \cos(ap^i)\Big]\right)^2, \tag{2.39}$$

which is the familiar dispersion relation of free Wilson fermions (eq. 2.27). It is now straight forward to solve the free Dirac equation on the lattice, leading to the following momentum space equations for the basis spinors

$$\Big(\gamma^\mu s_\mu - \mu\Big)u_s(\mathbf{p}) = 0, \qquad \Big(\gamma^\mu s_\mu + \mu\Big)v_s(\mathbf{p}) = 0. \tag{2.40}$$

The lattice solution of these equations is given as

$$u_s(\mathbf{p}) = \frac{1}{\sqrt{2s_0(s_0+\mu)}}\begin{pmatrix}\Big(s_0(\mathbf{p}) + \mu(\mathbf{p})\Big)\varphi_s \\ \sigma\cdot\mathbf{s}(\mathbf{p})\varphi_s\end{pmatrix}, \qquad \varphi_0 = \begin{pmatrix}1\\0\end{pmatrix}, \quad \varphi_1 = \begin{pmatrix}0\\1\end{pmatrix}, \tag{2.41}$$

$$v_s(\mathbf{p}) = \frac{1}{\sqrt{2s_0(s_0+\mu)}}\begin{pmatrix}\sigma\cdot\mathbf{s}(\mathbf{p})\chi_s \\ \Big(s_0(\mathbf{p}) + \mu(\mathbf{p})\Big)\chi_s\end{pmatrix}, \qquad \chi_0 = \begin{pmatrix}0\\1\end{pmatrix}, \quad \chi_1 = \begin{pmatrix}1\\0\end{pmatrix}. \tag{2.42}$$

The basis spinors on the lattice satisfy an ortho-normality relation

$$\begin{aligned} &\bar{u}_r(\mathbf{p})u_s(\mathbf{p}) = \frac{\mu}{s_0}\delta_{rs}, \qquad \bar{v}_r(\mathbf{p})v_s(\mathbf{p}) = -\frac{\mu}{s_0}\delta_{rs}, \\ &u_r^\dagger(\mathbf{p})u_s(\mathbf{p}) = \delta_{rs}, \qquad v_r^\dagger(\mathbf{p})v_s(\mathbf{p}) = \delta_{rs}. \end{aligned} \tag{2.43}$$

It is also possible to calculate the following spin sums

$$\sum_{s=1}^{2} u_\alpha^s(\mathbf{p})\bar{u}_\beta^s(\mathbf{p}) = \frac{1}{2s_0}(\gamma^\mu s_\mu + \mu)_{\alpha\beta}, \qquad \sum_{s=1}^{2} v_\alpha^s(\mathbf{p})\bar{v}_\beta^s(\mathbf{p}) = \frac{1}{2s_0}(\gamma^\mu s_\mu - \mu)_{\alpha\beta}. \tag{2.44}$$

The solution of the free Dirac spinor on the lattice now takes the following Fourier representation

$$\psi(x) = \frac{1}{V}\sum_{\mathbf{p}}\sum_{s=1}^{2}\sum_{c=1}^{3}\Big(a_{s,c}(\mathbf{p})u_s(\mathbf{p})\xi_c e^{-\mathrm{i}px} + b_{s,c}^\dagger(\mathbf{p})v_s(\mathbf{p})\xi_c e^{\mathrm{i}px}\Big), \tag{2.45}$$

where V is the spacial lattice volume. The operators $a_{s,c}(\mathbf{p})$ and $b_{s,c}(\mathbf{p})$ are the lattice counterparts of the creation and annihilation operators, satisfying the similar anti-commuting algebra as in the continuum, with Dirac deltas replaced by Kronecker deltas

$$\{a_{s,c}(\mathbf{p}), a_{s',c'}^\dagger(\mathbf{k})\} = \{b_{s,c}(\mathbf{p}), b_{s',c'}^\dagger(\mathbf{k})\} = V\delta_{ss'}\delta_{cc'}\delta_{\mathbf{p},\mathbf{k}}. \tag{2.46}$$

2.2.2 Stochastic Fermions on the Lattice

We discussed the low-cost stochastic fermion approach in (section 1.2.2), as a cost efficient way to calculate the statistical fermion propagator in a simulation. We now present, how this method can be used in a lattice regularized theory, presenting the lattice counterparts of the

continuum equations.

Replacing the creation and annihilation operators of the lattice spinor solution (eq. 2.45) by complex numbers, introducing two different fermion genders (eq. 1.48) and specifying the initial time $t_0 = 0$ leads to

$$\psi_{M/F}(t_0, \mathbf{x}) = \frac{1}{\sqrt{2}V} \sum_{\mathbf{n}} \sum_{s=1}^{2} \Big(\xi_s(\mathbf{p}) u_s(\mathbf{p}) e^{\mathrm{i}\frac{2\pi}{Na}\mathbf{nx}} \pm \eta_s(\mathbf{p}) v_s(\mathbf{p}) e^{-\mathrm{i}\frac{2\pi}{Na}\mathbf{nx}} \Big). \tag{2.47}$$

For vacuum initial conditions, the sampling of the complex numbers on the lattice is given by replacing the Dirac delta functions in (eq. 1.49) with discrete Kronecker deltas

$$\langle \xi_{s,a}(\mathbf{p}) \xi^{\star}_{r,b}(\mathbf{q}) \rangle_{N_{ens}} = V \delta_{\mathbf{pq}} \delta_{sr} \delta_{ab}, \qquad \langle \eta_{s,a}(\mathbf{p}) \eta^{\star}_{r,b}(\mathbf{q}) \rangle_{N_{ens}} = V \delta_{\mathbf{pq}} \delta_{sr} \delta_{ab}. \tag{2.48}$$

The same is true for the sampling of complex numbers in case of an ensemble of unpolarized thermal fermions of temperature T, with vanishing chemical potential $\mu = 0$

$$\begin{aligned} \langle \xi_{s,a}(\mathbf{p}) \xi^{\star}_{r,b}(\mathbf{q}) \rangle_{N_{ens}} &= V \delta_{\mathbf{pq}} \delta_{sr} \delta_{ab} \Big(1 - 2 n_{FD}(\mathbf{p}, T) \Big), \\ \langle \eta_{s,a}(\mathbf{p}) \eta^{\star}_{r,b}(\mathbf{q}) \rangle_{N_{ens}} &= V \delta_{\mathbf{pq}} \delta_{sr} \delta_{ab} \Big(1 - 2 n_{FD}(\mathbf{p}, T) \Big). \end{aligned} \tag{2.49}$$

In a simulation, the sampling of the complex numbers is realized in the following way:
The complex numbers are represented as (Euler-Moivre representation)

$$\xi_{s,a}(\mathbf{n}) = A_{s,a}(\mathbf{n}) e^{\mathrm{i}\phi_{s,a}(\mathbf{n})}, \qquad \xi_{s,a}(\mathbf{n}) = B_{s,a}(\mathbf{n}) e^{\mathrm{i}\theta_{s,a}(\mathbf{n})}. \tag{2.50}$$

The momentum independent amplitudes $A_{s,a}$ and $B_{s,a}$ are drawn from a Gaussian distribution with mean $\mu_G = 0$ and squared width $\sigma^2 = V$ (or $\sigma^2 = V(1 - 2n_{FD}(\mathbf{p}, T))$ in case of thermal fermions). The phases $\phi_{s,a}$ and $\theta_{s,a}$ are uniformly distributed in the interval $[0, 2\pi]$, making use of random numbers.

The lattice result of the equal time statistical propagator can now be determined by an ensemble average of stochastic low-cost fermions on the lattice, as seen in (eq. 1.47)

$$\begin{aligned} F_{\alpha\beta}(x, y) =& \langle \psi^{M/F}_{\alpha}(x) \bar{\psi}^{F/M}_{\beta}(y) \rangle_{N_{ens}} \\ =& \frac{1}{2V} \sum_{\mathbf{n}} \sum_{s=1}^{2} \Big(u^{s}_{\alpha}(\mathbf{p}) \bar{u}^{s}_{\beta}(\mathbf{p}) e^{\mathrm{i}\frac{2\pi}{Na}\mathbf{n}(\mathbf{x}-\mathbf{y})} - v^{s}_{\alpha}(\mathbf{p}) \bar{v}^{s}_{\beta}(\mathbf{p}) e^{-\mathrm{i}\frac{2\pi}{Na}\mathbf{n}(\mathbf{x}-\mathbf{y})} \Big). \end{aligned} \tag{2.51}$$

Inserting the spin sums (eq. 2.44) then leads to

$$\begin{aligned} F_{\alpha\beta}(x, y) &= \frac{1}{2V} \sum_{\mathbf{n}} \frac{1}{2s_0} \Big((\gamma^{\mu} s_{\mu} + \mu)_{\alpha\beta} e^{\mathrm{i}\frac{2\pi}{Na}\mathbf{n}(\mathbf{x}-\mathbf{y})} - (\gamma^{\mu} s_{\mu} - \mu)_{\alpha\beta} e^{-\mathrm{i}\frac{2\pi}{Na}\mathbf{n}(\mathbf{x}-\mathbf{y})} \Big) \\ &= \frac{1}{2V} \sum_{\mathbf{n}} \frac{1}{s_0} (\gamma^{i} s_i + \mu)_{\alpha\beta} e^{\mathrm{i}\frac{2\pi}{Na}\mathbf{n}(\mathbf{x}-\mathbf{y})}. \end{aligned} \tag{2.52}$$

2.3 Full Quantum Chromodynamics on the Lattice

Having discussed free lattice fermions and the doubling problem, let us return to full lattice QCD. As in case of the free theory, it is mandatory to add an additional Wilson term to the QCD Lagrangian to remove the unphysical doubler modes

$$W(x) = \frac{a}{2} \bar{\psi}(x) \Box_W \psi(x) = \frac{1}{2a} \sum_{i=1}^{3} \bar{\psi}(x) \Big[U_i(x) \psi(x + \hat{i}) - 2\psi(x) + U^{\dagger}_i(x - \hat{i}) \psi(x - \hat{i}) \Big]. \tag{2.53}$$

The lattice Lagrangian of the fermion sector of QCD is thus given as

$$\begin{aligned}\mathcal{L}_f =&\bar{\psi}(x)\mathrm{i}\gamma^0\partial_t\psi(x) - \left(m+\frac{3r}{a}\right)\bar{\psi}(x)\psi(x) \\ &+\frac{\mathrm{i}}{2a}\sum_{i=1}^{3}\Big[\bar{\psi}(x)\Big(\gamma^i-\mathrm{i}r\Big)U_i(x)\psi(x+\hat{i}) - \bar{\psi}(x)\Big(\gamma^i+\mathrm{i}r\Big)U_i^\dagger(x-\hat{i})\psi(x-\hat{i})\Big].\end{aligned} \tag{2.54}$$

The corresponding lattice Dirac equation, coupled to the Yang-Mills fields, can be found by making use of the Euler-Lagrange equation

$$\begin{aligned}0 =&\mathrm{i}\gamma^0\partial_t\psi(x) - \left(m+\frac{3r}{a}\right)\psi(x) \\ &+\frac{\mathrm{i}}{2a}\sum_{i=1}^{3}\Big[\Big(\gamma^i-\mathrm{i}r\Big)U_i(x)\psi(x+\hat{i}) - \Big(\gamma^i+\mathrm{i}r\Big)U_i^\dagger(x-\hat{i})\psi(x-\hat{i})\Big].\end{aligned} \tag{2.55}$$

The lattice Hamiltonian of the fermion sector is obtained from a Legendre transformation of (eq. 2.54)

$$\begin{aligned}\mathcal{H}_f = -\bar{\psi}(x)\Bigg[&\frac{\mathrm{i}}{2a}\sum_{i=1}^{3}\Big(\Big(\gamma^i-\mathrm{i}r\Big)U_i(x)\psi(x+\hat{i}) - \Big(\gamma^i+\mathrm{i}r\Big)U_i^\dagger(x-\hat{i})\psi(x-\hat{i})\Big) \\ &-\left(m+\frac{3r}{a}\right)\psi(x)\Bigg].\end{aligned} \tag{2.56}$$

We now have everything at hand to formulate QCD on a three dimensional lattice with real, continuous time. This result represents the starting point for the derivation of the semi-classical approximation, that will be presented in (chapter 4). The Lagrangian is given as the sum of the lattice Yang-Mills Lagrangian (eq. 2.9) and the lattice Lagrangian of the fermion sector (eq. 2.54)

$$\begin{aligned}\mathcal{L}_{QCD} =&\frac{1}{g^2a^4}\mathrm{Retr}\left[\bar{E}_i\bar{E}_i - 2\sum_{i<j}\Big(1-U_{ij}\Big)\right] + \mathrm{i}\bar{\psi}(x)\gamma^0\partial_t\psi(x) - \left(m+\frac{3r}{a}\right)\bar{\psi}(x)\psi(x) \\ &+\frac{\mathrm{i}}{2a}\sum_{i=1}^{3}\Big[\bar{\psi}(x)\Big(\gamma^i-\mathrm{i}r\Big)U_i(x)\psi(x+\hat{i}) - \bar{\psi}(x)\Big(\gamma^i+\mathrm{i}r\Big)U_i^\dagger(x-\hat{i})\psi(x-\hat{i})\Big].\end{aligned} \tag{2.57}$$

The corresponding Hamiltonian of lattice QCD is obtained from a Legendre transformation

$$\begin{aligned}\mathcal{H}_{QCD} =&\frac{1}{g^2a^4}\mathrm{Retr}\left[\bar{E}_i\bar{E}_i + 2\sum_{i<j}\Big(1-U_{ij}\Big)\right] + \left(m+\frac{3r}{a}\right)\bar{\psi}(x)\psi(x) \\ &-\frac{\mathrm{i}}{2a}\sum_{i=1}^{4}\Big[\bar{\psi}(x)\Big(\gamma^i-\mathrm{i}r\Big)U_i(x)\psi(x+\hat{i}) - \bar{\psi}(x)\Big(\gamma^i+\mathrm{i}r\Big)U_i^\dagger(x-\hat{i})\psi(x-\hat{i})\Big].\end{aligned} \tag{2.58}$$

Introducing the following rescaling of the fermion fields in terms of the lattice spacing a

$$\tilde{\psi}(x) = a^{\frac{3}{2}}\psi(x), \tag{2.59}$$

allows us to define a dimensionless version of the lattice QCD Lagrangian (eq. 2.57) and the lattice QCD Hamiltonian (eq. 2.58)

$$\bar{\mathcal{L}}_{QCD} = a^4g^2\mathcal{L}_{QCD}, \qquad \bar{\mathcal{H}}_{QCD} = a^4g^2\mathcal{H}_{QCD}. \tag{2.60}$$

3

Initial Conditions for the Yang-Mills Sector of QCD

In this chapter we give a brief overview on the early time physics in a highly energetic heavy ion collision. It marks the foundation for the derivation of the semi-classical approximation, allowing us to treat the Yang-Mills sector of QCD effectively classical. We will start the discussion with a general review of the phenomenology and the important physical concepts in a heavy ion collision. This will lead us to the phenomenon of gluon saturation at the early stage of the collision, that enters the definition of an effective model, allowing a description of the dynamics of the system in terms of classical Yang-Mills fields. We will present the genesis and applicability of this effective theory, referred to as Color-Glass-Condensate (CGC) and in a next step, we will discuss the general properties of the specific initial state, known as the Glasma. The Glasma represents the initial condition for the Yang-Mills sector in the semi-classical approximation and we will present how to initialize it on a three dimensional lattice with real-time. Finally, we discuss how to introduce a physical scale in our lattice system, specifying the lattice spacing a of the classical approximation.

3.1 Phenomenology of a Heavy Ion Collision

The popularity of heavy ion collisions is rooted in the nature of the strong interaction and its underlying quantum field theory, Quantum Chromodynamics (QCD). The phenomenon of confinement causes all constituents of QCD that carry color charge, namely the quarks and gluons, to appear only in bound, color-neutral states. The strength of interaction of quarks and gluons is mediated by the coupling g, that turns out not to be a constant, but a quantity depending on the energy scale of the system. It has been shown in [105, 106], that g decreases for increasing energy, leading to an asymptotically free theory at infinitely large energy. This can also be viewed in terms of distances: packing more and more hadrons into a small volume lowers the average inter-quark distance, hence their interaction is reduced more and more. As a consequence, the system becomes weakly coupled and eventually surpasses a phase transition where the bound states are traded with a system of free quarks and gluons. Such a system of

(quasi-)free quarks and gluons is called a Quark-Gluon-Plasma (QGP) and the underlying phase transition hence is a function of energy and density.

An intuitive choice for a system that could naturally create a highly energetic and dense medium is given from colliding two heavy nuclei at very high velocities. In fact, as prominently argued by Bjorken [12], such collisions create a hot and dense medium, that is very well describable in terms of hydrodynamics, where the system behaves like a fluid of quarks and gluons [9]. Observations in early experiments at the super proton synchrotron (SPS), later at the relativistic heavy ion collider (RHIC) and finally at the large hadron collider (LHC) supported the idea that indeed a QGP is created in a heavy ion collision. For a review on the history of the QGP see [107]. The phenomenology of a heavy ion collision, that is assumed to last for a duration of $\sim$ 10 fm is schematically shown in (figure 3.1).

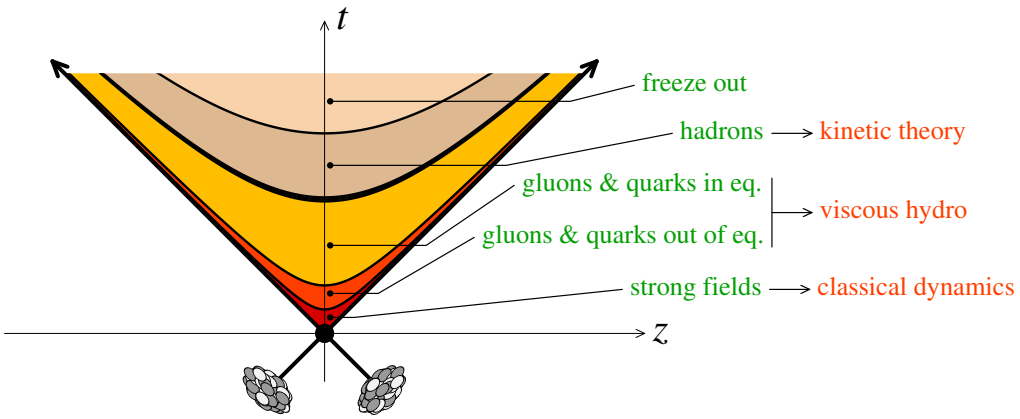

Figure 3.1: Illustration of the various stages in a heavy ion collision. Figure taken from [108].

The two incoming nuclei travel nearly at the speed of light and are taken to reside on the lightcone. Right after the collision, the system is out-of-equilibrium and dominated by overoccupied Yang-Mills fields. This marks the state of interest in our work and will be discussed further in this chapter. It is expected that the system becomes eligible for a description in terms of hydrodynamics after a hydrodynamization time of $\tau_{hydro} \sim 1$ fm [38]. Due to the rapid longitudinal expansion, the energy density of the plasma drops during the evolution and as a consequence, at some point a confinement transition happens and hadrons are formed again. This process has been described successfully in terms of kinetic transport models as provided for example by UrQMD [109] or SMASH [110]. Finally, the freeze out happens and all particles are confined again, causing the system to break down.

For a better understanding of the physics of the initial state, right after collision, it is first of all convenient to revisit the structure of a nucleus, or more simple a hadron. A hadron, as e.g. a proton, is not only constructed from its three valence quarks, but in fact the largest amount of its mass is contributed to binding energy, represented by the gluons and virtual quark-antiquark pairs (sea-quarks). For collisions of hadrons at low energies, the timescale of the internal dynamics of a hadron, as e.g. gluon exchange and the formation of sea quark pairs, is expected to be of the order of the timescale of the collision, making it impossible to study the hadron dynamics within perturbative QCD. The situation changes, when moving to large energies: the internal dynamics becomes affected by Lorentz time dilation and hence the timescale for gluon exchange and the lifetime of virtual sea-quark states is much longer, when

compared to the duration of the collision. As a consequence, all constituents of a hadron can be viewed as quasi-free during a high energetic collision. This concept manifests itself in the *parton model* [111], which approximates a high energetic hadron as a collection of quasi free constituents, called partons.

In a highly energetic system, a parton with large momentum can radiate softer partons in quantum processes, making a classification in terms of momentum necessary. It is convenient to introduce the Bjorken-x as the fraction of the longitudinal momentum carried by the parton over the exchanged momentum Q. In deep inelastic scattering experiments (DIS) the parton model has been exploited to probe the internal structure of a proton. We give the results from [68] for the single parton distribution functions of the gluons xg, the sea-quarks xS and the valence quarks xu_v and xd_v from DIS of a proton in (figure 3.2), at fixed momentum transfer of $Q^2 = 10$ GeV^2.

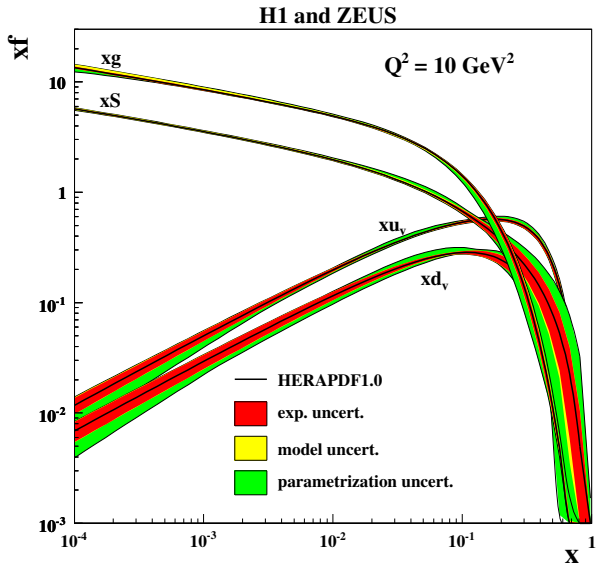

Figure 3.2: Parton distribution functions for a proton from DIS at $Q^2 = 10$ GeV^2. The single parton distribution functions of the gluons xg, the sea-quarks xS and the valence quarks xu_v and xd_v are plotted as a function of Bjorken-x. The plot is taken from [68].

For small x one finds, that the gluon content dominates the system, whereas the sea-quarks are suppressed by a factor of $\alpha_s = \frac{g^2}{4\pi}$. In the early phase of a heavy ion collision, processes involving even softer momenta of the order of $Q^2 \sim 2 - 3$ GeV^2 are of interest and the relevant Bjorken-x is assumed to be of order $x \sim 10^{-3}$ for LHC center-of-mass energies [112]. These observations lead to the assumption that the early stage of a heavy ion collision can be described within small-x physics and is dominated by the gluons.

3.2 Gluon Saturation and the MV-Model

Having discussed the dominance of gluons in the initial state of a heavy ion collision, the subsequent next step is, to define an appropriate effective theory for this specific regime. One of the first and most prominent models has been proposed by L.D. McLerran and R. Venugopalan in 1994 [18, 19, 20], which became popular as the *MV-model*. This model exploits the fact, that

at sufficiently small x, the gluon density tends to saturate at a specific transverse momentum scale Q_s, referred to as saturation scale. In the following we give a brief overview of the concept of *gluon saturation* and its consequences for the definition of an effective field theory.

The reason for the phenomenon of gluon saturation to appear, is a balancing of gluon emission and recombination $gg \to g$ at a specific transverse momentum scale. As discussed in the previous section, if the hadron or nucleus is boosted to high velocities, it can be described within the parton model. The highly energetic parton constituents of the hadron hence emit more and more gluons by bremsstrahlung. These gluons themselves can emit softer gluons, leading to a gluon cascade, formally known as $BFKL$-ladder. The dynamics follows the $BFKL$-equation for the gluon distribution $xG(x, Q^2)$, first studied by Balitsky, Lipatov, Kuraev and Fadin [113, 114]. Whereas the $BFKL$-construction assumes a dilute system and no interference terms between emitters are taken into account, in reality the emission of soft gluons inside the hadron increases the gluon density rapidly, making a density dependent description necessary. For sufficiently high gluon densities, destructive interference of gluons happens, due to the overlap of their wavefunctions, causing gluons from different cascades to recombine. This happens as soon as the product of the number of gluons per unit area with the cross-section of gluon recombination becomes larger than one,

$$\underbrace{\alpha_s Q^{-2}}_{gg\to g \text{ cross-section}} \times \underbrace{A^{-2/3} x G(x, Q^2)}_{\text{gluon surface density from atomic number and gluon distribution}} \geq 1. \tag{3.1}$$

As a consequence, as soon as the terms for gluon emission and recombination become parametrically of the same order, the system saturates. This happens at a specific transverse momentum scale Q_s that can be extracted from (eq. 3.1) as

$$Q^2 \leq Q_s^2 = \frac{\alpha_s x G(x, Q_s^2)}{A^{2/3}} \sim A^{1/3} x^{-0.3} \tag{3.2}$$

Saturation therefore becomes important, as soon as the typical momentum scale of the system is below the saturation scale Q_s. For nuclei at energies of the LHC, Q_s is expected to be of the order $Q_s^2 \approx 2 - 4$ GeV^2 and in fact the bulk of particle production in heavy ion collisions is controlled by saturation physics. The saturation domain is now characterized by two important features: On one hand it is dominated by non-linear gluon interactions, making advanced computational methods beyond perturbation theory necessary and on the other hand Q_s supersedes all softer momentum scales and thus controls the running of the coupling. The QCD coupling at the momentum scale of gluon saturation Q_s, for LHC center-of-mass energies can be extracted from (figure 3.3) and is of the order of $\alpha_s(Q_s^2) \approx 0.3$, corresponding to a coupling of $g \approx 2$. This is the standard value considered in simulations of the early phase of a heavy ion collision in the saturated regime [62].

Another view on gluon saturation results from the observation that a presence of large gluon densities corresponds to the presence of strong gluon fields $A \sim \mathcal{O}(\frac{1}{g})$. This causes the occupation numbers to become large $N = a^\dagger a \sim \frac{1}{\alpha_s}$ and hence quantum fluctuations are just a small correction to the strong, classical background field. Such a situation allows for a classical treatment of the Yang-Mills sector, which is the basis for the formulation of the MV-model.

The main assumptions of the MV-model can be understood best, considering the timescales in

a highly energetic nucleus. For simplicity, we restrict ourselves to one nucleus in the following to present the concept, but it can be extended to describe a collision of two nuclei. The nucleus is taken to move along the $z-$direction with a very large momentum p^{+1}, making it reside on the light-cone and Lorentz contracting it in longitudinal direction into a thin *pancake*. As a consequence, the fast parton constituents of the nucleus, as the valence quarks and large-x gluons, are affected by time dilation, whereas soft gluons at small-x have a much shorter lifetime. This creates a situation, where a separation of scales can be identified, with the long-lived large-x content of the nucleus formating an infinitely thin source of color-charge, that can be viewed as *frozen-in* throughout the collision, due to time dilation, whereas the small-x gluons remain dynamical. The MV-model relies on this separation of scales, treating the soft, small-x gluons as classical Yang-Mills fields in the presence of large-x valence degrees of freedom, that act as a static color source.

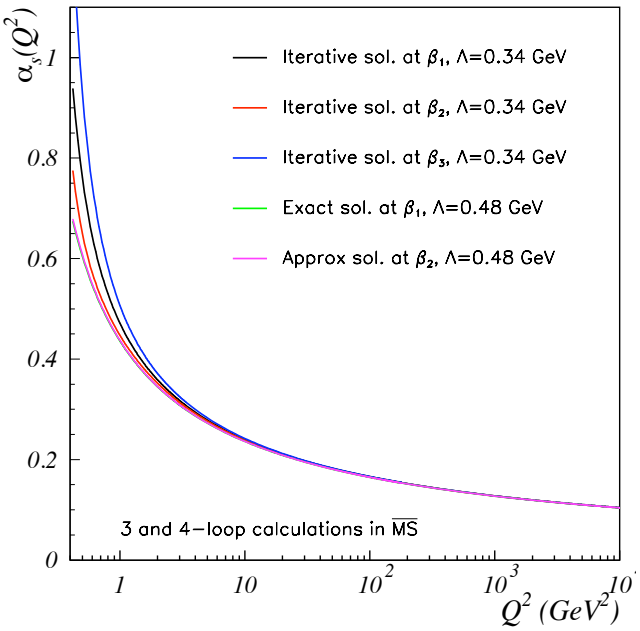

Figure 3.3: Running coupling of QCD in the perturbative regime. Calculation taken from [115].

In practice, the static sources can be integrated, generating a color current, that only has support in positive direction along the light-cone, because the sources are infinitely thin along the opposite, x^- direction

$$J_a^\mu = \delta^{\mu+}\delta(x^-)\rho_a(x^-, x_\perp). \tag{3.3}$$

The $\delta^{\mu+}$ forces the nucleus to reside on the light-cone and the distribution of color charge $\rho_a(x^-, x_\perp)$ is assumed to be given by a local Gaussian probability distribution $W_\Lambda[\rho]$, where Λ represents the cutoff for the separation of scales. The resulting correlation of color charge densities from the Gaussian distribution takes the form

$$\left\langle \rho^a(x_\perp, x^-)\rho^b(y_\perp, y^-)\right\rangle = \delta^{ab}\delta(x_\perp - y_\perp)\delta(x^- - y^-)\mu^2, \tag{3.4}$$

where we introduced the net color charge per unit area μ as a model parameter of the MV-model. This quantity is connected to the saturation momentum by

$$Q_s = g^2\mu, \tag{3.5}$$

[1]The index $\pm$ indicates light-cone coordinates, with $p^\pm = p^0 \pm p^z$

making the saturation scale Q_s the only dimensionful scale entering the MV-model. The dynamics of the small-x gluons is now governed by the classical Yang-Mills equation, with the large-x degrees of freedom entering the equation via the static color current

$$[D_\mu, F^{\mu\nu}] = J^\nu. \tag{3.6}$$

3.3 The Color-Glass Condensate

In the original proposed MV-model, a generic cutoff Λ has been introduced, to separate the static large-x and dynamical small-x degrees of freedom. In the Color-Glass Condensate (CGC) effective theory, this arbitrary cutoff dependence of the MV-model has been revisited. A crucial problem in the MV-model is, that close to the cutoff Λ, quantum fluctuations become important, which are not considered in the original model. It has been shown by a variety of authors, that these corrections can be resummed by means of a Wilsonian renormalization group procedure, introducing the JIMWLK-equation, named after Jalilian-Marian, Iancu, McLerran, Weigert, Leonidov and Kovner [116, 117, 118, 119]. Also see [120, 121] for a review on the subject. The JIMWLK-equation makes it possible to resum all quantum fluctuations in a small momentum strip between Λ and a new Λ', leading to the emergence of a cutoff $\tilde{\Lambda}$, that redefines the statistical weight $W_{\tilde{\Lambda}}[\rho]$. As a consequence, all quantum fluctuations close to the cutoff of the original MV-model can systematically be resummed and included in a redefinition of the cutoff.

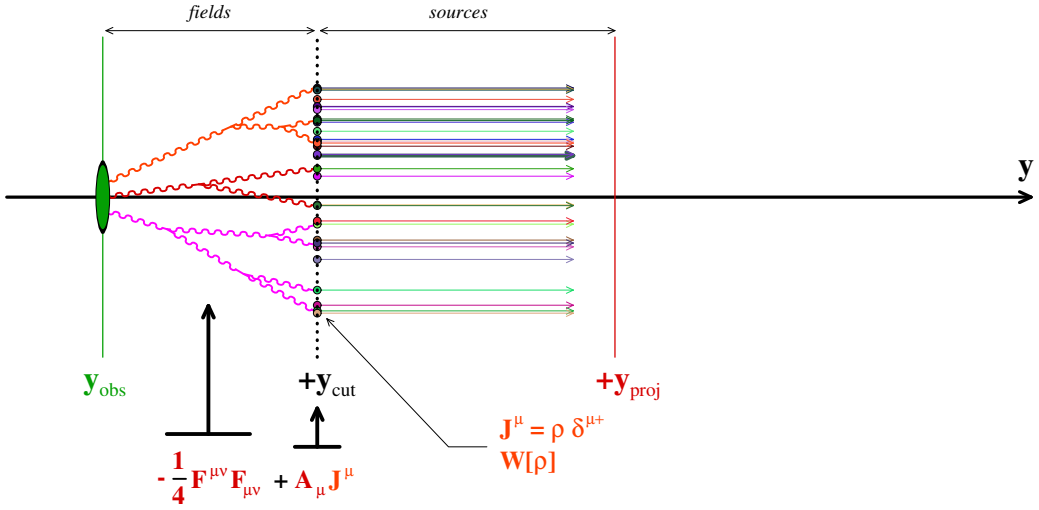

Figure 3.4: Degrees of freedom in the CGC effective theory. Illustration taken from [122]

Therefore, the concept of a separation of scales remains valid and is fundamental for the definition of the Color-Glass Condensate effective theory, as depicted in (figure 3.4). In this context, the name *Color-Glass Condensate* becomes understandable, as an effective theory for dynamical fields, in the background of an ensemble of *Color* sources, that are frozen in due to time dilation (*Glass*) and saturated (like in a *Condensate*), formating a static current that acts onto the system.

In the case of two colliding heavy nuclei, the following ansatz is made for the color current of the static background sources

$$J^{\mu,a} = \delta^{\mu+}\rho^{(1),a}(x^-, \mathbf{x}_\perp) + \delta^{\mu-}\rho^{(2),a}(x^+, \mathbf{x}_\perp), \tag{3.7}$$

where the $\delta^{\mu\pm}$ force the two incoming nuclei to reside on the positive and negative light-cone and $\rho^{(1/2)}$ is their corresponding color charge distribution. The collision axis is assumed to be the z-axis. The dynamical small-x gluons are thus obtained by solving the classical Yang-Mills equation of motion with the current entering as a source term

$$\left[D_\mu, F^{\mu\nu}\right] = \delta^{\nu+}\rho^{(1)}(x^-, \mathbf{x}_\perp) + \delta^{\nu-}\rho^{(2)}(x^+, \mathbf{x}_\perp). \tag{3.8}$$

For the solution of these equations, we can exploit the fact, that highly energetic collisions are nearly boost invariant in longitudinal direction. As a consequence, the solution of the classical Yang-Mills equations does not explicitly depend on rapidity and our problem becomes effectively $2+1$ dimensional.

The assumption of boost invariance allows us, to restrict our problem to the transverse plane and the solution in the forward light-cone is now constructed in the following way:
As depicted in (figure 3.5), the equation is first solved for each of the nuclei individually, corresponding to the regions (1) and (2).

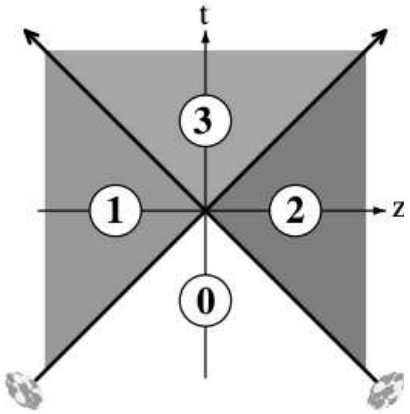

Figure 3.5: Space-time regions in a heavy ion collision, used in the solution of the classical Yang-Mills equation of the CGC effective theory, to construct the classical Yang-Mills fields in the forward lightcone, region (3). Illustration taken from [122].

From the solution of the Yang-Mills equation in space-time regions (1) and (2), often notated as $\alpha_\mu^{(1)}$ and $\alpha_\mu^{(2)}$, one can construct the solution in the forward lightcone region (3) in radial gauge $x^-A^+ + x^+A^- = 0$. This solution takes the form

$$A_i = \alpha_i^{(1)} + \alpha_i^{(2)}, \qquad A_{z/\eta} = 0, \tag{3.9}$$

$$E^i = 0, \qquad E^{z/\eta} = \mathrm{i}g\Big(\left[\alpha_1^{(1)}, \alpha_1^{(2)}\right] + \left[\alpha_2^{(1)}, \alpha_2^{(2)}\right]\Big) \tag{3.10}$$

[123], where E^i and $E^{z/\eta}$ are the transverse and longitudinal components of the classical color-electric field.[2] Next, we are going to discuss the construction of this solution on the lattice.

Another issue of the effective model is gauge ambiguity. The strong color fields have been discussed as intrinsic properties of the highly energetic nuclei, but they are dependent on a

[2]We introduced both z and η for the longitudinal direction, where the latter one denotes the space-time rapidity in Bjorken coordinates. Bjorken (or Milne) coordinates will be an important ingredient for the construction of a longitudinally expanding system and we will discuss them in (chapter 9).

particular frame or gauge choice. A way around is, to formulate the problem not in terms of gauge fields, but in terms of gauge invariant Wilson lines. Instead of assuming the distribution of color charge of the individual nuclei to be approximated as an infinitesimal thin sheet of color charge in transverse direction $\rho^a(x^\pm, \mathbf{x}_\perp) \to \delta(x^\pm)\rho^a(\mathbf{x}_\perp)$, as it has originally been proposed in the MV-model, we construct a set N_y of such sheets in longitudinal direction, allowing to compute Wilson lines through this set. As a result, one maintains gauge-covariance in that very direction, as pointed out in [124, 125].

3.3.1 The Color-Glass Condensate on the Lattice

Having presented the basic concepts of gluon saturation and the CGC as an effective theory for the saturated regime, we now want to construct the lattice discretized version. We follow the construction presented in [126] and the corresponding PhD thesis [127], that is itself based on the formalism presented in [39]. We use a construction from Wilson lines to prevent gauge ambiguity and additionally an infrared (IR) cutoff is introduced, when solving the Poisson equation of the CGC effective theory, making it possible to maintain color-neutrality, as pointed out in [128].

We first present how to construct the gauge link ensemble of the individual nuclei, corresponding to the regions (1) and (2) in (figure 3.5). Following this, we are able to construct the solution in the forward lightcone region (3). The gauge links of the individual nuclei are highlighted by an index $k \in \{(1), (2)\}$. As discussed in context of the continuum solution (eq. 3.9), the longitudinal direction is simply given by setting $A^k_{z/\eta} = 0$, which corresponds to choosing

$$U^k_{z/\eta} = 1, \tag{3.11}$$

for all longitudinal gauge links.

The strategy for the construction of the remaining links and chromo-electric fields on the lattice is the following:

First we draw the color charge densities of the individual nuclei $\rho^{(1)}$ and $\rho^{(2)}$ from the Gaussian distribution

$$\left\langle \rho^{k,a}_i(x_\perp)\rho^{k',b}_j(y_\perp)\right\rangle = \frac{g^2\mu^2}{N_y}\delta^{ab}\delta^{kk'}\delta(x_\perp - y_\perp), \tag{3.12}$$

where the Gaussian distribution is characterized by the color charge per unit area μ, extracted from the saturation scale Q_s. Additionally, we introduce a set of infinitesimal thin color-sheets N_y to construct the Wilson lines. Hence we have to repeat the drawing N_y times to obtain an ensemble of color sheets for the Wilson line construction, following [125]. The indices $i, j \in \{1, ..., N_y\}$ of the color charge density ρ count these sheets. Since all of these sheets are assumed to be infinitesimally thin, the position coordinate of the longitudinal direction is set to zero, making our problem effectively two dimensional, as discussed earlier.

Next, as familiar from electrodynamics, the next step is to construct a color potential Λ from the charge distribution obtained in the previous step. To do so, we have to solve the Poisson equation

$$\Big[\Delta_L + m^2\Big]\Lambda^{k,a}_i(x_\perp) = -\rho^{k,a}_i(x_\perp), \tag{3.13}$$

with Δ_L the two-dimensional lattice Laplace operator

$$\Delta_L \Lambda_i^{k,a}(x_\perp) = \frac{1}{a_\perp^2} \sum_{i \in x_\perp} \Big[\Lambda_i^{k,a}(x_\perp + \hat{i}) - 2\Lambda_i^{k,a}(x_\perp) + \Lambda_i^{k,a}(x_\perp - \hat{i}) \Big]. \tag{3.14}$$

We additionally introduced the infrared (IR) regulator m to the Poisson equation for the inversion of the Laplace operator, as discussed in [125].

The strategy for solving the Poisson equation on the lattice is discussed in [127] in detail and we will only sketch the procedure. The equation is solved by introducing a lattice Fourier transform, allowing us to write the color potential in momentum space as

$$\tilde{\Lambda}_i^{k,a}(p_1, p_2) = \frac{\tilde{\rho}_i^{k,a}(p_1, p_2)}{4 - e^{\mathrm{i}p_1} - e^{-\mathrm{i}p_1} - e^{\mathrm{i}p_2} - e^{-\mathrm{i}p_2} + m^2}. \tag{3.15}$$

The IR-cutoff eliminates the singularity of the zero mode $(p_1, p_2) = (0, 0)$, making the solution well defined on the reciprocal lattice. The position dependent color potential is thus extracted from a Fourier back-transformation.

Having created an ensemble of N_y different color potentials Λ_i, we construct the Wilson lines in longitudinal direction from

$$W^k(x_\perp) = \prod_{i=1}^{N_y} \exp\Big[\mathrm{i}\Lambda_i^{k,a}(x_\perp) T^a \Big], \tag{3.16}$$

with T^a the generator of the $SU(3)$ gauge group. Per construction one easily checks, that indeed $W^k(x_\perp) \in SU(3)$.

Finally, it is possible to construct the gauge link ensemble of the individual nuclei in a gauge invariant fashion from the Wilson lines

$$U_i^k(x_\perp) = W^k(x_\perp) W^{k\dagger}(x_\perp + \hat{i}). \tag{3.17}$$

Having constructed the gauge link ensemble of the individual nuclei in the space-time regions (1) and (2) in (figure 3.5), we now have to construct the solution in the forward lightcone, region (3), to obtain the initial gauge link ensemble for the simulation.

The lattice counterpart of (eq. 3.9) is given by [39]

$$\mathrm{tr}\Big[T^a \Big(\Big(U^{(1)} + U^{(2)}(x_\perp) \Big) \Big(1 + U^\dagger \Big) - \mathrm{h.c.} \Big) \Big] = 0. \tag{3.18}$$

For a $SU(3)$ group theory, there is no closed analytical solution of (eq. 3.18) making it necessary to extract the gauge links in the forward lightcone numerically. We initialize the gauge links as $U = \exp\big(\mathrm{i}\theta_a T^a\big)$, drawing an ensemble of θ_a and solving (eq. 3.18) iteratively, by updating the links U accordingly, until sufficient precision of 10^{-8} is reached. For details on the algorithm see [127].

Finally we have to initialize the chromo-electric fields. As it has been the case in the continuum (eq. 3.10), the transverse chromo-electric fields are taken to be zero, setting

$$E_\perp(x_\perp) = 0. \tag{3.19}$$

On the other hand, the longitudinal chromo-electric fields are constructed from the gauge link ensemble for the different space-time regions in (figure 3.5) [61, 129]

$$\begin{aligned} g a_\perp^2 E^a_{z/\eta}(x) = -\frac{\mathrm{i}}{2}\sum_{i=1}^{2} \mathrm{tr}\Big[T^a\Big(\Big[U_i(x)-1\Big]\Big[U_i^{(2)\dagger}(x) - U_i^{(1)\dagger}(x)\Big] - \text{h.c.} \\ + \Big[U_i^\dagger(x-\hat{i})-1\Big]\Big[U_i^{(2)}(x-\hat{i}) - U_i^{(1)}(x-\hat{i})\Big] - \text{h.c.}\Big)\Big]. \end{aligned} \tag{3.20}$$

3.4 The Glasma Initial State

In the previous section, we presented how to construct the initial gauge field ensemble from the CGC effective theory on the lattice. Keep in mind, that we constructed the gauge link ensemble in the transverse plane only, setting the longitudinal direction equal to zero. In this section, we will discuss how to extend the solution into longitudinal direction, arriving at a system that is known as the Glasma [37], an out-of-equilibrium state, initially dominated by gluon dynamics.

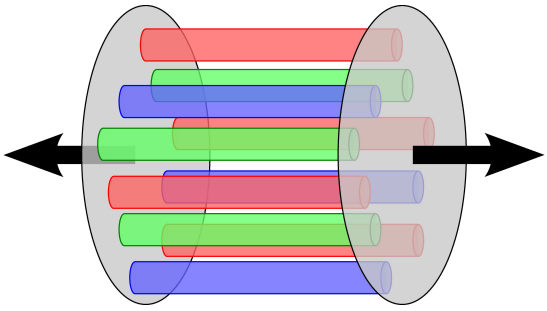

Figure 3.6: Color flux tubes of the Glasma in the early phase of a heavy ion collision, after $t \approx 0.1$ fm. The Glasma is created from boost invariant color electric and color magnetic fields, generated from the CGC effective theory. Illustration taken from [112].

Glasma is a coined word for the transitional state between the Color-*Glass* Condensate and the Quark-Gluon-*Plasma*. It evolves from the classical dynamics of the small-x gluons associated with the CGC, allowing a simulation of the Glasma within a classical field theory at early times. The state is characterized, by the appearance of boost invariant longitudinal color electric and color magnetic fields, forming so called color flux tubes, generated from the frozen in color charge distribution of the colliding nuclei.[3] A schematic illustration of this situation is given in (figure 3.6). To generate a similar system from our initial gauge link ensemble, presented in (section 3.3.1), we adapt the strategy presented in [60] for a static and in a second step for an expanding box, following [61]. The idea is to simply copy the generated gauge link configuration in the transverse plane at $z/\eta = 0$ to the other planes in longitudinal direction.

[3] In a naive picture, this can be viewed as some kind of capacitor, where the large-x, frozen-in color charges of the nuclei represent the capacitor plates. This also gives an intuitive understanding, why the perpendicular chromo-electric field components have to vanish.

For the static system, following [60], we assume a cubic box as a first approximation. This strategy exactly creates the desired color flux tube structure in longitudinal direction, that is characteristic for the Glasma initial state.

A challenging problem for the transitional state of the Glasma, is how the initial pressure of the system, determined from the CGC effective theory, is evolving. The crucial question hereby is, if a pressure isotropy can be reached by the system. A calculation of the pressure from the diagonal components of the energy momentum tensor $T^{\mu\nu} = \mathrm{diag}\big(\epsilon, P_T, P_T, P_L\big)$ for the CGC initial conditions reveals, that initially $P_T = \epsilon$, whereas $P_L = -\epsilon$, hence the longitudinal pressure is negative and exactly the opposite of the transverse pressure. As a consequence, the pressure of the system is highly anisotropic at initial times. The reason for the negative pressure in longitudinal direction is, that the longitudinal fields have positive energy density and thus stretching the color flux tubes further would require more positive energy in longitudinal direction. From that observation one can already guess, that erasing the color flux tube structure of the Glasma will turn out to be a crucial ingredient to move the system towards pressure isotropy. We will return to this statement later, when discussing our results.

The system is expected to move towards pressure isotropy, because of the success of hydrodynamics for a description of the Quark-Gluon-Plasma, already around a time of $t \approx 1$ fm. A necessary (but not sufficient) criteria for a hydrodynamization of the system and its approach towards local thermal equilibrium (LTE), is pressure isotropy. The question therefore is, if the dynamics of the classical gluons in the Glasma can drive the system towards pressure isotropy. This is especially challenging because such a process competes with the expansion in longitudinal direction. Due to the expansion, the system becomes more and more dilute and one would expect that the interaction between gluons (and quarks) nearly becomes turned off at some point, arriving at a situation of non-interacting quarks and gluons, also referred to as the free-streaming limit.

The question if pressure isotropy is reached in the Glasma has already been attacked in a variety of works, simulating the classical gluon dynamics within pure Yang-Mills simulations in a static and expanding system [58, 60, 61, 62]. It has been shown, that even in the static box, no pressure isotropy is reached for the Glasma initial conditions [60]. The reason for that is, that the initial conditions are boost invariant and the classical Yang-Mills equations preserve this boost invariance, hence the initial color flux tubes are never erased and no pressure isotropy is reached. A possible way out has first been presented by Venugopalan and Romatschke in [61], where they introduced rapidity fluctuations in longitudinal direction by hand, explicitly breaking the boost invariance. These rapidity fluctuations are motivated from quantum fluctuations in the Yang-Mills sector and later studied in a more systematic way, as NLO corrections to the CGC initial conditions by Gelis and Eppelbaum [63, 64]. To explicitly break boost invariance in longitudinal direction, the initial chromo-electric fields are modified, by introducing a perturbation

$$\begin{aligned} \delta E_i(x_\perp, z/\eta) &:= D_{z/\eta} F_i(x_\perp, z/\eta) \\ \delta E_{z/\eta}(x_\perp, z/\eta) &:= -D_i F_i(x_\perp, z/\eta), \end{aligned} \tag{3.21}$$

where $F_i(x_\perp, z/\eta)$ is a (at least) twice continuously differentiable function. Because we are only interested in longitudinal rapidity fluctuations, the dependence on the transverse coordinate is determined by random based generators $\xi_i(x_\perp)$, whereas we parametrize the rapidity fluctuation,

using a single longitudinal mode times a real-valued amplitude Δ that is chosen by hand

$$ga_\perp F_i(x_\perp, z/\eta) := f(z/\eta)\xi_i(x_\perp) = \Delta \cos\left(\frac{2\pi z/\eta}{L_{z/\eta}}\right)\xi_i(x_\perp). \tag{3.22}$$

In [126] and [60] it has been shown for a simulation of classical Yang-Mills theory in a static box, that such an explicit breaking of longitudinal boost invariance leads to the development of a plasma instability, referred to as chromo-Weibel instability, which is the $SU(3)$ counterpart of a Weibel instability familiar from electrodynamics [130]. This instability essentially erases the color flux tubes of the Glasma and drives the system towards pressure isotropy. An extension to the expanding system presented in [61] and [62] revealed the appearance of a Glasma instability as well, but no pressure isotropy could be reached, with the longitudinal expansion preventing the process and the free streaming limit being reached.

All these works only consider classical Yang-Mills theory to simulate the dynamics of the Glasma, but an explicit breaking of boost invariance already indicated, that quantum effects might play an important role for pressure isotropization. Besides the NLO quantum corrections to Yang-Mills theory, fermions, that are always of quantum nature, might play an important role for pressure isotropization. A first study in [73], for „Glasma type“ initial conditions already gave promising evidence, that a coupling to fermions might play an interesting role for the dynamics of the system. An analysis for an expanding system is still missing completely. In this work we want to study the effect of fermions on the Glasma state in a static box in detail, for a realistic set of parameters, connected to the heavy ion collision of *Pb-Pb* nuclei at center of mass energy of $\sqrt{s} = 5.02$ TeV, as recently studied at the LHC. In a next step, we want to extend this study to an expanding system. We assume that no quarks are trapped in the Quark-Gluon-Plasma after the collision and the quark chemical potential is set to zero. Quarks and anti-quarks can only be equally produced from gluon decay during the evolution of the Glasma, keeping the entropy constant.

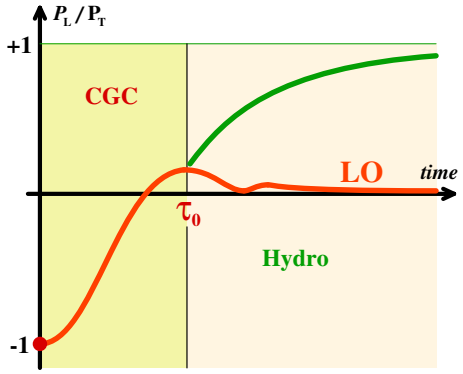

Figure 3.7: Matching between hydrodynamics and the CGC effective theory at leading order at the time τ_0. Illustration taken from [131].

We will test our system for pressure isotropization in the static and expanding box. It has been argued, that a system, that is already driven towards a (partial) pressure isotropy could be matched to hydrodynamics at the time of $\tau_0 \approx 1$ fm, as illustrated in (figure 3.7). As pointed out in the introduction, this can be extended by an intermediate step, where the dynamics of the system is described in terms of QCD kinetic theory after the classical regime

(see figure 1). Following this, the dynamical evolution towards local thermal equilibrium is governed by hydrodynamics, until it is possible to observe signatures of the Bose-Einstein and Fermi-Dirac distributions for the spectrum of the system in momentum space, making it possible to determine the equilibrium temperature of the medium.

3.5 Early Time Energy Density in a Heavy Ion Collision

A cutoff dependence is a general problem of lattice regularized theories, but it usually can be solved by systematically taking the continuum limit. This is not possible in a classical theory, because it is UV-divergent. This situation is familiar from Rayleigh-Jeans divergencies of the classical description of blackbody radiation, which is the reason why the classical approximation is sometimes referred to be Rayleigh-Jeans divergent. As a consequence, the classical theory remains cutoff dependent and a way to deal with such a theory is to match it to a continuum theory and extract the appropriate lattice spacing a. For our system, we want to perform such a matching for the energy density of the initial state in our lattice simulation, to an estimate of the energy density in the early stage of a heavy ion collision. The estimate is derived from a model based on gluon saturation [24, 22] and has been adapted to Pb-Pb collisions at the LHC with a center of mass energy of $\sqrt{s} = 5.02$ TeV in [132]. Performing a lattice simulation with different lattice spacings a then allows us to extract the appropriate lattice spacing for a matching of energy densities. We will present this procedure later, for a static and an expanding box and only discuss, how to estimate the initial energy density at this point.

Starting point for the estimation of the energy density of the initial state and corresponding momentum scale of gluon saturation Q_s, is the so called k_T-factorized spectrum of gluons per unit rapidity (Y), at transverse position $\mathbf{x}$ and per initial transverse momentum ($\mathbf{P}$) [133, 134]

$$\frac{dN_g}{d^2\mathbf{x}d^2\mathbf{P}dYdy} = \frac{g^2N_c}{4\pi^5\mathbf{P}^2(N_c^2-1)}\delta(Y-y)\int \Phi_{Pb}\left(\mathbf{x}+\frac{\mathbf{b}}{2},\mathbf{k}\right)\Phi_{Pb}\left(\mathbf{x}-\frac{\mathbf{b}}{2},\mathbf{P}-\mathbf{k}\right)\frac{d^2k}{(2\pi)^2}, \quad (3.23)$$

where g is the Yang-Mills coupling and N_c the number of colors. The individual Pb-nuclei are modeled as presented by Woods and Saxon [135], taking the estimated nucleus radius for Pb to be $r_{Pb} = 6.62$ fm and the diffusivity to be $a = 0.546$ fm. The impact parameter of the collision is set to $\mathbf{b} = 0$ (head-on collision), corresponding to the central rapidity regime ($Y = 0$). The functions Φ_{Pb} are then the unintegrated gluon distributions of the colliding Pb-nuclei, given from the Golec-Biernat-Wüsthoff (GBW) model [136]

$$\Phi_{Pb}(\mathbf{x},\mathbf{k}) = 4\pi^2\frac{N_c^2-1}{gN_c}\frac{\mathbf{k}^2}{Q_{s,Pb}^2}e^{-\frac{\mathbf{k}^2}{Q_{s,Pb}^2}}, \quad (3.24)$$

where the saturation scale of the Pb-nucleus $Q_{s,Pb}$ can be identified. Using these equations it is possible to analytically derive the gluon spectrum within the GBW-model and compute the energy density per unit rapidity

$$\left[\epsilon(\mathbf{x})\tau\right]_0 = \int\int |\mathbf{P}|d^2\mathbf{P}\frac{dN_g}{d^2\mathbf{x}d^2\mathbf{P}dYdy}. \quad (3.25)$$

Assuming that transverse momentum is dominated by the saturation scale $|\mathbf{P}| \sim Q_{s,Pb}$, makes it possible to solve the integrals analytically, obtaining the following result for the energy density

$$\left[\epsilon(\mathbf{x})\tau\right]_0 = \frac{N_c^2-1}{4g^2N_c\sqrt{\pi}}\frac{11Q_{s,Pb}^3}{2^{5/2}}. \quad (3.26)$$

The saturation scale $Q^2_{s,Pb}$ is parametrized as

$$Q^2_{s,Pb}(x,\mathbf{x}) = Q^2_{s,p}(x)\sigma_0 T_{Pb}(\mathbf{x}), \tag{3.27}$$

with x the longitudinal momentum fraction of the partons (Bjorken-x) and $T_{Pb}(\mathbf{x})$ the nuclear thickness function. The product $\sigma_0 T_{Pb}(\mathbf{x})$ effectively counts the number of nucleons (protons, neutrons) at transverse position $\mathbf{x}$ in a Pb-nucleus. We take $\sigma_0 = 2\pi B_G$, where $B_G = 4$ GeV^{-2} is the nucleus size, obtained from fits to HERA data [137, 138]. The quantity $Q^2_{s,p}(x)$ marks the average saturation scale of a proton and it can be parametrized in the following way

$$Q^2_{s,p}(x) = Q^2_{s,0} x^{-\lambda}(1-x)^{\delta}, \tag{3.28}$$

where $Q^2_{s,0} = 0.63$ GeV^2, $\lambda = 0.36$ and $\delta = 1$.

Combining (eq. 3.27) and (eq. 3.28) allows us to solve equation (eq. 3.26) for Pb-Pb collisions at LHC center-of-mass energies of $\sqrt{s} = 5.02$ TeV. We extract the saturation scale

$$Q^2_{s,Pb} = 3.586 \text{ GeV}^2, \qquad \rightarrow \qquad Q_{s,Pb} = 1.867 \text{ GeV}, \tag{3.29}$$

which matches very well the estimate of $Q_s \approx 2$ GeV for LHC energies, taken in the majority of studies of the CGC effective theory (for a review see [38]).

We calculate the energy density at the formation time of the Glasma $\tau_0 \approx 1/Q_{s,Pb} \approx 0.1$ fm [38], which is an order of magnitude smaller as the estimated hydrodynamization time of the system $\tau_{hydro} \approx 1$ fm. Evaluating (eq. 3.26) leads to the (average) initial energy density

$$\epsilon_0 \approx 281.45 \ \frac{\text{GeV}}{\text{fm}^3}. \tag{3.30}$$

This estimate matches very well previous estimates of the initial energy density in Pb-Pb collisions at the LHC, using hydrodynamic models [139]. For a standard choice of hydrodynamic parameters in simulations of the QGP, namely a shear viscosity of $\frac{\eta}{s} = \frac{2}{4\pi}$, a charged particle multiplicity of $\frac{dN_{ch}}{\eta} = 1600$, a constant $C_\infty = 0.87$ extracted from late stage viscous hydrodynamics [82, 140] and an entropy per charged particle at freeze-out of $\frac{S}{N_{ch}} = 7.5$ [141], one finds

$$\begin{aligned}\epsilon_0 \approx 270 \frac{\text{GeV}}{\text{fm}^3} \ & \left(\frac{\tau_0}{0.1\text{fm/c}}\right)^{-1}\left(\frac{C_\infty}{0.87}\right)^{-9/8}\left(\frac{\eta/s}{2/4\pi}\right)^{-1/2}\left(\frac{A_\perp}{128\text{fm}^2}\right)^{-3/2} \\ & \left(\frac{dN_{ch}/d\eta}{1600}\right)^{3/2}\left(\frac{\nu_{eff}}{40}\right)^{-1/2}\left(\frac{S/N_{ch}}{7.5}\right)^{3/2},\end{aligned} \tag{3.31}$$

where the initial time is taken to be $\tau_0 = 0.1$ fm and the transverse area of the Lorentz contracted Pb-nucleus is $A_\perp = 138$ fm^2. We find that this result for the initial state energy density is close to (eq. 3.30), validating our approach. Together with the saturation scale $Q_{s,Pb}$ and the estimated nucleus radius r_{Pb} for Pb, we will use this energy density to fix the lattice spacing in our simulation of the Glasma and therefore introduce a physical scale. Keep in mind, that these parameters are the only unit dependent parameters entering the simulation.

Part I

Simulating in a Static Box

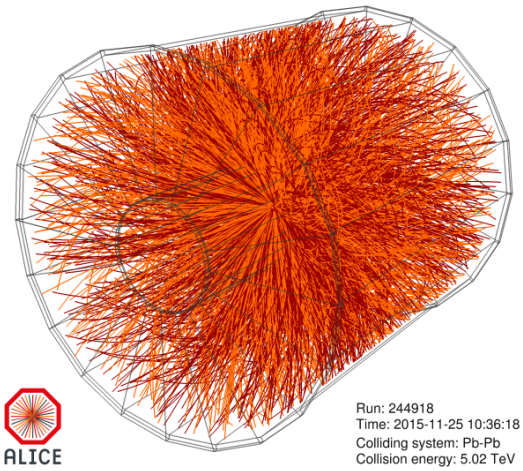

Event display of a *Pb-Pb* collision at the LHC,
observed in the ALICE experiment [142].

4

The Semi-Classical Approximation of QCD

In the following chapter we derive the semi-classical approximation of QCD in a static box. The whole derivation is motivated from the validity of a classical approximation for the Yang-Mills sector of QCD in the Glasma, discussed in the previous chapter. Initializing the Yang-Mills sector accordingly, we introduce fermions to our system and derive an effective partition function of QCD, as first presented in [72]. The aim of the section is to derive the equations of motion of the semi-classical approximation for all fields entering the simulation, namely the gauge links U_i, the fermion fields ψ and especially the chromo-electric fields E_i.

4.1 Evolution of Fermion Fields

We start our discussion with the derivation of the time evolution equation of fermion fields. The dynamics of fermions governed by the lattice Dirac equation (eq. 2.55). As discussed in (section 2.2), we use ensemble averages of stochastic low-cost fermions, to calculate expectation values involving fermion fields in our simulation. As a consequence, each individual gendered fermion field ψ_G of the ensemble N_{ens} has to be a solution of the lattice Dirac equation

$$\begin{aligned} 0 =& \mathrm{i}\gamma^0\partial_t\psi_G(x) - \left(m + \frac{3r}{a}\right)\psi_G(x) \\ &+ \frac{\mathrm{i}}{2a}\sum_{i=1}^{3}\Big[\big(\gamma^i - \mathrm{i}r\big)U_i(x)\psi_G(x+\hat{i}) - \big(\gamma^i + \mathrm{i}r\big)U_i^\dagger(x-\hat{i})\psi_G(x-\hat{i})\Big], \end{aligned} \tag{4.1}$$

with $G = \{M, F\}$ denoting the gender index.

We kept continuous real time when writing (eq. 4.1). In a simulation, the time dependence cannot be solved analytically in a closed form, making an additional discretization of time necessary. This is realized by introducing a temporal spacing a_t, with $t = n_t a_t$, $n_t \in \mathbb{N}$. This discretization has additional consequences on the numerics of the simulation, that we will discuss

later in (chapter 7). After discretizing time, (eq. 4.1) can be written as

$$\begin{aligned}\psi_G(x+\hat{t}) =&\psi_G(x-\hat{t}) - 2\mathrm{i}a_t\gamma^0\left(m+\frac{3r}{a}\right)\psi_G(x) \\ &- \frac{a_t}{a}\gamma^0\sum_{i=1}^{3}\Big(\big(\gamma^i-\mathrm{i}r\big)U_i(x)\psi_G(x+\hat{i}) - \big(\gamma^i+\mathrm{i}r\big)U_i^\dagger(x-\hat{i})\psi_G(x-\hat{i})\Big).\end{aligned} \tag{4.2}$$

The free Dirac equation is obtained by setting $U_i = 1$.

At initial time $t_0 = 0$, we do not have access to the field $\psi_G(x-\hat{t})$ entering (eq. 4.2) in the lattice simulation. A way out is to evolve our system by using the non-symmetric discrete time derivative once

$$\begin{aligned}\psi_G(x+\hat{t}) =&\psi_G(x) - \mathrm{i}a_t\gamma^0\left(m+\frac{3r}{a}\right)\psi_G(x) \\ &- \frac{a_t}{2a}\gamma^0\sum_{i=1}^{3}\Big(\big(\gamma^i-\mathrm{i}r\big)U_i(x)\psi_G(x+\hat{i}) - \big(\gamma^i+\mathrm{i}r\big)U_i^\dagger(x-\hat{i})\psi_G(x-\hat{i})\Big).\end{aligned} \tag{4.3}$$

4.2 Evolution of the Gauge Links

We derive the time evolution equation of the classical gauge links from the temporal lattice plaquette, using discretized time

$$U_{0i}(x) = U_0(x)U_i(x+\hat{0})U_0^\dagger(x+\hat{0})U_i^\dagger(x). \tag{4.4}$$

After applying temporal gauge $U_0 = 1$, this reduces to

$$U_{0i}(x) = U_i(x+\hat{0})U_i^\dagger(x) = U_i(x+\hat{t})U_i^\dagger(x) = e^{\mathrm{i}ga_taF_{0i}(x)+\mathcal{O}(a^3)}. \tag{4.5}$$

Making use of (eq. 2.7) it is now possible to write

$$U_i(x+\hat{t}) = e^{\mathrm{i}ga_taF_{0i}(x)}U_i(x), \tag{4.6}$$

where we neglected terms of order $\mathcal{O}(a^3)$. After identifying the chromo-electric fields (eq. 1.17), we arrive at the equation of motion for the gauge links

$$U_i(x+\hat{t}) = e^{\mathrm{i}ga_taE_i(x)}U_i(x). \tag{4.7}$$

4.3 The Semi-Classical Model

For the derivation of the time evolution equation of the chromo-electric fields we have to specify the semi-classical approximation. This is done by deriving the corresponding partition function, following [72] and in this chapter we will present the key results, adapted to our system. We take our system to be out-of-equilibrium, which happens to be the case for the Glasma initial state discussed in (section 3.4). Nevertheless, the following derivation is valid in more general equilibrium and non-equilibrium systems fulfilling the requirements that a) the bosonic sector of the theory can be treated classical to leading order and b) the initial state at a given time $t = t_0$ is well known.

The appropriate formalism for the derivation of the model is provided by the real-time formalism of the nonequilibrium quantum field theory. In the real-time formalism, time evolution is governed by a specific time contour $\mathcal{C}$, which is referred to as Schwinger-Keldysh contour [97]. Time evolution along the contour starts at an initial time $t = t_0$, where the initial state of the system is well known. It then proceeds forward up to a final time $t = t_f$, that can also be taken to infinity. This part of the contour is usually denoted $\mathcal{C}^+$. The contour is closed by proceeding backwards in time, back to the initial time $t = t_0$, usually denoted as $\mathcal{C}^-$. An illustration of the contour is given in (figure 4.1).

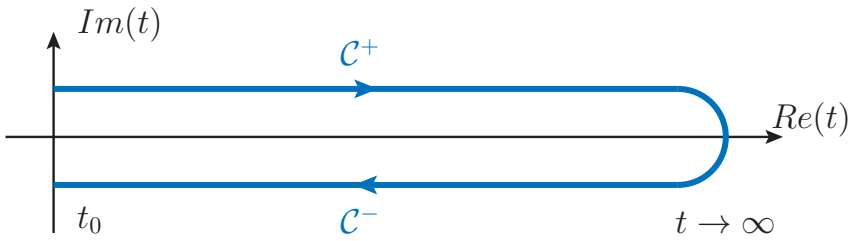

Figure 4.1: The Schwinger-Keldysh real time contour.

All information on the initial state of a system is given from the initial density matrix $\rho(t_0)$ and the fields entering the density matrix only depend on the initial time t_0. Making use of the Schwinger-Keldysh contour and the initial density matrix of the system, the real-time partition function of QCD can now be written as

$$Z_{\mathcal{C}} = \int\int \rho(t_0) e^{\mathrm{i}S_{YM}[A]+\mathrm{i}S_{\psi}[\bar{\psi},\psi,U]}[dA][d\bar{\psi}d\psi], \tag{4.8}$$

where the brackets [...] indicate the path integral measure. First we assume, that the initial density matrix can be split into a Yang-Mills and a fermion part, assuming vacuum fermions for the latter one. The fermion density matrix thus is quadratic in the fields and it can directly be included in the definition of the inverse fermion propagator on the real-time contour $\mathcal{C}$

$$S_f[\bar{\psi},\psi,A] = \int\int \bar{\psi}(x) D_{\mathcal{C}}^{-1}[A](x,y)\psi(y) d^4x d^4y. \tag{4.9}$$

As a consequence, it is possible to rewrite the partition function in the following way

$$\begin{aligned} Z_{\mathcal{C}} &= \int\int \rho(t_0) e^{\mathrm{i}S_{YM}[A]+\mathrm{i}S_{\psi}[\bar{\psi},\psi,U]}[dA][d\bar{\psi}d\psi] \\ &= \int\int \rho_A(t_0) e^{\mathrm{i}S_{YM}[A]+\mathrm{i}\int\int \bar{\psi}(x) D_{\mathcal{C}}^{-1}[A](x,y)\psi(y) d^4x d^4y}[dA][d\bar{\psi}d\psi]. \end{aligned} \tag{4.10}$$

Because this result is quadratic in the fermion fields, we can integrate these fields, introducing the so called fermion determinant

$$Z_{\mathcal{C}} = \int \rho_A(t_0) \det\left[D_{\mathcal{C}}^{-1}[A]\right] e^{\mathrm{i}S_{YM}[A]}[dA] = \int \rho_A(t_0) e^{\mathrm{Tr}\log[D_{\mathcal{C}}^{-1}[A]]+\mathrm{i}S_{YM}[A]}[dA], \tag{4.11}$$

where we used the trace-log (Jacobi) formula in the second step.

For the gauge field A_μ we assume, that it can be split into a leading order classical field $\bar{A}_\mu$ and a small quantum correction $\tilde{A}_\mu$

$$A_\mu(x) = \bar{A}_\mu(x) + \tilde{A}^{\pm}_\mu(x) = \bar{A}_\mu + \frac{1}{2}\mathrm{sgn}_{\mathcal{C}}\tilde{A}_\mu. \tag{4.12}$$
$$A^+_\mu(x) = \bar{A}_\mu(x) + \frac{1}{2}\tilde{A}_\mu(x), \qquad A^-_\mu(x) = \bar{A}_\mu(x) - \frac{1}{2}\tilde{A}_\mu(x).$$

The quantum field has to be taken on the forward $\mathcal{C}^+$ and backward $\mathcal{C}^-$ branch of the Schwinger-Keldysh contour (figure 4.1), which is indicated by $\pm$. It is now possible to integrate the classical and the quantum gauge fields independently in the partition function

$$Z_{\mathcal{C}} = \int \rho_A(t_0) e^{\mathrm{Tr}\log[D_{\mathcal{C}}^{-1}[A]] + \mathrm{i}S_{YM}[\bar{A},\tilde{A}]}[d\bar{A}][d\tilde{A}]. \tag{4.13}$$

The Yang-Mills action on the time contour $\mathcal{C}$ is given as

$$S_{YM}[\bar{A},\tilde{A}] = -\frac{1}{4}\int_{\mathcal{C}} F^a_{\mu\nu}[\bar{A},\tilde{A}](x)F^{\mu\nu,a}[\bar{A},\tilde{A}](x)d^4x. \tag{4.14}$$

In a next step, we linearize the Yang-Mills action in the quantum fluctuation $\mathcal{O}(\tilde{A})$, neglecting all higher order terms, which is justified due to the smallness of the fluctuation. The linearized field strength tensor reads

$$\begin{aligned} F^a_{\mu\nu} =& \partial_\mu\Big(\tilde{A}^{a\pm}_\nu + \bar{A}^a_\nu\Big) - \partial_\nu\Big(\tilde{A}^{a\pm}_\mu + \bar{A}^a_\mu\Big) - gf^{abc}\Big(\tilde{A}^{b\pm}_\mu + \bar{A}^b_\mu\Big)\Big(\tilde{A}^{c\pm}_\nu + \bar{A}^c_\nu\Big) \\ =& \Big(\partial_\mu\bar{A}^a_\nu - \partial_\nu\bar{A}^a_\mu\Big) + \Big(\partial_\mu\tilde{A}^{a,\pm}_\nu - \partial_\nu\tilde{A}^{a,\pm}_\mu\Big) - gf^{abc}\Big(\bar{A}^b_\mu\bar{A}^c_\nu + \bar{A}^b_\mu\tilde{A}^{c,\pm}_\nu + \tilde{A}^{b,\pm}_\mu\bar{A}^c_\nu\Big) + \mathcal{O}\Big(\tilde{A}^2\Big). \end{aligned} \tag{4.15}$$

Calculating the contraction and neglecting all higher order terms in $\tilde{A}$, leads to the linearized Yang-Mills action

$$S_{YM}[\tilde{A},\bar{A}] = -\frac{1}{4}\int_{\mathcal{C}} \bar{F}^{\mu\nu,a}\bar{F}^a_{\mu\nu} + 4\Big(\partial_\mu\tilde{A}^{a,\pm}_\nu\Big)\bar{F}^{\mu\nu,a} + 4gf^{abc}\tilde{A}^{a,\pm}_\nu\bar{A}^b_\mu\bar{F}^{\mu\nu,c}d^4x + \mathcal{O}(\tilde{A}^2), \tag{4.16}$$

where $\bar{F}^{\mu\nu}$ is constructed from classical fields $\bar{A}_\mu$ only. A detailed derivation can be found in (Appendix B.1). The first term in (eq. 4.16) vanishes due to the integration along the time contour $\mathcal{C}$. The reason for that is, that the classical field $\bar{A}$ is not branch dependent and the forward and backward terms cancel each other

$$\begin{aligned} -\frac{1}{4}\int_{\mathcal{C}} \bar{F}^{\mu\nu,a}\bar{F}^a_{\mu\nu}d^4x =& -\frac{1}{4}\int_{\mathcal{C}^+} \bar{F}^{\mu\nu,a}\bar{F}^a_{\mu\nu}d^4x - \frac{1}{4}\int_{\mathcal{C}^-} \bar{F}^{\mu\nu,a}\bar{F}^a_{\mu\nu}d^4x \\ =& -\frac{1}{4}\int_{\mathcal{C}^+} \bar{F}^{\mu\nu,a}\bar{F}^a_{\mu\nu}d^4x + \frac{1}{4}\int_{\mathcal{C}^+} \bar{F}^{\mu\nu,a}\bar{F}^a_{\mu\nu}d^4x = 0. \end{aligned} \tag{4.17}$$

For the middle term in (eq. 4.16) we use partial integration once

$$-\int_{\mathcal{C}} \Big(\partial_\mu\tilde{A}^{a,\pm}_\nu\Big)\bar{F}^{\mu\nu,a}d^4x = \int_{\mathcal{C}} \tilde{A}^{a,\pm}_\nu\partial_\mu\bar{F}^{\mu\nu,a}d^4x. \tag{4.18}$$

Explicitly inserting the ansatz of the gauge fields (eq. 4.12) and splitting the contour integration into an integration along the forward and the backward contour, we find the following result

for the linearized version of the Yang-Mills action

$$\begin{aligned} S_{YM}[\tilde{A},\bar{A}] =& \frac{1}{2}\int_{\mathcal{C}} \mathrm{sgn}_{\mathcal{C}} \tilde{A}^a_\nu \Big(\partial_\mu \bar{F}^{\mu\nu,a} - g f^{abc} \bar{A}^b_\mu \bar{F}^{\mu\nu,c}\Big) d^4x \\ =& \frac{1}{2}\int_{\mathcal{C}^+} \tilde{A}^a_\nu \Big(\partial_\mu \bar{F}^{\mu\nu,a} - g f^{abc} \bar{A}^b_\mu \bar{F}^{\mu\nu,c}\Big) d^4x - \frac{1}{2}\int_{\mathcal{C}^-} \tilde{A}^a_\nu \Big(\partial_\mu \bar{F}^{\mu\nu,a} - g f^{abc} \bar{A}^b_\mu \bar{F}^{\mu\nu,c}\Big) d^4x \\ =& \int_{\mathcal{C}^+} \tilde{A}^a_\nu \Big(\partial_\mu \bar{F}^{\mu\nu,a} - g f^{abc} \bar{A}^b_\mu \bar{F}^{\mu\nu,c}\Big) d^4x. \end{aligned} \tag{4.19}$$

Inserting this result into the total partition function of the system, we find

$$Z_{\mathcal{C}} = \int \rho_A(t_0) e^{\mathrm{Tr}\log[D_{\mathcal{C}}^{-1}[A]] + \mathrm{i}\int_{\mathcal{C}^+} \tilde{A}^a_\nu \left(\partial_\mu \bar{F}^{\mu\nu,a} - g f^{abc} \bar{A}^b_\mu \bar{F}^{\mu\nu,c}\right) d^4x} [d\bar{A}][d\tilde{A}]. \tag{4.20}$$

In a final step, we want to specify the fermion sector in more detail. Our aim is to explicitly evaluate the fermion determinant, by expanding $\mathrm{Tr}\log\Delta_{\mathcal{C}}^{-1}[A]$ in a Taylor series as a function of $\tilde{A}$. In general, the inverse fermion propagator on the real-time contour $\mathcal{C}$ can be written as

$$\mathrm{i}D_{\mathcal{C}}^{-1}[A] = \Big(\mathrm{i}\partial\!\!\!/ - g A\!\!\!/(x) - m\Big)\delta_{\mathcal{C}}(x,y) = \Big(\mathrm{i}\partial\!\!\!/ - g\Big(\bar{A\!\!\!/}(x) + \frac{1}{2}\mathrm{sgn}_{\mathcal{C}}\tilde{A\!\!\!/}\Big) - m\Big)\delta_{\mathcal{C}}(x,y). \tag{4.21}$$

Because we neglect all terms of order $\mathcal{O}(\tilde{A}^2)$, it is sufficient to calculate the first and second term of the Taylor series. Carrying out the derivative

$$\frac{\partial}{\partial \tilde{A}^a_\mu} \log D_{\mathcal{C}}^{-1}[A]\Big|_{\tilde{A}=0} = D_{\mathcal{C}}[\bar{A}] \frac{\partial}{\partial \tilde{A}^a_\mu} D_{\mathcal{C}}^{-1}[A]\Big|_{\tilde{A}=0} = D_{\mathcal{C}}[\bar{A}] \mathrm{i}g\gamma^\mu \frac{1}{2}\mathrm{sgn}_{\mathcal{C}} T^a, \tag{4.22}$$

allows us to write the Taylor series of the inverse propagator at $\tilde{A} = 0$

$$\begin{aligned} \mathrm{Tr}\log D_{\mathcal{C}}^{-1}[A] =& \mathrm{Tr}\left(\log D_{\mathcal{C}}^{-1}[A]\Big|_{\tilde{A}=0} + \frac{\partial}{\partial \tilde{A}^a_\mu}\log D_{\mathcal{C}}^{-1}[A]\Big|_{\tilde{A}=0} \tilde{A}^a_\mu + \mathcal{O}(\tilde{A}^2)\right) \\ =& \mathrm{Tr}\log D_{\mathcal{C}}^{-1}[\bar{A}] + \frac{\mathrm{i}g}{2}\mathrm{Tr}\Big(D_{\mathcal{C}}[\bar{A}]\mathrm{sgn}_{\mathcal{C}}\tilde{A\!\!\!/}\Big) + \mathcal{O}(\tilde{A}^2), \end{aligned} \tag{4.23}$$

where $D_{\mathcal{C}}[\bar{A}]$ denotes the fermion propagator evaluated in the background of the classical field $\bar{A}$. With the first term in (eq. 4.23) only being dependent on the classical field $\bar{A}$, it does not contribute to the partition function when integrating along the closed time contour $\mathcal{C}$, because again contributions on the forward and backward branch cancel each other.[1] The partition function now takes the following form

$$Z_{\mathcal{C}} = \int \rho_A(t_0) e^{\frac{ig}{2}\mathrm{Tr}\left(D_{\mathcal{C}}[\bar{A}]\mathrm{sgn}_{\mathcal{C}}\tilde{A\!\!\!/}\right) + \mathrm{i}\int_{\mathcal{C}^+} \tilde{A}^a_\nu \left(\partial_\mu \bar{F}^{\mu\nu,a} - g f^{abc} \bar{A}^b_\mu \bar{F}^{\mu\nu,c}\right) d^4x} [d\bar{A}][d\tilde{A}]. \tag{4.24}$$

The remaining term of the Taylor expanded fermion determinant can be connected to the statistical fermion propagator. This can be seen, starting from the propagator of fermions on the Schwinger-Keldysh contour

$$D_{\mathcal{C}}(x,y) = \langle T_{\mathcal{C}} \psi(x)\bar{\psi}(y)\rangle_{\bar{A}}\,, \tag{4.25}$$

[1] The capital trace Tr[...] denotes the super-trace that includes a position and time integration along the Schwinger-Keldysh contour.

where the operator $T_{\mathcal{C}}$ enforces time ordering along the contour and $\langle ... \rangle_{\bar{A}}$ indicates, that the correlation function has to be evaluated in the background of the classical field $\bar{A}$.
This propagator can be decomposed into Wightman-functions, commonly defined in the context of thermal- or non-equilibrium quantum field theory [97]

$$D_{\mathcal{C}}[\bar{A}](x,y) = \theta_{\mathcal{C}}(x_0,y_0)D^{>}[\bar{A}](x,y) + \theta_{\mathcal{C}}(y_0,x_0)D^{<}[\bar{A}](x,y), \tag{4.26}$$

with $\theta_{\mathcal{C}}(x_0,y_0)$ the generalized Heaviside function on the Schwinger-Keldysh contour. In terms of spinor fields, these Wightman-functions are given as

$$D^{>}_{\alpha\beta}[\bar{A}](x,y) = \langle \psi_\alpha(x)\bar{\psi}_\beta(y)\rangle_{\bar{A}}\,, \qquad D^{<}_{\alpha\beta}[\bar{A}](x,y) = -\langle \bar{\psi}_\beta(y)\psi_\alpha(x)\rangle_{\bar{A}}\,. \tag{4.27}$$

We can now use (eq. 4.26) to reformulate the fermion trace entering the partition function (eq. 4.24)

$$\begin{aligned}
\mathrm{Tr}\Big(D_{\mathcal{C}}[\bar{A}]\mathrm{sgn}_{\mathcal{C}}\tilde{\not{A}}\Big) &= \mathrm{Tr}\Big(\Big(\theta_{\mathcal{C}}(x_0,y_0)D^{>}[\bar{A}](x,y) + \theta_{\mathcal{C}}(y_0,x_0)D^{<}[\bar{A}](x,y)\Big)\mathrm{sgn}_{\mathcal{C}}\tilde{\not{A}}\Big) \\
&= \int\limits_{\mathcal{C}}\int\limits_{\mathbf{x}}\int\limits_{\mathcal{C}}\int\limits_{\mathbf{y}} \mathrm{tr}\Big(\Big(\theta_{\mathcal{C}}(x_0,y_0)\mathrm{sgn}_{\mathcal{C}}D^{>}[\bar{A}](x,y) - \theta_{\mathcal{C}}(x_0,y_0)\mathrm{sgn}_{\mathcal{C}}D^{<}[\bar{A}](x,y)\Big)\tilde{\not{A}}\Big)\delta_{\mathcal{C}}(x,y)d^4xd^4y \\
&= \int\limits_{\mathcal{C}^+}\int\limits_{\mathbf{x}} \mathrm{tr}\Big(\Big(D^{>}[\bar{A}](x,x) + D^{<}[\bar{A}](x,x)\Big)\tilde{\not{A}}(x)\Big)d^4x.
\end{aligned} \tag{4.28}$$

The Wightman-functions and the statistical propagator are related in the following way

$$F_{\bar{A}}(x,y) = \frac{1}{2}\Big(D^{>}[\bar{A}](x,y) + D^{<}[\bar{A}](x,y)\Big) = \frac{1}{2}\,\langle[\psi(x),\bar{\psi}(y)]\rangle_{\bar{A}}\,, \tag{4.29}$$

hence

$$\frac{\mathrm{i}g}{2}\mathrm{Tr}\Big(D_{\mathcal{C}}[\bar{A}]\mathrm{sgn}_{\mathcal{C}}\tilde{\not{A}}\Big) = \mathrm{i}g\int\limits_{\mathcal{C}^+}\int\limits_{\mathbf{x}} \mathrm{tr}\Big(F_{\bar{A}}(x,x)\tilde{\not{A}}(x)\Big)d^4x = \mathrm{i}g\int\limits_{\mathcal{C}^+}\int\limits_{\mathbf{x}} \mathrm{tr}\Big(F_{\bar{A}}(x,x)\gamma^\mu T^a\Big)\tilde{A}^a_\mu(x)d^4x. \tag{4.30}$$

It is now possible to identify a fermion color-current in the integrand of (eq. 4.30)

$$J^{\mu,a}_{\bar{A}}(x) = -g\mathrm{tr}\Big(F_{\bar{A}}(x,x)\gamma^\mu T^a\Big), \tag{4.31}$$

allowing us to write the fermion trace entering the partition function (eq. 4.24) in the following way

$$\frac{\mathrm{i}g}{2}\mathrm{Tr}\Big(\Delta_{\mathcal{C}}[\bar{A}]\mathrm{sgn}_{\mathcal{C}}\tilde{\not{A}}\Big) = -\mathrm{i}\int\limits_{\mathcal{C}^+} J^{\mu,a}_{\bar{A}}(x)\tilde{A}^a_\mu(x)d^4x. \tag{4.32}$$

The partition function of the model is then given as

$$Z_{\mathcal{C}} = \int \rho_A(t_0)e^{\,\mathrm{i}\int_{\mathcal{C}^+}\tilde{A}_\nu(x)\Big(\partial_\mu\bar{F}^{\mu\nu,a} - gf^{abc}\bar{A}^b_\mu\bar{F}^{\mu\nu,c} - J^{\nu,a}_{\bar{A}}(x)\Big)d^4x}[d\bar{A}][d\tilde{A}]. \tag{4.33}$$

In a final step we integrate the quantum fluctuation $\tilde{A}$, leading to the effective semi-classical model. Before doing so, we have to specify the initial density matrix of the gauge fields. We

assume, that the initial state is only dependent on the classical gauge fields $\bar{A}$, which is indeed the case for the Glasma in our simulation.[2] Performing the integration we find

$$Z_{\mathcal{C}} = \int \rho_A[\bar{A}(t_0)]\delta\Big[\partial_\mu \bar{F}^{\mu\nu,a} - g f^{abc}\bar{A}^b_\mu \bar{F}^{\mu\nu,c} - J^{\nu,a}_{\bar{A}}\Big][d\bar{A}]. \tag{4.34}$$

It is possible to identify the classical Yang-Mills equation of the gauge fields $\bar{A}$ in (eq. 4.34), familiar from (eq. 1.21). The fermions enter this equation via a color current $J^{\nu,a}_{\bar{A}}$. The delta function thus enforces an evolution equation for the semi-classical system

$$\partial_\mu \bar{F}^{\mu\nu,a} - g f^{abc}\bar{A}^b_\mu \bar{F}^{\mu\nu,c} = J^{\nu,a}_{\bar{A}} = -g\mathrm{tr}\Big(F_{\bar{A}}(x,x)\gamma^\nu T^a\Big). \tag{4.35}$$

This equation will be referred to as the equation of motion of the semi-classical model.

We derived (eq. 4.35) in the $N_f = 1$ flavor case. The derivation can easily be extended to an arbitrary number of degenerate flavors. Considering N_f degenerate flavors, the flavor trace of the statistical fermion propagator, entering the fermion current (eq. 4.31), simply picks up an additional factor of N_f. This will be of great use later, when considering degenerate up- and down-quarks.

It is possible to derive the equation of motion for the chromo-electric field from (eq. 4.35), setting $\nu = i$

$$\partial_0 F^{0i,a}(x) + \partial_j F^{ji,a}(x) - g f^{abc} A^b_j(x) F^{ji,c}(x) = J^{i,a}_{\bar{A}}(x). \tag{4.36}$$

Identifying the chromo-electric fields (eq. 1.17) leads to the evolution equation

$$\partial_t E^a_i(x) = -J^{i,a}_{\bar{A}}(x) + \partial_j F^{ji,a}(x) - g f^{abc} A^b_j(x) F^{ji,c}(x). \tag{4.37}$$

When setting $\nu = 0$ in the evolution equation of the semi-classical model (eq. 4.35) an additional equation is found, that imposes a constraint on the systems dynamics

$$\partial_i F^{i0,a}[\bar{A}](x) - g f^{abc}\bar{A}^b_i(x) F^{i0,c}[\bar{A}](x) = J^{0,a}_{\bar{A}}. \tag{4.38}$$

This equation is referred to as Gauss constraint and will be discussed in detail at the end of this chapter.

4.3.1 The Semi-Classical Model on the Lattice

Having derived the semi-classical model and the corresponding evolution equation (eq. 4.35) in the continuum, let us discretize the results, making it accessible in a lattice simulation. For the Yang-Mills part, that enters (eq. 4.37), it is straight forward to replace the continuum Yang-Mills equation by its lattice counterpart, making use of (eq. 2.14),

$$\partial_t E^a_i(x) = -J^{i,a}_{\bar{A}}(x) + \frac{2}{ga^3}\sum_{j\neq i}\mathrm{Im}\mathrm{tr}\Big[T^a\Big(U_{ji}(x) + U_{-ji}(x)\Big)\Big]. \tag{4.39}$$

[2] In [72] it has been pointed out, that in general one could also Wigner transform the density matrix with respect to the quantum fluctuation field $\tilde{A}$, linearizing it in the quantum fluctuation. Afterwards one could proceed integrating the quantum fluctuation $\tilde{A}$, leading to a more general definition of the model.

The discretization of the fermion current $J^{i,a}_{\tilde{A}}(x)$ is realized, by making use of the lattice inverse Dirac operator, discussed in (section 2.3),

$$D^{-1}_{\mathcal{C}}[A](x,x) = \frac{1}{2a_\mu}\Big(\big(\gamma^\mu - \mathrm{i}r\big)U_\mu(y)\delta_{x+\hat{\mu},y} - \big(\gamma^\mu + \mathrm{i}r\big)U^\dagger_\mu(x-\hat{\mu})\delta_{x-\hat{\mu},y}\Big) - \Big(m + \frac{3r}{a}\Big)\delta_{x,y}, \tag{4.40}$$

where we additionally discretized the time direction, indicating $a_0 = a_t$ and $a_i = a$. We formally include U_0 as well, although it is set to one in temporal gauge.

As presented in the continuum (eq. 4.23), we now perform a Taylor series for the inverse lattice propagator

$$\begin{aligned}&\frac{\partial}{\partial\tilde{A}^a_\mu(x)}D^{-1}_{\mathcal{C}}[A](x,x) \\ &\quad= \frac{1}{2a_\mu}\Big(\big(\gamma^\mu - \mathrm{i}r\big)\frac{\partial}{\partial\tilde{A}^a_\mu(x)}U_\mu(x)\delta_{x+\hat{\mu},y} - \big(\gamma^\mu + \mathrm{i}r\big)\frac{\partial}{\partial\tilde{A}^a_\mu(x)}U^\dagger_\mu(x-\hat{\mu})\delta_{x-\hat{\mu},y}\Big),\end{aligned} \tag{4.41}$$

where the derivative of the gauge link is given as

$$\frac{\partial}{\partial\tilde{A}^a_\mu(x)}U_\mu(x) = \frac{\partial}{\partial\tilde{A}^a_\mu(x)}\exp\left[\mathrm{i}ga_\mu\Big(\bar{A}^a_\mu(x) + \frac{1}{2}\mathrm{sgn}_{\mathcal{C}}\tilde{A}^a_\mu(x)\Big)T^a\right] = \frac{\mathrm{i}g}{2}a_\mu\mathrm{sgn}_{\mathcal{C}}T^aU_\mu(x). \tag{4.42}$$

Comparing (eq. 4.41) and (eq. 4.42) to (eq. 4.22), we find a similar structure on the lattice, making it straight forward to repeat the previous steps presented for the continuum, to derive the following lattice version of the current [72]

$$J^{\nu,a}_{\tilde{A}}(x) = -\frac{g}{2}\Big(\mathrm{tr}\Big(F(x+\hat{\nu},x)\big(\gamma^\nu - \mathrm{i}r\big)T^aU_\nu(x)\Big) + \mathrm{tr}\Big(F(x,x+\hat{\nu})\big(\gamma^\nu + \mathrm{i}r\big)U^\dagger_\nu(x)T^a\Big)\Big). \tag{4.43}$$

The current picks up two terms, due to the structure of (eq. 4.41), but it is possible to simplify it, using

$$\begin{aligned}F(x,x+\hat{\nu}) = F^\dagger(x+\hat{\nu},x) =& \frac{1}{2}\Big\langle\Big[\psi(x+\hat{\nu}),\bar{\psi}(x)\Big]\Big\rangle^\dagger \\ =& \gamma^0\frac{1}{2}\Big\langle\Big[\psi(x),\bar{\psi}^\dagger(x+\hat{\nu})\Big]\Big\rangle\gamma^0 = \gamma^0F(x,x+\hat{\nu})\gamma^0.\end{aligned} \tag{4.44}$$

Making use of this property and the cyclicity of the trace, we find

$$\begin{aligned}\mathrm{tr}\Big(F(x,x+\hat{\nu})\big(\gamma^\nu + \mathrm{i}r\big)U^\dagger_\nu(x)T^a\Big) =& \mathrm{tr}\Big(F^\dagger(x+\hat{\nu},x)\big(\gamma^0\gamma^\nu\gamma^0 + \mathrm{i}r\big)U^\dagger_\nu(x)T^a\Big) \\ =& \mathrm{tr}\Big(\Big(T^aU_\mu(x)\big(\gamma^\mu - \mathrm{i}r\big)F(x+\hat{\mu},x)\Big)^\dagger\Big) \\ =& \mathrm{tr}^\star\Big(F(x+\hat{\mu},x)\big(\gamma^\mu - \mathrm{i}r\big)T^aU_\mu(x)\Big).\end{aligned} \tag{4.45}$$

The fermion current can now be written as

$$\begin{aligned}J^{\nu,a}_{\tilde{A}}(x) =& -\frac{g}{2}\Big(\mathrm{tr}\Big(F(x+\hat{\nu},x)\big(\gamma^\nu - \mathrm{i}r\big)T^aU_\nu(x)\Big) + \mathrm{tr}^\star\Big(F(x+\hat{\nu},x)\big(\gamma^\nu - \mathrm{i}r\big)T^aU_\nu(x)\Big)\Big) \\ =& -g\mathrm{Retr}\Big(F(x+\hat{\nu},x)\big(\gamma^\nu - \mathrm{i}r\big)T^aU_\nu(x)\Big).\end{aligned} \tag{4.46}$$

We find the following lattice version of the chromo-electric field equation of motion of the semi-classical approximation

$$\partial_t E_i^a(x) = g\mathrm{Retr}\Big(F(x+\hat{i},x)\big(\gamma^i - \mathrm{i}r\big)T^a U_i(x)\Big) + \frac{2}{ga^3}\sum_{j\neq i}\mathrm{Imtr}\Big[T^a\Big(U_{ji}(x) + U_{-ji}(x)\Big)\Big]. \tag{4.47}$$

As discussed in (section 2.2.2), the statistical propagator that enters the fermion current (eq. 4.46) can be evaluated in a simulation as an ensemble average of stochastic low-cost fermions.

4.3.2 The Gauss Constraint

From the equation of motion of the semi-classical model (eq. 4.35), we identified an additional constraint (eq. 4.38), referred to as Gauss constraint. This non-abelian variant of Gauss law has to be satisfied at every time-step of a lattice simulation. It is possible to rewrite (eq. 4.38) as a function of the chromo-electric field (eq. 1.17)

$$\partial_i E_i^a(x) - g f^{abc}\bar{A}_i^b(x)E_i^c(x) = -g\mathrm{tr}\Big(F_{\bar{A}}(x,x)\gamma^0 T^a\Big). \tag{4.48}$$

Looking at the left-hand side of the equation, we note that it can be written as

$$\begin{aligned}\Big[D_i, E_i(x)\Big] &= \partial_i E_i(x) + \mathrm{i}g\bar{A}_i^a(x)E_i^b(x)\Big[T^a, T^b\Big] \\ &= \partial_i E_i(x) - g f^{abc}T^a\bar{A}_i^b(x)E_i^c(x) = -gT^a\mathrm{tr}\Big(F_{\bar{A}}(x,x)\gamma^0 T^a\Big).\end{aligned} \tag{4.49}$$

In case of a $U(1)$ theory, (eq. 4.49) would reproduce the familiar Gauss law of electrodynamics, which explains the origin of the name.

Within the CGC effective theory, derived in (section 3.3.1), one would expect the Gauss constraint to be satisfied at all time-steps in a simulation, but in fact the constraint can be violated due to numerical reasons [126]. A numerical violation can happen due to rounding errors, that particularly play an important role in pure Yang-Mills simulations [143]. In our simulation, there is another source for numerical uncertainties, which is the statistical nature of fermion expectation values, that are calculated as ensemble averages of stochastic low-cost fermions. Although the error decreases with $1/\sqrt{N_{ens}}$, we would require very huge ensembles to minimize the error, which are numerically out of reach. We will investigate this further in (chapter 7). A way to restore the Gauss constraint in a simulation has first been presented in [143] for a pure Yang-Mills theory, providing an algorithm, that is able to restore Gauss law at every time-step of the simulation. We will adapt this algorithm to a simulation including fermions.

With the fermion fields and the chromo-electric fields being located on the lattice points, it is possible to define a parallel transport along a direction $\hat{i}$ to the nearest neighbor lattice point

$$E_i(x) \quad \rightarrow \quad U_i^\dagger(x)E_i(x)U_i(x). \tag{4.50}$$

Following [143] the amount of Gauss violation at a lattice point in a pure Yang-Mills theory is given as the difference of chromo-electric flux leaving a link subtracting the flux entering the link

$$0 = \frac{1}{a}\sum_i\Big[E_i(x) - U_i^\dagger(x-\hat{i})E_i(x-\hat{i})U_i(x-\hat{i})\Big]. \tag{4.51}$$

One easily proves by taking the continuum limit, that the given ansatz for the lattice reproduces the continuum Gauss law (eq. 4.48)

$$\begin{aligned} 0 =& \frac{1}{a}\sum_i \Big[E_i(x) - U_i^\dagger(x-\hat{i})E_i(x-\hat{i})U_i(x-\hat{i})\Big] \\ =& \sum_i \left[\frac{E_i(x)-E_i(x-\hat{i})}{a} + \mathrm{i}gA_i^a(x-\hat{x})E_i^b(x-\hat{i})\Big[T^a,T^b\Big]\right] + \mathcal{O}(a) \\ =& \sum_i \Big[\partial_i E_i(x) - gf^{abc}T^aA_i^b(x-\hat{x})E_i^c(x-\hat{i})\Big] + \mathcal{O}(a). \end{aligned} \tag{4.52}$$

With the presence of fermions (eq. 4.51) becomes

$$\frac{1}{a}\sum_i \Big[E_i(x) - U_i^\dagger(x-\hat{i})E_i(x-\hat{i})U_i(x-\hat{i})\Big] = -gT^a\mathrm{Retr}\Big(F(x+\hat{0},x)\gamma^0T^a\Big), \tag{4.53}$$

in temporal gauge $U_0 = 1$. One easily checks by inserting (eq. 4.52), that the continuum Gauss law (eq. 4.48) is reproduced, when taking the continuum limit.

If the Gauss constraint is violated at a given time-step in the simulation, (eq. 4.53) picks up a finite value

$$C(x) := \sum_i \Big[\bar{E}_i(x) - U_i^\dagger(x-\hat{i})\bar{E}_i(x-\hat{i})U_i(x-\hat{i})\Big] + g^2T^a\mathrm{Retr}\Big(\bar{F}(x+\hat{0},x)\gamma^0T^a\Big), \tag{4.54}$$

where $C(x)$ is a matrix in color space, defined at every lattice point $\mathbf{x}$ at time t. We can define the time dependent amount of Gauss violation, by taking a lattice average

$$C(t) = \sqrt{\frac{1}{V}\sum_{\mathbf{x}} \mathrm{tr}\Big(C^\dagger(x)C(x)\Big)}. \tag{4.55}$$

We now restore Gauss law in a simulation by using the following algorithm [143]:
First, we evaluate $C(t)$ at a given time-step to check if Gauss law is satisfied. If not, the chromo-electric fields are modified, introducing the following shift

$$\tilde{E}_i(x) \;\rightarrow\; \tilde{E}_i(x) + \gamma\Big[U_i(x)C(x+\hat{i})U_{-i}(x+\hat{i}) - C(x)\Big]. \tag{4.56}$$

Now, we evaluate $C(t)$ again and check for convergence. The algorithm stops as soon as the Gauss constraint is satisfied to sufficient precision. The constant γ, appearing in the definition of the shift (eq. 4.56), is a numerical fine tuning parameter and has to be chosen appropriately.

5

Renormalization of the Semi-Classical Model

In this chapter we will discuss a renormalization procedure for the semi-classical effective theory presented in the previous chapter. There are two important facts to keep in mind:
When constructing the Glasma initial state for the Yang-Mills sector of the theory in (chapter 3), we assumed that the gauge fields are classical to leading order. The amplitudes of the classical gauge fields are thus of the order $\bar{A} \sim \mathcal{O}(1/g)$ and these fields cannot participate in quantum corrections within the semi-classical effective theory, due to the classicality. In the language of Feynman diagrams, this translates to the fact, that gauge fields can not enter as internal lines and especially there are no closed loops constructed from gauge lines. The situation is different for the fermion fields. According to Paulis exclusion principle, fermions are always of quantum nature. As a consequence, closed fermion loops can be present in the semi-classical model.
On the other hand, it is impossible to perform a continuum limit in the lattice regularized semi-classical effective theory, because the classical Yang-Mills fields are UV-divergent (Rayleigh-Jeans divergences). As a consequence, the theory is naturally regularized by the momentum cutoff of the lattice and loop diagrams are not divergent anymore. Nevertheless, fermion loops impose a correction to the classical gauge fields $\bar{A}$, making a rigorous treatment in terms of a renormalization procedure necessary, to achieve the correct dynamics of the system. This has first been pointed out in context of stochastic low-cost fermions coupled to scalar fields in [101] and we will adapt the procedure to our model.

5.1 Strategy of the Renormalization

How the semi-classical approximation can be affected by divergencies, that arise from fermion loop contributions, becomes clear when studying the trace of the equal position statistical propagator, that enters the fermion color-current of the equation of motion of the classical Yang-Mills fields (eq. 4.31). This becomes utterly clear when expanding the current in terms of the classical gauge field $\bar{A}$ to n-th order, creating a series of fermion loop diagrams with n external boson lines. As stated in [101] these diagrams are (potentially) divergent in $d = 3 + 1$ dimensions making a renormalization procedure necessary.

It is possible to study such divergencies in a simple „toy-model“, considering the trace of

a equal position statistical propagator $F(x,x)$, evaluated from vacuum fermions, that enter the semi-classical model as initial condition. Inserting the result of the vacuum statistical propagator (eq. 1.47), a quick calculation leads to

$$\mathrm{tr}\Big(F(x,x)\Big) = \mathrm{tr}\bigg(\int \frac{p_i\gamma^i + m}{2\sqrt{\mathbf{p}^2+m^2}}\frac{d^3p}{(2\pi)^3}\bigg) \sim \int \frac{4m}{2|p|}\frac{d^3p}{(2\pi)^3} \sim \int_0^\infty \frac{m}{p}p^2dp, \tag{5.1}$$

which is obviously divergent. The fact that expectation values of bilinear field operators at equal position are divergent is well known and has e.g. been studied in [144].

The strategy of renormalization is now based on a wave function renormalization, entering the Yang-Mills sector. The corresponding Z-factor can be derived from a fermion loop correction to the classical field $\bar{A}$. As discussed in [101], for the computation of the renormalization Z-factor we linearize the equation of motion, keeping the first fermion loop correction to the classical gauge field. This technique has first been discussed in [98, 145] for a model of overoccupied, classical scalar fields interacting with fermions. In a next step, one can identify the fermion self energy $\Sigma(x-z)$, making it possible to evaluate the renormalization Z-factor in the following way [101]

$$\delta Z = \frac{\partial^2\Sigma(k_0,\mathbf{k})}{\partial k_0^2}\bigg|_{\mathbf{k}=0}, \tag{5.2}$$

where we choose the renormalization scale to be $\mathbf{k}=0$.
A Fourier transformation in k_0 allows us to rewrite this equation as

$$\delta Z = N_f \int_0^\infty \frac{t^2}{2}\Sigma(t,\mathbf{k})\bigg|_{\mathbf{k}=0} dt. \tag{5.3}$$

This integral can only be solved under the assumption, that the oscillatory parts entering the integrand from the fermion self energy are incoherent at large times and can be averaged away [101].

In the following, we adapt this procedure to classical $SU(3)$ gauge fields coupled to fermions. The Z-factor then enters the Yang-Mills part of the equation of motion and the observables from a counterterm renormalization. We emphasize that this approach matches previous studies of classical $SU(2)$ gauge fields, coupled to scalar Higgs fields and low-cost fermions, presented in [146, 147].

5.2 One-Loop Semi-Classical Equation of Motion

For the derivation of the fermion one-loop semi-classical equation of motion of the semi-classical model, we start from the Lagrangian of one-flavor QCD (eq. 1.2). We first take the familiar ansatz for the gauge field (eq. 4.12) and linearize the Lagrangian of the Yang-Mills sector in the quantum fluctuation $\tilde{A}$, as discussed in (Appendix B.1)

$$\mathcal{L}[\tilde{A},\bar{A}] = -\frac{1}{4}\bar{F}^{\mu\nu,a}\bar{F}^a_{\mu\nu} - \frac{1}{4}\tilde{G}^{\mu\nu,a,\pm}\tilde{G}^{a,\pm}_{\mu\nu} - \Big(\partial_\mu\tilde{A}^{a,\pm}_\nu\Big)\bar{F}^{\mu\nu,a} - gf^{abc}\tilde{A}^{a,\pm}_\nu\bar{A}^b_\mu\bar{F}^{\mu\nu,c} + \mathcal{O}(\tilde{A}^2). \tag{5.4}$$

We kept the non-interacting dynamics term of the quantum fluctuation $\tilde{A}$, that is formally of second order

$$\tilde{G}^{a,\pm}_{\mu\nu} = \partial_\mu \tilde{A}^{a,\pm}_\nu - \partial_\nu \tilde{A}^{a,\pm}_\mu. \tag{5.5}$$

The fermion fields have to be evaluated on the Schwinger-Keldysh contour (figure 4.1) as well. We introduce an index $\pm$, indicating if the field is located on the upper or the lower branch of the contour. With the ansatz for the gauge fields (eq. 4.12), the Lagrangian of the fermion sector can now be written as

$$\begin{aligned}\mathcal{L}_f &= \bar{\psi}^\pm \Big[\mathrm{i}\gamma^\mu \partial_\mu - g\gamma^\mu \Big(\bar{A}^a_\mu + \tilde{A}^{a,\pm}_\mu \Big) T^a - m \Big] \psi^\pm \\ &= \bar{\psi}^\pm \Big(\mathrm{i}\gamma^\mu \partial_\mu - m \Big) \psi^\pm - g\bar{\psi}^\pm \gamma^\mu \bar{A}^a_\mu T^a \psi^\pm - g\bar{\psi}^\pm \gamma^\mu \tilde{A}^{a,\pm}_\mu T^a \psi^\pm,\end{aligned} \tag{5.6}$$

following [145] the effective Lagrangian of QCD on the Schwinger-Keldysh contour is therefore given as

$$\begin{aligned}\mathcal{L}(A^\pm_\mu, \bar{\psi}^\pm, \psi^\pm) =& \mathcal{L}(A^+_\mu, \bar{\psi}^+, \psi^+) - \mathcal{L}(A^-_\mu, \bar{\psi}^-, \psi^-) \\ =& \mathcal{L}_{free}(\tilde{A}^\pm_\mu, \bar{\psi}^\pm, \psi^\pm) - \Big(\partial_\mu \tilde{A}^{a,+}_\nu - \partial_\mu \tilde{A}^{a,+}_\nu \Big) \bar{F}^{\mu\nu,a} - g f^{abc} \Big(\tilde{A}^{a,+}_\nu - \tilde{A}^{a,-}_\nu \Big) \bar{A}^b_\mu \bar{F}^{\mu\nu,c} \\ & - g\bar{\psi}^+ \gamma^\mu \Big(\bar{A}^a_\mu + \tilde{A}^{a,+}_\mu \Big) T^a \psi^+ + g\bar{\psi}^- \gamma^\mu \Big(\bar{A}^a_\mu + \tilde{A}^{a,-}_\mu \Big) T^a \psi^-,\end{aligned} \tag{5.7}$$

where we identified the free Lagrangian of the theory. Using partial integration once, the effective action is then given as

$$\begin{aligned}S_{eff}[A^\pm_\mu, \bar{\psi}^\pm, \psi^\pm] = \int & \mathcal{L}_{free}(\tilde{A}^\pm_\mu, \bar{\psi}^\pm, \psi^\pm) + \Big(\tilde{A}^{a,+}_\nu - \tilde{A}^{a,-}_\nu \Big) \Big[\partial_\mu \bar{F}^{\mu\nu,a} - g f^{abc} \bar{A}^b_\mu \bar{F}^{\mu\nu,c} \Big] \\ & - g\bar{\psi}^+ \gamma^\mu \Big(\bar{A}^a_\mu + \tilde{A}^{a,+}_\mu \Big) T^a \psi^+ + g\bar{\psi}^- \gamma^\mu \Big(\bar{A}^a_\mu + \tilde{A}^{a,-}_\mu \Big) T^a \psi^- d^4x.\end{aligned} \tag{5.8}$$

As discussed in [98], the equation of motion of the theory can now be derived from

$$\Big\langle \tilde{A}^{d,+}_\alpha(y) \Big\rangle = \int \tilde{A}^{d,+}_\alpha(y) e^{\mathrm{i}S_{eff}[A^\pm_\mu, \bar{\psi}^\pm, \psi^\pm]} [d\tilde{A}_\mu][d\bar{\psi}^\pm][d\psi^\pm] = 0. \tag{5.9}$$

The procedure can easily be demonstrated in a pure Yang-Mills theory, by expanding the exponential in orders of $\mathcal{O}(\tilde{A})$

$$\begin{aligned}e^{S_{eff}[A^\pm_\mu]} =& e^{\mathrm{i}S^{free}_{eff}[\tilde{A}_\mu]} \exp\left(\mathrm{i} \int \Big(\tilde{A}^{a,+}_\nu - \tilde{A}^{a,-}_\nu \Big) \Big[\partial_\mu \bar{F}^{\mu\nu,a} - g f^{abc} \bar{A}^b_\mu \bar{F}^{\mu\nu,c} \Big] d^4x \right) \\ =& e^{\mathrm{i}S^{free}_{eff}[\tilde{A}_\mu]} \left(1 + \mathrm{i} \int \Big(\tilde{A}^{a,+}_\nu - \tilde{A}^{a,-}_\nu \Big) \Big[\partial_\mu \bar{F}^{\mu\nu,a} - g f^{abc} \bar{A}^b_\mu \bar{F}^{\mu\nu,c} \Big] d^4x + \mathcal{O}(\tilde{A}^2) \right).\end{aligned} \tag{5.10}$$

Evaluating the expectation value leads to

$$\begin{aligned}\Big\langle \tilde{A}^{d,+}_\alpha(y) \Big\rangle =& \int \tilde{A}^{d,+}_\alpha(y) e^{\mathrm{i}S^{free}_{eff}[\tilde{A}_\mu]} \\ & \times \left(1 + \mathrm{i} \int \Big(\tilde{A}^{a,+}_\nu - \tilde{A}^{a,-}_\nu \Big) \Big[\partial_\mu \bar{F}^{\mu\nu,a} - g f^{abc} \bar{A}^b_\mu \bar{F}^{\mu\nu,c} \Big] d^4x + \mathcal{O}(\tilde{A}^2) \right) \Big[d\tilde{A}_\mu \Big] \\ =& \Big\langle \tilde{A}^{d,+}_\alpha(y) \Big\rangle_0 \\ & + \mathrm{i} \int \Big(\Big\langle \tilde{A}^{d,+}_\alpha(y) \tilde{A}^{a,+}_\nu \Big\rangle_0 - \Big\langle \tilde{A}^{d,+}_\alpha(y) \tilde{A}^{a,-}_\nu \Big\rangle_0 \Big) \Big[\partial_\mu \bar{F}^{\mu\nu,a} - g f^{abc} \bar{A}^b_\mu \bar{F}^{\mu\nu,c} \Big] d^4x \\ =& 0,\end{aligned} \tag{5.11}$$

where we introduced the single-field expectation value with respect to the free theory

$$\left\langle \tilde{A}^{d,+}_{\alpha}(y)\right\rangle_0 = \int \tilde{A}^{d,+}_{\alpha}(y) e^{\mathrm{i}S^{free}_{eff}[\tilde{A}_\mu]} D\tilde{A}_\mu = 0. \tag{5.12}$$

Since the two point functions satisfy $\left\langle \tilde{A}^{d,+}_{\alpha}(y)\tilde{A}^{a,+}_{\nu}\right\rangle_0 \neq \left\langle \tilde{A}^{d,+}_{\alpha}(y)\tilde{A}^{a,-}_{\nu}\right\rangle_0$, we can deduce the Yang-Mills equation as the equation of motion of the classical Yang-Mills theory

$$\partial_\mu \bar{F}^{\mu\nu,a}(x) - g f^{abc}\bar{A}^b_\mu(x)\bar{F}^{\mu\nu,c}(x) = 0. \tag{5.13}$$

Having demonstrated the procedure in pure Yang-Mills theory, let us now turn to the full theory, including fermions. We already derived the full equation of motion of the semi-classical model in (section 4.3) and therefore restrict ourselves to the one-loop version here. Expanding the Yang-Mills sector of (eq. 5.9) in $\mathcal{O}(\tilde{A})$ we find

$$\begin{aligned}\left\langle \tilde{A}^{d,+}_{\alpha}(y)\right\rangle =& \int \Bigg(\tilde{A}^{d,+}_{\alpha}(y) e^{\mathrm{i}\int \mathcal{L}_{free}(\tilde{A}^{\pm}_\mu,\bar{\psi}^{\pm},\psi^{\pm}) - g\bar{\psi}^+\gamma^\mu\left(\bar{A}^a_\mu+\tilde{A}^{a,+}_\mu\right)T^a\psi^+ + g\bar{\psi}^-\gamma^\mu\left(\bar{A}^a_\mu+\tilde{A}^{a,-}_\mu\right)T^a\psi^- d^4x} \\ &\times \left[1 + \mathrm{i}\int \left(\tilde{A}^{a,+}_\nu - \tilde{A}^{a,-}_\nu\right)\left[\partial_\mu \bar{F}^{\mu\nu,a} - g f^{abc}\bar{A}^b_\mu \bar{F}^{\mu\nu,c}\right] d^4x\right]\Bigg)\left[d\tilde{A}_\mu\right]\left[d\bar{\psi}\right]\left[d\psi\right] \\ =&0.\end{aligned} \tag{5.14}$$

The remaining exponential still contains all interaction terms with fermion fields to arbitrary order, which enter the fermion current (eq. 4.31) derived in (section 4.3). For a derivation of the one-loop equation of motion, we make use of the assumption of the CGC effective theory, that $\mathcal{O}(g\bar{A})$ is small, because classical field modes are highly occupied, allowing us to only keep interaction terms of fermions and classical gauge fields, that are linear in the classical field. Within this assumption, we linearize our theory, making it possible to derive the one-loop equation of motion. After neglecting all terms that are of higher order, (eq. 5.9) reduces to

$$\begin{aligned}\left\langle \tilde{A}^{d,+}_{\alpha}(y)\right\rangle =& \mathrm{i}\int \left(\left\langle \tilde{A}^{d,+}_{\alpha}(y)\tilde{A}^{a,+}_{\nu}(x)\right\rangle_0 - \left\langle \tilde{A}^{d,+}_{\alpha}(y)\tilde{A}^{a,-}_{\nu}(x)\right\rangle_0 \right)\left[\partial_\mu \bar{F}^{\mu\nu,a} - g f^{abc}\bar{A}^b_\mu \bar{F}^{\mu\nu,c}\right] d^4x \\ &+ \mathrm{i}g\int \Big(\left\langle \tilde{A}^{d,+}_{\alpha}(y)\tilde{A}^{a,-}_{\nu}(x)\right\rangle_0 \left\langle \bar{\psi}^-(x)\gamma^\nu T^a \psi^-(x)\right\rangle_0 \\ &\qquad - \left\langle \tilde{A}^{d,+}_{\alpha}(y)\tilde{A}^{a,+}_{\nu}(x)\right\rangle_0 \left\langle \bar{\psi}^+(x)\gamma^\nu T^a \psi^+(x)\right\rangle_0 \Big) d^4x \\ &- g^2 \int\int \left\langle \tilde{A}^{d,+}_{\alpha}(y)\tilde{A}^{a,+}_{\nu}(x)\right\rangle_0 \Big(\left\langle \bar{\psi}^+(x)\gamma^\nu T^a \psi^+(x)\bar{\psi}^+(z)\gamma^\mu T^b \psi^+(z)\right\rangle_0 \\ &\qquad - \left\langle \bar{\psi}^+(x)\gamma^\nu T^a \psi^+(x)\bar{\psi}^-(z)\gamma^\mu T^b \psi^-(z)\right\rangle_0 \Big)\bar{A}^b_\mu(z) d^4x d^4z \\ &\quad + \left\langle \tilde{A}^{d,+}_{\alpha}(y)\tilde{A}^{a,-}_{\nu}(x)\right\rangle_0 \Big(\left\langle \bar{\psi}^-(x)\gamma^\nu T^a \psi^-(x)\bar{\psi}^-(z)\gamma^\mu T^b \psi^-(z)\right\rangle_0 \\ &\qquad - \left\langle \bar{\psi}^-(x)\gamma^\nu T^a \psi^-(x)\bar{\psi}^+(z)\gamma^\mu T^b \psi^+(z)\right\rangle_0 \Big)\bar{A}^b_\mu(z) d^4x d^4z \\ =&0,\end{aligned} \tag{5.15}$$

where we introduced the fermion expectation value

$$\left\langle \bar{\psi}^-(x)\gamma^\nu T^a \psi^-(x)\right\rangle_0 = \langle 0|\, \bar{\psi}^-(x)\gamma^\nu T^a \psi^-(x)\,|0\rangle = \int \bar{\psi}^-(x)\gamma^\nu T^a \psi^-(x) e^{\mathrm{i}S^{free}_{eff}[\bar{\psi}^{\pm},\psi^{\pm}]}\left[d\bar{\psi}\right]\left[d\psi\right], \tag{5.16}$$

taken with respect to the non-interacting vacuum $|0\rangle$.

It is now possible to deduce the following one-loop equations of motion from (eq. 5.15)

$$\partial_\mu \bar{F}^{\mu\nu,a} - g f^{abc} \bar{A}^b_\mu \bar{F}^{\mu\nu,c} - g \left\langle \bar{\psi}^+(x)\gamma^\nu T^a \psi^+(x) \right\rangle + \mathrm{i}g^2 \int \Big(\left\langle \bar{\psi}^+(x)\gamma^\nu T^a \psi^+(x) \bar{\psi}^+(z)\gamma^\mu T^b \psi^+(z) \right\rangle - \left\langle \bar{\psi}^+(x)\gamma^\nu T^a \psi^+(x) \bar{\psi}^-(z)\gamma^\mu T^b \psi^-(z) \right\rangle \Big) \bar{A}^b_\mu(z) d^4z = 0, \tag{5.17}$$

$$\partial_\mu \bar{F}^{\mu\nu,a} - g f^{abc} \bar{A}^b_\mu \bar{F}^{\mu\nu,c} - g \left\langle \bar{\psi}^-(x)\gamma^\nu T^a \psi^-(x) \right\rangle - \mathrm{i}g^2 \int \Big(\left\langle \bar{\psi}^-(x)\gamma^\nu T^a \psi^-(x) \bar{\psi}^-(z)\gamma^\mu T^b \psi^-(z) \right\rangle - \left\langle \bar{\psi}^-(x)\gamma^\nu T^a \psi^-(x) \bar{\psi}^+(z)\gamma^\mu T^b \psi^+(z) \right\rangle \Big) \bar{A}^b_\mu(z) d^4z = 0. \tag{5.18}$$

One can demonstrate, that these equations are equivalent, identifying the fermion self energy

$$\Sigma^{\mu\nu,ab}(t-t', \mathbf{x}-\mathbf{z}) = ig^2 \mathrm{tr}\Big[D^<(t-t', \mathbf{x}-\mathbf{z})\gamma^\mu T^b D^<(t'-t, \mathbf{z}-\mathbf{x})\gamma^\nu T^a - D^>(t-t', \mathbf{x}-\mathbf{z})\gamma^\mu T^b D^<(t'-t, \mathbf{z}-\mathbf{x})\gamma^\nu T^a \Big], \tag{5.19}$$

with $D^{\lessgtr}$ denoting the Wightman-functions, familiar from (section 4.3). With the help of (eq. 5.19) and the definition of the statistical propagator (eq. 1.44), (eq. 5.17) and (eq. 5.18) lead to the fermion one-loop equation of motion of the classical Yang-Mills fields $\bar{A}$

$$\partial_\mu \bar{F}^{\mu\nu,a} - g f^{abc} \bar{A}^b_\mu \bar{F}^{\mu\nu,c} - 2g \mathrm{tr}\Big[F(x,x)\gamma^\nu T^a \Big] + \int_0^t \Sigma^{\mu\nu,ab}(x-z) \bar{A}^b_\mu(z) d^4z = 0. \tag{5.20}$$

A detailed derivation of this result can be found in (Appendix B.2).

5.3 Calculation of the Z-factor

In a first step, we perform a spacial Fourier transformation for the calculation of the Z-factor. The corresponding Fourier transformed classical gauge field is given as

$$\bar{A}^\mu_{\mathbf{k}}(t) = \int \bar{A}^\mu(t, \mathbf{x}) e^{-\mathrm{i}\mathbf{k}\mathbf{x}} d^3x, \tag{5.21}$$

The fermion self energy, that enters (eq. 5.20), can then be rewritten by making use of the convolution theorem for Fourier transformations

$$\int_0^t \Sigma^{\mu\nu,ab}_{\mathbf{k}}(t-t') \bar{A}^b_{\mathbf{k},\mu}(t') dt' = \mathrm{i}g^2 \int_0^t \int \mathrm{tr}\Big[D^<_{\mathbf{p}}(t-t')\gamma^\mu T^b D^>_{\mathbf{p}-\mathbf{k}}(t'-t)\gamma^\nu T^a - D^>_{\mathbf{p}}(t-t')\gamma^\mu T^b D^<_{\mathbf{p}-\mathbf{k}}(t'-t)\gamma^\nu T^a \Big] \frac{d^3p}{(2\pi)^3} \bar{A}^b_{\mathbf{k},\mu}(t') dt'. \tag{5.22}$$

In a next step, we insert the Wightman functions in momentum space. With the semi-classical model being specified at the first time-step in our simulation, where we couple the classical

Yang-Mills fields of the Glasma to vacuum fermions, we evaluate the Wightman functions with respect to free fermions, using the non-interacting vacuum

$$D^{>}_{\mathbf{p},nm}(t,t') = \delta_{nm} D^{>}_{\mathbf{p}}(t,t') = \frac{\delta_{nm}}{2\omega_{\mathbf{p}}}\Big(\not{p} + m\Big)e^{-\mathrm{i}E_{\mathbf{p}}(t-t')}, \tag{5.23}$$

$$D^{<}_{\mathbf{p},nm}(t,t') = \delta_{nm} D^{y}_{\mathbf{p}}(t,t') = -\frac{\delta_{nm}}{2\omega_{\mathbf{p}}}\gamma^0\Big(\not{p} - m\Big)\gamma^0 e^{\mathrm{i}E_{\mathbf{p}}(t-t')}. \tag{5.24}$$

A detailed derivation can be found in (Appendix B.3).
It is now possible to evaluate the color traces of the self energy $\Sigma^{\mu\nu,ab}$

$$\begin{aligned}\mathrm{tr}\Big[D^{<}_{\mathbf{p}}(t-t')\gamma^\mu T^b D^{>}_{\mathbf{p}-\mathbf{k}}(t'-t)\gamma^\nu T^a\Big] =& \delta_{ij}T^b_{jn}\delta_{nm}T^a_{mi}\mathrm{tr}\Big[D^{<}_{\mathbf{p}}(t-t')\gamma^\mu D^{>}_{\mathbf{p}-\mathbf{k}}(t'-t)\gamma^\nu\Big] \\ =& \mathrm{tr}\Big[T^bT^a\Big]\mathrm{tr}\Big[D^{<}_{\mathbf{p}}(t-t')\gamma^\mu D^{>}_{\mathbf{p}-\mathbf{k}}(t'-t)\gamma^\nu\Big] \\ =& \frac{1}{2}\delta^{ab}\mathrm{tr}\Big[D^{<}_{\mathbf{p}}(t-t')\gamma^\mu D^{>}_{\mathbf{p}-\mathbf{k}}(t'-t)\gamma^\nu\Big].\end{aligned} \tag{5.25}$$

A similar calculation can be done for the second term.
In a next step, we have a look at Dirac space

$$D^{<}_{\mathbf{p}}(t-t')\gamma^\mu D^{>}_{\mathbf{p}-\mathbf{k}}(t'-t)\gamma^\nu = -\frac{1}{4\omega_{\mathbf{p}}\omega_{\mathbf{p}-\mathbf{k}}}\Big[\gamma^0\Big(\not{p} - m\Big)\gamma^0\gamma^\mu\Big(\Big(\not{p} - \not{k}\Big) + m\Big)\gamma^\nu\Big]e^{\mathrm{i}(\omega_{\mathbf{p}}+\omega_{\mathbf{p}-\mathbf{k}})(t-t')}, \tag{5.26}$$

$$D^{>}_{\mathbf{p}}(t-t')\gamma^\mu D^{<}_{\mathbf{p}-\mathbf{k}}(t'-t)\gamma^\nu = -\frac{1}{4\omega_{\mathbf{p}}\omega_{\mathbf{p}-\mathbf{k}}}\Big[\Big(\not{p} + m\Big)\gamma^\mu\gamma^0\Big(\Big(\not{p} - \not{k}\Big) - m\Big)\gamma^0\gamma^\nu\Big]e^{-\mathrm{i}(\omega_{\mathbf{p}}+\omega_{\mathbf{p}-\mathbf{k}})(t-t')}. \tag{5.27}$$

Evaluating the Dirac traces then leads to

$$\begin{aligned}\mathrm{tr}\Big[\Big(\not{p} + m\Big)\gamma^\mu\gamma^0\Big(\Big(\not{p} - \not{k}\Big) - m\Big)\gamma^0\gamma^\nu\Big] =& 4\eta^{\mu\nu}\Big(\omega_{\mathbf{p}}\omega_{\mathbf{p}-\mathbf{k}} + \mathbf{p}(\mathbf{p}-\mathbf{k}) - m^2\Big) \\ &+ \sum_{\alpha,\beta} 4\eta^{\mu\alpha}\eta^{\nu\beta}\Big(p_\alpha(p-k)^\beta - p_\beta(p-k)^\alpha\Big),\end{aligned} \tag{5.28}$$

$$\begin{aligned}\mathrm{tr}\Big[\gamma^0\Big(\not{p} - m\Big)\gamma^0\gamma^\mu\Big(\Big(\not{p} - \not{k}\Big) + m\Big)\gamma^\nu\Big] =& 4\eta^{\mu\nu}\Big(\omega_{\mathbf{p}}\omega_{\mathbf{p}-\mathbf{k}} + \mathbf{p}(\mathbf{p}-\mathbf{k}) - m^2\Big) \\ &+ \sum_{\alpha,\beta} 4\eta^{\mu\alpha}\eta^{\nu\beta}\Big(p^\alpha(p-k)_\beta - p^\beta(p-k)_\alpha\Big).\end{aligned} \tag{5.29}$$

A detailed derivation of this result can be found in (Appendix B.4).

In total we find the following result for the traces of Wightman functions of free fermions

$$\begin{aligned}\mathrm{tr}\Big[D^{<}_{\mathbf{p}}(t-t')\gamma^\mu D^{>}_{\mathbf{p}-\mathbf{k}}(t'-t)\gamma^\nu\Big] = -\frac{e^{\mathrm{i}(\omega_{\mathbf{p}}+\omega_{\mathbf{p}-\mathbf{k}})(t-t')}}{\omega_{\mathbf{p}}\omega_{\mathbf{p}-\mathbf{k}}}\Big[&\eta^{\mu\nu}\Big(\omega_{\mathbf{p}}\omega_{\mathbf{p}-\mathbf{k}} + \mathbf{p}(\mathbf{p}-\mathbf{k}) - m^2\Big) \\ &+ \sum_{\alpha,\beta}\eta^{\mu\alpha}\eta^{\nu\beta}\Big(p^\alpha(p-k)_\beta - p^\beta(p-k)_\alpha\Big)\Big],\end{aligned} \tag{5.30}$$

$$\begin{aligned}\mathrm{tr}\Big[D^{>}_{\mathbf{p}}(t-t')\gamma^\mu D^{<}_{\mathbf{p}-\mathbf{k}}(t'-t)\gamma^\nu\Big] = -\frac{e^{-\mathrm{i}(\omega_{\mathbf{p}}+\omega_{\mathbf{p}-\mathbf{k}})(t-t')}}{\omega_{\mathbf{p}}\omega_{\mathbf{p}-\mathbf{k}}}\Big[&\eta^{\mu\nu}\Big(\omega_{\mathbf{p}}\omega_{\mathbf{p}-\mathbf{k}} + \mathbf{p}(\mathbf{p}-\mathbf{k}) - m^2\Big) \\ &+ \sum_{\alpha,\beta}\eta^{\mu\alpha}\eta^{\nu\beta}\Big(p_\alpha(p-k)^\beta - p_\beta(p-k)^\alpha\Big)\Big].\end{aligned} \tag{5.31}$$

Inserting these results into the Fourier transformed fermion self-energy, we arrive at

$$\begin{aligned}\Sigma^{\mu\nu,ab}_{\mathbf{k}}(t-t') &= \frac{\mathrm{i}}{2}\delta^{ab}g^2\int\frac{1}{\omega_{\mathbf{p}}\omega_{\mathbf{p}-\mathbf{k}}}\eta^{\mu\nu}\Big(\omega_{\mathbf{p}}\omega_{\mathbf{p}-\mathbf{k}}+\mathbf{p}(\mathbf{p}-\mathbf{k})-m^2\Big)\Big(e^{-\mathrm{i}(\omega_{\mathbf{p}}+\omega_{\mathbf{p}-\mathbf{k}})(t-t')}-e^{\mathrm{i}(\omega_{\mathbf{p}}+\omega_{\mathbf{p}-\mathbf{k}})(t-t')}\Big)\\ &\quad+\frac{1}{\omega_{\mathbf{p}}\omega_{\mathbf{p}-\mathbf{k}}}\sum_{\alpha,\beta}\eta^{\mu\alpha}\eta^{\nu\beta}\Big(\Big(p_\alpha(p-k)^\beta-p_\beta(p-k)^\alpha\Big)e^{-\mathrm{i}(\omega_{\mathbf{p}}+\omega_{\mathbf{p}-\mathbf{k}})(t-t')}\\ &\quad-\Big(p^\alpha(p-k)_\beta-p^\beta(p-k)_\alpha\Big)e^{\mathrm{i}(\omega_{\mathbf{p}}+\omega_{\mathbf{p}-\mathbf{k}})(t-t')}\Big)\frac{d^3p}{(2\pi)^3}.\end{aligned} \tag{5.32}$$

It is now possible to simplify this result, by identifying

$$\frac{\mathrm{i}}{2}\Big(e^{-\mathrm{i}(\omega_{\mathbf{p}}+\omega_{\mathbf{p}-\mathbf{k}})(t-t')}-e^{\mathrm{i}(\omega_{\mathbf{p}}+\omega_{\mathbf{p}-\mathbf{k}})(t-t')}\Big)=\sin\Big((\omega_{\mathbf{p}}+\omega_{\mathbf{p}-\mathbf{k}})(t-t')\Big). \tag{5.33}$$

As discussed in [101], we choose the scale of renormalization to be $\mathbf{k}$=0,

$$\begin{aligned}\Sigma^{\mu\nu,ab}_{\mathbf{0}}(t-t') &= \delta^{ab}g^2\int\eta^{\mu\nu}\left(1+\frac{\mathbf{p}^2-m^2}{\omega^2_{\mathbf{p}}}\right)\sin\Big(2\omega_{\mathbf{p}}(t-t')\Big)\\ &\quad+\frac{\mathrm{i}}{2}\frac{1}{\omega^2_{\mathbf{p}}}\sum_{\alpha,\beta}\eta^{\mu\alpha}\eta^{\nu\beta}\Big(\Big(p_\alpha p^\beta-p_\beta p^\alpha\Big)e^{-\mathrm{i}2\omega_{\mathbf{p}}(t-t')}-\Big(p^\alpha p_\beta-p^\beta p_\alpha\Big)e^{\mathrm{i}2\omega_{\mathbf{p}}(t-t')}\Big)\frac{d^3p}{(2\pi)^3}.\end{aligned} \tag{5.34}$$

This result can also be written in the following way, after performing some algebra

$$\Sigma^{\mu\nu,ab}_{\mathbf{0}}(t)=\delta^{ab}g^2\int 2\eta^{\mu\nu}\frac{\mathbf{p}^2}{\omega^2_{\mathbf{p}}}\sin\Big(2\omega_{\mathbf{p}}t\Big)+\frac{\mathrm{i}}{\omega^2_{\mathbf{p}}}\sum_{\alpha,\beta}\eta^{\mu\alpha}\eta^{\nu\beta}\Big(p_\alpha p^\beta-p_\beta p^\alpha\Big)\cos\Big(2\omega_{\mathbf{p}}t\Big)\frac{d^3p}{(2\pi)^3}. \tag{5.35}$$

From (eq. 5.3), we are now able to calculate δZ

$$\delta Z=N_f\int_0^\infty\frac{t^2}{2}\Sigma_{\mathbf{0}}(t)dt, \tag{5.36}$$

where we stripped of δ^{ab} and $\eta^{\mu\nu}$ and formally kept a factor N_f for the number of degenerate fermion flavors.

There are two contributions to the time integral. The first contribution is of the form

$$\int_0^\infty t^2\sin(2\omega_{\mathbf{p}}t)dt=\frac{1}{4\omega^3_{\mathbf{p}}}\lim_{t\to\infty}\Big(-2\omega^2_{\mathbf{p}}t^2\cos(2\omega_{\mathbf{p}}t)+2\omega_{\mathbf{p}}t\sin(2\omega_{\mathbf{p}}t)\Big)-\frac{1}{4\omega^3_{\mathbf{p}}}. \tag{5.37}$$

As discussed in [101], we assume that the oscillatory contributions to the integral are incoherent at large times and can be averaged away, allowing us to neglect these oscillations

$$\int_0^\infty t^2\sin(2\omega_{\mathbf{p}}t)dt=-\frac{1}{4\omega^3_{\mathbf{p}}}. \tag{5.38}$$

The same is true for the second contribution, that is purely oscillatory

$$\begin{aligned}\int_0^\infty t^2\cos(2\omega_{\mathbf{p}}t)dt =&\frac{1}{4\omega_{\mathbf{p}}^3}\Big[\Big(2\omega_{\mathbf{p}}^2t^2-1\Big)\sin(2\omega_{\mathbf{p}}t)+2\omega_{\mathbf{p}}t\cos(2\omega_{\mathbf{p}}t)\Big]_0^\infty \\ =&\frac{1}{4\omega_{\mathbf{p}}}\lim_{t\to\infty}\Big[\Big(2\omega_{\mathbf{p}}^2t^2-1\Big)\sin(2\omega_{\mathbf{p}}t)+2\omega_{\mathbf{p}}t\cos(2\omega_{\mathbf{p}}t)\Big].\end{aligned} \tag{5.39}$$

In total we found the following renormalization factor

$$\delta Z=\int_0^\infty\frac{t^2}{2}\Sigma_{\mathbf{0}}dt=-g^2N_f\int\frac{\mathbf{p}^2}{4\omega_{\mathbf{p}}^5}\frac{d^3p}{(2\pi)^3}. \tag{5.40}$$

Comparing this result to the result in [101], derived for a model of classical scalar fields coupled to fermions, we find that both results agree up to an additional factor, that arises from the evaluation of the $SU(3)$ color traces. The agreement is not surprising, because the interaction of fermion and classical fields has a similar structure in both cases and the key difference is essentially the additional color degree of freedom, manifesting itself in the color traces.

5.3.1 Lattice Implementation of the Z-Factor

In the previous section, we presented how to calculate the wave function renormalization Z-factor for the semi-classical approximation of QCD. This derivation has been presented in the continuum, making a translation to the lattice necessary, to determine the Z-factor in a lattice simulation of the effective theory. The lattice counterpart of the continuum Wightman functions of free vacuum fermions (eq. 5.23) is obtained in similar fashion, as in the continuum (Appendix B.3). For the lattice derivation, we make use of the free Dirac spinor on the lattice (eq. 2.45), leading to

$$S^{>}_{\mathbf{p},ab}(t,t')=\frac{\delta_{ab}}{2s_0(\mathbf{p})}\Big(\not{s}(\mathbf{p})+\mu(\mathbf{p})\Big)_{\alpha\beta}e^{-\mathrm{i}\omega_{\mathbf{p}}(t-t')}, \tag{5.41}$$

$$S^{<}_{\mathbf{p},ab}(t,t')=-\frac{\delta_{ab}}{2s_0(\mathbf{p})}\gamma^0\Big(\not{s}(\mathbf{p})-\mu(\mathbf{p})\Big)\gamma^0e^{\mathrm{i}\omega_{\mathbf{p}}(t-t')}. \tag{5.42}$$

It is now possible to use these results to calculate the lattice variant of the fermion self-energy

$$\Sigma^{\mu\nu,ab}_{\mathbf{k}}(t-t')=\frac{\mathrm{i}g^2}{V}\sum_{\mathbf{p}}\mathrm{tr}\Big[S^{<}_{\mathbf{p}}(t-t')\gamma^\mu T^bS^{>}_{\mathbf{p}-\mathbf{k}}(t'-t)\gamma^\nu T^a-S^{>}_{\mathbf{p}}(t-t')\gamma^\mu T^bS^{<}_{\mathbf{p}-\mathbf{k}}(t'-t)\gamma^\nu T^a\Big]. \tag{5.43}$$

Repeating the previous steps, setting the scale of renormalization to $\mathbf{k}$=0 again, we find the following lattice version of the fermion self energy, that enters the fermion one-loop equation of motion of the classical Yang-Mills fields

$$\Sigma^{\mu\nu,ab}_{\mathbf{0}}(t)=\delta^{ab}g^2\frac{1}{V}\sum_{\mathbf{p}}2\eta^{\mu\nu}\frac{\mathbf{s}^2}{s_0^2}\sin\Big(2\omega_{\mathbf{p}}t\Big)+\frac{\mathrm{i}}{s_0^2}\eta^{\mu\alpha}\eta^{\nu\beta}\Big(s_\alpha s^\beta-s_\beta s^\alpha\Big)\cos\Big(2\omega_{\mathbf{p}}t\Big). \tag{5.44}$$

It is now possible to derive the lattice renormalization Z-factor from the lattice fermion self-energy in similar fashion, by solving the time integral (eq. 5.3). Carrying out the calculation leads to a similar result as in case of the continuum, but this time the momentum integration

is traded with a sum over the regularized lattice momenta and the momenta and dispersion relation are replaced by the lattice counterparts (eq. 2.38)

$$\delta Z = -\frac{g^2}{4V} N_f \sum_{\mathbf{p}} \frac{\mathbf{s}^2(\mathbf{p})}{s_0^5(\mathbf{p})}. \tag{5.45}$$

This result is naturally regulated by the lattice momentum cutoff and therefore finite. As a consequence, δZ is cutoff dependent, which is no surprise because we are dealing with a semi-classical theory, where no continuum limit can be performed and all quantities, including the physical observables, remain cutoff dependent in general.

5.4 Counterterm Renormalization

Having derived the Z-factor for the semi-classical model, we can now use it to renormalize our theory, following the procedure presented in [146]. The renormalization is done by introducing a counterterm to the action of the classical Yang-Mills sector of QCD

$$S_C = -\int \frac{(Z-1)}{4} F^{\mu\nu,a} F^a_{\mu\nu} d^4x. \tag{5.46}$$

The Z-factor is defined as $Z = 1 + \delta Z$.
Adding the counterterm to the action of QCD (eq. 1.1), the renormalized action takes the form

$$\begin{aligned} S_R = S + S_C &= \int -\frac{1}{4} F^{\mu\nu,a} F^a_{\mu\nu} + \bar{\psi}\Big(\mathrm{i}\gamma^\mu D_\mu - m\Big)\psi d^4x - \int \frac{(Z-1)}{4} F^{\mu\nu,a} F^a_{\mu\nu} d^4x \\ &= \int -\frac{Z}{4} F^{\mu\nu,a} F^a_{\mu\nu} + \bar{\psi}\Big(\mathrm{i}\gamma^\mu D_\mu - m\Big)\psi d^4x. \end{aligned} \tag{5.47}$$

The corresponding renormalized lattice Lagrangian (eq. 2.57) can then be written as

$$\begin{aligned} \mathcal{L}_R =& Z\mathrm{Retr}\left[E_i E_i - \frac{2}{g^2 a^4} \sum_{i<j} \Big(1 - U_{ij}\Big)\right] + \mathrm{i}\bar{\psi}(x)\gamma^0 \partial_t \psi(x) - \left(m + \frac{3r}{a}\right)\bar{\psi}(x)\psi(x) \\ &+ \frac{\mathrm{i}}{2a} \sum_{i=1}^{3} \Big[\bar{\psi}(x)\Big(\gamma^i - \mathrm{i}r\Big) U_i(x)\psi(x+\hat{i}) - \bar{\psi}(x)\Big(\gamma^i + \mathrm{i}r\Big) U_i^\dagger(x-\hat{i})\psi(x-\hat{i})\Big]. \end{aligned} \tag{5.48}$$

A similar result is found for the renormalized lattice Hamilton density of QCD (eq. 2.58)

$$\begin{aligned} \mathcal{H}_R =& Z\mathrm{Retr}\left[E_i E_i + \frac{2}{g^2 a^4} \sum_{i<j} \Big(1 - U_{ij}\Big)\right] + \bar{\psi}(x)\left(m + \frac{3r}{a}\right)\psi(x) \\ &- \frac{\mathrm{i}}{2a} \sum_{i=1}^{3} \Big[\bar{\psi}(x)\Big(\gamma^i - \mathrm{i}r\Big) U_i(x)\psi(x+\hat{i}) - \bar{\psi}(x)\Big(\gamma^i + \mathrm{i}r\Big) U_i^\dagger(x-\hat{i})\psi(x-\hat{i})\Big]. \end{aligned} \tag{5.49}$$

5.4.1 Renormalized Equation of Motion

The derivation of the semi-classical model, presented in (section 4.3) is unchanged, when starting from the renormalized Lagrangian (eq. 5.48). The equation of motion for the lattice chromo-electric fields simply picks up the Z-factor

$$Z\partial_t E^a_i(x) = \frac{2}{ga^3} Z \sum_{j\neq i} \mathrm{Imtr}\Big[T^a\Big(U_{ji}(x) + U_{-ji}(x)\Big)\Big] + g\mathrm{Retr}\Big[F\Big(x+\hat{i}, x\Big)\Big(\gamma^i - \mathrm{i}r\Big) T^a U_i(x)\Big]. \tag{5.50}$$

A similar modification happens to the Gauss constraint of the model

$$\frac{Z}{a}\sum_i \Big[E_i - U_i^\dagger(x-\hat{i})E_i(x-\hat{i})U_i(x-\hat{i})\Big] = -gT^a\mathrm{Retr}\Big(F(x+\hat{0},x)\gamma^0 T^a\Big). \tag{5.51}$$

The color matrix $C(x)$, that measures the amount of Gauss violation and enters the algorithm for a restoration of Gauss law, is now given as

$$C(x) = \frac{Z}{a}\sum_i \Big[E_i - U_i^\dagger(x-\hat{i})E_i(x-\hat{i})U_i(x-\hat{i})\Big] + gT^a\mathrm{Retr}\Big(F(x+\hat{0},x)\gamma^0 T^a\Big). \tag{5.52}$$

The update equation for the chromo-electric fields (eq. 4.56), as well as the fermion and gauge link evolution equations (eq. 4.1) and (eq. 4.7) remain unchanged.

6
Static Box Observables

Having discussed the derivation of the semi-classical effective theory in (chapter 4), as well as its renormalization in (chapter 5), let us now turn to the definition of the observables that will be evaluated in the lattice simulation of the effective theory. As pointed out in (chapter 3), we are particularly interested in the pressure and the occupation of energy-modes of the system, making it possible to measure the evolution of the initial pressure anisotropy of the CGC and study the validity of the semi-classical approximation. Furthermore, we will determine the energy density in the simulation to connect it to the estimated energy density of the early phase in a heavy ion collision (section 3.5), allowing us to fix the lattice spacing a.

6.1 The Energy-Momentum Tensor of Quantum Chromodynamics

We will define the energy and pressure observables of our system, by making use of the energy-momentum tensor of QCD, where the diagonal elements represent the energy density and pressure. As expected, the resulting observables are gauge invariant and we do not have to fix the remaining gauge degree of freedom in our system. One has to keep in mind, that the Glasma initial state of the Yang-Mills sector is a non-equilibrium state and as a consequence, the definition of a pressure should not be understood in context of an equilibrium statistical (quantum-)field theory. We define the pressure of the non-equilibrium system essentially as the spacial diagonal component of the corresponding energy-momentum tensor. To introduce the basic concepts, we will stick to continuum physics at first and discretize our results in a next step.

The symmetrized energy-momentum tensor of QCD can be found e.g. in [148]

$$T^{\mu\nu}_{\mathrm{QCD}} = -\eta^{\mu\nu}\mathcal{L}_{\mathrm{QCD}} - ZF^{\mu\alpha,a}F^{\nu}_{\ \alpha\ a} + \frac{1}{2}\bar{\psi}\mathrm{i}D^{(\mu}\gamma^{\nu)}\psi + \frac{1}{2}\bar{\psi}\mathrm{i}\overleftarrow{D}^{(\mu}\gamma^{\nu)}\psi. \tag{6.1}$$

We introduced the following short notation for the covariant derivative

$$D^{(\mu}\gamma^{\nu)} = \frac{1}{2}\Big(D^{\mu}\gamma^{\nu} + D^{\nu}\gamma^{\mu}\Big), \tag{6.2}$$

with an arrow above a covariant derivative indicating, that it has to be taken to the left

$$\bar{\psi}\overleftarrow{D}^{\mu} = -\partial^{\mu}\bar{\psi} + \mathrm{i}g\bar{\psi}A^{\mu}. \tag{6.3}$$

The energy-momentum tensor can now be split into the different sectors of QCD, a Yang-Mills part $T^{\mu\nu}_{YM}$ and a fermion part $T^{\mu\nu}_{\psi}$

$$\begin{aligned} T^{\mu\nu}_{QCD} =& \underbrace{\frac{Z}{4}\eta^{\mu\nu}F^{\alpha\beta,a}F^{a}_{\alpha\beta} - ZF^{\mu\alpha,a}F^{\nu\ a}_{\ \alpha}}_{:=T^{\mu\nu}_{YM}} \\ & \underbrace{-\eta^{\mu\nu}\bar{\psi}\Big(\mathrm{i}\gamma^{\alpha}D_{\alpha} - m\Big)\psi + \frac{1}{4}\Big(\bar{\psi}\mathrm{i}D^{\mu}\gamma^{\nu}\psi + \bar{\psi}\mathrm{i}D^{\nu}\gamma^{\mu}\psi + \bar{\psi}\mathrm{i}\overleftarrow{D}^{\mu}\gamma^{\nu}\psi + \bar{\psi}\mathrm{i}\overleftarrow{D}^{\nu}\gamma^{\mu}\psi\Big)}_{:=T^{\mu\nu}_{\psi}}. \end{aligned} \tag{6.4}$$

We will use this splitting to define the energy density and pressure for each of the sectors individually.

6.1.1 Yang-Mills Sector of the QCD Energy-Momentum Tensor

We start our discussion for the Yang-Mills sector of the theory. The energy-momentum tensor of the Yang-Mills sector can be written in the following way

$$T^{\mu\nu}_{YM} = \frac{Z}{4}\eta^{\mu\nu}F^{\alpha\beta,a}F^{a}_{\alpha\beta} - ZF^{\mu\alpha,a}F^{\nu\ ,a}_{\ \alpha} = \frac{Z}{4}\eta^{\mu\nu}\eta^{\alpha\gamma}\eta^{\beta\delta}F^{a}_{\gamma\delta}F^{a}_{\alpha\beta} - Z\eta^{\mu\alpha}\eta^{\nu\beta}\eta^{\gamma\delta}F^{a}_{\alpha\gamma}F^{a}_{\beta\delta}. \tag{6.5}$$

The corresponding energy density is given as the 00-component of the tensor

$$T^{00}_{YM} = \epsilon_{YM} = \frac{Z}{4}\eta^{00}\eta^{\alpha\gamma}\eta^{\beta\delta}F^{a}_{\gamma\delta}F^{a}_{\alpha\beta} - Z\eta^{0\alpha}\eta^{0\beta}\eta^{\gamma\delta}F^{a}_{\alpha\gamma}F^{a}_{\beta\delta} = \frac{Z}{4}F^{\alpha\beta,a}F^{a}_{\alpha\beta} - ZF^{0\alpha,a}F^{0\ ,a}_{\ \alpha} \tag{6.6}$$

Identifying the chromo-electric fields (eq. 1.17) then leads to

$$\epsilon_{YM} = ZE^{a2}_{i} - \frac{Z}{2}\Big[E^{a2}_{i} - Z\sum_{i<j}F^{a2}_{ij}\Big] = Z\mathrm{tr}\Big[E^{2}_{i} + \sum_{i<j}F^{2}_{ij}\Big] \equiv \mathcal{H}_{YM}. \tag{6.7}$$

By comparing this result to the Hamiltonian of pure Yang-Mills theory (eq. 2.11) we find that both equations agree, as it should be the case in a conservative system.
The pressure can be calculated from the spacial components of (eq. 6.5)

$$\begin{aligned} T^{ii}_{YM} = P_{YM,i} =& \frac{Z}{4}\eta^{ii}\eta^{\alpha\gamma}\eta^{\beta\delta}F^{a}_{\gamma\delta}F^{a}_{\alpha\beta} - Z\eta^{i\alpha}\eta^{i\beta}\eta^{\gamma\delta}F^{a}_{\alpha\gamma}F^{a}_{\beta\delta} \\ =& -\frac{Z}{4}F^{\alpha\beta,a}F^{a}_{\alpha\beta} - ZF_{i}^{\ 0,a}F^{a}_{i0} - \sum_{j\neq i}F_{i}^{\ j,a}F^{a}_{ij}. \end{aligned} \tag{6.8}$$

Identifying the chromo-electric fields (eq. 1.17) again, we find

$$P_{YM,i} = Z\mathrm{Tr}\Big[\sum_{k\neq i}E^{2}_{k} - E^{2}_{i} + 2\sum_{j\neq i}F^{2}_{ij} - \sum_{k<j}F^{2}_{kj}\Big]. \tag{6.9}$$

We use this result to define the longitudinal pressure, which is oriented parallel to the beam axis in a heavy ion collision and the transverse pressure, which is oriented perpendicular

to the beam axis. Choosing the beam axis along z-direction, the longitudinal pressure is given by the z-component of (eq. 6.8)

$$P_{YM}^{L} = P_{YM,z} = Z\mathrm{tr}\Big[E_1^2 + E_2^2 - E_3^2 + F_{13}^2 + F_{23}^2 - F_{12}^2\Big]. \tag{6.10}$$

The transverse pressure is thus defined as

$$P_{YM}^{T} = \frac{1}{2}\Big(P_{YM,x} + P_{YM,y}\Big) = Z\mathrm{tr}\Big[E_3^2 + F_{12}^2\Big]. \tag{6.11}$$

For the sake of completeness, the following splitting of the energy density of the Yang-Mills sector into longitudinal and transverse contributions can be found in the literature (see e.g. [126])

$$\epsilon_{YM}^{T} = Z\mathrm{tr}\Big[E_1^2 + E_2^2 + F_{13}^2 + F_{23}^2\Big], \qquad \epsilon_{YM}^{L} = Z\mathrm{tr}\Big[E_3^2 + F_{12}^2\Big]. \tag{6.12}$$

Using these definitions, the pressure and energy density of the Yang-Mills sector are related in the following way

$$P_{YM}^{T} = \epsilon_{YM}^{L}, \qquad P_{YM}^{L} = \epsilon_{YM}^{T} - \epsilon_{YM}^{L}. \tag{6.13}$$

For the calculation it might be useful as well, to split the energy density into a chromo-electric and a chromo-magnetic part. This is simply done by identifying all terms containing the chromo-electric fields as chromo-electric and all other terms as the chromo-magnetic part.

6.1.2 Fermion Sector of the QCD Energy-Momentum Tensor

Next we have a look at the energy-momentum tensor of the fermion sector of QCD

$$T_{\psi}^{\mu\nu} = -\eta^{\mu\nu}\bar{\psi}\Big(\mathrm{i}\gamma^{\alpha}D_{\alpha} - m\Big)\psi + \frac{1}{4}\Big(\bar{\psi}\mathrm{i}D^{\mu}\gamma^{\nu}\psi + \bar{\psi}\mathrm{i}D^{\nu}\gamma^{\mu}\psi + \bar{\psi}\mathrm{i}\overleftarrow{D^{\mu}}\gamma^{\nu}\psi + \bar{\psi}\mathrm{i}\overleftarrow{D^{\nu}}\gamma^{\mu}\psi\Big). \tag{6.14}$$

The energy density is again obtained from the 00-component

$$T_{\psi}^{00} = \epsilon_{\psi} = -\bar{\psi}\Big(\mathrm{i}\gamma^{\alpha}D_{\alpha} - m\Big)\psi + \frac{1}{2}\Big(\bar{\psi}\mathrm{i}\gamma^{0}\partial_t\psi + \bar{\psi}\mathrm{i}\gamma^{0}\overleftarrow{\partial}_t\psi\Big), \tag{6.15}$$

Making use of the Lagrangian of the fermion sector of QCD (eq. 1.2), we find

$$\epsilon_{\psi} = -\bar{\psi}(x)\Big(\mathrm{i}\gamma^{i}D_i - m\Big)\psi(x) \equiv \mathcal{H}_f(x). \tag{6.16}$$

As already seen in case of the Yang-Mills sector, the result (eq. 6.16) is equivalent to the Hamilton density of the fermion sector (eq. 1.25).

The pressure is defined from the spacial diagonal components of (eq. 6.14)

$$P_i^{\psi} = T_{\psi}^{ii} = -\eta^{ii}\bar{\psi}\Big(\mathrm{i}\gamma^{\alpha}D_{\alpha} - m\Big)\psi + \frac{1}{2}\Big(\bar{\psi}\mathrm{i}D^{i}\gamma^{i}\psi + \bar{\psi}\mathrm{i}\overleftarrow{D^{i}}\gamma^{i}\psi\Big). \tag{6.17}$$

We can simplify this, using the fact that the Dirac equation explicitly enters the Lagrangian of the fermion sector (eq. 1.5). With the Dirac equation representing the evolution equation of the fermion fields in our simulation, it is satisfied at every time-step

$$\mathcal{L}_f = \bar{\psi}\underbrace{\Big(\mathrm{i}\gamma^{0}\partial_t + \mathrm{i}\gamma^{i}D_i - m\Big)\psi}_{=0} = 0. \tag{6.18}$$

As a result, the pressure observable reduces to [144]

$$P_i^{\psi} = T_{\psi}^{ii} = \frac{1}{2}\Big(\bar{\psi}\mathrm{i}D^i\gamma^i\psi + \bar{\psi}\mathrm{i}\overleftarrow{D^i}\gamma^i\psi\Big). \tag{6.19}$$

It is now straight forward to define a longitudinal and transverse pressure for the fermion sector, as presented for the Yang-Mills sector.

In contrast to the Yang-Mills sector, where the gauge fields are assumed to be classical, fermion spinors are quantum operators. As a consequence, the energy density (eq. 6.16) and the pressure (eq. 6.19) of the fermion sector are operator valued. When evaluating these observables, this has to be done with respect to the partition function of the semi-classical model (eq. 4.34)

$$\langle\mathcal{O}(x)\rangle = \int \mathcal{O}(x)\rho_A[\bar{A}(t_0)]\delta\Big[\partial_\mu\bar{F}^{\mu\nu,a} - gf^{abc}\bar{A}_\mu^b\bar{F}^{\mu\nu,c} - J_{\bar{A}}^{\nu,a}\Big][d\bar{A}]. \tag{6.20}$$

We will discuss how to evaluate these observables in a lattice simulation in the following.

6.2 Lattice Discretization of the Observables

Having defined the energy and pressure observables of both, the Yang-Mills and fermion sector in our semi-classical effective theory of QCD, let us discretize these results, making an evaluation in a real-time lattice simulation possible.

It is straight forward to discretize the observables of the Yang-Mills sector (eq. 6.7) and (eq. 6.8), by replacing the field-strength tensor components by the lattice counterparts given from (eq. 2.9)

$$\bar{\epsilon}_{YM}(x) = g^2a^4\epsilon_{YM}(x) = Z\mathrm{Retr}\Big[\bar{E}_i^2(x) + 2\sum_{i<j}\Big[1 - U_{ij}(x)\Big]\Big], \tag{6.21}$$

$$\bar{P}_{YM}^T = g^2a^4P_{YM}^T = Z\mathrm{Retr}\Big[\bar{E}_3^2 + 2(1 - U_{12})\Big], \tag{6.22}$$

$$\bar{P}_{YM}^L = g^2a^4P_{YM}^L = Z\mathrm{Retr}\Big[\bar{E}_1^2 + \bar{E}_2^2 - \bar{E}_3^2 + 2(1 + U_{12} - U_{13} - U_{23})\Big], \tag{6.23}$$

where we defined the energy density and pressure in lattice units, rescaling the observables in terms of the lattice spacing a and the coupling g.

For the discretization of the fermion sector, we have to introduce the Wilson term (eq. 2.53) to take care of the fermion doubling problem on the lattice. On top of this, as discussed in the previous section, we have to take the expectation value with respect to the semi-classical partition function (eq. 4.34), because fermion fields are operator valued. In case of the energy density of the fermion sector (eq. 6.16), this manifests itself in

$$\begin{aligned}\epsilon_\psi = &-\frac{\mathrm{i}}{2a}\sum_i\Big(\Big\langle\bar{\psi}(x)\Big(\gamma^i - \mathrm{i}r\Big)U_i(x)\psi(x+\hat{i})\Big\rangle - \Big\langle\bar{\psi}(x)\Big(\gamma^i + \mathrm{i}r\Big)U_i^\dagger(x-\hat{i})\psi(x-\hat{i})\Big\rangle\Big) \\ &+ \frac{1}{a}\Big(am + 3r\Big)\Big\langle\bar{\psi}(x)\psi(x)\Big\rangle.\end{aligned} \tag{6.24}$$

As discussed for the evaluation of the fermion current, that enters the equation of motion of the chromo-electric fields (eq. 5.50), the expectation values can be evaluated by making use

of the statistical propagator (eq. 1.44). Rewriting the first term of (eq. 6.24)

$$\begin{aligned}\Big\langle\bar\psi(x)\Big(\gamma^i-\mathrm{i}r\Big)U_i(x)\psi(x+\hat\imath)\Big\rangle &=\Big\langle\bar\psi_{\alpha,c}(x)\Big(\gamma^i_{\alpha\beta}-\delta_{\alpha\beta}\mathrm{i}r\Big)U_{i,cd}(x)\psi_{\beta,d}(x+\hat\imath)\Big\rangle \\ &=\Big\langle\bar\psi_{\alpha,c}(x)\psi_{\beta,d}(x+\hat\imath)\Big\rangle\Big(\gamma^i_{\alpha\beta}-\delta_{\alpha\beta}\mathrm{i}r\Big)U_{i,cd}(x),\end{aligned} \tag{6.25}$$

we can split the expectation value into

$$\Big\langle\bar\psi_{\alpha,c}(x)\psi_{\beta,d}(x+\hat\imath)\Big\rangle=\frac{1}{2}\Big(\Big\langle\bar\psi_{\alpha,c}(x)\psi_{\beta,d}(x+\hat\imath)\Big\rangle+\Big\langle\bar\psi_{\alpha,c}(x)\psi_{\beta,d}(x+\hat\imath)\Big\rangle\Big). \tag{6.26}$$

Because the fermion spinors are given at different spacial positions, we can make use of (eq .1.31)

$$\{\psi_{\beta,d}(x+\hat\imath),\bar\psi_{\alpha,c}(x)\}=\psi_{\beta,d}(x+\hat\imath)\bar\psi_{\alpha,c}(x)+\bar\psi_{\alpha,c}(x)\psi_{\beta,d}(x+\hat\imath)=0, \tag{6.27}$$

making it possible to identify the statistical propagator, by anti-commuting the first term

$$\Big\langle\bar\psi_{\alpha,c}(x)\psi_{\beta,d}(x+\hat\imath)\Big\rangle=-\frac{1}{2}\Big\langle\Big[\tilde\psi_{\beta,d}(x+\hat\imath),\bar\psi_{\alpha,c}(x)\Big]\Big\rangle=-F_{\beta\alpha,dc}(x+\hat\imath,x). \tag{6.28}$$

With this result, the fermion expectation values in (eq. 6.24) can be calculated by making use of the statistical propagator

$$\begin{aligned}\Big\langle\bar\psi(x)\Big(\gamma^i-\mathrm{i}r\Big)U_i(x)\psi(x+\hat\imath)\Big\rangle &=-F_{\beta\alpha,dc}(x+\hat\imath,x)\Big(\gamma^i_{\alpha\beta}-\delta_{\alpha\beta}\mathrm{i}r\Big)U_{i,cd}(x) \\ &=-\operatorname{tr}\Big[F(x+\hat\imath,x)\Big(\gamma^i-\mathrm{i}r\Big)U_i(x)\Big].\end{aligned} \tag{6.29}$$

In similar fashion we find

$$\Big\langle\bar\psi(x)\Big(\gamma^i+\mathrm{i}r\Big)U_i^\dagger(x-\hat\imath)\psi(x-\hat\imath)\Big\rangle=-\mathrm{tr}\Big[F(x-\hat\imath,x)\Big(\gamma^i+\mathrm{i}r\Big)U_i^\dagger(x-\hat\imath)\Big]. \tag{6.30}$$

In the mass term of (eq. 6.24), the spinor fields are taken at equal position

$$\Big\langle\bar\psi(x)\psi(x)\Big\rangle=\Big\langle\bar\psi_{\alpha,c}(x)\psi_{\alpha,c}(x)\Big\rangle=\frac{1}{2}\Big(\Big\langle\bar\psi_{\alpha,c}(x)\psi_{\alpha,c}(x)\Big\rangle+\Big\langle\bar\psi_{\alpha,c}(x)\psi_{\alpha,c}(x)\Big\rangle\Big). \tag{6.31}$$

Nevertheless using (eq. 1.31) leads to

$$\{\psi_{\alpha,c}(x),\bar\psi_{\alpha,c}(x)\}=\psi_{\alpha,c}(x)\bar\psi_{\alpha,c}(x)+\bar\psi_{\alpha,c}(x)\psi_{\alpha,c}(x)=\underbrace{\gamma^0_{\alpha\alpha}}_{=\mathrm{tr}\gamma^0=0}\delta_{cc}\delta_{\mathbf{x},\mathbf{x}}=0. \tag{6.32}$$

As a consequence, the mass term can also be calculated by making use of the statistical fermion propagator

$$\Big\langle\bar\psi(x)\psi(x)\Big\rangle=-\mathrm{tr}\Big[F(x,x)\Big]=-\frac{1}{a^3}\mathrm{tr}\Big[\bar F(x,x)\Big], \tag{6.33}$$

where we introduced a rescaled, dimensionless lattice version of the statistical propagator in the second step. Combining all results, we find the following lattice energy density of the fermion sector

$$\begin{aligned}\bar\epsilon_\psi(x)=g^2a^4\epsilon_\psi(x)=g^2\frac{\mathrm{i}}{2}\sum_i\Big(&\mathrm{tr}\Big[\bar F(x+\hat\imath,x)\Big(\gamma^i-\mathrm{i}r\Big)U_i(x)\Big] \\ &-\mathrm{tr}\Big[\bar F(x-\hat\imath,x)\Big(\gamma^i+\mathrm{i}r\Big)U_i^\dagger(x-\hat\imath)\Big]\Big)-g^2\Big(\bar m+3r\Big)\mathrm{tr}\Big[\bar F(x,x)\Big].\end{aligned} \tag{6.34}$$

In the simulation, the statistical propagator of fermion fields can be evaluated from ensemble averages of stochastic low-cost fermions (eq. 1.51). As discussed already in the context of the equations of motion in (section 4.3), when considering N_f degenerate fermion flavors, all traces of the statistical propagator pick up an additional factor of N_f.

The pressure of the fermion sector can be derived in similar fashion. After including the Wilson term[1] and taking the expectation value, one finds

$$\begin{aligned} P_i(x) =& -\left\langle \bar{\psi}(x)\Big(\mathrm{i}\gamma^i D_i + \frac{ra}{2}\Box_i^W\Big)\psi(x)\right\rangle \\ =& -\frac{\mathrm{i}g^2}{2}\Big[\left\langle \bar{\psi}(x)\big(\gamma^i - \mathrm{i}r\big)U_i(x)\psi(x+\hat{i})\right\rangle + 2\mathrm{i}r\left\langle \bar{\psi}(x)\psi(x)\right\rangle \\ & - \left\langle \bar{\psi}(x)\big(\gamma^i + \mathrm{i}r\big)U_i^\dagger(x-\hat{i})\psi(x-\hat{i})\right\rangle\Big], \end{aligned} \tag{6.35}$$

The expectation values can then be evaluated by making use of the statistical propagator. Introducing dimensionless lattice fields, we obtain

$$\begin{aligned} \bar{P}_i^\psi = g^2a^4P_{i,\psi} = g^2\frac{\mathrm{i}}{2}\Bigg(& \mathrm{tr}\Big[\bar{F}(x+\hat{i},x)\big(\gamma^i - \mathrm{i}r\big)U_i(x)\Big] + 2\mathrm{i}r\mathrm{tr}\Big[\bar{F}(x,x)\Big] \\ & - \mathrm{tr}\Big[\bar{F}(x-\hat{i},x)\big(\gamma^i + \mathrm{i}r\big)U_i^\dagger(x-\hat{i})\Big]\Bigg). \end{aligned} \tag{6.36}$$

The total energy density and pressure of the system is then given as the sum of the individual sectors.

In most cases, we will perform a lattice average for the energy density and pressure

$$\langle\mathcal{O}(t)\rangle_{av} = \frac{1}{V}\sum_{\mathbf{x}}\mathcal{O}(t,\mathbf{x}). \tag{6.37}$$

This allows us to study the time dependence of the observables only.

6.2.1 Computing the Error for Stochastic Fermions

In the stochastic low-cost approach for the calculation of the statistical propagator, the ensemble averages over N_{ens} gendered fermions are of Gaussian type and can be understood as evaluating the mean

$$\mu\Big(\mathcal{O}(\psi,\bar{\psi})\Big) = \langle\mathcal{O}(\psi,\bar{\psi})\rangle_{N_{ens}}. \tag{6.38}$$

In this section, we will discuss how to evaluate the standard deviation for averages of stochastic low-cost fermions, making it possible to estimate a statistical error for the energy density and pressure observables of the fermion sector

$$\Delta\mathcal{O}(x) = \frac{\sigma(x)}{\sqrt{N_{ens}}}. \tag{6.39}$$

[1] Recall that in the derivation of the energy-momentum tensor, one takes the derivative of the Lagrangian with respect to the field derivative [149]. The Wilson term enters the lattice Lagrangian as a derivative operator itself, and as a consequence, one picks up an additional contribution from the Wilson term, when deriving the lattice pressure of the fermion sector.

The standard deviation is defined as

$$\sigma^2\Big(\mathcal{O}(\psi,\bar{\psi})\Big) = \langle \mathcal{O}^2(\psi,\bar{\psi})\rangle_{N_{ens}} - \langle \mathcal{O}(\psi,\bar{\psi})\rangle^2_{N_{ens}}\,. \tag{6.40}$$

In a first step we have to square our observable for the energy density (eq. 6.24) and take the expectation value with respect to the semi-classical partition function (eq. 4.34) afterwards.

The squared energy density of the fermion sector is given as

$$\begin{aligned}\epsilon^2_\psi(x) = &-\frac{1}{4}\sum_{i,j}\Bigg[\Big\langle \bar{\psi}(x)\Big(\gamma^i - \mathrm{i}r\Big)U_i(x)\psi(x+\hat{i})\bar{\psi}(x)\Big(\gamma^j - \mathrm{i}r\Big)U_j(x)\psi(x+\hat{j})\Big\rangle \\ &\quad + \Big\langle \bar{\psi}(x)\Big(\gamma^i + \mathrm{i}r\Big)U_i^\dagger(x-\hat{i})\psi(x-\hat{i})\bar{\psi}(x)\Big(\gamma^j + \mathrm{i}r\Big)U_j^\dagger(x-\hat{j})\psi(x-\hat{j})\Big\rangle \\ &\quad - 2\Big\langle \bar{\psi}(x)\Big(\gamma^i - \mathrm{i}r\Big)U_i(x)\psi(x+\hat{i})\bar{\psi}(x)\Big(\gamma^j + \mathrm{i}r\Big)U_j^\dagger(x-\hat{j})\psi(x-\hat{j})\Big\rangle\Bigg] \\ &- \mathrm{i}\Big(m+3r\Big)\sum_i\Big\langle \bar{\psi}(x)\psi(x)\bar{\psi}(x)\Big(\gamma^i - \mathrm{i}r\Big)U_i(x)\psi(x+\hat{i})\Big\rangle \\ &+ \mathrm{i}\Big(m+3r\Big)\sum_i\Big\langle \bar{\psi}(x)\psi(x)\bar{\psi}(x)\Big(\gamma^i + \mathrm{i}r\Big)U_i^\dagger(x-\hat{i})\psi(x+\hat{i})\Big\rangle \\ &+ \Big(m+3r\Big)^2\Big\langle \bar{\psi}(x)\psi(x)\bar{\psi}(x)\psi(x)\Big\rangle.\end{aligned} \tag{6.41}$$

We have to evaluate expectation values of the form

$$\begin{aligned}\sum_{i,j}\Big\langle \bar{\psi}^a_\alpha(x)\Big(\gamma^i - \mathrm{i}r\Big)_{\alpha\beta}U_i^{ab}(x)\psi^b_\beta(x+\hat{i})\bar{\psi}^c_\mu(x)\Big(\gamma^j - \mathrm{i}r\Big)_{\mu\nu}U_j^{cd}(x)\psi^d_\nu(x+\hat{j})\Big\rangle \\ = \sum_{i,j}\Big\langle \bar{\psi}^a_\alpha(x)\psi^b_\beta(x+\hat{i})\bar{\psi}^c_\mu(x)\psi^d_\nu(x+\hat{j})\Big\rangle\Big(\gamma^i - \mathrm{i}r\Big)_{\alpha\beta}U_i^{ab}(x)\Big(\gamma^j - \mathrm{i}r\Big)_{\mu\nu}U_j^{cd}(x).\end{aligned} \tag{6.42}$$

This can be done by making use of the Wick theorem for fermion fields and afterwards using the statistical propagator (eq. 1.44) to rewrite the result

$$\begin{aligned}\Big\langle \bar{\psi}^a_\alpha(x)\psi^b_\beta(x+\hat{i})\bar{\psi}^c_\mu(x)\psi^d_\nu(x+\hat{j})\Big\rangle =&\Big\langle \bar{\psi}^a_\alpha(x)\psi^b_\beta(x+\hat{i})\Big\rangle\Big\langle \bar{\psi}^c_\mu(x)\psi^d_\nu(x+\hat{j})\Big\rangle \\ &- \Big\langle \bar{\psi}^a_\alpha(x)\psi^d_\nu(x+\hat{j})\Big\rangle\Big\langle \bar{\psi}^c_\mu(x)\psi^b_\beta(x+\hat{i})\Big\rangle \\ =&F^{ba}_{\beta\alpha}(x+\hat{i},x)F^{dc}_{\nu\mu}(x+\hat{j},x) - F^{da}_{\nu\alpha}(x+\hat{j},x)F^{bc}_{\beta\mu}(x+\hat{i},x).\end{aligned} \tag{6.43}$$

Using this, (eq. 6.42) is given as

$$\begin{aligned}\sum_{i,j}\Big\langle \bar{\psi}^a_\alpha(x)\psi^b_\beta(x+\hat{i})\bar{\psi}^c_\mu(x)\psi^d_\nu(x+\hat{j})\Big\rangle\Big(\gamma^i - \mathrm{i}r\Big)_{\alpha\beta}U_i^{ab}(x)\Big(\gamma^j - \mathrm{i}r\Big)_{\mu\nu}U_j^{cd}(x) \\ = \sum_{i,j}\mathrm{tr}\Big(F(x+\hat{i},x)\Big(\gamma^i - \mathrm{i}r\Big)U_i(x)\Big)\mathrm{tr}\Big(F(x+\hat{j},x)\Big(\gamma^j - \mathrm{i}r\Big)U_j(x)\Big) \\ - \sum_{i,j}\mathrm{tr}\Big(F(x+\hat{j},x)\Big(\gamma^i - \mathrm{i}r\Big)U_i(x)F(x+\hat{i},x)\Big(\gamma^j - \mathrm{i}r\Big)U_j(x)\Big).\end{aligned} \tag{6.44}$$

We observe, that this splits into two terms, with the first one canceling one contribution to the single squared single expectation value of the fermion energy density operator. All

other terms of (eq. 6.41) can be treated in similar fashion and introducing dimensionless lattice fields, we finally find

$$\begin{aligned}\langle\bar{\epsilon}^2_\psi(x)\rangle = \langle\bar{\epsilon}_\psi(x)\rangle^2 + \frac{g^4}{4}\sum_{i,j}\Bigg[&\mathrm{tr}\Big(\bar{F}(x+\hat{j},x)\big(\gamma^i-\mathrm{i}r\big)U_i(x)\bar{F}(x+\hat{i},x)\big(\gamma^j-\mathrm{i}r\big)U_j(x)\Big)\\ &+\mathrm{tr}\Big(\bar{F}(x-\hat{j},x)\big(\gamma^i+\mathrm{i}r\big)U_i^\dagger(x-\hat{i})\bar{F}(x-\hat{i},x)\big(\gamma^j+\mathrm{i}r\big)U_j^\dagger(x-\hat{j})\Big)\\ &-2\mathrm{tr}\Big(\bar{F}(x-\hat{j},x)\big(\gamma^i-\mathrm{i}r\big)U_i(x)\bar{F}(x+\hat{i},x)\big(\gamma^j+\mathrm{i}r\big)U_j^\dagger(x-\hat{j})\Big)\Bigg]\\ &+\mathrm{i}g^4\big(\bar{m}+3r\big)\sum_i\Bigg[\mathrm{tr}\Big(\bar{F}(x+\hat{i},x)\bar{F}(x,x)\big(\gamma^i-\mathrm{i}r\big)U_i(x)\Big)\\ &-\mathrm{tr}\Big(\bar{F}(x-\hat{i},x)\bar{F}(x,x)\big(\gamma^i+\mathrm{i}r\big)U_i^\dagger(x-\hat{i})\Big)\Bigg]\\ &-g^4\big(\bar{m}+3r\big)^2\mathrm{tr}\Big(\bar{F}(x,x)\bar{F}(x,x)\Big).\end{aligned} \tag{6.45}$$

With the help of (eq. 6.40) we can now derive the standard deviation and finally the standard error (eq. 6.39). It is straight forward to repeat the procedure for the pressure observable

$$\begin{aligned}\langle\bar{P}^2_{i,\psi}(x)\rangle = \langle\bar{P}_{i,\psi}(x)\rangle^2 + \frac{g^4}{4}\Bigg[&\mathrm{tr}\Big(\bar{F}(x+\hat{i},x)\big(\gamma^i-\mathrm{i}r\big)U_i(x)\bar{F}(x+\hat{i},x)\big(\gamma^i+\mathrm{i}r\big)U_i(x)\Big)\\ &-2\mathrm{tr}\Big(\bar{F}(x-\hat{i},x)\big(\gamma^i-\mathrm{i}r\big)U_i(x)\bar{F}(x+\hat{i},x)\big(\gamma^i+\mathrm{i}r\big)U_i^\dagger(x-\hat{i})\Big)\\ &+\mathrm{tr}\Big(\bar{F}(x-\hat{i},x)\big(\gamma^i+\mathrm{i}r\big)U_i^\dagger(x-\hat{i})\bar{F}(x-\hat{i},x)\big(\gamma^i+\mathrm{i}r\big)U_i^\dagger(x-\hat{i})\Big)\Bigg]\\ &+\mathrm{i}g^4r\Bigg[\mathrm{tr}\Big(\bar{F}(x+\hat{i},x)\bar{F}(x,x)\big(\gamma^i-\mathrm{i}r\big)U_i(x)\Big)\\ &-\mathrm{tr}\Big(\bar{F}(x-\hat{i},x)\bar{F}(x,x)\big(\gamma^i+\mathrm{i}r\big)U_i^\dagger(x-\hat{i})\Big)\Bigg]-g^4r^2\mathrm{tr}\Big(\bar{F}(x,x)\bar{F}(x,x)\Big).\end{aligned} \tag{6.46}$$

Keep in mind that the index i is not summed in case of the pressure and denotes the spacial direction.

6.2.2 Initial Values and Renormalization

In the simulation, we initialize the gauge and fermion sector independently and couple both sectors at the first time-step of the simulation. At initial time $t_0 = 0$, the sectors are thus still uncoupled and we have to evaluate the energy density and pressure of the fermion sector with respect to the free non-interacting vacuum, setting $U_i = 1$. It is well known from the continuum, that this leads to divergencies of fermion expectation values, due to vacuum contributions of fermion fields in a quantum field theory [149]. This infinite vacuum contribution has to be subtracted when defining the physical observables. On a lattice, the theory is naturally regulated by the lattice momentum cutoff, hence the vacuum contribution is finite, but it has to be removed as well to define physical quantities.

In this section, we first identify the appearance of such vacuum contributions in the lattice

fermion energy density and pressure observables. Afterwards, we discuss how to subtract them in our simulation. Although we are mainly dealing with vacuum fermions in later simulations, we will discuss the more general case of thermal fermions of temperature T. The initialization of thermal fermions has previously been discussed in (section 1.2), where a thermal distribution enters the expectation value of a commutator of creation and annihilation operators (eq. 1.41).

With all fermion observables being formulated with use of the statistical propagator, let us first investigate the propagator itself. For thermal fermions, its lattice Fourier representation can be written as

$$\begin{aligned} F_{\alpha\beta}(x,y) &= \frac{1}{2V^2}\sum_{\mathbf{p},\mathbf{k}}\sum_{s,r}\Bigg(\Big\langle\Big[a_s(\mathbf{p}),a_r^\dagger(\mathbf{k})\Big]\Big\rangle u_{s,\alpha}(\mathbf{p})\bar{u}_{r,\beta}(\mathbf{k})e^{-\mathrm{i}px+\mathrm{i}ky} \\ &\qquad + \Big\langle\Big[\hat{b}_s^\dagger(\mathbf{p}),\hat{b}_r(\mathbf{k})\Big]\Big\rangle v_{s,\alpha}(\mathbf{p})\bar{v}_{r,\beta}(\mathbf{k})e^{\mathrm{i}px-\mathrm{i}ky}\Bigg) \\ &= \frac{1}{2V}\sum_{\mathbf{p}}\Big(1-2n_{FD}(\mathbf{p},T)\Big)\Bigg(\frac{\Big(\gamma^\mu s_\mu(\mathbf{p})+\mu\Big)_{\alpha\beta}}{2s_0}e^{-\mathrm{i}p(x-y)} - \frac{\Big(\gamma^\mu s_\mu(\mathbf{p})-\mu\Big)_{\alpha\beta}}{2s_0}e^{\mathrm{i}p(x-y)}\Bigg), \end{aligned} \tag{6.47}$$

where we used (eq. 1.41) and carried out the spin sums (eq. 2.44). The distribution function $n_{FD}(\mathbf{p},T)$ is the Fermi-Dirac distribution (eq. 1.43) and the vacuum result is easily obtained by setting $n_{FD}(\mathbf{p},T)=0$. The following combination of traces of the statistical propagator enters the energy density (eq. 6.34) and pressure (eq. 6.36) observables of the fermion sector

$$\begin{aligned} &\mathrm{tr}\Big[F(x+\hat{i},x)\Big(\gamma^i-\mathrm{i}r\Big)\Big] - \mathrm{tr}\Big[F(x-\hat{i},x)\Big(\gamma^i-\mathrm{i}r\Big)\Big] \\ &\qquad = \frac{2N_c}{V}\sum_{\mathbf{p}}\frac{1-2n_{FD}(\mathbf{p},T)}{s_0}\Bigg(\Big(s^i-\mathrm{i}r\mu\Big)e^{\mathrm{i}\frac{2\pi}{N_i}q_i} - \Big(s^i+\mathrm{i}r\mu\Big)e^{-\mathrm{i}\frac{2\pi}{N_i}q_i}\Bigg), \end{aligned} \tag{6.48}$$

where we inserted the lattice momenta $p^i=\frac{2\pi}{N_i a}q_i,\ q_i\in\{-\frac{N_i}{2}+1,...,\frac{N_i}{2}\}$ and $N_c=3$ denotes the number of colors. This can be simplified using

$$s^i = \sin\Big(ap^i\Big) = \sin\left(\frac{2\pi}{N_i}q_i\right) = \frac{1}{2i}\Big(e^{\mathrm{i}\frac{2\pi}{N_i}q_i} - e^{-\mathrm{i}\frac{2\pi}{N_i}q_i}\Big), \tag{6.49}$$

$$\cos\Big(ap^i\Big) = \cos\left(\frac{2\pi}{N_i}q_i\right) = \frac{1}{2}\Big(e^{\mathrm{i}\frac{2\pi}{N_i}q_i} + e^{-\mathrm{i}\frac{2\pi}{N_i}q_i}\Big), \tag{6.50}$$

leading to

$$\begin{aligned} &\mathrm{tr}\Big[F(x+\hat{i},x)\Big(\gamma^i-\mathrm{i}r\Big)\Big] - \mathrm{tr}\Big[F(x-\hat{i},x)\Big(\gamma^i-\mathrm{i}r\Big)\Big] \\ &\qquad = \frac{\mathrm{i}4N_c}{V}\sum_{\mathbf{p}}\frac{1-2n_{FD}(\mathbf{p},T)}{s_0}\Big(\sin^2\Big(ap^i\Big) - r\mu\cos\Big(ap^i\Big)\Big). \end{aligned} \tag{6.51}$$

Inserting this into the free fermion energy density (eq. 6.34) we find

$$\bar{\epsilon} = \frac{2N_c g^2}{V}\sum_{\mathbf{p}}\frac{1-2n_{FD}(\mathbf{p},T)}{s_0}\Bigg[-\sum_{i=1}^{3}\sin^2(ap^i) - \mu\Bigg(\bar{m}+r\sum_{i=1}^{3}\Big(1-\cos(ap^i)\Big)\Bigg)\Bigg]. \tag{6.52}$$

Identifying the lattice mass and the lattice momenta of free Dirac fermions (eq. 2.38) we finally have

$$\bar{\epsilon} = -\frac{2N_c g^2}{V} \sum_{\mathbf{p}} s_0(\mathbf{p}) \Big(1 - 2n_{FD}(\mathbf{p}, T)\Big). \tag{6.53}$$

First note, that the result (eq. 6.54) is position independent, as expected for a free gas of fermions with a temperature T. Furthermore the result is finite, because the momenta $\mathbf{p}$ are regulated by the lattice momentum cutoff.
We obtain the vacuum solution by setting $n_{FD}(\mathbf{p}, T) = 0$. This result is non-vanishing and referred to as vacuum energy

$$\bar{\epsilon}^{vac} = -\frac{2N_c g^2}{V} \sum_{\mathbf{p}} s_0 \overset{a\to 0}{\to} -\infty. \tag{6.54}$$

The renormalized energy density can now be defined by subtracting the vacuum energy[2]

$$\bar{\epsilon}^R = \bar{\epsilon} - \bar{\epsilon}^{vac} = \frac{4N_c g^2}{V} \sum_{\mathbf{p}} s_0 \; n_{FD}(\mathbf{p}, T). \tag{6.55}$$

This result is the lattice version of the energy density of a free gas of fermions and the prefactor $g_\psi = 4N_c$ is the degeneracy factor, given by the number of spins, colors and fermion/anti-fermion.

At initial time $t_0 = 0$, we calculate this vacuum energy (eq. 6.54) in our simulation, when evaluating (eq. 6.34)

$$\bar{\epsilon}^{vac}_\psi = \bar{\epsilon}_\psi(t_0) = \frac{1}{V} \sum_{\mathbf{x}} \langle 0| \, \hat{\mathcal{H}}_\psi(t_0, \mathbf{x}) \, |0\rangle \, . \tag{6.56}$$

Hence its initial value defines an additive renormalization constant, that has to be subtracted at every time-step in the simulation, to obtain the physical energy density.

It is straight forward to repeat this discussion for the fermion pressure (eq. 6.36), leading to the following contribution at initial time

$$\bar{P}^\psi_i = -g^2 \frac{2N_c}{V} \sum_{\mathbf{p}} \frac{1 - 2n_{FD}(\mathbf{p}, T)}{s_0} \left(\sin^2(ap^i) + \mu r \Big(1 - \cos(ap^i)\Big) \right). \tag{6.57}$$

We find by setting $n_{FD}(\mathbf{p}, T) = 0$, that the fermion pressure observable has a vacuum contribution as well, that has to be subtracted to define the physical observable

$$\bar{P}^{\psi,R}_i = \bar{P}^\psi_i - \bar{P}^{\psi,vac}_i. \tag{6.58}$$

This renormalization procedure for the observables also matches the procedure of calculating physical expectation values from normal ordered operators. As discussed in (section 1.2), normal ordered operators are constructed such, that vacuum contributions are no longer present. Following this concept, our renormalization procedure is nothing but normal ordering the operator. It is straight forward to check that, starting from the operator and enforcing normal order, reproducing our results.

[2]The vacuum energy is sometimes referred to as $T = 0$ contribution in the context of statistical quantum field theory, where the renormalization procedure is known as additive renormalization. [150]

6.3 Occupation

We want to define a measure for the occupation of field modes in our semi-classical system in a gauge invariant way. This can be done by making use of a gauge independent observable, which is provided by the energy density of the system. We will use the Fourier transform of the energy density to identify the Fourier modes as energy modes of the system, providing information on the occupation of modes. We will crosscheck this procedure numerically by comparing it to a gauge dependent definition of the occupation of modes presented in [40, 43]. The additional gauge degree of freedom will be fixed using the Coulomb condition and a relaxation algorithm.

6.3.1 Gauge Invariant Occupation of Energy Modes

We follow the definition that has first been presented in [126] for a pure Yang-Mills simulation and extend it to a system including fermions. As pointed out already, our starting point is the gauge invariant energy density

$$\bar{\epsilon}(x) = \bar{\epsilon}_{YM}(x) + \bar{\epsilon}_{\psi}(x). \tag{6.59}$$

In a first step, we perform the lattice Fourier transform of the energy density

$$\tilde{\bar{\epsilon}}(t, \mathbf{p}) = \frac{1}{\sqrt{|\Lambda|}} \sum_{\mathbf{x}\in\Lambda} \bar{\epsilon}(t, \mathbf{x}) e^{-\mathrm{i}\mathbf{x}\mathbf{p}} = \frac{1}{\sqrt{V}} \sum_{\mathbf{n}\in\Lambda} \bar{\epsilon}(t, \mathbf{x}) e^{-\mathrm{i}\frac{2\pi}{N_i} n_i k_i}, \tag{6.60}$$

where we define the position and momentum space lattice according to

$$\Lambda = \Big\{ \mathbf{x} = (x, y, z); \quad x_i = a n_i; \quad n_i \in \Big[0, 1, ..., N_i - 1\Big] \Big\}, \tag{6.61}$$

$$\tilde{\Lambda} = \Big\{ \mathbf{p} = (p_x, p_y, p_z); \quad p_i = \frac{2\pi}{a N_i} k_i; \quad k_i \in \Big[-N_i/2 + 1, ..., 0, ..., N_i/2 \Big] \Big\}. \tag{6.62}$$

The Fourier transform can be split into a Yang-Mills and fermion part as well

$$\tilde{\bar{\epsilon}}(t, \mathbf{p}) = \tilde{\bar{\epsilon}}_{YM}(t, \mathbf{p}) + \tilde{\bar{\epsilon}}_{\psi}(t, \mathbf{p}). \tag{6.63}$$

In context of a Fourier transformation, we have to treat the zero-momentum $\mathbf{p} = (0, 0, 0)$ with specific care. Recalling the definition of the (discrete) Fourier transform and setting $\mathbf{p} = \mathbf{0}$, we find

$$\tilde{\bar{\epsilon}}(t, \mathbf{0}) = \tilde{\bar{\epsilon}}_0(t) = \frac{1}{\sqrt{V}} \sum_{\mathbf{x}} \bar{\epsilon}(t, \mathbf{x}) = \sqrt{V} \bar{\epsilon}(t). \tag{6.64}$$

The zeroth Fourier mode therefore is nothing but the lattice average of the energy density itself and can not be interpreted as a specific energy mode of our system. As a consequence, we exclude it in our definition.

The definition of the occupation of energy modes is motivated by the energy density of a free gas of bosons or fermions [151]

$$\epsilon = \int \omega_{\mathbf{p}} n(\mathbf{p}) d^3 p, \tag{6.65}$$

where $n(\mathbf{p})$ denotes the distribution function and $\omega_{\mathbf{p}}$ the energy of the specific modes. For a free gas on the lattice, the energy of a mode corresponds to the lattice dispersion relation. In case of massless Yang-Mills fields it is given as

$$\omega_{\mathbf{p}}^2 \quad \rightarrow \quad \frac{1}{a^2}\hat{p}^2 = \frac{4}{a^2}\sum_{i=1}^{3}\sin^2\left(\frac{ap^i}{2}\right), \tag{6.66}$$

where $\hat{p}$ takes discrete values in an interval of

$$\frac{1}{a}\hat{p} \in \left[0, \frac{2}{a}\sqrt{3\sin^2\pi/2}\right] = \left[0, \frac{2\sqrt{3}}{a}\right]. \tag{6.67}$$

We discussed the lattice dispersion relation of massive Wilson fermion fields of mass $\bar{m} = am$ already in (section 2.2.1), obtaining

$$\omega_{\mathbf{p}}^2 \quad \rightarrow \quad \frac{1}{a^2}s_0^2 = \frac{1}{a^2}\sum_{i=1}^{3}\sin^2\left(ap^i\right) + \frac{1}{a^2}\mu^2(\mathbf{p}), \tag{6.68}$$

with the lattice mass μ (eq. 2.38). It takes discrete values in the interval of

$$\frac{1}{a}s_0 \in \left[m, \frac{1}{a}\sqrt{3\sin(\pi) + (m + 3(1-\cos(\pi)))^2}\right] = \left[m, m + \frac{6}{a}r\right]. \tag{6.69}$$

Every lattice momentum p_i is associated with a specific value $\omega_{\mathbf{p}}$ of either the fermion or the boson lattice dispersion relation. Note that this mapping is unique, but its inversion is not unique: for some values of $\omega_{\mathbf{p}}$ there exist multiple momenta of p_i, e.g.

$$\omega_{\mathbf{p}} \quad \rightarrow \quad \hat{p} = \sin\left(\frac{\pi}{N_i}n\right) \quad \text{for} \quad \begin{cases} \mathbf{p} = \left(\sin\left(\frac{\pi}{N_i}n\right), 0, 0\right) \\ \mathbf{p} = \left(0, \sin\left(\frac{\pi}{N_i}n\right), 0\right) \\ \mathbf{p} = \left(0, 0, \sin\left(\frac{\pi}{N_i}n\right)\right). \end{cases} \tag{6.70}$$

We call $\Gamma_{\mathbf{p}}$ the set of momenta $\mathbf{p}$ with equal lattice dispersion relation $\omega_{\mathbf{p}}$.

The energy density in momentum space is a function of the lattice momenta p^i and it takes different values for different momenta of the set $\mathbf{p} \in \Gamma_{\mathbf{p}}$. We therefore perform an average for momenta in the set $\Gamma_{\mathbf{p}}$. The result corresponds to the occupation of one specific energy mode $\omega_{\mathbf{p}}$, defining the gauge invariant occupation of energy modes as

$$n(t, \omega_{\mathbf{p}}) = \frac{1}{\omega_{\mathbf{p}}}\left\langle\left|\tilde{\bar{\epsilon}}(t, \mathbf{p})\right|\right\rangle_{\mathbf{p}} = \frac{1}{\omega_{\mathbf{p}}}\left(\frac{1}{|\Gamma_{\mathbf{p}}|}\sum_{\mathbf{p}\in\Gamma_{\mathbf{p}}}\left|\tilde{\bar{\epsilon}}(t, \mathbf{p})\right|\right). \tag{6.71}$$

This definition is motivated from (eq. 6.65) and provides a gauge invariant possibility to calculate the occupation of energy modes. Although we are in an interacting system, an analysis in [40] has shown, that it is reasonable in a system dominated by classical modes to approximate the dispersion relation $\omega_{\mathbf{p}}$ using the free lattice dispersion.

We have defined the occupation of energy modes (eq. 6.71) without restricting to fermions or bosons. The corresponding observables are given by replacing the Fourier transformed

energy density with the energy density of the fermion or the Yang-Mills sector and the lattice dispersion relation (eq. 6.66) or (eq. 6.68)

$$g^2 a^3 n_{YM}(t,\hat{p}) = \bar{n}_{YM}(t,\hat{p}) = \frac{1}{\hat{p}} \left\langle \left| \tilde{\bar{\epsilon}}_{YM}(t,\mathbf{p}) \right| \right\rangle_{\mathbf{p}}, \tag{6.72}$$

$$g^2 a^3 n_{\psi}(t,\hat{p}) = \bar{n}_{\psi}(t,\hat{p}) = \frac{1}{s_0} \left\langle \left| \tilde{\bar{\epsilon}}_{\psi}(t,\mathbf{p}) \right| \right\rangle_{\mathbf{p}}. \tag{6.73}$$

We defined the dimensionless lattice version of the observable, introducing the appropriate rescaling in terms of the lattice spacing a.

The definitions (eq. 6.72) provide a measure for the occupation of energy modes, hence it can also be used to discuss the classicality of our system. We expect the system to be initially dominated by an overoccupation of classical field modes, which should manifest itself in a large occupation of low energy modes in the Yang-Mills sector. With the fermion sector being initialized as vacuum fermions, all energy modes have to be unoccupied at initial time. We are now able to measure how high energy modes become occupied during the evolution of the system, possibly causing the classical approximation to break down at a late stage of the simulation.

Keeping in mind, that the definition of the occupation of energy modes discussed in this section does not match the Bose-Einstein or Fermi-Dirac distribution of modes in equilibrium statistical (quantum-)field theory.
This can easily be seen, by a check of dimension: The distribution function of equilibrium statistical physics has dimension 1, whereas

$$[n_{YM}(t,\omega_{\mathbf{p}})] \sim \frac{[\epsilon_{YM/\psi}]}{[\omega_{\mathbf{p}}]} \sim \frac{1}{\mathrm{fm}^3}, \tag{6.74}$$

has the dimension of a density, hence we can interpret it as an occupation number density [126]

$$n_{YM}(t,\hat{p}) = \frac{N_{YM}(t,\hat{p})}{V}. \tag{6.75}$$

To monitor the occupation of high energy modes during the evolution of the system, it is useful to define a specific reduction of the occupation of energy modes (eq. 6.72). As discussed in (section 3.4), the construction of the Glasma state from the CGC effective theory is realized by copying the effectively two dimensional solution of the Poisson equation to the other transverse planes in longitudinal direction, generating color flux tubes. As a result, when plotting the occupation of energy modes as a function of longitudinal momentum, the distribution is peaked at $p_z = 0$. We will later confirm this numerically when discussing our simulation results. To measure how energy modes with momenta $pz \neq 0$ become more and more occupied during the evolution of the system, we define the occupation of energy modes as a function of longitudinal momentum, by averaging the occupation in the transverse planes

$$n(t,p_z) = \frac{1}{N_x N_y} \sum_{p_x,p_y} \frac{1}{\omega_{\mathbf{p}}} \left\langle \left| \tilde{\epsilon}(t,\mathbf{p}) \right| \right\rangle_{\mathbf{p}}. \tag{6.76}$$

6.3.2 Gauge Variant Occupation

To justify the validity of our gauge invariant approach for the calculation of the occupation of energy modes, we want to compare it to the gauge variant definition, familiar from the

literature [43]. The gauge variant occupation has only be defined in a pure Yang-Mills theory and therefore we restrict ourselves to the Yang-Mills sector. Starting point of the gauge variant definition is the Hamilton function of the Yang-Mills sector, that is derived from the Hamiltonian (eq. 1.18) by integrating the position dependence

$$H_{YM}(t) = \int \mathcal{H}_{YM}(t,\mathbf{x})d^3x = \int \mathrm{tr}\Big[E_i(x)E_i(x) + \sum_{i<j} F_{ij}(x)F_{ij}(x)\Big]d^3x. \tag{6.77}$$

In the previous section, we already discussed that the total energy in a free theory is given by the free dispersion relation $\omega_{\mathbf{k}} = \sqrt{\mathbf{k}^2 + m^2}$, weighted with the occupation number $n(\mathbf{k})$

$$H = \int \omega_{\mathbf{k}} n(\mathbf{k}) d^3k, \tag{6.78}$$

where we replaced the energy by the Hamilton function, which is possible in a conservative system.

Applying a Fourier transform for the chromo-electric part of the Hamiltonian, we find

$$\begin{aligned} H \sim \int \mathrm{Retr}\Big[E_i(x)E_i(x)\Big]d^3x &= \int\int \mathrm{Retr}\Big[E_i(t,\mathbf{k})E_i(t,\mathbf{p})\Big]\int e^{-\mathbf{i}\mathbf{x}(\mathbf{k}+\mathbf{p})}d^3x\frac{d^3k}{(2\pi)^3}\frac{d^3p}{(2\pi)^3} \\ &= \int \mathrm{Retr}\Big[E_i(t,\mathbf{k})E_i(t,-\mathbf{k})\Big]\frac{d^3k}{(2\pi)^3} = \int \mathrm{Retr}|E_i(t,\mathbf{k})|^2\frac{d^3k}{(2\pi)^3}. \end{aligned} \tag{6.79}$$

In [43] it has been argued, that the chromo-electric and chromo-magnetic modes are equally distributed, when taking a time average, making it possible to approximate

$$\overline{H} = \int \omega(\mathbf{k})n(\mathbf{k})d^3k \approx \int 2\mathrm{Retr}|E_i(t,\mathbf{k})|^2\frac{d^3k}{(2\pi)^3}, \tag{6.80}$$

where the over-line indicates a time average and the additional factor of 2 counts the contribution of the chromo-magnetic part. We can now conclude from a comparison to (eq. 6.78), that

$$n(\mathbf{k}) = \frac{2}{(2\pi)^3\omega_{\mathbf{k}}}\mathrm{Retr}|E_i(k)|^2, \tag{6.81}$$

where we use the same argument as previously, that the dispersion relation can be taken as (quasi-) free.

On the lattice, the free dispersion relation $\omega_{\mathbf{p}}$ will again be replaced by the lattice Yang-Mills dispersion relation. Also note, that the definition (eq. 6.81) has the same dimension as the gauge invariant definition (eq. 6.72). As stated in the beginning, the definition of the occupation of modes (eq. 6.81) requires an additional gauge fixing procedure. We choose Coulomb gauge

$$0 = \nabla\mathbf{A}, \tag{6.82}$$

and fix the gauge on the lattice, making use of a relaxation algorithm [102].

6.3.3 Fermion Spectrum

Having discussed a gauge variant definition for the occupation of modes in the Yang-Mills sector of QCD we want to present a possibility to evaluate the occupation in the fermion sector

as well. A possible definition of a quark production rate has been proposed in [74]. We will briefly review the derivation and afterwards adapt the result to our static system. The quark number per momentum fraction is derived in [74] by making use of the LSZ-reduction formula for the production of quark-antiquark pairs. They define a probability P_1 to produce one quark-antiquark pair and generalize to n-pairs afterwards. The mean number of produced pairs per momentum fraction, given from the first moment $\sum_n nP_n$, can then be written as

$$\frac{dN_q}{d^3p} = \frac{1}{(2\pi)^3}\sum_{s,r=1}^{2}\sum_{a,b=1}^{N_c}\int\frac{d^3k}{(2\pi)^3}\left|\left(\psi^{0+}_{\mathbf{p},r,b}\middle|\psi^{-}_{\mathbf{k},s,a}\right)_t\right|^2, \tag{6.83}$$

with the free spinor mode-function

$$\psi^{0+}_{\mathbf{p},r,b} = u_r(\mathbf{p})e^{-\mathrm{i}px}. \tag{6.84}$$

The scalar product is defined as

$$\left|\left(\psi^{0+}_{\mathbf{k},r,b}\middle|\psi^{-}_{\mathbf{p},s,a}\right)_t\right|^2 = \int\int\psi^{0+,\dagger}_{\mathbf{p},r,b}(t,\mathbf{x})\psi^{-}_{\mathbf{k},s,a}(t,\mathbf{x})\psi^{-,\dagger}_{\mathbf{k},s,a}(t,\mathbf{y})\psi^{0+}_{\mathbf{p},r,b}(t,\mathbf{y})d^3xd^3y. \tag{6.85}$$

For the details on the derivation see Appendix A of [74].

We will now use the stochastic low-cost gendered fermions (eq. 1.48) to define the following combination of gendered spinors

$$\psi^{-}_{\eta}(x) := \frac{1}{\sqrt{2}}\Big(\psi_M(x) - \psi_F(x)\Big) = \int\sum_{r=1}^{2}\sum_{b=1}^{N_c}\eta_{r,b}(\mathbf{k})\psi^{-}_{\mathbf{k},r,b}(x)\frac{d^3k}{(2\pi)^3}, \tag{6.86}$$

where we identified the mode-functions $\psi^{\pm}_{\mathbf{k},r,b}(t,\mathbf{x})$. At initial time $t_0 = 0$, these are given by the vacuum solution of free Dirac fermions

$$\psi^{+}_{\mathbf{k},r,b}(t_0,\mathbf{x}) = \psi^{0+}_{\mathbf{k},r,b}(t_0,\mathbf{x}) = u_{r,b}(\mathbf{k})e^{-\mathrm{i}kx}, \tag{6.87}$$

$$\psi^{-}_{\mathbf{k},r,b}(t_0,\mathbf{x}) = \psi^{0-}_{\mathbf{k},r,b}(t_0,\mathbf{x}) = v_{r,b}(\mathbf{k})e^{\mathrm{i}kx}. \tag{6.88}$$

Using (eq. 6.86) and taking an ensemble average, we are left with

$$\begin{aligned}\left\langle\psi^{-}_{\eta}(x)\psi^{-\dagger}_{\eta}(y)\right\rangle_{Ens} &= \int\int\sum_{r,r'}^{2}\sum_{b,b'}^{N_c}\underbrace{\left\langle\eta_{r,b}(\mathbf{k})\eta^{*}_{r'b'}(\mathbf{k}')\right\rangle_{Ens}}_{=(2\pi)^3\delta(\mathbf{k}-\mathbf{k}')\delta_{rr'}\delta_{bb'}}\psi^{-}_{\mathbf{k},r,b}(x)\psi^{-\dagger}_{\mathbf{k}',r',b'}(y)\frac{d^3k}{(2\pi)^3}\frac{d^3k'}{(2\pi)^3}\\ &= \int\sum_{r=1}^{2}\sum_{b=1}^{N_c}\psi^{-}_{\mathbf{k},r,b}(x)\psi^{-\dagger}_{\mathbf{k},r,b}(y)\frac{d^3k}{(2\pi)^3},\end{aligned} \tag{6.89}$$

where we used (eq. 1.49). We can now substitute

$$\begin{aligned}&\sum_{s=1}^{2}\sum_{a=1}^{N_c}\int\left|\left(\psi^{0+}_{\mathbf{k},r,b}\middle|\psi^{-}_{\mathbf{p},s,a}\right)_t\right|^2\frac{d^3k}{(2\pi)^3} \\ &\quad= \int\int\psi^{0+,\dagger}_{\mathbf{p},r,b}(t,\mathbf{x})\sum_{s=1}^{2}\sum_{a=1}^{N_c}\int\psi^{-}_{\mathbf{k},s,a}(t,\mathbf{x})\psi^{-,\dagger}_{\mathbf{k},s,a}(t,\mathbf{y})\frac{d^3k}{(2\pi)^3}\psi^{0+}_{\mathbf{p},r,b}(t,\mathbf{y})d^3xd^3y \\ &\quad= \int\int\psi^{0+,\dagger}_{\mathbf{p},r,b}(t,\mathbf{x})\left\langle\psi^{-}_{\eta}(t,\mathbf{x})\psi^{-\dagger}_{\eta}(t,\mathbf{y})\right\rangle_{Ens}\psi^{0+}_{\mathbf{p},r,b}(t,\mathbf{y})d^3xd^3y \\ &\quad= \left\langle\int\psi^{0+,\dagger}_{\mathbf{p},r,b}(t,\mathbf{x})\psi^{-}_{\eta}(t,\mathbf{x})d^3x\int\psi^{-\dagger}_{\eta}(t,\mathbf{y})\psi^{0+}_{\mathbf{p},r,b}(t,\mathbf{y})d^3y\right\rangle_{Ens} = \left\langle\left|\left(\psi^{0+,\dagger}_{\mathbf{p},r,b}\middle|\psi^{-}_{\eta}\right)_t\right|^2\right\rangle_{Ens}.\end{aligned} \tag{6.90}$$

We have shown, that it is possible to evaluate the quark spectrum using stochastic low cost via

$$\frac{dN_q}{d^3p} = \frac{1}{2(2\pi)^3}\sum_{r=1}^{2}\sum_{b=1}^{N_c}\left\langle\left|\left(\psi^{0+,\dagger}_{\mathbf{p},r,b}\middle|\psi_M - \psi_F\right)_t\right|^2\right\rangle_{N_{ens}}. \tag{6.91}$$

This result can be simplified even further in case of the static box, by explicitly inserting the mode functions at initial time (eq. 6.87) in the last line of (eq. 6.90)

$$\begin{aligned}\left\langle \int \psi^{0+,\dagger}_{\mathbf{p},r,b}(t,\mathbf{x})\psi^{-}_{\eta}(t,\mathbf{x})d^3x \int \psi^{-\dagger}_{\eta}(t,\mathbf{y})\psi^{0+}_{\mathbf{p},r,b}(t,\mathbf{y})d^3y\right\rangle_{N_{ens}} \\ =\left\langle u^{\dagger}_{r,b}(\mathbf{p})\int \psi^{-}_{\eta}(t,\mathbf{x})e^{-\mathrm{i}\mathbf{p}\mathbf{x}}d^3x\int \psi^{-\dagger}_{\eta}(t,\mathbf{y})e^{\mathrm{i}\mathbf{p}\mathbf{y}}d^3y u_{r,b}(\mathbf{p})\right\rangle_{N_{ens}} \\ =\left\langle \tilde{\psi}^{-\dagger}_{\eta}(t,\mathbf{p})u_{r,b}(\mathbf{p})u^{\dagger}_{r,b}(\mathbf{p})\tilde{\psi}^{-}_{\eta}(t,\mathbf{p})\right\rangle_{N_{ens}},\end{aligned} \tag{6.92}$$

where we identified the Fourier transformation. Inserting this into (eq. 6.92) and performing a spin sum (eq. 1.37), makes it possible to write the quark production rate in the following way

$$\frac{dN_q}{d^3p} = \frac{N_c}{2\omega_{\mathbf{p}}(2\pi)^3}\left\langle \bar{\psi}^{-}_{\eta}(t,\mathbf{p})\left(\omega_{\mathbf{p}}\gamma^0 + \gamma^i p^i + m\right)\psi^{-}_{\eta}(t,\mathbf{p})\right\rangle_{N_{ens}}. \tag{6.93}$$

Explicitly inserting (eq. 6.86) finally leads to the quark number per momentum fraction

$$\frac{dN_q}{d^3p} = \frac{N_c}{2(2\pi)^3}\left\langle \left(\bar{\psi}_M(t,\mathbf{p}) - \bar{\psi}_F(t,\mathbf{p})\right)\frac{\omega_{\mathbf{p}}\gamma^0 + \gamma^i p^i + m}{2\omega_{\mathbf{p}}}\left(\psi_M(t,\mathbf{p}) - \psi_F(t,\mathbf{p})\right)\right\rangle_{N_{ens}}. \tag{6.94}$$

When discretizing (eq. 6.94) we have to replace the integrals by lattice sums and the dispersion relation by the corresponding lattice dispersion relation of Wilson fermions (eq. 2.27)

$$\frac{dN_q}{d^3p} = \frac{N_c}{2(2\pi)^3}\left\langle \left(\bar{\psi}_M(t,\mathbf{p}) - \bar{\psi}_F(t,\mathbf{p})\right)\frac{s_0(\mathbf{p})\gamma^0 + \gamma^i s^i(\mathbf{p}) + \mu(\mathbf{p})}{2s_0(\mathbf{p})}\left(\psi_M(t,\mathbf{p}) - \psi_F(t,\mathbf{p})\right)\right\rangle_{N_{ens}}. \tag{6.95}$$

The total quark number is finally given by summing the momenta

$$N_q = \frac{N_c}{2}\sum_{\mathbf{p}}\left\langle \left(\bar{\psi}_M(t,\mathbf{p}) - \bar{\psi}_F(t,\mathbf{p})\right)\frac{s_0(\mathbf{p})\gamma^0 + \gamma^i s^i(\mathbf{p}) + \mu(\mathbf{p})}{2s_0(\mathbf{p})}\left(\psi_M(t,\mathbf{p}) - \psi_F(t,\mathbf{p})\right)\right\rangle_{N_{ens}}. \tag{6.96}$$

It is possible to derive the total anti-quark number in similar fashion,

$$N_{\bar{q}} = \frac{N_c}{2}\sum_{\mathbf{p}}\left\langle \left(\bar{\psi}_M(t,\mathbf{p}) + \bar{\psi}_F(t,\mathbf{p})\right)\frac{s_0(\mathbf{p})\gamma^0 + \gamma^i s^i(\mathbf{p}) - \mu(\mathbf{p})}{2s_0(\mathbf{p})}\left(\psi_M(t,\mathbf{p}) + \psi_F(t,\mathbf{p})\right)\right\rangle_{N_{ens}}. \tag{6.97}$$

In a simulation, we expect $N_q = N_{\bar{q}}$, because we start from the vacuum state with zero entropy.

In [74] it has been argued that the given definition of the quark and anti-quark number is gauge invariant. Strictly speaking this is only true considering the limit $t \to \infty$, which is why we fix Coulomb gauge when evaluating (eq. 6.96) and (eq. 6.97) at every time-step in our simulation.

7

The Simulation in a Static Box

In this chapter we will discuss the realization of the semi-classical approximation of QCD in a real-time lattice simulation. We will provide results of different tests of the lattice implementation of the model, studying its numerical properties in detail. Additionally we will provide a matching procedure for the semi-classical approximation, allowing us to introduce a physical scale to our system, fixing the lattice spacing a.

7.1 Lattice Implementation of the Semi-Classical Equations of Motion

In (chapter 4), we presented the real-time equations of motion of the semi-classical model. As pointed out earlier, it is not possible to solve the time dependence of these equations in a closed form, making a discretization necessary. This discretization of the temporal direction has consequences on the numerics, when solving the equations of motion, as well as on the fermion doubling problem, arising the question, if temporal doublers are present as well. In this section, we present the lattice implementation of the equations of motion and discuss an algorithm that governs the time evolution.

Having discretized time, the equations of motion become „update“ equations, that move the fields from the current time-slice t_i to a new time-slice $t_i + a_t$, with a_t denoting the temporal spacing. This procedure follows a *leap-frog* construction:
First we update the chromo-electric fields to the new time slice, making use of the fermion fields and gauge links defined on the current time slice. Next we proceed with the fermion fields and afterwards the gauge links, moving all fields to the new time slice $t + a_t$. Additionally one has to assure that the Gauss constraint (eq. 4.53) is satisfied during the evolution of the system. For this purpose, we fix Gauss law using the algorithm discussed in (section 4.3.2), after the fields have been moved to the new time-slice.

We give the lattice equations of motion using dimensionless lattice quantities, rescaled in terms of the lattice spacing a and the coupling g. The update equations are given as:

- **Chromo-electric fields:**
  For the chromo-electric fields we have the following update equation, obtained from (eq. 5.50)

$$\begin{aligned}\bar{E}_i^a(x+\hat{t}) =& \bar{E}_i^a(x) + 2\bar{a}_t \sum_{j\neq i} \mathrm{Im tr}\Big[T^a\Big(U_{ji}(x) + U_{-ji}(x)\Big)\Big] \\ &+ \frac{g^2\bar{a}_t}{2Z}\mathrm{Re tr}\Big(\Big\langle \tilde{\psi}_M(x+\hat{i})\bar{\tilde{\psi}}_F(x) + \tilde{\psi}_F(x+\hat{i})\bar{\tilde{\psi}}_M(x)\Big\rangle_{N_{ens}}\Big(\gamma^i - \mathrm{i}r\Big)T^a U_i(x)\Big),\end{aligned} \tag{7.1}$$

  where we expressed the statistical propagators explicitly in terms of an ensemble average of low-cost fermions.

- **Fermion fields:**
  The time evolution of the low-cost fermion fields ψ_G is governed by the Dirac equation (eq. 4.1)

$$\begin{aligned}\tilde{\psi}_G(x+\hat{t}) =& \tilde{\psi}_G(x-\hat{t}) - 2\mathrm{i}\bar{a}_t\gamma^0\Big(\bar{m} + 3r\Big)\tilde{\psi}_G(x) \\ &- \bar{a}_t\gamma^0\sum_{i=1}^{3}\Big(\Big(\gamma^i - \mathrm{i}r\Big)U_i(x)\tilde{\psi}_G(x+\hat{i}) - \Big(\gamma^i + \mathrm{i}r\Big)U_i^\dagger(x-\hat{i})\tilde{\psi}_G(x-\hat{i})\Big).\end{aligned} \tag{7.2}$$

  As discussed in (section 4.1), we have to use the non central derivative at the very first time-step of the evolution, because the field $\tilde{\psi}_G(x-\hat{i})$ is not accessible.

- **Gauge links:**
  The update equation for the gauge links has been derived in (section 4.2)

$$U_i(x+\hat{t}) = e^{\mathrm{i}\bar{a}_t\bar{E}_i(x)}U_i(x). \tag{7.3}$$

  In the simulation we evaluate the exponential function by approximating it via a Taylor series up to 15th order, to reach sufficient precision.

- **Gauss constraint:**
  The dimensionless color matrix $C(x)$ for restoring Gauss law is computed in the following way, as argued in (section 5.4.1)

$$\begin{aligned}C(x) = Z\sum_i \Big[\bar{E}_i(x) - & U_i^\dagger(x-\hat{i})\bar{E}_i(x-\hat{i})U_i(x-\hat{i})\Big] \\ &+ \frac{g^2}{2}T^a\mathrm{Re tr}\Big[\Big\langle \tilde{\psi}_M(x+\hat{t})\bar{\tilde{\psi}}_F(x) + \tilde{\psi}_F(x+\hat{t})\bar{\tilde{\psi}}_M(x)\Big\rangle_{N_{ens}}\gamma^0 T^a\Big],\end{aligned} \tag{7.4}$$

  where we replaced the statistical propagator by an ensemble average of low-cost fermions. If Gauss law is violated, we restore it by updating the chromo-electric fields according to (eq. 4.56) iteratively.

7.2 Free Gas of Fermions

A first test for the implementation of fermions in our lattice simulation is provided by comparing the energy density and pressure of a free gas of fermions calculated in the simulation, to the

analytic result familiar from statistical mechanics. In our simulation, the energy density of free fermions is simply given by setting $U_i = 1$ in (eq. 6.34). It is now possible to calculate the energy density of a free gas of fermions of temperature T from the lattice simulation, by initializing the low cost fermion fields from a thermal distribution, using (eq. 2.49). We will calculate the energy density for different temperatures T, with a fixed fermion mass of

$$\bar{m} = am = 0.1, \quad \rightarrow \quad a = \frac{0.1}{m}. \tag{7.5}$$

We use these relations to fix the lattice spacing of our system as well.

We have already seen in (section 6.2.2) , that it is possible to calculate the energy density of a free thermal gas of fermions analytically on the lattice, with the (renormalized) result given as

$$a^4\epsilon = \frac{4N_c}{V}\sum_{\mathbf{p}} s_0(\mathbf{p}) n_{FD}(\mathbf{p}, T). \tag{7.6}$$

It is possible to replace the momentum sum by a continuous integration over the first Brioullin zone in this equation, leading to

$$a^4\epsilon = \frac{g_\psi}{(2\pi)^3}\int_{-\pi}^{\pi}\int_{-\pi}^{\pi}\int_{-\pi}^{\pi} s_0(\bar{\mathbf{p}}) n_{FD}(\bar{\mathbf{p}}, \bar{T}) d^3\bar{p}, \tag{7.7}$$

with $\bar{p}_i = ap_i$ and the degeneracy factor $g_\psi = 4N_c$. One has to keep in mind, that the fermion lattice dispersion relation s_0 enters the Fermi-Dirac distribution as well

$$n_{FD}(\bar{\mathbf{p}}, \bar{T}) = \frac{1}{e^{\frac{s_0(\bar{\mathbf{p}})}{a\bar{T}}} + 1}, \tag{7.8}$$

where we defined $\bar{T} = aT$.

It is straight forward to calculate (eq. 7.7) numerically in python. To study the discretization error of Wilson fermions on the lattice, let us compare the lattice discretized result to the continuum result as well. In the continuum, the energy density of a free gas of relativistic fermions is given as [151]

$$\epsilon_\psi = \frac{g_\psi}{(2\pi)^3}\int \omega_{\mathbf{p}} n(\mathbf{p}, T) d^3p, \tag{7.9}$$

with the free dispersion relation given by the relativistic energy momentum relation $\omega_{\mathbf{p}}^2 = \mathbf{p}^2 + m^2$. To compare this to the lattice result, we have to restrict the momentum integration to the first Brioullin zone

$$a^4\epsilon_\psi(x) = \frac{g_\psi}{(2\pi)^3}\int_{-\pi}^{\pi}\int_{-\pi}^{\pi}\int_{-\pi}^{\pi} \bar{\omega}_{\mathbf{p}} n(\bar{\mathbf{p}}, \bar{T}) d^3\bar{p}, \tag{7.10}$$

where we have rescaled the momentum $\bar{p}_i = ap_i$, rewriting the dispersion relation accordingly

$$\omega_{\mathbf{p}} = \frac{1}{a}\bar{\omega}_{\mathbf{p}} = \sqrt{\frac{1}{a^2}\bar{\mathbf{p}}^2 + \frac{1}{a^2}\bar{m}^2}, \qquad d^3p = \frac{1}{a^3}d^3\bar{p}. \tag{7.11}$$

We calculate the integral (eq. 7.10) numerically and compare it to the lattice results in (figure 7.1).

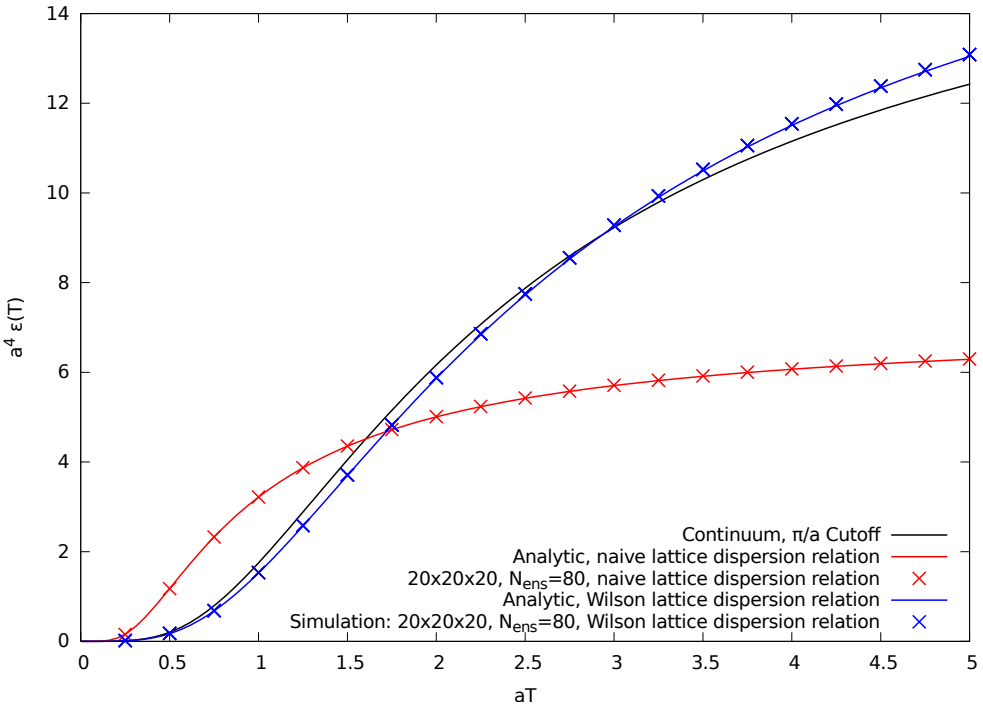

Figure 7.1: Energy density of a free gas of fermions, comparing the continuum result with momentum cutoff (eq. 7.10), the lattice Brioullin zone integrated result (eq. 7.7) and a result evaluated in a lattice simulation using an ensemble of stochastic low-cost fermions of size $N_{ens} = 80$, on a lattice with $20 \times 20 \times 20$ points. The fermion mass is taken to be $am = 0.1$.

In (figure 7.1) it is clearly evident, that the energy density calculated from (eq. 7.7) and in the lattice simulation match. We additionally included a crosscheck for naive fermions, setting $r = 0$, removing the Wilson term.

Furthermore, we observe that the energy density calculated from naive fermions has a significant offset when compared to the continuum result. The reason for that is, that the lattice dispersion relation for naive fermion drops to zero at the edges of the Brioullin zone (see figure 2.2). The contribution of large momenta therefore is underestimated, when compared to the continuum dispersion relation, which is in fact maximized at the edges of the Brioullin zone. Because large momenta become more and more important at large temperatures T the offset for naive fermions increases. Additionally keep in mind, that the lattice dispersion relation enters the Fermi-Dirac distribution as well, hence large momenta are also weighted differently when using naive fermions. This demonstrates, why it is important to introduce a Wilson term, although a continuum limit is not possible in our scenario.

Because no continuum limit has been performed, there is still an offset between the continuum and the lattice Wilson fermion energy density present in (figure 7.1). As discussed in (section 2.2.1), the additional mass of the doubler modes prevents the unphysical behavior of the lattice dispersion relation close to the edges of the Brioullin zone, but as observed in (figure 2.2), we do not achieve perfect agreement with the continuum dispersion relation, as long as we do not take the continuum limit $a \to 0$. This finite offset translates to the energy density as well.

Having discussed the energy density of a free gas of fermions, let us now turn to the pressure. In the simulation, we calculate the pressure of free fermions, by setting $U_i = 1$ in (eq. 6.36). In (section 6.2.2), we already calculated the analytic expression for the renormalized pressure of free fermions of temperature T on the lattice

$$a^4 P_{i,\psi} = \frac{g_\psi}{V} \sum_{\mathbf{p}} \frac{\sin^2\left(ap^i\right) + r\mu\Big(1 - \cos(ap^i)\Big)}{s_0} n_{FD}(\mathbf{p}, \bar{T}). \tag{7.12}$$

As presented already, we replace the sum by an integration over the Brioullin zone and additionally, because the pressure of a free gas of fermions is uniform in all spacial directions, we write $P = \frac{1}{3}\sum_i P_i$ and obtain

$$a^4 P_\psi = \frac{g_\psi}{3(2\pi)^3} \int_{-\pi}^{\pi}\int_{-\pi}^{\pi}\int_{-\pi}^{\pi} \frac{\sum_{i=1}^{3} \sin^2(\bar{p}^i) + r\mu \sum_{i=1}^{3}\Big(1 - \cos(\bar{p}^i)\Big)}{s_0} n_{FD}(\bar{\mathbf{p}}, \bar{T}) d^3\bar{p}. \tag{7.13}$$

Again we want to compare (eq. 7.13) to its continuum counterpart. In statistical physics, the pressure is given as the momentum transfer per fermion times the flux of fermions hitting a wall [151]. Let us assume the particles flow along the x-axis, so the flux is given as

$$v_x n_{FD}(\mathbf{p}, T) d^3p. \tag{7.14}$$

The momentum transfer is thus given as p_x and the pressure can be calculated from

$$P_\psi = \frac{g_\psi}{(2\pi)^3} \int p_x v_x n_{FD}(\mathbf{p}, T) d^3p. \tag{7.15}$$

We can now replace the velocity by its relation to the relativistic momentum $v_x = \frac{p_x}{\omega_{\mathbf{p}}}$, leading to

$$P_\psi = \frac{g_\psi}{(2\pi)^3} \int \frac{p_x^2}{\omega_{\mathbf{p}}} n_{FD}(\mathbf{p}) d^3p. \tag{7.16}$$

Finally we use, that this can be written uniformly in every spacial direction, replacing $p_x^2 = \frac{1}{3}\mathbf{p}^2$. We found the following result for the pressure of a free gas of fermions

$$P_\psi = \frac{g_\psi}{3(2\pi)^3} \int \frac{\mathbf{p}^2}{\omega_{\mathbf{p}}} n(\mathbf{p}, T) d^3p. \tag{7.17}$$

To compare to the lattice result, we now restrict the integration to the first Brioullin zone, introducing the lattice momentum cutoff $\frac{\pi}{a}$[1]

$$a^4 P_\psi = \frac{g_\psi}{3(2\pi)^3} \int_{-\pi}^{\pi}\int_{-\pi}^{\pi}\int_{-\pi}^{\pi} \frac{\bar{\mathbf{p}}^2}{\bar{\omega}_{\mathbf{p}}} n(\bar{\mathbf{p}}, \bar{T}) d^3\bar{p}. \tag{7.18}$$

[1]Naively one may wonder from comparing (eq. 7.18) to (eq. 7.13), why the squared momentum $\mathbf{p}^2$ is not simply replaced by the squared lattice momentum $\mathbf{s}^2$. The reason for that can be understood recalling that $\mathbf{s}^2$ has unphysical roots at the edges of the Brioullin zone as well, which is obviously not the case for $\mathbf{p}^2$, hence the Wilson term corrects this misbehavior leading to an appropriate approximation of the continuum result.

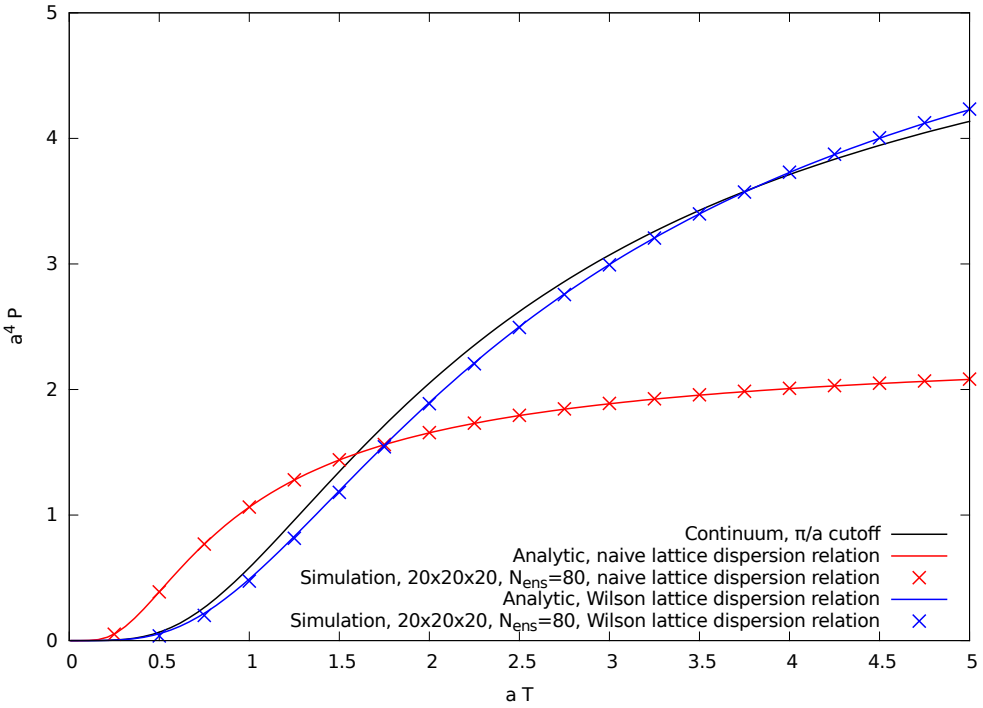

Figure 7.2: Pressure of a free gas of fermions as a function of T, comparing the continuum result with lattice momentum cutoff (eq. 7.18), to the lattice Brioullin zone integrated result (eq. 7.13) and a result evaluated in a lattice simulation with an ensemble of stochastic low-cost fermions of size $N_{ens} = 80$, on a lattice with $20 \times 20 \times 20$ points. The fermion mass is taken to be $am = 0.1$.

We compare the different results in (figure 7.2). We observe a similar behavior as in the case of the energy density when comparing the result of the pressure for Wilson and naive fermions in (figure 7.2). As expected, the result evaluated in the simulation and the lattice result (eq. 7.13) agree. Furthermore, we observe a similar offset between the continuum pressure (eq. 7.18) and the lattice counterpart (eq. 7.13) that is again rooted in discretization effects, that are only vanishing in the continuum limit $a \to 0$.

7.3 Initialization of Vacuum Stochastic Fermions

In the simulation, we compute fermion expectation values making use of ensemble averages of statistical low-cost fermions, which introduces a statistical error, that is reduced when increasing the ensemble size N_{ens}. This statistical error in the fermion sector does not only have consequences for the computation of observables, but more importantly for the equations of motion themselves. As seen in (section 4.3), a fermion color current enters the chromo-electric field equations of motion (eq. 5.50) and the Gauss constraint (eq. 5.51). In this section we will have a detailed look at the current at initial time $t_0 = 0$ by comparing a result calculated in the simulation to the analytic result.

The fermion color current (eq. 4.31), evaluated from an ensemble average of stochastic low-cost fermions is given as

$$a^3 J^{\mu,a}(x) = \frac{g^2}{2} \mathrm{Retr}\Big(\Big\langle \tilde{\psi}_M(x+\hat{\imath})\tilde{\bar{\psi}}_F(x) + \tilde{\psi}_F(x+\hat{\imath})\tilde{\bar{\psi}}_M(x) \Big\rangle_{N_{ens}} \big(\gamma^\mu - \mathrm{i}\delta_{\mu i} r\big) T^a U_\mu(x) \Big). \quad (7.19)$$

At initial time the fermion color current can be calculated analytically by using the result of the free fermion statistical propagator on the lattice (eq. 2.52). We find for the spacial part

$$a^3 J^{i,a}(t_0, \mathbf{x}) = -\frac{2g^2}{V} \sum_{\mathbf{n}} \frac{s^i(\mathbf{n}) + \mathrm{i}\mu(\mathbf{n})}{s_0(\mathbf{n})} \mathrm{tr}\Big(T^a U_i(x)\Big) e^{-\frac{2\pi}{N}\mathbf{n}a}. \tag{7.20}$$

We will compare this result (eq. 7.20) to the fermion color current (eq. 7.19) calculated in the simulation. Because the current is a vector in color and Lorentz space, we only give the result for one component, setting $i = 1$ and $a = 1$, having checked for the other components as well.

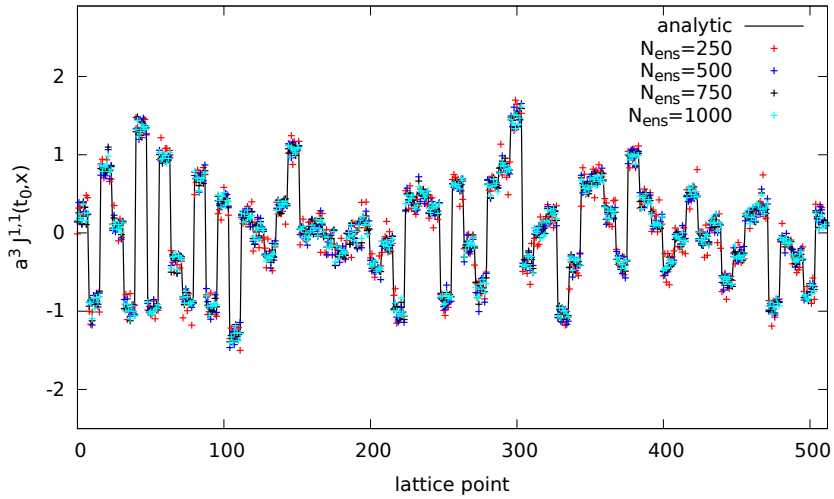

Figure 7.3: $J^{1,1}$ component of the fermion color current (eq. 7.19) at initial time, calculated in a lattice simulation on a $8 \times 8 \times 8$ lattice with Wilson fermions of mass $am = 0.1$, for different ensemble sizes N_{ens} and compared to the analytic result (eq. 7.20). The x-axis counts all lattice points.

We compare both results in (figure 7.3). The simulation has been performed on a small lattice of $8 \times 8 \times 8$ points, manageable on a local machine for large stochastic fermion ensembles N_{ens}. We consider fermions of mass $am = 0.1$ and compute the fermion color current, that enters the equations of motion at the first time-step. The result has been plotted as a function of the spacial lattice points, labeling all points in a straight forward list. As expected, better precision is achieved when increasing the ensemble size N_{ens}. For a sufficiently large ensemble the approximation matches the analytic result.

Having discussed the spacial part of the current (eq. 7.19) let us now turn to the temporal part of the current (eq. 4.31), that enters the Gauss constraint (eq. 5.51). At initial time we find the following analytic result

$$J^{0,a}(t_0, \mathbf{x}) = g^2 \mathrm{Retr}\Big(F\Big(x + \hat{i}, x\Big)\gamma^0 T^a\Big) = -\frac{g^2}{V} \sum_{\mathbf{p}} \sum_{s=1}^{2} \bar{v}_s(\mathbf{p})\gamma^0 v_s(\mathbf{p}) e^{\mathrm{i}\omega_{\mathbf{p}} a_t} \underbrace{\mathrm{tr} T^a}_{=0} = 0. \tag{7.21}$$

Choosing the same lattice size as previously with $8 \times 8 \times 8$ points and a lattice fermion mass of $\bar{m} = 0.1$, we compare the result in the lattice simulation (eq. 7.19) to the analytic result (eq. 7.21) in (figure 7.4). We observe, that the current calculated from an ensemble average of low-cost fermions fluctuates around the analytical value and the amplitude of the fluctuation is reduced when increasing the ensemble size N_{ens}.

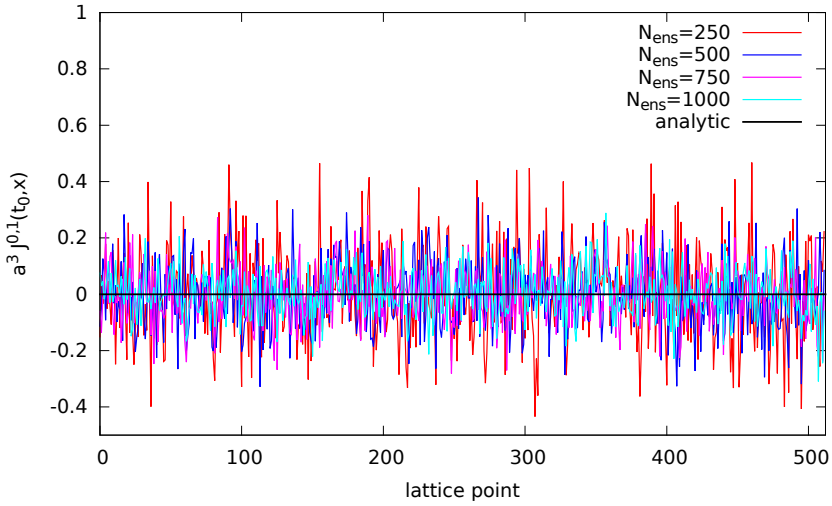

Figure 7.4: $J^{0,1}$ component of the fermion color current (eq. 7.19) at initial time, calculated in a lattice simulation on a $8 \times 8 \times 8$ lattice with Wilson fermions of mass $am = 0.1$, for different ensemble sizes N_{ens} and compared to the analytic result (eq. 7.20). The x-axis counts all lattice points.

As discussed in (section 4.3.2), the Gauss constraint (eq. 5.51) should be satisfied to a fairly high precision. At initial time, the gauge link ensemble generated from the CGC satisfies the Gauss constraint per construction. In (figure 7.4) we observe, that the fermion sector introduces a significant statistical uncertainty to the Gauss constraint, arriving at a situation where Gauss law is not satisfied at initial time, although it should in principle be the case from an analytical perspective.

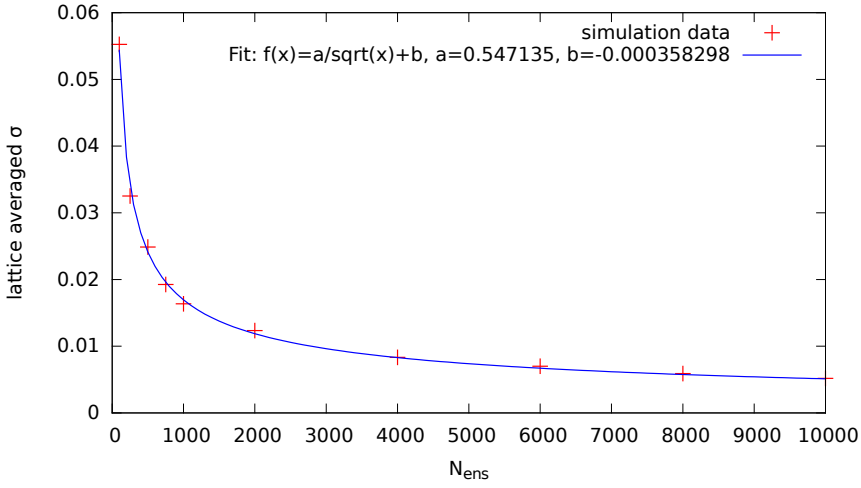

Figure 7.5: Standard deviation σ of the $J^{0,1}$ component of the fermion color current (eq. 7.19), when compared to the continuum result (eq. 7.21) as a function of the stochastic fermion ensemble size N_{ens}. A lattice average has been performed. The error drops with $\frac{1}{\sqrt{N_{ens}}}$, as indicated by the fit.

It is not possible to choose the stochastic fermion ensemble N_{ens} that large, that the Gauss constraint is satisfied up to machine precision at initial time, because the error only decreases with $\frac{1}{\sqrt{N_{ens}}}$, as can be seen in (figure 7.5). To achieve sufficient precision, one would have to move to tremendously large ensembles, that are not numerically feasible. As a way

out, we match the temporal component of the fermion color current to the analytical result at initial time, setting it zero. For all other time-steps we apply the algorithm described in (section 4.3.2), to restore Gauss law.

7.3.1 Restoration of Gauss Law

To restore Gauss law at every time-step of the simulation, we use the algorithm of [143], previously presented in (section 4.3.2). In (figure 7.6) we demonstrate this procedure on a lattice with $20 \times 20 \times 20$ points in a simulation with Wilson fermions of mass $am = 0.01$ and an ensemble size of $N_{ens} = 200$. The restoration algorithm uses an optimization parameter of $\gamma = 0.06$, that turned out to give good results while optimizing the computational time. We will use the same choice later, in a simulation of the semi-classical effective model on larger lattices.

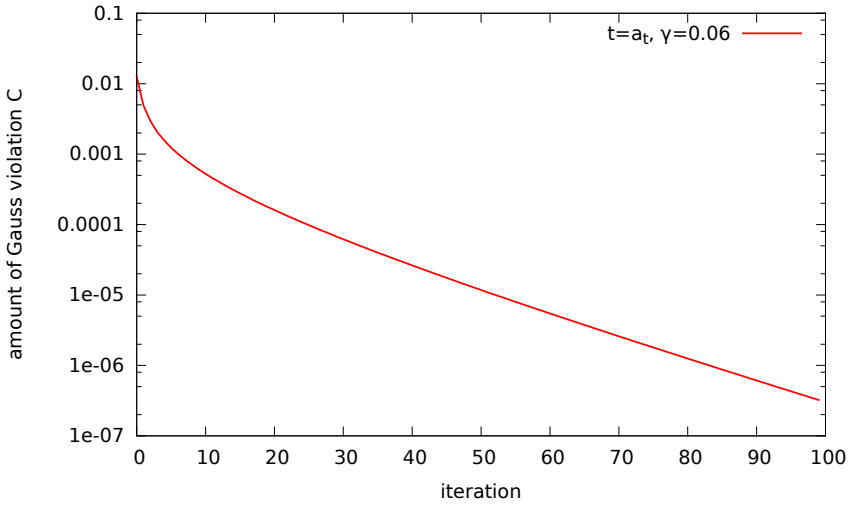

Figure 7.6: Restoration of Gauss law, making use of the algorithm presented in [143]. The simulation has been performed on a lattice of size $20 \times 20 \times 20$, with Wilson fermions of mass $am = 0.01$ and an ensemble size of $N_{ens} = 750$. The $\gamma-$parameter is set to $\gamma = 0.06$.

We have plotted the amount of Gauss violation $C(t)$ on a logarithmic scale as a function of the iteration step of the restoration algorithm, at the second time-step of the simulation. We observe, that the amount of Gauss violation decreases exponentially for every iteration of the algorithm. Because every iteration requires a re-computation of a fermion expectation value, that takes a significant computational time, we accept Gauss law to be sufficiently restored for $C \lesssim 10^{-6}$, to keep the computational time feasible. This value is reasonable, when compared to the statistical error imposed by the computation of fermion expectation values within the low-cost method.

7.3.2 Stochastic Fermion Ensemble Dependence

Having discussed the statistical error imposed by the ensemble average of low-cost fermions, let us check for the ensemble size N_{ens} dependence of the observables in general. For the validity of the method, the observables calculated in the simulation should not depend on the chosen ensemble size N_{ens}, which can be realized by choosing it sufficiently large. We test the ensemble size dependence for the energy density of the fermion sector (eq. 6.34)[2] in a simulation on a

[2]We also investigated the pressure of the fermion sector (eq. 6.36), obtaining similar results.

lattice of size $60 \times 60 \times 60$. This will turn out to correspond to a lattice spacing a, that is smaller than the lattice spacing we will extract in a matching procedure later. As a consequence, if fermion observables turn out to be independent on the chosen ensemble size N_{ens} on the given lattice, we conclude that the choice of N_{ens} is also appropriate on coarser lattices.

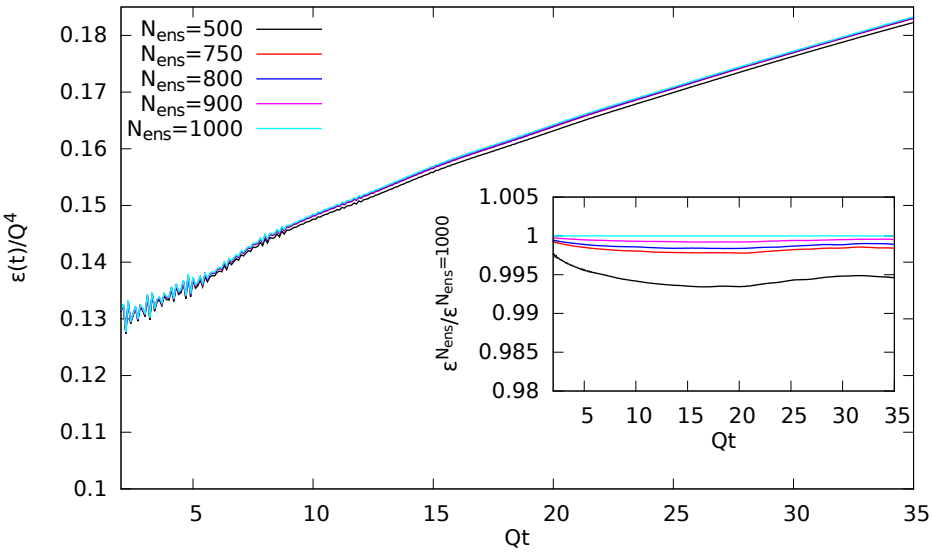

Figure 7.7: Dependence for the energy density of the fermion sector (eq. 6.34) on the stochastic fermion ensemble size N_{ens}. The simulations have been performed on a lattice of size $60 \times 60 \times 60$.

We observe in (figure 7.7), that beyond a choice of $N_{ens} \geq 750$, the results of the fermion energy density of the fermion sector (eq. 6.34) do not significantly vary. A larger deviation is observed, when choosing a smaller ensemble size of $N_{ens} = 500$. This becomes more evident by looking at the inlay plot in (figure 7.7), where we plot the deviation of the energy density for different choices of N_{ens} from the result with $N_{ens} = 1000$. We find that the deviation for the choices of $N_{ens} \in \{750, 800, 900\}$ is only of the order of 0.3% and therefore negligible. Choosing a smaller ensemble of $N_{ens} = 500$ leads to a stronger deviation of the order of 0.6%. To optimize the computational time, that blows up for large choices of N_{ens}, we stick to the choice of $N_{ens} = 750$ in later simulations. For tests of the lattice implementation of the semi-classical approximation on a local machine, we will usually stick to smaller ensembles, having checked for ensemble dependence as well.

7.4 Discretizing Minkowski Time

As pointed out earlier, the lattice implementation of the equations of motion of the semi-classical effective theory required a discretization of time, introducing a temporal spacing a_t. In (section 2.2), we rigorously discussed the phenomenon of fermion doubling on a spacial lattice, introducing the spacial Wilson term to remove the doublers. When additionally discretizing the time direction, the question arises if temporal doublers appear as well. In this section we will argue, that temporal doublers are not excited in our simulations, as long as we keep a strong anisotropy $a_t/a \ll 1$. We will furthermore provide a numerical test to check if temporal doublers are indeed unexcited during the evolution of the system, following the discussion in [146].

In general, the choice of a_t is not arbitrary but limited by the Courant-Friedrichs-Levi condition [152], which is a constraint for a numerical integrator of partial differential equations, as for example the leap-frog method, that has to be satisfied to achieve convergence. It relates the spacial step-size Δx of the integrator, in our case given by the lattice spacing a, to the temporal step-size Δt, given by the temporal spacing a_t. Both spacings have to satisfy the following relation [127]

$$\sqrt{3}\frac{|v|\Delta t}{\Delta x} \ll 1, \tag{7.22}$$

where the prefactor $\sqrt{3}$ is determined from the number of directions and $|v|$ is the propagation velocity, given as $|v| = 1$ in natural units. This approximately translates to the lattice spacings in the following way

$$\frac{a_t}{a} = \bar{a_t} \ll 1. \tag{7.23}$$

In practice, we will limit our choices of a_t to $a_t \in \{0.05a, 0.03a, 0.02a\}$, obviously satisfying (eq. 7.23).

With this in mind, let us return to the question if there are additional fermion doublers present, when discretizing time. We initialize the fermion fields according to fermion fields according to the vacuum solution with continuous Minkowski time (eq. 2.45), hence temporal doublers are initially not excited. To argue, that these doubler modes remain unexcited during the evolution, let us study the appearance of temporal doublers in the free theory first. As discussed in (section 2.2.1) the lattice propagator with real Minkowksi time can be derived from (cf. eq. 2.32)

$$\left(\mathrm{i}\gamma^0\partial_t + \frac{\mathrm{i}}{2a}\gamma^i\left(\delta_{\mathbf{y},\mathbf{x}+\hat{i}} - \delta_{\mathbf{y},\mathbf{x}-\hat{i}}\right) - m\delta_{\mathbf{y},\mathbf{x}}\right)D(t-t',\mathbf{x},\mathbf{y}) = \mathrm{i}\delta(t-t')\delta_{\mathbf{x},\mathbf{y}}. \tag{7.24}$$

Applying a spacial Fourier transform, we arrive at

$$\int\left(\mathrm{i}\gamma^0\partial_t + \frac{\mathrm{i}}{2a}\gamma^i\left(e^{\mathrm{i}p^i a} - e^{-\mathrm{i}p^i a}\right) - m\right)D(t,\mathbf{p})e^{\mathrm{i}\mathbf{p}\mathbf{x}}\frac{d^3p}{(2\pi)^3} = 0. \tag{7.25}$$

It is now possible to identify the spacial lattice momenta s^i, writing

$$\left(\mathrm{i}\gamma^0\partial_t + \frac{1}{a}\gamma^i s_i - m\right)D(t,\mathbf{p}) = 0. \tag{7.26}$$

This differential equation can easily be solved analytically and we find the following solution

$$D(t,\mathbf{p}) = \frac{m+\gamma^i s_i}{2\omega_{\mathbf{p}}}\cos(\omega_{\mathbf{p}}t) - \frac{\mathrm{i}}{2}\gamma^0\sin(\omega_{\mathbf{p}}t), \tag{7.27}$$

with $\omega_{\mathbf{p}}$ the (naive) lattice dispersion relation, obtained from (eq. 2.27) by setting $r = 0$. The spacial doublers could now be removed by introducing a spacial Wilson term, but we ignore them for a second and discretize the time direction instead, using (eq. 2.31)

$$\left(\frac{\mathrm{i}}{2}\gamma^0\left(\nabla_t^f + \nabla_t^b\right) + \gamma^i s_i - m\right)D(t,\mathbf{p}) = 0. \tag{7.28}$$

As seen for the spacial direction, this leads to a „lattice momentum“ in temporal direction of the form

$$s_0 = \frac{1}{a_t}\sin(p^0 a_t). \tag{7.29}$$

As a consequence, we require the solution of the Dirac equation on the lattice to satisfy $s_0 = \omega_{\mathbf{p}}$. If we now consider a lattice with a strong anisotropy $a_t \ll a$, we can expand s_0 in terms of a_t, because $\omega_{\mathbf{p}} \sim \mathcal{O}(1/a)$ and $a_t/a \ll 1$ is very small. When doing so, we have to be careful, because there are two possible solutions in the first Brioullin zone, namely a physical solution and one close to the edge of the Brioullin zone, representing the doubler solution [101]

$$\omega_{\mathbf{p}} \approx p^0, \qquad \omega_{\mathbf{p}} \approx \frac{\pi}{a_t} - p^0. \tag{7.30}$$

Because $\omega_{\mathbf{p}} \sim \mathcal{O}(a^{-1})$, we can already see, that the doubler solution becomes very heavy for strong anisotropic lattices, with $a_t \ll a$ and is most likely not excited in the evolution of our system, if (eq. 7.23) is satisfied. This can be studied in more detail by looking at the lattice propagators of the two different dispersion relations

$$D_1(t,\mathbf{p}) = \frac{m + \gamma^i s_i}{2\omega_{\mathbf{p}}}\cos(\omega_{\mathbf{p}} t) - \frac{\mathrm{i}}{2}\gamma^0 \sin(\omega_{\mathbf{p}} t), \tag{7.31}$$

$$D_2(t,\mathbf{p}) = \frac{m + \gamma^i s_i}{2\omega_{\mathbf{p}}}\cos(\omega_{\mathbf{p}} t)(-1)^s - \frac{\mathrm{i}}{2}\gamma^0 \sin(\omega_{\mathbf{p}} t)(-1)^{s+1}, \tag{7.32}$$

where D_1 represents the physical lattice propagator and D_2 the propagator of the doubler modes, that fluctuates in sign for every time-step ($t = sa_t$), due to the additional shift by $\frac{\pi}{a_t}$ in the lattice dispersion relation.

Although we have studied this in context of free fermions, the fluctuating character of the doubler modes does not change, when coupling our theory to gauge fields. We can exploit the sign changes of the doubler mode propagator, to test the excitement of temporal doubler modes during the evolution of our system. We do this by averaging the two closest time-steps in the following way [146]:
We first define

$$\psi_p(x) = \frac{\psi(x+a_t) + \psi(x)}{2} + \frac{\psi(x) + \psi(x-a_t)}{2}, \tag{7.33}$$

$$\psi_d(x) = \frac{\psi(x+a_t) - \psi(x)}{2} - \frac{\psi(x) - \psi(x-a_t)}{2}. \tag{7.34}$$

Using these definitions, we can calculate the following expectation values

$$\frac{1}{2}\left\langle \psi^\dagger_{p,M/F}(t,\mathbf{x})\psi_{p,M/F}(t,\mathbf{x})\right\rangle_{N_{ens}}, \qquad \frac{1}{2}\left\langle \psi^\dagger_{d,M/F}(t,\mathbf{x})\psi_{d,M/F}(t,\mathbf{x})\right\rangle_{N_{ens}}, \tag{7.35}$$

and compute their lattice average. Because the physical solution does not differ in sign, we expect the closest time-step expectation value to cancel in the second case, whereas it does not cancel in the first case. For the doubler solution, the situation is vice versa. One easily checks this for vacuum fermions, by calculating the expectation values analytically, inserting

the explicit formulas for the free stochastic low-cost fermions (eq. 2.47)

$$\frac{1}{2}\left\langle \psi^{\dagger}_{p,M/F}(t,\mathbf{x})\psi_{p,M/F}(t,\mathbf{x})\right\rangle_{N_{ens}} = \frac{1}{4V}\sum_{\mathbf{p}}\left(\cos\left(p^0 a_t\right)+1\right)^2, \tag{7.36}$$

$$\frac{1}{2}\left\langle \psi^{\dagger}_{d,M/F}(t,\mathbf{x})\psi_{d,M/F}(t,\mathbf{x})\right\rangle_{N_{ens}} = \frac{1}{4V}\sum_{\mathbf{p}}\left(\cos\left(p^0 a_t\right)-1\right)^2. \tag{7.37}$$

For the physical solution $p^0 \approx \omega_{\mathbf{p}}$ we have

$$\cos\left(p^0 a_t\right) = \cos\left(\omega_{\mathbf{p}} a_t\right) \approx 1 + \mathcal{O}\left(\frac{a_t}{a}\right), \tag{7.38}$$

leading to

$$\frac{1}{2}\left\langle \psi^{\dagger}_{p,M/F}(t,\mathbf{x})\psi_{p,M/F}(t,\mathbf{x})\right\rangle_{N_{ens}} \approx 1, \qquad \frac{1}{2}\left\langle \psi^{\dagger}_{d,M/F}(t,\mathbf{x})\psi_{d,M/F}(t,\mathbf{x})\right\rangle_{N_{ens}} \approx 0. \tag{7.39}$$

Whereas for the unphysical doubler solution $p^0 \approx \frac{\pi}{a_t} - \omega_{\mathbf{p}}$ (if only doubler modes would be excited and no physical modes), we expect

$$\cos\left(p^0 a_t\right) \approx \cos\left(\pi - \omega_{\mathbf{p}} a_t\right) \approx -1 + \mathcal{O}\left(\frac{a_t}{a}\right), \tag{7.40}$$

leading to

$$\frac{1}{2}\left\langle \psi^{\dagger}_{p,M/F}(t,\mathbf{x})\psi_{p,M/F}(t,\mathbf{x})\right\rangle_{N_{ens}} \approx 0, \qquad \frac{1}{2}\left\langle \psi^{\dagger}_{d,M/F}(t,\mathbf{x})\psi_{d,M/F}(t,\mathbf{x})\right\rangle_{N_{ens}} \approx 1. \tag{7.41}$$

We use this method to check if temporal doubler modes stay unexcited during the evolution of our system in (figure 7.8). We compute (eq. 7.35) in a simulation of the semi-classical effective model, on a lattice of $20 \times 20 \times 20$ points, using a stochastic low-cost fermion ensemble of size $N_{ens} = 100$, with Wilson fermions of mass $am = 0.1$ and a temporal spacing of $\frac{a_t}{a} = 0.02 \ll 1$. We verify that temporal doublers are not excited in the simulation, when choosing a small temporal spacing, justifying our approach of not taking a temporal Wilson term into account.

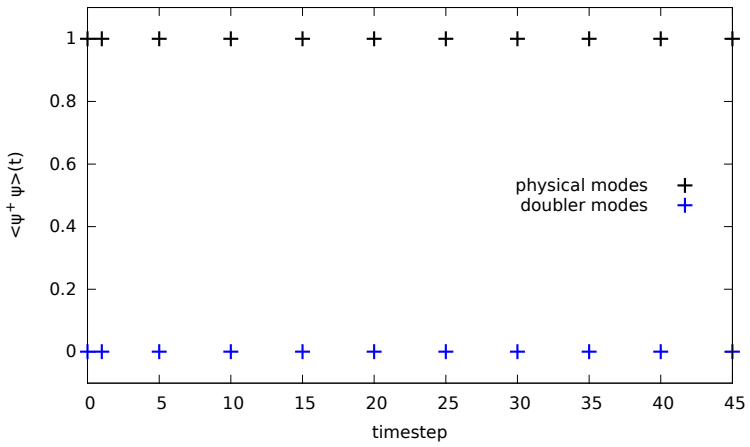

Figure 7.8: Physical modes and temporal doubler modes calculated using (eq. 7.35) in a simulation of the semi-classical model on a $20 \times 20 \times 20$ lattice, using a stochastic low-cost fermion ensemble of size $N_{ens} = 100$, Wilson fermions of mass $am = 0.1$ and a temporal spacing of $a_t = 0.02a$.

7.4.1 Initial Oscillations when Solving the Lattice Dirac Equation

Let us discuss another phenomenon that is connected to time discretization in the solution of the equations of motion of the semi-classical model. When coupling vacuum fermions to the ensemble of gauge links U_i, the fermion fields are significantly modified, when evolving the coupled system the first time. With the fermions being intialized as vacuum fields, the energy modes are initially unoccupied, whereas in the Yang-Mills fields, classical modes are even overoccupied and carry a large anisotropy. As a consequence, the system is sensitive to the time discretization a_t and one observes additional oscillations in the observables as e.g. the energy density (eq. 6.34). As expected, these oscillations are significantly reduced when moving to smaller temporal spacings. We demonstrate this using a lattice of $20 \times 20 \times 20$ points and a low-cost fermion ensemble of massive $am = 0.01$ fermions of size $N_{ens} = 70$. We vary the temporal spacing in the simulation and give the results as a function of the different a_t in (figure 7.9).

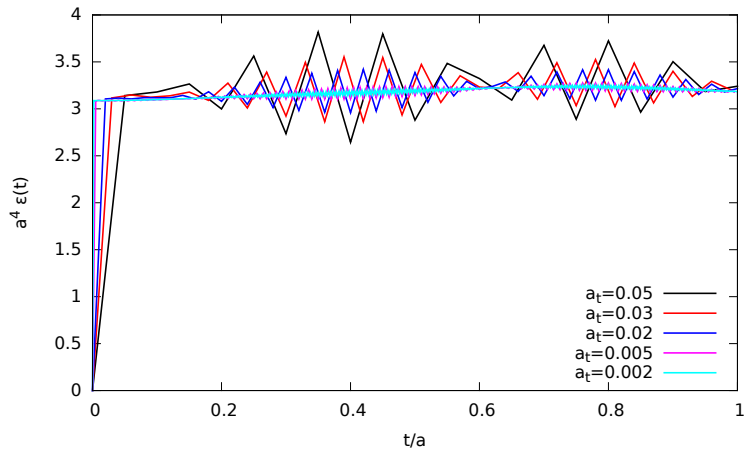

Figure 7.9: Energy density of the fermion sector (eq. 6.34) for different temporal spacings a_t. The simulation has been performed on a $20 \times 20 \times 20$ lattice, for an ensemble of massive stochastic low-cost fermions of mass $am = 0.01$ and ensemble size $N_{ens} = 70$.

We indeed observe, that oscillations at initial times are significantly reduced when moving to smaller temporal spacings a_t. Note that for $a_t = 0.05$, which is a typical literature choice in pure Yang-Mills simulations (compare e.g. [61]), the oscillations are still large. On the opposite, for very small spacings below $a_t \leq 0.005$ the oscillations are nearly removed completely. On the downside, such a small temporal spacing blows up the computational time, demanding a huge number of time-steps for a simulation that lasts (at least) up to the estimated hydrodynamization time of $t \approx 1$ fm. As a compromise, we stick to the spacing of $a_t = 0.02$ in most of our simulations. Nevertheless note, that the solution (eq. 6.34) is still stable for coarse temporal spacings.

The sudden jump in the fermion energy density, which is present in (figure 7.9) at the initial time-step, happens because we assume the Yang-Mills and fermion sector of our theory to be initially uncoupled and initialize each of the sectors individually. At the first time-step we couple both sectors and the gauge links of the Yang-Mills sector do not only enter the equations of motion, but also the energy density and pressure observables of the fermion sector. As a consequence, we observe a sudden jump in these observables at the first time-step, that is often referred to as a quantum quench. We are going to discuss this in more detail, when presenting the simulation results.

7.5 Scale Setting

In (chapter 4), we pointed out that it is not possible to perform a continuum limit for a lattice theory including classical fields, due to the appearance of Rayleigh-Jeans divergencies. As a consequence, we cannot remove the lattice cutoff dependence of our observables. A way out is to connect the lattice spacing a to a physical scale in a matching procedure. Such a procedure is known as a scale setting and has been performed in numerous scenarios (see e.g. [36]).

In (section 3.5), we discussed the physical parameters entering the CGC effective theory, namely the saturation scale Q_s and the nucleus size. Because the saturation scale cannot directly be measured, we presented a model to estimate the saturation scale and the initial energy density for *Pb-Pb* collisions at LHC center-of-mass energies of $\sqrt{s} = 5.02$ TeV (compare to eq. 3.29 and eq. 3.30)

$$Q_s \approx 1.867 \text{ GeV}, \qquad \epsilon_0 = 281.45 \, \frac{\text{GeV}}{\text{fm}^3}. \tag{7.42}$$

The idea of the scale setting procedure is to match the lattice averaged energy density calculated in our simulation, using (eq. 6.34 and eq. 6.21) to the estimated energy density of the initial state in a heavy ion collision. This procedure allows us to fix the lattice spacing a to a physically motivated value.

The box size is fixed by connecting the transverse lattice area $L_\perp^2$ to the area of the colliding nuclei, assuming that they totally overlap in the collision („head-on“ collision). As discussed in (chapter 3), the incoming nuclei are Lorentz contracted in beam direction due to their high velocity and can therefore be approximated as effectively two dimensional

$$L_\perp^2 = a_\perp^2 N_\perp^2 \approx \pi R^2, \tag{7.43}$$

with R denoting the nucleus radius of a *Pb*-atom, estimated as $R_{Pb} \approx 6.6$ fm [132, 139]. The lattice extent in perpendicular direction is thus given as

$$L_\perp^2 \approx \pi R_{Pb}^2 \approx 138 \text{ fm}^2, \quad \rightarrow \quad L_\perp \approx 12 \text{ fm} \approx 60 \, \frac{1}{\text{GeV}} \tag{7.44}$$

This can be connected to the lattice spacing in the following way

$$a_\perp = \frac{L_\perp}{N_\perp} \approx \frac{12}{N_\perp} \text{ fm} \approx \frac{60}{N_\perp} \, \frac{1}{\text{GeV}}. \tag{7.45}$$

For later convenience, it is useful to derive a dimensionless scale, connecting the saturation scale and the length scale of the system

$$Q_s L_\perp \approx 111 = g^2 \bar{\mu}, \tag{7.46}$$

where $\bar{\mu}$ is the color charge per unit area in lattice units.

As discussed in (section 3.4), we choose a cubic box for our static system

$$N_z = N_\perp \quad \rightarrow \quad V = N_z N_\perp^2 = N_\perp^3. \tag{7.47}$$

We can now fix the lattice spacing a, by performing simulations with different lattice extents N, keeping the physical parameters box size and saturation scale constant. We extract the specific lattice spacing a, where the estimated energy density (eq. 3.30) and the lattice averaged energy density approximately match. A perfect matching will not be possible, because we are restricted to a choice of an even integer number for the lattice extent N.

The energy density in physical units is extracted from the simulation by calculating the total energy density as a sum of (eq. 6.21) and (eq. 6.34)

$$\epsilon(t) = \frac{1}{g^2 a^4}\bar{\epsilon}(t). \tag{7.48}$$

The physical coupling at the saturation scale Q_s has been determined in (section 3.2) as $g \approx 2$, combining this with (eq. 7.45) we find

$$\epsilon(t) = \frac{1}{a^4 g^2}\bar{\epsilon}(t) = \frac{N_\perp^4}{g^2\ (12)^3\ 60}\bar{\epsilon}(t)\frac{\text{GeV}}{\text{fm}^3}. \tag{7.49}$$

We now run a series of simulations of varying lattice spacing and extract the corresponding energy density. We will fit these results using a standard polynomial function, making it possible to extract the appropriate lattice spacing a.

We perform the matching, choosing a fermion of mass $am = 0.01$, which is sufficiently small to be unaffected from discretization effects, as discussed in (section 2.2). The temporal spacing is chosen to be $\bar{a}_t = 0.02$, satisfying the Courant-Levi condition (eq. 7.23). The results are given in (figure 7.10).

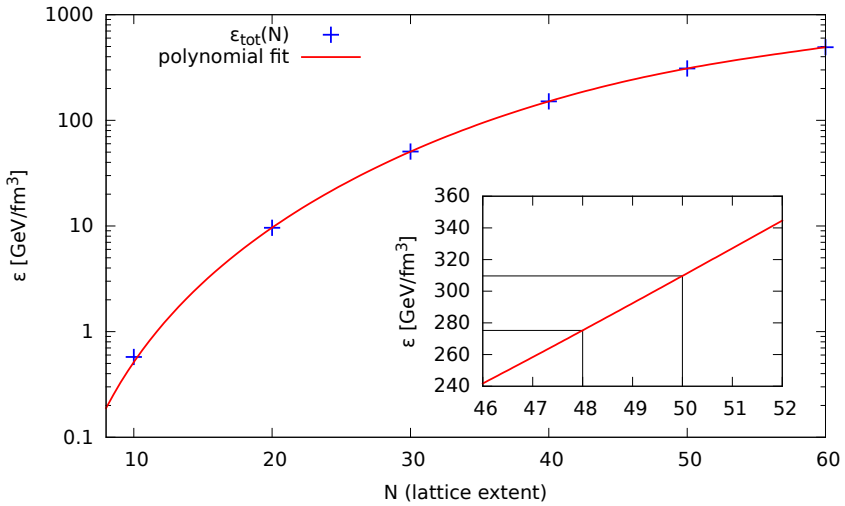

Figure 7.10: Lattice averaged energy density in a simulation of the semi-classical approximation in the static box, for different lattice spacings a, as a function of the lattice extent N, using (eq. 7.45). The fermion ensemble is of size $N_{ens} = 750$, the fermion mass is $am = 0.01$, the temporal spacing is chosen to be $a_t = 0.02a$ and the saturation scale, that enters the CGC initial conditions $Q_s = 1.867$ GeV.

From the inlay plot in (figure 7.10) it is possible to extract the lattice spacing for approximately matching energy densities. We identify the perfect value to be located between $\frac{12}{48}\text{fm} > a > \frac{12}{50}\text{fm}$.[3]

[3] As stated previously we have restricted ourselves to even integer numbers for the lattice extent.

Because the estimated energy density of the initial state (eq. 3.30) is a strongly model dependent quantity, with a significant uncertainty itself, we choose the smaller value for the lattice spacing $a = \frac{12}{50}$ fm, because finer lattices naturally provide better resolutions. We extracted the following lattice spacing a from the matching procedure

$$a \approx \frac{12}{50} \text{ fm} = 0.24 \text{ fm} = 1.2 \frac{1}{\text{GeV}}. \tag{7.50}$$

We can now use this result to discuss the scale of the fermion masses entering the simulation. We choose the following values

$$m = \frac{0.01}{a} \approx \frac{0.01}{1.2} \text{ GeV} \approx 8.33 \text{ MeV} \sim \mathcal{O}(m_{u/d}), \tag{7.51}$$

$$m = \frac{0.1}{a} \approx \frac{0.1}{1.2} \text{ GeV} \approx 80.3 \text{ MeV} \sim \mathcal{O}(m_s), \tag{7.52}$$

where the first choice is parametrically of the order of the light quark masses, namely the up- and down-quark and the second choice of the order of the strange quark mass.
To discuss the ultra-relativistic limit, we will also check a mass of

$$m = \frac{0.001}{a} \approx \frac{0.001}{1.2} \text{ GeV} \approx 0.833 \text{ MeV}. \tag{7.53}$$

Larger masses are naturally excluded, because of the condition set from the lattice dispersion relation of Wilson fermions, discussed in (section 2.2).

In case of two fermions with degenerate masses, we take $N_f = 2$. As a consequence, the quench at the first time-step is modified, because we have doubled the degrees of freedom in the fermion sector. We therefore have to repeat the matching procedure, again choosing a fermion of mass $am = 0.01$ and a temporal spacing of $a_t = 0.02a$. The results are given in (figure 7.11).

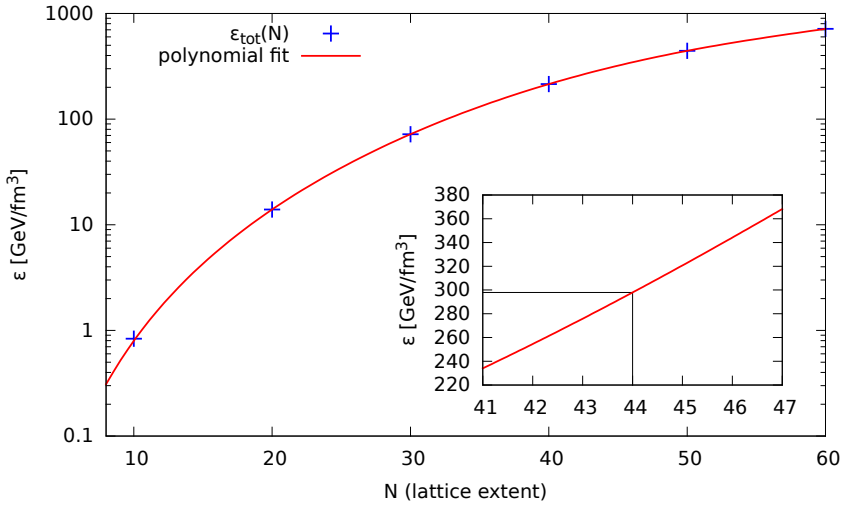

Figure 7.11: Lattice averaged energy density in a simulation of the semi-classical approximation in the static box with two flavors $N_f = 2$, for different lattice spacings a, as a function of the lattice extent N, using (eq. 7.45). The fermion ensemble is of size $N_{ens} = 750$, the fermion mass is $am = 0.01$, the temporal spacing is chosen to be $a_t = 0.02a$ and the saturation scale, that enters the CGC initial conditions $Q_s = 1.867$ GeV.

As discussed previously we identify the appropriate lattice spacing a as

$$a \approx \frac{12}{44}\ \text{fm} = 0.27\ \text{fm} = \frac{60}{44}\ \frac{1}{\text{GeV}} = 1.363\ \frac{1}{\text{GeV}}. \tag{7.54}$$

In a highly energetic system, the masses of the up- and down-quark can be taken to be of the same order $m_u \sim m_d$, making it possible to approximate these to be degenerate. In our simulation we choose the fermion masses to be

$$m = \frac{0.01}{a} = \frac{0.01}{1.363}\ \text{GeV} \approx 7.34\ \text{MeV} \sim \mathcal{O}(m_{u/d}), \tag{7.55}$$

$$m = \frac{0.001}{a} = \frac{0.001}{1.363}\ \text{GeV} \approx 0.734\ \text{MeV}, \tag{7.56}$$

where the first choice is parametrically of the same order as the masses of the up- and down-quark and the second choice is taken to investigate if the ultra-relativistic limit is reached.

Finally, we have to repeat the matching procedure for a pure Yang-Mills simulation, that will be used for a comparison to the simulations including fermions. When doing so, we keep all physical parameters as box size and saturation scale Q_s GeV unchanged. The result is given in (figure 7.12).

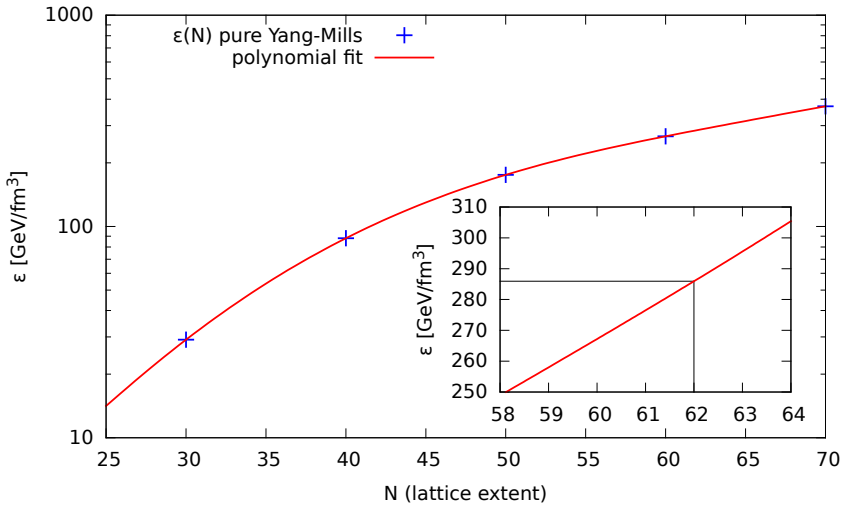

Figure 7.12: Lattice averaged energy density in a pure Yang-Mills simulation in the static box, for different lattice spacings a, as a function of the lattice extent N, using (eq. 7.45). The simulation has been performed with a temporal spacing of $a_t = 0.02a$, keeping the physical parameters box size and saturation scale $Q_s = 1.867$ GeV constant, when compared to the simulation with fermions.

We extract the following lattice spacing a from the matching procedure in (figure 7.12)

$$a \approx \frac{12}{62}\text{fm} \approx 0.19\ \text{fm}. \tag{7.57}$$

8

Results for the Static Box

In the following we will present the results of a simulation of the semi-classical effective theory of QCD in a static box. As discussed in (chapter 3), the classical Yang-Mills fields are initialized by making use of the Color Glass Condensate effective theory, formating the Glasma at initial time. The fermion fields are initialized as vacuum fermion fields and the Yang-Mills and fermion sector are coupled at the first time-step of the simulation.

In (section 7.5) we extracted the appropriate lattice spacing for a simulation in a static box, making use of a matching procedure for the energy density of the initial Glasma state. We extracted a lattice spacing of $a = \frac{12}{N}\text{fm} \approx 0.24$ fm. The static box is assumed to be cubic, and the length is fixed, by using the estimated radius of the incoming Pb-nuclei, setting the number of lattice points to $50 \times 50 \times 50$. As discussed in (section 7.1), integrating the equations of motion of the semi-classical theory on the lattice in a leap-frog scheme, required a discretization of Minkowski time. If not stated differently, we choose $a_t = 0.02a$ for the temporal spacing, which satisfies on one hand the Courant-Levi condition (eq. 7.23) and leads to numerically fairly stable results at early time-steps, as discussed in (section 7.4.1).

As discussed in (section 3.3.1), we follow the strategy of [126] for the initialization of gauge links, making use of the CGC effective theory on the lattice. We therefore choose the following parameters for the initialization: The number of longitudinal infinitesimally thin color sheets, used for the construction of the color current from Wilson lines, is set to $N_y = 30$. For the infrared, we use a cutoff of $m/Q = 0.1$ when solving the Poisson equation on the lattice. The UV-cutoff is provided by the lattice cutoff, where the momentum in each direction is limited by $p_{\text{max}} = \frac{\pi}{a}$.

For the physical initial conditions, we use a saturation scale of $Q_s = 1.867$ GeV, which is the appropriate estimate for Pb-Pb central collisions with a center-of-mass energy of $\sqrt{s} = 5.02$ GeV at the LHC, as discussed in (section 3.5). The corresponding coupling has been extracted in (chapter 3.2) from the QCD running coupling for fixed momentum transfer at the saturation scale Q_s and is set to $g = 2$. Fermion observables are computed, using stochastic low-cost fermions (see section 2.2.2), choosing an ensemble of size $N_{ens} = 750$, as discussed in (section

7.3.2). The parameter γ entering the Gauss law restoration algorithm (see chapter 4.3.2) is set to $\gamma = 0.06$.

We compare the results for the semi-classical effective theory of QCD to a pure Yang-Mills simulation. The pure Yang-Mills simulation has been constructed in such a way, that all physical parameters match the parameters of the simulation including fermions. To fix the corresponding lattice spacing, we have repeated the matching procedure for the initial energy density in (section 7.5), leading to a lattice spacing of $a \approx \frac{12}{62} \approx 0.1934$ fm. The corresponding number of lattice points is given as $62 \times 62 \times 62$.

We will first present the results for different choices of fermion mass m. These masses are chosen parametrically of the same order as the masses of the up- and down-quark and the strange quark (eq. 7.51). Next, we compare these results to a pure Yang-Mills simulation, where we additionally modified the Glasma initial conditions, by explicitly breaking longitudinal boost invariance, introducing a quantum rapidity fluctuation of magnitude Δ (eq. 3.22). Following this, we test our model for different choices of the coupling g. Finally we discuss the effect on the system, when having two degenerate quark flavors $N_f = 2$ present in the simulation. The mass is chosen of the same order as the mass of the up-/down-quark (eq. 7.55).

8.1 Simulations in a Static Box with Different Fermion Masses

We will first present the results for simulations of the semi-classical effective theory of QCD in a static box, including fermions of different mass m. The fermion masses are chosen as (see eq. 7.51)

$$m = 0.01\frac{1}{a} \approx 8.33 \text{ MeV} \sim \mathcal{O}(m_{u/d}), \qquad m = 0.1\frac{1}{a} \approx 83.3 \text{ MeV} \sim \mathcal{O}(m_s), \tag{8.1}$$

where the former one is parametrically of the order of the up-/down-quark mass and the latter one of the order of the mass of the strange quark. Additionally, we discuss the result for fermions of mass

$$m = 0.001\frac{1}{a} = 0.833 \text{ MeV}, \tag{8.2}$$

making it possible to check for the ultra-relativistic limit.

8.1.1 Energy Density

Let us first study the energy density of the system. We plot the lattice average of the total energy density, as well as its splitting into the contributions to the Yang-Mills and fermion sector. Because there is no energy gain or loss in a static box, we expect the lattice averaged total energy density to be constant. We indicate the errors of the observables determined from ensemble averages of stochastic low-cost fermions by color bands.

In (figure 8.1) we observe, that the total energy of the system is indeed constant. Furthermore, the lattice averaged total energy density is of the same order as the estimated energy density of the initial state (eq. 3.30), discussed in (section 3.5). The slight deviation is rooted in

the fact, that we are limited to a choice of an even integer number for the lattice extent N, leading to a slightly larger total energy density in our simulation. Nevertheless, the estimated initial energy density (eq. 3.30) is a model dependent quantity, that has not been measured in the experiment, making the agreement sufficient.

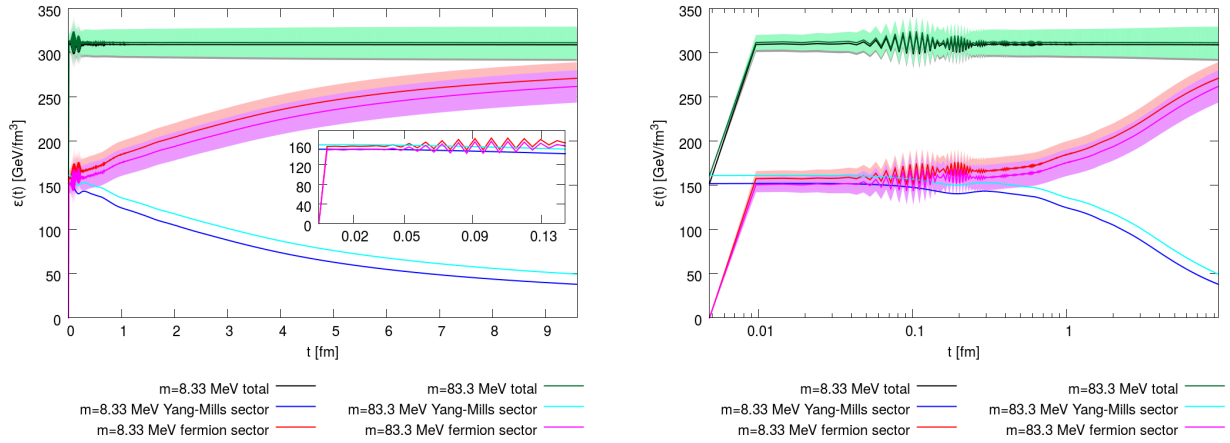

Figure 8.1: Energy density in simulations for different fermion masses $m = 8.33$ MeV and $m = 83.3$ MeV, on a $50 \times 50 \times 50$ lattice, with spacing $a = 0.24$ fm, coupling $g = 2$ and a stochastic fermion ensemble size of $N_{ens} = 750$. On the right-hand side, time is plotted logarithmically.

The early time oscillations in the fermion sector have already been discussed in (section 7.4.1) and happen due to the limitation in resolution, caused from the time discretization. One clearly notes, that these discretization effects diminish throughout the simulation. Furthermore, we observe a jump of the energy density at the initial time-step, especially when looking at the right plot of (figure 8.1). The reason for that is a quench, that happens at the first time-step, when coupling the Yang-Mills and fermion sector of the effective theory.

Initially, only the Yang-Mills sector contributes to the energy density, due to the initialization of the gauge links with respect to the CGC effective theory. The fermions on the other hand are initialized as free vacuum fermions and hence do not contribute to the energy density. As a consequence, before both sectors are coupled at the first time-step, they are represented by individual density matrices ρ with corresponding Hamilton operators $\hat{H}$. For the Yang-Mills sector, one has the classical Hamilton function of the CGC effective theory and for the fermions the free Hamilton operator of fermions $\mathcal{H}^{free}$. As soon as both sectors are coupled at the first time-step, the evolution of the system is governed by a new, interacting Hamilton operator of the total system $\hat{H}^{int}$. As a consequence, the gauge links U_i now enter the fermion evolution equation and observables (and vice versa). Such a sudden change for the evolution of a system at a specific time-step is characterized by an unsteadiness in the observables and referred to as (quantum) quench.

During the evolution of the system, more and more energy is transfered from the Yang-Mills to the fermion sector. This effect is more present for lighter fermions, that can naturally acquire more kinetic energy, although the effect is not very present for the two masses considered. We expect the energy of the fermion and Yang-Mills sector to saturate at late times, leading to a situation where the energy exchange between sectors is balanced. This state is not yet reached for the final time in our simulation, but we can extract the asymptotes by fitting

the data to functions of the form

$$\epsilon^{fit}(t) = a + b \cdot e^{-c \cdot t}. \tag{8.3}$$

We give the result of the fitting procedure in (figure 8.2). The simulation data is indicated as bold line, whereas the fit is plotted as dotted line. As a crosscheck, the total energy density is obtained from summing the fits for the Yang-Mills and fermion sector.

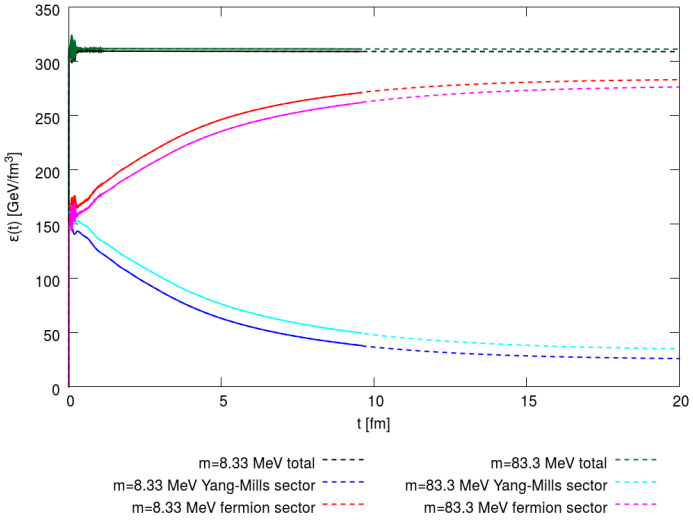

Figure 8.2: Energy density in simulations with different fermion masses $m = 8.33$ MeV and $m = 83.3$ MeV, on a $50 \times 50 \times 50$ lattice, with spacing $a = 0.24$ fm, coupling $g = 2$ and a stochastic fermion ensemble size of $N_{ens} = 750$. The data is fitted to (eq. 8.3), making it possible to extract the asymptotes.

Note that this state of balanced energy transfer between the Yang-Mills and fermion sector is reached far beyond the estimated hydrodynamisation time of $\tau_{hydro} \approx 1$ fm. Based on that, we can already conclude, that most likely no equilibrium state is reached for a simulation of the Glasma coupled to fermions within the time estimates for equilibration, using the framework of the semi-classical effective theory of QCD.

We close the discussion of the energy density, by comparing a simulation with fermions of mass $m = 8.33$ MeV to a simulation with fermions of lower mass $m = 0.833$ MeV. The idea is to study, how strongly the dynamics of the system is modified when moving towards the ultra-relativistic limit of massless fermions.

Comparing the energy density for the two different masses in (figure 8.3), we find that the difference is negligible. We can conclude, that we are already close to the ultra-relativistic limit for a choice of $m \leq 8.33$ MeV for the fermion mass. The reason for that is most likely rooted in the fact, that the fermion mass is small, when compared to the momentum scale of the highly energetic Glasma state. Extending this discussion to larger fermion masses is not possible, because the dynamics of lattice Wilson fermions becomes significantly modified, as discussed in (section 2.2).

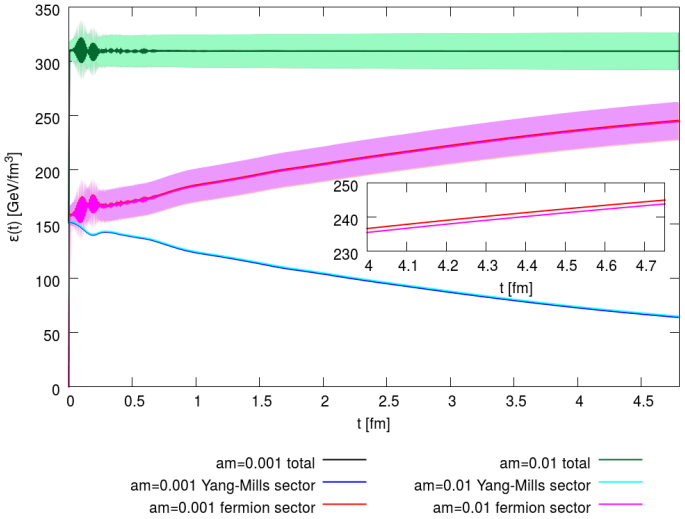

Figure 8.3: Energy Density in simulations with different fermion masses $m = 0.833$ MeV and $m = 8.33$ MeV, on a $50 \times 50 \times 50$ lattice, with spacing $a = 0.24$ fm, coupling $g = 2$ and a stochastic fermion ensemble size of $N_{ens} = 750$.

8.1.2 Pressure Isotropization

Let us now turn to the question if a pressure isotropy is reached in the simulation. As discussed in (section 3.4), the initial Glasma state is characterized by a strong pressure anisotropy for the longitudinal pressure P_L compared to the transverse pressure P_T, with the initial ratio given as $P_L/P_T = -1$. Because of the success of hydrodynamics after an estimated time of $t_{hydro} = 1$ fm, we require the system to move towards (at least partial) thermal equilibrium, where (partial) pressure isotropy marks a necessary condition.

As discussed in (section 3.4), it has already been shown in [60] that a pure Yang-Mills simulation of the Glasma does not isotropize. Isotropization could only be achieved by explicitly breaking the longitudinal boost invariance on the level of the initial conditions, motivated from quantum rapidity fluctuations (eq. 3.22). In this section, we want to study if a coupling to fermions, that are inherently of quantum nature, has a comparable effect on the system and can drive it towards pressure isotropy as well.

In (figure 8.4), we compare the ratio P_L/P_T for simulations with fermions of masses $m = 8.33$ MeV and $m = 83.3$ MeV. We observe that the system moves towards pressure isotropy in both cases. For a comparison, we additionally included the pressure ratio of a pure Yang-Mills simulation, that shows no isotropization, as expected. Perfect isotropy $P_L/P_T = 1$ is not reached in the simulation with fermions, but the initial anisotropy of $P_L/P_T = -1$ of the Glasma is erased rapidly. The difference for the two masses is only marginal. It can be explained, by the fact that lighter fermions acquire more energy, as seen in (figure 8.1), but it can also be rooted in discretization effects.

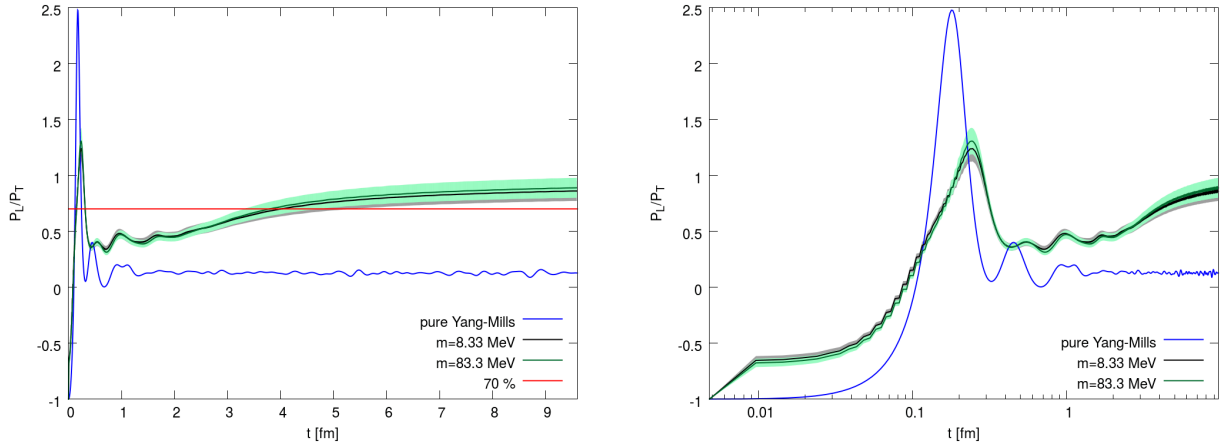

Figure 8.4: Longitudinal to transverse pressure ratio for simulations with fermions of mass $m = 8.33$ MeV and $m = 83.3$ MeV, on a $50 \times 50 \times 50$ lattice, with spacing $a = 0.24$ fm, coupling $g = 2$ and a stochastic fermion ensemble of size $N_{ens} = 750$. On the right-hand side, time is plotted logarithmically.

As characteristic for the Glasma, the initial anisotropy is given as $P_L/P_T = -1$. As soon as both sectors are coupled, the system enters an oscillatory phase, that is present in all cases, in a pure Yang-Mills simulation, as well as in a simulation with fermions. In the latter one, the oscillations are significantly reduced in amplitude. Also note, that the quench at the first time-step, that has previously been discussed in context of the energy density (figure 8.1), is present as well. The oscillatory phase approximately lasts until $t \approx 1$ fm, which is of the order of the hydrodynamization time. The crucial difference between the system including fermions and the pure Yang-Mills system is, that in the latter one the pressure ratio drops to zero after the oscillatory phase, reaching the free streaming limit, which is characterized by $P_L \to 0$. On the opposite, the system including fermions already reaches a pressure ratio of $P_L/P_T \approx 0.5$ after the oscillatory phase, followed by a phase, where the pressure is slowly approaching isotropy.

In (chapter 3), it has been suggested to match either to hydrodynamics or to QCD kinetic theory at a specific time [50]. Following [153] we suggest a ratio of $P_L/P_T \geq 0.7$ in (figure 8.4), although this ratio is reached far beyond the expected hydrodynamization time $t \approx 4$ fm $> t_{hydro} = 1$ fm. As discussed in [38], QCD effective kinetic theory (EKT) is expected to be valid early at the order of $t_{EKT} \approx 0.3$ fm, which happens to be very close to the peak of the initial oscillatory phase, observable in (figure 8.4). Finally note, that having reached a ratio of $P_L/P_T \approx 0.5$ at the hydrodynamization time of $t_{hydro} = 1$ fm, matches well previous studies in [154], where a matching to relativistic hydrodynamics has been proposed, also presented in [155, 156, 157, 158].

Having discussed masses of the order of the up-/down-quark mass and the mass of the strange quark, let us consider a mass of $m = 0.833$ MeV, which is below the mass of the up-quark, to test for the ultra-relativistic limit. We give the longitudinal to transverse pressure ratio in (figure 8.5). As it has already been observed in case of the energy density (figure 8.3), we do not find a significant difference for the two masses considered, supporting our previous observation, that the dynamics becomes independent on m, due to the validity of the ultra-relativistic limit.

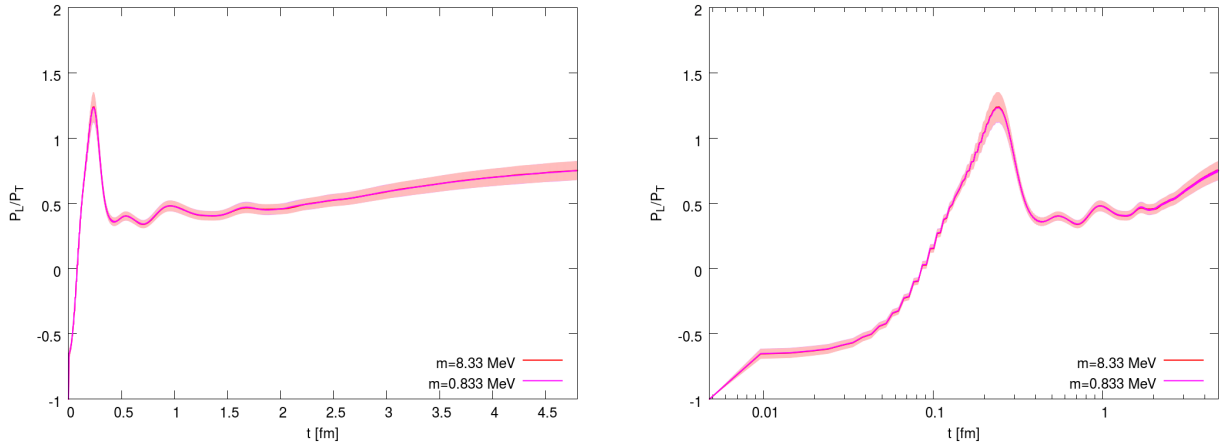

Figure 8.5: Longitudinal to transverse pressure ratio for simulations with fermions of mass $m = 0.833$ MeV and $m = 8.33$ MeV, on a $50 \times 50 \times 50$ lattice, with spacing $a = 0.24$ fm, coupling $g = 2$ and a stochastic fermion ensemble of size $N_{ens} = 750$. On the right-hand side, time is plotted logarithmically.

Another observable of interest in our simulation, is the pressure to energy ratio P/ϵ. In a pure Yang-Mills simulation, the system approaches [61, 62]

$$\frac{P_L}{\epsilon} \to 0, \qquad \frac{P_T}{\epsilon} \to \frac{1}{2}, \tag{8.4}$$

which is referred to as the free streaming limit.

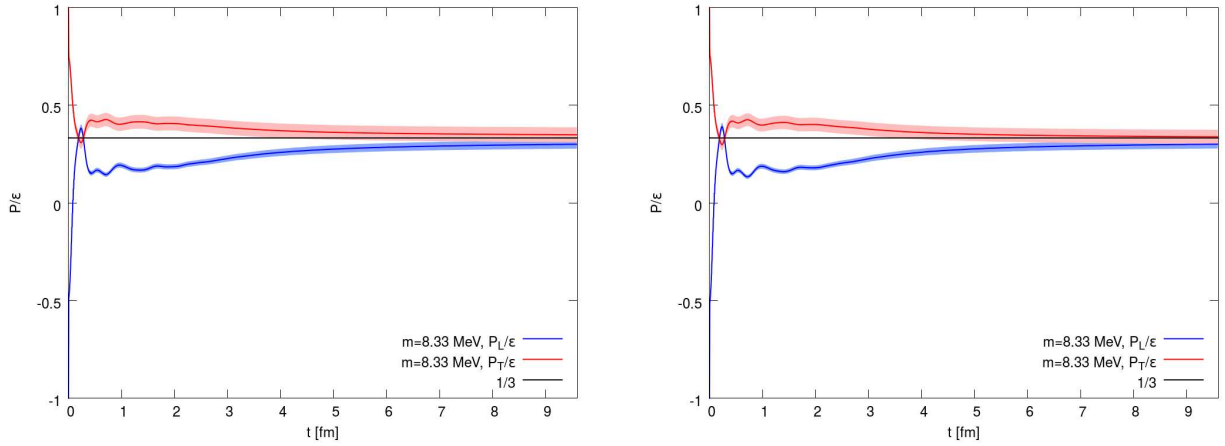

Figure 8.6: Pressure to energy ratio for a simulation with fermions of mass $m = 8.33$ MeV (left) and $m = 83.3$ MeV (right), on a $50 \times 50 \times 50$ lattice, with spacing $a = 0.24$ fm, coupling $g = 2$ and a stochastic fermion ensemble of size $N_{ens} = 750$.

It has been shown in [60], that an explicit breaking of longitudinal boost invariance in a pure Yang-Mills simulation in a static box, drives the ratio towards the limit

$$\frac{P_{T/L}}{\epsilon} \to \frac{1}{3}, \tag{8.5}$$

which is familiar from an ultra-relativistic free gas.

We give the results for the pressure to energy ratio of our semi-classical system with fermions of mass $m = 8.33$ MeV and $m = 83.3$ MeV in (figure 8.6). It is clearly visible, that the limit $P_L/P_T \to 1/3$ is approached during the evolution, although it is not yet perfectly reached, matching our previous observation for the longitudinal to transverse pressure ratio. Keep in mind, that the exact limit of $P_i/\epsilon \to 1/3$ is only reached in case of ultra-relativistic particles and we expect to reach a constant value slightly below in case of fermions with a finite mass $m = 83.3$ MeV [159].

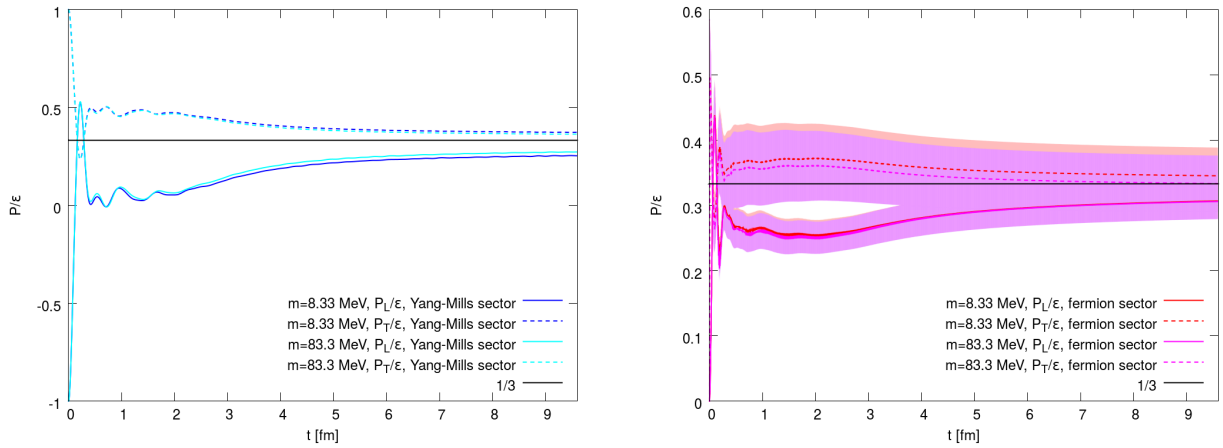

Figure 8.7: Pressure to energy ratio of the Yang-Mills sector (left) and the fermion sector (right) for different fermion masses $m = 8.33$ MeV and $m = 83.3$ MeV, on a $50 \times 50 \times 50$ lattice, with a stochastic fermion ensemble of size $N_{ens} = 750$ and coupling $g = 2$.

The limit $P/\epsilon \sim 1/3$ is also reached for the Yang-Mills and fermion sector individually (figure 8.7). In general we observe, that the transverse direction approaches the equilibrium value slightly faster, which seems to be reasonable, because initially the pressure in longitudinal direction is far more off its equilibrium value. We will use the observation, that the fermion sector approaches the equilibrium value of $P/\epsilon \to 1/3$, to match the energy density of the fermion sector to a free gas of fermions later, making it possible to extract a quasi-temperature of the system.

8.1.3 Profile of the Energy Density

In the following, we want to study the process of pressure isotropization, caused from a coupling of the Yang-Mills fields of the Glasma to fermions. In a first step, we have a look at the profile of the energy density. This is motivated by the observation, that the energy density of the Yang-Mills sector is characterized by lines of constant energy in longitudinal direction for the Glasma. This can easily be understood, recalling the longitudinal color-flux tubes present in the Glasma. In a simulation of pure Yang-Mills theory, the equations of motion preserve longitudinal boost invariance and the initial profile of the energy density is conserved. This can be seen in (figure 8.8), where we have plotted the profile of the longitudinal chromo-electric part of the energy density in a pure Yang-Mills simulation at different times. The profile shows the longitudinal lines of constant energy, only influenced by fluctuations.

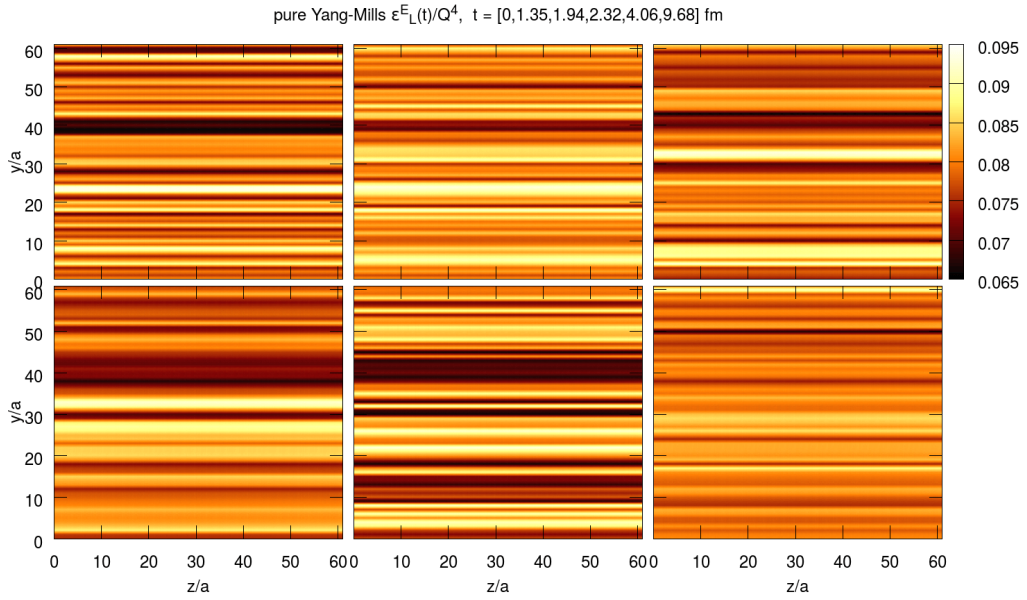

Figure 8.8: Profile of the longitudinal chromo-electric energy density $\epsilon_L^E(t)$ in a pure Yang-Mills simulation at times $t = \{0, 1.35, 1.94, 2.32, 4.06, 9.68\}$ fm. A lattice average has been performed for the x-direction. Simulations have been performed on a $62 \times 62 \times 62$ lattice, with lattice spacing $a \approx 0.19$ fm and a coupling of $g = 2$.

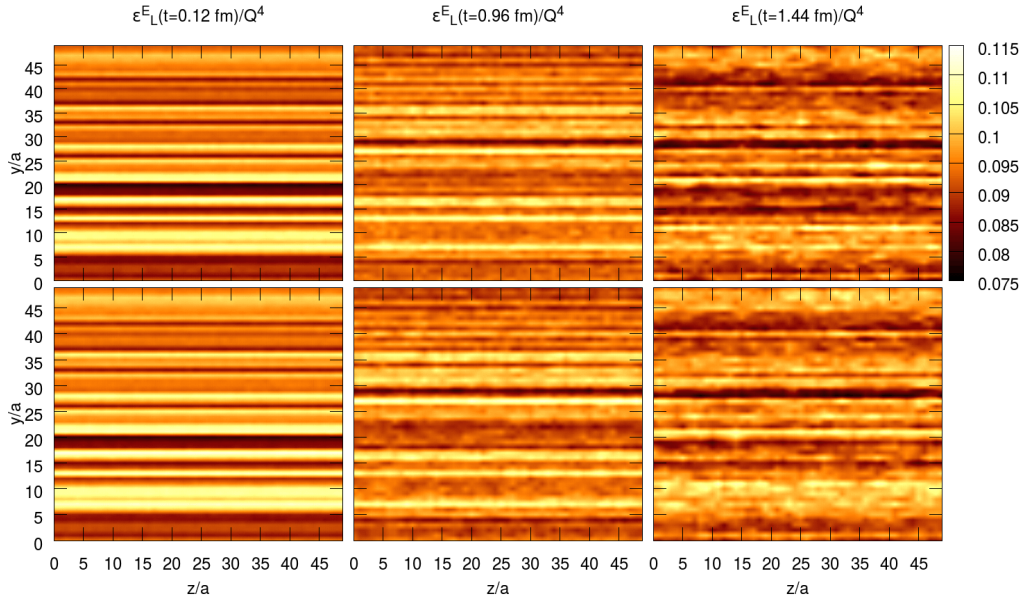

Figure 8.9: Profile of the longitudinal chromo-electric energy density $\epsilon_L^E(t)$ for a simulation with fermions of mass $m = 8.33$ MeV (top) and fermions of mass $m = 83.3$ MeV (bottom), at times $t \in \{0.12, 0.96, 1.44\}$ fm. A lattice averaged has been taken in x-direction. The simulations have been performed on a $50 \times 50 \times 50$ lattice, with spacing $a = 0.24$ fm, coupling $g = 2$ and a stochastic fermion ensemble of size $N_{ens} = 750$.

We now want to study, how the energy density profile is changed in a simulation of the Glasma coupled to fermions. In (figure 8.9) we plot the profile of the longitudinal component of the chromo-electric energy density, with a lattice average taken in x-direction, for a simulation with fermions of mass $m = 8.33$ MeV (top) and a simulation with fermions of mass $m = 83.3$

MeV (bottom) at early times. Plotting the transverse component of the energy density of the chromo-electric field, or the longitudinal or transverse component of the energy density of the chromo-magnetic field reveals a similar picture [126], hence the plots are not given here.

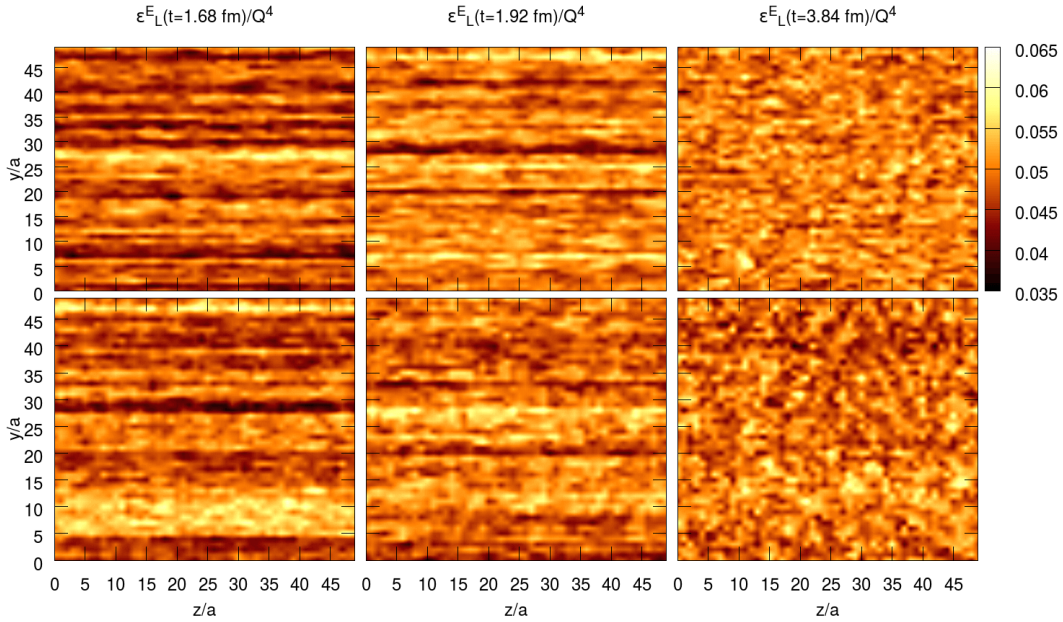

Figure 8.10: Profile of the longitudinal chromo-electric energy density $\epsilon_L^E(t)$ for a simulation with fermions of mass $m = 8.33$ MeV (top) and fermions of mass $m = 83.3$ MeV (bottom), at times $t \in \{1.68, 1.92, 3.84\}$ fm. A lattice averaged has been taken in x-direction. The simulations have been performed on a $50 \times 50 \times 50$ lattice, with spacing $a = 0.24$ fm, coupling $g = 2$ and a stochastic fermion ensemble of size $N_{ens} = 750$.

We find, that the initial lines of constant energy are slowly erased in a simulation with fermions present. At the hydrodynamization time $t_{hydro} = 1$ fm, a „melting“ of the lines can be observed for both masses. Continuing the evolution in time, depicted in (figure 8.10), the lines are completely erased and we arrive at a spacial homogeneous energy density, characterized by random local fluctuations. We emphasize that this effect is essentially caused by the interaction of the classical Yang-Mills fields with the fermions produced in the Glasma, because it is not present in the pure Yang-Mills simulation (figure 8.8).

Having studied the profile of the energy density of the Yang-Mills sector, let us turn to the fermion sector. We plot the longitudinal part of the fermion energy density $\epsilon_L^{\psi}(t)$ in (figure 8.11), where a lattice average has been taken in x-direction. We observe, that the fermions partially copy the initial structure of the longitudinal lines of constant energy at initial times. This is most likely the case, because the gauge links directly enter the energy density observable of the fermion sector (eq. 6.34), as soon as both sectors are coupled at the first time-step. As a consequence, the initial energy density profile of the fermion sector resembles the profile of the longitudinal chromo-electric part of the energy density (figure 8.9). Nevertheless, the lines of constant energy in longitudinal direction are only slightly visible and quickly erased during the evolution of the system, when compared to the Yang-Mills sector. This matches our previous observation for the pressure to energy ratio of the individual Yang-Mills and fermion sector in (figure 8.7), where we observed that the fermion sector reaches $P/\epsilon \to 1/3$ faster than the Yang-Mills sector.

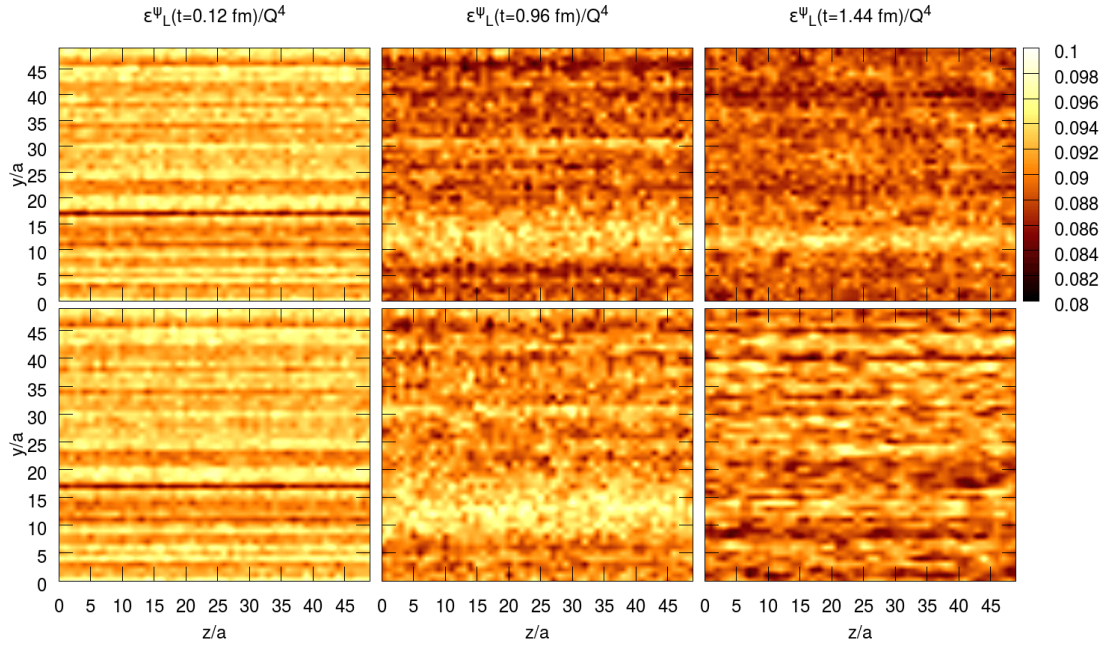

Figure 8.11: Profile of the longitudinal energy density of the fermion sector $\epsilon_L^{\Psi}(t)$ for a simulation with fermions of mass $m = 8.33$ MeV (top) and fermions of mass $m = 83.3$ MeV (bottom), at times $t \in \{0.12, 0.96, 1.44\}$ fm. A lattice averaged has been taken in x-direction. The simulations have been performed on a $50 \times 50 \times 50$ lattice, with spacing $a = 0.24$ fm, coupling $g = 2$ and a stochastic fermion ensemble of size $N_{ens} = 750$.

We can conclude that shifting energy back- and fourth between the Yang-Mills and fermion sector during the evolution of the system erases the lines of constant energy, characteristic for the initial Glasma state and causes the energy density to become homogeneous. We will compare this process to the idea of explicitly breaking boost invariance on the level of the initial conditions later.

8.1.4 Gauge Invariant Occupation of Energy Modes

Having discussed how signals of isotropization can be found in the profile of the energy density, let us finally turn to the occupation of energy modes. We have defined the gauge invariant occupation of energy modes in (section 6.3.1), making use of the Fourier transform of the energy density, weighted by the appropriate lattice dispersion relation of bosons or fermions. With the fermions being initialized as vacuum fermions, their energy modes are completely unoccupied before the fermion- and Yang-Mills sector are coupled at the first time-step in the simulation. On the other hand, we expect low energy modes to be highly occupied in the Yang-Mills sector, due to the overoccupied classical field modes in the Glasma. Keep in mind, that we have initialized the Yang-Mills sector, by solving the Poisson equation in the transverse plane and later copied the result into longitudinal direction, setting $U_z = 1$ and generating the characteristic color flux-tubes of the Glasma (see section 3.4). As a consequence, energy modes with $p_z = 0$ are not occupied at initial time.

Having seen previously, that there is no significant difference for the two different fermion masses considered $m = 8.33$ MeV and $m = 83.3$ MeV, we restrict our discussion to the lighter

mass. We plot the occupation of energy modes (eq. 6.71) for the Yang-Mills sector in (figure 8.12). The energy modes $\omega_{\mathbf{p}}$ are given by the lattice dispersion relation of massless bosons (eq. 6.66).

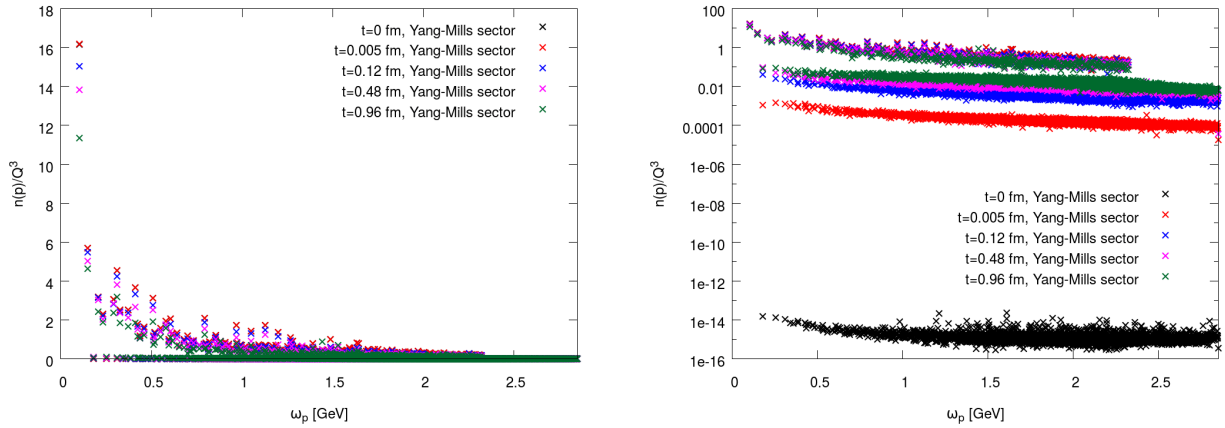

Figure 8.12: Occupation of energy modes in the Yang-Mills sector for a simulation with fermions of mass $m = 8.33$ MeV. The simulation has been performed on a $50 \times 50 \times 50$ lattice, with lattice spacing $a = 0.24$ fm, coupling $g = 2$ and a stochastic fermion ensemble of size $N_{ens} = 750$. The y-axis is logarithmically scaled on the right-hand side.

As expected, we observe that the distribution is peaked for low energy modes at initial times. When evolving in time, higher energy modes become more and more occupied, as can be seen on the right-hand side of (figure 8.12). It is furthermore possible to identify two separated ribbons at initial times, where the upper ribbon corresponds to energy modes with $p_z = 0$. The energy modes with $p_z \neq 0$ are unoccupied at initial time, as can be seen from the black lower ribbon on the right-hand side of (figure 8.12), which is located at numerical zero. During the evolution of the system, these modes become more and more occupied, causing the ribbon to move up.

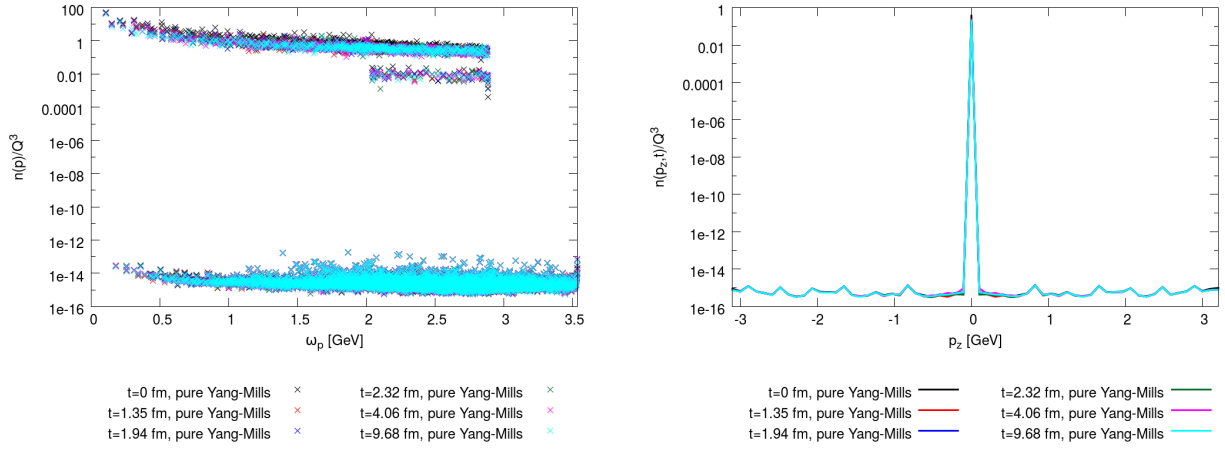

Figure 8.13: Occupation of energy modes in a pure Yang-Mills simulation (left) and a lattice average of the occupation in the transverse plane (right). The simulation has been performed on a $62 \times 62 \times 62$ lattice, with lattice spacing $a = 0.19$ fm and coupling $g = 2$. The physical parameters as box size, energy and saturation scale Q_s are kept constant, when compared to a simulation with fermions.

The situation is completely different for a pure Yang-Mills simulation. We plot the occupation of energy modes in a pure Yang-Mills simulation in (figure 8.13). In contrast to the simulation

with fermions, the occupation of energy modes is not modified during the evolution of the system. Especially, energy modes with $p_z \neq 0$ are not occupied. The reason for that is that the classical Hamilton equations of motion of the pure Yang-Mills system (section 2.1) preserve boost invariance. As a consequence, the boost invariant construction of the initial conditions is preserved, which translates to the occupation of energy modes.

On the opposite, in a simulation with fermions present, energy is transferred back and forth between the Yang-Mills and fermion sector, due to the coupling of the sectors in (eq. 4.1) and a back-coupling of fermions onto the Yang-Mills fields in (eq. 5.50). Because of that, the energy modes of the fermion sector become occupied, as soon as both sectors couple at the first time-step. We demonstrate this for the fermion sector by plotting the occupation of energy modes as a function of the lattice dispersion relation for Wilson fermions (eq. 6.68) in (figure 8.14). As can be seen in the left-hand plot, the low energy modes become more and more occupied, because energy is transfered from the Yang-Mills to the fermion sector during the evolution. This shift of energy between sectors slows down, as soon as a balanced situation is reached at late times, as discussed in the context of the energy density (figure 8.2). The energy back-transfer from the fermion sector to the Yang-Mills sector now causes the energy modes with $p_z \neq 0$ and high energy modes to become occupied during the evolution of the system, as seen in (figure 8.12).

On top of that, we observe in (figure 8.14) that the two ribbon structure is slightly present in the fermion sector at early times. This matches our previous observation for the energy density profile of the fermion sector, where we have seen that the longitudinal lines of constant energy of the Yang-Mills sector are copied to the fermion sector at early times (figure 8.11). Nevertheless we emphasize, that the splitting between $p_z = 0$ and $p_z \neq 0$ modes is much less present in the fermion sector and on top of that quickly erases.

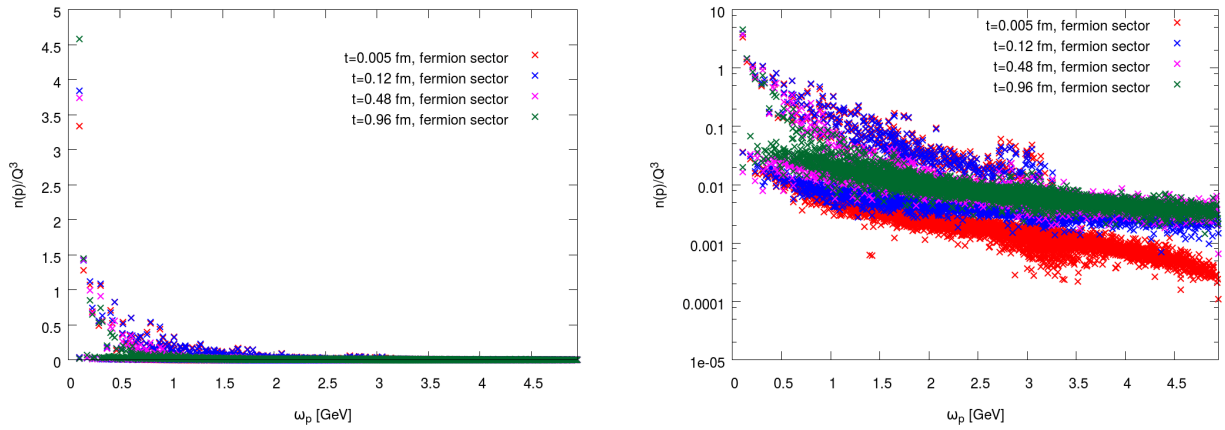

Figure 8.14: Occupation of energy modes in the fermion sector for a simulation with fermions of mass $m = 8.33$ MeV. The simulation has been performed on a $50 \times 50 \times 50$ lattice, with lattice spacing $a = 0.24$ fm, coupling $g = 2$ and a stochastic fermion ensemble of size $N_{ens} = 750$. The y-axis is logarithmically scaled on the right-hand side.

In (figure 8.15) we give the occupation of energy modes of the Yang-Mills and fermion sector for large times. We observe in both cases, that energy modes tend towards an equal occupation, which happens to be the case much faster in the fermion sector than in the Yang-Mills sector. At a time of $t \approx 4$ fm, where we have observed a longitudinal to transverse pressure ratio

of approximately $P_L/P_T \approx 0.7$, the occupation of energy modes already flattens out in both sectors, indicating that high energy modes become equally occupied when compared to low energy modes. We conclude, that an equilibration of the occupation of energy modes seems to go hand in hand with the observation of pressure isotropization. This is especially underlined by the finding, that both phenomena are not present in a pure Yang-Mills simulation.

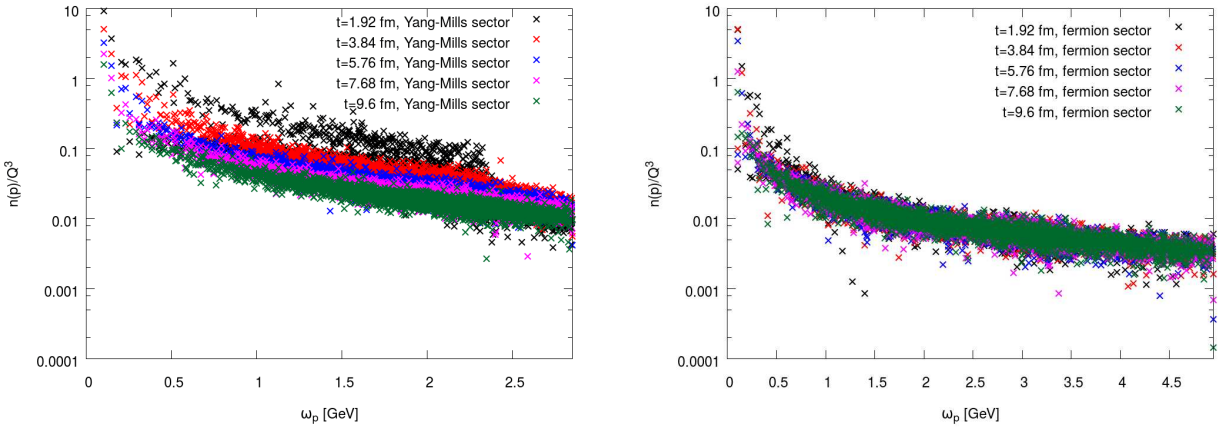

Figure 8.15: Occupation of energy modes in the Yang-Mills sector (left) and the fermion sector (right) at large times t for a simulation with fermions of mass $m = 8.33$ MeV, as a function of the lattice dispersion relation of massless gauge fields and Wilson fermions. The simulation has been performed on a $50 \times 50 \times 50$ lattice, with lattice spacing $a = 0.24$ fm, coupling $g = 2$ and a stochastic fermion ensemble of size $N_{ens} = 750$.

The previous observations are supported when investigating the average of the occupation of energy modes in the transverse momentum planes, as a function of longitudinal momentum. As stated in the beginning, only the energy modes in the $p_z = 0$ transverse momentum plane are occupied at initial time, due to properties of the Glasma (see section 3.4). As stated previously, in case of a pure Yang-Mills simulation, this situation is unchanged during the evolution of the system, as can be seen in the right-hand plot in (figure 8.13).

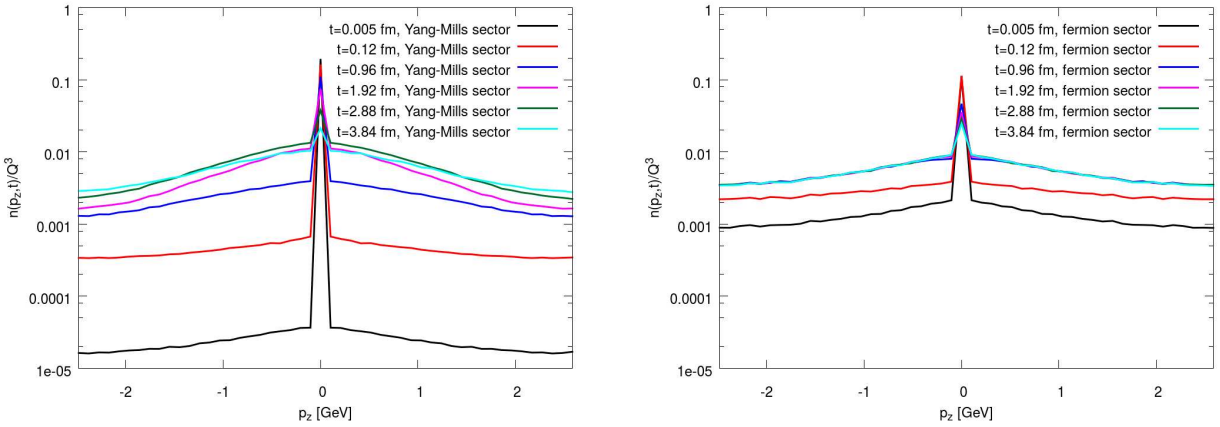

Figure 8.16: Lattice averaged occupation of energy modes in the transverse plane for the Yang-Mills sector (left) and the fermion sector (right), as a function of longitudinal momentum, for a simulation including fermions of mass $m = 8.33$ MeV. The simulation has been performed on a $50 \times 50 \times 50$ lattice, with lattice spacing $a = 0.24$ fm, coupling $g = 2$ and a stochastic fermion ensemble of size $N_{ens} = 750$.

This observation differs for a simulation with fermions of mass 8.33 MeV, as can be seen in (figure 8.16). In both cases we observe that energy modes with $p_z \neq 0$ become more and more occupied by time. As a consequence, we observe in (figure 8.16), that the initial peak at $p_z = 0$ decreases during the evolution of the system. Note that the total decrease in the Yang-Mills sector happens, because a part of the energy is transferred to the fermion sector. For the fermion sector we observe in (figure 8.16), that the peak at $p_z = 0$ is copied at initial times, supporting our previous observations. Following that, the peak decreases in analogy to the Yang-Mills sector, leading to a situation where the fermion energy modes become approximately equally occupied at late times.

Having observed, that high energy modes become more and more occupied during the evolution of the system, the question arises, if it is still valid to approximate the Yang-Mills sector as classical at late times. To study this in more detail, we have a look at the percentage of occupied low energy modes, compared to the total amount of available modes in the system. We set the boundary for low energy modes to be

$$\omega_{\mathbf{p}}^{bound} = \alpha_s Q_s \approx 0.6 \text{ GeV}, \tag{8.6}$$

where $\alpha_s = \frac{g^2}{4\pi}$ is the strong parameter and $Q_s = 1.867$ GeV the saturation scale. We plot the ratio for the two simulations, including fermions of different mass $m = 8.33$ MeV and $m = 83.3$ MeV, in (figure 8.17). We find, that the initial percentage of $\sim 38\%$ decreases rapidly during the evolution of the system. At the final time of the simulation, the ratio of occupied low energy modes has already dropped below $\sim 10\%$, making it possible to conclude, that the Yang-Mills sector is no longer dominated by soft modes and Yang-Mills fields can no longer be taken to be overoccupied. As a consequence it is reasonable to argue that the classical approximation reaches its limit of validity.

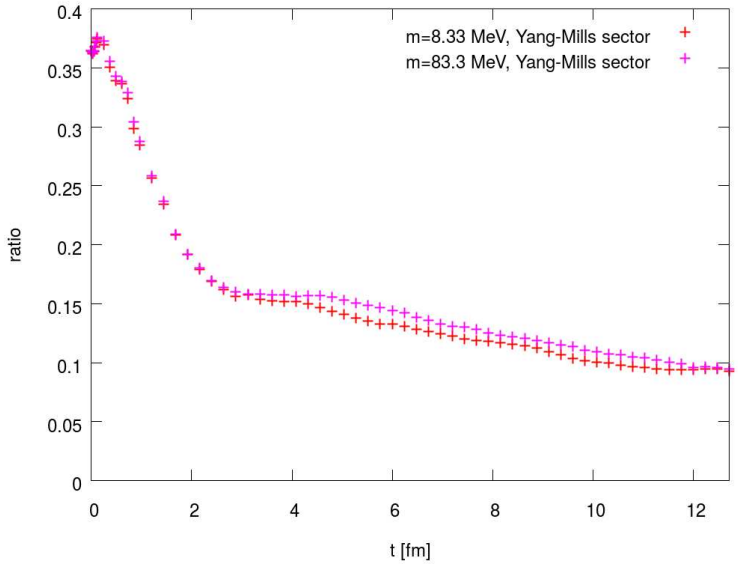

Figure 8.17: Ratio of occupied low energy modes compared to the total occupation of energy modes for two simulations with fermions of mass $m = 8.33$ MeV and $m = 83.3$ MeV. Low energy modes are classified until a cutoff of $\omega_{\mathbf{p}}^{bound} = \alpha_s Q_s \approx 0.6$ GeV. The simulations have been performed on a $50 \times 50 \times 50$ lattice, with a lattice spacing of $a = 0.24$ fm, coupling $g = 2$ and a stochastic fermion ensemble of size $N_{ens} = 750$.

8.1.5 Gauge Variant Occupation and Quark-Antiquark Production

In the previous section, we presented the results for the occupation of energy modes, calculated in a gauge invariant way. To further validate this approach, we compare it to the gauge variant definitions of the occupation of modes, familiar from the literature. As discussed in (section 6.3.2), we follow the approach of [43] and [40] to study the occupation of modes in the Yang-Mills sector, by making use of the Fourier transform of the chromo-electric field (eq. 6.81). For the fermion sector we follow [74], calculating a quasi quark- and anti-quark number, making use of (eq. 6.96) and (eq. 6.97).

In (figure 8.18) we give the results of the gauge variant occupation of modes and the transverse averaged occupation, as a function of longitudinal momentum, for the Yang-Mills sector of a simulation with fermions of mass $m = 8.33$ MeV. Both gauge variant observables have been calculated after fixing Coulomb gauge, making use of a relaxation algorithm [102]. When comparing the gauge variant occupation of modes to the gauge invariant definition given in (figure 8.12), (figure 8.15) and (figure 8.16) we find very good qualitative agreement. In all cases it is possible to identify the two separated ribbons at initial time, caused by the choice of initial conditions. These ribbons move towards each other during the evolution of the system, causing modes with $p_z \neq 0$ to become occupied as well. At late times high energy modes become more and more occupied in all cases.

For the fermion sector, the definition of the gauge variant occupation of modes is different, when compared to the definition for the Yang-Mills sector. The latter one uses the Fourier transform of the chromo-electric fields, whereas the definition for the fermion sector (eq. 6.94) uses projections of the full interacting fermion spinors at time t onto the free vacuum spinors. On the other hand, the gauge invariant definition of the occupation of energy modes in the fermion sector (eq. 6.71) uses a Fourier transform of the energy density as well. As a consequence, the gauge links enter the gauge variant definition only implicitly, from the equation of motion of the fermions, whereas they explicitly enter the energy density (eq. 6.34).

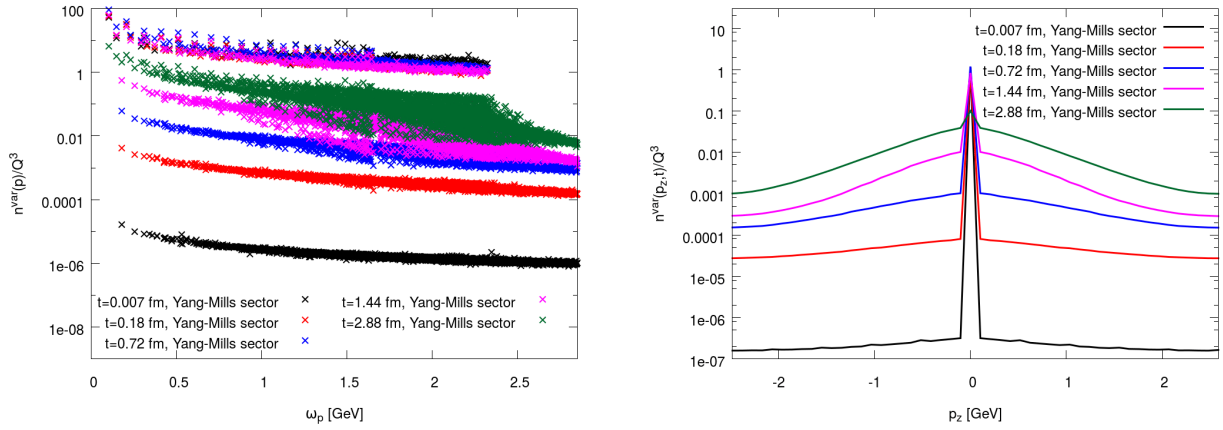

Figure 8.18: Gauge variant occupation of modes (left) and averaged occupation in the transverse plane, as a function of longitudinal momentum (right) for the Yang-Mills sector of a simulation with fermions of mass $m = 8.33$ MeV. The observables are calculated after fixing Coulomb gauge. The simulation has been performed on a $50 \times 50 \times 50$ lattice, with lattice spacing $a = 0.24$ fm, coupling $g = 2$ and a stochastic fermion ensemble of size $N_{ens} = 750$.

In (figure 8.19) we plot the gauge variant occupation of modes for the fermion sector, as well as the lattice averaged occupation in the transverse plane as a function of longitudinal momentum.

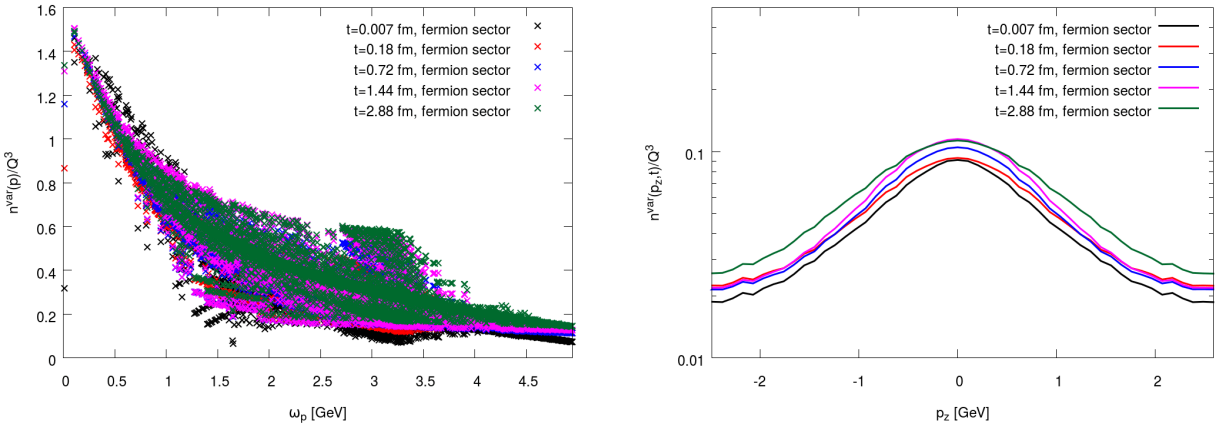

Figure 8.19: Gauge variant occupation of modes (left) and lattice averaged occupation in the transverse plane, as a function of longitudinal momentum (right) for the fermion sector of a simulation with fermions of mass $m = 8.33$ MeV. The observables are calculated after fixing Coulomb gauge. The simulation has been performed on a $50 \times 50 \times 50$ lattice, with lattice spacing $a = 0.24$ fm, coupling $g = 2$ and a stochastic fermion ensemble of size $N_{ens} = 750$.

When comparing these to the gauge invariant definition (figure 8.14) and (figure 8.16), we again find qualitative agreement, although the gauge variant results differ in shape. The reason for that essentially is, that the gauge links do not enter the definition of the gauge variant occupation of the fermion sector, as stated previously. Having validated, that the two ribbon structure and the peak observed at $p_z = 0$ is an artifact from the Yang-Mills sector, we do not observe it in case of the gauge variant definition for the fermion sector. Nevertheless, we observe that hard modes become more and more occupied for the gauge variant definition as well, thus observing qualitative agreement when compared to the gauge invariant definition, validating our approach.

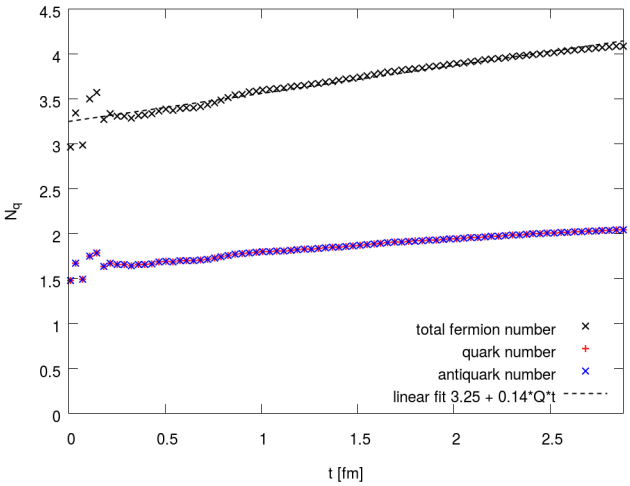

Figure 8.20: Evolution of the quark number (eq. 6.96) and anti-quark number (eq. 6.97) in a simulation with fermions of mass of $m = 8.33$ MeV. The simulation has been performed on a $50 \times 50 \times 50$ lattice, with spacing $a = 0.24$ fm, coupling $g = 2$ and a stochastic fermion ensemble of size $N_{ens} = 750$.

Finally, we have a look at fermion production, making use of the quasi fermion and anti-fermion number (eq. 6.96) and (eq. 6.97). Because we start with symmetric initial conditions, namely the free vacuum, we expect no difference for quark- and anti-quark production. The quark/anti-quark number is given in (figure 8.20). We observe, that indeed fermions and anti-fermions are produced to equal parts. The total production of fermions has been fitted using a linear fit, to demonstrate that our findings in a static box match previous results for a longitudinal expanding system, discussed in [75].

8.1.6 Towards a Temperature

Having observed in a simulation with fermions in (section 8.1.2), that the fermion sector approaches the ultra-relativistic limit of $P/\epsilon \to 1/3$, we use this observation to attribute a (quasi-)temperature[1] to the system. This is done in a matching procedure, where we match the lattice averaged energy density of the fermions, calculated at late times, to the energy density of the free gas of fermions (figure 7.1). With the ultra-relativistic limit being reached, the approach is justified because fermions in the Glasma can be expected to behave quasi free at late times. We now take the late time asymptote of the lattice averaged energy density of the fermion sector, derived from a fit in (figure 8.2), to extract the corresponding temperature of the free gas of fermions as a (quasi-)temperature of the system.

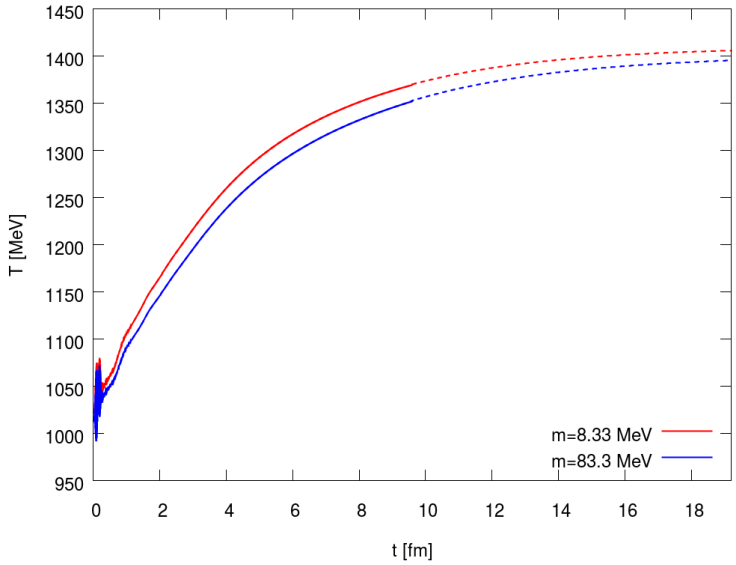

Figure 8.21: Temperature extracted from a matching of the energy density of the fermion sector for two simulations with fermion masses of $m = 8.33$ MeV and $m = 83.3$ MeV, to the energy of a free gas of fermions, extracting the corresponding temperature. The simulation has been performed on a $50 \times 50 \times 50$ lattice, with spacing $a = 0.24$ fm, coupling $g = 2$ and a stochastic fermion ensemble of size $N_{ens} = 750$ and $g = 2$.

The matching procedure is demonstrated in (figure 8.21). At late times it is possible to extract a temperature of the order of ~ 1400 MeV for both fermion masses. This result is a factor of ~ 10 times larger than the Hagedorn temperature, which marks a necessary lower

[1] We refer to the temperature as a quasi-temperature, because pressure isotropy is not a sufficient but only a necessary condition to thermalize a system.

limit for the appearance of a non-hadronic state. Essentially, this temperature is also a factor of ~ 4 times larger, than the expected temperature of ~ 300 MeV for *Pb-Pb* collisions at the LHC from experimental data [160]. Besides limitations from the matching procedure, assuming that it is valid to treat the fermion sector as a free gas at late times, the strong difference can also be rooted in the assumption of a static box. In reality, the QGP is a rapidly longitudinal (and also transverse) expanding system. As a consequence, the energy density drops as a function of time, because the volume significantly increases. This expansion would therefore lead to a lower temperature within our matching procedure. On top of that we have seen, that the semi-classical approximation reaches its limit of validity at late times, because energy modes become more and more equally occupied. This imposes an additional restriction onto the validity of the extracted temperature.

8.2 Explicit Breaking of Longitudinal Boost Invariance

Having discussed the influence of fermions onto the Glasma within the semi-classical approach, observing (partial-)pressure isotropy at late times, we will compare these results to the isotropization process observed in a pure Yang-Mills simulation with an explicit breaking of longitudinal boost invariance. A key difference between the approaches is, that the fermion fields are present at every time-step of the simulation, whereas the violation of boost invariance is caused by a quantum fluctuation, that only enters on the level of the initial conditions in the CGC effective theory (eq. 3.22). It has been demonstrated in [126] and [60], that a presence of these fluctuations in the initial state causes a chromo-Weibel instability, which is the non-abelian counterpart of a Weibel instability, first discussed in the context of electrodynamics [130]. The chromo-Weibel instability in a pure Yang-Mills simulation can then be traced back to the appearance of a non-linear turbulent cascade for the occupation of high energy modes, caused by the fluctuating current in the initial state. This becomes observable as well by a development of filaments in the energy density profile, which we will validate later in this section. To do so, we will discuss different seeds for the initial quantum fluctuation, where a choice of $\Delta = 0.1$ has been estimated to be a realistic choice for quantum fluctuations in the Yang-Mills sector [61].

The lattice spacing for the simulation of a pure Yang-Mills system has been extracted in a matching procedure for the energy density in (section 7.5), keeping the total energy of the system, the box size and the saturation scale Q_s constant, when compared to simulations with fermions. The appropriate lattice spacing has been extracted to be $a = 0.194$ fm, with a lattice extent of $62 \times 62 \times 62$ points. We emphasize, that the physical situation is comparable to the system including fermions and only the resolution in terms of a changes.

Before turning to the comparison of a pure Yang-Mills simulation to a system with fermions, let us discuss a simulation including fermions of mass $m = 8.33$ MeV, where we additionally break the longitudinal boost invariance, introducing a quantum fluctuation (eq. 3.22) of magnitude $\Delta = 0.1$. Our aim is to study if the dynamics of the system is influenced in the static box, when both mechanisms are present.

An explicit breaking of boost invariance manifests itself already in a modified occupation of energy modes at initial time in the Yang-Mills sector, given in (figure 8.22). We observe, that additional energy modes are occupied when introducing the fluctuation. As a consequence, the

previously studied two ribbon structure is weakened. This translates to the lattice averaged occupation of energy modes in the transverse plane such, that energy modes with $p_z \neq 0$ are already occupied at $t = 0$, given on the right of (figure 8.22).

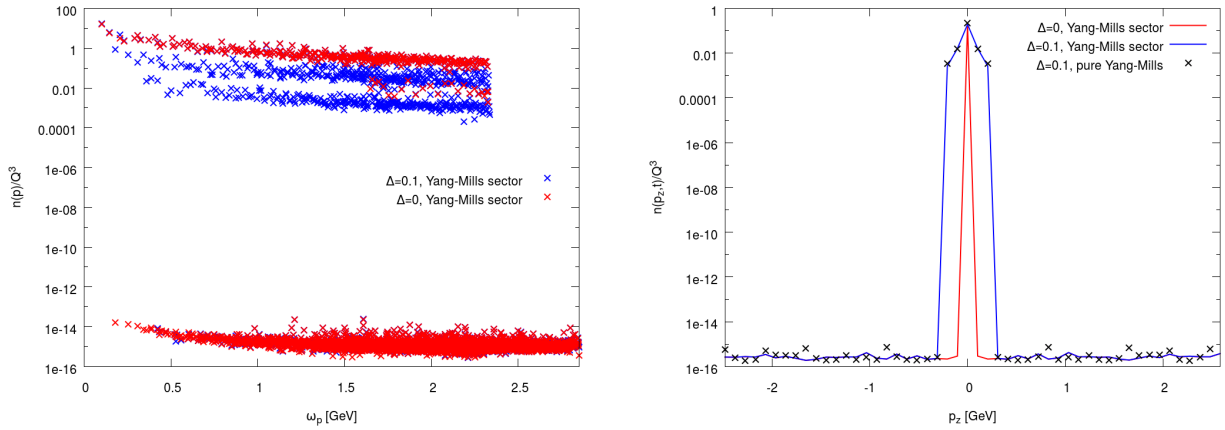

Figure 8.22: Occupation of energy modes (left) and lattice averaged occupation of energy modes in the transverse plane, as a function of longitudinal momentum (right), in the Yang-Mills sector of simulations with and without an initial quantum fluctuations of magnitude $\Delta = 0.1$, at initial time $t = 0$. The simulation has been performed on a $50 \times 50 \times 50$ lattice, with spacing $a = 0.24$ fm, coupling $g = 2$ and fermions of mass $m = 8.33$ MeV, using a stochastic fermion ensemble of size $N_{ens} = 750$.

In a next step, we compare the longitudinal to transverse pressure ratio and the pressure to energy ratio of a simulation with fermions of mass $m = 8.33$ MeV, with and without an initial quantum fluctuation in (figure 8.23).

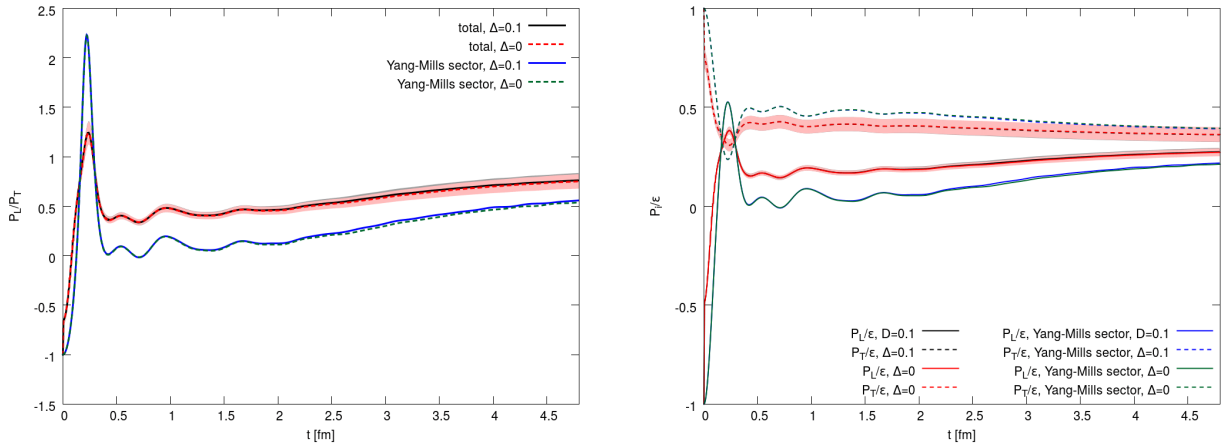

Figure 8.23: Longitudinal to transverse pressure ratio (left) and pressure to energy ratio (right) for simulations with and without an initial quantum fluctuation in the Yang-Mills sector of strength $\Delta = 0.1$. The simulation has been performed on a $50 \times 50 \times 50$ lattice, with spacing $a = 0.24$ fm, coupling $g = 2$ and fermions of mass $m = 8.33$ MeV, using a stochastic fermion ensemble of size $N_{ens} = 750$.

We find, that although the initial state is modified in one simulation, there is only a negligible difference in the two simulations. Especially at early times the data matches perfectly. This observation is still valid, when investigating the ratio in the Yang-Mills sector only. Because the

initial quantum fluctuation only enters the Yang-Mills sector, we can therefore conclude, that the dynamics of a simulation with fermions is not significantly influenced when including an explicit breaking of boost invariance. Moreover, the evolution is dominated by the interaction with fermions in the static box.

The next step is to compare the semi-classical system with fermions of mass $m = 8.33$ MeV to a pure Yang-Mills simulation. In the latter case, we impose an explicit breaking of longitudinal boost invariance to the initial state, introducing a quantum fluctuation of different strength $\Delta \in \{0.001, 0.01, 0.1\}$. The results for the longitudinal to transverse pressure ratio, as well as the pressure to energy ratio are given in (figure 8.24).

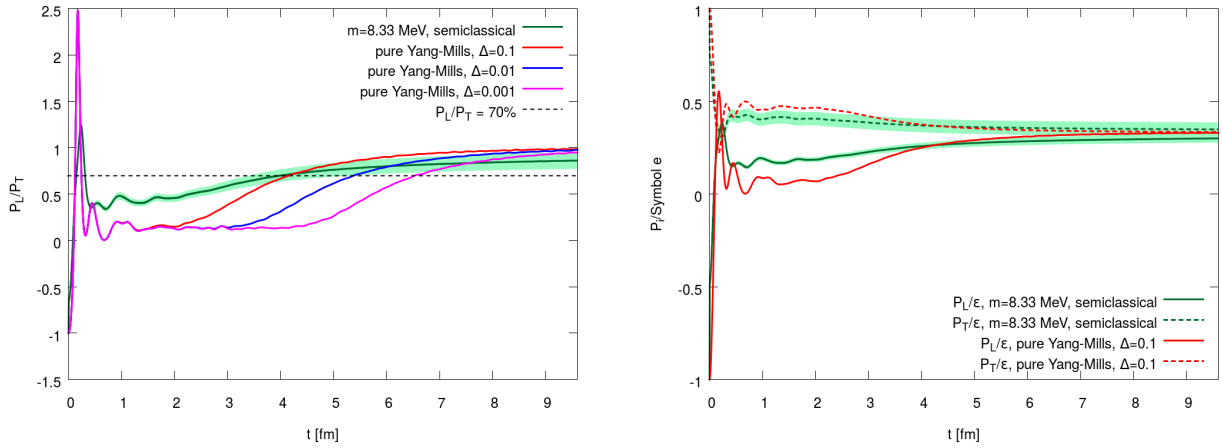

Figure 8.24: Longitudinal to transverse pressure ratio (left) and pressure to energy ratio (right) for a simulation including fermions of mass $m = 8.33$ MeV, compared to a pure Yang-Mills simulation with an explicit breaking of boost invariance of varying strength Δ. The simulation with fermions has been performed on a $50 \times 50 \times 50$ lattice, with lattice spacing $a = 0.24$ fm and a stochastic fermion ensemble of size $N_{ens} = 750$. The pure Yang-Mills simulation has been performed on a $62 \times 62 \times 62$ lattice with spacing $a = 0.19$. All physical parameters as total energy, box size, saturation scale and coupling $g = 2$ are kept equivalently in all simulations.

We observe, that the strength of the quantum fluctuation Δ controls, how fast the pure Yang-Mills system isotropizes. In general, we find that the system coupled to fermions moves faster towards partial pressure isotropy at early times. Independently on the choice of Δ, the longitudinal to transverse pressure ratio of the pure Yang-Mills simulation drops to a value close to zero after the initial oscillatory phase. Following this, the actual isotropization process is then driven by a chromo-weibel instability, as discussed in [126]. This process sets in, as soon as the instability has been spread over the complete lattice, driving the system relatively fast towards pressure isotropy. We will validate this statement later, by investigating the energy density profile and the occupation of energy modes. When increasing the strength Δ of the initial quantum fluctuation in the Yang-Mills sector, the chromo-Weibel stability develops faster and hence pressure isotropy is reached earlier.

In (section 8.1.2) we already saw, that the simulation with fermions does not reach $P_L/P_T \approx 1$ at late times, whereas this seems to be the case in a pure Yang-Mills simulation with broken boost invariance. This can now be understood from comparing the two different processes of isotropization: While isotropization in pure Yang-Mills theory is driven from a chromo-Weibel

instability, that spreads over the whole lattice after sufficient time-steps, the isotropization in a simulation with fermions happens due to the interaction with fermions, starting right from the first time-step. We have argued, that the energy transfer between the fermion and the Yang-Mills sector slows down, as soon as a balance at late times is reached and energy modes become equally occupied. Because more and more energy is transfered to the fermion sector, the anisotropy in the Yang-Mills sector is no longer erased as soon as this balance is reached. On top of that, the classical approximation reaches its limit of validity at late times, making a further investigation with a different theoretical approach necessary.

This discussion is supported from comparing the occupation of energy modes in a simulation with fermions to a pure Yang-Mills simulation with broken boost invariance (figure 8.25). At early times, high energy modes are much faster occupied for a system with fermions (left), because the energy transfer between sectors is immediately present, as soon as both sectors have been coupled. On the other hand, we observe a cascade for the occupation of energy modes in a pure Yang-Mills system with broken boost invariance (right), caused by the chromo-Weibel instability. In the static box, this turns out to be slower than a coupling to fermions at early times.

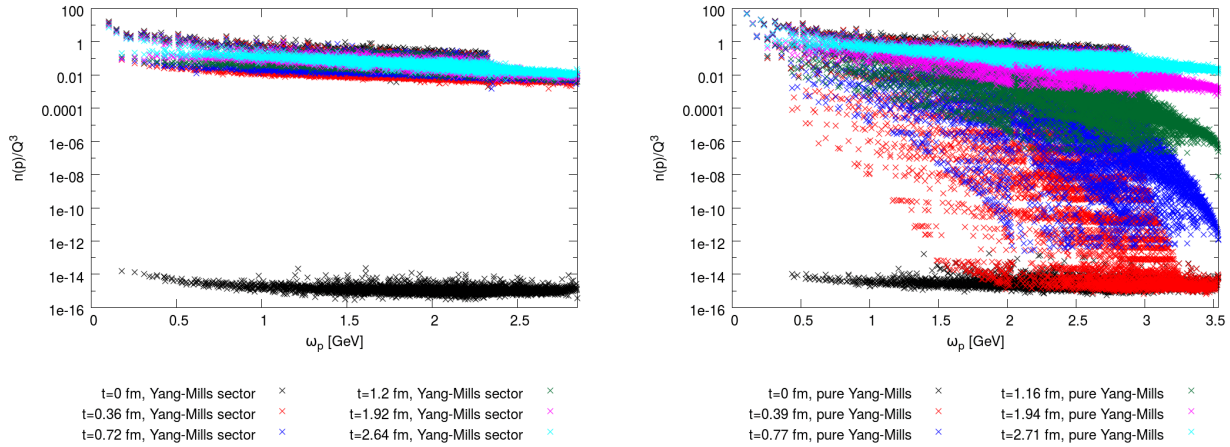

Figure 8.25: Occupation of energy modes in the Yang-Mills sector for a system with fermions of mass $m = 8.33$ MeV (left) and a pure Yang-Mills system with an initial quantum fluctuation of $\Delta = 0.1$ (right). The simulation of the system with fermions has been performed on a $50 \times 50 \times 50$ lattice, with spacing $a = 0.24$ fm and a stochastic fermion ensemble of size $N_{ens} = 750$. The pure Yang-Mills system on a $62 \times 62 \times 62$ lattice with spacing $a = 0.19$ fm. All physical parameters as total energy, box size, saturation scale and coupling $g = 2$ are kept equivalently in all simulations.

To study how the chromo-Weibel instability spreads over the whole lattice by time, let us finally have a look at the energy density profile of a pure Yang-Mills simulation with broken longitudinal boost invariance. We give the profile of the longitudinal chromo-electric energy density, with a quantum fluctuation of magnitude $\Delta = 0.1$, in (figure 8.26).

Comparing it to the energy density profile of a simulation with fermions of mass $m = 8.33$ MeV, (figure 8.9) and (figure 8.10), we find that the initial state shows the characteristic longitudinal lines of constant energy as well, but this time it is possible to observe additional shadowed regions around $z/a \sim 15$ and $z/a \sim 50$ in the energy density profile. These appear due to the modification of the initial state by (eq. 3.22) and their presence is governed by the magnitude

of the fluctuation in longitudinal direction $\Delta = 0.1$.[2]

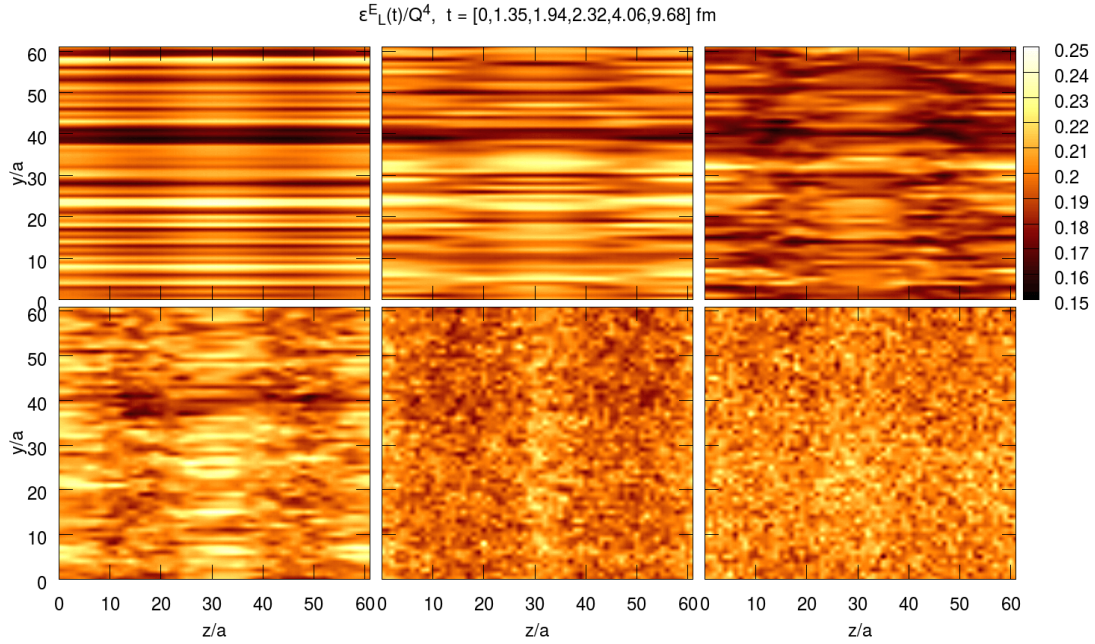

Figure 8.26: Profile of the longitudinal energy density $\epsilon_L^E(t)$ for a pure Yang-Mills simulation with an explicit breaking of longitudinal boost invariance of magnitude $\Delta = 0.1$, at times $t \in \{0, 1.35, 1.94, 2.32, 4.06, 9.68\}$ fm. A lattice average has been taken in x-direction. The simulations have been performed on a $62 \times 62 \times 62$ lattice, with spacing $a = 0.19$ fm and coupling $g = 2$.

During the evolution of the system, filaments arise along these shaded regions, that are caused by the chromo-Weibel instability. In time, the instability spreads over the whole lattice and we observe how the longitudinal lines of constant energy are more and more erased, leading to a situation, where the energy density profile is homogenized and dominated by local fluctuations. As in case of a system coupled to fermions, we conclude, that a homogenization of the energy density goes hand in hand with the development of an isotropization process for the pressure of the system.

Importantly, the longitudinal lines of constant energy are clearly present in the energy density profile of the pure Yang-Mills system around the hydrodynamization time of $t_{hydro} \approx 1$ fm, in contrast to the simulation with fermions, where the lines are already partly erased at every lattice point (see figure 8.9). The reason for that is, that the instability has not yet been spread over the whole lattice. Moreover, at t_{hydro} only the regions close to the maxima of the quantum fluctuation are influenced, as can be seen in (figure 8.26). This supports our previous conclusion, that pressure isotropization initially takes longer in pure Yang-Mills simulation with broken boost invariance, because it takes longer until the chromo-Weibel instability develops. Nevertheless, as soon as the instability has grown, the system is rapidly driven towards pressure isotropy.

[2]The fluctuation is modeled as a cos-function in (eq. 3.22), causing the observed structure of maxima and minima along longitudinal direction in the energy density profile.

8.3 Dependence on the Choice of Coupling

In this section, we will study the dependence on the coupling g, that controls the strength of the interaction of the classical fields with the fermion fields. It enters not only the chromo-electric field equation of motion (eq. 5.50), that controls the back-coupling of fermions onto the Yang-Mills fields, but also the observables themselves. Varying the value of the coupling g therefore is a test, how adapting the interaction strength between the Yang-Mills and fermion sector influences the dynamics of the system. Because the physical reality at the early stage in a heavy ion collision requires a choice of $g \approx 2$, it is not possible to repeat a matching procedure for the energy density for smaller couplings. As a consequence, we leave the model parameters as box size, saturation scale Q_s and lattice spacing a constant. The results for the longitudinal to transverse pressure ratio and the pressure to energy ratio for a simulation with fermions of mass $m = 8.33$ MeV and three different choices of coupling $g \in \{0.01, 0.1, 0.5\}$ are given in (figure 8.27). To reduce computational time, the simulations have been performed with a temporal spacing of $a_t = 0.03a$, that still satisfies the Courant-Levi condition (eq. 7.23).

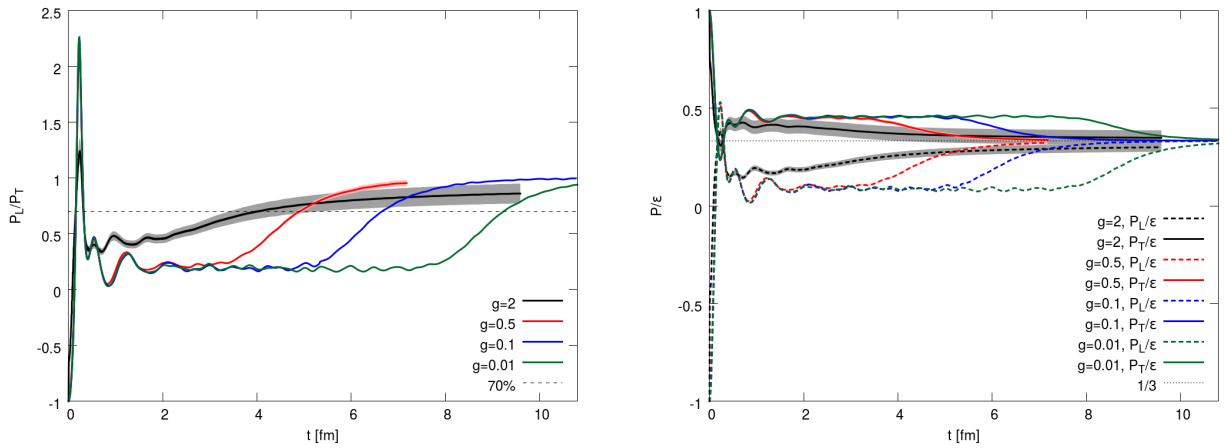

Figure 8.27: Longitudinal to transverse pressure ratio (left) and pressure to energy ratio (right) for simulations with different couplings $g \in \{2, 0.5, 0.1, 0.01\}$. The simulations have been performed at a fixed saturation scale of $Q_s = 1.867$ GeV, on a $50 \times 50 \times 50$ lattice, with spacing $a = 0.24$ fm, including fermions of mass $m = 8.33$ MeV and a stochastic fermion ensemble of size $N_{ens} = 750$.

We find, that pressure isotropy is reached in all cases. In contrast to the simulation with coupling $g = 2$, the longitudinal to transverse pressure ratio for all other choices of g drops to a small fraction close to zero after the initial oscillatory phase. The system therefore does not move towards partial isotropy at early times, especially not around the estimated hydrodynamization time of $t_{hydro} = 1$ fm. The actual process of isotropization sets in later, determined from the strength of the coupling g, with the smallest coupling taking the longest time. The same observations are true for the pressure to energy ratio, given on the right-hand side of (figure 8.27), where the ratio in all simulations moves towards the equilibrium value of 1/3, in decreasing order as a function of the coupling.

At late times we find, that the system moves closer towards perfect pressure isotropy $P_L/P_T \to 1$ for smaller coupling. The reason for this can be understood by recalling that the energy transfer between the fermion and Yang-Mills sector, that causes high energy modes to become occupied, marks a necessary ingredient for pressure isotropization. We argued, that this process is slowed

down as soon as a balanced situation between Yang-Mills and fermion sector is reached at late times for $g = 2$, with a significant amount of energy stored in the fermion sector. For small couplings, both sectors are coupled weaker and hence the energy transfer is reduced. As a consequence, isotropization sets in later, as observed in (figure 8.27), but on the other hand, less energy is transfered to the fermion sector. Because a balanced situation at late times is not reached as rapidly as it is the case for $g = 2$, isotropization is not slowed down for smaller g. This picture is supported from an investigation of the occupation of energy modes in the Yang-Mills sector for simulations with different coupling in (figure 8.28). As expected, we find that energy modes are occupied slower for small couplings g.

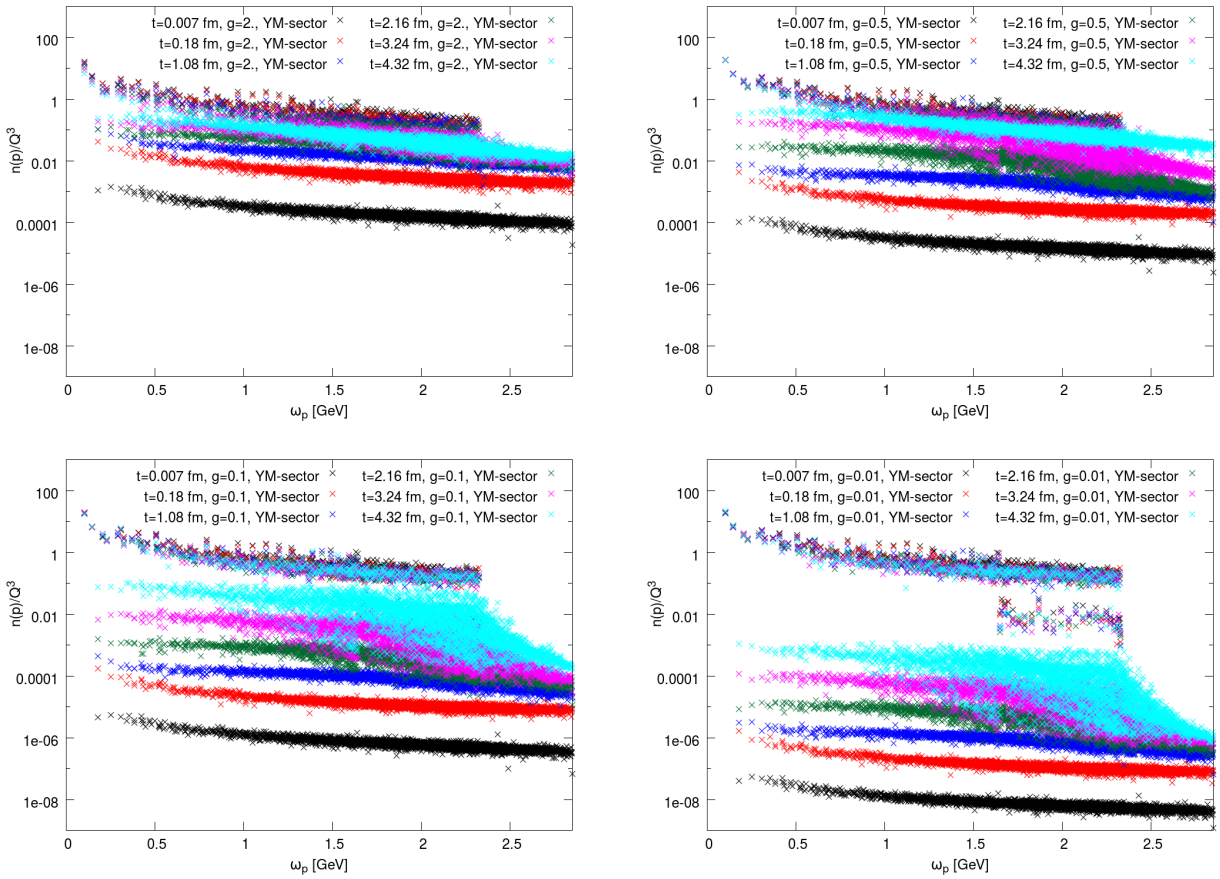

Figure 8.28: Occupation of energy modes in the Yang-Mills sector for simulations with fermions of mass $m = 8.33$ MeV and different couplings $g \in \{2, 0.5, 0.1, 0.01\}$ (top left to bottom right). The simulations have been performed at a fixed saturation scale of $Q_s = 1.867$ GeV, on a $50 \times 50 \times 50$ lattice, with spacing $a = 0.24$ fm and a stochastic fermion ensemble of size $N_{ens} = 750$.

In general, we find by comparing (figure 8.28) and (figure 8.27), that pressure isotropization only sets in, as soon as the two ribbon structure of the initial state has sufficiently been erased. These observations are of course supported by the lattice average of the occupation of energy modes in transverse direction, plotted as a function of longitudinal momentum for the Yang-Mills sector in (figure 8.29). For the couplings $g = 2$ and $g = 0.5$ we observe that this occupation is equalized and the initial peak at $p_z = 0$ is diminished. In the other two cases of smaller couplings, we are not yet close to an equalized situation and pressure isotropization sets in at a later time. Also note, that it is already possible to observe a slow down for

$g = 2$ in the Yang-Mills sector, because more and more energy has been transfered to the fermion sector, as can be seen in (figure 8.1) as well.

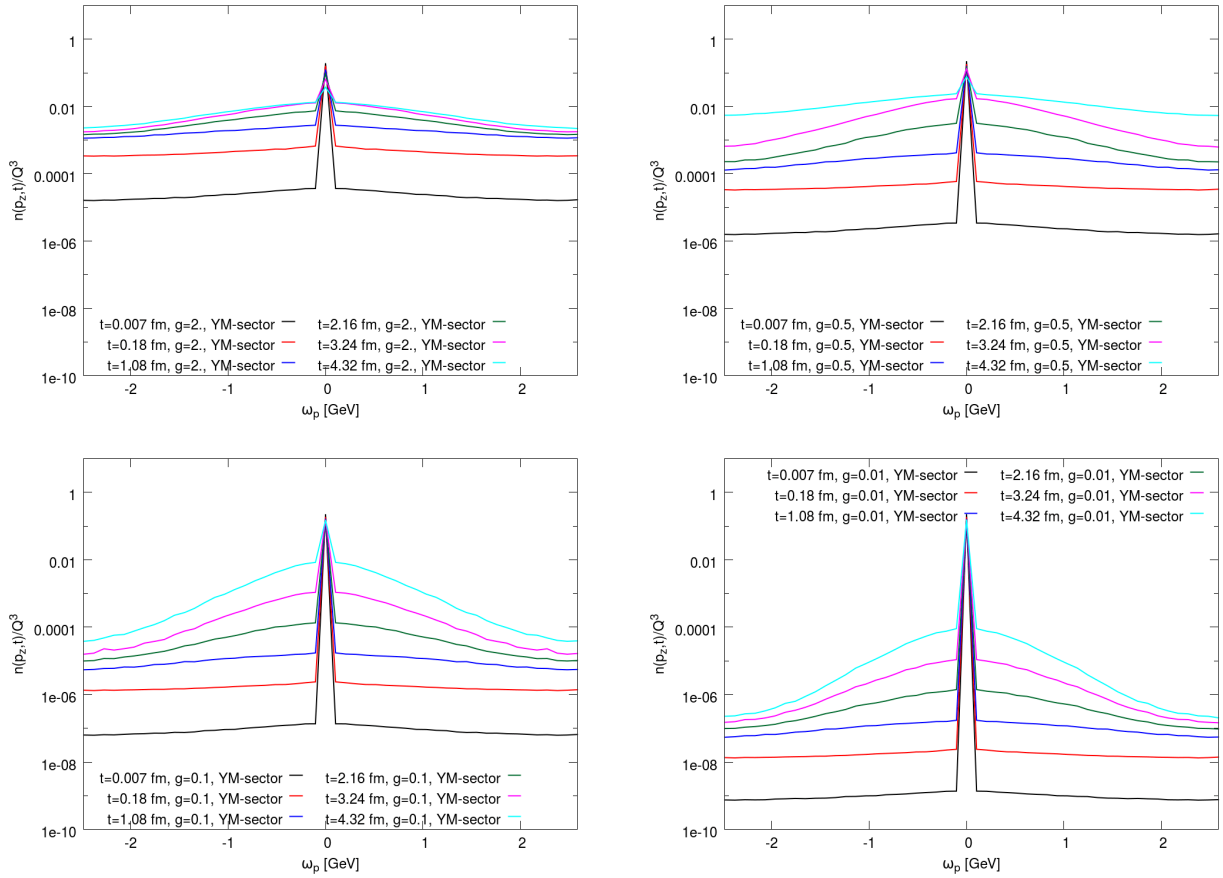

Figure 8.29: Lattice averaged occupation of energy modes in the transverse plane in the Yang-Mills sector, as a function of longitudinal momentum, for simulations including fermions of mass $m = 8.33$ MeV and different couplings $g \in \{2, 0.5, 0.1, 0.01\}$ (top left to bottom right). The simulations have been performed at a fixed saturation scale of $Q_s = 1.867$ GeV, on a $50 \times 50 \times 50$ lattice, with spacing $a = 0.24$ fm and a stochastic fermion ensemble of size $N_{ens} = 750$.

The reduced interaction between fermions and gauge fields for small couplings also manifests itself in the dominance of low energy modes in the Yang-Mills sector. In (figure 8.30) we plot the percentage of occupied low energy modes, compared to the total amount of available modes in the system. The low energy modes are again classified up to a cutoff (eq. 8.6). As expected, we find that low energy modes dominate the Yang-Mills sector more, the smaller the coupling. Additionally, for small values of g, the percentage even increases at initial time. The reason for that is rooted in the initial conditions: At initial time, only modes with $p_z = 0$ are occupied. As a consequence, there are still low energy modes with $p_z \neq 0$ available at the first time-steps of a simulation. For a vivid interaction between the fermion and Yang-Mills sector, as it is the case when choosing $g = 2$, not only these low energy modes are occupied, but high energy modes are rapidly occupied as well. This situation changes, if g is reduced. For small couplings a significantly smaller amount of energy is transfered to the fermion sector. As a consequence, a smaller fraction of this energy is transfered back to the Yang-Mills sector, due to the back-coupling of fermions onto the Yang-Mills sector. Naturally, an occupation of the

low energy modes is preferred, causing the percentage in (figure 8.30) to move up.

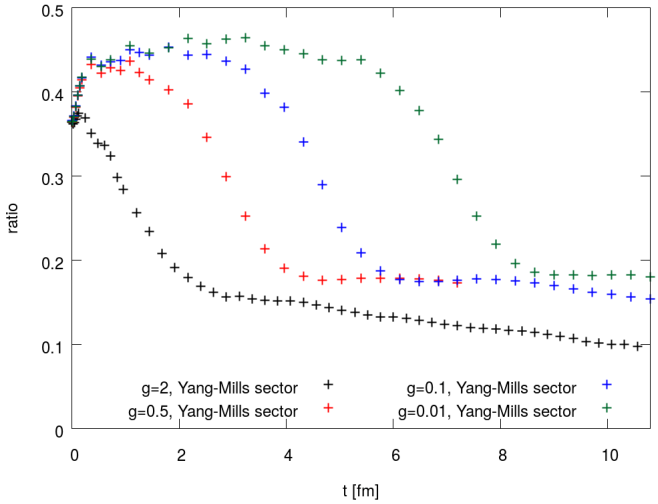

Figure 8.30: Ratio of occupied low energy modes compared to the total occupation of energy modes for simulations with fermions of mass $m = 8.33$ MeV and different choices of coupling $g \in \{0.01, 0.1, 0.5, 2\}$. Low energy modes are classified up to a cutoff of $\omega_{\mathbf{p}}^{bound} = \alpha_s Q_s \approx 0.6$ GeV. The simulations have been performed at a fixed saturation scale of $Q_s = 1.867$ GeV, on a $50 \times 50 \times 50$ lattice, with spacing $a = 0.24$ fm and a stochastic fermion ensemble of size $N_{ens} = 750$.

8.4 Two Degenerate Quark Flavors

Finally, let us investigate a simulation with two degenerate quark flavors present. We want to study, if a doubling of the degrees of freedom in the fermion sector influences the dynamics of the system. With the masses of the up- and down-quark being close together and having seen, that we are close to the ultra-relativistic limit in the highly energetic Glasma in (section 8.1.1), it is justified to consider the up- and down-quark to be approximately degenerate. We have performed a matching procedure for the energy density in the $N_f = 2$ flavor case in (section 7.5), to extract the appropriate lattice spacing of $a = 0.27$ fm and we keep the box size constant, choosing a lattice of $44 \times 44 \times 44$ points. The fermion mass is chosen to be $m = 0.01/a \approx 7.34$ MeV, hence we are at the order of the up- and down-quark mass. To check for the ultra-relativistic limit again, we compare the results to a mass of $m \approx 0.734$ MeV.

In (figure 8.31) we give the longitudinal to transverse pressure ratio comparing a simulation with one fermion of mass $m = 8.34$ MeV, a simulation with two degenerate fermions of mass $m = 7.34$ MeV and of mass $m = 0.734$ MeV. We find, that the results for the two simulations with degenerate fermions present coincide, hence we are close to the ultra-relativistic limit. On top of that, for two degenerate flavors, the initial pressure anisotropy is diminished even faster at early times. This is intuitive, because we have doubled the degrees of freedom in the fermion sector, enhancing the energy exchange between the fermion and Yang-Mills sector, that plays an important role for the genesis of an isotropization process. Within the hydrodynamization time of $t_{hydro} = 1$ fm, the longitudinal to transverse pressure ratio even surpasses $P_L/P_T \approx 0.6$ and a ratio of $P_L/P_T = 0.7$ is already reached around $t \approx 3$ fm, which is a significant speed up when compared to the one flavor case in (section 8.1.2).

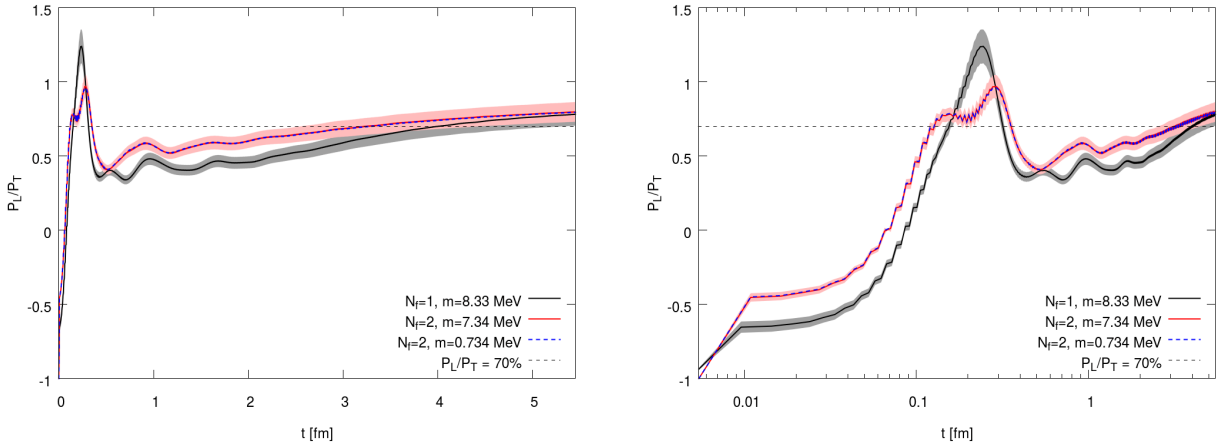

Figure 8.31: Longitudinal to transverse pressure ratio for a simulation with one fermion of mass $m = 8.33$ MeV, a simulation with two degenerate fermions of mass $m = 7.34$ MeV and a simulation with two degenerate fermions of mass $m = 0.734$ MeV. The simulation parameters as box size, saturation scale, energy density, coupling $g = 2$ and ensemble size $N_{ens} = 750$ are kept constant in all simulations. The $N_f = 1$ simulation has been performed on a $50 \times 50 \times 50$ lattice, with spacing $a = 0.24$ fm and the $N_f = 2$ simulations on a $44 \times 44 \times 44$ lattice, with spacing $a = 0.27$ fm.

For late times, the ratios of the one and two flavor case move towards each other. This goes hand in hand with the fermion sector acquiring more and more energy in both simulations, as depicted on the left of (figure 8.32).[3] As argued previously, as soon as the energy transfer between sectors reaches a balance, isotropization slows down and the two curves in (figure 8.31) move towards each other. This observation is supported by the pressure to energy ratio, given on the right-hand side of (figure 8.32). As expected, the two flavor system tends towards $P_i/\epsilon = 1/3$ faster, when compared to the one flavor system.

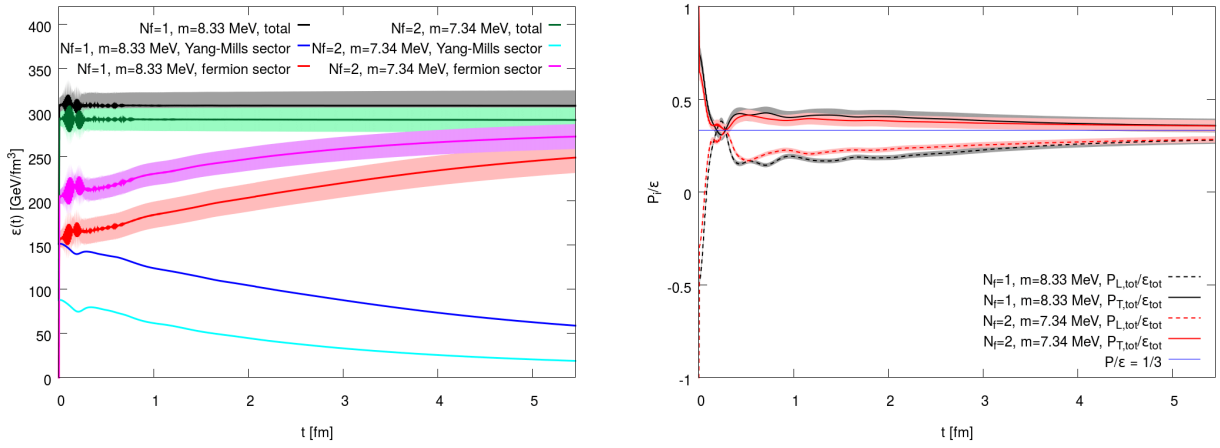

Figure 8.32: Energy density (left) and pressure to energy ration (right), in a simulation with one fermion of mass $m = 8.33$ MeV and with two degenerate fermions of mass $m = 7.34$ MeV. The simulation parameters as box size, saturation scale, energy density, coupling $g = 2$ and ensemble size $N_{ens} = 750$ are kept constant in all simulations. The $N_f = 1$ simulation has been performed on a $50 \times 50 \times 50$ lattice, with spacing $a = 0.24$ fm and the $N_f = 2$ simulation on a $44 \times 44 \times 44$ lattice, with spacing $a = 0.27$ fm.

[3] The small difference in the total lattice averaged energy density for the one and two flavor system is rooted in the restriction to even integer numbers for the lattice extent, when performing the matching procedure.

Part II

Simulating in an Expanding Box

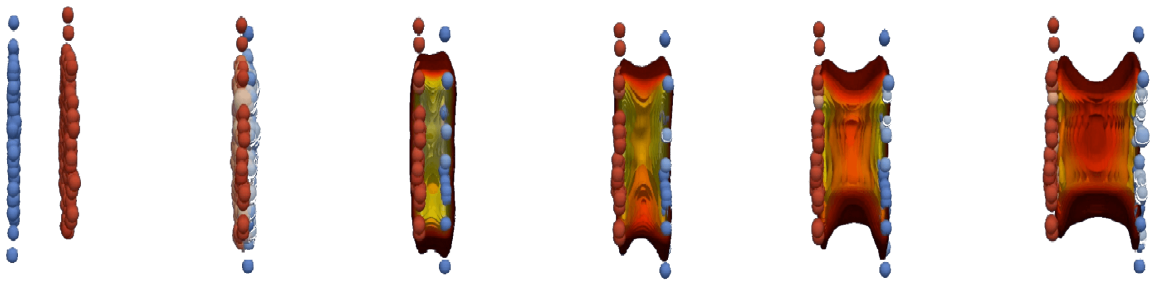

Visualization of the early phase in a heavy ion collision [161].

9 The Expanding System

In the following chapter, we want to extend the previously discussed semi-classical model from a static to a longitudinally expanding box. In fact, a longitudinally expanding system matches much better the physical reality of a heavy ion collision: The QGP-plasma, expands in all spacial directions, but with the ions being accelerated along the beam direction one can expect the longitudinal expansion to dominate, especially at initial times. For this reason we neglect a transverse expansion in our ansatz.

As stated previously, we consider the beam along the z-direction, therefore we require a coordinate system that is able to describe a longitudinally expansion in z-direction. Such a system has first been discussed by Bjorken [12], describing the QGP in terms of relativistic hydrodynamics. The Bjorken flow model uses a comoving coordinate system referred to as Milne or Bjorken coordinates, where the longitudinal expansion is inherent in the definition of the coordinate system. In this chapter we will introduce this coordinate system and present how to formulate QCD in Milne coordinates.

9.1 Milne Coordinates

Milne coordinates are related to Cartesian coordinates in the following way

$$\begin{aligned} \tau &= \sqrt{t^2 - z^2}, & t &= \tau \cosh \eta \\ \eta &= \operatorname{atan}\left(\frac{z}{t}\right) = \frac{1}{2} \ln\left(\frac{t+z}{t-z}\right), & z &= \tau \sinh \eta \\ \mathbf{x}_\perp &= (x, y). \end{aligned} \tag{9.1}$$

The quantity τ replaces the Minkowski time t and can be interpreted as a proper time of the system. The z-direction is replaced by the space-time rapidity η, which is a dimensionless quantity.

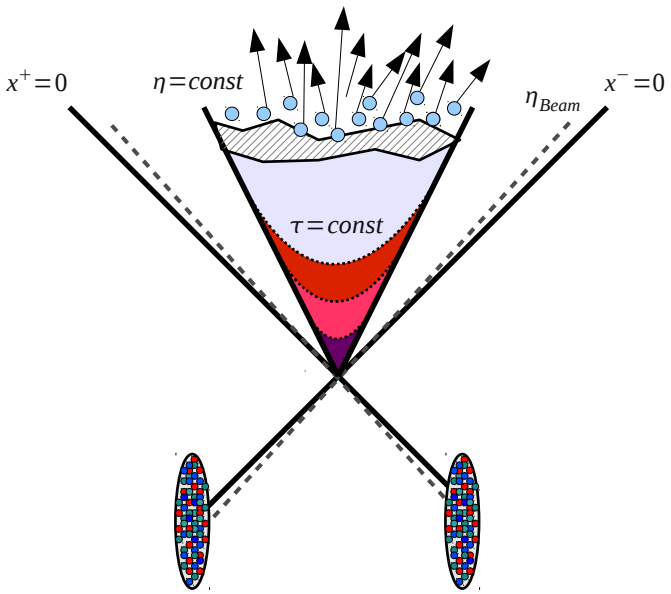

Figure 9.1: Minkowski diagram for two colliding nuclei, residing on the lightcone. Figure taken from [58]

In (figure 9.1), the proper time τ and the space-time rapidity η are depicted in a Minkowski diagram for a heavy ion collision. The two incoming nuclei reside on the lightcone and the plasma is formated after the collision. Its expansion in longitudinal direction for increasing proper time τ can be observed in the Minkowski diagram, by considering a fixed space-time rapidity η. We will later discuss how to fix η in our lattice simulation, restricting ourself to the area of central rapidity. In an experiment typically two units of space-time rapidity can be covered [62].

In general, the four-vector of Milne coordinates can be written as

$$x^\mu = (\tau, x, y, \eta). \tag{9.2}$$

In contrast to the Minkowski metric, the new coordinate system has a non-trivial metric $g_{\mu\nu}$, derived from

$$g_{\mu\nu} = \frac{\partial x^\alpha}{\partial x'^\mu} \eta_{\alpha\beta} \frac{\partial x^\beta}{\partial x'^\nu}. \tag{9.3}$$

Using (eq. 9.1) one derives

$$g_{\mu\nu} = \mathrm{diag}\left(1, -1, -1, -\tau^2\right), \qquad g^{\mu\nu} = \mathrm{diag}\left(1, -1, -1, -\frac{1}{\tau^2}\right), \qquad g_{\mu\nu} g^{\nu\alpha} = \delta_\mu{}^\alpha. \tag{9.4}$$

When integrating position and proper time one has to include a Jacobi determinant in the integration measure, which can be calculated from the metric of Milne coordinates (eq. 9.4)

$$\det g_{\mu\nu} = g = -\tau^2, \qquad dV = \sqrt{-g} d\tau d^2x_\perp d\eta. \tag{9.5}$$

When changing the coordinate system one has to transform the derivative operator accordingly

$$\frac{\partial}{\partial x^\beta} = \frac{\partial x'^\alpha}{\partial x^\beta} \frac{\partial}{\partial x'^\alpha} = \Lambda_\beta{}^\alpha \frac{\partial}{\partial x'^\alpha}. \tag{9.6}$$

$$\partial_\alpha = \Lambda_\alpha^{\ \beta}\partial'_\beta, \qquad \rightarrow \qquad \begin{pmatrix}\partial_t\\ \partial_x\\ \partial_y\\ \partial_z\end{pmatrix} = \begin{pmatrix}\cosh\eta & 0 & 0 & -\frac{1}{\tau}\sinh\eta\\ 0 & 1 & 0 & 0\\ 0 & 0 & 1 & 0\\ -\sinh\eta & 0 & 0 & \frac{1}{\tau}\cosh\eta\end{pmatrix}\begin{pmatrix}\partial_\tau\\ \partial_x\\ \partial_y\\ \partial_\eta\end{pmatrix}. \tag{9.7}$$

The Cartesian time and z-direction derivative operators are therefore replaced by

$$\begin{aligned}\partial_t &= \cosh\eta\ \partial_\tau - \frac{1}{\tau}\sinh\eta\ \partial_\eta,\\ \partial_z &= -\sinh\eta\ \partial_\tau + \frac{1}{\tau}\cosh\eta\ \partial_\eta,\end{aligned} \tag{9.8}$$

in Milne coordinates. These transformations of the derivative operators in Milne coordinates have important consequences for the Dirac equation, that we will discuss in the next section.

9.1.1 The Dirac Equation in Milne Coordinates

When introducing Milne coordinates, the time and z-direction derivative operators in the free Dirac equation (eq. 1.28) are replaced by (eq. 9.8)

$$\gamma^0\partial_0 + \gamma^3\partial_3 = \gamma^0\bigg(\cosh\eta\ \partial_\tau - \frac{1}{\tau}\sinh\eta\ \partial_\eta\bigg) + \gamma^3\bigg(-\sinh\eta\ \partial_\tau + \frac{1}{\tau}\cosh\eta\ \partial_\eta\bigg). \tag{9.9}$$

In (Appendix C.1) we show, that this can be rewritten as

$$\gamma^0\partial_0 + \gamma^3\partial_3 = \gamma^0 e^{-\eta\gamma^0\gamma^3}\partial_\tau + \frac{1}{\tau}\gamma^3 e^{-\eta\gamma^0\gamma^3}\partial_\eta, \tag{9.10}$$

allowing us to write the Dirac equation in Milne coordinates in the following way

$$\bigg[\mathrm{i}\gamma^0 e^{-\eta\gamma^0\gamma^3}\partial_\tau + \frac{\mathrm{i}}{\tau}\gamma^3 e^{-\eta\gamma^0\gamma^3}\partial_\eta + \mathrm{i}\gamma^i\partial_i - m\bigg]\psi(x) = 0. \tag{9.11}$$

It is possible to simplify (eq. 9.11) further by multiplying it with $e^{-\frac{\eta}{2}\gamma^0\gamma^3}$ from the left and commute this factor with the gamma matrices, using $\{\gamma^0,\gamma^i\} = \{\gamma^0,\gamma^3\} = \{\gamma^3,\gamma^i\} = 0$

$$\begin{aligned}0 &= e^{-\frac{\eta}{2}\gamma^0\gamma^3}\bigg[\mathrm{i}\gamma^0 e^{-\eta\gamma^0\gamma^3}\partial_\tau + \frac{\mathrm{i}}{\tau}\gamma^3 e^{-\eta\gamma^0\gamma^3}\partial_\eta + \mathrm{i}\gamma^i\partial_i - m\bigg]\psi(x)\\ &= \bigg[\mathrm{i}\gamma^0 e^{-\frac{\eta}{2}\gamma^0\gamma^3}\partial_\tau + \frac{\mathrm{i}}{\tau}\gamma^3 e^{-\frac{\eta}{2}\gamma^0\gamma^3}\partial_\eta + \mathrm{i}\gamma^i e^{-\frac{\eta}{2}\gamma^0\gamma^3}\partial_i - m e^{-\frac{\eta}{2}\gamma^0\gamma^3}\bigg]\psi(x).\end{aligned} \tag{9.12}$$

Letting the η-derivative operator act on the matrix exponential one can simplify this result

$$\begin{aligned}\frac{\mathrm{i}}{\tau}\gamma^3\partial_\eta\Big(e^{-\frac{\eta}{2}\gamma^0\gamma^3}\psi(x)\Big) &= \frac{\mathrm{i}}{\tau}\gamma^3\gamma^3\gamma^0\frac{1}{2}e^{-\frac{\eta}{2}\gamma^0\gamma^3}\psi(x) + \frac{\mathrm{i}}{\tau}\gamma^3 e^{-\frac{\eta}{2}\gamma^0\gamma^3}\partial_\eta\psi(x)\\ &= -\frac{\mathrm{i}}{2\tau}\gamma^0 e^{-\frac{\eta}{2}\gamma^0\gamma^3}\psi(x) + \frac{\mathrm{i}}{\tau}\gamma^3 e^{-\frac{\eta}{2}\gamma^0\gamma^3}\partial_\eta\psi(x).\end{aligned} \tag{9.13}$$

Substitution leads to

$$\bigg[\mathrm{i}\gamma^0\partial_\tau + \frac{\mathrm{i}}{\tau}\gamma^3\partial_\eta + \frac{\mathrm{i}}{2\tau}\gamma^0 + \mathrm{i}\gamma^i\partial_i - m\bigg]e^{-\frac{\eta}{2}\gamma^0\gamma^3}\psi(x) = 0. \tag{9.14}$$

Finally we make use of

$$\mathrm{i}\gamma^0\partial_\tau\Big(\sqrt{\tau}\psi(x)\Big) = \mathrm{i}\gamma^0\frac{1}{2\sqrt{\tau}}\psi(x) + \mathrm{i}\gamma^0\sqrt{\tau}\psi(x), \tag{9.15}$$

hence multiplying the Dirac equation with $\sqrt{\tau}$ leads to

$$\left[\mathrm{i}\gamma^0\partial_\tau + \frac{\mathrm{i}}{\tau}\gamma^3\partial_\eta + \mathrm{i}\gamma^i\partial_i - m\right]\underbrace{\sqrt{\tau}e^{-\frac{\eta}{2}\gamma^0\gamma^3}\psi(x)}_{:=\hat{\psi}(\tau,\mathbf{x}_\perp,\eta)} = 0. \tag{9.16}$$

In the last step we redefined the spinor, following the strategy first proposed in [74]. The given redefinition will turn out to be very useful when solving the Dirac equation in an expanding geometry. In the following, the redefined spinor will be referred to as expanding box spinor. The associated scalar product of fermions in Milne coordinates is given as [74]

$$\int \psi^\dagger(\tau,\mathbf{x}_\perp,\eta)\tau e^{-\eta\gamma^0\gamma^3}\psi(\tau,\mathbf{x}_\perp,\eta)dx_\perp d\eta = \int \hat{\psi}^\dagger(\tau,\mathbf{x}_\perp\eta)\hat{\psi}(\tau,\mathbf{x}_\perp,\eta)dx_\perp d\eta. \tag{9.17}$$

Another important consequence of the redefinition of the spinor in the expanding geometry is that the dimension is reduced by a factor of $\sqrt{[length]}$, due to the additional factor of $\sqrt{\tau}$ entering the spinor definition

$$\Big[\hat{\psi}(\tau,\mathbf{x}_\perp,\eta)\Big] \sim \frac{1}{[length]}. \tag{9.18}$$

In the next section we will discuss, how this translates to the fermion Lagrangian and especially how the corresponding action can be written.

An interaction of fermion fields with the gauge fields is introduced to (eq. 9.16), by replacing the derivative operator by their covariant counterpart

$$\partial_i \quad\to\quad D_i, \qquad\qquad \partial_\eta \quad\to\quad D_\eta. \tag{9.19}$$

This leads to the full interacting Dirac equation in an expanding geometry

$$\left[\mathrm{i}\gamma^0\partial_\tau + \frac{\mathrm{i}}{\tau}\gamma^3 D_\eta + \mathrm{i}\gamma^i D_i - m\right]\hat{\psi}(\tau,\mathbf{x}_\perp,\eta) = 0. \tag{9.20}$$

We have chosen $A_\tau = 0$ in (eq. 9.20), also known as Fock-Schwinger gauge, eliminating one of two gauge degrees of freedom.

9.2 The Lagrangian in an Expanding Box

Having discussed the Dirac equation in an expanding box, let us now turn to the definition of the Lagrange density and action of QCD in an expanding geometry, making use of Milne coordinates. For the action of the Yang-Mills sector of QCD, introducing Milne coordinates and including the correct integration measure (eq. 9.5), leads to

$$S_{YM}[A] = \int -\frac{1}{2}\mathrm{tr}\Big[F^{\mu\nu}F_{\mu\nu}\Big]\tau d\tau d^2x_\perp d\eta. \tag{9.21}$$

Explicitly writing the contraction of the field-strength tensor in Milne coordinates, we find

$$\begin{aligned} F_{\mu\nu}F^{\mu\nu} = F_{\mu\nu}g^{\mu\alpha}g^{\nu\beta}F_{\alpha\beta} =& 2\Big[F_{\tau 1}g^{\tau\tau}g^{11}F_{\tau 1} + F_{\tau 2}g^{\tau\tau}g^{22}F_{\tau 2} + F_{\tau\eta}g^{\tau\tau}g^{\eta\eta}F_{\tau\eta} \\ &+ F_{12}g^{11}g^{22}F_{12} + F_{1\eta}g^{11}g^{\eta\eta}F_{1\eta} + F_{2\eta}g^{22}g^{\eta\eta}F_{2\eta}\Big] \\ =& -2\left[F_{\tau 1}^2 + F_{\tau 2}^2 + \frac{1}{\tau^2}F_{\tau\eta}^2 - F_{12}^2 - \frac{1}{\tau^2}F_{1\eta}^2 - \frac{1}{\tau^2}F_{2\eta}^2\right] \\ =& -2\left[F_{\tau i}^2 + \frac{1}{\tau^2}F_{\tau\eta}^2 - F_{12}^2 - \frac{1}{\tau^2}F_{i\eta}^2\right], \end{aligned} \tag{9.22}$$

where we used the metric (eq. 9.4). The Yang-Mills action can now be written as

$$S_{YM}[A] = \int \mathrm{tr}\left[\tau F_{\tau i}^2 + \frac{1}{\tau}F_{\tau\eta}^2 - \tau F_{12}^2 - \frac{1}{\tau}F_{i\eta}^2\right] d\tau d^2x_\perp d\eta. \tag{9.23}$$

For the derivation of the corresponding equations of motion of the classical theory, one would have to make use of the variational principle to minimize the action

$$\delta S = 0. \tag{9.24}$$

A crucial difference to the static case is, that one has to take care of the additional factor of τ, entering the Yang-Mills action due to the Jacobian (eq. 9.5). The procedure has in detail been discussed in [162, 163] and it turned out to be convenient to redefine the Lagrangian of Yang-Mills theory in an expanding geometry,

$$\mathcal{L}_{YM}^{exp}[A] = \mathrm{tr}\left[\tau F_{\tau i}^2 + \frac{1}{\tau}F_{\tau\eta}^2 - \tau F_{12}^2 - \frac{1}{\tau}F_{i\eta}^2\right] = -\frac{\tau}{2}\mathrm{tr}\Big[F^{\mu\nu}F_{\mu\nu}\Big], \tag{9.25}$$

where we included the additional factor τ in the definition of the Lagrangian [61]. On the one hand, this changes the dimensionality of the Lagrangian by a factor of *length*, but on the other hand it significantly simplifies the derivation of the equations of motion, allowing us to simply apply the Euler-Lagrange equation.

To derive the corresponding Hamiltonian of the theory, let us perform a Legendre transformation of (eq. 9.25). To do so, we have to derive the conjugate fields at first, that can again be interpreted as chromo-electric fields E. In contrast to the static box, the chromo-electric fields now split into a transverse and a longitudinal field,

$$\begin{aligned} E_i^a(x) = \frac{\partial\mathcal{L}_{YM}^{exp}}{\partial\Big(\partial_\tau A_i^a(x)\Big)} =& \frac{\partial}{\partial\Big(\partial_\tau A_i^a(x)\Big)}\mathrm{tr}\left[\tau F_{\tau j}^2 + \frac{1}{\tau}F_{\tau\eta}^2 - \tau F_{12}^2 - \frac{1}{\tau}F_{j\eta}^2\right] = \tau\frac{\partial}{\partial\Big(\partial_\tau A_i^a(x)\Big)}\mathrm{tr}\Big[F_{\tau j}^2\Big] \\ =& \frac{\tau}{2}\frac{\partial}{\partial\Big(\partial_\tau A_i^a(x)\Big)}\Big(\partial_\tau A_j^b(x)\Big)^2 = \tau\partial_\tau A_i^a(x) = \tau F_{\tau i}^a(x), \end{aligned} \tag{9.26}$$

$$\begin{aligned} E_\eta^a(x) = \frac{\partial\mathcal{L}_{YM}^{exp}}{\partial\Big(\partial_\tau A_\eta^a(x)\Big)} =& \frac{\partial}{\partial\Big(\partial_\tau A_\eta^a(x)\Big)}\mathrm{tr}\left[\tau F_{\tau j}^2 + \frac{1}{\tau}F_{\tau\eta}^2 - \tau F_{12}^2 - \frac{1}{\tau}F_{j\eta}^2\right] = \frac{1}{\tau}\frac{\partial}{\partial\Big(\partial_\tau A_\eta^a(x)\Big)}\mathrm{tr}\Big[F_{\tau\eta}^2\Big] \\ =& \frac{1}{2\tau}\frac{\partial}{\partial\Big(\partial_\tau A_\eta^a(x)\Big)}\Big(\partial_\tau A_\eta^b(x)\Big)^2 = \frac{1}{\tau}\partial_\tau A_\eta^a(x) = \frac{1}{\tau}F_{\tau\eta}^a(x), \end{aligned} \tag{9.27}$$

Making use of these definitions, we can rewrite the Lagrangian of the Yang-Mills sector (eq. 9.25) in the following way

$$\mathcal{L}_{YM}^{exp} = \mathrm{tr}\left[\frac{1}{\tau}E_i^2 + \tau E_\eta^2 - \tau F_{12}^2 - \frac{1}{\tau}F_{i\eta}^2\right]. \tag{9.28}$$

The corresponding Hamiltonian of Yang-Mills theory in an expanding box is then given as

$$\mathcal{H}_{YM}^{exp} = \mathrm{tr}\left[\frac{1}{\tau}E_i^2 + \frac{1}{\tau}F_{\eta i}^2 + \tau E_\eta^2 + \tau F_{xy}^2\right]. \tag{9.29}$$

One easily checks, that this result does not have the dimension of an energy density, because of the redefinition of the Lagrangian in the expanding box. We will discuss how to connect it to the energy density of the Yang-Mills sector later.

For the fermion sector of QCD in an expanding box, the Lagrangian is deduced from the Dirac equation (eq. 9.20) as it has been the case in the static box

$$\mathcal{L}_f^{exp} = \hat{\bar{\psi}}\left[\mathrm{i}\gamma^0\partial_\tau + \frac{\mathrm{i}}{\tau}\gamma^3 D_\eta + \mathrm{i}\gamma^i D_i - m\right]\hat{\psi}. \tag{9.30}$$

As expected, it has the same reduced dimensionality as the Lagrangian of the Yang-Mills sector, due to the redefinition of the spinor. The action is thus given by using (eq. 9.17), leading to

$$S_f = \int \hat{\bar{\psi}}\left[\mathrm{i}\gamma^0\partial_\tau + \frac{\mathrm{i}}{\tau}\gamma^3 D_\eta + \mathrm{i}\gamma^i D_i - m\right]\hat{\psi} d\tau d^2x_\perp d\eta. \tag{9.31}$$

Of course, the dimensionality of the action is unchanged when compared to the static box, as it should be the case. Finally, it is straight forward to derive the Hamiltonian of the fermion sector from (eq. 9.30), making use of a Legendre transformation. Summing the result with the previously derived Hamiltonian of the Yang-Mills sector (eq. 9.29), we find the Hamiltonian of QCD in an expanding geometry

$$\mathcal{H}_{QCD}^{exp} = \mathrm{tr}\left[\frac{1}{\tau}E_i^2 + \frac{1}{\tau}F_{\eta i}^2 + \tau E_\eta^2 + \tau F_{xy}^2\right] - \frac{\mathrm{i}}{\tau}\hat{\bar{\psi}}\gamma^3 D_\eta\hat{\psi} - \mathrm{i}\hat{\bar{\psi}}\gamma^i D_i\hat{\psi} + m\hat{\bar{\psi}}\hat{\psi}. \tag{9.32}$$

This result has dimension $\sim \frac{1}{L^3}$, because we derived it from the expanding box Lagrangian of reduced dimensionality. It can therefore not be directly interpreted as the energy density of the system [61].

The action of QCD in the expanding box is simply given by summing the Yang-Mills and fermion sector

$$S_{QCD} = \int\left(\mathrm{tr}\left[\tau F_{\tau i}^2 + \frac{1}{\tau}F_{\tau\eta}^2 - \tau F_{12}^2 - \frac{1}{\tau}F_{i\eta}^2\right] + \hat{\bar{\psi}}\left[\mathrm{i}\gamma^0\partial_\tau + \frac{\mathrm{i}}{\tau}\gamma^3 D_\eta + \mathrm{i}\gamma^i D_i - m\right]\hat{\psi}\right) d\tau d^2x_\perp d\eta, \tag{9.33}$$

with corresponding Lagrangian

$$\mathcal{L}_{QCD}^{exp} = \mathrm{tr}\left[\tau F_{\tau i}^2 + \frac{1}{\tau}F_{\tau\eta}^2 - \tau F_{12}^2 - \frac{1}{\tau}F_{i\eta}^2\right] + \hat{\bar{\psi}}\left[\mathrm{i}\gamma^0\partial_\tau + \frac{\mathrm{i}}{\tau}\gamma^3 D_\eta + \mathrm{i}\gamma^i D_i - m\right]. \tag{9.34}$$

10

Initial Conditions for the Expanding System

In this chapter we will discuss the initial conditions of the semi-classical approximation of QCD in the expanding box. As it has been the case for the static system, the Yang-Mills sector is initialized, solving the Poisson equation of the CGC effective theory, creating the Glasma. The fermions enter the simulation as free vacuum fermions, making it necessary to solve the corresponding free Dirac equation (eq. 9.20) in the expanding geometry.

10.1 Initialization of the Gauge Fields

The construction of the ensemble of gauge links $\{U_i\}$ in the expanding box is completely equivalent to what has been discussed in (section 3.3.1). At first, the gauge links are initialized in the transverse plane, which is not affected by the expansion in the longitudinal direction. As a consequence, we can reuse all equations of (section 3.3.1). The gauge link ensemble is thus defined in a single transverse slice at $\eta = 0$. Afterwards we extend it in longitudinal direction, as discussed in (section 3.4), by copying it to the other space-time rapidity planes, creating the familiar color-flux tube structure of the Glasma. When doing so, we set all longitudinal gauge links to one

$$U_\eta = 1. \tag{10.1}$$

This construction requires us to specify the longitudinal extent of the three dimensional lattice. In contrast to the static box, where we assumed a cubic lattice, the longitudinal and transverse direction in an expanding geometry have to be treated independently. We have to specify the units of space-time rapidity that will be covered by the transverse lattice extent in our simulation, corresponding to the area indicated in (figure 9.1). We choose

$$L_\eta = 3. \tag{10.2}$$

units of space-time rapidity for the longitudinal lattice extent.[1] This area matches well the central rapidity regime, that is covered by the experiment [61].

[1] In most of the literature $L_\eta = 2.$ is chosen. We chose a slightly larger area, having obtained numerically more stable results in a simulation with fermions.

As in the static box, the chromo-electric fields are only defined in the longitudinal direction at initial time, hence we set the transverse direction to zero

$$E_\perp(x) = 0. \tag{10.3}$$

In the longitudinal direction they can be constructed from the gauge link ensemble of the CGC in similar fashion as in the static box, solving

$$\begin{aligned}\bar{E}^a_\eta(x) = -\frac{\mathrm{i}}{2}\sum_{i=1}^{2}\mathrm{tr}\Bigg[T^a\Bigg(\Big[U_i(x)-1\Big]\Big[U_i^{(2)\dagger}(x)-U_i^{(1)\dagger}(x)\Big] \\ + \Big[U_i^\dagger(x-\hat{i})-1\Big]\Big[U_i^{(2)}(x-\hat{i})-U_i^{(1)}(x-\hat{i})\Big]\Bigg)-\mathrm{h.c.}\Bigg].\end{aligned} \tag{10.4}$$

10.2 Vacuum Fermions in an Expanding Geometry

As stated in the introduction, the fermion fields are initialized as free vacuum fermions. In an expanding geometry, this turns out to be more involved as in the static case, due to the non-linearity of the Dirac equation in Milne coordinates (eq. 9.20). Before turning to the solution of the equation, let us in general discuss the concept of longitudinal boost invariance of fermion spinors. In a next step, we will first solve the spacial part of (eq. 9.20) and finally the non-linear proper time dependent part. We finish the discussion by normalizing the vacuum solution of the spinor and relate it to the static box solution. Finally we discretize our result, making it accessible in a lattice simulation.

10.2.1 Boost Invariance of a Fermion Spinor

In analogy to the static box, we take the ansatz for the Fourier decomposition of an expanding box spinor

$$\begin{aligned}\hat{\psi}(\tau,\mathbf{x}_\perp,\eta) = \int\sum_{s=1}^{2}\sum_{a=1}^{N_c}\Big(&\hat{a}_{s,a}(\mathbf{k}_\perp,y_k)\hat{\psi}^{+}_{\mathbf{k}_\perp,y_k,s,a}(\tau,\mathbf{x}_\perp,\eta) \\ &+\hat{b}^\dagger_{s,a}(\mathbf{k}_\perp,y_k)\hat{\psi}^{-}_{\mathbf{k}_\perp,y_k,s,a}(\tau,\mathbf{x}_\perp,\eta)\Big)\frac{d^2k_\perp}{(2\pi)^2}dy_k,\end{aligned} \tag{10.5}$$

where we introduced $\psi^{0\pm}_{s,\mathbf{p}}(x)$ as mode functions and identified the momentum rapidity $y_p = \frac{p_z}{E_\mathbf{p}}$. The mode functions are constructed such, that they solve the expanding box Dirac equation

$$\Big[\mathrm{i}\gamma^0\partial_\tau + \mathrm{i}\gamma^i\partial_i + \frac{\mathrm{i}}{\tau}\gamma^3\partial_\eta - m\Big]\hat{\psi}^{\pm}_{\mathbf{k}_\perp,y_k,s,a}(\tau,\mathbf{x}_\perp,\eta) = 0. \tag{10.6}$$

As it is the case for the initial conditions of the Yang-Mills sector, the spinors that enter our system require to be longitudinal boost invariant as well. To study how longitudinal boost invariance manifests itself for a fermion spinor, let us first discuss how a static box vacuum spinor transforms under a boost in longitudinal direction. The mode functions of a free Dirac spinor in a static box are given as (compare to eq. 6.87)

$$\psi^{0+}_{s,\mathbf{p}}(x) = u_s(\mathbf{p})e^{-\mathrm{i}px} = u_s(\mathbf{p})e^{-\mathrm{i}E_\mathbf{p}t}e^{\mathrm{i}\mathbf{p}\mathbf{x}} = u_s(\mathbf{p})e^{-\mathrm{i}E_\mathbf{p}t}e^{\mathrm{i}\mathbf{p}_\perp\mathbf{x}_\perp}e^{\mathrm{i}p_z z}, \tag{10.7}$$

$$\psi^{0-}_{s,\mathbf{p}}(x) = v_s(\mathbf{p})e^{\mathrm{i}px} = v_s(\mathbf{p})e^{\mathrm{i}E_\mathbf{p}t}e^{-\mathrm{i}\mathbf{p}\mathbf{x}} = v_s(\mathbf{p})e^{\mathrm{i}E_\mathbf{p}t}e^{-\mathrm{i}\mathbf{p}_\perp\mathbf{x}_\perp}e^{-\mathrm{i}p_z z}. \tag{10.8}$$

We now perform a Lorentz boost in longitudinal direction, setting $y_p = 0$ at initial time in the comoving frame. For the time component t a longitudinal boost leads to

$$\begin{aligned} t \quad \rightarrow \quad t' =& t\cosh(y_p) - z\sinh(y_p) = \frac{1}{2}\Big[t\Big(e^{y_p} + e^{-y_p}\Big) - z\Big(e^{y_p} - e^{-y_p}\Big)\Big] \\ =& \frac{1}{2}\sqrt{(t-z)(t+z)}\left[e^{y_p}\sqrt{\frac{t-z}{t+z}} + e^{-y_p}\sqrt{\frac{t+z}{t-z}}\right] \\ =& \frac{1}{2}\underbrace{\sqrt{t^2-z^2}}_{=\tau}\left[e^{y_p}\exp\Bigg(\underbrace{\ln\left(\sqrt{\frac{t-z}{t+z}}\right)}_{=-\frac{1}{2}\ln\left(\frac{t+z}{t-z}\right)=-\eta}\Bigg) + e^{-y_p}\exp\Bigg(\underbrace{\ln\left(\sqrt{\frac{t+z}{t-z}}\right)}_{=\frac{1}{2}\ln\left(\frac{t+z}{t-z}\right)=\eta}\Bigg)\right] \\ =& \frac{1}{2}\tau\Big[e^{y_p-\eta} + e^{-y_p+\eta}\Big] = \tau\cosh(y_p-\eta), \end{aligned} \tag{10.9}$$

where we identified the proper time τ and the space-time rapidity η. We define

$$E_{\mathbf{p}}(y_p = 0) = \sqrt{\mathbf{p}_\perp^2 + m^2} := M_{\mathbf{p}}, \tag{10.10}$$

leading to the following transformation of the time dependent part of the Fourier kernel, when performing a boost in z-direction

$$e^{-\mathrm{i}E_{\mathbf{p}}t} \quad \overset{\text{z-boost}}{\rightarrow} \quad e^{-M_{\mathbf{p}}\tau\cosh(y_p-\eta)}, \qquad e^{\mathrm{i}E_{\mathbf{p}}t} \quad \overset{\text{z-boost}}{\rightarrow} \quad e^{M_{\mathbf{p}}\tau\cosh(y_p-\eta)}. \tag{10.11}$$

For the basis spinors, we have to Lorentz boost the spinors in the longitudinal direction [149]

$$S(\Lambda) = \exp\Big(\mathrm{i}\Theta_{03}S^{03}\Big) = \exp\left(\frac{1}{2}y_p\gamma^0\gamma^3\right), \qquad S^{\mu\nu} = \frac{\mathrm{i}}{4}\Big[\gamma^\mu, \gamma^\nu\Big]. \tag{10.12}$$

The basis spinor then transforms according to

$$u_s(\mathbf{p}) \quad \overset{\text{z-boost}}{\rightarrow} \quad S(\Lambda)u_s(\mathbf{p}_\perp, y_p = 0) = e^{\frac{1}{2}y_p\gamma^0\gamma^3}u_s(\mathbf{p}_\perp, y_p = 0), \tag{10.13}$$

$$v_s(\mathbf{p}) \quad \overset{\text{z-boost}}{\rightarrow} \quad S(\Lambda)v_s(\mathbf{p}_\perp, y_p = 0) = e^{\frac{1}{2}y_p\gamma^0\gamma^3}v_s(\mathbf{p}_\perp, y_p = 0). \tag{10.14}$$

Combining both results (eq. 10.11) and (eq. 10.13), we find the following rapidity dependence of the static box mode functions

$$\psi^{0+}_{s,\mathbf{p}}(x) \quad \overset{\text{z-boost}}{\rightarrow} \quad \psi^{0+}_{s,\mathbf{p}_\perp,y_p}(\tau,\mathbf{x}_\perp,\eta) = e^{\frac{1}{2}y_p\gamma^0\gamma^3}u_s(\mathbf{p}_\perp, y_p = 0)e^{-\mathrm{i}M_{\mathbf{p}_\perp}\tau\cosh(y_p-\eta)}e^{\mathrm{i}\mathbf{p}_\perp\mathbf{x}_\perp}, \tag{10.15}$$

$$\psi^{0-}_{s,\mathbf{p}}(x) \quad \overset{\text{z-boost}}{\rightarrow} \quad \psi^{0-}_{s,\mathbf{p}_\perp,y_p}(\tau,\mathbf{x}_\perp,\eta) = e^{\frac{1}{2}y_p\gamma^0\gamma^3}v_s(\mathbf{p}_\perp, y_p = 0)e^{\mathrm{i}M_{\mathbf{p}_\perp}\tau\cosh(y_p-\eta)}e^{-\mathrm{i}\mathbf{p}_\perp\mathbf{x}_\perp}. \tag{10.16}$$

When defining the expanding box spinor in (eq. 9.16), the given boosted spinors are modified by multiplying them with

$$\hat{\psi}^{0+}_{s,\mathbf{p}_\perp,y_p}(\tau,\mathbf{x}_\perp,\eta) = \sqrt{\tau}e^{\frac{1}{2}(y_p-\eta)\gamma^0\gamma^3}u_s(\mathbf{p}_\perp, y_p = 0)e^{-\mathrm{i}M_{\mathbf{p}_\perp}\tau\cosh(y_p-\eta)}e^{\mathrm{i}\mathbf{p}_\perp\mathbf{x}_\perp}, \tag{10.17}$$

$$\hat{\psi}^{0-}_{s,\mathbf{p}_\perp,y_p}(\tau,\mathbf{x}_\perp,\eta) = \sqrt{\tau}e^{\frac{1}{2}(y_p-\eta)\gamma^0\gamma^3}v_s(\mathbf{p}_\perp, y_p = 0)e^{\mathrm{i}M_{\mathbf{p}_\perp}\tau\cosh(y_p-\eta)}e^{-\mathrm{i}\mathbf{p}_\perp\mathbf{x}_\perp}. \tag{10.18}$$

We find that for the definition of the spinor in an expanding system, the rapidity dependence only enters as a difference of momentum and spacetime rapidity $y_p - \eta$, making the spinor longitudinal boost invariant, as discussed in [74].

This simple rapidity dependence of the expanding box spinor can be used to simplify (eq. 10.5). To do so, let us consider an arbitrary function $f = f(y_p - \eta)$ that only depends on the difference of rapidities: A Fourier transformation with respect to y_p then leads to

$$\tilde{f}(\nu,\eta) = \int f(y_p-\eta)e^{\mathrm{i}\nu y_p}dy_p, \qquad f(y_p,\eta) = \int \tilde{f}(\nu,\eta)e^{-\mathrm{i}\nu y_p}\frac{d\nu}{2\pi}. \tag{10.19}$$

Because we know, that the function in position space depends only on the difference of rapidities $f(y_p,\eta) = f(y_p-\eta)$, the Fourier transform picks up a trivial η dependence, with

$$\tilde{f}(\nu,\eta) = e^{\mathrm{i}\nu\eta}\tilde{f}(\nu), \tag{10.20}$$

because

$$f(y_p,\eta) = \int \tilde{f}(\nu,\eta)e^{-\mathrm{i}\nu y_p}\frac{d\nu}{2\pi} = \int \tilde{f}(\nu)e^{-\mathrm{i}\nu(y_p-\eta)}\frac{d\nu}{2\pi} = f(y_p-\eta). \tag{10.21}$$

Making use of (eq. 10.21) we can rewrite the expanding box spinor in the following way

$$\hat{\psi}^{\pm}_{\mathbf{k}_\perp,y_k,s,a}(\tau,\mathbf{x}_\perp,\eta) \quad \rightarrow \quad \hat{\psi}^{\pm}_{\mathbf{k}_\perp,\nu,s,a}(\tau,\mathbf{x}_\perp,\eta) = \int \hat{\psi}^{\pm}_{\mathbf{k}_\perp,y_k,s,a}(\tau,\mathbf{x}_\perp,\eta)e^{\mathrm{i}\nu y_k}dy_k. \tag{10.22}$$

We can now trade our y_k with a ν dependence in (eq. 10.5), performing a Fourier transformation with respect to ν and arrive at

$$\hat{\psi}(\tau,\mathbf{x}_\perp,\eta) = \int \sum_{s=1}^{2}\sum_{a=1}^{N_c}\left(\hat{a}_{s,a}(\mathbf{k}_\perp,\nu)\hat{\psi}^{+}_{\mathbf{k}_\perp,\nu,s,a}(\tau,\mathbf{x}_\perp,\eta) + \hat{b}^{\dagger}_{s,a}(\mathbf{k}_\perp,\nu)\hat{\psi}^{-}_{\mathbf{k}_\perp,\nu,s,a}(\tau,\mathbf{x}_\perp,\eta)\right)\frac{d^2k_\perp}{(2\pi)^2}\frac{d\nu}{2\pi}, \tag{10.23}$$

where the rapidity dependence of the mode functions is simply given as

$$\hat{\psi}^{\pm}_{\mathbf{k}_\perp,\nu,s,a}(\tau,\mathbf{x}_\perp,\eta) = e^{\mathrm{i}\nu\eta}\hat{\psi}^{\pm}_{\mathbf{k}_\perp,\nu,s,a}(\tau,\mathbf{x}_\perp). \tag{10.24}$$

The corresponding Dirac equation of the mode functions then reduces to

$$\left[\mathrm{i}\gamma^0\partial_\tau + \mathrm{i}\gamma^i\partial_i - \frac{1}{\tau}\nu\gamma^3 - m\right]\hat{\psi}^{\pm}_{\mathbf{k}_\perp,\nu,s,a}(\tau,\mathbf{x}_\perp) = 0. \tag{10.25}$$

10.2.2 Solution of the Free Dirac Equation in Milne Coordinates: Differential Equation

Let us now solve the free Dirac equation of the mode functions (eq. 10.25). We start with the position dependence, making the familiar ansatz from the static box

$$\hat{\psi}^{\pm}_{\mathbf{k}_\perp,\nu,s,a}(\tau,\mathbf{x}_\perp) = e^{\pm\mathrm{i}\mathbf{x}_\perp\mathbf{k}_\perp}\hat{\psi}^{\pm}_{\mathbf{k}_\perp,\nu,s,a}(\tau). \tag{10.26}$$

Inserting this into (eq. 10.25) we find

$$0 = \left[\mathrm{i}\gamma^0\partial_\tau \mp \gamma^i k^i_\perp - \frac{1}{\tau}\nu\gamma^3 - m\right]e^{\pm\mathrm{i}\mathbf{x}_\perp\mathbf{k}_\perp}\hat{\psi}^{\pm}_{\mathbf{k}_\perp,\nu,s,a}(\tau). \tag{10.27}$$

Note that the remaining equation (eq. 10.27) is only a differential equation for the proper time τ, but it is non-linear because of the additional $1/\tau$ dependence. To solve this equation, we have to diagonalize it at first. We do this by stripping of the factor $e^{\pm i\mathbf{x}_\perp\mathbf{k}_\perp}$ and applying another time derivative

$$\begin{aligned}\partial_\tau^2\hat{\psi}^\pm_{\mathbf{k}_\perp,\nu,s,a}(\tau) &= -i\gamma^0\partial_\tau\Big[\pm\gamma^i k^i_\perp + \frac{1}{\tau}\nu\gamma^3 + m\Big]\hat{\psi}^\pm_{\mathbf{k}_\perp,\nu,s,a}(\tau) \\ &= -i\gamma^0\Big[\pm\gamma^i k^i_\perp + \frac{1}{\tau}\nu\gamma^3 + m\Big]\partial_\tau\hat{\psi}^\pm_{\mathbf{k}_\perp,\nu,s,a}(\tau) + \frac{i}{\tau^2}\nu\gamma^0\gamma^3\hat{\psi}^\pm_{\mathbf{k}_\perp,\nu,s,a}(\tau).\end{aligned} \tag{10.28}$$

We can now reuse (eq. 10.27) to substitute the term $\partial_\tau\hat{\psi}^\pm_{\mathbf{k}_\perp,\nu,s,a}(\tau)$. The first term of (eq. 10.28) is then given as

$$\begin{aligned}&-i\gamma^0\Big[\pm\gamma^i k^i_\perp + \frac{1}{\tau}\nu\gamma^3 + m\Big](-i)\gamma^0\Big[\pm\gamma^i k^i_\perp + \frac{1}{\tau}\nu\gamma^3 + m\Big] \\ &\quad= -\Big[-\gamma^i k^i_\perp\gamma^j k^j_\perp \mp \frac{1}{\tau}\nu k^i_\perp\underbrace{\{\gamma^i,\gamma^3\}}_{=0} + \frac{1}{\tau^2}\nu^2 + m^2\Big] = -\Big[k^2_\perp + \frac{1}{\tau^2}\nu^2 + m^2\Big],\end{aligned} \tag{10.29}$$

where we used that

$$-\gamma^i k^i_\perp\gamma^j k^j_\perp = -\frac{1}{2}\big(\gamma^i\gamma^j + \gamma^i\gamma^j\big)k^i_\perp k^j_\perp = -\frac{1}{2}\{\gamma^i,\gamma^j\}k^i_\perp k^j_\perp = -\eta^{ij}k^i_\perp k^j_\perp = k^i_\perp k^i_\perp = k^2_\perp. \tag{10.30}$$

We can now identify $M_{k_\perp}$, previously defined in (eq. 10.10), rewriting (eq. 10.28) in the following form

$$\partial_\tau^2\hat{\psi}^\pm_{\mathbf{k}_\perp,\nu,s,a}(\tau) = -\Big[M^2_{k_\perp} + \frac{1}{\tau^2}\nu^2 - \frac{i}{\tau^2}\nu\gamma^0\gamma^3\Big]\hat{\psi}^\pm_{\mathbf{k}_\perp,\nu,s,a}(\tau). \tag{10.31}$$

When multiplied by τ^2, this can be written in a more compact form

$$\Big[\tau^2\partial_\tau^2 + \tau^2 M^2_{k_\perp} - i\nu\big(i\nu + \gamma^0\gamma^3\big)\Big]\hat{\psi}^\pm_{\mathbf{k}_\perp,\nu,s,a}(\tau) = 0. \tag{10.32}$$

This equation already looks very much like a variant of the Bessel equation [164], but it is still a non-diagonal, matrix valued equation, because of the $\gamma^0\gamma^3$ term. We can eliminate this dependence and diagonalize the equation by making use of projection operators

$$P^\pm = \frac{1}{2}\big(1 \pm \gamma^0\gamma^3\big). \tag{10.33}$$

Making use of the following properties of the projection operators

$$\gamma^0\gamma^3P^+ = P^+, \qquad \gamma^0\gamma^3P^- = -P^-, \qquad P^+ + P^- = 1, \tag{10.34}$$

we can rewrite (eq. 10.32)

$$\begin{aligned}0 &= \Big[\tau^2\partial_\tau^2 + \tau^2 M^2_{k_\perp} - i\nu\big(i\nu + \gamma^0\gamma^3\big)\Big]\big(P^+ + P^-\big)\hat{\psi}^\pm_{\mathbf{k}_\perp,\nu,s,a}(\tau) \\ &= \Big[\tau^2\partial_\tau^2 + \tau^2 M^2_{k_\perp} - i\nu\big(i\nu + 1\big)\Big]P^+\hat{\psi}^\pm_{\mathbf{k}_\perp,\nu,s,a}(\tau) + \Big[\tau^2\partial_\tau^2 + \tau^2 M^2_{k_\perp} - i\nu\big(i\nu - 1\big)\Big]P^-\hat{\psi}^\pm_{\mathbf{k}_\perp,\nu,s,a}(\tau).\end{aligned} \tag{10.35}$$

The resulting equations for the projections of the mode function $P^{\pm}\hat{\psi}^{\pm}_{\mathbf{k}_\perp,\nu,s,a}(\tau)$ are diagonal and have to be satisfied individually. We conclude, that as soon as we find their solution, we can construct the full solution of (eq. 10.32).

We make the following ansatz for the time dependence of $\hat{\psi}^{\pm}_{\mathbf{k}_\perp,\nu,s,a}(\tau)$

$$\begin{aligned}\hat{\psi}^{\pm}_{\mathbf{k}_\perp,\nu,s,a}(\tau) &= P^{+}\hat{\psi}^{\pm}_{\mathbf{k}_\perp,\nu,s,a}(\tau) + P^{-}\hat{\psi}^{\pm}_{\mathbf{k}_\perp,\nu,s,a}(\tau) \\ &= T^{\pm}_{\mathbf{k}_\perp,\nu}(\tau)P^{+}\hat{\psi}^{\pm}_{\mathbf{k}_\perp,\nu,s,a} + \tilde{T}^{\pm}_{\mathbf{k}_\perp,\nu}(\tau)P^{-}\hat{\psi}^{\pm}_{\mathbf{k}_\perp,\nu,s,a},\end{aligned} \tag{10.36}$$

where $T^{\pm}_{\mathbf{k}_\perp,\nu}(\tau)$ and $\tilde{T}^{\pm}_{\mathbf{k}_\perp,\nu}(\tau)$ are scalar functions. These functions have to satisfy the non-linear differential equations

$$\Big[\tau^2\partial_\tau^2 + \tau^2 M_{k_\perp}^2 - \mathrm{i}\nu\Big(\mathrm{i}\nu+1\Big)\Big]T^{\pm}_{\mathbf{k}_\perp,\nu}(\tau) = 0, \tag{10.37}$$

$$\Big[\tau^2\partial_\tau^2 + \tau^2 M_{k_\perp}^2 - \mathrm{i}\nu\Big(\mathrm{i}\nu-1\Big)\Big]\tilde{T}^{\pm}_{\mathbf{k}_\perp,\nu}(\tau) = 0. \tag{10.38}$$

Both equations are a variant of the Bessel equation [164] and their solution is constructed from Bessel functions[2]

$$T^{\pm}_{\mathbf{k}_\perp,\nu}(\tau) = \sqrt{\tau}\Big(c_1^{\pm}J_{\mathrm{i}\nu+\frac{1}{2}}\Big(M_{\mathbf{k}_\perp}\tau\Big) + c_2^{\pm}Y_{\mathrm{i}\nu+\frac{1}{2}}\Big(M_{\mathbf{k}_\perp}\tau\Big)\Big), \tag{10.39}$$

$$\tilde{T}^{\pm}_{\mathbf{k}_\perp,\nu}(\tau) = \sqrt{\tau}\Big(\tilde{c}_1^{\pm}J_{\mathrm{i}\nu-\frac{1}{2}}\Big(M_{\mathbf{k}_\perp}\tau\Big) + \tilde{c}_2^{\pm}Y_{\mathrm{i}\nu-\frac{1}{2}}\Big(M_{\mathbf{k}_\perp}\tau\Big)\Big). \tag{10.40}$$

We use the integration constants $c^{\pm}_{1/2}$ and $\tilde{c}^{\pm}_{1/2}$ to rewrite our result in terms of Hankel functions, which will turn out to be useful later. To do so, we set $c_2^{+} = -\mathrm{i}c_1^{+} = c^{+}$ and $c_2^{-} = \mathrm{i}c_1^{-} = c^{-}$ (and the same for the $\tilde{c}_i^{\pm}$), arriving at

$$T^{\pm}_{\mathbf{k}_\perp,\nu}(\tau) = c^{\pm}\sqrt{\tau}H^{(2)/(1)}_{\mathrm{i}\nu+\frac{1}{2}}\Big(M_{\mathbf{k}_\perp}\tau\Big), \qquad \tilde{T}^{\pm}_{\mathbf{k}_\perp,\nu}(\tau) = \tilde{c}^{\pm}\sqrt{\tau}H^{(2)/(1)}_{\mathrm{i}\nu-\frac{1}{2}}\Big(M_{\mathbf{k}_\perp}\tau\Big), \tag{10.41}$$

where the Hankel functions are given as

$$H^{(1)}_{\mathrm{i}\nu\pm\frac{1}{2}}\Big(M_{\mathbf{k}_\perp}\tau\Big) = J_{\mathrm{i}\nu\pm\frac{1}{2}}\Big(M_{\mathbf{k}_\perp}\tau\Big) + \mathrm{i}Y_{\mathrm{i}\nu\pm\frac{1}{2}}\Big(M_{\mathbf{k}_\perp}\tau\Big), \tag{10.42}$$

$$H^{(2)}_{\mathrm{i}\nu\pm\frac{1}{2}}\Big(M_{\mathbf{k}_\perp}\tau\Big) = J_{\mathrm{i}\nu\pm\frac{1}{2}}\Big(M_{\mathbf{k}_\perp}\tau\Big) - \mathrm{i}Y_{\mathrm{i}\nu\pm\frac{1}{2}}\Big(M_{\mathbf{k}_\perp}\tau\Big). \tag{10.43}$$

Up to this point, we found the following solution of the free Dirac equation in Milne coordinates (eq. 10.25)

$$\hat{\psi}^{\pm}_{\mathbf{k}_\perp,\nu,s,a}(\tau) = \sqrt{\tau}\Big(c^{\pm}H^{(2)/(1)}_{\mathrm{i}\nu+\frac{1}{2}}\Big(M_{\mathbf{k}_\perp}\tau\Big)P^{+} + \tilde{c}^{\pm}H^{(2)/(1)}_{\mathrm{i}\nu-\frac{1}{2}}\Big(M_{\mathbf{k}_\perp}\tau\Big)P^{-}\Big)\hat{\psi}^{\pm}_{\mathbf{k}_\perp,\nu,s,a}. \tag{10.44}$$

10.2.3 Solution of the Free Dirac Equation in Milne Coordinates: Matrix Equation

Having solved the differential equation for the mode functions (eq. 10.25) by diagonalizing the equation, we now have to insert the solution (eq. 10.44) into the non-diagonalized equation.

[2]Note the explicit factor of $\sqrt{\tau}$ appearing, which matches the definition of the expanding box spinor (eq. 9.16).

After a lengthy calculation that can be found in (Appendix C.2), one arrives at

$$0 = \sqrt{\tau}\left[\tilde{c}^{\pm} H^{(2)/(1)}_{i\nu-\frac{1}{2}}\left(M_{\mathbf{k}_\perp}\tau\right)P^{-} + c^{\pm} H^{(2)/(1)}_{i\nu+\frac{1}{2}}\left(M_{\mathbf{k}_\perp}\tau\right)P^{+}\right]\left[\pm M_{\mathbf{k}_\perp}\gamma^0 \mp \gamma^i k^i_\perp - m\right]\hat{\psi}^{\pm}_{\mathbf{k}_\perp,\nu,s,a}. \tag{10.45}$$

The leftmost term of (eq. 10.45) has been checked for roots, identifying only the pole at $\tau = 0$, characteristic for the expanding geometry. Because we have to consider a finite initial time in a simulation in an expanding box, we can eliminate this term, leading to

$$\left[\pm M_{\mathbf{k}_\perp}\gamma^0 \mp \gamma^i k^i_\perp - m\right]\hat{\psi}^{\pm}_{\mathbf{k}_\perp,\nu,s,a} = \begin{pmatrix} \pm M_{\mathbf{k}_\perp}\gamma^0 - m & \mp k^i_\perp \sigma_i \\ \pm k^i_\perp \sigma_i & \mp M_{\mathbf{k}_\perp} - m \end{pmatrix}\hat{\psi}^{\pm}_{\mathbf{k}_\perp,\nu,s,a} = 0. \tag{10.46}$$

This algebraic matrix valued equation has a similar structure as the momentum space free Dirac equation in the static box (eq. 1.34), hence we make the following ansatz for the expanding box mode functions

$$\hat{\psi}^{\pm}_{\mathbf{k}_\perp,\nu,s,a} = \begin{pmatrix} \varphi(\mathbf{k}_\perp,\nu) \\ \chi(\mathbf{k}_\perp,\nu) \end{pmatrix}. \tag{10.47}$$

We find two equations, that are effectively two dimensional

$$(\mp M_{\mathbf{k}_\perp} + m)\varphi(\mathbf{k}_\perp,\nu) \pm k^i_\perp \sigma_i \chi(\mathbf{k}_\perp,\nu) = 0, \tag{10.48}$$

$$(\mp M_{\mathbf{k}_\perp} - m)\chi(\mathbf{k}_\perp,\nu) \pm k^i_\perp \sigma_i \varphi(\mathbf{k}_\perp,\nu) = 0. \tag{10.49}$$

Starting with the solution for ψ^+, the second equation of (eq. 10.48) leads to

$$\chi(\mathbf{k}_\perp,\nu) = \frac{k^i_\perp \sigma_i}{M_{\mathbf{k}_\perp} + m}\varphi(\mathbf{k}_\perp,\nu). \tag{10.50}$$

Inserting this result into the first equation of (eq. 10.48), we find

$$(-M_{\mathbf{k}_\perp} + m)\varphi(\mathbf{k}_\perp,\nu) + \frac{k^i_\perp \sigma_i k^j_\perp \sigma_j}{M_{\mathbf{k}_\perp} + m}\varphi(\mathbf{k}_\perp,\nu) = 0. \tag{10.51}$$

Using the following identity

$$k^i_\perp \sigma_i k^j_\perp \sigma_j = \frac{1}{2}\underbrace{\{\sigma_i,\sigma_j\}}_{=2\delta_{ij}} k^i_\perp k^j_\perp = \mathbf{k}^2_\perp = M^2_{\mathbf{k}_\perp} - m^2 = (M_{\mathbf{k}_\perp} - m)(M_{\mathbf{k}_\perp} + m), \tag{10.52}$$

we find

$$(-M_{\mathbf{k}_\perp} + m)\varphi(\mathbf{k}_\perp,\nu) + \frac{(M_{\mathbf{k}_\perp} - m)(M_{\mathbf{k}_\perp} + m)}{M_{\mathbf{k}_\perp} + m}\varphi(\mathbf{k}_\perp,\nu) = 0. \tag{10.53}$$

Note that this equation is always satisfied, independently on the choice of φ. As a consequence, we have the freedom of choosing φ, which is familiar from solving the free Dirac equation in the static box

$$\varphi_1 = \begin{pmatrix} 1 \\ 0 \end{pmatrix}, \qquad \varphi_2 = \begin{pmatrix} 0 \\ 1 \end{pmatrix}. \tag{10.54}$$

Making use of (eq. 10.50), we are now able to construct the first basis spinor

$$u_s(\mathbf{k}_\perp, y_k = 0) = N \begin{pmatrix} \varphi_s \\ \frac{k_\perp^i \sigma_i}{M_{\mathbf{k}_\perp}+m}\varphi_s \end{pmatrix}, \tag{10.55}$$

where we included a normalization constant N that has to be specified later. Note, that in contrast to the basis spinor in the static box (eq. 1.35), the result in the expanding box is no longer rapidity dependent, which is connected to the longitudinal boost invariance, discussed earlier. We are now able to repeat the calculation for ψ^-, leading to

$$v_s(\mathbf{k}_\perp, y_k = 0) = N \begin{pmatrix} \frac{k_\perp^i \sigma_i}{M_{\mathbf{k}_\perp}+m}\chi_s \\ \chi_s \end{pmatrix}, \tag{10.56}$$

where χ_s is given as

$$\chi_1 = \begin{pmatrix} 0 \\ 1 \end{pmatrix}, \qquad \chi_2 = \begin{pmatrix} 1 \\ 0 \end{pmatrix}. \tag{10.57}$$

We want our basis spinors to be orthonormal, as it has been the case in the static box (eq. 1.39). We can achieve this by fixing the normalization constant N, deriving

$$\begin{aligned} u_s^\dagger(\mathbf{k}_\perp, y_k = 0) u_r(\mathbf{k}_\perp, y_k = 0) =& |N|^2 \delta_{rs} \frac{2M_{\mathbf{k}_\perp}}{M_{\mathbf{k}_\perp}+m}, \\ v_s^\dagger(\mathbf{k}_\perp, y_k = 0) v_r(\mathbf{k}_\perp, y_k = 0) =& |N|^2 \delta_{rs} \frac{2M_{\mathbf{k}_\perp}}{M_{\mathbf{k}_\perp}+m}. \end{aligned} \tag{10.58}$$

To achieve ortho-normality, we set the normalization factor N to

$$N = \sqrt{\frac{M_{\mathbf{k}_\perp}+m}{2M_{\mathbf{k}_\perp}}}, \tag{10.59}$$

to reproduce the properties of the basis spinors (eq. 1.39) and (eq. 1.37).

10.2.4 Normalization of the Free Expanding Box Spinor

Having constructed the solution of the free Dirac equation in an expanding geometry, we finally have to identify the integration constants. Before doing so, we use the freedom to rewrite the integration constants, setting

$$c^\pm = -\mathrm{i} e^{\mp \mathrm{i}\frac{\pi}{4}} b^\pm, \qquad \tilde{c}^\pm = -\mathrm{i} e^{\pm \mathrm{i}\frac{\pi}{4}} b^\pm. \tag{10.60}$$

This allows us to write the solution of the free Dirac equation in a more compact form

$$\hat{\psi}^+_{\mathbf{k}_\perp,\nu,s,a}(\tau) = -\mathrm{i} b^+ \sqrt{\tau} \Big(e^{-\mathrm{i}\frac{\pi}{4}} H^{(2)}_{\mathrm{i}\nu+\frac{1}{2}}\big(M_{\mathbf{k}_\perp}\tau\big) P^+ + e^{\mathrm{i}\frac{\pi}{4}} H^{(2)}_{\mathrm{i}\nu-\frac{1}{2}}\big(M_{\mathbf{k}_\perp}\tau\big) P^- \Big) u_{s,a}(\mathbf{k}_\perp, y_k = 0), \tag{10.61}$$

$$\hat{\psi}^-_{\mathbf{k}_\perp,\nu,s,a}(\tau) = -\mathrm{i} b^- \sqrt{\tau} \Big(e^{\mathrm{i}\frac{\pi}{4}} H^{(1)}_{\mathrm{i}\nu+\frac{1}{2}}\big(M_{\mathbf{k}_\perp}\tau\big) P^+ + e^{-\mathrm{i}\frac{\pi}{4}} H^{(1)}_{\mathrm{i}\nu-\frac{1}{2}}\big(M_{\mathbf{k}_\perp}\tau\big) P^- \Big) v_{s,a}(\mathbf{k}_\perp, y_k = 0). \tag{10.62}$$

We require two conditions to fix the integration constants b^+ and b^-. A first condition is provided by a connection of the spinor to the static box solution. As a second condition we

consider the large time asymptotes of the expanding box spinors, taking $\tau \gg 1$. For large times, the asymptotes of the Hankel functions are given as

$$H^{(1)}_{\mathrm{i}\nu\pm\frac{1}{2}}\Big(M_{\mathbf{k}_\perp}\tau\Big) \approx \sqrt{\frac{2}{\pi M_{\mathbf{k}_\perp}\tau}} e^{\mathrm{i}\Big(M_{\mathbf{k}_\perp}\tau - \frac{\mathrm{i}\nu\pi}{2} \mp \frac{\pi}{4} - \frac{\pi}{4}\Big)}, \tag{10.63}$$
$$H^{(2)}_{\mathrm{i}\nu\pm\frac{1}{2}}\Big(M_{\mathbf{k}_\perp}\tau\Big) \approx \sqrt{\frac{2}{\pi M_{\mathbf{k}_\perp}\tau}} e^{-\mathrm{i}\Big(M_{\mathbf{k}_\perp}\tau - \frac{\mathrm{i}\nu\pi}{2} \mp \frac{\pi}{4} - \frac{\pi}{4}\Big)}.$$

Inserting those leads to

$$\hat{\psi}^{+}_{\mathbf{k}_\perp,\nu,s,a}(\tau) \overset{\tau\gg 1}{=} -\mathrm{i}b^{+}\sqrt{\frac{2}{\pi M_{\mathbf{k}_\perp}}} e^{-\mathrm{i}M_{\mathbf{k}_\perp}\tau} e^{-\frac{\nu\pi}{2}} e^{\mathrm{i}\frac{\pi}{4}} u_{s,a}(\mathbf{k}_\perp, y_k = 0), \tag{10.64}$$
$$\hat{\psi}^{-}_{\mathbf{k}_\perp,\nu,s,a}(\tau) \overset{\tau\gg 1}{=} -\mathrm{i}b^{-}\sqrt{\frac{2}{\pi M_{\mathbf{k}_\perp}}} e^{\mathrm{i}M_{\mathbf{k}_\perp}\tau} e^{\frac{\nu\pi}{2}} e^{-\mathrm{i}\frac{\pi}{4}} v_{s,a}(\mathbf{k}_\perp, y_k = 0). \tag{10.65}$$

At very large $\tau \gg 1$ the equation of motion of the mode functions (eq. 10.25) becomes effectively two dimensional

$$\Big[\mathrm{i}\gamma^0\partial_\tau \mp \gamma^i k^i_\perp - m + \mathcal{O}\Big(\frac{1}{\tau}\Big)\Big]\hat{\psi}^{\pm}_{\mathbf{k}_\perp,\nu,s,a} = \Big[\pm M_{\mathbf{k}_\perp}\gamma^0 \mp \gamma^i k^i_\perp - m\Big] u/v_{s,a}(\mathbf{k}_\perp, y_k = 0) = 0. \tag{10.66}$$

As a result we conclude, that the solution (eq. 10.61) should not be ν dependent in this limit, identifying

$$b^{+} = e^{\frac{\nu\pi}{2}} a, \qquad b^{-} = e^{-\frac{\nu\pi}{2}} a. \tag{10.67}$$

The solution (eq. 10.61) can then be written as

$$\hat{\psi}^{+}_{\mathbf{k}_\perp,\nu,s,a}(\tau, \mathbf{x}_\perp, \eta) = -\mathrm{i}a e^{\mathrm{i}\nu\eta + \mathbf{k}_\perp\mathbf{x}_\perp} e^{\frac{\nu\pi}{2}} \sqrt{\tau} \tag{10.68}$$
$$\times \Big(e^{-\mathrm{i}\frac{\pi}{4}} H^{(2)}_{\mathrm{i}\nu+\frac{1}{2}}\Big(M_{\mathbf{k}_\perp}\tau\Big)P^{+} + e^{\mathrm{i}\frac{\pi}{4}} H^{(2)}_{\mathrm{i}\nu-\frac{1}{2}}\Big(M_{\mathbf{k}_\perp}\tau\Big)P^{-}\Big) u_{s,a}(\mathbf{k}_\perp, y_k = 0),$$
$$\hat{\psi}^{-}_{\mathbf{k}_\perp,\nu,s,a}(\tau, \mathbf{x}_\perp, \eta) = -\mathrm{i}a e^{\mathrm{i}\nu\eta - \mathbf{k}_\perp\mathbf{x}_\perp} e^{-\frac{\nu\pi}{2}} \sqrt{\tau} \tag{10.69}$$
$$\times \Big(e^{\mathrm{i}\frac{\pi}{4}} H^{(1)}_{\mathrm{i}\nu+\frac{1}{2}}\Big(M_{\mathbf{k}_\perp}\tau\Big)P^{+} + e^{-\mathrm{i}\frac{\pi}{4}} H^{(1)}_{\mathrm{i}\nu-\frac{1}{2}}\Big(M_{\mathbf{k}_\perp}\tau\Big)P^{-}\Big) v_{s,a}(\mathbf{k}_\perp, y_k = 0),$$

and in total the spinor is given as

$$\psi(\tau, \mathbf{x}_\perp, \eta) = \int \sum_{s=1}^{2}\sum_{a=1}^{N_c} \Big(\hat{a}_{s,a}(\mathbf{k}_\perp, \nu)\hat{\psi}^{+}_{\mathbf{k}_\perp,\nu,s,a}(\tau, \mathbf{x}_\perp, \eta) + \hat{b}^{\dagger}_{s,a}(\mathbf{k}_\perp, \nu)\hat{\psi}^{-}_{\mathbf{k}_\perp,\nu,s,a}(\tau, \mathbf{x}_\perp, \eta)\Big)\frac{d^2k_\perp}{(2\pi)^2}\frac{d\nu}{2\pi}. \tag{10.70}$$

To fix the remaining integration constant, let us consider the norm of the expanding box spinor, making use of the scalar product in the expanding geometry (eq. 9.17)

$$\int |\psi(x)|^2 d^3x = \int\int \hat{\psi}^{\dagger}(\tau, \mathbf{x}_\perp, \eta)\hat{\psi}(\tau, \mathbf{x}_\perp, \eta) d^2x_\perp d\eta \tag{10.71}$$

Inserting the spinor solution (eq. 10.68), a lengthy calculation that can be found in (Appendix C.3), leads to

$$\int |\psi(x)|^2 d^3x = |a|^2 \tau \int \sum_{s=1}^{2}\sum_{a=1}^{N_c} \Big[\hat{a}^\dagger_{s,a}(\mathbf{k}_\perp,\nu)\hat{a}_{s,a}(\mathbf{k}_\perp,\nu) e^{\nu\pi}\Big(\big|H^{(2)}_{\mathrm{i}\nu+\frac{1}{2}}\big(M_{\mathbf{k}_\perp}\tau\big)\big|^2 + \big|H^{(2)}_{\mathrm{i}\nu-\frac{1}{2}}\big(M_{\mathbf{k}_\perp}\tau\big)\big|^2\Big) + \hat{b}_{s,a}(\mathbf{k}_\perp,\nu)\hat{b}^\dagger_{s,a}(\mathbf{k}_\perp,\nu) e^{-\nu\pi}\Big(\big|H^{(1)}_{\mathrm{i}\nu+\frac{1}{2}}\big(M_{\mathbf{k}_\perp}\tau\big)\big|^2 + \big|H^{(1)}_{\mathrm{i}\nu-\frac{1}{2}}\big(M_{\mathbf{k}_\perp}\tau\big)\big|^2\Big)\Big] \frac{d^2k_\perp}{(2\pi)^2}\frac{d\nu}{2\pi}. \tag{10.72}$$

Let us compare this result to the familiar result in the static box

$$\int |\psi(x)|^2 d^3x = \int \sum_{s=1}^{2}\sum_{a=1}^{N_c} \Big(\hat{a}^\dagger_{s,a}(\mathbf{k})\hat{a}_{s,a}(\mathbf{k}) + \hat{b}_{s,a}(\mathbf{k})\hat{b}^\dagger_{s,a}(\mathbf{k})\Big) \frac{d^3k}{(2\pi)^3}. \tag{10.73}$$

The solution of the free spinor in the expanding box should of course be a solution of the Dirac equation at all times, hence also at late times $\tau \gg 1$. We now use the late time asymptotes of the Hankel functions (eq. 10.63)

$$\big|H^{(2)}_{\mathrm{i}\nu+\frac{1}{2}}\big(M_{\mathbf{k}_\perp}\tau\big)\big|^2 \approx \frac{2}{\pi M_{\mathbf{k}_\perp}\tau} e^{-\pi\nu}, \qquad \big|H^{(2)}_{\mathrm{i}\nu-\frac{1}{2}}\big(M_{\mathbf{k}_\perp}\tau\big)\big|^2 \approx \frac{2}{\pi M_{\mathbf{k}_\perp}\tau} e^{-\pi\nu} \tag{10.74}$$

$$\big|H^{(1)}_{\mathrm{i}\nu+\frac{1}{2}}\big(M_{\mathbf{k}_\perp}\tau\big)\big|^2 \approx \frac{2}{\pi M_{\mathbf{k}_\perp}\tau} e^{\pi\nu}, \qquad \big|H^{(1)}_{\mathrm{i}\nu-\frac{1}{2}}\big(M_{\mathbf{k}_\perp}\tau\big)\big|^2 \approx \frac{2}{\pi M_{\mathbf{k}_\perp}\tau} e^{\pi\nu}, \tag{10.75}$$

to rewrite (eq. 10.72)

$$\int |\psi(x)|^2 d^3x = |a|^2 \frac{4}{\pi M_{\mathbf{k}_\perp}} \int \sum_{s=1}^{2}\sum_{a=1}^{N_c} \Big[\hat{a}^\dagger_{s,a}(\mathbf{k}_\perp,\nu)\hat{a}_{s,a}(\mathbf{k}_\perp,\nu) + \hat{b}_{s,a}(\mathbf{k}_\perp,\nu)\hat{b}^\dagger_{s,a}(\mathbf{k}_\perp,\nu)\Big] \frac{d^2k_\perp}{(2\pi)^2}\frac{d\nu}{2\pi}. \tag{10.76}$$

From a comparison to the static box result[3] (eq. 10.73), we conclude

$$|a|^2 = \frac{\pi M_{\mathbf{k}_\perp}}{4}, \quad \Rightarrow \quad a = \frac{1}{2}\sqrt{M_{\mathbf{k}_\perp}\pi}. \tag{10.77}$$

We found the following solutions for the mode functions

$$\hat{\psi}^+_{\mathbf{k}_\perp,\nu,s,a}(\tau,\mathbf{x}_\perp,\eta) = -\frac{\mathrm{i}}{2}\sqrt{\pi M_{\mathbf{k}_\perp}\tau}\, e^{\mathrm{i}\nu\eta+\mathrm{i}\mathbf{k}_\perp\mathbf{x}_\perp} e^{\frac{\nu\pi}{2}} \times \Big(e^{-\mathrm{i}\frac{\pi}{4}} H^{(2)}_{\mathrm{i}\nu+\frac{1}{2}}\big(M_{\mathbf{k}_\perp}\tau\big)P^+ + e^{\mathrm{i}\frac{\pi}{4}} H^{(2)}_{\mathrm{i}\nu-\frac{1}{2}}\big(M_{\mathbf{k}_\perp}\tau\big)P^-\Big) u_{s,a}(\mathbf{k}_\perp, y_k = 0), \tag{10.78}$$

$$\hat{\psi}^-_{\mathbf{k}_\perp,\nu,s,a}(\tau,\mathbf{x}_\perp,\eta) = -\frac{\mathrm{i}}{2}\sqrt{\pi M_{\mathbf{k}_\perp}\tau}\, e^{\mathrm{i}\nu\eta-\mathrm{i}\mathbf{k}_\perp\mathbf{x}_\perp} e^{-\frac{\nu\pi}{2}} \times \Big(e^{\mathrm{i}\frac{\pi}{4}} H^{(1)}_{\mathrm{i}\nu+\frac{1}{2}}\big(M_{\mathbf{k}_\perp}\tau\big)P^+ + e^{-\mathrm{i}\frac{\pi}{4}} H^{(1)}_{\mathrm{i}\nu-\frac{1}{2}}\big(M_{\mathbf{k}_\perp}\tau\big)P^-\Big) v_{s,a}(\mathbf{k}_\perp, y_k = 0), \tag{10.79}$$

that enters the Fourier representation of the free spinor in an expanding geometry

$$\hat{\psi}(\tau,\mathbf{x}_\perp,\eta) = \int \sum_{s=1}^{2}\sum_{a=1}^{N_c} \Big(\hat{a}_{s,a}(\mathbf{k}_\perp,\nu)\hat{\psi}^+_{\mathbf{k}_\perp,\nu,s,a}(\tau,\mathbf{x}_\perp,\eta) + \hat{b}^\dagger_{s,a}(\mathbf{k}_\perp,\nu)\hat{\psi}^-_{\mathbf{k}_\perp,\nu,s,a}(\tau,\mathbf{x}_\perp,\eta)\Big) \frac{d^2k_\perp}{(2\pi)^2}\frac{d\nu}{2\pi}. \tag{10.80}$$

[3] As seen earlier, the late time behavior of the expanding box solution should be connected to the static result, since the box becomes infinitely large in η direction, hence the effect of expansion can be neglected and the solution becomes effectively two dimensional.

10.3 Lattice Discretization of the Free Spinor in an Expanding Geometry

In this final section, we want to discretize the result of the free spinor in an expanding geometry (eq. 10.80). We start the discussion, by discretizing the η-direction. On the lattice, we replace the continuous derivative operator by

$$\frac{\mathrm{i}}{\tau}\gamma^3\partial_\eta = \frac{\mathrm{i}}{2a_\eta\tau}\Big(\gamma^3\delta_{\eta+\hat{a}_\eta,\eta} - \gamma^3\delta_{\eta-\hat{a}_\eta,\eta}\Big). \tag{10.81}$$

The Dirac equation for the mode functions (eq. 10.25) now reads

$$\begin{aligned} 0 &= \left[\mathrm{i}\gamma^0\partial_\tau + \mathrm{i}\gamma^i\partial_i + \frac{\mathrm{i}}{2a_\eta\tau}\gamma^3\Big(e^{\mathrm{i}\nu a_\eta} - e^{-\mathrm{i}\nu a_\eta}\Big) - m\right]e^{\mathrm{i}\nu\eta}\hat{\psi}^{\pm}_{\mathbf{k}_\perp,\nu,s,a}(\tau,\mathbf{x}_\perp) \\ &= \left[\mathrm{i}\gamma^0\partial_\tau + \mathrm{i}\gamma^i\partial_i - \frac{1}{a_\eta\tau}\sin\Big(a_\eta\nu\Big) - m\right]e^{\mathrm{i}\nu\eta}\hat{\psi}^{\pm}_{\mathbf{k}_\perp,\nu,s,a}(\tau,\mathbf{x}_\perp), \end{aligned} \tag{10.82}$$

where we were able to identified the lattice momentum s^ν for the longitudinal direction. The transverse direction can be treated in a similar fashion, introducing the discrete lattice derivative operator and identifying the lattice momenta

$$0 = \left[\mathrm{i}\gamma^0\partial_\tau \mp \frac{1}{a_\perp}\gamma^i\sin\Big(a_\perp k^i_\perp\Big) - \frac{1}{a_\eta\tau}\sin\Big(a_\eta\nu\Big) - m\right]e^{\pm\mathrm{i}\mathbf{x}_\perp\mathbf{k}_\perp}\hat{\psi}^{\pm}_{\mathbf{k}_\perp,\nu,s,a}(\tau). \tag{10.83}$$

As discussed in case of the static box, we do not discretize time at this point, but we require a discretization later, to solve the equations of motion in a leap-frog scheme in the lattice simulation.

It is now straight forward to repeat all previous steps to solve the time dependent part of the expanding box Dirac equation on the lattice (eq. 10.83). We will repeat the calculation, because it is possible to construct the result from the continuum solution (eq. 10.78) by substituting

$$\nu \;\rightarrow\; \frac{1}{a_\eta}\sin\Big(a_\eta\nu\Big), \qquad k^i_\perp \;\rightarrow\; \frac{1}{a_\perp}\sin\Big(a_\perp k^i_\perp\Big) = \frac{1}{a_\perp}s^i_\perp, \tag{10.84}$$

Revisiting the solution of the time dependent part of the continuum free expanding box Dirac equation, we have a look at the following intermediate result (eq. 10.45), which is now expressed in terms of lattice momenta

$$\begin{aligned} 0 = \sqrt{\tau}\Bigg[\tilde{c}^{\pm}H^{(2)/(1)}_{\mathrm{i}\frac{\mathrm{i}}{a_\eta}\sin(a_\eta\nu)-\frac{1}{2}}\Big(M_{\mathbf{k}_\perp}\tau\Big)P^- + c^{\pm}H^{(2)/(1)}_{\frac{\mathrm{i}}{a_\eta}\sin(a_\eta\nu)+\frac{1}{2}}\Big(M_{\mathbf{k}_\perp}\tau\Big)P^+\Bigg] \\ \times\left[\pm M_{\mathbf{k}_\perp}\gamma^0 \mp \frac{1}{a_\perp}\gamma^i s^i_\perp - m\right]\hat{\psi}^{\pm}_{\mathbf{k}_\perp,\nu,s,a}. \end{aligned} \tag{10.85}$$

As it has been the case in the continuum, checking the left-hand term for roots,does not reveal any, besides the initial time singularity in an expanding geometry $\tau = 0$. As discussed previously, we exclude the singularity in a simulation by specifying a finite initial time, allowing us to get rid of the time dependent term. We find the following lattice version of the matrix equation

$$0 = \left[\pm M_{\mathbf{k}_\perp}\gamma^0 \mp \frac{1}{a_\perp}\gamma^i s^i_\perp - m\right]\hat{\psi}^{\pm}_{\mathbf{k}_\perp,\nu,s,a}. \tag{10.86}$$

We now note, that $M_{\mathbf{k}_\perp}$ can be identified as the lattice counterpart of the effective dispersion relation in case of an expanding box. It is effectively two dimensional and the η-dependence has been eliminated due to the boost invariance. The equation is solved for

$$M_{\mathbf{k}_\perp} = \sqrt{\frac{1}{a_\perp^2} s_i^2(\mathbf{k}_\perp) + \frac{1}{a_\perp^2}\bar{m}^2} = \frac{1}{a_\perp}\sqrt{s_i^2(\mathbf{k}_\perp) + \bar{m}^2}. \tag{10.87}$$

When comparing the lattice dispersion relation (eq. 10.87) to its continuum counterpart (eq. 10.10), it is straight forward to see, that the lattice dispersion relation in the expanding box (eq. 10.87) suffers from the same problem as discussed in the static box. We have additional poles at the edges of the Brioullin zone and the dispersion relation „bends“ towards these edges. To cure this problem, we introduce a transverse Wilson term

$$0 = \left[\pm M_{\mathbf{k}_\perp}\gamma^0 \mp \frac{1}{a_\perp}\gamma^i s_\perp^i - \left(m + \frac{r_\perp}{a_\perp}\sum_{i=1}^{2}\left(1 - \cos\left(a_\perp k_\perp^i\right)\right)\right)\right]\hat{\psi}^{\pm}_{\mathbf{k}_\perp,\nu,s,a}. \tag{10.88}$$

The lattice dispersion relation now reads

$$M_{\mathbf{k}_\perp} = \frac{1}{a_\perp}\sqrt{s_i^2(\mathbf{k}_\perp) + \mu^2(\mathbf{k}_\perp)}, \qquad \mu(\mathbf{k}_\perp) = \bar{m} + r_\perp \sum_{i=1}^{2}\left(1 - \cos\left(a_\perp k_\perp^i\right)\right), \tag{10.89}$$

where we defined the lattice mass, including the transverse Wilson term. We can now solve (eq. 10.88) to obtain the basis spinors[4]

$$u_s(\mathbf{k}_\perp) = \sqrt{\frac{\bar{M}_{\mathbf{k}_\perp} + \mu(\mathbf{k}_\perp)}{2\bar{M}_{\mathbf{k}_\perp}}}\begin{pmatrix} \varphi_s \\ \frac{s_\perp^i \sigma_i}{\bar{M}_{\mathbf{k}_\perp} + \mu(\mathbf{k}_\perp)}\varphi_s \end{pmatrix}, \quad v_s(\mathbf{k}_\perp) = \sqrt{\frac{\bar{M}_{\mathbf{k}_\perp} + \mu(\mathbf{k}_\perp)}{2\bar{M}_{\mathbf{k}_\perp}}}\begin{pmatrix} \frac{s_\perp^i \sigma_i}{\bar{M}_{\mathbf{k}_\perp} + \mu^2(\mathbf{k}_\perp)}\chi_s \\ \chi_s \end{pmatrix}. \tag{10.90}$$

The lattice mode functions in the expanding box, that enter the free solution of the Dirac spinor, can now be written as

$$\begin{aligned}\hat{\psi}^{+}_{\mathbf{k}_\perp,\nu,s,a}(\tau,\mathbf{x}_\perp,\eta) &= -\frac{\mathrm{i}}{2}\sqrt{\pi\bar{M}_{\mathbf{k}_\perp}\bar{\tau}}e^{\mathrm{i}\nu\eta + \mathrm{i}\mathbf{k}_\perp\mathbf{x}_\perp}e^{\frac{\pi}{2a_\eta}\sin(a_\eta\nu)} \qquad (10.91)\\ &\times\left(e^{-\mathrm{i}\frac{\pi}{4}}H^{(2)}_{\frac{\mathrm{i}}{a_\eta}\sin(a_\eta\nu)+\frac{1}{2}}\left(\bar{M}_{\mathbf{k}_\perp}\bar{\tau}\right)P^+ + e^{\mathrm{i}\frac{\pi}{4}}H^{(2)}_{\frac{\mathrm{i}}{a_\eta}\sin(a_\eta\nu)-\frac{1}{2}}\left(\bar{M}_{\mathbf{k}_\perp}\bar{\tau}\right)P^-\right)u_{s,a}(\mathbf{k}_\perp, y_k = 0),\\ \hat{\psi}^{-}_{\mathbf{k}_\perp,\nu,s,a}(\tau,\mathbf{x}_\perp,\eta) &= -\frac{\mathrm{i}}{2}\sqrt{\pi\bar{M}_{\mathbf{k}_\perp}\bar{\tau}}e^{\mathrm{i}\nu\eta - \mathrm{i}\mathbf{k}_\perp\mathbf{x}_\perp}e^{-\frac{\pi}{2a_\eta}\sin(a_\eta\nu)} \qquad (10.92)\\ &\times\left(e^{\mathrm{i}\frac{\pi}{4}}H^{(1)}_{\frac{\mathrm{i}}{a_\eta}\sin(a_\eta\nu)+\frac{1}{2}}\left(\bar{M}_{\mathbf{k}_\perp}\bar{\tau}\right)P^+ + e^{-\mathrm{i}\frac{\pi}{4}}H^{(1)}_{\frac{\mathrm{i}}{a_\eta}\sin(a_\eta\nu)-\frac{1}{2}}\left(\bar{M}_{\mathbf{k}_\perp}\bar{\tau}\right)P^-\right)v_{s,a}(\mathbf{k}_\perp, y_k = 0).\end{aligned}$$

For the Fourier representation of the free spinor on the lattice, integrals are replaced by sums

$$\hat{\psi}(\tau,\mathbf{x}_\perp,\eta) = \frac{1}{V}\sum_{\mathbf{k}_\perp,\nu}\sum_{s=1}^{2}\sum_{a=1}^{N_c}\left(\hat{a}_{s,a}(\mathbf{k}_\perp,\nu)\hat{\psi}^{+}_{\mathbf{k}_\perp,\nu,s,a}(\tau,\mathbf{x}_\perp,\eta) + \hat{b}^\dagger_{s,a}(\mathbf{k}_\perp,\nu)\hat{\psi}^{-}_{\mathbf{k}_\perp,\nu,s,a}(\tau,\mathbf{x}_\perp,\eta)\right). \tag{10.93}$$

Details on the implementation in a real-time lattice simulation can be found in (Appendix C.3.1).

[4]The bar above $\bar{M}_{\mathbf{k}_\perp} = a_\perp M_{\mathbf{k}_\perp}$ indicates rescaling in terms of the lattice spacing $a_\perp$. The index i is only summed from $i \in \{1, 2\}$.

11

Equations of Motion for the Expanding System

Having discussed the formalism and the initial conditions for a semi-classical simulation in an expanding box, we now derive the model and present the corresponding equations of motion in this section. As it has been the case in the static box, the equations of motion of the semi-classical approximation will be derived from the semi-classical partition function and the Dirac equation. The main difference is, that the longitudinal expansion will manifest itself in a splitting of the gauge link and the chromo-electric field equation into a longitudinal and transverse part. We start our discussion with the time evolution equation of the gauge links and the fermion fields. In a next step, we introduce the semi classical model in the expanding box and derive the corresponding equation of motion for the chromo-electric field, as well as the Gauss constraint. We close the chapter with a comment on renormalization. As discussed in the context of the static box, we discretize the proper time in this section, introducing a temporal spacing $a_\tau \ll a_\perp$.

11.1 Evolution Equation of the Gauge Links

The evolution equation of the gauge links is again found from the temporal plaquette. When applying the Fock-Schwinger gauge ($A_\tau = 0$) to eliminate one of the two gauge degrees of freedom, we find

$$U_{\tau\mu}(x) = U_\mu(x+\hat{\tau})U_\mu^\dagger(x) = \exp\Big(\mathrm{i}g a_\tau a_\mu F_{\tau\mu}(x) + \mathcal{O}(a^3)\Big). \tag{11.1}$$

It is now possible to identify the expanding box chromo-electric fields (eq. 9.26) and (eq. 9.27). Because of the splitting of the expanding box chromo-electric fields, into a transverse and a longitudinal part, we obtain two equations of motion for the transverse and longitudinal gauge links

$$U_i(x+\hat{\tau}) = \exp\left(\mathrm{i}\frac{a_\tau}{\tau}E_i(x)\right)U_i(x), \tag{11.2}$$

$$U_\eta(x+\hat{\tau}) = \exp\Big(\mathrm{i}a_\tau a_\eta \tau E_\eta(x)\Big)U_\eta(x). \tag{11.3}$$

Making use of the discretized proper time with spacing a_τ, it is straight forward to implement the equation of motion in a real-time lattice simulation.

11.2 Equation of Motion of the Fermion Fields

The equation of motion of the expanding box spinor has already been derived in (section 9.1.1) and is given by the Dirac equation in Milne coordinates. The coupling to the classical gauge field is realized by replacing the derivative operators by their covariant counterpart

$$\left[\mathrm{i}\gamma^0\partial_\tau + \mathrm{i}\gamma^i D_i + \mathrm{i}\frac{1}{\tau}\gamma^3 D_\eta - m + \frac{r_\perp}{2}a_\perp \Box_W^\perp\right]\hat{\psi}(x) = 0, \tag{11.4}$$

where we have formally introduced a transverse Wilson term. Discretizing the covariant derivatives we find the following lattice version of the equation

$$\begin{aligned}\partial_\tau\hat{\psi}_G(x) = &-\frac{1}{2a_\perp}\gamma^0\sum_{i=1}^{2}\Big[\big(\gamma^i - \mathrm{i}r_\perp\big)U_i(x)\hat{\psi}_G(x+\hat{i}) - \big(\gamma^i + \mathrm{i}r_\perp\big)U_i^\dagger(x-\hat{i})\hat{\psi}_G(x-\hat{i})\Big] \\ &-\frac{1}{2a_\eta\tau}\gamma^0\gamma^3\Big[U_\eta(x)\hat{\psi}_G(x+\hat{\eta}) - U_\eta^\dagger(x-\hat{\eta})\hat{\psi}_G(x-\hat{\eta})\Big] - \mathrm{i}\left(m + \frac{2r_\perp}{a_\perp}\right)\gamma^0\hat{\psi}_G(x),\end{aligned} \tag{11.5}$$

where we also applied a gender index to the spinors, because the Dirac equation is the evolution equation of each of the gendered fermions in the stochastic ensemble N_{ens}. As discussed already, when implementing the given equation (eq. 11.5) in a real-time lattice simulation, we have to discretize the proper time

$$\partial_\tau\hat{\psi}_G(x) = \frac{1}{2a_\tau}\Big(\hat{\psi}_G(x+\hat{\tau}) - \hat{\psi}_G(x-\tau)\Big). \tag{11.6}$$

At the first time-step, we do not have access to the field $\hat{\psi}_G(x-\hat{\tau})$ and therefore use only a forward time derivative once

$$\partial_\tau\hat{\psi}_G(x) = \frac{1}{a_\tau}\Big(\hat{\psi}_G(x+\hat{\tau}) - \hat{\psi}_G(x)\Big). \tag{11.7}$$

Introducing dimensionless lattice quantities[1], by rescaling all quantities in terms of the lattice spacing $a_\perp$, setting

$$\hat{\bar{\psi}}(x) = a_\perp\hat{\psi}(x), \tag{11.8}$$

and introducing $\bar{a}_\tau = a_\tau/a_\perp$, $\bar{\tau} = \tau/a_\perp$, $\bar{m} = a_\perp m$, we arrive at the following equation of motion of the fermion fields, which can directly be implemented in a lattice simulation

$$\begin{aligned}\hat{\bar{\psi}}_G(x+\hat{\tau}) = &\hat{\bar{\psi}}_G(x-\hat{\tau}) - \bar{a}_\tau\gamma^0\sum_{i=1}^{2}\Big[\big(\gamma^i - \mathrm{i}r_\perp\big)U_i(x)\hat{\bar{\psi}}_G(x+\hat{i}) - \big(\gamma^i + \mathrm{i}r_\perp\big)U_i^\dagger(x-\hat{i})\hat{\bar{\psi}}_G(x-\hat{i})\Big] \\ &-\frac{\bar{a}_\tau}{a_\eta\bar{\tau}}\gamma^0\gamma^3\Big[U_\eta(x)\hat{\bar{\psi}}_G(x+\hat{\eta}) - U_\eta^\dagger(x-\hat{\eta})\hat{\bar{\psi}}_G(x-\hat{\eta})\Big] - 2\mathrm{i}\bar{a}_\tau\big(\bar{m} + 2r_\perp\big)\gamma^0\hat{\bar{\psi}}_G(x)\end{aligned} \tag{11.9}$$

[1]Keep in mind, that the spinor in the expanding box is of reduced dimension when compared to the static box, given by $\psi \sim length^{-1}$.

11.3 The Semi-Classical Model in an Expanding Box

Let us now formulate the semi-classical model in the expanding box. We adopt the procedure presented in the context of the static box in (section 4.3) and assume the Yang-Mills fields to be overoccupied and dominated by classical modes. This allows us to use the ansatz (eq. 4.12) for the Yang-Mills fields and linearize the action in the quantum fluctuation $\tilde{A}$. As discussed in (chapter 9), an important difference for Yang-Mills theory in the expanding box, is that one has to take care of the non-trivial metric of Milne coordinates. The linearized Yang-Mills action (eq. 4.16) in the expanding box is then given as

$$S_{YM}[A] \approx \int_{\mathcal{C}^+} \tilde{A}^a_\nu(x)\Big[\partial_\mu F^{\mu\nu,a}[\bar{A}](x) - g f^{abc}\bar{A}^b_\mu(x) F^{\mu\nu,c}[\bar{A}](x)\Big]\tau d\tau d^2x_\perp d\eta, \tag{11.10}$$

where we included the Jacobian (eq. 9.5) in the integration measure. For the fermion sector, we start from (eq. 9.33) and introduce the inverse propagator to rewrite the action

$$\begin{aligned} S_f[\hat{\psi},\hat{\bar{\psi}}] &= \int \hat{\bar{\psi}}(x)\Big[\mathrm{i}\gamma^0\partial_\tau + \mathrm{i}\gamma^i D_i + \frac{\mathrm{i}}{\tau}\gamma^3 D_\eta - m\Big]\hat{\psi}(x) d\tau d^2x_\perp d\eta \\ &= \int \hat{\bar{\psi}}(x)\mathrm{i}D_{\mathcal{C}}[A]^{-1}(x,y)\hat{\psi}(y) d^4x d^4y, \end{aligned} \tag{11.11}$$

where we introduced the following short notation $x = (\tau, \mathbf{x}_\perp, \eta)$ and $y = (\tau, \mathbf{x}'_\perp, \eta')$. The inverse propagator is given as

$$\mathrm{i}D^{-1}_{\mathcal{C}}[A] = \Big(\mathrm{i}\not{\partial} - g\Big(\not{\bar{A}}(x) + \frac{1}{2}\mathrm{sgn}_{\mathcal{C}}\not{\tilde{A}}\Big) - m\Big)\delta_{\mathcal{C}}(x,x), \tag{11.12}$$

where we introduced Feynman slash notation in the expanding geometry, which is defined in the following way

$$\not{\bar{A}}(x) = \gamma^\mu \bar{A}_\mu(x) = \gamma^0\bar{A}_0(x) + \sum_{i=1}^{2}\gamma^i\bar{A}_i(x) + \frac{1}{\tau}\gamma^3\bar{A}_3(x). \tag{11.13}$$

Integrating the fermion fields, specifies the effective partition function of the semi-classical model

$$Z_{\mathcal{C},exp} = \int \rho_A(\tau_0)\det\Big[D^{-1}_{\mathcal{C}}[A]\Big]e^{\mathrm{i}S_{YM}[A]}[dA] = \int \rho_A(\tau_0)e^{\mathrm{Trlog}\Big(D^{-1}_{\mathcal{C}}[A]\Big)+\mathrm{i}S_{YM}[A]}[dA]. \tag{11.14}$$

As it has been the case in the static box, we use a Taylor expansion for the fermion determinant, expanding it in terms of the quantum gauge field $\tilde{A}_\mu$. To do so, we take the derivative with respect to $\tilde{A}$ at first

$$\frac{\partial}{\partial\tilde{A}_\mu}\log\Big(D^{-1}_{\mathcal{C}}[A]\Big)\Big|_{\tilde{A}=0} = D_{\mathcal{C}}[\bar{A}]\frac{\partial}{\partial\tilde{A}_\mu}D^{-1}_{\mathcal{C}}[A]\Big|_{\tilde{A}=0} = D_{\mathcal{C}}[\bar{A}]\mathrm{i}g\gamma^\mu\frac{1}{2}\mathrm{sgn}_{\mathcal{C}}, \tag{11.15}$$

where we use short notation for the γ-matrices

$$\mu \in \{0, i, \eta\}, \quad \text{with} \quad \gamma^\eta = \frac{1}{\tau}\gamma^3. \tag{11.16}$$

We therefore find

$$\mathrm{Tr}\,\log D^{-1}_{\mathcal{C}}[A] \approx \mathrm{Tr}\,\log D^{-1}_{\mathcal{C}}[A]\Big|_{\tilde{A}=0} + \frac{\mathrm{i}g}{2}\mathrm{Tr}\Big[D_{\mathcal{C}}[\bar{A}]\mathrm{sgn}_{\mathcal{C}}\underbrace{\Big(\gamma^0\tilde{A}_0 + \gamma^i\tilde{A}_i + \frac{1}{\tau}\gamma^3\tilde{A}_\eta\Big)}_{\equiv\not{\tilde{A}}}\Big] + \mathcal{O}(\tilde{A}^2). \tag{11.17}$$

As discussed in the static box, the first term cancels on the forward and backward branch of the (proper-)time contour (figure 4.1) and we are left with

$$\frac{\mathrm{i}g}{2}\mathrm{Tr}\Big[D_{\mathcal{C}}[\bar{A}]\mathrm{sgn}_{\mathcal{C}}\tilde{A}\Big] = \mathrm{i}g\int_{\tau_0}^{\tau_f}\int \mathrm{tr}\Big[\hat{F}_{\bar{A}}(x,x)\gamma^{\mu}T^a\Big]\tilde{A}^a_{\mu}(x)d\tau d^2x_{\perp}d\eta, \tag{11.18}$$

where we identified the statistical propagator. Now we can define the fermion current in the expanding box, using the short notation for the gamma matrices (eq. 11.16)

$$J^{\mu,a}_{\bar{A},exp} = -g\mathrm{tr}\Big[\hat{F}_{\bar{A}}(x,x)\gamma^{\mu}T^a\Big]. \tag{11.19}$$

In a final step, we integrate the quantum field $\tilde{A}$, arriving at the partition function of the semi-classical approximation of QCD in a longitudinally expanding geometry

$$Z_{\mathcal{C},exp} = \int \rho_{\bar{A}}(\tau_0)\delta\Big[\partial_{\mu}\tau F^{\mu\nu,a}[\bar{A}](x) - g\tau f^{abc}\bar{A}^b_{\mu}(x)F^{\mu\nu,c}[\bar{A}](x) - J^{\nu,a}_{\bar{A},exp}\Big][d\bar{A}]. \tag{11.20}$$

From this result, we can deduce the equation of motion of the semi-classical model, in an expanding system

$$\partial_{\mu}\tau F^{\mu\nu,a}[\bar{A}](x) - g\tau f^{abc}\bar{A}^b_{\mu}(x)F^{\mu\nu,c}[\bar{A}](x) = J^{\nu,a}_{\bar{A},exp} = -g\mathrm{tr}\Big[\hat{F}_{\bar{A}}(x,x)\gamma^{\nu}T^a\Big]. \tag{11.21}$$

The evolution equation of the chromo-electric field now splits into a longitudinal and a transverse part. The transverse part is derived by setting $\nu = i$, with $i \in \{1,2\}$ and the longitudinal part is derived by setting $\nu = \eta$. Identifying the transverse chromo-electric field (eq. 9.26), the corresponding equation of motion of the field is given as

$$\begin{aligned}\partial_{\tau}E^a_i(x) =& \tau\sum_{j\neq\eta}\Big(\partial_j F^a_{ji}[\bar{A}](x) - gf^{abc}\bar{A}^b_j(x)F^c_{ji}[\bar{A}](x)\Big) \\ &+\frac{1}{\tau}\Big(\partial_{\eta}F_{\eta i}[\bar{A}](x) - gf^{abc}\bar{A}^b_{\eta}(x)F^c_{\eta i}[\bar{A}](x)\Big) + g\mathrm{tr}\Big[\hat{F}_{\bar{A}}(x,x)\gamma^i T^a\Big].\end{aligned} \tag{11.22}$$

In the longitudinal direction, we find the following equation, after identifying the longitudinal chromo-electric field (eq. 9.27)

$$\partial_{\tau}E^a_{\eta}(x) = \frac{1}{\tau}\sum_{j=1}^{2}\Big(\partial_j F^a_{j\eta}[\bar{A}](x) - gf^{abc}\bar{A}^b_j(x)F^c_{j\eta}[\bar{A}](x)\Big) + \frac{g}{\tau}\mathrm{tr}\Big[\hat{F}_{\bar{A}}(x,x)\gamma^3 T^a\Big]. \tag{11.23}$$

In a final step, we discretize (eq. 11.22) and (eq. 11.23), making it accessible in a real-time lattice simulation. When doing so, one has to keep in mind, that we are dealing with two different kinds of lattice spacing in the expanding geometry: In transverse direction the lattice spacing $a_{\perp}$ of dimension *length* and in longitudinal direction the dimensionless lattice spacing a_{η}. In transverse direction, we have to include the Wilson term as well, when discretizing the equation of motion. All in all, we arrive at the following expanding box chromo-electric field equations of motion on the lattice

$$\begin{aligned}\bar{E}^a_i(x+\tau) = \bar{E}^a_i(x) &+ 2\bar{a}_{\tau}\mathrm{Im}\mathrm{tr}\Big[T^a\bar{\tau}\sum_{i\neq j}\Big(U_{ji}(x) + U_{-ji}(x)\Big) + \frac{1}{\bar{\tau}\bar{a}^2_{\eta}}T^a\Big(U_{\eta i}(x) + U_{-\eta i}(x)\Big)\Big] \\ &+ g^2\bar{a}_{\tau}\mathrm{Re}\mathrm{tr}\Big[\hat{\bar{F}}(x+\hat{i},x)\Big(\gamma^i - \mathrm{i}r_{\perp}\Big)T^a U_i(x)\Big],\end{aligned} \tag{11.24}$$

$$\bar{E}^a_{\eta}(x+\tau) = \bar{E}^a_{\eta}(x) + \frac{2\bar{a}_{\tau}}{\bar{\tau}\bar{a}_{\eta}}\sum_{i=1}^{2}\mathrm{Im}\mathrm{tr}\Big[T^a\Big(U_{-i\eta}(x) + U_{i\eta}(x)\Big)\Big] + \frac{g^2\bar{a}_{\tau}}{\bar{\tau}}\mathrm{Re}\mathrm{tr}\Big[\hat{\bar{F}}(x+\hat{\eta},x)\gamma^3 T^a U_{\eta}(x)\Big], \tag{11.25}$$

where we rescaled all quantities in terms of the lattice spacing $a_\perp$ and discretized the proper time by

$$\partial_{\bar{\tau}} \bar{E}_i^a(x) = \frac{1}{\bar{a}_\tau}\Big(\bar{E}_i^a(x+\hat{\tau}) - \bar{E}_i^a(x)\Big). \tag{11.26}$$

The statistical propagator, that enters the expanding box fermion current (eq. 11.19) can be calculated in the simulation, making use of an ensemble average of stochastic low-cost fermions. Neglecting the fermion contribution, reproduces the familiar evolution equations of the chromo-electric fields in an expanding system of pure Yang-Mills theory [61].

11.3.1 Gauss Constraint

The $\nu = 0$ component of the equation of motion of the semi-classical model in the expanding box (eq. 11.21) can be interpreted as the expanding box variant of the Gauss constraint

$$\begin{aligned}\tau \sum_{i=1}^{2} \partial_i F^{i\tau,a}[\bar{A}](x) + \tau \partial_\eta F^{\eta\tau,a}[\bar{A}](x) - g\tau f^{abc} \sum_{i=1}^{2} \bar{A}_i^b(x) F^{i\tau,c}[\bar{A}](x) \\ - g\tau f^{abc} \bar{A}_\eta^b(x) F^{\eta\tau,c}[\bar{A}](x) = -g\mathrm{tr}\Big[\hat{F}_{\bar{A}}(x,x)\gamma^0 T^a\Big].\end{aligned} \tag{11.27}$$

Identifying the chromo-electric fields (eq. 9.26) and (eq. 9.27), this equation can be written as

$$\begin{aligned}\sum_{i=1}^{2} \Big(\partial_i E_i[\bar{A}](x) - g T^a f^{abc} \bar{A}_i^b(x) E_i^c[\bar{A}](x)\Big) \\ + \Big(\partial_\eta E_\eta[\bar{A}](x) - g T^a f^{abc} \bar{A}_\eta^b(x) E_\eta^c[\bar{A}](x)\Big) = -g T^a \mathrm{tr}\Big[\hat{F}_{\bar{A}}(x,x)\gamma^0 T^a\Big]\end{aligned} \tag{11.28}$$

When discretizing the equation, we replace

$$\sum_{i=1}^{2} \Big(\partial_i E_i[\bar{A}](x) - g T^a f^{abc} \bar{A}_i^b(x) E_i^c[\bar{A}](x)\Big) = \frac{1}{a_\perp} \sum_{i=1}^{2} \Big(E_i(x) - U_i^\dagger(x-\hat{i}) E_i(x-\hat{i}) U_i(x-\hat{i})\Big), \tag{11.29}$$

for the transverse part and in a similar fashion for the longitudinal part

$$\Big(\partial_\eta E_\eta[\bar{A}](x) - g T^a f^{abc} \bar{A}_\eta^b(x) E_\eta^c[\bar{A}](x)\Big) = \frac{1}{a_\eta}\Big(E_\eta(x) - U_\eta^\dagger(x-\hat{\eta}) E_\eta(x-\hat{\eta}) U_\eta(x-\hat{\eta})\Big). \tag{11.30}$$

For the fermion current we apply the Fock-Schwinger gauge $A_\tau = 0$

$$-g T^a \mathrm{tr}\Big[\hat{F}_{\bar{A}}(x,x)\gamma^0 T^a\Big] = -g T^a \mathrm{tr}\Big[\hat{F}(x+\hat{\tau},x)\gamma^0 T^a\Big]. \tag{11.31}$$

We can now define the color-matrix $C(x)$, that is used in the algorithm to restore the Gauss constraint [143]

$$\begin{aligned}C(x) = g^2 T^a \mathrm{tr}\Big[\hat{\bar{F}}(x+\hat{\tau},x)\gamma^0 T^a\Big] + \sum_{i=1}^{2} \Big(\bar{E}_i(x) - U_i^\dagger(x-\hat{i}) \bar{E}_i(x-\hat{i}) U_i(x-\hat{i})\Big) \\ + \frac{1}{a_\eta}\Big(\bar{E}_\eta(x) - U_\eta^\dagger(x-\hat{\eta}) \bar{E}_\eta(x-\hat{\eta}) U_\eta(x-\hat{\eta})\Big).\end{aligned} \tag{11.32}$$

We already introduced dimensionless lattice fields, by rescaling the fields in terms of $a_\perp$. The proper time dependent measure of the amount of Gauss violation can thus be defined as

$$C(\tau) = \sqrt{\frac{1}{V}\sum_{\mathbf{x}_\perp,\eta} \mathrm{tr}\Big[C^\dagger(x)C(x)\Big]}. \tag{11.33}$$

For the restoration of Gauss law, the chromo-electric fields are updated according to

$$\bar{E}_i(x) \;\rightarrow\; \bar{E}_i(x) + \gamma\Big[U_i(x)C(x+\hat{i})U_i^\dagger(x) - C(x)\Big] \tag{11.34}$$

$$\bar{E}_\eta(x) \;\rightarrow\; \bar{E}_\eta(x) + \gamma\Big[U_\eta(x)C(x+\hat{\eta})U_\eta^\dagger(x) - C(x)\Big]. \tag{11.35}$$

11.4 Renormalization

Finally, let us comment on a renormalization procedure for the semi-classical model in the expanding box. As it has been the case in the static box, our theory is naturally regularized by the lattice momentum cutoff, that can not be removed due to the UV-divergence of the semi-classical model in the continuum limit. As a consequence, renormalization plays the role of weighting the fermion and gauge sector appropriately, to maintain the correct dynamics of the system.

In analogy to the static box, the renormalization Z-factor can be evaluated from the fermion self energy, derived from the effective one-loop equation of motion of the semi-classical model (eq. 5.20). It is straight forward to repeat the derivation in the expanding box, leading to[2]

$$\partial_\mu \tau \bar{F}^{\mu\nu,a} - g\tau f^{abc}\bar{A}^b_\mu \bar{F}^{\mu\nu,c} - 2g\mathrm{tr}\Big[\hat{F}(x,x)\gamma^\nu T^a\Big] + \int \hat{\Sigma}^{\mu\nu,ab}(x-z)\bar{A}^b_\mu(z)d^4z = 0. \tag{11.36}$$

Choosing the scale of renormalization, setting $\mathbf{k} = 0$, the fermion self-energy in the expanding box can be written as

$$\begin{aligned}\Sigma^{\mu\nu,ab}_{\mathbf{0}}(\tau-\tau') = \mathrm{i}g^2 \int \mathrm{tr}\Big[&\hat{D}^<_{\mathbf{p}_\perp,\nu_p}(\tau-\tau')\gamma^\mu T^b \hat{D}^>_{\mathbf{p}_\perp,\nu_p}(\tau'-\tau)\gamma^\nu T^a \\ &- \hat{D}^>_{\mathbf{p}_\perp,\nu_p}(\tau-\tau')\gamma^\mu T^b \hat{D}^<_{\mathbf{p}_\perp,\nu_p}(\tau'-\tau)\gamma^\mu T^b\Big]\frac{d^2p_\perp d\nu_p}{(2\pi)^3}.\end{aligned} \tag{11.37}$$

The renormalization Z-factor has to be time and frame independent. Furthermore, it should preserve the longitudinal boost invariance and should not be depending on the initial time. We therefore derive it from the large time limit of the expanding box spinors, with the limit naturally satisfying both conditions. The large proper time mode functions are given as

$$\hat{\psi}^+_{\mathbf{k}_\perp,\nu,s,a}(\tau,\mathbf{x}_\perp,\eta) \overset{\tau\gg 1}{=} -\frac{\mathrm{i}}{\sqrt{2}} e^{-\mathrm{i}M_{\mathbf{k}_\perp}\tau + \mathrm{i}\mathbf{k}_\perp\mathbf{x}_\perp + \mathrm{i}\nu\eta} e^{\mathrm{i}\frac{\pi}{4}} u_{s,a}(\mathbf{k}_\perp), \tag{11.38}$$

$$\hat{\psi}^-_{\mathbf{k}_\perp,\nu,s,a}(\tau,\mathbf{x}_\perp,\eta) \overset{\tau\gg 1}{=} -\frac{\mathrm{i}}{\sqrt{2}} e^{\mathrm{i}M_{\mathbf{k}_\perp}\tau - \mathrm{i}\mathbf{k}_\perp\mathbf{x}_\perp - \mathrm{i}\nu\eta} e^{-\mathrm{i}\frac{\pi}{4}} v_{s,a}(\mathbf{k}_\perp). \tag{11.39}$$

[2]The hat indicates, that the statistical propagator and fermion self-energy has to be evaluated by making use of the expanding box spinors (eq. 9.16).

Using these expressions, we obtain the following lattice version of the expanding box spinor at large proper times

$$\hat{\psi}(\tau, x_\perp, \eta) \overset{\tau \gg 1}{=} -\frac{\mathrm{i}}{\sqrt{2}V} \sum_{\mathbf{k}_\perp,\nu} \sum_{s=1}^{2} \sum_{a=1}^{N_c} \Big(\hat{a}_{s,a}(\mathbf{k}_\perp,\nu) e^{-\mathrm{i}M_{\mathbf{k}_\perp}\tau + \mathrm{i}\mathbf{k}_\perp\mathbf{x}_\perp + \mathrm{i}\nu\eta} e^{\mathrm{i}\frac{\pi}{4}} u_{s,a}(\mathbf{k}_\perp) \\ + \hat{b}^\dagger_{s,a}(\mathbf{k}_\perp,\nu) e^{\mathrm{i}M_{\mathbf{k}_\perp}\tau - \mathrm{i}\mathbf{k}_\perp\mathbf{x}_\perp - \mathrm{i}\nu\eta} e^{-\mathrm{i}\frac{\pi}{4}} v_{s,a}(\mathbf{k}_\perp) \Big). \tag{11.40}$$

We can now derive the Wightman functions $\hat{D}^{\lessgtr}_{\mathbf{p}_\perp,\nu_p}(\tau - \tau')$ of free fermions in an expanding geometry. On the lattice we have

$$\hat{D}^{>}_{\mathbf{p}_\perp,\nu,\alpha\beta} = \sum_{\mathbf{x}_\perp,\eta} e^{-\mathrm{i}\mathbf{p}_\perp\mathbf{x}_\perp - \mathrm{i}\eta\nu} \Big\langle \hat{\psi}_\alpha(\tau, \mathbf{x}_\perp, \eta) \hat{\bar{\psi}}_\beta(\tau', \mathbf{0}) \Big\rangle, \tag{11.41}$$

$$\hat{D}^{<}_{\mathbf{p}_\perp,\nu,\alpha\beta} = -\sum_{\mathbf{x}_\perp,\eta} e^{-\mathrm{i}\mathbf{p}_\perp\mathbf{x}_\perp - \mathrm{i}\eta\nu} \Big\langle \hat{\bar{\psi}}_\beta(\tau', \mathbf{0}) \hat{\psi}_\alpha(\tau, \mathbf{x}_\perp, \eta) \Big\rangle. \tag{11.42}$$

The derivation is identical to the derivation of the Wightman functions in the static box (compare to Appendix B.3), leading to

$$\Big\langle \hat{\psi}_\alpha(\tau, \mathbf{x}_\perp, \eta) \hat{\bar{\psi}}_\beta(\tau', \mathbf{0}) \Big\rangle = \frac{1}{V} \sum_{\mathbf{k}_\perp,\nu} \frac{1}{2M_{\mathbf{k}_\perp}} \Big(\gamma^0 M_{\mathbf{k}_\perp} + \gamma^i s_i(\mathbf{k}_\perp) + \mu(\mathbf{k}_\perp) \Big)_{\alpha\beta} e^{-\mathrm{i}M_{\mathbf{k}_\perp}(\tau - \tau') + \mathrm{i}\mathbf{k}_\perp\mathbf{x}_\perp + \mathrm{i}\eta\nu}. \tag{11.43}$$

$$\Big\langle \hat{\bar{\psi}}_\beta(\tau', \mathbf{0}) \hat{\psi}_\alpha(\tau, \mathbf{x}_\perp, \eta) \Big\rangle = \frac{1}{V} \sum_{\mathbf{k}_\perp,\nu} \frac{1}{2M_{\mathbf{k}_\perp}} \Big(\gamma^0 M_{\mathbf{k}_\perp} + \gamma^i s_i(\mathbf{k}_\perp) - \mu(\mathbf{k}_\perp) \Big)_{\alpha\beta} e^{\mathrm{i}M_{\mathbf{k}_\perp}(\tau - \tau') - \mathrm{i}\mathbf{k}_\perp\mathbf{x}_\perp - \mathrm{i}\eta\nu}. \tag{11.44}$$

We are now able to repeat all the steps presented previously in context of the static box in (section 5.3). The only difference is, that our result in the expanding box is effectively two dimensional, due to the longitudinal boost invariance

$$\delta Z = -\frac{g^2}{4V_\perp} \sum_{\mathbf{k}_\perp} \frac{\mathbf{s}^2(\mathbf{k}_\perp)}{M^5_{\mathbf{k}_\perp}}, \tag{11.45}$$

where $V_\perp = N_x N y$. We also note, that the familiar fermion dispersion relation of the expanding geometry enters (eq. 11.45).

We are now able to perform a systematic counterterm renormalization for the semi-classical theory in the expanding box. This procedure leads to the following equations of motion of the chromo-electric fields

$$\bar{E}^a_i(x + \tau) = \bar{E}^a_i(x) + 2\bar{a}_\tau \mathrm{Im tr} \Big[T^a \bar{\tau} \sum_{i \neq j} \Big(U_{ji}(x) + U_{-ji}(x) \Big) + \frac{1}{\bar{\tau} a^2_\eta} T^a \Big(U_{\eta i}(x) + U_{-\eta i}(x) \Big) \Big] \\ + g^2 \frac{\bar{a}_\tau}{Z} \mathrm{Re tr} \Big[\hat{\bar{F}}(x + \hat{\imath}, x) \Big(\gamma^i - \mathrm{i} r_\perp \Big) T^a U_i(x) \Big], \tag{11.46}$$

$$\bar{E}^a_\eta(x + \tau) = \bar{E}^a_\eta(x) + \frac{2\bar{a}_\tau}{\bar{\tau} a_\eta} \sum_{i=1}^{2} \mathrm{Im tr} \Big[T^a \Big(U_{-i\eta}(x) + U_{i\eta}(x) \Big) \Big] + \frac{g^2 \bar{a}_\tau}{Z\bar{\tau}} \mathrm{Re tr} \Big[\hat{\bar{F}}(x + \hat{\eta}, x) \gamma^3 T^a U_\eta(x) \Big], \tag{11.47}$$

and to the following color matrix $C(x)$, that enters the restoration of Gauss law

$$C(x) = g^2 T^a \mathrm{tr}\Big[\hat{\bar{F}}(x+\hat{\tau},x)\gamma^0 T^a\Big] + Z\sum_{i=1}^{2}\Big(\bar{E}_i(x) - U_i^\dagger(x-\hat{i})\bar{E}_i(x-\hat{i})U_i(x-\hat{i})\Big) \qquad (11.48)$$
$$+\frac{Z}{a_\eta}\Big(\bar{E}_\eta(x) - U_\eta^\dagger(x-\hat{\eta})\bar{E}_\eta(x-\hat{\eta})U_\eta(x-\hat{\eta})\Big).$$

12 Expanding Box Observables

Having derived the equations of motion of the semi-classical approximation of QCD in the expanding geometry, we finally have to specify the observables, that will be measured in a lattice simulation of the system. As done in the static box, we derive the energy density and pressure from the diagonal components of the QCD energy-momentum tensor. To do so we have to specify the tensor in the expanding box at first. The same is true for the gauge invariant occupation of energy modes and we will again define it from the Fourier transform of the energy density. Having observed good agreement, when comparing the gauge variant and gauge invariant definition of the occupation of energy modes in the static box, we will restrict ourselves to the gauge invariant definition in the expanding box.

12.1 QCD Energy-Momentum Tensor in an Expanding Box

The energy-momentum tensor of a field theory can in general be derived from Noethers theorem, by considering translations in time and space for the Lagrangian of the theory (see e.g. [149]). In this section, we sketch the derivation of a tensor associated to these translations, from the Lagrangian of the expanding system (eq. 9.34). From Noethers theorem, this tensor can be derived from

$$\Theta^{\mu\nu}_{exp} = \frac{\partial \mathcal{L}^{exp}}{\partial\left(\partial_\mu A^a_\alpha\right)}\partial^\nu A^a_\alpha + \frac{\partial \mathcal{L}^{exp}}{\partial\left(\partial_\mu \psi\right)}\partial^\nu \psi - g^{\mu\nu}\mathcal{L}^{exp}. \tag{12.1}$$

Restricting ourselves to the Yang-Mills sector at first, we find

$$\Theta^{\mu\nu}_{exp,YM} = -\tau Z F^{\mu\alpha,a}\partial^\nu A^a_\alpha + \frac{Z}{4}\tau g^{\mu\nu} F^{\alpha\beta,a}F^a_{\alpha\beta}, \tag{12.2}$$

in a straight forward calculation. This result is neither symmetric nor gauge invariant. This problem is well known as non-uniqueness of the energy-momentum tensor in Yang-Mills theories and a solution has first been proposed in [165]. The idea is to add an additional, divergence free tensor to the given result. This has to be done in such a way, that the

resulting new tensor is symmetric and gauge invariant. In our case, the Belinfante tensor in an expanding system is given as

$$\chi^{\mu\beta\nu} = -2\frac{\partial \mathcal{L}_{exp}}{\partial F^a_{\mu\beta}} A^{\nu,a} = \tau F^{\mu\beta,a} A^{\nu,a}. \tag{12.3}$$

Adding this tensor and using the Yang-Mills equations of motion of the expanding box, we find the following symmetrized and gauge invariant result

$$T^{\mu\nu}_{exp,YM} = -\tau Z F^{\mu\beta,a} F^{\nu}_{\ \beta\ a} + \frac{1}{4} g^{\mu\nu} \tau F^{\alpha\beta,a} F^a_{\alpha\beta}. \tag{12.4}$$

Due to the appearance of an additional factor of τ, the resulting tensor does not have the same dimension as the energy-momentum tensor in a static box (eq. 6.5). Because of that it is not possible to naively identify the diagonal components of the tensor as physical quantities. We will discuss how to connect the diagonal components of (eq. 12.4) to the physical observables later in this section.[1]

It is straight forward to repeat the calculation for the Lagrangian of the fermion sector of QCD in an expanding system (eq. 9.30), leading to

$$\begin{aligned} T^{\mu\nu}_{\psi} =& - g^{\mu\nu} \hat{\bar{\psi}} \Big(\mathrm{i}\gamma^i D_i + \frac{\mathrm{i}}{\tau}\gamma^3 D_\eta - m + r\frac{a_\perp}{2}\Box^\perp_W \Big) \hat{\psi} \\ &+ \frac{1}{4}\Big(\hat{\bar{\psi}} \mathrm{i} D^\mu \gamma^\nu \hat{\psi} + \hat{\bar{\psi}} \mathrm{i} D^\nu \gamma^\mu \hat{\psi} + \hat{\bar{\psi}} \mathrm{i} \overleftarrow{D}^\mu \gamma^\nu \hat{\psi} + \hat{\bar{\psi}} \mathrm{i} \overleftarrow{D}^\nu \gamma^\mu \hat{\psi} \Big), \end{aligned} \tag{12.5}$$

where we have formally included the transverse Wilson term and used short notation for

$$\gamma^\eta = \frac{1}{\tau}\gamma^3. \tag{12.6}$$

Note that this result has the same dimension as the Yang-Mills tensor (eq. 12.4).

12.1.1 Energy Density and Pressure in Yang-Mills Theory

Let us start the derivation of the energy density and pressure by restricting ourselves to the Yang-Mills theory. The energy density should be connected to the 00-component of the tensor (eq. 12.4)

$$\begin{aligned} T^{00}_{exp,YM} =& - \tau Z F^{0\beta,a} F^{0}_{\ \beta\ a} + \frac{Z}{4} g^{00} \tau F^{\alpha\beta,a} F^a_{\alpha\beta} \\ =& \frac{\tau Z}{2}\left[F^{a2}_{\tau i} + \frac{1}{\tau^2} F^{a2}_{\tau\eta} + F^{a2}_{12} + \frac{1}{\tau^2} F^{a2}_{i\eta} \right] = Z\mathrm{tr}\left[\tau F^2_{\tau i} + \frac{1}{\tau} F^2_{\tau\eta} + \tau F^2_{12} + \frac{1}{\tau} F^2_{i\eta} \right]. \end{aligned} \tag{12.7}$$

It is possible to identify the chromo-electric fields (eq. 9.26) and (eq. 9.27), arriving at

$$T^{00}_{exp,YM} = Z\mathrm{tr}\left[\frac{1}{\tau} E^2_i + \tau E^2_\eta + \tau F^2_{12} + \frac{1}{\tau} F^2_{i\eta} \right] \equiv \mathcal{H}_{exp,YM}. \tag{12.8}$$

[1] In fact, the name *energy-momentum tensor* seems not to be appropriate in this case, because the tensor has a different dimensionality. The resulting tensor should more likely be viewed as the tensor associated to translations in time and space of the expanding box Lagrangian of the semi-classical model in the expanding box, derived within Noethers' theorem.

As expected, the result is identical to the Hamiltonian of Yang-Mills theory in the expanding box, (eq. 9.29). The corresponding Hamilton function is now given by integrating position[2]

$$H_{YM} = \int \mathcal{H}^{exp}_{YM} d^2x_\perp d\eta = \int Z\mathrm{tr}\left[\frac{1}{\tau}E_i^2 + \tau E_\eta^2 + \tau F_{12}^2 + \frac{1}{\tau}F_{i\eta}^2\right] d^2x_\perp d\eta. \tag{12.9}$$

The Hamilton function represents the energy of the system, which is observable in an experiment. On the other hand we know that the energy can also be written as

$$H_{YM} = \int \epsilon_{YM}(\tau, \mathbf{x}_\perp, \eta)\tau d^2x_\perp d\eta, \tag{12.10}$$

where $\epsilon_{YM}(\tau, \mathbf{x}_\perp, \eta)$ is the energy density of the system in Milne coordinates. Comparing both equations, we can deduce the physical energy density from the 00-component of the tensor (eq. 12.4) of Yang-Mills theory in the expanding box

$$\epsilon_{YM}(\tau, \mathbf{x}_\perp, \eta) = \frac{Z}{\tau}\mathcal{H}^{exp}_{YM} = \mathrm{tr}\left[\frac{1}{\tau^2}E_i^2 + E_\eta^2 + F_{12}^2 + \frac{1}{\tau^2}F_{i\eta}^2\right]. \tag{12.11}$$

We point out, that this result is equivalent to the definition in [61]. We have derived the energy density in the expanding box the other way around: We derived a gauge invariant tensor from the Lagrangian of the semi-classical approximation of QCD in the expanding box, using Noethers theorem. Afterwards, we connected the diagonal components of the resulting tensor to the measurable energy density.

The lattice discretized version of the energy density of Yang-Mills theory in the expanding box, is given as

$$g^2 a_\perp^4 \epsilon_{YM}(\tau, \mathbf{x}_\perp, \eta) = Z\mathrm{Retr}\left[\frac{1}{\bar\tau^2}\bar E_i^2 + \bar E_\eta^2 + 2\Big(1 - U_{12}\Big) + \frac{2}{a_\eta^2\bar\tau^2}\sum_{i=1}^{2}\Big(1 - U_{i\eta}\Big)\right]. \tag{12.12}$$

We already rescaled this result in terms of the lattice spacing $a_\perp$, making it dimensionless. In analogy to the static box, we can additionally define a longitudinal and a transverse, as well as chromo-electric and chromo-magnetic part of the energy density

$$g^2 a_\perp^4 \epsilon_L^E(\tau) = \frac{Z}{V}\sum_{\mathbf{x}} \mathrm{tr}\bar E_\eta^2, \qquad g^2 a_\perp^4 \epsilon_T^E(\tau) = \frac{Z}{V}\sum_{\mathbf{x}} \frac{1}{\bar\tau^2}\sum_{i=1}^{2}\mathrm{tr}\bar E_i^2, \tag{12.13}$$

$$g^2 a_\perp^4 \epsilon_L^B(\tau) = \frac{Z}{V}\sum_{\mathbf{x}} 2\mathrm{Retr}\Big(1 - U_{12}\Big), \qquad g^2 a_\perp^4 \epsilon_T^B(\tau) = \frac{Z}{V}\sum_{\mathbf{x}} \frac{2}{a_\eta^2\tau^2}\sum_{i=1}^{2}\mathrm{Retr}\Big(1 - U_{i\eta}\Big), \tag{12.14}$$

where we have taken a lattice average as well.

We now repeat the previous discussion for the pressure. This can be done in a straight forward way in case of the transverse pressure, starting from the ii-component of the tensor (eq. 12.4), with $i \in \{1, 2\}$

$$\begin{aligned} T^{ii}_{exp,YM} =& -\tau Z F^{i\beta,a} F^{i\ a}_{\ \beta} + \frac{Z}{4} g^{ii}\tau F^{\alpha\beta,a}F^a_{\alpha\beta} \\ =& -\tau Z F^{a2}_{\tau i} + \frac{Z}{2\tau}F^{a2}_{\tau\eta} + \frac{Z}{\tau}F^{a2}_{i\eta} + \frac{\tau Z}{2}F^{a2}_{12} + \frac{Z}{2}\sum_{i=2}^{2}\left(\tau F^{a2}_{\tau i} - \frac{Z}{\tau}F^{a2}_{i\eta}\right). \end{aligned} \tag{12.15}$$

[2]The factor of $\sqrt{-g} = \tau$ does not appear in the integration, because we already included it in the definition of the Yang-Mills Lagrangian for an expanding geometry, (eq. 9.25).

After identifying the chromo-electric fields (eq. 9.26) and (eq. 9.27), this can be written as

$$T^{ii}_{exp,YM} = -\frac{Z}{\tau}E_i^{a2}(x) + \frac{\tau Z}{2}E_\eta^{a2} + \frac{Z}{\tau}F_{i\eta}^{a2} + \frac{\tau Z}{2}F_{12}^{a2} + \frac{Z}{2\tau}\sum_{i=1}^{2}\Big(E_i^{a2} - F_{i\eta}^{a2}\Big). \tag{12.16}$$

We can now define the transverse component of the tensor on the lattice, discretizing the tensor and rescaling all fields in terms of $a_\perp$, making them dimensionless

$$g^2 a_\perp^3 T^{YM}_{exp,T} = \frac{g^2 a_\perp^3}{2}\sum_{i=1}^{2} T^{ii}_{exp,YM} = \bar{\tau} Z \mathrm{Re\ tr}\Big(\bar{E}_\eta^2(x) + 2\Big(1 - U_{12}\Big)\Big). \tag{12.17}$$

The longitudinal direction is given by the $\eta\eta$-component of the tensor (eq. 12.4),

$$\begin{aligned} T^{\eta\eta}_{YM} =& -\tau Z F^{\eta\beta,a}F^{\ \ a}_{\eta\ \ \beta} + \frac{Z}{4}g^{\eta\eta}\tau F^{\alpha\beta,a}F^a_{\alpha\beta} = -\frac{Z}{\tau^3}g^{\alpha\beta}F^a_{\eta\alpha}F^a_{\eta\beta} - \frac{Z}{4\tau}F^{\alpha\beta,a}F^a_{\alpha\beta} \\ =& -\frac{Z}{2\tau^3}F_{\tau\eta}^{a2} + \frac{Z}{2\tau^3}\sum_{i=1}^{2}F_{i\eta}^{a2} + \frac{Z}{2\tau}F_{\tau i}^{a2} - \frac{Z}{2\tau}F_{12}^{a2}. \end{aligned} \tag{12.18}$$

Making use of the chromo-electric fields (eq. 9.26) and (eq. 9.27) again and discretizing the result, using dimensionless lattice quantities, we find

$$g^2 a_\perp^5 T^{\eta\eta}_{YM} = \frac{Z}{\bar{\tau}}\mathrm{Re\ tr}\Big(\bar{E}_\eta^2 + \frac{2}{a_\eta^2\bar{\tau}^2}\sum_{i=1}^{2}\Big(1 - U_{i\eta}\Big) + \frac{1}{\bar{\tau}^2}\bar{E}_i^2 - 2\Big(1 - U_{12}\Big)\Big). \tag{12.19}$$

Comparing the transverse and the longitudinal component (eq. 12.17) and (eq. 12.19), one notices, that they have a different dimensionality. This occurs because of the additional appearance of a factor of $1/\tau^2$ in the longitudinal component, due to the metric of Milne coordinates (eq. 9.4). This appearance changes the dimensionality of the longitudinal component by a factor of $lenght^2$. We follow [61] and compensate this, by additionally including an explicit factor of τ^2 in the longitudinal component

$$g^2 a_\perp^3 \bar{\tau}^2 T^{\eta\eta}_{YM} = \bar{\tau} Z \mathrm{Re\ tr}\Big(\bar{E}_\eta^2 + \frac{2}{a_\eta^2\bar{\tau}^2}\sum_{i=1}^{2}\Big(1 - U_{i\eta}\Big) + \frac{1}{\bar{\tau}^2}\bar{E}_i^2 - 2\Big(1 - U_{12}\Big)\Big) \tag{12.20}$$

We can now define the pressure of the system in a similar fashion as presented in case of the energy density[3]

$$\bar{P}_T^{YM} = g^2 a_\perp^4 P_T^{YM} = Z\mathrm{Re\ tr}\Big(\bar{E}_\eta^2(x) + 2\Big(1 - U_{12}\Big)\Big), \tag{12.21}$$

$$\bar{P}_L^{YM} = g^2 a_\perp^4 P_L^{YM} = Z\mathrm{Re\ tr}\Big(E_\eta^2 + \frac{2}{a_\eta^2\tau^2}\sum_{i=1}^{2}\Big(1 - U_{i\eta}\Big) + \frac{1}{\tau^2}E_i^2 - 2\Big(1 - U_{12}\Big)\Big). \tag{12.22}$$

This result can also be written as a function of the longitudinal and transverse components of the chromo-electric and chromo-magnetic energy density

$$\bar{P}_T^{YM}(\tau) = \Big(\bar{\epsilon}_L^E(\tau) + \bar{\epsilon}_L^B(\tau)\Big), \tag{12.23}$$

$$\bar{P}_L^{YM}(\tau) = \Big(\bar{\epsilon}_T^E(\tau) + \bar{\epsilon}_T^B(\tau) - \bar{\epsilon}_L^E(\tau) - \bar{\epsilon}_L^B(\tau)\Big). \tag{12.24}$$

[3]We emphasize that this definition again matches the definition in [61].

12.1.2 Energy Density and Pressure of the Fermion Sector of QCD

Let us now turn to the derivation of the energy density and pressure for the fermion sector of QCD. Again, the starting point is provided by the tensor (eq. 12.5), derived from the Lagrangian of the fermion sector of QCD in an expanding geometry. As done in case of the Yang-Mills sector, we will connect the 00-component of the tensor to the physical energy density in the expanding box. The 00-component is given as

$$T^{\tau\tau}_{\psi,exp} = -\, g^{\tau\tau}\mathcal{L}^{exp}_f + \frac{1}{4}\Big(\hat{\bar{\psi}}\mathrm{i}D^\tau\gamma^0\hat{\psi} + \hat{\bar{\psi}}\mathrm{i}D^\tau\gamma^0\hat{\psi} + \hat{\bar{\psi}}\mathrm{i}\overleftarrow{D}^\tau\gamma^0\hat{\psi} + \hat{\bar{\psi}}\mathrm{i}\overleftarrow{D}^\tau\gamma^0\hat{\psi}\Big) = -\mathcal{L}^{exp}_\psi + \hat{\bar{\psi}}\mathrm{i}\gamma^0 D_\tau\hat{\psi}. \tag{12.25}$$

Discretizing this result, we find

$$\begin{aligned} T^{\tau\tau}_{\psi,exp} =& \Bigg[\hat{\bar{\psi}}\Big(m + \frac{2r_\perp}{a_\perp}\Big)\hat{\psi} - \frac{\mathrm{i}}{2a_\eta\tau}\Big(\hat{\bar{\psi}}(x)\gamma^3 U_\eta(x)\hat{\psi}(x+\hat{\eta}) - \hat{\bar{\psi}}(x)\gamma^3 U^\dagger_\eta(x-\hat{\eta})\hat{\psi}(x-\hat{\eta})\Big) \\ & - \frac{\mathrm{i}}{2a_\perp}\sum_{i=1}^{2}\Big(\hat{\bar{\psi}}(x)\big(\gamma^i - \mathrm{i}r_\perp\big)U_i(x)\hat{\psi}(x+\hat{i}) - \hat{\bar{\psi}}(x)\big(\gamma^i + \mathrm{i}r_\perp\big)U^\dagger_i(x-\hat{i})\hat{\psi}(x-\hat{i})\Big)\Bigg], \end{aligned} \tag{12.26}$$

where we included the transverse Wilson term as well. As observed in case of the Yang-Mills sector, this result is equivalent to the Hamiltonian of the fermion sector of QCD in an expanding geometry (eq.9.32)

$$T^{\tau\tau}_{\psi,exp} \equiv \mathcal{H}^{exp}_f. \tag{12.27}$$

In contrast to the Yang-Mills sector, where the gauge fields are assumed to be classical to leading order, the fermion fields are of quantum nature, hence (eq. 12.26) is an operator. The observable therefore has to be calculated by taking an expectation value of (eq. 12.26) with respect to the semi-classical partition function (eq. 11.20). As it has been the case in the static box, taking the expectation value allows us to rewrite the observable in terms of the statistical propagator

$$\begin{aligned} g^2 a_\perp^3 T^{\tau\tau}_{\psi,exp} =& \frac{g^2}{V}\sum_{\mathbf{x}}\Bigg[-\big(\bar{m} + 2r_\perp\big)\mathrm{tr}\Big[\hat{\bar{F}}(x,x)\Big] \\ & + \frac{\mathrm{i}}{2a_\eta\bar{\tau}}\Bigg(\mathrm{tr}\Big[\hat{\bar{F}}(x+\hat{\eta},x)\gamma^3 U_\eta(x)\Big] - \mathrm{tr}\Big[\hat{\bar{F}}(x-\hat{\eta},x)\gamma^3 U^\dagger_\eta(x-\hat{\eta})\Big] \\ & + \frac{\mathrm{i}}{2}\sum_{i=1}^{2}\Big(\mathrm{tr}\Big[\hat{\bar{F}}(x+\hat{i},x)\big(\gamma^i - \mathrm{i}r\big)U_i(x)\Big] - \mathrm{tr}\Big[\hat{\bar{F}}(x-\hat{i},x)\big(\gamma^i + \mathrm{i}r\big)U^\dagger_i(x-\hat{i})\Big]\Big)\Bigg)\Bigg], \end{aligned} \tag{12.28}$$

where we introduced dimensionless lattice quantities, by rescaling in terms of the lattice spacing $a_\perp$. In the lattice simulation, the statistical propagator can be calculated from an ensemble average of stochastic low-cost fermions, as discussed in (section 2.2.2). Keeping in mind, that at initial time τ_0, the statistical fermion propagator is calculated with respect to the free vacuum $|0\rangle$. When doing so, we already discussed in context of the static box in (section 6.2.2), that the fermion expectation values pick up a vacuum contribution, that is infinite in the continuum limit, but naturally regularized on the lattice. Consequently, we have to subtract this vacuum contribution to obtain the correct expectation value.

The total energy of the system is given from integrating (eq. 12.28), making use of the definition of the scalar product of the expanding box spinors (eq. 9.17)

$$H_f = \int \mathcal{H}_f^{exp} d^2x_\perp d\eta. \tag{12.29}$$

As presented previously in context of Yang-Mills theory, we now use the total energy of the fermion sector, to connect (eq. 12.28) to the energy density, making use of (eq. 12.10)

$$\bar{\epsilon}_{\psi,exp} = g^2 a_\perp^4 \epsilon_{\psi,exp} = \frac{g^2 a_\perp^4}{\tau} \mathcal{H}_f^{exp}. \tag{12.30}$$

We can now repeat all previous steps for the spacial diagonal components of (eq. 12.5), connecting them with the pressure of the system. We start with the 11-component

$$\begin{aligned} T^{11}_{\psi,exp} =& - g^{11}\mathcal{L}_f^{exp} + \frac{1}{4}\Big(\hat{\bar{\psi}}\mathrm{i}g^{11}D_1\gamma^1\hat{\psi} + \hat{\bar{\psi}}\mathrm{i}g^{11}D_1\gamma^1\hat{\psi} + \hat{\bar{\psi}}\mathrm{i}g^{11}\overleftarrow{D}_1\gamma^1\hat{\psi} + \hat{\bar{\psi}}\mathrm{i}g^{11}\overleftarrow{D}_1\gamma^1\hat{\psi}\Big) \\ =& \mathcal{L}_f^{exp} - \frac{1}{2}\Big(\hat{\bar{\psi}}\mathrm{i}D_1\gamma^1\hat{\psi} + \hat{\bar{\psi}}\mathrm{i}\overleftarrow{D}_1\gamma^1\hat{\psi}\Big). \end{aligned} \tag{12.31}$$

We now use, that the expanding box Dirac equation (eq. 9.20) is satisfied at every time-step of the simulation. Because it directly enters the Lagrangian of the fermion sector (eq. 9.30), it does not contribute in (eq. 12.31) and can be eliminated

$$T^{11}_{\psi,exp} = - \frac{\mathrm{i}}{2}\Big(\hat{\bar{\psi}}D_1\gamma^1\hat{\psi} + \hat{\bar{\psi}}\overleftarrow{D}_1\gamma^1\hat{\psi}\Big) = -\mathrm{i}\hat{\bar{\psi}}D_1\gamma^1\hat{\psi}. \tag{12.32}$$

In a next step, we discretize the result and introduce rescaled, dimensionless lattice quantities. Furthermore, we take the expectation value with respect to the partition function of the semi-classical effective theory (eq. 11.20), making it possible to identify the statistical fermion propagator

$$\begin{aligned} g^2 a_\perp^3 T^{11}_{\psi,exp} = \frac{\mathrm{i}g^2}{2}\Bigg(&\mathrm{tr}\Big[\hat{\bar{F}}\Big(x+\hat{1},x\Big)\Big(\gamma^1 - \mathrm{i}r_\perp\Big)U_1(x)\Big] + 2\mathrm{i}r_\perp \mathrm{tr}\Big[\hat{\bar{F}}(x,x)\Big] \\ &- \mathrm{tr}\Big[\hat{\bar{F}}\Big(x-\hat{1},x\Big)\Big(\gamma^1 + \mathrm{i}r_\perp\Big)U_1^\dagger(x-\hat{1})\Big]\Bigg). \end{aligned} \tag{12.33}$$

A similar calculation can easily be repeated for the 22-component of (eq. 12.5) and combining both, we are able to define the transverse component

$$\begin{aligned} g^2 a_\perp^3 T^T_{\psi,exp} = \frac{g^2 a_\perp^3}{2}\sum_{i=1}^{2} T^{ii}_{\psi,exp} = \frac{\mathrm{i}g^2}{4}\sum_{i=1}^{2}\Bigg(&\mathrm{tr}\Big[F\Big(x+\hat{i},x\Big)\Big(\gamma^i - \mathrm{i}r_\perp\Big)U_i(x)\Big] + 2\mathrm{i}r_\perp \mathrm{tr}\Big[\hat{F}(x,x)\Big] \\ &- \mathrm{tr}\Big[F\Big(x-\hat{i},x\Big)\Big(\gamma^i + \mathrm{i}r_\perp\Big)U_i^\dagger(x-\hat{i})\Big]\Bigg). \end{aligned} \tag{12.34}$$

Next we consider the longitudinal direction, given by the $\eta\eta$-direction of (eq. 12.5)

$$\begin{aligned} T^{\eta\eta}_{\psi,exp} =& - g^{\eta\eta}\mathcal{L}_f^{exp} + \frac{1}{4}\Big(\hat{\bar{\psi}}\mathrm{i}g^{\eta\eta}D_\eta\frac{1}{\tau}\gamma^3\hat{\psi} + \hat{\bar{\psi}}\mathrm{i}g^{\eta\eta}D_\eta\frac{1}{\tau}\gamma^3\hat{\psi} + \hat{\bar{\psi}}\mathrm{i}g^{\eta\eta}\overleftarrow{D}_\eta\frac{1}{\tau}\gamma^3\hat{\psi} + \hat{\bar{\psi}}\mathrm{i}g^{\eta\eta}\frac{1}{\tau}\overleftarrow{D}_\eta\gamma^3\hat{\psi}\Big) \\ =& \frac{1}{\tau^2}\mathcal{L}_f^{exp} - \frac{1}{2\tau^3}\Big(\hat{\bar{\psi}}\mathrm{i}D_\eta\gamma^3\hat{\psi} + \hat{\bar{\psi}}\mathrm{i}\overleftarrow{D}_\eta\gamma^3\hat{\psi}\Big). \end{aligned} \tag{12.35}$$

Again we can eliminate the Lagrangian, making use of the Dirac equation (eq. 9.20)

$$T^{\eta\eta}_{\psi,exp} = -\frac{1}{2\tau^3}\left(\hat{\bar{\psi}}\mathrm{i}D_\eta\gamma^3\hat{\psi} + \hat{\bar{\psi}}\mathrm{i}\overleftarrow{D}_\eta\gamma^3\hat{\psi}\right) = -\frac{1}{\tau^3}\hat{\bar{\psi}}\mathrm{i}D_\eta\gamma^3\hat{\psi}. \tag{12.36}$$

As discussed previously in the context of the Yang-Mills sector, the result differs in dimensionality when compared to the transverse direction, due to the additional contribution of $1/\tau^2$, entering from the metric of Milne coordinates (eq. 9.4). We compensate this in similar fashion as presented in case of the Yang-Mills sector, defining

$$\tau^2 T^{\eta\eta}_{\psi,exp} = -\frac{1}{\tau}\hat{\bar{\psi}}\mathrm{i}D_\eta\gamma^3\hat{\psi}. \tag{12.37}$$

In a final step, we discretize the result, introducing dimensionless, rescaled fields and take the expectation with respect to the partition function of the semi-classical effective theory (eq. 11.20),

$$g^2 a_\perp^3 \tau^2 T^{\eta\eta}_{\psi,exp} = \frac{\mathrm{i}g^2}{2a_\eta\bar{\tau}}\left(\mathrm{tr}\left[\hat{\bar{F}}\big(x+\hat{\eta},x\big)\gamma^3 U_\eta(x)\right] - \mathrm{tr}\left[\hat{\bar{F}}\big(x-\hat{\eta},x\big)\gamma^3 U^\dagger_\eta(x-\hat{\eta})\right]\right). \tag{12.38}$$

As discussed in the context of the energy density, we have to renormalize the expectation values at initial time, making it finally possible to define the pressure of the fermion sector in analogy to the Yang-Mills sector

$$g^2 a_\perp^4 P^T_{\psi,exp} = g^2 a_\perp^4 \frac{1}{\tau} T^T_{\psi,exp}, \tag{12.39}$$

$$g^2 a_\perp^4 P^L_{\psi,exp} = g^2 a_\perp^4 \frac{1}{\tau}\big(\tau^2 T^L_{\psi,exp}\big). \tag{12.40}$$

The traces of statistical propagators can be evaluated in the lattice simulation by making use of ensemble averages of stochastic low-cost fermions.

12.1.3 Longitudinal Rapidity Fluctuations

As discussed in (section 3.4), in a pure Yang-Mills simulation of the Glasma, no pressure isotropy has been reached, because the boost invariance of the initial state is preserved by the covariant Hamilton equations of motion [61, 62]. We showed in (section 8.2), that pressure isotropy is reached in a static box, when explicitly breaking longitudinal boost invariance. The isotropization is then caused from the development of a chromo-Weibel instability. In the expanding box pressure isotropization is still prevented by the rapid longitudinal expansion of the system, also when explicitly breaking boost invariance, as pointed out in [61, 62]. Nevertheless it is possible to identify the development of an instability in the expanding system. It has been shown in [61] that the evolution of this instability can be studied from the Fourier transform of the longitudinal pressure component of the Yang-Mills sector

$$\tilde{P}^L_{YM}(\tau,\nu) = \int\int e^{\mathrm{i}\eta\nu} P_L(\tau, x_\perp, \eta) d\eta d^2 x_\perp. \tag{12.41}$$

The transverse direction has simply been integrated. The discretized version of (eq. 12.41) is therefore given as

$$\tilde{P}^L_{YM}(\tau,\nu) = \frac{1}{N_\perp^2}\sum_{\mathbf{x}_\perp}\frac{1}{N_\eta}\sum_\eta e^{\mathrm{i}\nu\eta} P_L(\tau, x_\perp, \eta). \tag{12.42}$$

Note that the given quantity (eq. 12.42) is not an observable quantity in an experiment. Only the $\nu = 0$ component corresponds to the longitudinal pressure, that can indeed be measured. Besides this, the $\nu \neq 0$ components of the Fourier transformed pressure give interesting information on the evolution of the system. As argued in [61] one can show, that in the boost invariant case, the quantity (eq. 12.42) is strictly zero, except of the $\nu = 0$ component. On the other hand, for non-vanishing quantum fluctuations of magnitude Δ, (eq. 12.42) picks up a contribution in longitudinal Fourier modes with $\nu \neq 0$ [61]. In practice, we will restrict ourselves to $\nu = 1$ because it maximizes the Fourier transform besides the $\nu = 0$ case.

The reason for this behavior is connected to the physical interpretation of the Fourier conjugate of the space-time rapidity η, the wave number ν. It can be interpreted as a measure to quantify inhomogenity along the longitudinal beam axis [112]. An observable with $\nu = 0$ thus represents the boost invariant „background“, whereas the other components can be interpreted as fluctuations on that background. If these fluctuations increase exponentially during the evolution of the system, such a process is known as the development of a (quantum) instability. For more details see [112].

We will use this approach to search for an instability in the semi-classical effective theory of QCD as well, that could possibly be caused from the interaction of the classical Yang-Mills fields of the Glasma with fermions. We emphasize, that the scenario with fermions is different when compared to the pure Yang-Mills simulation, because quantum fluctuations do not enter from a modification of the initial conditions (eq. 3.22) only, but dynamically at every time-step of the simulation. The idea therefore is, to measure the effect of the back-coupling of fermions onto the Yang-Mills fields, in the rapidity distribution of the Fourier transformed longitudinal pressure of the Yang-Mills sector and compare it to the pure Yang-Mills scenario.

12.2 Gauge Invariant Occupation of Energy Modes

To study the occupation of energy modes, that provides interesting insights into the dynamics of the system and the validity of the classical approximation, we define the gauge invariant occupation of energy modes in the expanding box. As in case of the static box, starting point for the gauge invariant definition is the Fourier transform of the energy density. In case of an expanding geometry, it is constructed by combining the Fourier transform of transverse position $\mathbf{x}_\perp$ and the Fourier transform of the space-time rapidity η

$$\tilde{\bar{\epsilon}}(\tau, \mathbf{k}_\perp, \nu) = \frac{1}{\sqrt{V_\perp}} \sum_{n_x=0}^{N_x-1} \sum_{n_y=0}^{N_y-1} e^{-\mathrm{i} \sum_{i=1}^{2} \bar{k}_i n_i} \frac{1}{\sqrt{N_\eta}} \sum_{n_\eta=0}^{N_\eta-1} \bar{\epsilon}(\tau, \mathbf{x}_\perp, \eta) e^{-\mathrm{i}\bar{\nu} n_\eta}, \tag{12.43}$$

where we defined $\bar{k}_i = a_\perp k_i$ and $\bar{\nu} = a_\eta \nu$ and the reciproke lattice is given as

$$\tilde{\Lambda} = \Big\{ \mathbf{k} = \big(\mathbf{k}_\perp, \nu\big); \quad k_{\perp,i} = \frac{2\pi}{a_\perp N_{\perp,i}} n_{\perp,i}, \nu = \frac{2\pi}{a_\eta N_\eta} n_\eta, \tag{12.44}$$
$$n_{\perp,i} \in \big[-N_{\perp,1}/2 + 1, ..., 0, ..., N_{\perp,i}/2 \big], n_\eta \in \big[-N_\eta/2 + 1, ..., 0, ..., N_\eta/2 \big] \Big\}.$$

The most important difference in the definition of the occupation of energy modes in the expanding geometry, when compared to the static box, is the lattice dispersion relation of

the fields, that enters the definition. The definition of the occupation of energy modes in the static box is frame dependent. Adopting this definition in the expanding box would lead to a situation, where the longitudinal modes change by time and no longitudinal boost invariance is given. As a consequence, an invariant definition can only be provided if we restrict ourselves to the transverse planes with fixed longitudinal Fourier mode ν. In [58] it has been argued that this approach is reasonable in a highly anisotropic system, with the characteristic transverse momenta being much larger than the longitudinal ones

$$\omega_{\mathbf{p}}^2 \approx \mathbf{p}_\perp^2, \qquad \omega_{\mathbf{p}}^2 \approx M_{\mathbf{p}_\perp}^2, \tag{12.45}$$

for massless bosons and massive fermions respectively. Note, that the latter one matches our previous observation for the solution of the free Dirac equation in an expanding geometry in (section 10.2), where $M_{\mathbf{p}_\perp}$ has been identified as the effectively two-dimensional dispersion relation of fermions in the expanding box. Because of the Glasma initial conditions (section 3.4), only energy modes with $\nu = 0$ are initially occupied in the Yang-Mills sector. When evolving the system in time, we expect the occupation of energy modes to spread from the plane with $\nu = 0$ to the other planes.

For the definition of the gauge invariant occupation of energy modes in the expanding box, we weight the Fourier modes of the energy density (eq. 12.43) with the corresponding lattice dispersion relation, either for the massless gauge fields or the massive fermion fields. The effective two dimensional dispersion relation in the different rapidity planes, is given as

$$\hat{p}^2 = \frac{4}{a_\perp^2} \sum_{i=1}^{2} \sin^2\left(\frac{a_\perp p^i}{2}\right), \tag{12.46}$$

in case of massless Yang-Mills fields and in case of the fermion sector it has already been derived in (eq. 10.10)

$$\omega_{\mathbf{p}}^2 = M_{\mathbf{p}_\perp}^2 = \frac{1}{a_\perp^2} \sum_{i=1}^{2} \sin\left(a_\perp p^i\right) + \mu^2(\mathbf{p}_\perp). \tag{12.47}$$

We define the occupation of modes in the transverse plane at fixed longitudinal Fourier mode ν as

$$\bar{n}_{YM}(\tau, \nu, \hat{p}) = \frac{1}{\hat{p}} \Big\langle \Big| \tilde{\bar{\epsilon}}_{YM}(\tau, \nu, \mathbf{p}_\perp) \Big| \Big\rangle_{\mathbf{p}_\perp}, \tag{12.48}$$

$$\bar{n}_{\psi}(\tau, \nu, M_{\mathbf{p}_\perp}) = \frac{1}{M_{\mathbf{p}_\perp}} \Big\langle \Big| \tilde{\bar{\epsilon}}_{\psi}(\tau, \nu, \mathbf{p}_\perp) \Big| \Big\rangle_{\mathbf{p}_\perp}, \tag{12.49}$$

where $\Big\langle ... \Big\rangle_{\mathbf{p}_\perp}$ marks the average of modes with the same dispersion relation in the rapidity plane. We will also compute the averages of the occupation in the transverse plane $\bar{n}_{YM}(\tau, \nu)$ and $\bar{n}_{\psi}(\tau, \nu)$, to demonstrate how planes with $\nu \neq 0$ become occupied during the evolution of the system.

13
Results for the Expanding Box

In this chapter we give the results of simulations of the semi-classical approximation of QCD in a longitudinal expanding system. We initialize the Yang-Mills fields by making use of the CGC effective theory, creating the Glasma at initial time. We furthermore introduce vacuum fermions to the Glasma and couple the Yang-Mills and fermion fields at the first time-step of the simulation. As discussed in (chapter 9), the longitudinal expansion of the system has been realized by introducing Milne (Bjorken) coordinates.

We do not modify the parameters for the construction of the initial gauge link ensemble, presented in [126] and previously discussed in (chapter 8). We choose the infrared cutoff for the solution of the Poisson equation to be $m/Q = 0.1$ and the number of infinitesimally thin color sheets $N_y = 30$. The UV-momentum cutoff is provided by the lattice cutoff $p_i = \frac{\pi}{a_i}$. We introduced an additional index for the lattice spacing a_i, because we have to deal with two different spacings in case of a longitudinal expanding system, a transverse lattice spacing $a_\perp$ and a dimensionless longitudinal lattice spacing a_η. As discussed in (section 3.5), the physical parameters entering the CGC effective theory are chosen such, that they correspond to *Pb-Pb* collisions at center-of-mass energies of $\sqrt{s} = 5.02$ TeV at the LHC. The corresponding momentum scale for gluon saturation is given as $Q_s = 1.867$ GeV and the appropriate coupling at the saturation scale is given as $g \approx 2$.

Fermion observables are computed by making use of the stochastic low-cost method (section 2.2.2), choosing a stochastic fermion ensemble of size $N_{ens} = 750$. Because the expanding geometry has a singularity at $\tau = 0$, we have to choose a finite initial time τ_0. As initial time we choose a time of $\tau_0 = 0.1$ fm, which is assumed to be the formation time of the Glasma [38], but enters the solution of vacuum fermions in an expanding box (eq. 10.80) as well. We choose a value of $\gamma = 0.01$ for the parameter entering the restoration algorithm of Gauss law (eq. 11.34), having observed good convergence for this choice.

In the following, we will discuss how to introduce a physical scale in a simulation in a longitudinally expanding box at first. Next, our main focus will lie on a comparison of simulations with fermions of different mass. These fermion masses are again chosen to be

of the order of the up/down- and strange quark mass. Following this, we will compare the results of the simulations with fermions of different mass to the dynamics of a pure Yang-Mills system, with an explicitly breaking of boost invariance. Finally we discuss various choices of g to test our model for a dependence on the coupling and investigate a simulation with two degenerate fermions present, setting $N_f = 2$.

13.1 Scale Setting

As stated previously, the longitudinal and the transverse direction have to be discretized independently in a longitudinally expanding box. We therefore introduce a dimensionless longitudinal lattice spacing[1] a_η and a transverse spacing $a_\perp$ of dimension *length*. The latter one is fixed within a matching procedure for the energy density, as discussed already in context of the static box. The estimated energy density of the early phase of a heavy ion collision at $\tau \approx 0.1$ fm has been given in (eq. 3.5). We will measure the energy density of our system in the simulation, choosing different lattice spacings $a_\perp$. In a next step it is possible to extract the appropriate lattice spacing $a_\perp$, where the lattice averaged energy density of our system at initial time, matches the early time estimate of the energy density of the Glasma.

Keeping the transverse box size fixed, making use of the estimated size of the incoming Lorentz-contracted *Pb*-nucleus, the transverse lattice spacing in physical units is given as

$$a_\perp = \frac{12}{N_\perp} \text{ fm}. \tag{13.1}$$

As in case of the static box, we are restricted to a choice of an even integer number for the lattice extent in transverse direction $N_\perp$.

Before presenting the results of the matching procedure for the transverse lattice spacing, let us specify the longitudinal lattice spacing a_η first. As discussed in (section 10.1), we choose our longitudinal lattice extent to cover $\eta = 3$ units of space-time rapidity, corresponding in good approximation to the central rapidity region, which is accessible in the experiment. The dimensionless longitudinal lattice spacing is then given as

$$a_\eta = \frac{3}{N_\eta}. \tag{13.2}$$

In practice, we choose $N_\eta = 40$ for the longitudinal lattice extent in most of our simulations, but we will test our results for a dependence on a_η later.

To solve the equations of motion of the semi-classical model in an expanding box, using a leap-frog integrator, we have to specify the temporal spacing a_τ as well. When discretizing the temporal direction, we have to take care of the Courant-Levi condition. Due to the appearance of an additional lattice spacing in longitudinal direction and the necessity of setting an initial time in Milne coordinates, we are dealing with an additional Courant-Levi constraint in case of the expanding box. On the one hand, we have the familiar condition from the static box

$$a_\tau < a_\perp, \tag{13.3}$$

[1] The lattice spacing is dimensionless, because the space-time rapidity η is dimensionless itself, when introducing Milne coordinates (eq. 9.1).

on the other hand, we require[2]

$$a_\tau < a_\eta \tau. \tag{13.4}$$

We choose $\tau_0 = 0.1$ fm as initial time, leading to the following initial time-step

$$n_{\tau_0} = \frac{0.1 \text{ fm}}{\bar{a}_\tau a_\perp}, \tag{13.5}$$

where we introduced the temporal spacing in lattice units $\bar{a}_\tau = a_\tau / a_\perp$. With this result, we derive the following constraint from (eq. 13.4), that has to be satisfied

$$1 < a_\eta n_{\tau_0} = a_\eta \frac{0.1 \text{ fm}}{\bar{a}_\tau a_\perp}. \tag{13.6}$$

We find that this requirement is proportional to $\sim \frac{1}{\bar{a}_\tau}$, which motivates a small choice of $\bar{a}_\tau = 0.01$ for the temporal spacing in lattice units, leading to numerically stable results. Note that this choice naturally satisfies (eq. 13.3) as well.

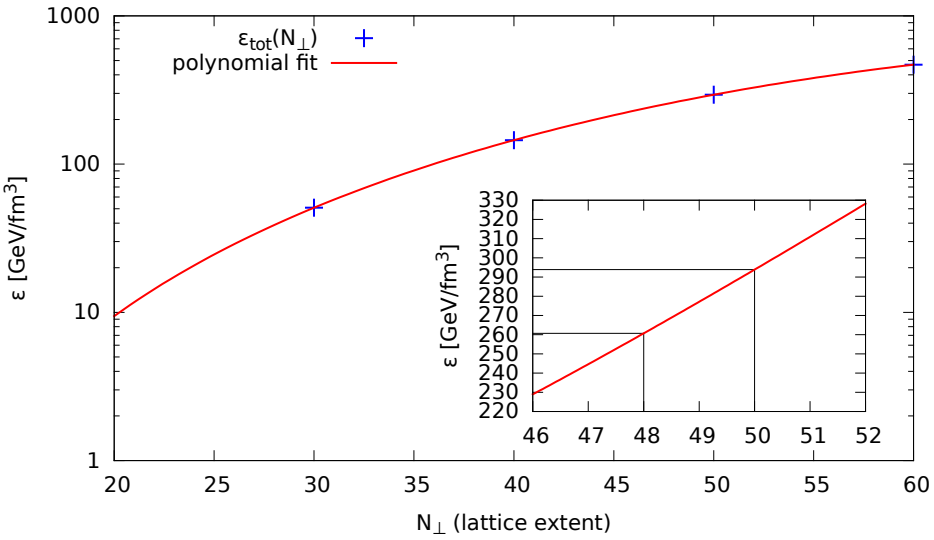

Figure 13.1: Lattice averaged energy density in a simulation of the semi-classical model for different lattice spacings $a_\perp$ in the expanding box. The energy density has been computed at an initial time of $\tau_0 = 0.1$ fm with a fixed fermion mass of $am = 0.01$ and an ensemble size of $N_{ens} = 750$. The longitudinal lattice extend is given as $N_\eta = 40$ with longitudinal lattice spacing $a_\eta = 0.075$. The total energy density ϵ is extracted at initial times as a function of the transverse lattice extent $N_\perp$.

The simulations for the matching procedure have been performed with fermions of (lattice dimensionless) mass $\bar{m} = 0.01$. We give the results for the matching procedure, as a function of the transverse lattice extent $N_\perp$ in (figure 13.1). We can extract the lattice spacing for approximately matching energy densities from the inlay plot, with the corresponding lattice extent given as $N_\perp = 50$

$$a_\perp = \frac{12}{N_\perp} \approx 0.24 \text{ fm}. \tag{13.7}$$

[2]The appearance of the additional factor of τ in the Courant-Levi condition is rooted in the Jacobian $\sqrt{-g} = \tau$.

Note, that this choice matches our previous result for the static box in (chapter 7.5). We emphasize, that the condition $a_\perp > a_\eta$ is satisfied for the given choice of parameters. The initial time-step for the initialization is given as

$$n_{\tau_0} = \frac{0.1 \text{ fm}}{\bar{a}_\tau a_\perp} = 41.67 \approx 42. \tag{13.8}$$

One quickly verifies, that this choice satisfies the second Courant-Levi condition (eq. 13.4)

$$1 < n_{\tau_0} a_\eta = 3.15. \tag{13.9}$$

We choose the following fermion masses in later simulations

$$\bar{m} = 0.01 \;\rightarrow\; m = 8.33 \text{ MeV} \sim \mathcal{O}(m_{u/d}), \quad \bar{m} = 0.1 \;\rightarrow\; m = 83.3 \text{ MeV} \sim \mathcal{O}(m_s), \tag{13.10}$$

which parametrically match the mass of the up-/down-quark and the mass of the strange quark.

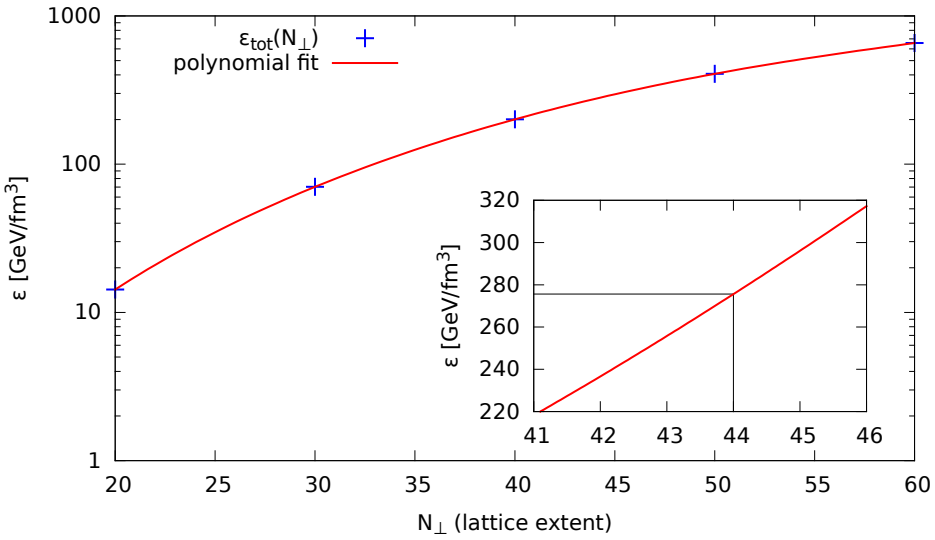

Figure 13.2: Lattice averaged energy density in a simulation of the semi-classical model for different lattice spacings $a_\perp$ in the expanding box. The energy density has been computed at an initial time of $\tau_0 = 0.1$ fm, in a simulation with two fermions of degenerate mass $am = 0.01$ and an ensemble size of $N_{ens} = 750$. The longitudinal lattice extend is given as $N_\eta = 40$ with longitudinal lattice spacing $a_\eta = 0.075$. The total energy density ϵ is extracted at initial times as a function of the transverse lattice extent $N_\perp$.

We repeat the matching procedure for two degenerate quarks, setting $N_f = 2$. The result is given in (figure 13.2). It is possible to extract the following lattice spacing for approximately matching energy densities, with a corresponding lattice extent of $N_\perp = 44$

$$a_\perp = \frac{12}{N_\perp} = \frac{12}{44} \text{ fm}. \tag{13.11}$$

The initial time-step is then given as

$$n_{\tau_0} = \frac{0.1 \text{ fm}}{\bar{a}_\tau a_\perp} = 36.67 \approx 37. \tag{13.12}$$

This result satisfies the second Courant-Levi condition (eq. 13.4) as well

$$1 < n_{\tau_0} a_\eta = 2.775. \tag{13.13}$$

In future simulations we choose the following quark mass

$$\bar{m} = 0.01 \quad \rightarrow \quad m = 7.34 \text{ MeV} \sim \mathcal{O}(m_{u/d}), \tag{13.14}$$

that parametrically matches the mass of the up-/down-quark.

Finally we perform a matching for a pure Yang-Mills simulation in an expanding geometry. We keep all parameters unchanged, varying only the transverse lattice spacing $a_\perp$ as a function of the lattice extent and give the results in (figure 13.3).

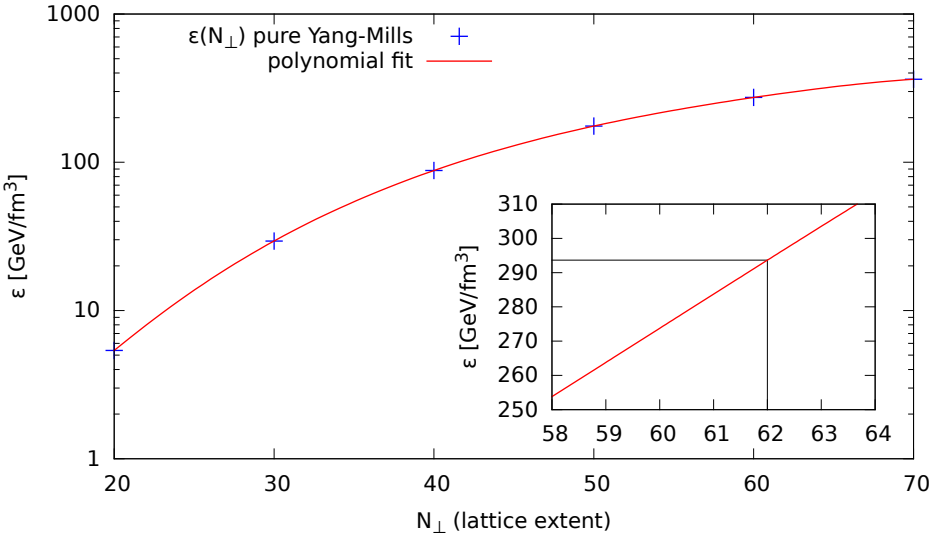

Figure 13.3: Lattice averaged energy density in a simulation of the semi-classical model for different lattice spacings $a_\perp$ in the expanding box. The energy density has been computed at an initial time of $\tau_0 = 0.1$ fm in a pure Yang-Mills simulation. The longitudinal lattice extend is given as $N_\eta = 40$ with longitudinal lattice spacing $a_\eta = 0.075$. The total energy density ϵ is extracted at initial times as a function of the transverse lattice extent $N_\perp$.

From the inlay plot of (figure 13.3), we are able to extract the lattice spacing in a pure Yang-Mills simulation

$$a_\perp = \frac{12}{N_\perp} = \frac{12}{62} \text{ fm}. \tag{13.15}$$

The corresponding initial time-step is then given as

$$n_{\tau_0} = \frac{0.1 \text{ fm}}{\bar{a}_\tau a_\perp} = 51.67 \approx 52, \tag{13.16}$$

and the second Courant-Levi condition (eq 13.4) is satisfied

$$1 < n_{\tau_0} a_\eta = 3.9. \tag{13.17}$$

13.2 Simulations in an Expanding Box with Different Fermion Masses

We start our discussion for an expanding box by comparing results from simulations with fermions of different mass. As discussed already, these masses are parametrically of the order of the mass of the up-/down-quark and the strange quark, choosing $m = 8.33$ MeV and $m = 83.3$ MeV. Our main goal is to test the system for pressure isotropization, measuring the longitudinal to transverse pressure ratio, as well as the pressure to energy ratio. To gain more insights into the dynamics of the system, we will investigate the profile of the energy density, as well as the occupation of energy modes.

13.2.1 Energy Density

Let us start with an investigation of the energy density of the system with fermions. The energy density has been matched to the estimated energy density of the Glasma (section 3.5) at the formation time of $\tau_0 = 0.1$ fm. In contrast to the static box, the energy density of the system will no longer be constant, because of the longitudinal expansion of the system and therefore decrease by time. In (figure 13.4) we give the energy density for a simulation of the semi-classical effective theory in an expanding box, choosing two different fermion masses of $m = 8.33$ MeV (left) and $m = 83.3$ MeV (right).

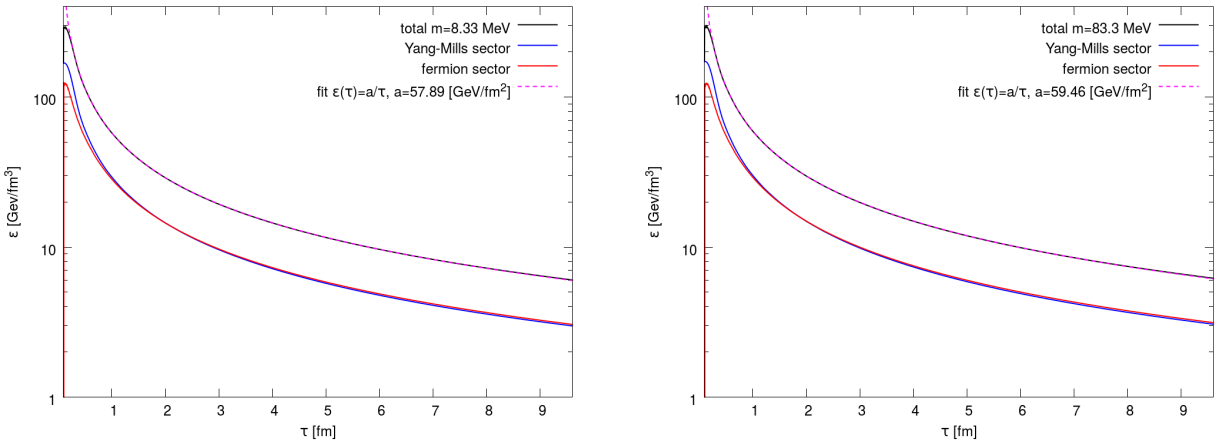

Figure 13.4: Energy density in a simulation with fermions of mass $m = 8.33$ MeV (left) and $m = 83.3$ MeV (right). The simulation has been performed on a $50 \times 50 \times 40$ lattice, with coupling $g = 2$, a transverse lattice spacing of $a_\perp = 0.24$ fm and a longitudinal lattice spacing of $a_\eta = 0.075$, setting the initial time to $\tau_0 = 0.1$ fm. A stochastic fermion ensemble of size $N_{ens} = 750$ has been used.

The y-axis in (figure 13.4) has been plotted on a logarithmic scale. As expected, the energy density decreases in the expanding system as a function of proper time τ. To extract the time dependence, we have fitted the total energy density using

$$\epsilon(\tau) = a\tau^b + c, \tag{13.18}$$

extracting for both masses $b \approx -1$. This scaling behavior of the energy density along $\frac{1}{\tau}$ is familiar from the free-streaming limit in a heavy ion collision, where the quarks and gluons move (quasi-)free in the medium.

When comparing (figure 13.4) to the results of the static box (figure 8.1), one notices that less energy is transfered from the Yang-Mills to the fermion sector. The rapid expansion competes with the interaction between the sectors and hence the energy transfer is reduced. This finding does not strongly dependent on the tested fermion masses, which matches previous observations in the static box. Also note, that we observe the quench at the first time-step, familiar from the static box as well.

13.2.2 Pressure

Let us now turn to the question if pressure isotropy is reached in the expanding box. As a first observable, we give the longitudinal to transverse pressure ratio in a simulation with fermions of mass $m = 8.33$ MeV and $m = 83.3$ MeV in (figure 13.5). In both cases, no pressure isotropy is reached, independently on the chosen fermion mass. On the opposite, the ratio drops to zero instead. This is equivalent to a vanishing longitudinal pressure $P_L = 0$ at late times, hence the expansion in the longitudinal direction dominates the dynamics of the system. This matches observations in pure Yang-Mills simulations of the Glasma, where no pressure isotropy is achieved as well and the free-streaming limit is reached.

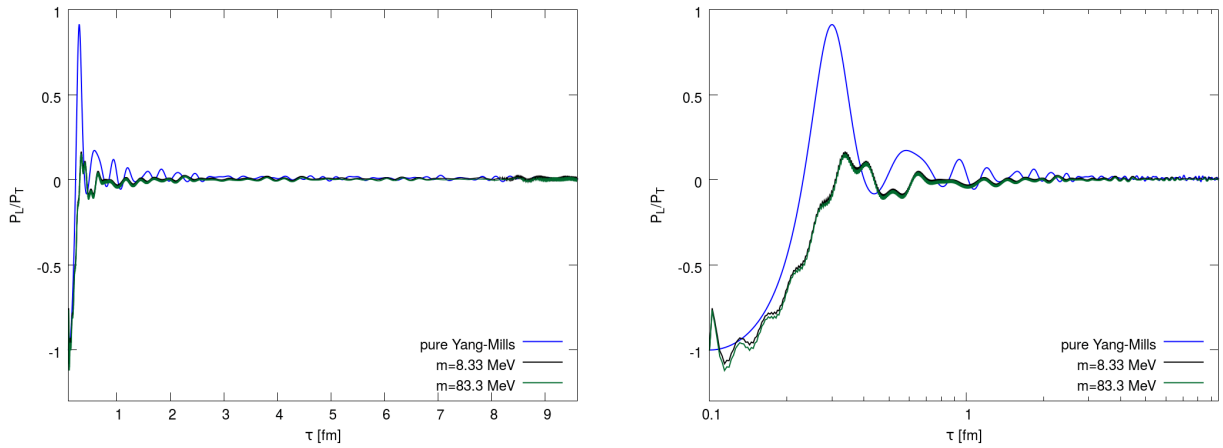

Figure 13.5: Longitudinal to transverse pressure ratio in a simulation with fermions of mass $m = 8.33$ MeV and a simulation with fermions of mass $m = 83.3$ MeV. The simulations have been performed on a $50 \times 50 \times 40$ lattice, with coupling $g = 2$, a transverse lattice spacing of $a_\perp = 0.24$ fm and a longitudinal lattice spacing of $a_\eta = 0.075$, setting the initial time to $\tau_0 = 0.1$ fm. A stochastic fermion ensemble of size $N_{ens} = 750$ has been used. For comparison, the result of a pure Yang-Mills simulation with equivalent physical parameters is shown as well. In the right-hand plot, the x-axis is plotted logarithmically.

On the right-hand side of (figure 13.5), one can clearly see, that the simulation with fermions enters an oscillatory phase at early times. In contrast to the the pure Yang-Mills simulation, the total amplitude of these oscillations is reduced, but the frequency is enhanced by the coupling to fermions. We will trace back the effect of the fermions on to the system in the following sections.

In (figure 13.6) we give the pressure to energy ratio for the two systems including fermions of different mass. In the static box we have seen, that approaching pressure isotropy goes hand in hand with approaching the (ultra-relativistic) limit of $P_i/\epsilon = 1/3$ for the pressure to energy

ratio. In case of the expanding box, neither of the limits is approached.

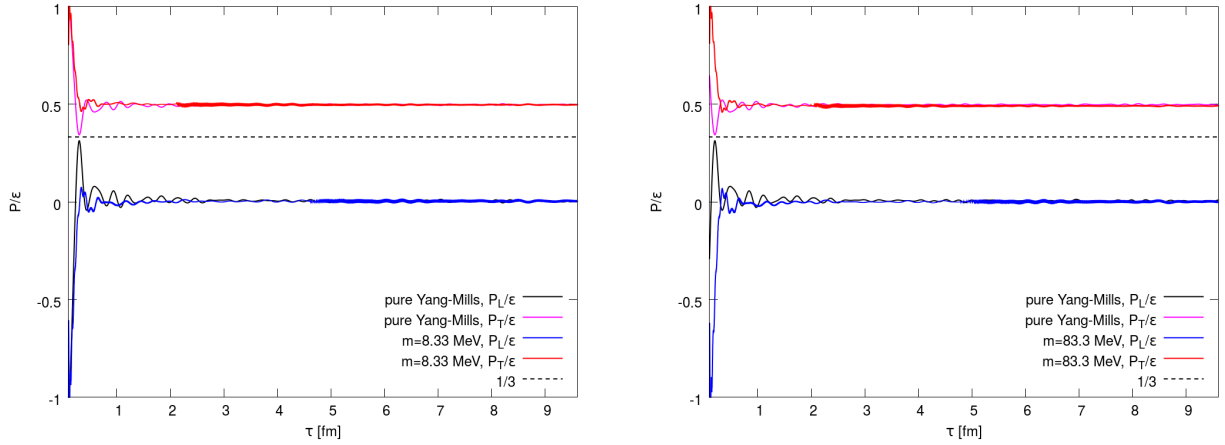

Figure 13.6: Pressure to energy ratio for a simulation with a fermion of mass $m = 8.33$ MeV (left) and a fermion of mass $m = 83.3$ MeV (right). The simulation has been performed on a $50 \times 50 \times 40$ lattice, with coupling $g = 2$, a transverse lattice spacing of $a_\perp = 0.24$ fm and a longitudinal lattice spacing of $a_\eta = 3/N_\eta$, setting the initial time to $\tau_0 = 0.1$ fm. A stochastic fermion ensemble of size $N_{ens} = 750$ has been used. For comparison, the result of a pure Yang-Mills simulation with equivalent physical parameters is shown as well.

With the longitudinal pressure dropping to zero, the longitudinal pressure to energy ratio drops to zero as well. On the other hand, the transverse pressure to energy ratio approaches a constant value of $\frac{P_T}{\epsilon} = \frac{1}{2}$. This result is familiar from pure Yang-Mills simulations in an expanding box (see e.g. [166]) and is yet another manifestation of the free-streaming limit. We conclude, that the longitudinal expansion dominates the dynamics of the system, causing the fermions and (classical) bosons to behave (quasi-)free at late times, making it impossible to reach an isotropy.

We have shown, that a coupling to fermions does not drive the system towards pressure isotropy in the expanding box. This arises the question in which sense the dynamics of the system is influenced by the coupling to fermions, when compared to a pure Yang-Mills simulation. To study this, we use a method first discussed in [61, 62] in context of an explicit breaking of boost invariance on the level of the initial conditions. It has been argued in [61], that a breaking of boost invariance induces an instability, that could drive the system towards pressure isotropy[3], but this instability is not strong enough to succeed over the rapid longitudinal expansion. Our goal is, to look for traces of a similar effect in case of a simulation of the Glasma in a longitudinal expanding box, coupled to fermions.

As argued in (section 12.1.3), a possible observable for such an instability is the Fourier transformed longitudinal pressure of the Yang-Mills sector. An instability can then be observed in exponentially increasing contributions to higher order Fourier modes of the observable. We derived the corresponding lattice quantity in (eq. 12.42). Because of the longitudinal boost invariant construction of the initial Glasma state from the CGC effective theory, the unperturbed system does not pick up a contribution to these Fourier modes, with the trivial mode $\nu = 0$ being the exception. To validate this statement numerically, we have plotted

[3] Which is actually the case in a static box, see [60].

the next to lowest order $\nu_0 = 1$ of the Fourier transformed longitudinal pressure in a pure Yang-Mills simulation on the left of (figure 13.7). We indeed find, that the contribution is equivalent to zero, up to machine precision.

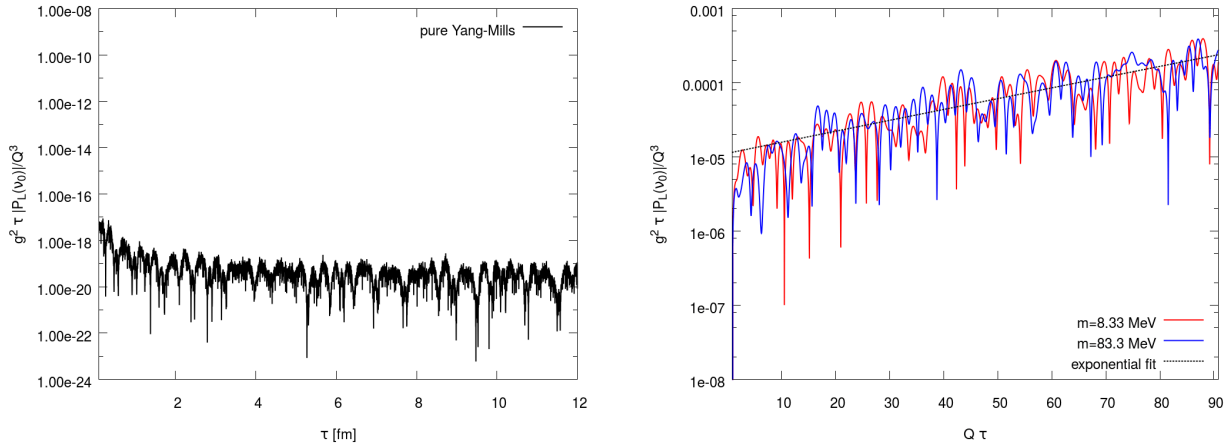

Figure 13.7: Fourier mode $\nu_0 = 1$ of the Fourier transformed longitudinal pressure of the Yang-Mills sector, for a pure Yang-Mills simulation (left) and two simulations including fermions of mass $m = 8.33$ MeV and 83.3 MeV. The simulations with fermions have been performed on a $50 \times 50 \times 40$ lattice, with coupling $g = 2$, a transverse lattice spacing of $a_\perp = 0.24$ fm and a longitudinal lattice spacing of $a_\eta = 0.075$, setting the initial time to $\tau_0 = 0.1$ fm. A stochastic fermion ensemble of size $N_{ens} = 750$ has been used. The pure Yang-Mills simulation uses equivalent physical parameters as initial time, total energy, saturation scale and box size.

On the right-hand side of (figure 13.7) we give the results of the contribution to the Fourier mode $\nu_0 = 1$ for two simulations including fermions of mass $m = 8.33$ MeV and 83.3 MeV. We observe, that indeed a contribution is picked up. To demonstrate that this contribution is exponentially increasing, we have fitted the data to a function of the form

$$g^2\tau|P_L(\nu_0)|/Q^3 \sim a\exp\left(bQ\tau\right) + c. \tag{13.19}$$

The fit parameter could be extracted to be $b \approx 0.032$. Because of the exponential increase, this can be referred to as a pressure instability, induced by the coupling to fermions. We conclude, that due to the coupling to fermions, a pressure instability arises in our system, but it is not strong enough to drive the system towards pressure isotropy.

13.2.3 Occupation of Energy Modes and Energy Density Profile

Although pressure isotropy is not reached in a simulation with fermions in the expanding box, we have seen that the dynamics of the system is influenced by the coupling to fermions. To study the dynamics in more detail, let us investigate the profile of the energy density at first. We restrict ourselves to the chromo-electric longitudinal part of the energy density and perform an average in x-direction. We give the results for a simulation including fermions of mass $m = 8.33$ MeV in (figure 13.8) and of mass $m = 83.3$ MeV in (figure 13.9).

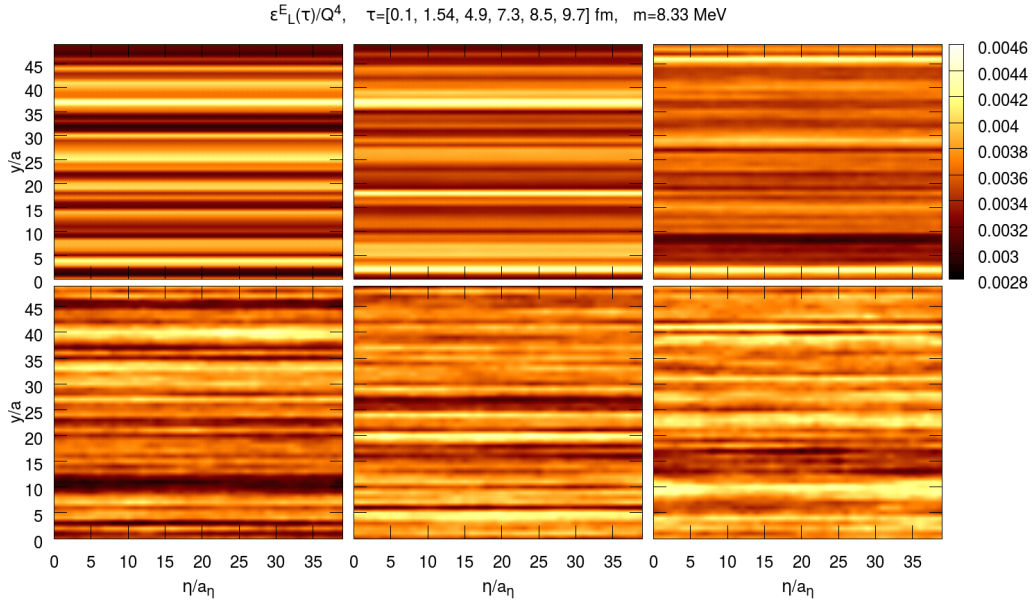

Figure 13.8: Profile of the longitudinal chromo-electric energy density $\epsilon_L^E(t)$ in a simulation with fermions of mass $m = 8.33$ MeV at times $\tau = \{0.1, 1.54, 4.9, 7.3, 8.5, 9.7\}$ fm (top left to bottom right). The simulation has been performed on a $50 \times 50 \times 40$ lattice, with coupling $g = 2$, a transverse lattice spacing of $a_\perp = 0.24$ fm and a longitudinal lattice spacing of $a_\eta = 0.075$, setting the initial time to $\tau_0 = 0.1$ fm. A stochastic fermion ensemble of size $N_{ens} = 750$ has been used and the x-direction has been averaged.

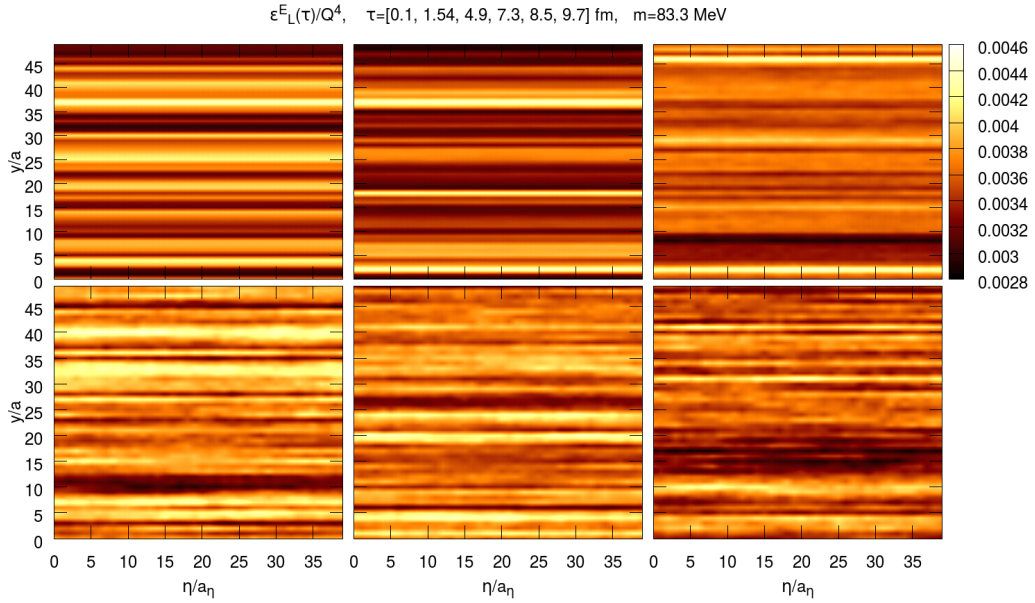

Figure 13.9: Profile of the longitudinal chromo-electric energy density $\epsilon_L^E(t)$ in a simulation with fermions of mass $m = 83.3$ MeV at times $\tau = \{0.1, 1.54, 4.9, 7.3, 8.5, 9.7\}$ fm (top left to bottom right). The simulation has been performed on a $50 \times 50 \times 40$ lattice, with coupling $g = 2$, a transverse lattice spacing of $a_\perp = 0.24$ fm and a longitudinal lattice spacing of $a_\eta = 0.075$, setting the initial time to $\tau_0 = 0.1$ fm. A stochastic fermion ensemble of size $N_{ens} = 750$ has been used and the x-direction has been averaged.

In both cases, we identify the lines of constant energy along longitudinal direction, caused by

the color-flux tubes of the Glasma. When comparing to the results in a static box, (figure 8.9) and (figure 8.10), we see that this initial structure is much better preserved during the evolution of the system. For the static box, we argued, that a homogenization of the energy density, that goes hand in hand with an occupation of high energy modes, is a necessary condition for pressure isotropization to develop. Observing no similar process in the expanding box supports the finding, that no pressure isotropy is reached.

Nevertheless, the lines of constant energy are slightly affected from the energy transfer between the Yang-Mills and fermion sector in the expanding box. This becomes utterly clear, when comparing to a pure Yang-Mills simulation in the expanding box (figure 13.10), where the lines of constant energy are not at all affected during the evolution of the system. Their modification in an expanding box can therefore clearly be traced back to be rooted in the interaction between fermion and Yang-Mills fields.

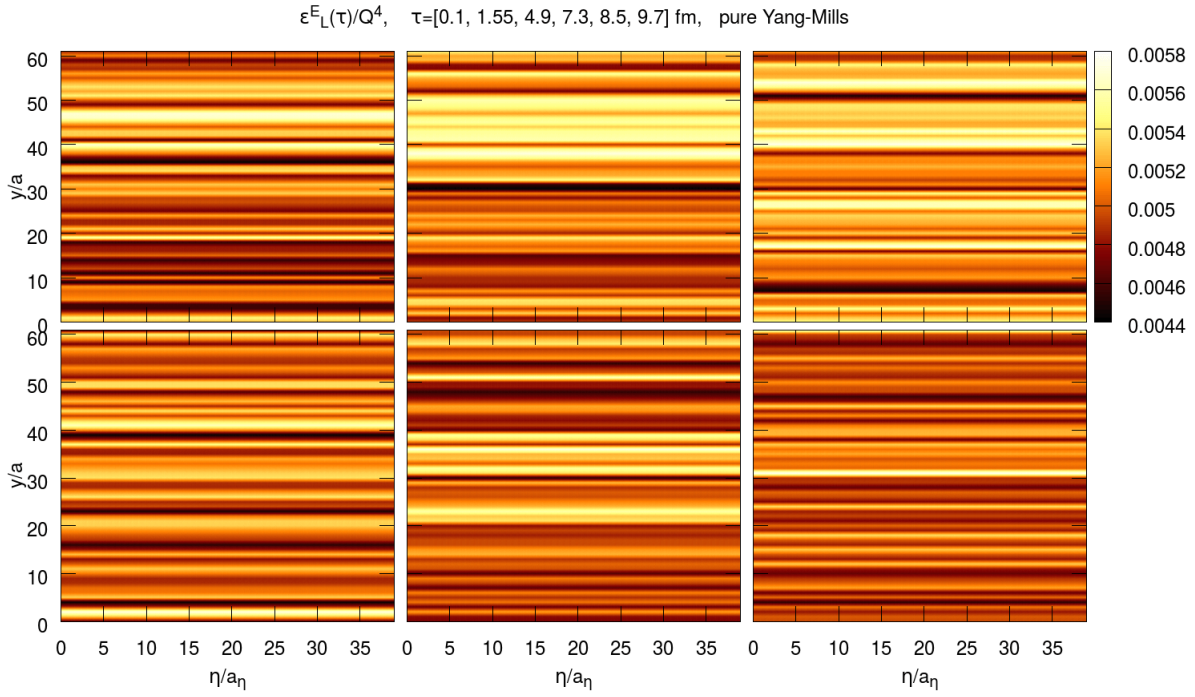

Figure 13.10: Profile of the longitudinal chromo-electric energy density $\epsilon_L^E(t)$ in a pure Yang-Mills simulation at times $\tau = \{0.1, 1.55, 4.9, 7.3, 8.5, 9.7\}$ fm (top left to bottom right). The simulation has been performed on a $62 \times 62 \times 40$ lattice, with coupling $g = 2$, a transverse lattice spacing of $a_\perp \approx 0.19$ fm and a longitudinal lattice spacing of $a_\eta = \frac{3}{N_\eta}$, setting the initial time to $\tau_0 = 0.1$ fm. The x-direction has been averaged and all physical parameters as energy, saturation scale Q_s and nucleus size are kept constant when compared to the simulation with fermions.

Finally let us turn to the occupation of energy modes. In general, the lattice averaged energy density decreases by an overall factor of $\sim \frac{1}{\tau}$ during the evolution, as seen in (figure 13.4). With the gauge invariant occupation of energy modes being derived from the Fourier transform of the energy density, it is affected by this decrease as well. To compensate this effect, making the occupation of energy modes comparable at different time-steps, we multiply (eq. 12.48) by a factor of τ.

Having observed only marginal differences for simulations with fermions of mass $m = 8.33$ MeV and with fermions of mass $m = 83.3$ MeV, we restrict our discussion to the smaller mass. As discussed in (section 12.2), an evaluation of the occupation of energy modes in the expanding box is only possible when restricting ourselves to the transverse planes, labeled by the longitudinal Fourier mode ν. In (figure 13.11) we plot the occupation of energy modes in the transverse planes as a function of the lattice dispersion relation of the Yang-Mills fields (eq. 12.46), or the fermion fields (eq. 10.10).

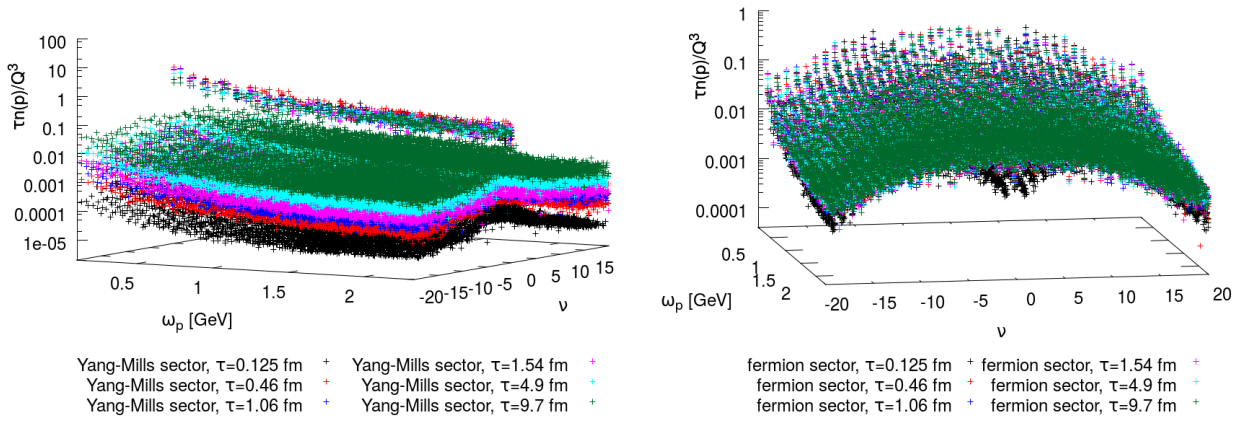

Figure 13.11: Occupation of energy modes in the transverse planes as a function of the lattice dispersion relation $\omega_{\mathbf{p}}$ and the longitudinal Fourier mode ν, for a simulation with fermions of mass $m = 8.33$ MeV. We give the result for the Yang-Mills sector on the left-hand side and the result for the fermion sector on the right-hand side. The simulation has been performed on a $50 \times 50 \times 40$ lattice, with coupling $g = 2$, a transverse lattice spacing of $a_\perp = 0.24$ fm and a longitudinal lattice spacing of $a_\eta = 0.075$, setting the initial time to $\tau_0 = 0.1$ fm. A stochastic fermion ensemble of size $N_{ens} = 750$ has been used.

In case of the fermion sector, plotted on the right-hand side in (figure 13.11), we find that the energy modes in the transverse planes are equally occupied, with low energy modes slightly favored. This is in total correspondence to what we have seen in case of the static box (figure 8.14). A key difference between the static and the expanding system is the occupation of energy modes in the Yang-Mills sector, given on the left-hand side of (figure 13.11). As familiar from the static box and rooted in the construction of the initial conditions, we observe that low energy modes in the plane with $\nu = 0$ initially dominate the system. For the static system we found, that this initial dominance is erased within the evolution of the system and high energy modes are occupied during the evolution, until finally, a nearly balanced situation is reached (compare to figure 8.15 and figure 8.16). This is certainly not the case in the expanding system, where a clear separation between the plane with $\nu = 0$ and the other planes remains visible right until the final time of the simulation.

Nevertheless it is possible to observe, that high energy modes become occupied during the simulation, due to an energy exchange between the Yang-Mills and fermion sector, although the exchanged is reduced. This is essentially caused by a coupling of the classical Yang-Mills fields to fermions, comparing it to the occupation of energy modes in a pure Yang-Mills

simulation, given in (figure 13.12). Because the boost invariance of the Glasma is preserved by the equations of motion in the pure Yang-Mills system, the occupation of energy modes does not change during the evolution of the system, matching our previous observation for the energy density profile (figure 13.10).

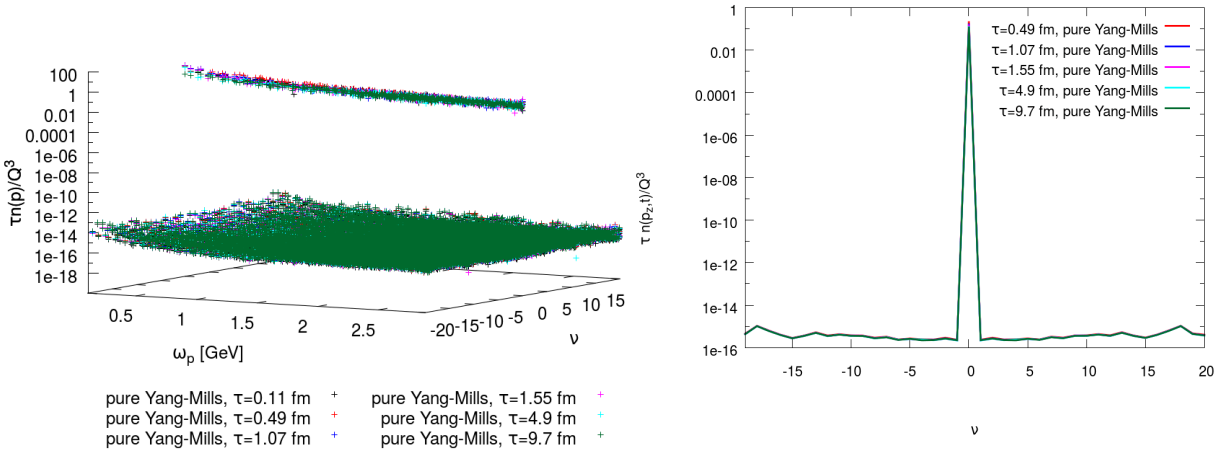

Figure 13.12: Occupation of energy modes in the transverse planes (left) and an average of these planes (right), as a function of the longitudinal Fourier mode ν, for a pure Yang-Mills simulation. The simulation has been performed on a $62 \times 62 \times 40$ lattice, with coupling $g = 2$, a transverse lattice spacing of $a_\perp \approx 0.19$ fm and a longitudinal lattice spacing of $a_\eta = 0.075$, setting the initial time to $\tau_0 = 0.1$ fm. All physical parameters as energy, saturation scale Q_s and nucleus size are kept constant when compared to the simulation with fermions.

The evolution of the occupation of energy modes in planes with $\nu \neq 0$ can be studied, looking at the averaged occupation in the transverse planes as a function of the longitudinal Fourier mode ν, given for a simulation with fermions of mass $m = 8.33$ in (figure 13.13). We restricted ourselves to the Yang-Mills sector, having already seen in (figure 13.11), that energy modes in the fermion sector are equally occupied during the evolution of the system.

In the Yang-Mills sector, the averaged occupation of energy modes in the transverse plane is initially sharply peaked at $\nu = 0$, as expected for the Glasma. We find that this peak is diminished very slowly by time. Plotting the y-axis logarithmically, on the right-hand side of (figure 13.13) reveals that energy modes in the transverse planes with $\nu \neq 0$ become occupied during the evolution of the system, but this happens rather slowly, when compared to the static box (figure 8.16). In general the initial distribution is erased much slower in the expanding box. This happens, because on the one hand the longitudinal expansion counteracts the interaction of the classical Yang-Mills fields with the fermion fields and hence the energy exchange between the sectors is significantly reduced and on the other hand, more and more low energy longitudinal modes are created because of the rapid expansion, preserving the dominance of low modes in our system. As a consequence, this also influences the validity of the classical approximation. In the expanding system, higher order energy modes are occupied much slower than it has been the case in the static box (figure 8.17) and therefore the dominance of low energy modes, associated with overoccupied classical Yang-Mills fields is preserved, supporting the validity of the classical approximation.

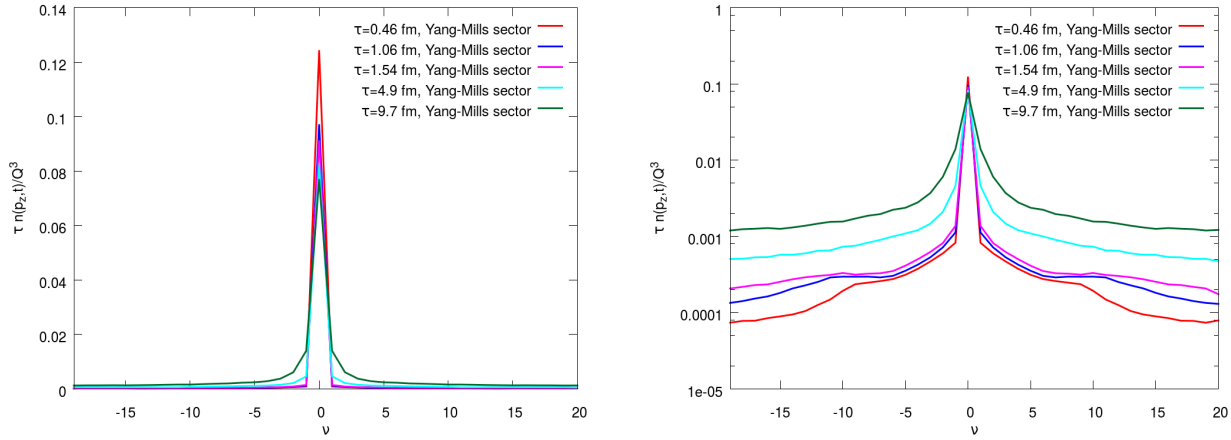

Figure 13.13: Average of the occupation of energy modes in the transverse planes, as a function of the longitudinal Fourier mode ν, for the Yang-Mills sector of a simulation with fermions of mass $m = 8.33$ MeV in an expanding box. The simulation has been performed on a $50 \times 50 \times 40$ lattice, with coupling $g = 2$, a transverse lattice spacing of $a_\perp = 0.24$ fm and a longitudinal lattice spacing of $a_\eta = 0.075$, setting the initial time to $\tau_0 = 0.1$ fm. A stochastic fermion ensemble of size $N_{ens} = 750$ has been used.

13.3 Discretization in Longitudinal Direction

We fixed the longitudinal lattice spacing a_η by choosing an area of 3 units of space-time rapidity η to be covered by the longitudinal lattice extent. The lattice spacing has thus been given as $a_\eta = 3/N_\eta$. We have chosen, without further specification, $N_\eta = 40$, leading to numerically stable results with manageable computational time, while satisfying $a_\eta < a_\perp$. In this section, we vary $N_\eta \in \{40, 50, 60\}$, moving to finer lattice spacings a_η. If the choice of $N_\eta = 40$ is reasonable, we expect our previous results not to vary significantly. All other parameters entering the simulation are left constant.

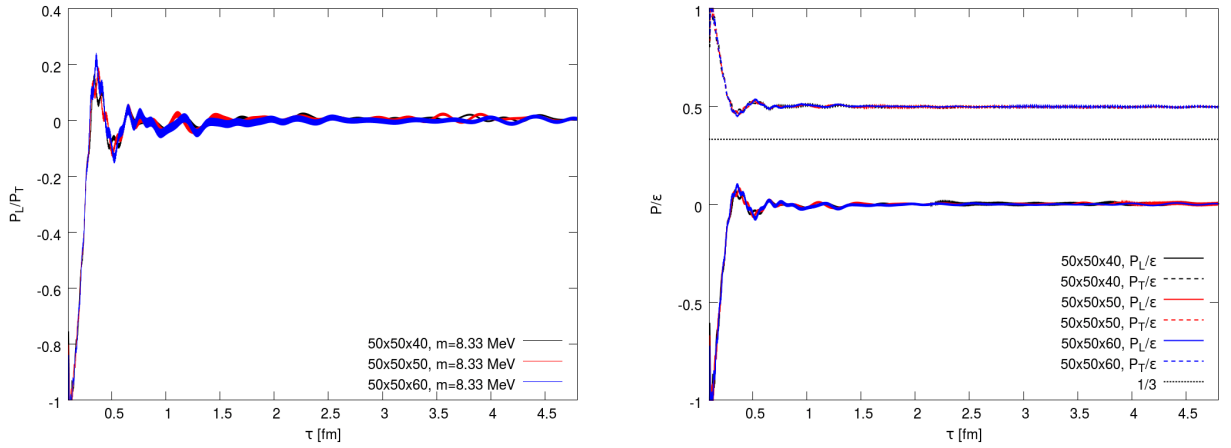

Figure 13.14: Longitudinal to transverse pressure ratio (left) and pressure to energy ratio (right) for a simulation with fermions of mass $m = 8.33$ MeV, choosing different longitudinal spacings $a_\eta \in \{0.075, 0.06, 0.05\}$. The simulation has been performed with a fixed transverse lattice extent $N_\perp = 50$, with lattice spacing $a_\perp = 0.24$ fm, a coupling $g = 2$, initial time $\tau_0 = 0.1$ fm and a stochastic fermion ensemble of size $N_{ens} = 750$.

In (figure 13.14) we compare the longitudinal to transverse pressure ratio (left) and the pressure to energy ratio (right) in a simulation including fermions of mass $m = 8.33$ MeV, for different choices of a_η. We find that independently on the choice of a_η, no pressure isotropy is reached in all three cases. The results only differ in small fluctuations, that are caused numerically and are most likely rooted in a different construction of initial conditions for the Yang-Mills sector and a different initialization of fermions for the choices of a_η. Moreover the results agree in amplitude, shape and evolution, finding no dependence of the physical results on the choice of a_η.

This observation is supported by the pressure to energy ratio of the individual sectors, given in (figure 13.15). We see that neither the evolution of the Yang-Mills, nor the evolution of the fermion sector changes, making it possible to conclude that a choice of $a_\eta = 0.075$ is sufficiently fine.

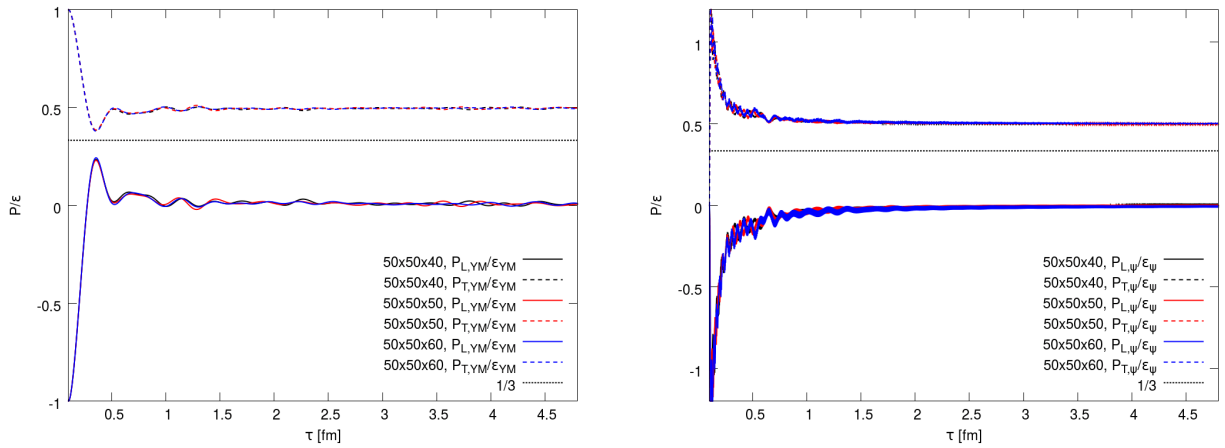

Figure 13.15: Pressure to energy ratio for the Yang-Mills sector (left) and the fermion sector (right) in a simulation with fermions of mass $m = 8.33$ MeV for different longitudinal lattice spacing $a_\eta \in \{0.075, 0.06, 0.05\}$. The simulation has been performed with a fixed transverse lattice extent $N_\perp = 50$, with lattice spacing $a_\perp = 0.24$ fm, a coupling $g = 2$, initial time $\tau_0 = 0.1$ fm and a stochastic fermion ensemble of size $N_{ens} = 750$.

13.4 Explicitly Breaking Longitudinal Boost Invariance

Having studied the influence of fermions in a simulation of the semi-classical effective theory in an expanding box, we want to compare our results to a pure Yang-Mills simulation with an explicit breaking of longitudinal boost invariance, introducing a quantum fluctuation in longitudinal direction of magnitude Δ (eq. 3.22). Such a system has previously been studied in [61, 62] and it has been shown, that a pressure instability (eq. 12.42) develops. On the downside, this instability is not strong enough to succeed over the rapid longitudinal expansion and drive the system towards pressure isotropy. On the opposite, the system reaches the free-streaming limit, where the classical Yang-Mills fields propagate quasi-free.

We compare the longitudinal to transverse pressure ratio and the pressure to energy ratio in pure Yang-Mills simulations with different choices of fluctuation strength $\Delta \in \{0, 0.01, 0.1\}$, to a simulation with a fermion of mass $m = 8.33$ MeV in (figure 13.16). To compare all simulations, we keep the parameters total energy, longitudinal lattice extent, spacing a_η, transverse box size, saturation scale Q_s and the initial time τ_0 constant. We find in all cases, that no pressure

isotropy is reached and the pressure to energy ratio approaches the free-streaming limit, where the longitudinal pressure drops to zero and $P_T/\epsilon \to 1/2$.

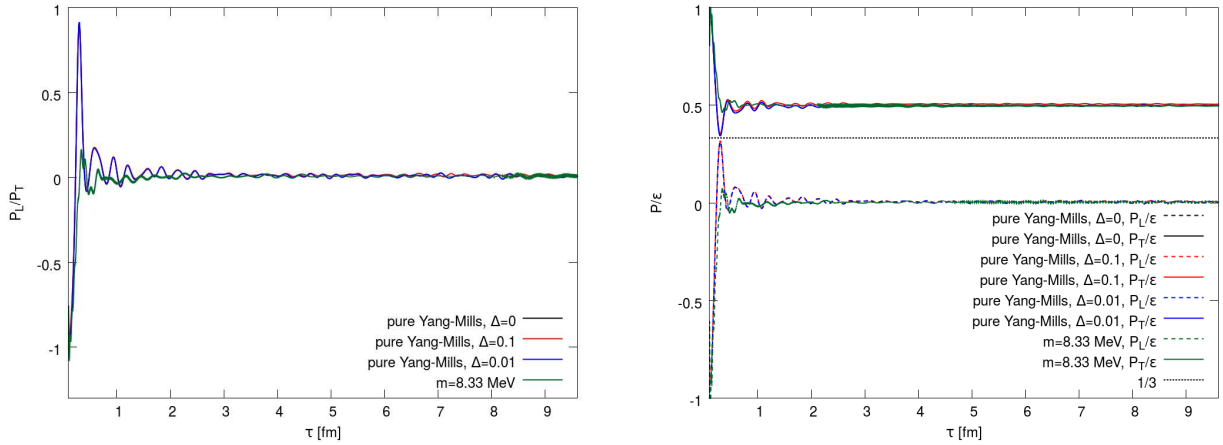

Figure 13.16: Longitudinal to transverse pressure ratio (left) and pressure to energy ratio (right), for a pure Yang-Mills simulations with an explicit breaking of longitudinal boost invariance of magnitude $\Delta = \{0, 0.01, 0.1\}$ and a simulation including fermions of mass $m = 8.33$ MeV. The simulation including fermions has been performed on a $50 \times 50 \times 40$ lattice, with transverse lattice spacing $a_\perp = 0.24$ fm and a stochastic fermion ensemble of size $N_{ens} = 750$. The pure Yang-Mills simulations have been performed on a $62 \times 62 \times 40$ lattice, with transverse lattice spacing $a_\perp = 0.19$ fm. In all simulations, the initial time is set to $\tau_0 = 0.1$ fm and the longitudinal lattice spacing is fixed to $a_\eta = 0.075$. All physical parameters as total energy, saturation scale Q_s and transverse lattice size are constant in all simulations.

Next, we want to investigate possible differences for the simulation with fermions and the pure Yang-Mills simulations with an explicit breaking of boost invariance. For this purpose we study the profile of the energy density and compare it to the energy density profile of a simulation with fermions (figure 13.8) and (figure 13.9). We restrict ourselves to the fluctuation of amplitude $\Delta = 0.1$ and give the chromo-electric energy density in (figure 13.17). A lattice average in x-direction has been performed.

For early times, it is possible to identify the lines of constant energy, which are slightly modified due to the appearance of vertically shaded regions. As discussed in the context of the static box, these shaded regions are caused from the rapidity fluctuation (eq. 3.22) entering the initial condition of the Glasma and their strength is controlled by Δ. During the evolution of the system, it is possible to observe the development of filaments along the shaded regions, which extent over the whole lattice more and more. At the final time, the longitudinal lines of constant energy are nearly completely erased. This is again an evidence for the development of a chromo-Weibel instability, discussed in the context of the static box (figure 8.26), that homogenizes the energy density, as soon as it it is spread over the whole lattice. We emphasize, that this observation matches the previous study of an equivalent system in [61, 62].

When comparing to the energy density profile of a simulation with fermions of mass $m = 8.33$ MeV (figure 13.8), we find that the energy density in the latter case is homogenized slower. The reason for that has to be rooted in the fact, that the homogenization is caused by two completely different processes. On the one hand from a chromo-Weibel instability, that spreads over the

whole lattice by time and on the other hand, by an energy exchange between the fermion and Yang-Mills sector, which is slowed down, because of the rapid longitudinal expansion of the system. On top of that, the fermions are initialized to preserve boost invariance as well, which is why it takes more time for an instability to develop in this case.

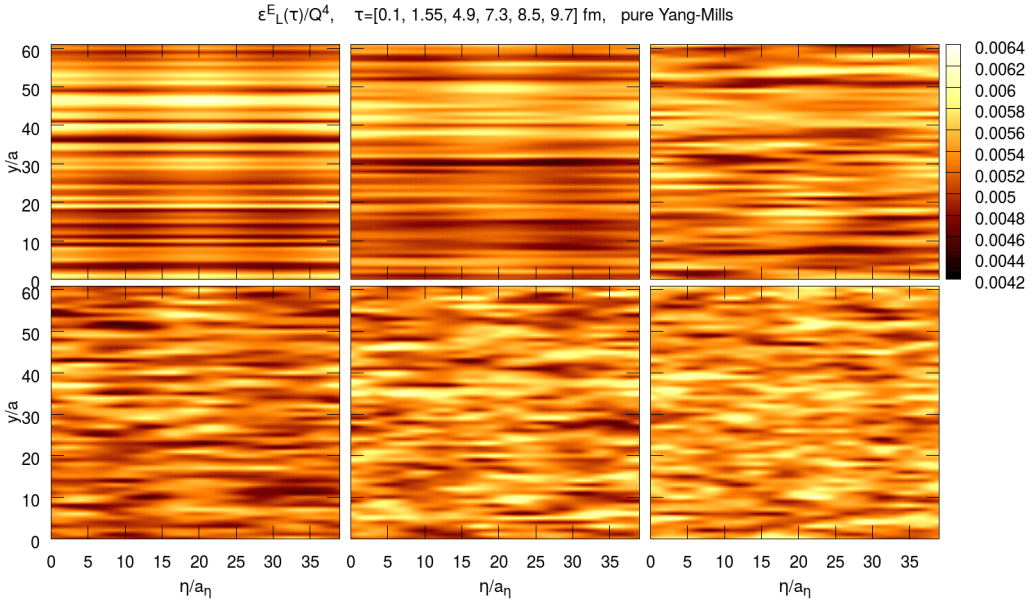

Figure 13.17: Profile of the longitudinal chromo-electric energy density $\epsilon_L^E(t)$ for a pure Yang-Mills simulation with an explicit breaking of boost invariance of magnitude $\Delta = 0.1$ at times $\tau = \{0.1, 1.55, 4.9, 7.3, 8.5, 9.7\}$ fm (top left to bottom right). The simulation has been performed on a $62 \times 62 \times 40$ lattice, with transverse lattice spacing $a_\perp = 0.19$ fm and longitudinal lattice spacing $a_\eta = 0.075$. The x-direction has been averaged and the coupling is chosen to be $g = 2$. All physical parameters as total energy, saturation scale Q_s and transverse box size are kept constant when compared to a simulation with fermions.

Finally, we give the results for the occupation of energy modes in the transverse planes and an average in these planes, as a function of the longitudinal Fourier mode ν, for pure Yang-Mills simulations with fluctuations of $\Delta = 0.01$ and $\Delta = 0.1$ in (figure 13.18) and (figure 13.19). We observe that some energy modes with $\nu \neq 0$ are now occupied at initial time, due to the introduction of the rapidity fluctuation in longitudinal direction (eq. 3.22). This effect becomes more present, when choosing a larger amplitude Δ for the fluctuation. In analogy to the static box, we observe a cascade for the occupation of energy modes, where higher energy modes are occupied more and more during the evolution of the system. This happens to be faster when choosing a larger Δ.

Comparing these results to the occupation of energy modes in the transverse planes for a simulation with fermions (figure 13.11) and (figure 13.13), the key difference is, that the initial peak remains present in a simulation with fermions. Although the energy transfer between the fermion and Yang-Mills sector leads to an occupation of high energy modes, we do not observe a similar cascade as in case of a chromo-Weibel instability. In the latter case, energy modes are evenly occupied to a maximum at $\nu = 0$, leading to a triangular shape of the peak, whereas in a simulation with fermions, the distribution is more sharply peaked around $\nu = 0$.

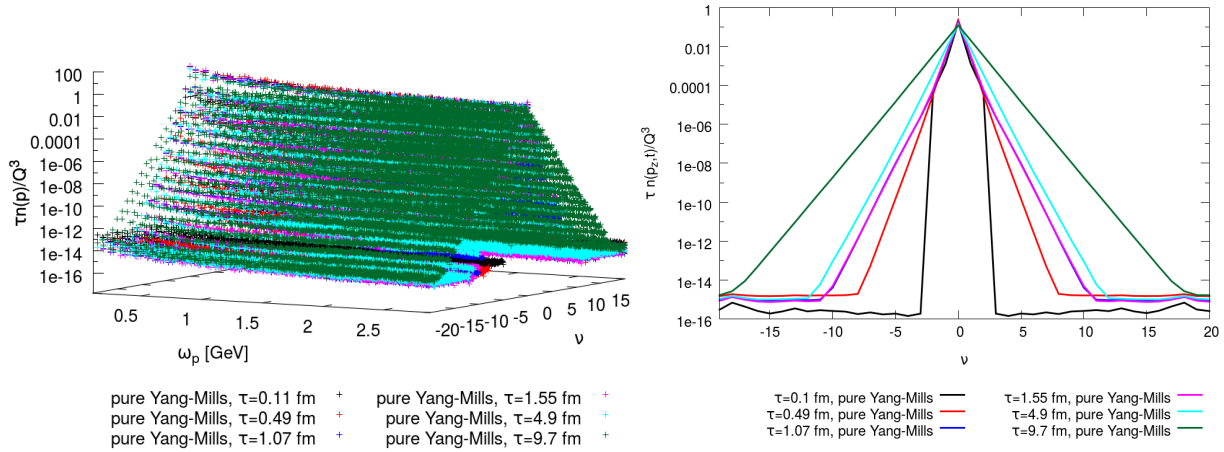

Figure 13.18: Occupation of energy modes in the transverse planes (left) and an average of these planes (right), as a function of the longitudinal Fourier mode ν, for a pure Yang-Mills simulation with an explicit breaking of boost invariance of strength $\Delta = 0.01$. The simulation has been performed on a $62 \times 62 \times 40$ lattice, with transverse lattice spacing $a_\perp = 0.19$ fm, initial time $\tau_0 = 0.1$ fm, coupling $g = 2$ and a longitudinal lattice spacing of $a_\eta = 0.075$. All physical parameters as energy, saturation scale Q_s and nucleus size are kept constant when compared to the simulation with fermions.

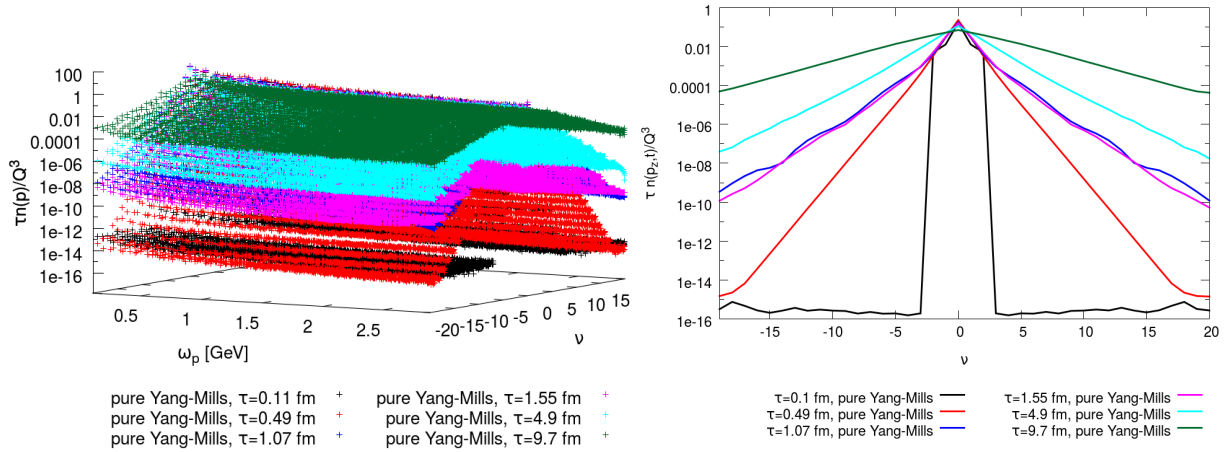

Figure 13.19: Occupation of energy modes in the transverse planes (left) and an average of these planes (right), as a function of the longitudinal Fourier mode ν, for a pure Yang-Mills simulation with an explicit breaking of boost invariance of strength $\Delta = 0.1$. The simulation has been performed on a $62 \times 62 \times 40$ lattice, with transverse lattice spacing $a_\perp = 0.19$ fm, initial time $\tau_0 = 0.1$ fm, coupling $g = 2$ and a longitudinal lattice spacing of $a_\eta = 0.075$. All physical parameters as energy, saturation scale Q_s and nucleus size are kept constant when compared to the simulation with fermions.

We have seen, that a chromo-Weibel instability develops in a pure Yang-Mills simulation in the expanding box, if longitudinal boost invariance is explicitly broken, but it is not strong enough to drive the system towards pressure isotropy. The same has been true for a coupling to fermions and as a consequence, we now want to study what happens when both effects are combined. We simulate a system with fermions of mass $m = 8.33$ MeV and introduce a quantum

fluctuation of amplitude $\Delta = 0.1$. In (figure 13.20) we give the result for the longitudinal to transverse pressure ratio (left) and the pressure to energy ratio (right) of the system.

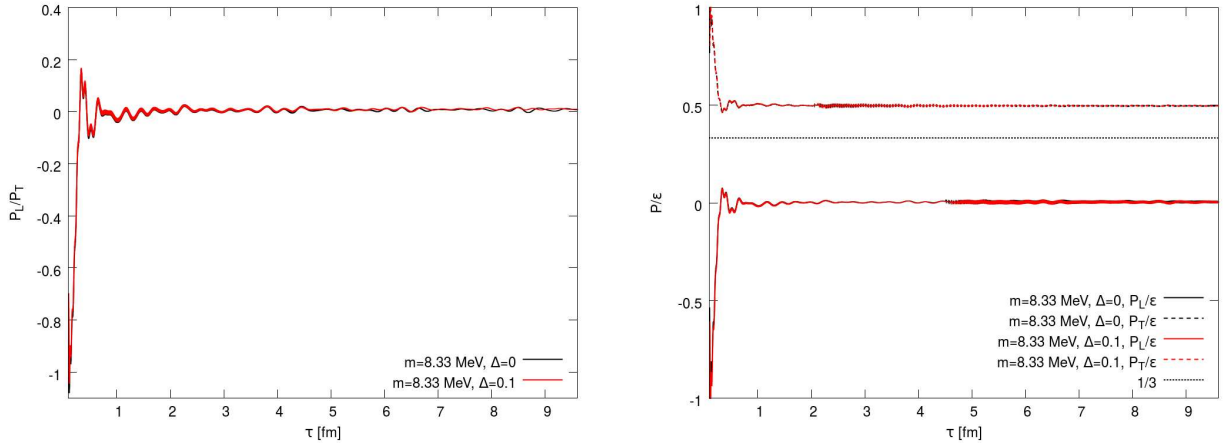

Figure 13.20: Longitudinal to transverse pressure ratio (left) and pressure to energy ratio (right) for a simulation with fermions of mass $m = 8.33$ MeV, with and without an explicit breaking of boost invariance of strength $\Delta = 0.1$. The simulation has been performed on a $50 \times 50 \times 40$ lattice, with transverse lattice spacing $a_\perp = 0.24$ fm, initial time $\tau_0 = 0.1$ fm, coupling $g = 2$, longitudinal lattice spacing $a_\eta = 0.075$ and a stochastic fermion ensemble of size $N_{ens} = 750$.

We find no difference for the pressure ratio, when comparing to a simulation with fermions only. In both cases, the dynamics of the system is dominated by the longitudinal expansion and no isotropy is reached. To study the interplay of both mechanisms, we investigate the occupation of energy modes in the Yang-Mills sector, given in (figure 13.21).

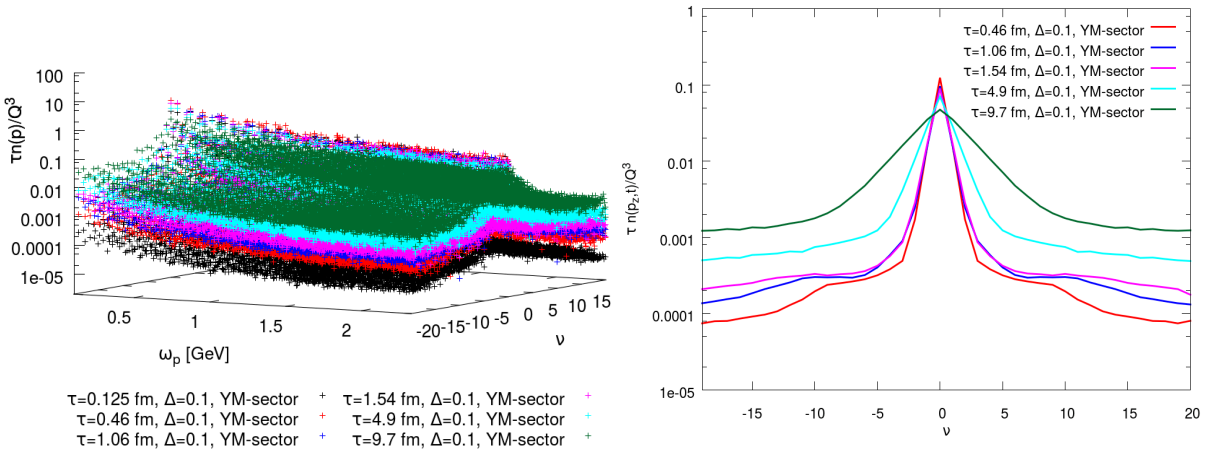

Figure 13.21: Occupation of energy modes in the transverse planes (left) and an average of these planes (right) as a function of the longitudinal Fourier mode ν, for a simulation including fermions of mass $m = 8.33$ MeV and an explicit breaking of longitudinal boost invariance of strength $\Delta = 0.1$. The simulation has been performed on a $50 \times 50 \times 40$ lattice, with coupling $g = 2$, a transverse lattice spacing of $a_\perp = 0.24$ fm and a longitudinal lattice spacing of $a_\eta = 0.075$, setting the initial time to $\tau_0 = 0.1$ fm. A stochastic fermion ensemble of size $N_{ens} = 750$ has been used.

It is clearly visible, that high energy modes become occupied during the evolution of the system. When comparing the right-hand plot in (figure 13.21) to the simulation with fermions and without an explicit breaking of longitudinal boost invariance (figure 13.13), we find that the peak at $\nu = 0$ of the initial state remains present in (figure 13.21), but it is broadened. This happens due to the additional instability induced by the explicit breaking of boost invariance. On the other hand, low momentum modes are occupied earlier, when compared to a pure Yang-Mills simulation with an initial quantum fluctuation of strength $\Delta = 0.1$ (figure 13.19). This happens because of the additional energy exchange between the fermion and Yang-Mills sector in a simulation with fermions. On top of that, the separation of the occupation in the $\nu = 0$ plane, compared to planes with $\nu \neq 0$ is much more present without a longitudinal rapidity fluctuation (figure 13.11) as it is the case with a fluctuation (figure 13.21).

13.5 Coupling Dependence

Having studied the evolution of the Glasma coupled to fermions in the expanding box, with an appropriate coupling of $g \approx 2$, let us now test our model for its dependence on the coupling. As presented for the static box, we choose couplings of $g \in \{0.01, 0.1, 0.5\}$ and compare the results to the realistic choice. Because the strength of the coupling mediates the interaction of classical gluons and fermions, we expect the occupation of high energy modes to slow down even further. Subsequently, no pressure isotropy should be reached by the expanding system in any of these cases. To compare to a simulation with $g = 2$, we do not vary the transverse lattice spacing $a_\perp = 0.24$ fm and keep the longitudinal lattice spacing $a_\eta = 0.075$ and extent $N_\eta = 40$ constant as well, covering 3 units of space-time rapidity. All physical parameters as the transverse lattice size and the saturation scale Q_s are left constant. The simulations have been performed choosing a fermion mass of $m = 8.33$ MeV and a stochastic fermion ensemble of $N_{ens} = 750$.

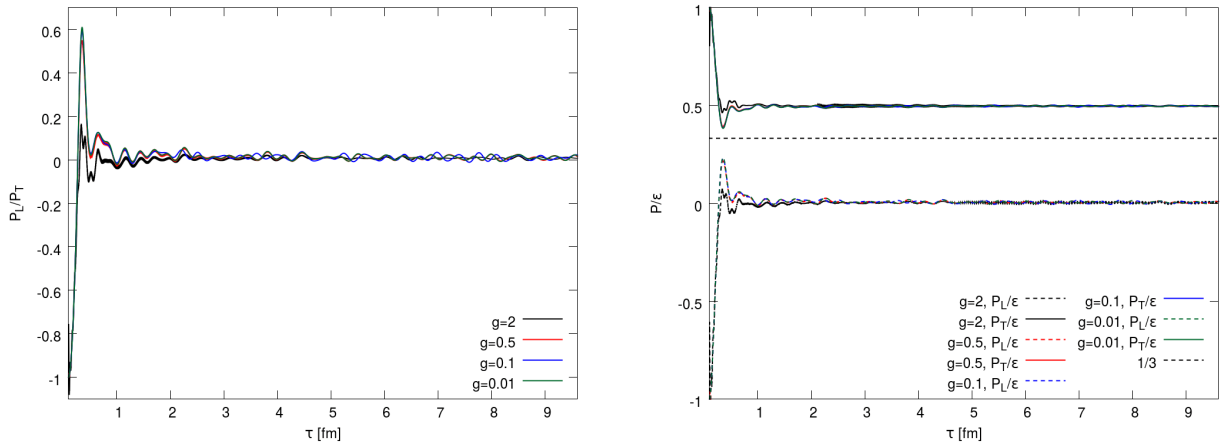

Figure 13.22: Longitudinal to transverse pressure ratio (left) and pressure to energy ratio (right) for simulations with fermions of mass $m = 8.33$ MeV and different choices of coupling $g \in \{0.01, 0.1, 0.5, 2\}$. The simulations have been performed on a $50 \times 50 \times 40$ lattice, with transverse lattice spacing $a_\perp = 0.24$ fm, longitudinal lattice spacing of $a_\eta = 0.075$. The initial time is chosen to be $\tau_0 = 0.1$ fm and the stochastic fermion ensemble size is given as $N_{ens} = 750$.

In (figure 13.22) we give the longitudinal to transverse pressure ratio (left) and the pressure to energy ratio (right) for the different choices of coupling g. As expected, we observe in all

cases, that neither a pressure isotropy is reached, nor the ultra-relativistic limit of $P_i/\epsilon \to 1/3$ for the pressure to energy ratio. On the opposite, the longitudinal pressure P_L drops to zero after an initial oscillatory phase and the free-streaming limit, characterized by $P_T/\epsilon \to 1/2$ as well, is reached. The only difference can be noticed at early times, where it is possible to observe that the amplitude of the initial oscillatory phase is modified by the different choices of g. This is essentially a consequence of the reduced interaction strength between the Yang-Mills and fermion sector, where the latter one acquires less energy for smaller choices of g, hence its contribution to the total pressure of the system is reduced. As a result, the dynamics of the whole system resembles much more the dynamics of a pure Yang-Mills system for small choices of g.

The reduced influence of fermions onto the dynamics of the system for small choices of g, also manifests itself on the level of the contribution to the $\nu \neq 0$ modes of the Fourier transfered longitudinal pressure of the Yang-Mills sector (eq. 12.42). In (section 13.2.2), we where able to identify an exponentially increasing instability, that could in principle drive the system towards pressure isotropy, but is prevented by the longitudinal expansion. In (figure 13.23), we give the results of the instability for different couplings, setting $\nu_0 = 1$. It is possible to identify an exponentially increasing instability in all cases, but we find that the order of magnitude varies for the different choices of coupling[4].

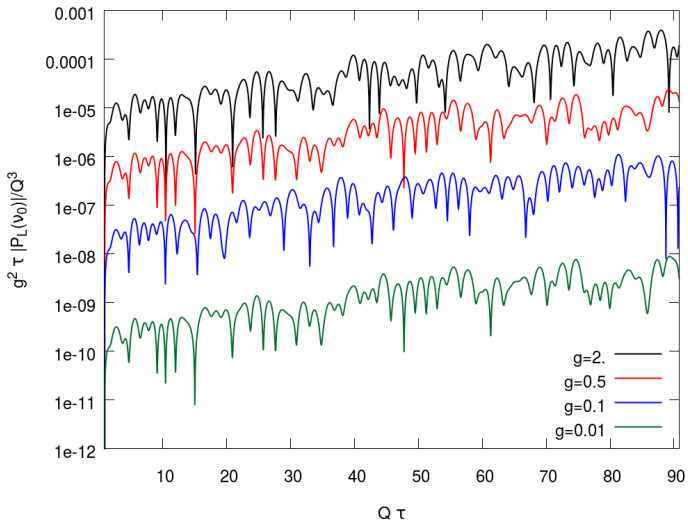

Figure 13.23: Fourier mode $\nu_0 = 1$ of the Fourier transformed longitudinal pressure of the Yang-Mills sector, for simulations including fermions of mass $m = 8.33$ MeV, with different couplings $g \in \{0.01, 0.1, 0.5, 2\}$. The simulations have been performed on a $50 \times 50 \times 40$ lattice, with transverse lattice spacing $a_\perp = 0.24$ fm, longitudinal lattice spacing of $a_\eta = 0.075$. The initial time is chosen to be $\tau_0 = 0.1$ fm and the stochastic fermion ensemble size is given as $N_{ens} = 750$.

This translates to the occupation of energy modes in the transverse plane. We give the results for different couplings $g \in \{0.5, 0.1, 0.01\}$ of the occupation and an average in the transverse planes in (figure 13.24), (figure 13.25) and (figure 13.26). Again we restricted ourselves to the Yang-Mills sector. Comparing these results to the occupation for $g = 2$ (figure 13.11), we find that for larger choices of g high energy modes are occupied earlier. This is especially evident,

[4]Note that these differences are beyond $\mathcal{O}(g^2)$.

when looking at the lattice averages of the occupation in the transverse planes, plotted on the right-hand side. Nevertheless, the initial peak at $\nu = 0$, caused from the construction of the Glasma initial conditions remains present for all choices of coupling g. Note that the difference for $g = 2$ and $g = 0.5$ is approximately one order of magnitude. As discussed previously, the reason for this observation is, that the interaction between fermions and classical gauge fields is further reduced in the expanding box, when lowering the coupling g.

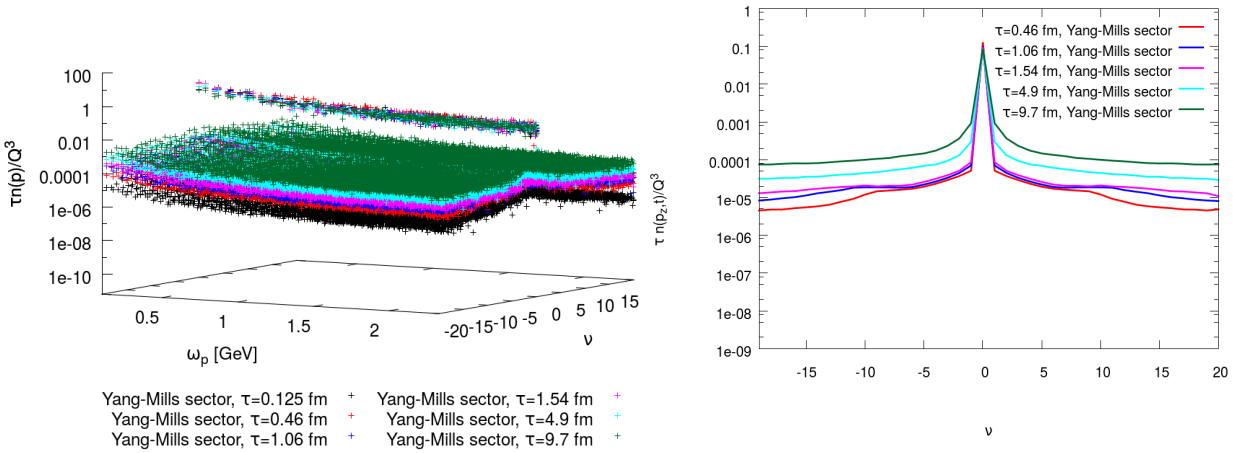

Figure 13.24: Occupation of energy modes in the transverse planes (left) and an average of these planes (right), as a function of the longitudinal Fourier mode ν, for a simulation including fermions of mass $m = 8.33$ MeV. The simulation has been performed on a $50 \times 50 \times 40$ lattice, with initial time $\tau_0 = 0.1$ fm, transverse lattice spacing $a_\perp = 0.24$ fm, longitudinal lattice spacing of $a_\eta = 0.075$. The coupling is chosen to be $g = 0.5$ and the stochastic fermion ensemble size is $N_{ens} = 750$.

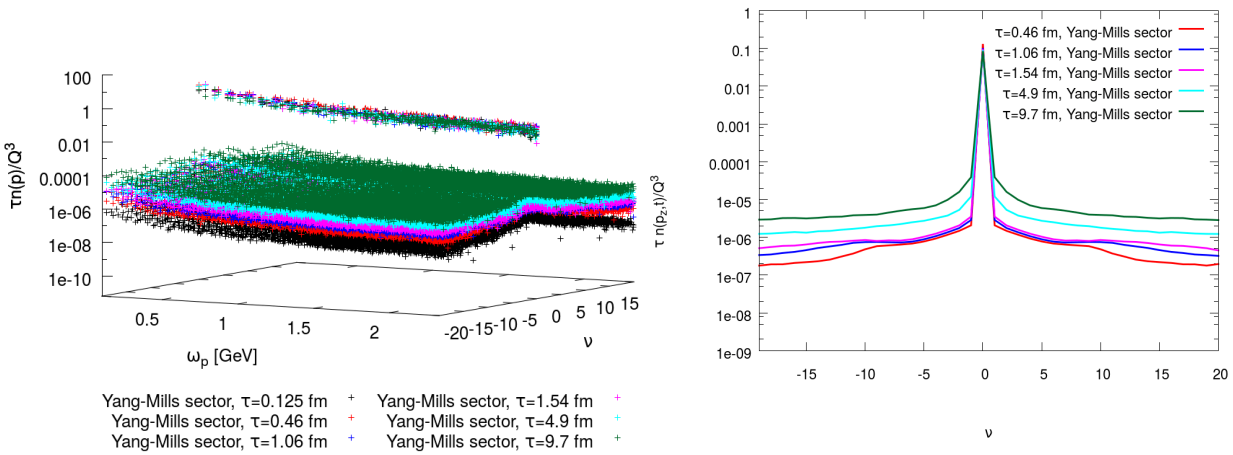

Figure 13.25: Occupation of energy modes in the transverse planes (left) and an average of these planes (right), as a function of the longitudinal Fourier mode ν, for a simulation including fermions of mass $m = 8.33$ MeV. The simulation has been performed on a $50 \times 50 \times 40$ lattice, with initial time $\tau_0 = 0.1$ fm, transverse lattice spacing $a_\perp = 0.24$ fm, longitudinal lattice spacing of $a_\eta = 0.075$. The coupling is chosen to be $g = 0.1$ and the stochastic fermion ensemble size is $N_{ens} = 750$.

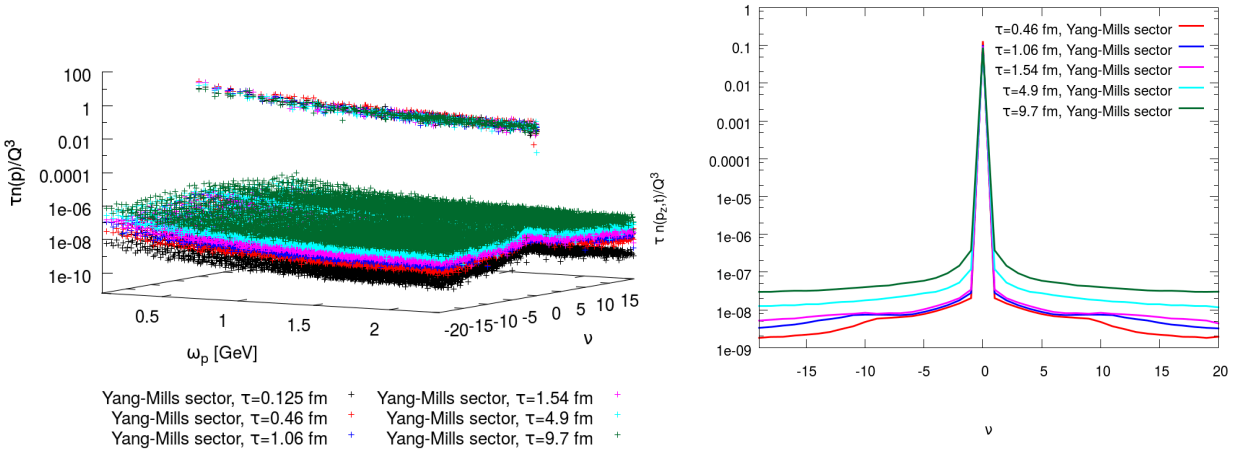

Figure 13.26: Occupation of energy modes in the transverse planes (left) and an average of these planes (right), as a function of the longitudinal Fourier mode ν, for a simulation including fermions of mass $m = 8.33$ MeV. The simulation has been performed on a $50 \times 50 \times 40$ lattice, with initial time $\tau_0 = 0.1$ fm, transverse lattice spacing $a_\perp = 0.24$ fm, longitudinal lattice spacing of $a_\eta = 0.075$. The coupling is chosen to be $g = 0.01$ and the stochastic fermion ensemble size is $N_{ens} = 750$.

13.6 Slow Expansion

Although we found, that the coupling of the classical Yang-Mills fields of the Glasma to fermion fields leads to a pressure isotropy in the static box, this could not be observed in a longitudinally expanding box. Essentially, we identified the rapid longitudinal expansion as the reason that pressure isotropy is prevented. This arises the question what happens, if the expansion is slowed down. Because the expansion is inherently embedded in the geometry of the system, from choosing Milne coordinates (eq. 9.1), the simplest way to „slow down“ the expansion is to initialize the system at a later time τ_0 [58]. One easily convinces oneself, regarding (figure 9.1), that the expansion of such a system is slowed down.

With pressure isotropization being driven from the back-coupling of the fermion fields onto the classical Yang-Mills fields, or by an explicit breaking of boost invariance, we study both mechanisms in the following. In one simulation, we couple the system to fermions of mass $m = 8.33$ MeV only and in a second simulation, we combine this with a longitudinal quantum fluctuation of magnitude $\Delta = 0.1$. The simulations have been performed with a constant transverse lattice spacing $a_\perp = 0.24$ fm to maintain comparability to the previous simulations. The lattice extent is chosen to be $50 \times 50 \times 40$, with longitudinal lattice spacing of $a_\eta = 0.075$, covering 3 units of space-time rapidity. The physical parameters as saturation scale and transverse lattice size are kept constant. To slow down the expansion, we choose an initial time of $\tau \approx 2$ fm.[5] We emphasize, that this choice is already beyond the estimated hydrodynamization time of $\tau_{hydro} = 1$ fm and therefore only represents a test for our model to study, if pressure

[5] With the energy of the system, that is initialized at $\tau_0 = 2$ fm being different when compared to a simulation initialized at $\tau_0 = 0.1$ fm, a matching can not be performed, because the given estimate for the energy of the Glasma is only valid at $\tau_0 = 0.1$ fm.

isotropization is indeed prevented by a rapid expansion. With the initial time of $\tau_0 \approx 2$ fm being much larger than $\tau_0 = 0.1$, we are able to use a coarser temporal spacing, while satisfying the Courant-Levi condition (eq. 13.4). We choose $a_\tau = 0.03 a_\perp$.

In (figure 13.27) we give the result for the longitudinal to transverse pressure ratio (left) and the pressure to energy ratio (right) for a slowly expanding system. Although no pressure isotropy is reached, we indeed find that the longitudinal to transverse pressure ratio does not drop to zero, as it has been the case previously, when initializing at $\tau_0 = 0.1$ fm (figure 13.5). On top of that, it is possible to observe that the pressure ratio moves towards isotropy earlier, in a simulation where fermions and the initial quantum fluctuation in the Yang-Mills sector have been combined, which supports our previous analysis as well. Nevertheless, the ratio is still far from a pressure isotropy. The same is true for the pressure to energy ratio, as can be seen in the right-hand plot of (figure 13.27). These observations support our previous conclusion, that the rapid longitudinal expansion prevents the system from isotropizing.

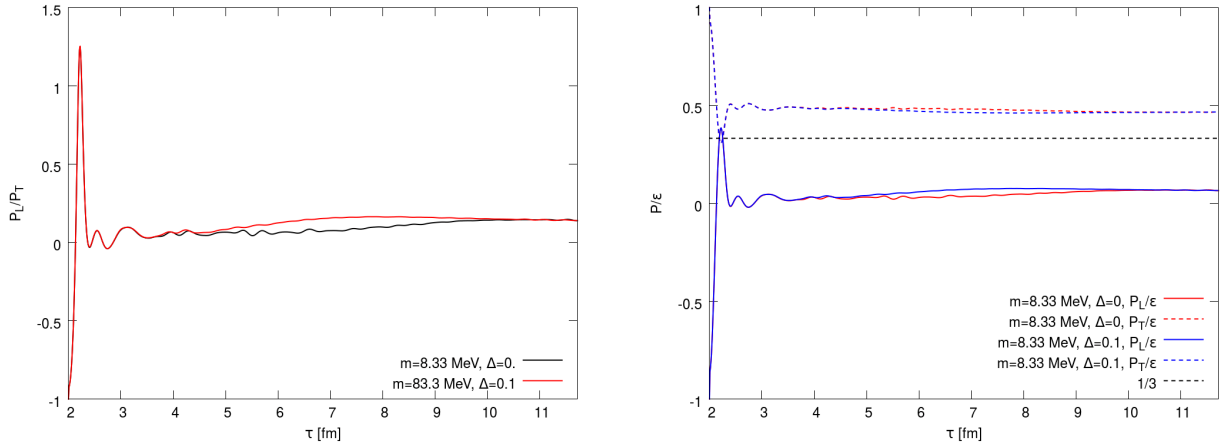

Figure 13.27: Longitudinal to transverse pressure ratio (left) and pressure to energy ratio (right) for simulations with fermions of mass $m = 8.33$ MeV, with and without an explicit breaking of boost invariance of strength $\Delta = 0.1$. The initial time is set to $\tau_0 \approx 2$ fm, corresponding geometrically to a slow longitudinally expanding system. The simulations have been performed on a $50 \times 50 \times 40$ lattice, with transverse lattice spacing $a_\perp = 0.24$ fm, longitudinal lattice spacing of $a_\eta = 0.075$. The coupling is $g = 2$ and the stochastic fermion ensemble size is given as $N_{ens} = 750$.

Following the discussion of the previous chapter, we expect the energy density profile of the two simulations in a slowly expanding system to homogenize. We give the profile of the longitudinal chromo-electric part of the energy density for the slow expanding simulations including fermions, with and without an explicit breaking of longitudinal boost invariance in (figure 13.29) and (figure 13.28). Starting from the longitudinal lines of constant energy of the Glasma, we find that the energy density profile homogenizes in both cases. As expected, this happens to be faster in case of a simulation where fermions and an explicit breaking of boost invariance are combined. In this case, it is also possible to identify the shaded regions at initial time that are caused by the quantum fluctuation of magnitude $\Delta = 0.1$. Later on, an instability arises along these regions, that spreads over the whole lattice by time. In contrast, without an explicit breaking of boost invariance, the energy exchange between the fermion and Yang-Mills sector homogenizes the energy density at every lattice point.

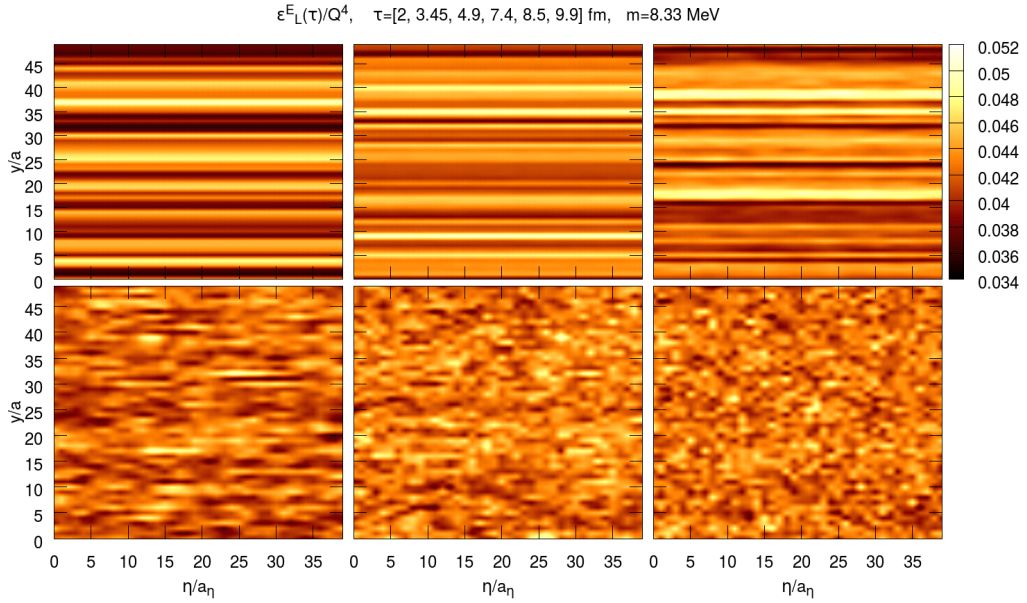

Figure 13.28: Profile of the longitudinal chromo-electric energy density $\epsilon_L^E(t)$ in a simulation with fermions of mass $m = 8.33$ MeV at times $\tau = \{2, 3.45, 4.9, 7.4, 8.5, 9.9\}$ fm (top left to bottom right). The initial time is set to $\tau_0 \approx 2$ fm, corresponding geometrically to a slow longitudinally expanding system. The simulation has been performed on a $50 \times 50 \times 40$ lattice, with transverse lattice spacing $a_\perp = 0.24$ fm and a longitudinal lattice spacing of $a_\eta = 0.075$. The coupling is $g = 2$ and the stochastic fermion ensemble size is given as $N_{ens} = 750$.

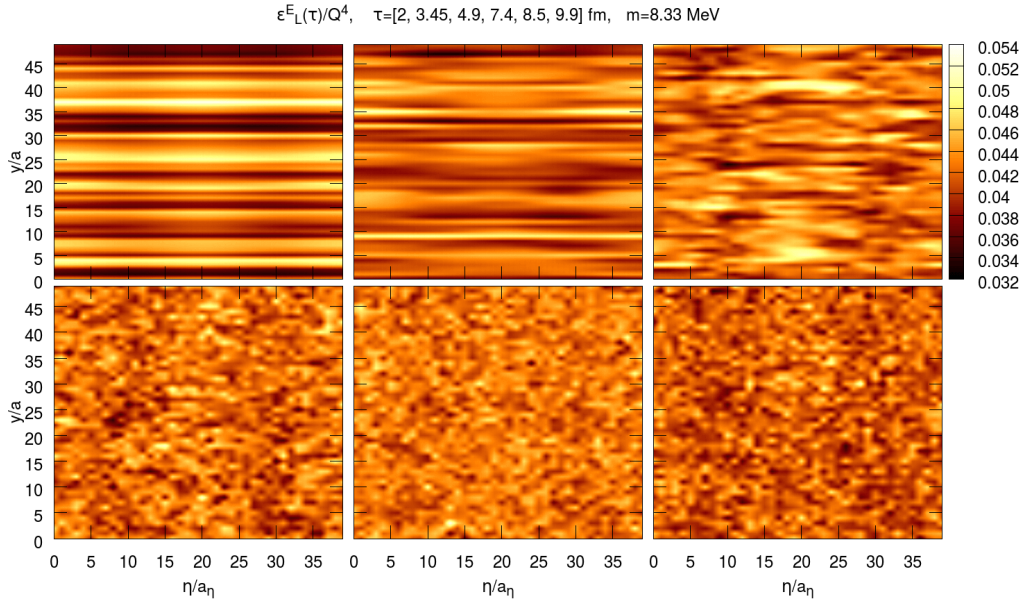

Figure 13.29: Profile of the longitudinal chromo-electric energy density $\epsilon_L^E(t)$ in a simulation with fermions of mass $m = 8.33$ MeV and with an explicit breaking of boost invariance of strength $\Delta = 0.1$, at times $\tau = \{2, 3.45, 4.9, 7.4, 8.5, 9.9\}$ fm (top left to bottom right). The initial time is set to $\tau_0 \approx 2$ fm, corresponding geometrically to a slow longitudinally expanding system. The simulation has been performed on a $50 \times 50 \times 40$ lattice, with transverse lattice spacing $a_\perp = 0.24$ fm and a longitudinal lattice spacing of $a_\eta = 0.075$. The coupling is $g = 2$ and the stochastic fermion ensemble size is given as $N_{ens} = 750$.

Finally, we have a look at the occupation of energy modes in the transverse planes, as well as at an average in these planes. We give the results for the Yang-Mills sector in a simulation with fermions only in (figure 13.30) and the result for a simulation with an additional quantum fluctuation of magnitude $\Delta = 0.1$ in (figure 13.31).

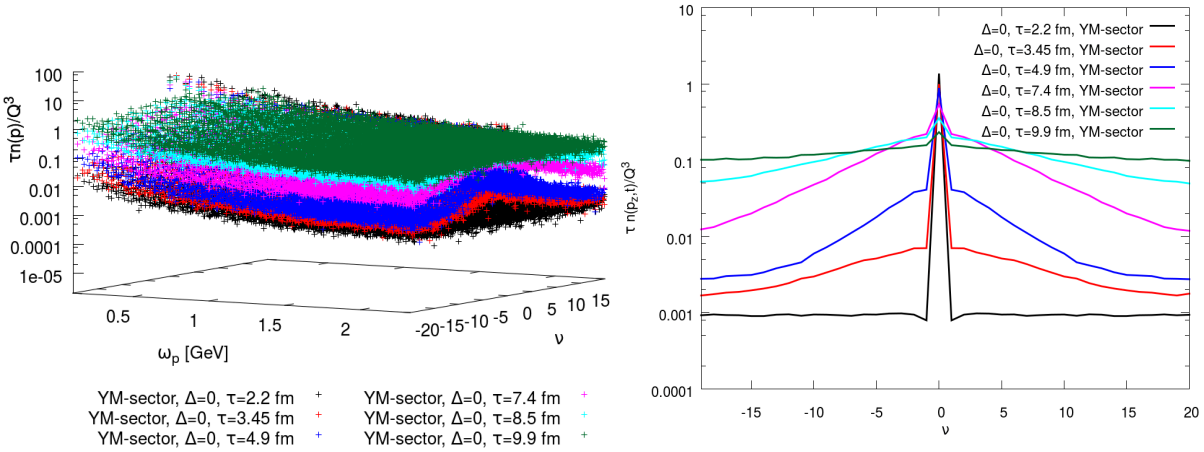

Figure 13.30: Occupation of energy modes in the transverse planes (left) and an average of these planes (right), as a function of the longitudinal Fourier mode ν, for a simulation including fermions of mass $m = 8.33$ MeV. The initial time is set to $\tau_0 \approx 2$ fm, corresponding geometrically to a slow longitudinally expanding system. The simulation has been performed on a $50 \times 50 \times 40$ lattice, with transverse lattice spacing $a_\perp = 0.24$ fm and a longitudinal lattice spacing of $a_\eta = 0.075$. The coupling is chosen to be $g = 2$ and the stochastic fermion ensemble size is $N_{ens} = 750$.

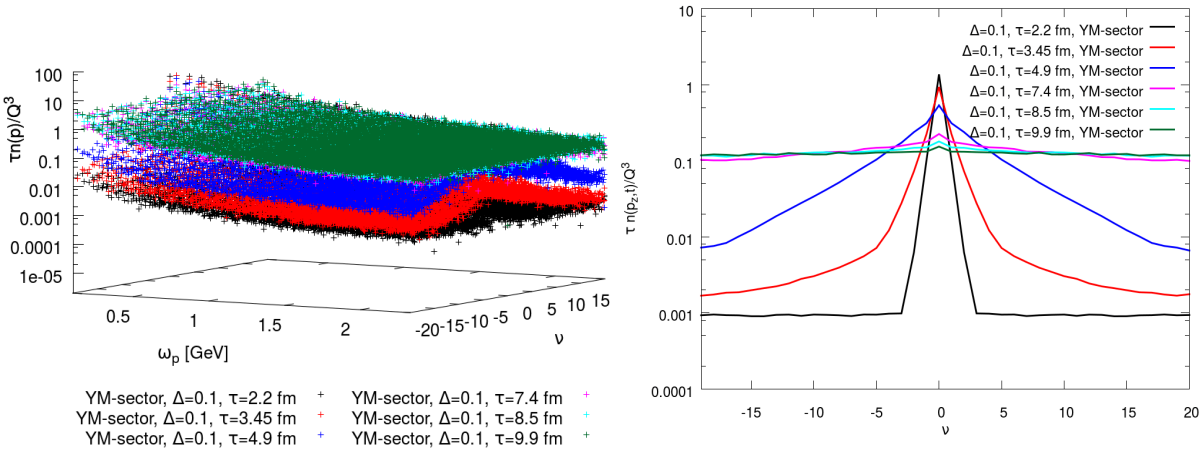

Figure 13.31: Occupation of energy modes in the transverse planes (left) and an average of these planes (right), as a function of the longitudinal Fourier mode ν, for a simulation including fermions of mass $m = 8.33$ MeV and a fluctuation of strength $\Delta = 0.1$. The initial time is set to $\tau_0 \approx 2$ fm, corresponding geometrically to a slow longitudinally expanding system. The simulation has been performed on a $50 \times 50 \times 40$ lattice, with transverse lattice spacing $a_\perp = 0.24$ fm and a longitudinal lattice spacing of $a_\eta = 0.075$. The coupling is chosen to be $g = 2$ and the stochastic fermion ensemble size is $N_{ens} = 750$.

In contrast to the occupation of energy modes in a rapidly expanding system, (figure 13.11) and (figure 13.13), the initial peak is erased during the evolution of the system and high energy modes become approximately equally occupied. This happens to be the case in both simulations, with and without an explicit breaking of longitudinal boost invariance. The main difference for the two scenarios is how the occupation of energy modes in the transverse planes proceeds. In a simulation with fermions only, the peak at $\nu = 0$ is much better pronounced and it is broadened when additionally breaking boost invariance, leading to a shape that resembles the triangular shape, familiar from the pure Yang-Mills case (figure 13.19). This supports our conclusion, that there is an interplay of both mechanisms, hence the occupation of high energy modes is governed by an energy exchange between the fermion and Yang-Mills sector, plus an instability caused by the explicit breaking of boost invariance.

With the occupation of energy modes becoming approximately equal at late times in case of a slowly expanding system, the classical approximation of the Yang-Mills sector can be expected to reach its limit of validity, as discussed in the context of the static box already. The overoccupation of classical field modes is erased during the evolution, causing the classicality to break down. This could also explain, why a slow down of the isotropization is observed in (figure 13.27) at late times. With the fail of the classical approximation at late times, the dynamics of the system is no longer well described in terms of the semi-classical model.

13.7 Two Degenerate Quark Flavors

Finally, let us investigate a simulation with two fermions of degenerate mass in the expanding box, setting the number of flavors to $N_f = 2$. In case of the static box, we have already seen that doubling the degrees of freedom in the fermion sector enhances the isotropization process. Having observed no pressure isotropy in the rapidly longitudinal expanding box, we will test if this situation changes, when considering two fermion flavors. We extracted the transverse lattice spacing in case of two degenerate fermions to be $a_\perp \approx 0.27$ fm, with a transverse lattice extent of $N_\perp = 44$, within a matching procedure presented in the beginning of this chapter. For the longitudinal lattice spacing we choose $a_\eta = 0.075$, with $N_\eta = 40$, covering 3 units of space-time rapidity η. The mass of the two degenerate quarks is given as $m = 7.34$ MeV, which is parametrically of the order of the mass of the up-/down quark.

In (figure 13.32), we give the result for the longitudinal to transverse pressure ratio (left) and the pressure to energy ratio (right) in a simulation with $N_f = 1$ and $N_f = 2$ degenerate fermions. We find in both cases, that the longitudinal pressure drops to zero after an initial oscillatory phase and no pressure isotropy is reached. At the same time, the free streaming limit is approached by the system, with the transverse pressure to energy ratio taking the value of $P_T/\epsilon \to 1/2$. In contrast to the static box, we do not observe a significant difference regarding pressure isotropization, when considering two degenerate quark flavors and still no isotropy is reached. The only difference is present in the initial oscillatory phase, where the frequency in case of a simulation with fermions turns out to be even higher in a simulation with two fermions present, which has to be connected to the fact that the degrees of freedom in the fermion sector have been doubled.

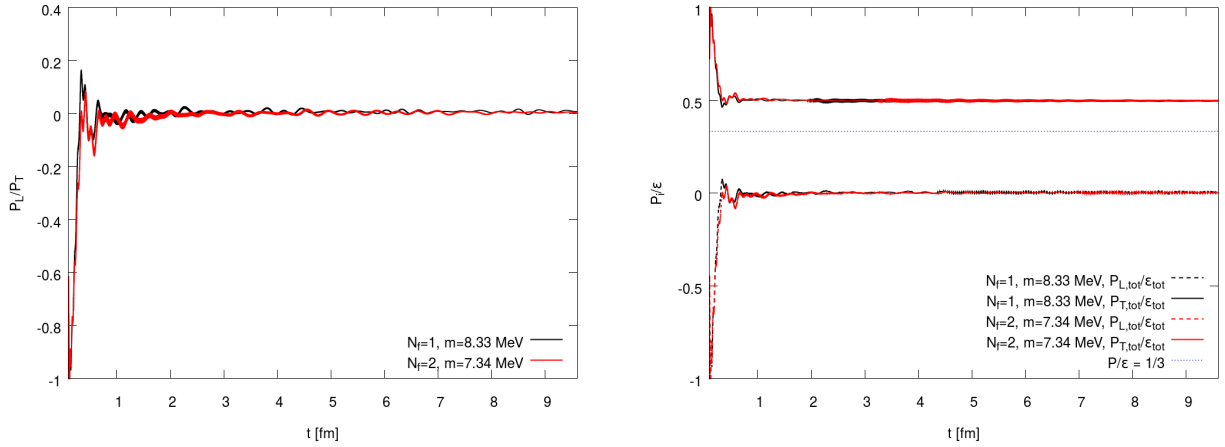

Figure 13.32: Longitudinal to transverse pressure ratio (left) and pressure to energy ratio (right) for a simulation with $N_f = 1$ fermions of mass $m = 8.33$ MeV and $N_f = 2$ fermions of mass $m = 7.34$ MeV. The simulation for $N_f = 1$ has been performed on a $50 \times 50 \times 40$ lattice, with $a_\perp = 0.24$ fm and for $N_f = 2$ on a $44 \times 44 \times 40$ lattice, with $a_\perp = 0.27$ fm. The longitudinal lattice spacing is $a_\eta = 0.075$, the initial time is set to $\tau_0 = 0.1$ fm, the coupling to $g = 2$ and the fermion ensemble size is $N_{ens} = 750$.

This is supported by the occupation of energy modes in the transverse plane and the lattice average in these planes. We give the occupation for the Yang-Mills sector, in the two flavor case in (figure 13.33). Comparing it to the one flavor case (figure 13.11) and (figure 13.13), we find that there is only a small deviation for occupied high energy modes. As expected, high energy modes become occupied slightly earlier in case of two flavors, which can be seen best for the lattice averaged occupation in the transverse plane. Nevertheless, the rapid longitudinal expansion dominates the dynamics of the system, not leading to an approximately equal occupation of energy modes at late times.

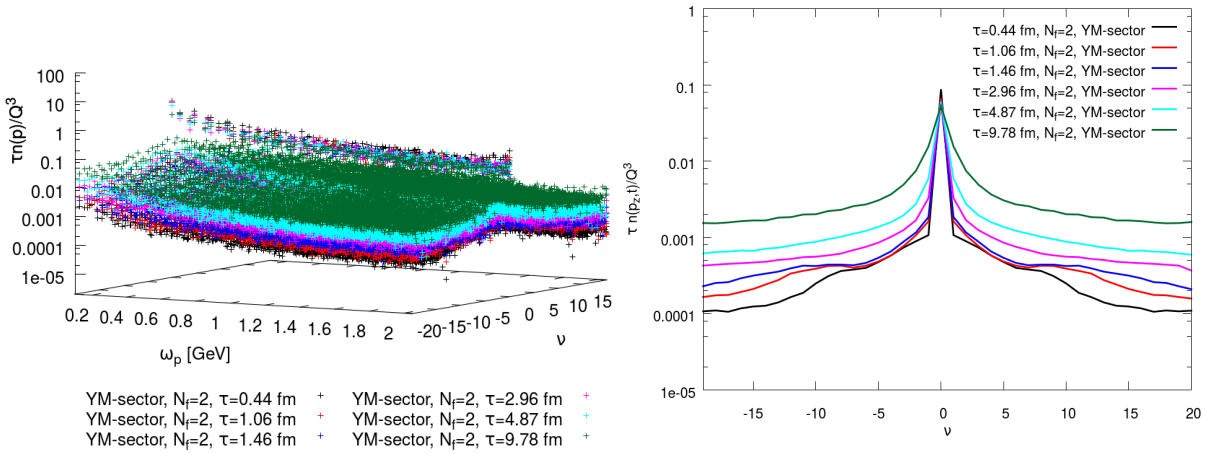

Figure 13.33: Occupation of energy modes in the transverse planes (left) and an average of these planes (right) as a function of the longitudinal Fourier mode ν, for a simulation with $N_f = 2$ fermions of mass $m = 7.34$ MeV. The simulation has been performed on a lattice with $44 \times 44 \times 40$ points, with $a_\perp = 0.27$ fm. The longitudinal lattice spacing is $a_\eta = 0.075$, the initial time is set to $\tau_0 = 0.1$ fm, the coupling to $g = 2$ and the fermion ensemble size is $N_{ens} = 750$.

Conclusion and Research Perspectives

In this thesis we investigated the impact of fermions coupled to classical Yang-Mills fields of the Glasma, on the dynamics of the system, in a static and a longitudinally expanding box. The non-equilibrium Glasma has been constructed from the Color-Glass-Condensate effective theory for the early phase of a heavy ion collision, after $\tau \approx 0.1$ fm and used as an initial condition for the Yang-Mills sector, whereas the fermions entered as vacuum fermions. The dynamics has been governed from the equations of motion of a semi-classical approximation of QCD, where we have seen, that the fermions enter as a color current. We presented a systematic renormalization and derived the observables, measured in the lattice simulation. With the classical lattice theory being UV-divergent and a continuum limit therefore not being possible, we fixed the lattice spacing, by matching the energy density to an estimate for the early phase of a heavy ion collision, based on a saturation model [132].

We found in the static box, that in contrast to pure Yang-Mills simulations, the initially highly anisotropic pressure of the Glasma isotropizes, when coupling the system to fermions. We additionally found, that the limit of $P/\epsilon \to 1/3$, familiar from an ultra-relativistic gas of free particles, is reached for the pressure to energy ratio, for both, the total system and the individual fermion and Yang-Mills sector. We saw, that this observation is not strongly dependent on the fermion mass, testing for masses that are parametrically of the order of the strange-quark mass and the up/down-quark mass. We identified a redistribution from overoccupied low, to high energy modes, caused from an energy exchange between the Yang-Mills and fermion sector, as a necessity for the development of pressure isotropy. This process essentially compares to the energy cascade necessary for thermalization (cf. [58]) and caused from a chromo-Weibel instability in a pure Yang-Mills system with broken boost invariance. We found, that the process is supported, when doubling the degrees of freedom in the fermion sector, setting $N_f = 2$, but suppressed, when reducing the interaction strength of fermions and Yang-Mills fields, namely the coupling g. All in all, a coupling to fermions drives the Glasma towards pressure isotropy in a static box. However, no perfect isotropy is reached at the time where hydrodynamics is expected to become applicable $t_{hydro} \approx 1$ fm, but the system is far from the free-streaming limit.

From a matching of the late time energy density of the fermion sector to the energy density of a free gas, we extracted a temperature of the order of $T \sim 1400$ MeV, that is much larger than an estimate of $T \sim 300$ MeV for the QGP from experimental data [160]. This approach is limited, because we neglected the longitudinal expansion of the system and treated the fermions as a free gas at late times. On top of that, we saw that the overoccupation of low energy modes is erased during the evolution. As a consequence, classical field modes are no longer overoccupied and the approximation breaks down at late times in the static box.

In a second part of this work, we extended the model to a longitudinally expanding box, presenting the equations of motion and observables and the vacuum solution of the Dirac

equation in Milne coordinates, used as an initial condition for the fermion sector. The lattice spacing could again be fixed from a matching procedure. We performed simulations in the central rapidity region, using the formation time of the Glasma $\tau \approx 0.1$ fm as an initial time. We found, that no pressure isotropization is reached in the expanding box, independent on fermion masses, parametrically of the order of the up/down- and strange-quark mass. On the opposite, the system falls into the free-streaming limit, where the fermions and classical gluons evolve (quasi-)free at late times. It was possible to identify the characteristics of the free-streaming limit, familiar from pure Yang-Mills simulations. We saw, that the energy density decreases with $\sim \frac{1}{\tau}$, the longitudinal pressure drops to zero and the ratio of the transverse pressure to energy reaches $P_T/\epsilon \to 1/2$.

Although the coupling to fermions leads to an occupation of high energy modes in the expanding box as well, this turns out to happen much slower than in the static box and no approximate uniform occupation is reached at late times, leading to no pressure isotropization. An arising instability, identified in the Fourier transformed longitudinal pressure of the Yang-Mills sector, is not strong enough to succeed over the rapid longitudinal expansion and pressure isotropy is prevented. This remains to be true, when additionally breaking longitudinal boost invariance in the Yang-Mills sector, or considering two degenerate fermions. That this is indeed rooted in the rapid longitudinal expansion of the system could be demonstrated, by investigating a slowly expanding system, where the free-streaming limit is not reached, when coupling to fermions.

For the occupation of energy modes, the reduced energy exchange between the sectors and the generation of additional low energy modes in longitudinal direction due to the expansion, causes low energy modes to remain overoccupied in the expanding box. As a consequence, the classical approximation does not break down at late times, in contrast to the static box. On the downside, we have seen that pressure isotropy can only be reached in a system, where the occupation of energy modes is equalized. In general, it turns out that reaching pressure isotropy competes with the validity of the classical approximation.

In a future work, one could use the results of this thesis for a matching to QCD kinetic theory and/or hydrodynamics as discussed e.g. in [50]. Another approach could be a treatment of the Yang-Mills UV-modes in a systematic way, using either Vlasov equations [167, 168, 169], or the NLO calculations presented in [63, 64]. On top of that, considering nuclei of finite thickness, has turned out to be a promising improvement of the model [65, 66, 67]. For the fermions, it could be interesting to initialize them in the background of the static color sources of the CGC effective theory. A formalism for the expanding box has been presented in[74], but it has (yet) never been realized in a simulation.

Finally, having seen that the overoccupation of classical field modes breaks down when moving towards pressure isotropy, an important question is a running of coupling. Due to the breakdown, it is no longer valid to take the coupling to be fixed at the scale of gluon saturation Q_s from the CGC. One would expect a running towards strong coupling, that could have important consequences on the thermalization of the system [170]. Especially quantum effects would become more important for the dynamics of the system and an inclusion would be inevitable, also putting the applicability of perturbative methods under question and demanding a different theoretical description.

A

Appendix A - Quantum Chromodynamics on the Lattice

A.1 Pauli matrices

The Pauli matrices are given as

$$\sigma^1 = \begin{pmatrix} 0 & 1 \\ 1 & 0 \end{pmatrix}, \qquad \sigma^2 = \begin{pmatrix} 0 & -\mathrm{i} \\ \mathrm{i} & 0 \end{pmatrix}, \qquad \sigma^3 = \begin{pmatrix} 1 & 0 \\ 0 & -1 \end{pmatrix}. \tag{A.1}$$

A.2 Dirac matrices

The gamma matrices in the Dirac basis are given as

$$\gamma^0 = \begin{pmatrix} \mathbb{1} & 0 \\ 0 & -\mathbb{1} \end{pmatrix}, \qquad \gamma^i = \begin{pmatrix} 0 & -\sigma^i \\ \sigma^i & 0 \end{pmatrix}, \tag{A.2}$$

with σ^i denoting the Pauli matrices (eq. A.1). We do not specify the euclidean Dirac matrix γ^4, that only appears in the euclidean formulation of lattice QCD, because we consider real time only.

A.3 Generators of SU(3)

The generators of the $SU(3)$ Lie-group are given as

$$T^a = \frac{\lambda^a}{2}. \tag{A.3}$$

They satisfy the following Lie-algebra

$$\left[T^a, T^b\right] = \mathrm{i} f^{abc} T^c, \tag{A.4}$$

with structure constants f^{abc} given as

$$\begin{aligned} f^{123} &= 1, \\ f^{147} = -f^{156} = f^{246} = -f^{257} = f^{345} = -f^{367} &= \frac{1}{2}, \\ f^{458} = f^{678} &= \frac{\sqrt{3}}{2}. \end{aligned} \tag{A.5}$$

All other structure constants, not related to the given ones by permutation, are vanishing.

The generators of $SU(3)$ Yang-Mills theory T^a, with $a \in \{1, ..., N_c^2 - 1\}$ are defined from the Gell-Mann matrices λ^a

$$\begin{aligned} \lambda^1 &= \begin{pmatrix} 0 & 1 & 0 \\ 1 & 0 & 0 \\ 0 & 0 & 0 \end{pmatrix}, \quad \lambda^2 = \begin{pmatrix} 0 & -\mathrm{i} & 0 \\ \mathrm{i} & 0 & 0 \\ 0 & 0 & 0 \end{pmatrix}, \quad \lambda^3 = \begin{pmatrix} 1 & 0 & 0 \\ 0 & -1 & 0 \\ 0 & 0 & 0 \end{pmatrix}, \\ \lambda^4 &= \begin{pmatrix} 0 & 0 & 1 \\ 0 & 0 & 0 \\ 1 & 0 & 0 \end{pmatrix}, \quad \lambda^5 = \begin{pmatrix} 0 & 0 & -\mathrm{i} \\ 0 & 0 & 0 \\ \mathrm{i} & 0 & 0 \end{pmatrix}, \\ \lambda^6 &= \begin{pmatrix} 0 & 0 & 0 \\ 0 & 0 & 1 \\ 0 & 1 & 0 \end{pmatrix}, \quad \lambda^7 = \begin{pmatrix} 0 & 0 & 0 \\ 0 & 0 & -\mathrm{i} \\ 0 & \mathrm{i} & 0 \end{pmatrix}, \quad \lambda^8 = \frac{1}{\sqrt{3}} \begin{pmatrix} 1 & 0 & 0 \\ 0 & 1 & 0 \\ 0 & 0 & -2 \end{pmatrix}. \end{aligned} \tag{A.6}$$

A.4 Derivation of the lattice Yang-Mills equation

We present the derivation of the classical Yang-Mills equation on the lattice by making use of dimensionless quantities, rescaling all using the lattice spacing a. As discussed in (section 2.1), the classical equation of motion of the lattice chromo-electric field can be derived from

$$\begin{aligned} \partial_{\bar{t}} \bar{E}_i^a(x) =& -g^2 a^4 \frac{\partial \mathcal{H}_{YM}}{\partial \tilde{A}_i^a(x)} = -\frac{\partial}{\partial \bar{A}_i^a(x)} \mathrm{Retr}\left[\bar{E}_k(y)\bar{E}_k(y) + 2\sum_{k<j} \Big(1 - U_{kj}(y)\Big) \right] \\ =& 2\frac{\partial}{\partial \bar{A}_i^a(x)} \sum_{k<j} \mathrm{Retr}\Big[U_k(y) U_j(y+\hat{k}) U_k^\dagger(y+\hat{j}) U_j^\dagger(y) \Big]. \end{aligned} \tag{A.7}$$

Taking the derivatives we find

$$\frac{\partial}{\partial \bar{A}_i^a(x)} U_k(y) = \frac{\partial}{\partial \bar{A}_i^a(x)} e^{\mathrm{i}\bar{A}_k^b(y)T^b} = \mathrm{i}\delta_{ab} T^b e^{\mathrm{i}\bar{A}_k^b(y)T^b} \delta_{xy}\delta_{ik} = \mathrm{i}T^a \delta_{xy}\delta_{ik} U_k(y), \tag{A.8}$$

$$\frac{\partial}{\partial \bar{A}_i^a(x)} U_j(y+\hat{k}) = \mathrm{i}T^a \delta_{ij}\delta_{x,y+\hat{k}} U_j(y+\hat{k}), \tag{A.9}$$

$$\frac{\partial}{\partial \bar{A}_i^a(x)} U_j^\dagger(y) = \frac{\partial}{\partial \bar{A}_i^a(x)} e^{-\mathrm{i}\bar{A}_j^b(y)T^b} = -\mathrm{i}\delta_{ab}\delta_{ij}\delta_{xy} e^{-\mathrm{i}\bar{A}_j^b(y)T^b} T^b = -\mathrm{i}\delta_{ij}\delta_{xy} U_j^\dagger(y) T^a, \tag{A.10}$$

$$\frac{\partial}{\partial \bar{A}_i^a(x)} U_k^\dagger(y+\hat{j}) = -\mathrm{i}\delta_{ik}\delta_{x,y+\hat{j}} U_k^\dagger(y+\hat{j}) T^a. \tag{A.11}$$

Using these results leads to

$$\begin{aligned}\partial_{\bar{t}}\bar{E}_i^a(x) = 2\sum_{k<j}\mathrm{Retr}\Bigg[\mathrm{i}T^a\Big(&U_k(y)U_j(y+\hat{k})U_k^\dagger(y+\hat{j})U_j^\dagger(y)\delta_{ik}\delta_{xy}\\ &+U_j(y+\hat{k})U_k^\dagger(y+\hat{j})U_j^\dagger(y)U_k(y)\delta_{ij}\delta_{x,y+\hat{k}}\\ &-U_j^\dagger(y)U_k(y)U_j(y+\hat{k})U_k^\dagger(y+\hat{j})\delta_{ik}\delta_{x,y+\hat{j}}\\ &-U_k(y)U_j(y+\hat{k})U_k^\dagger(y+\hat{j})U_j^\dagger(y)\delta_{ij}\delta_{xy}\Big)\Bigg],\end{aligned} \tag{A.12}$$

where we used the cyclicity of the trace. It is now possible to identify the lattice plaquettes, leading to

$$\begin{aligned}\partial_{\bar{t}}\bar{E}_i^a(x) &= 2\sum_{k<j}\mathrm{Retr}\Bigg[\mathrm{i}T^a\Big(U_{kj}(y)\delta_{ik}\delta_{xy}+U_{j,-k}(y+\hat{k})\delta_{ij}\delta_{x,y+\hat{k}}\\ &\qquad -U_{-jk}(y+\hat{j})\delta_{ik}\delta_{x,y+\hat{j}}-U_{kj}(y)\delta_{ij}\delta_{xy}\Big)\Bigg]\\ &= 2\sum_{k<j}\mathrm{Retr}\Bigg[\mathrm{i}T^a\Big(U_{kj}(x)\delta_{ik}+U_{j,-k}(x)\delta_{ij}-U_{-jk}(x)\delta_{ik}-U_{kj}(x)\delta_{ij}\Big)\Bigg].\end{aligned} \tag{A.13}$$

Finally, we use $\mathrm{Re}(\mathrm{i}z) = -\mathrm{Im}(z)$ and $\mathrm{Imtr}\Big[T^aU_{ji}(x)\Big] = -\mathrm{Imtr}\Big[T^aU_{ij}(x)\Big]$, and make use of the Kronecker deltas for Lorentz indices

$$\begin{aligned}\partial_{\bar{t}}\bar{E}_i^a(x) &= 2\mathrm{Imtr}\Bigg[T^a\sum_{i<j}\Big(U_{ji}(x)+U_{-ji}(x)\Big)+T^a\sum_{i>j}\Big(U_{ji}(x)+U_{-ji}(x)\Big)\Bigg]\\ &= 2\sum_{j\neq i}\mathrm{Imtr}\Big[T^a\Big(U_{ji}(x)+U_{-ji}(x)\Big)\Big],\end{aligned} \tag{A.14}$$

with $T^{a\dagger} = T^a$ and $U_{ij}^\dagger(x) = U_{ji}(x)$.

A.5 Equivalence of the lattice and the continuum equation

In this appendix we briefly motivate, how the continuum equation of motion for the chromoelectric field can be reproduced from the corresponding lattice equation of motion, when taking the continuum limit $a \to 0$. This is possible to show from (eq. 2.13), making use of the Baker-Campbell-Hausdorff formula

$$e^Xe^Y = e^{X+Y+\frac{1}{2}[X,Y]+\frac{1}{12}[X,[X,Y]]-\frac{1}{12}[Y,[X,Y]]}, \tag{A.15}$$

with X and Y denoting two arbitrary matrices of the same dimension. We use the Baker-Campbell-Hausdorff formula to rewrite the lattice plaquette entering the equation of motion

of the chromo-electric field (eq. 2.13), neglecting all terms of the order $\mathcal{O}(a^4)$

$$
\begin{aligned}
U_{ji}(x) =& e^{\mathrm{i}agA_j(x)} e^{\mathrm{i}agA_i(x+\hat{j})} e^{-\mathrm{i}agA_j(x+\hat{i})} e^{-\mathrm{i}agA_i(x)} \qquad \text{(A.16)}\\
=& \exp\Bigg[\mathrm{i}ag\Big(\big(A_i(x+\hat{j}) - A_i(x)\big) - \big(A_j(x+\hat{i}) - A_j(x)\big)\Big)\\
&- \frac{1}{2}a^2g^2\Big(\big[A_j(x), A_i(x+\hat{j})\big] + \big[A_j(x+\hat{i}), A_i(x)\big]\Big)\\
&+ \frac{1}{2}a^2g^2\big[A_j(x) + A_i(x+\hat{j}), A_j(x+\hat{i}) + A_i(x)\big]\\
&- \frac{\mathrm{i}}{12}a^3g^3\Big(\big[A_j(x), \big[A_j(x), A_i(x+\hat{j})\big]\big] - \big[A_i(x+\hat{j}), \big[A_j(x), A_i(x+\hat{j})\big]\big]\\
&\qquad - \big[A_j(x+\hat{i}), \big[A_j(x+\hat{i}), A_i(x)\big]\big] + \big[A_i(x), \big[A_j(x+\hat{i}), A_i(x)\big]\big]\Big)\\
&- \frac{\mathrm{i}}{4}a^3g^3\Big(\big[A_j(x) + A_i(x+\hat{j}), \big[A_j(x+\hat{i}), A_i(x)\big]\big]\\
&\qquad - \big[\big[A_j(x), A_i(x+\hat{j})\big], A_j(x+\hat{i}) + A_i(x)\big]\Big)\\
&+ \frac{\mathrm{i}}{12}a^3g^3\Big(\big[A_j(x) + A_i(x+\hat{j}), \big[A_j(x) + A_i(x+\hat{j}), A_j(x+\hat{i}) + A_i(x)\big]\big]\\
&\qquad + \big[A_j(x+\hat{i}) + A_i(x), \big[A_j(x) + A_i(x+\hat{j}), A_j(x+\hat{i}) + A_i(x)\big]\big]\Big) + \mathcal{O}(a^4)\Bigg]
\end{aligned}
$$

It is possible to simplify the majority of the commutators, by making use of

$$A_i(x+\hat{j}) = A_i(x) + a\partial_j A_i(x) + \mathcal{O}(a^2). \qquad \text{(A.17)}$$

Inserting this and simplifying the commutators in a tedious calculation finally leads to

$$
\begin{aligned}
U_{ji}(x) = \exp\Bigg(&\mathrm{i}a^2g\big(\partial_j A_i(x) - \partial_i A_j(x)\big) - a^2g^2\big[A_j(x), A_i(x)\big] + \frac{1}{2}a^3g^2\Big(2\big[\partial_j A_i(x), A_j(x)\big]\\
&- 2\big[\partial_i A_j(x), A_i(x)\big] + \big[\partial_j A_i(x), A_i(x)\big] - \big[\partial_i A_j(x), A_j(x)\big]\Big) \qquad \text{(A.18)}\\
&- \frac{\mathrm{i}}{2}a^3g^3\Big(\big[A_j(x), \big[A_j(x), A_i(x)\big]\big] + \big[A_i(x), \big[A_j(x), A_i(x)\big]\big]\Big) + \mathcal{O}(a^4)\Bigg).
\end{aligned}
$$

It is possible to repeat all previous steps for the plaquette U_{-ji}, this time making use of

$$A_i(x-\hat{j}) = A_i(x) - a\partial_j A_i(x) + \mathcal{O}(a^2). \qquad \text{(A.19)}$$

After expanding the exponential function, the sum of both plaquettes is given as

$$
\begin{aligned}
&U_{ij}(x) + U_{-ji}(x) \qquad \text{(A.20)}\\
&\quad = 2 + \mathrm{i}a^3g\Big(\partial_j\partial_j A_i(x) - \partial_i\partial_j A_j(x)\Big) + \mathrm{i}^2a^3g^2\Big(\big[\partial_j A_j(x), A_i(x)\big] + \big[A_j(x), \partial_j A_i(x)\big]\Big)\\
&\qquad + \mathrm{i}^2a^3g^2\Big(\big[A_j(x), \partial_j A_i(x)\big] - \big[A_j(x), \partial_i A_j(x)\big] + \mathrm{i}g\big[A_j(x), \big[A_j(x), A_i(x)\big]\big]\Big).
\end{aligned}
$$

We can now insert the continuum field strength tensor (eq. 1.12) and use

$$
\begin{aligned}
\partial_j F_{ji}(x) =& \partial_j\partial_j A_i(x) - \partial_j\partial_i A_j(x) + \mathrm{i}g\partial_j\big[A_j(x), A_i(x)\big] \qquad \text{(A.21)}\\
=& \partial_j\partial_j A_i(x) - \partial_j\partial_i A_j(x) + \mathrm{i}g\Big(\big[\partial_j A_j(x), A_i(x)\big] + \big[A_j(x), \partial_j A_i(x)\big]\Big),
\end{aligned}
$$

finally obtaining

$$\begin{aligned} U_{ij}(x) + U_{-ji}(x) =& 2 + \mathrm{i}a^3 g\Big(\partial_j F_{ji}(x) + \mathrm{i}g\big[A_j(x), F_{ji}(x)\big]\Big) + \mathcal{O}(a^4) \\ =& 2 + \mathrm{i}a^3 g\Big(\partial_j F^b_{ji}(x) T^b - g f^{bdde} T^b A^d_j(x) F^e_{ji}(x)\Big) + \mathcal{O}(a^4). \end{aligned} \tag{A.22}$$

We can now take the color trace

$$\begin{aligned} 2\mathrm{tr}\Big[T^a\Big(U_{ij}(x) + U_{-ji}(x)\Big)\Big] =& 2\mathrm{tr}\Big[2T^a + \mathrm{i}a^3 g\Big(\partial_j F^b_{ji}(x) T^b T^a - g f^{bdde} T^b T^a A^d_j(x) F^e_{ji}(x)\Big)\Big] \\ =& 4\underbrace{\mathrm{tr} T^a}_{=0} + \mathrm{i}a^3 g\Big(\partial_j F^b_{ji}(x) 2\underbrace{\mathrm{tr}\big[T^b T^a\big]}_{=\frac{1}{2}\delta^{ab}} - g f^{bde} 2\underbrace{\mathrm{tr}\big[T^b T^a\big]}_{=\frac{1}{2}\delta^{ab}} A^d_j(x) F^e_{ji}(x)\Big) \\ =& \mathrm{i}a^3 g\Big(\partial_j F^a_{ji} - g f^{abc} A^b_j(x) F^c_{ji}(x)\Big). \end{aligned} \tag{A.23}$$

Inserting this result into (eq. 2.13) we find

$$\begin{aligned} \partial_{\tilde{t}} \tilde{E}^a_i(x) = g a^3 \partial_t E^a_i(x) =& 2\sum_{j\neq i} \mathrm{Im}\mathrm{tr}\Big[T^a\Big(U_{ji}(x) + U_{-ji}(x)\Big)\Big] \\ =& \sum_{j\neq i} \mathrm{Im}\Big[\mathrm{i}a^3 g\Big(\partial_j F^a_{ji} - g f^{abc} A^b_j(x) F^c_{ji}(x)\Big)\Big] \\ =& g a^3 \sum_{j\neq i}\Big[\partial_j F^a_{ji} - g f^{abc} A^b_j(x) F^c_{ji}(x)\Big], \end{aligned} \tag{A.24}$$

demonstrating the equivalence of continuum and lattice equation of motion, in the limit $a \to 0$.

A.6 Naive Free Fermion Propagator on a Minkowski lattice

The (naive) Dirac operator of free fermions on a Minkowski lattice is given as

$$\begin{aligned} &\bar{\psi}(x)\Big(\mathrm{i}\gamma^0 \delta(x^0 - y^0)\partial_{y^0}\delta_{\mathbf{xy}} + \sum_{i=1}^{3} \frac{\mathrm{i}}{2a}\gamma^i\Big(\delta_{\mathbf{x}+\hat{i},\mathbf{y}} - \delta_{\mathbf{x}-\hat{i},\mathbf{y}}\Big)\delta(x^0 - y^0) - m\delta_{\mathbf{xy}}\delta(x^0 - y^0)\Big)\psi(y) \\ &= \bar{\psi}(x) D(x,y)\psi(y). \end{aligned} \tag{A.25}$$

The lattice propagator of a free Dirac field is now given by inverting the Dirac operator. The inversion is done in momentum space, preforming a spacial discrete Fourier transformation and a continuous Fourier transformation in time

$$\tilde{D}(p,q) = \frac{1}{|\Lambda|}\int \sum_{\mathbf{x},\mathbf{y}\in\Lambda} e^{-\mathrm{i}px} D(x,y) e^{\mathrm{i}qy} dx_0 dy_0, \tag{A.26}$$

with $\Lambda = \Big\{x^i | x^i = a n^i, n^i \in (0, ..., N_i)\Big\}$ the (isotropic) spacial lattice. Note that

$$\begin{aligned} \sum_{\mathbf{x},\mathbf{y}\in\Lambda} e^{-\mathrm{i}px}\delta_{x+\hat{i},y} e^{\mathrm{i}qy} &= \sum_{\mathbf{x}\in\Lambda} e^{-\mathrm{i}px} e^{\mathrm{i}q(x+\hat{\mu})} = \sum_{\mathbf{x}\in\Lambda} e^{-\mathrm{i}(p-q)x} e^{\mathrm{i}q^i a}, \\ \sum_{\mathbf{x},\mathbf{y}\in\Lambda} e^{-\mathrm{i}px}\delta_{x-\hat{i},y} e^{\mathrm{i}qy} &= \sum_{\mathbf{x}\in\Lambda} e^{-\mathrm{i}px} e^{\mathrm{i}q(x-\hat{i})} = \sum_{\mathbf{x}\in\Lambda} e^{-\mathrm{i}(p-q)x} e^{-\mathrm{i}q^i a}. \end{aligned} \tag{A.27}$$

We arrive at

$$\tilde{D}(p,q) = \frac{1}{|\Lambda|}\int \sum_{\mathbf{x}\in\Lambda}\Bigg(-\gamma^0 q_0 + \sum_{i=1}^{3} \underbrace{\frac{\mathrm{i}}{2a}\gamma^i\Big(e^{\mathrm{i}q^i a} - e^{-\mathrm{i}q^i a}\Big)}_{=-\frac{1}{a}\gamma^i\sin(q_i a)} - m\Bigg) e^{-\mathrm{i}(p-q)x} dx_0. \tag{A.28}$$

We found

$$\tilde{D}(p) = -\gamma^0 p_0 - \frac{1}{a}\sum_{i=1}^{3}\gamma^i \sin\Big(p_i a\Big) - m. \tag{A.29}$$

To invert the operator, let us consider

$$\begin{aligned}\tilde{D}(p) =& \Bigg(-\gamma^0 p_0 - \frac{1}{a}\sum i = 1^3 \gamma^i \sin\Big(p_i a\Big) - m\Bigg) \frac{-\gamma^0 p_0 - \frac{1}{a}\sum_{i=1}^{3}\gamma^i \sin\Big(p_i a\Big) + m}{-\gamma^0 p_0 - \frac{1}{a}\sum_{i=1}^{3}\gamma^i \sin\Big(p_i a\Big) + m} \\ =& \frac{p_0^2 + \sum_{i,j=1}^{3}\frac{1}{a^2}\eta^{ij}\sin(p_i a)\sin(p_j a) - m^2}{-\gamma^0 p_0 - \sum_{i=1}^{3}\frac{1}{a}\gamma^i \sin\Big(p_i a\Big) + m},\end{aligned} \tag{A.30}$$

where we used

$$\Big\{\gamma^\mu, \gamma^\nu\Big\} = 2\eta^{\mu\nu}. \tag{A.31}$$

Inverting the Dirac operator then leads to

$$\tilde{D}^{-1}(p) = -\frac{\gamma^0 p_0 + \sum_{i=1}^{3}\frac{1}{a}\gamma^i \sin\Big(p_i a\Big) - m}{p_0^2 + \sum_{i,j=1}^{3}\frac{1}{a^2}\eta^{ij}\sin(p_i a)\sin(p_j a) - m^2}. \tag{A.32}$$

B

Appendix B - Derivation of the Semi-Classical Model in the Static Box

B.1 Linearization of the Yang-Mills Action

In this appendix, we linearize the Yang-Mills action on the real-time Schwinger-Keldysh contour (figure 4.1)

$$S_{YM}[\bar{A},\tilde{A}] = -\frac{1}{4}\int_{\mathcal{C}} F^a_{\mu\nu}[\bar{A},\tilde{A}](x)F^{\mu\nu,a}[\bar{A},\tilde{A}](x)d^4x, \tag{B.1}$$

in the quantum fluctuation $\tilde{A}_\mu$. Using the ansatz (eq. 4.12), the linearized field-strength-tensor is given as

$$F^a_{\mu\nu} = \Big(\partial_\mu \bar{A}^a_\nu - \partial_\nu \bar{A}^a_\mu\Big) + \Big(\partial_\mu \tilde{A}^{a,\pm}_\nu - \partial_\nu \tilde{A}^{a,\pm}_\mu\Big) - g f^{abc}\Big(\bar{A}^b_\mu \bar{A}^c_\nu + \bar{A}^b_\mu \tilde{A}^{c,\pm}_\nu + \tilde{A}^{b,\pm}_\mu \bar{A}^c_\nu\Big) + \mathcal{O}\big(\tilde{A}^2\big). \tag{B.2}$$

To shorten the notation, we define

$$\tilde{G}^{a,\pm}_{\mu\nu} = \partial_\mu \tilde{A}^{a,\pm}_\nu - \partial_\nu \tilde{A}^{a,\pm}_\mu, \qquad \bar{G}^a_{\mu\nu} = \partial_\mu \bar{A}^a_\nu - \partial_\nu \bar{A}^a_\mu, \tag{B.3}$$

leading to

$$F^a_{\mu\nu}[\tilde{A},\bar{A}] = \bar{G}^a_{\mu\nu} + \tilde{G}^{a,\pm}_{\mu\nu} - g f^{abc}\Big(\bar{A}^b_\mu \bar{A}^c_\nu + \bar{A}^b_\mu \tilde{A}^{c,\pm}_\nu + \tilde{A}^{b,\pm}_\mu \bar{A}^c_\nu\Big) + \mathcal{O}\big(\tilde{A}^2\big). \tag{B.4}$$

We now have to consider the contraction of the field-strength-tensor with itself. We neglect all $\mathcal{O}(\tilde{A}^2)$ contributions and the lengthy calculation can significantly be simplified by making use of the following identities

$$\begin{aligned} f^{abc}\bar{G}^a_{\mu\nu}\Big(\bar{A}^{\mu,b}\tilde{A}^{\nu,c,\pm} + \tilde{A}^{\mu,b,\pm}\bar{A}^{\nu,c}\Big) &= f^{abc}\bar{G}^a_{\mu\nu}\bar{A}^{\mu,b}\tilde{A}^{\nu,c,\pm} + f^{acb}\bar{G}^a_{\nu\mu}\tilde{A}^{\nu,c,\pm}\bar{A}^{\mu,b} \\ &= 2 f^{abc}\bar{G}^a_{\mu\nu}\bar{A}^{\mu,b}\tilde{A}^{\nu,c,\pm}, \end{aligned} \tag{B.5}$$

and

$$\begin{aligned} & f^{abc}f^{ade}\Big(\bar{A}^{\mu,b}\tilde{A}^{\nu,c,\pm}\bar{A}^{d}_{\mu}\bar{A}^{e}_{\nu}+\tilde{A}^{\mu,b,\pm}\bar{A}^{\nu,c}\bar{A}^{d}_{\mu}\bar{A}^{e}_{\nu}+\bar{A}^{\mu,b}\bar{A}^{\nu,c}\bar{A}^{d}_{\mu}\tilde{A}^{e,\pm}_{\nu}+\bar{A}^{\mu,b}\bar{A}^{\nu,c}\tilde{A}^{d,\pm}_{\mu}\bar{A}^{e}_{\nu}\Big) \qquad \text{(B.6)}\\ =&f^{abc}f^{aed}\bar{A}^{\mu,b}\tilde{A}^{\nu,c,\pm}\bar{A}^{d}_{\mu}\bar{A}^{e}_{\nu}+f^{acb}f^{ade}\tilde{A}^{\nu,c,\pm}\bar{A}^{\mu,b}\bar{A}^{e}_{\nu}\bar{A}^{d}_{\mu}+f^{abc}f^{aed}\bar{A}^{\mu,d}\bar{A}^{\nu,e}\bar{A}^{b}_{\mu}\tilde{A}^{c,\pm}_{\nu}\\ &+f^{acb}f^{ade}\bar{A}^{\nu,d}\bar{A}^{\mu,e}\tilde{A}^{b,\pm}_{\nu}\bar{A}^{c}_{\mu}\\ =&4f^{abc}f^{aed}\bar{A}^{\mu,b}\tilde{A}^{\nu,c,\pm}\bar{A}^{d}_{\mu}\bar{A}^{e}_{\nu}. \end{aligned}$$

As well as

$$\begin{aligned} f^{abc}\tilde{G}^{a,\pm}_{\mu\nu}\bar{A}^{\mu,b}\bar{A}^{\nu,c} =&f^{abc}\Big(\partial_{\mu}\tilde{A}^{a,\pm}_{\nu}-\partial_{\nu}\tilde{A}^{a,\pm}_{\mu}\Big)\bar{A}^{\mu,b}\bar{A}^{\nu,c} \qquad \text{(B.7)}\\ =&f^{abc}\Big(\partial_{\mu}\tilde{A}^{a,\pm}_{\nu}\Big)\bar{A}^{\mu,b}\bar{A}^{\nu,c}-f^{acb}\Big(\partial_{\mu}\tilde{A}^{a,\pm}_{\nu}\Big)\bar{A}^{\nu,c}\bar{A}^{\mu,b}=2f^{abc}\Big(\partial_{\mu}\tilde{A}^{a,\pm}_{\nu}\Big)\bar{A}^{\mu,b}\bar{A}^{\nu,c}, \end{aligned}$$

and

$$\tilde{G}^{\mu\nu,a,\pm}\bar{G}^{a}_{\mu\nu}=\Big(\partial_{\mu}\tilde{A}^{a,\pm}_{\nu}-\partial_{\nu}\tilde{A}^{a,\pm}_{\mu}\Big)\bar{G}^{\mu\nu,a}=\partial_{\mu}\tilde{A}^{a,\pm}_{\nu}\bar{G}^{\mu\nu,a}-\partial_{\mu}\tilde{A}^{a,\pm}_{\nu}\bar{G}^{\nu\mu,a}=2\Big(\partial_{\mu}\tilde{A}^{a,\pm}_{\nu}\Big)\bar{G}^{\mu\nu,a}. \quad \text{(B.8)}$$

Combining all results, we arrive at

$$\begin{aligned} F^{\mu\nu,a}F^{a}_{\mu\nu} =&\bar{G}^{\mu\nu,a}\bar{G}^{a}_{\mu\nu}+4\Big(\partial_{\mu}\tilde{A}^{a,\pm}_{\nu}\Big)\bar{G}^{\mu\nu,a} \qquad \text{(B.9)}\\ &-4gf^{abc}\bar{G}^{a}_{\mu\nu}\bar{A}^{\mu,b}\tilde{A}^{\nu,c,\pm}-2gf^{abc}\bar{G}^{a}_{\mu\nu}\bar{A}^{\mu,b}\bar{A}^{\nu,c}-4gf^{abc}\Big(\partial_{\mu}\tilde{A}^{a,\pm}_{\nu}\Big)\bar{A}^{\mu,b}\bar{A}^{\nu,c}\\ &+g^{2}f^{abc}f^{ade}\bar{A}^{\mu,b}\bar{A}^{\nu,c}\bar{A}^{d}_{\mu}\bar{A}^{e}_{\nu}+4g^{2}f^{abc}f^{aed}\bar{A}^{\mu,b}\tilde{A}^{\nu,c,\pm}\bar{A}^{d}_{\mu}\bar{A}^{e}_{\nu}\\ =&\bar{G}^{\mu\nu,a}\bar{G}^{a}_{\mu\nu}-2gf^{abc}\bar{G}^{a}_{\mu\nu}\bar{A}^{\mu,b}\bar{A}^{\nu,c}+g^{2}f^{abc}f^{ade}\bar{A}^{\mu,b}\bar{A}^{\nu,c}\bar{A}^{d}_{\mu}\bar{A}^{e}_{\nu}\\ &+4\Big(\partial_{\mu}\tilde{A}^{a,\pm}_{\nu}\Big)\Big[\bar{G}^{\mu\nu,a}-gf^{abc}\bar{A}^{\mu,b}\bar{A}^{\nu,c}\Big]-4g\bar{A}^{b}_{\mu}\tilde{A}^{c,\pm}_{\nu}f^{abc}\Big[\bar{G}^{\mu\nu,a}-gf^{ade}\bar{A}^{\mu,d}\bar{A}^{\nu,e}\Big]\\ =&\bar{F}^{\mu\nu,a}\bar{F}^{a}_{\mu\nu}+4\Big(\partial_{\mu}\tilde{A}^{a,\pm}_{\nu}\Big)\bar{F}^{\mu\nu,a}-4gf^{abc}\bar{A}^{b}_{\mu}\tilde{A}^{c,\pm}_{\nu}\bar{F}^{\mu\nu,a}. \end{aligned}$$

After renaming some indices, we find the following result for the linearized Yang-Mills action

$$S_{YM}[\tilde{A},\bar{A}]=-\frac{1}{4}\int_{\mathcal{C}}\Big(\bar{F}^{\mu\nu,a}\bar{F}^{a}_{\mu\nu}+4\Big(\partial_{\mu}\tilde{A}^{a,\pm}_{\nu}\Big)\bar{F}^{\mu\nu,a}+4gf^{abc}\tilde{A}^{a,\pm}_{\nu}\bar{A}^{b}_{\mu}\bar{F}^{\mu\nu,c}\Big)d^{4}x+\mathcal{O}(\tilde{A}^{2}). \quad \text{(B.10)}$$

B.2 Derivation of the Fermion Self Energy

Before turning to the derivation of (eq. 5.20), let us introduce some useful propagators and identities for real time statistical quantum field theory. In the real time formalism, the fermion propagator is defined on the Schwinger-Keldysh time contour (figure 4.1) and therefore becomes matrix valued, because fields can either be located on the upper or lower branch of the contour. As a consequence, the fields entering the propagator can either be located on the same branch

$$D^{++}(x,y)=\langle\psi^{+}(x)\bar{\psi}^{+}(y)\rangle\,, \qquad D^{--}(x,y) \qquad =\langle\psi^{-}(x)\bar{\psi}^{-}(y)\rangle\,, \qquad \text{(B.11)}$$

or mix branches

$$D^{+-}(x,y)=\langle\psi^{+}(x)\bar{\psi}^{-}(y)\rangle\,, \qquad D^{-+}(x,y) \qquad =\langle\psi^{-}(x)\bar{\psi}^{+}(y)\rangle\,. \qquad \text{(B.12)}$$

These definitions are related to the Wightman-functions, cf. (chapter 5.3)

$$D^{++}(x,y) = D^{>}(x,y)\Theta(x_0-y_0) + D^{<}(x,y)\Theta(y_0-x_0) \tag{B.13}$$
$$D^{--}(x,y) = D^{>}(x,y)\Theta(y_0-x_0) + D^{<}(x,y)\Theta(x_0-y_0) \tag{B.14}$$
$$D^{+-}(x,y) = -D^{<}(x,y) \tag{B.15}$$
$$D^{-+}(x,y) = -D^{>}(x,y), \tag{B.16}$$

where $\Theta(y_0 - x_0)$ denotes the Heaviside-function. At equal time and equal position, these relations simplify in the following way

$$D^{++}(x,x) = D^{>}(x,x)\Theta(x_0-x_0) + D^{<}(x,x)\Theta(x_0-x_0) = D^{>}(x,x) + D^{<}(x,x) \tag{B.17}$$
$$D^{--}(x,x) = D^{>}(x,x)\Theta(x_0-x_0) + D^{<}(x,x)\Theta(x_0-x_0) = D^{>}(x,x) + D^{<}(x,x) \tag{B.18}$$
$$\Rightarrow D^{++}(x,x) = D^{--}(x,x). \tag{B.19}$$

To evaluate the four-point vacuum expectation values of fermion fields entering (eq. 5.17) and (eq. 5.18), we have to make use of the Wick theorem

$$\langle \psi_1^{\pm}\psi_2^{\pm}\bar{\psi}_3^{\pm}\bar{\psi}_4^{\pm}\rangle \sim -\langle \psi_1^{\pm}\bar{\psi}_3^{\pm}\rangle \langle \psi_2^{\pm}\bar{\psi}_4^{\pm}\rangle = D^{\pm\pm}(x_1-x_3)D^{\pm\pm}(x_2-x_4). \tag{B.20}$$

Using these relations, the first four-point fermion vacuum expectation value entering (eq. 5.17) can be evaluated using real-time propagators,

$$\begin{aligned}
\Big\langle \bar{\psi}^{+}(x)\gamma^{\nu}T^{a}\psi^{+}(x)\bar{\psi}^{+}(z)\gamma^{\mu}T^{b}\psi^{+}(z)\Big\rangle =& \Big\langle \bar{\psi}^{+}_{\alpha,i}(x)\gamma^{\nu}_{\alpha\beta}T^{a}_{ij}\psi^{+}_{\beta,j}(x)\bar{\psi}^{+}_{\delta,n}(z)\gamma^{\mu}_{\delta\sigma}T^{b}_{nm}\psi^{+}_{\sigma,m}(z)\Big\rangle \\
=& \Big\langle \bar{\psi}^{+}_{\alpha,i}(x)\psi^{+}_{\beta,j}(x)\bar{\psi}^{+}_{\delta,n}(z)\psi^{+}_{\sigma,m}(z)\Big\rangle \gamma^{\nu}_{\alpha\beta}T^{a}_{ij}\gamma^{\mu}_{\delta\sigma}T^{b}_{nm} \\
=& \Big\langle \psi^{+}_{\beta,j}(x)\bar{\psi}^{+}_{\alpha,i}(x)\Big\rangle \Big\langle \psi^{+}_{\sigma,m}(z)\bar{\psi}^{+}_{\delta,n}(z)\Big\rangle \gamma^{\nu}_{\alpha\beta}T^{a}_{ij}\gamma^{\mu}_{\delta\sigma}T^{b}_{nm} \\
& - \Big\langle \psi^{+}_{\beta,j}(x)\bar{\psi}^{+}_{\delta,n}(z)\Big\rangle \Big\langle \psi^{+}_{\sigma,m}(z)\bar{\psi}^{+}_{\alpha,i}(x)\Big\rangle \gamma^{\nu}_{\alpha\beta}T^{a}_{ij}\gamma^{\mu}_{\delta\sigma}T^{b}_{nm} \\
=& \mathrm{tr}\Big(\Big\langle \psi^{+}(x)\bar{\psi}^{+}(x)\Big\rangle \gamma^{\nu}T^{a}\Big)\mathrm{tr}\Big(\Big\langle \psi^{+}(z)\bar{\psi}^{+}(z)\Big\rangle \gamma^{\mu}T^{b}\Big) \\
& - \mathrm{tr}\Big(\Big\langle \psi^{+}_{\beta,j}(x)\bar{\psi}^{+}_{\delta,n}(z)\Big\rangle \gamma^{\mu}T^{b} \Big\langle \psi^{+}_{\sigma,m}(z)\bar{\psi}^{+}_{\alpha,i}(x)\Big\rangle \gamma^{\nu}T^{a}\Big) \\
=& \mathrm{tr}\Big(D^{++}(x,x)\gamma^{\nu}T^{a}\Big)\mathrm{tr}\Big(D^{++}(z,z)\gamma^{\mu}T^{b}\Big) \\
& - \mathrm{tr}\Big(D^{++}(x,z)\gamma^{\mu}T^{b}D^{++}(z,x)\gamma^{\nu}T^{a}\Big).
\end{aligned} \tag{B.21}$$

For the other four-point expectation values in (eq. 5.17) and (eq. 5.18) one finds a similar result,

$$\begin{aligned}
\Big\langle \bar{\psi}^{-}(x)\gamma^{\nu}T^{a}\psi^{-}(x)\bar{\psi}^{-}(z)\gamma^{\mu}T^{b}\psi^{-}(z)\Big\rangle =& \mathrm{tr}\Big(D^{--}(x,x)\gamma^{\nu}T^{a}\Big)\mathrm{tr}\Big(D^{--}(z,z)\gamma^{\mu}T^{b}\Big) \\
& - \mathrm{tr}\Big(D^{--}(x,z)\gamma^{\mu}T^{b}D^{--}(z,x)\gamma^{\nu}T^{a}\Big),
\end{aligned} \tag{B.22}$$

$$\begin{aligned}
\Big\langle \bar{\psi}^{+}(x)\gamma^{\nu}T^{a}\psi^{+}(x)\bar{\psi}^{-}(z)\gamma^{\mu}T^{b}\psi^{-}(z)\Big\rangle =& \mathrm{tr}\Big(D^{++}(x,x)\gamma^{\nu}T^{a}\Big)\mathrm{tr}\Big(D^{--}(z,z)\gamma^{\mu}T^{b}\Big) \\
& - \mathrm{tr}\Big(D^{+-}(x,z)\gamma^{\mu}T^{b}D^{-+}(z,x)\gamma^{\nu}T^{a}\Big),
\end{aligned} \tag{B.23}$$

$$\begin{aligned}\left\langle \bar{\psi}^-(x)\gamma^\nu T^a\psi^-(x)\bar{\psi}^+(z)\gamma^\mu T^b\psi^+(z)\right\rangle =&\mathrm{tr}\Big(D^{--}(x,x)\gamma^\nu T^a\Big)\mathrm{tr}\Big(D^{++}(z,z)\gamma^\mu T^b\Big)\\ &-\mathrm{tr}\Big(D^{-+}(x,z)\gamma^\mu T^b D^{+-}(z,x)\gamma^\nu T^a\Big).\end{aligned} \tag{B.24}$$

The combination of four-point vacuum expectation values entering (eq. 5.17) hence can be written as

$$\begin{aligned}&\left\langle \bar{\psi}^+(x)\gamma^\nu T^a\psi^+(x)\bar{\psi}^+(z)\gamma^\mu T^b\psi^+(z)\right\rangle - \left\langle \bar{\psi}^+(x)\gamma^\nu T^a\psi^+(x)\bar{\psi}^-(z)\gamma^\mu T^b\psi^-(z)\right\rangle\\ =&\mathrm{tr}\Big(D^{++}(x,x)\gamma^\nu T^a\Big)\mathrm{tr}\Big(D^{++}(z,z)\gamma^\mu T^b\Big) - \mathrm{tr}\Big(D^{++}(x,z)\gamma^\mu T^b D^{++}(z,x)\gamma^\nu T^a\Big)\\ &-\mathrm{tr}\Big(D^{++}(x,x)\gamma^\nu T^a\Big)\mathrm{tr}\Big(D^{--}(z,z)\gamma^\mu T^b\Big) + \mathrm{tr}\Big(D^{+-}(x,z)\gamma^\mu T^b D^{-+}(z,x)\gamma^\nu T^a\Big)\\ =&-\mathrm{tr}\Big(D^{++}(x,z)\gamma^\mu T^b D^{++}(z,x)\gamma^\nu T^a\Big) + \mathrm{tr}\Big(D^{+-}(x,z)\gamma^\mu T^b D^{-+}(z,x)\gamma^\nu T^a\Big),\end{aligned} \tag{B.25}$$

and in case of (eq. 5.18)

$$\begin{aligned}&\left\langle \bar{\psi}^-(x)\gamma^\nu T^a\psi^-(x)\bar{\psi}^-(z)\gamma^\mu T^b\psi^-(z)\right\rangle - \left\langle \bar{\psi}^-(x)\gamma^\nu T^a\psi^-(x)\bar{\psi}^+(z)\gamma^\mu T^b\psi^+(z)\right\rangle\\ =&-\mathrm{tr}\Big(D^{--}(x,z)\gamma^\mu T^b D^{--}(z,x)\gamma^\nu T^a\Big) + \mathrm{tr}\Big(D^{-+}(x,z)\gamma^\mu T^b D^{+-}(z,x)\gamma^\nu T^a\Big).\end{aligned} \tag{B.26}$$

In a next step, we replace the real-time propagators by Wightman-functions, using the relations (eq. B.13) introduced earlier

$$\begin{aligned}&\mathrm{tr}\Big[D^{++}(x,z)\gamma^\mu T^b D^{++}(z,x)\gamma^\nu T^a\Big]\\ &=\mathrm{tr}\Big[\Big(D^>(x,z)\Theta(x_0-z_0)+D^<(x,z)\Theta(z_0-x_0)\Big)\gamma^\mu T^b\\ &\qquad\Big(D^>(z,x)\Theta(z_0-x_0)+D^<(z,x)\Theta(x_0-z_0)\Big)\gamma^\nu T^a\Big]\\ &=\mathrm{tr}\Big[D^>(x,z)\gamma^\mu T^b D^<(z,x)\gamma^\nu T^a\Big]\Theta(x_0-z_0)+\mathrm{tr}\Big[D^<(x,z)\gamma^\mu T^b D^>(z,x)\gamma^\nu T^a\Big]\Theta(z_0-x_0)\\ &+\Big(\mathrm{tr}\Big[D^>(x,z)\gamma^\mu T^b D^>(z,x)\gamma^\nu T^a\Big]+\mathrm{tr}\Big[D^<(x,z)\gamma^\mu T^b D^<(z,x)\gamma^\nu T^a\Big]\Big)\Theta(x_0-z_0)\Theta(z_0-x_0),\end{aligned} \tag{B.27}$$

where we used that $\Theta^2(x_0-z_0)=\Theta(x_0-z_0)$. In a similar way we find

$$\begin{aligned}&\mathrm{tr}\Big[D^{--}(x,z)\gamma^\mu T^b D^{--}(z,x)\gamma^\nu T^a\Big]\\ &=\mathrm{tr}\Big[\Big(D^>(x,z)\Theta(z_0-x_0)+D^<(x,z)\Theta(x_0-z_0)\Big)\gamma^\mu T^b\\ &\qquad\Big(D^>(z,x)\Theta(x_0-z_0)+D^<(z,x)\Theta(z_0-x_0)\Big)\gamma^\nu T^a\Big]\\ &=\mathrm{tr}\Big[D^>(x,z)\gamma^\mu T^b D^<(z,x)\gamma^\nu T^a\Big]\Theta(z_0-x_0)+\mathrm{tr}\Big[D^<(x,z)\gamma^\mu T^b D^>(z,x)\gamma^\nu T^a\Big]\Theta(x_0-z_0)\\ &+\Big(\mathrm{tr}\Big[D^>(x,z)\gamma^\mu T^b D^>(z,x)\gamma^\nu T^a\Big]+\mathrm{tr}\Big[D^<(x,z)\gamma^\mu T^b D^<(z,x)\gamma^\nu T^a\Big]\Big)\Theta(x_0-z_0)\Theta(z_0-x_0).\end{aligned} \tag{B.28}$$

For the branch mixing propagators, we find

$$\mathrm{tr}\Big[D^{+-}(x,z)\gamma^\mu T^b D^{-+}(z,x)\gamma^\nu T^a\Big] = \mathrm{tr}\Big[D^{<}(x,z)\gamma^\mu T^b D^{>}(z,x)\gamma^\nu T^a\Big], \tag{B.29}$$

$$\mathrm{tr}\Big[D^{-+}(x,z)\gamma^\mu T^b D^{+-}(z,x)\gamma^\nu T^a\Big] = \mathrm{tr}\Big[D^{>}(x,z)\gamma^\mu T^b D^{<}(z,x)\gamma^\nu T^a\Big]. \tag{B.30}$$

When integrating with respect to z, the double Heaviside contribution is vanishing

$$\int_{-\infty}^{\infty} \Theta(x_0-z_0)\Theta(z_0-x_0)f(z)dz_0 = \int_{x_0}^{x_0} f(z)dz_0 = F(x_0)-F(x_0) = 0, \tag{B.31}$$

therefore it can be neglected.

Combining all results, we can rewrite the fermion four-point interaction in (eq. 5.17) as

$$\begin{aligned}
&\mathrm{i}g^2\int\Big(\Big\langle\bar\psi^+(x)\gamma^\nu T^a\psi^+(x)\bar\psi^+(z)\gamma^\mu T^b\psi^+(z)\Big\rangle - \Big\langle\bar\psi^+(x)\gamma^\nu T^a\psi^+(x)\bar\psi^-(z)\gamma^\mu T^b\psi^-(z)\Big\rangle\Big)\bar A^b_\mu(z)d^4z\\
&\quad=\mathrm{i}g^2\int\Big(\mathrm{tr}\Big[D^{<}(x,z)\gamma^\mu T^b D^{>}(z,x)\gamma^\nu T^a\Big]\Big(1-\Theta(z_0-x_0)\Big)\\
&\qquad-\mathrm{tr}\Big[D^{>}(x,z)\gamma^\mu T^b D^{<}(z,x)\gamma^\nu T^a\Big]\Theta(x_0-z_0)\Big)\bar A^b_\mu(z)d^4z.
\end{aligned} \tag{B.32}$$

Making use of the identity $\Big(1-\Theta(z_0-x_0)\Big) = \Theta(x_0-z_0)$ we finally find

$$\begin{aligned}
&\mathrm{i}g^2\int\Big(\mathrm{tr}\Big[D^{<}(x,z)\gamma^\mu T^b D^{>}(z,x)\gamma^\nu T^a\Big] - \mathrm{tr}\Big[D^{>}(x,z)\gamma^\mu T^b D^{<}(z,x)\gamma^\nu T^a\Big]\Big)\bar A^b_\mu(z)\Theta(x_0-z_0)d^4z\\
&=\mathrm{i}g^2\int\Theta(x_0-z_0)\mathrm{tr}\Big[D^{<}(x,z)\gamma^\mu T^b D^{>}(z,x)\gamma^\nu T^a - D^{>}(x,z)\gamma^\mu T^b D^{<}(z,x)\gamma^\nu T^a\Big]\bar A^b_\mu(z)d^4z.
\end{aligned} \tag{B.33}$$

We can repeat this calculation for the four-point fermion interaction of (eq. 5.18)

$$\begin{aligned}
&-\mathrm{i}g^2\int\Big(\Big\langle\bar\psi^-(x)\gamma^\nu T^a\psi^-(x)\bar\psi^-(z)\gamma^\mu T^b\psi^-(z)\Big\rangle\\
&\qquad\qquad-\Big\langle\bar\psi^-(x)\gamma^\nu T^a\psi^-(x)\bar\psi^+(z)\gamma^\mu T^b\psi^+(z)\Big\rangle\Big)\bar A^b_\mu(z)d^4z\\
&=\mathrm{i}g^2\int\Theta(x_0-z_0)\mathrm{tr}\Big[D^{<}(x,z)\gamma^\mu T^b D^{>}(z,x)\gamma^\nu T^a - D^{>}(x,z)\gamma^\mu T^b D^{<}(z,x)\gamma^\nu T^a\Big]\bar A^b_\mu(z)d^4z,
\end{aligned} \tag{B.34}$$

leading to the identical result.
For the tadpole contributions in (eq. 5.17) and (eq. 5.18) it is possible to write

$$\Big\langle\bar\psi^+(x)\gamma^\nu T^a\psi^+(x)\Big\rangle = \mathrm{tr}\Big[D^{++}(x,x)\gamma^\nu T^a\Big] = 2\mathrm{tr}\Big[F(x,x)\gamma^\nu T^a\Big], \tag{B.35}$$

$$\Big\langle\bar\psi^-(x)\gamma^\nu T^a\psi^+(x)\Big\rangle = \mathrm{tr}\Big[D^{--}(x,x)\gamma^\nu T^a\Big] = 2\mathrm{tr}\Big[F(x,x)\gamma^\nu T^a\Big], \tag{B.36}$$

where we used (eq. B.17) and identified the statistical propagator

$$D^{++}(x,x) = D^{>}(x,x) + D^{<}(x,x) = 2F(x,x). \tag{B.37}$$

We found, that (eq. 5.17) and (eq. 5.18) are identical

$$\partial_\mu \bar{F}^{\mu\nu,a} - g f^{abc} \bar{A}^b_\mu \bar{F}^{\mu\nu,c} - 2g\mathrm{tr}\Big[F(x,x)\gamma^\nu T^a\Big] \tag{B.38}$$
$$+ \mathrm{i}g^2 \int \Theta(x_0 - z_0)\mathrm{tr}\Big[D^<(x,z)\gamma^\mu T^b D^>(z,x)\gamma^\nu T^a - D^>(x,z)\gamma^\mu T^b D^<(z,x)\gamma^\nu T^a\Big]\bar{A}^b_\mu(z)d^4z = 0.$$

Identifying $x_0 = t$ and $z_0 = t'$ in (eq. B.38) and use $t = 0$ as initial time, it is possible to introduce the fermion self energy Σ

$$\begin{aligned}
&\mathrm{i}g^2 \int \Theta(x_0 - z_0)\mathrm{tr}\Big[D^<(x,z)\gamma^\mu T^b D^>(z,x)\gamma^\nu T^a - D^>(x,z)\gamma^\mu T^b D^<(z,x)\gamma^\nu T^a\Big]\bar{A}^b_\mu(z)d^4z \\
&\quad = \mathrm{i}g^2 \int_0^t \mathrm{tr}\Big[D^<(t-t',\mathbf{x}-\mathbf{z})\gamma^\mu T^b D^>(t'-t,\mathbf{z}-\mathbf{x})\gamma^\nu T^a \\
&\qquad\qquad - D^>(t-t',\mathbf{x}-\mathbf{z})\gamma^\mu T^b D^<(t'-t,\mathbf{z}-\mathbf{x})\gamma^\nu T^a\Big]\bar{A}^b_\mu(t',\mathbf{z})dt'd^3z \\
&\quad = \int_0^t \Sigma^{\mu\nu,ab}(t-t',\mathbf{x}-\mathbf{z})\bar{A}^b_\mu(t',\mathbf{z})dt'd^3z,
\end{aligned} \tag{B.39}$$

which leads to the familiar form of the equation of motion (eq. 5.20)

$$\partial_\mu \bar{F}^{\mu\nu,a} - g f^{abc} \bar{A}^b_\mu \bar{F}^{\mu\nu,c} - 2g\mathrm{tr}\Big[F(x,x)\gamma^\nu T^a\Big] + \int_0^t \Sigma^{\mu\nu,ab}(x-z)\bar{A}^b_\mu(z)d^4z = 0. \tag{B.40}$$

B.3 Wightman-Functions of Free Vacuum Fermions

In this appendix, we will derive the result for the Wightman-functions of free fermions, evaluated with respect to the vacuum state (eq. 5.23).
Recalling the definition of the Wightman-functions

$$D^>_{\alpha\beta}(x,y) = \left\langle \psi_\alpha(x)\bar{\psi}_\beta(y)\right\rangle, \qquad D^<_{\alpha\beta}(x,y) = -\left\langle \bar{\psi}_\beta(y)\psi_\alpha(x)\right\rangle, \tag{B.41}$$

we first apply a spacial Fourier transformation. Because the Wightman-functions are only dependent on spacial differences in case of vacuum fermions, we find

$$D^>_{\mathbf{p},\alpha\beta}(t,t') = \int e^{-\mathrm{i}\mathbf{px}}\left\langle \psi_\alpha(t,\mathbf{x})\bar{\psi}_\beta(t',\mathbf{0})\right\rangle d^3x \tag{B.42}$$

$$D^<_{\mathbf{p},\alpha\beta}(t,t') = -\int e^{-\mathrm{i}\mathbf{px}}\left\langle \bar{\psi}_\beta(t',\mathbf{0})\psi_\alpha(t,\mathbf{x})\right\rangle d^3x. \tag{B.43}$$

Next we insert the Fourier decomposition of the fermion spinor (eq. 1.29)

$$\psi_\alpha(t,\mathbf{x}) = \int \sum_{s=1}^{2}\left(a_s(\mathbf{k})u_{\alpha,s}(\mathbf{k})e^{-\mathrm{i}\omega_\mathbf{k}t+\mathrm{i}\mathbf{kx}} + b^\dagger_{\alpha,s}(\mathbf{k})v_s(\mathbf{k})e^{\mathrm{i}\omega_\mathbf{k}t-\mathrm{i}\mathbf{kx}}\right)\frac{d^3k}{(2\pi)^3}. \tag{B.44}$$

Inserting leads to

$$\left\langle \psi_\alpha(t,\mathbf{x})\bar{\psi}_\beta(t',\mathbf{0})\right\rangle = \int\int \sum_{s,r=1}^{2} \langle 0|\, a_s(\mathbf{k})a^\dagger_r(\mathbf{q})\,|0\rangle\, u_{\alpha,s}(\mathbf{k})\bar{u}_{\beta,r}(\mathbf{q})e^{-\mathrm{i}\omega_\mathbf{k}t+\mathrm{i}\omega_\mathbf{q}t'+\mathrm{i}\mathbf{kx}}\frac{d^3k}{(2\pi)^3}\frac{d^3q}{(2\pi)^3}, \tag{B.45}$$

where we have neglected all vacuum expectation values with annihilation operators acting on the vacuum state.
The remaining vacuum expectation value is solved, by making use of the commutator (eq. 1.30)

$$\langle 0|\, a_s(\mathbf{k}) a_r^\dagger(\mathbf{q})\, |0\rangle = (2\pi)^3 \delta_{rs}\delta(\mathbf{k}-\mathbf{q})\, \langle 0\,|\,0\rangle - \langle 0|\, a_r^\dagger(\mathbf{q}) a_s(\mathbf{k})\, |0\rangle = (2\pi)^3 \delta_{rs}\delta(\mathbf{k}-\mathbf{q}). \tag{B.46}$$

We arrive at

$$\begin{aligned}\left\langle \psi_\alpha(t,\mathbf{x})\bar{\psi}_\beta(t',\mathbf{0})\right\rangle &= \int \sum_{s=1}^{2} u_{\alpha,s}(\mathbf{k})\bar{u}_{\beta,s}(\mathbf{k}) e^{-\mathrm{i}\omega_\mathbf{k}(t-t')+\mathrm{i}\mathbf{kx}} \frac{d^3k}{(2\pi)^3} \\ &= \int \frac{1}{2\omega_\mathbf{k}} \left(\not{k}+m\right)_{\alpha\beta} e^{-\mathrm{i}\omega_\mathbf{k}(t-t')+\mathrm{i}\mathbf{kx}} \frac{d^3k}{(2\pi)^3},\end{aligned} \tag{B.47}$$

where we performed the spin sum using (eq. 1.37) in the last step.

For the other Wightman-function we have

$$\left\langle \bar{\psi}_\beta(t',\mathbf{0})\psi_\alpha(t,\mathbf{x})\right\rangle = \int\int \sum_{s,r=1}^{2} \langle 0|\, b_r(\mathbf{q}) b_s^\dagger(\mathbf{k})\, |0\rangle\, v_{\alpha,s}(\mathbf{k})\bar{v}_{\beta,r}(\mathbf{q}) e^{-\mathrm{i}\omega_\mathbf{q} t' + \mathrm{i}\omega_\mathbf{k} t - \mathrm{i}\mathbf{kx}} \frac{d^3k}{(2\pi)^3}\frac{d^3q}{(2\pi)^3}. \tag{B.48}$$

Using

$$\langle 0|\, b_s(\mathbf{k}) b_r^\dagger(\mathbf{q})\, |0\rangle = (2\pi)^3 \delta_{rs}\delta(\mathbf{k}-\mathbf{q}), \tag{B.49}$$

then leads to

$$\begin{aligned}\left\langle \bar{\psi}_\beta(t',\mathbf{0})\psi_\alpha(t,\mathbf{x})\right\rangle &= \int \sum_{s=1}^{2} v_{\alpha,s}(\mathbf{k})\bar{v}_{\beta,r}(\mathbf{k}) e^{\mathrm{i}\omega_\mathbf{k}(t-t')-\mathrm{i}\mathbf{kx}} \frac{d^3k}{(2\pi)^3} \\ &= \int \frac{1}{2\omega_\mathbf{k}} \left(\not{k}-m\right)_{\alpha\beta} e^{\mathrm{i}\omega_\mathbf{k}(t-t')-\mathrm{i}\mathbf{kx}} \frac{d^3k}{(2\pi)^3}.\end{aligned} \tag{B.50}$$

Inserting these results now leads to

$$\begin{aligned} D^{>}_{\mathbf{p},\alpha\beta}(t,t') &= \int e^{-\mathrm{i}\mathbf{px}} \left\langle \psi_\alpha(t,\mathbf{x})\bar{\psi}_\beta(t',\mathbf{0})\right\rangle d^3x \\ &= \int e^{-\mathrm{i}\mathbf{px}} \int \frac{1}{2\omega_\mathbf{k}} \left(\not{k}+m\right)_{\alpha\beta} e^{-\mathrm{i}\omega_\mathbf{k}(t-t')+\mathrm{i}\mathbf{kx}} \frac{d^3k}{(2\pi)^3} d^3x \\ &= \int \frac{1}{2\omega_\mathbf{k}} \left(\not{k}+m\right)_{\alpha\beta} e^{-\mathrm{i}\omega_\mathbf{k}(t-t')} \int e^{-\mathrm{i}\mathbf{x}(\mathbf{p}-\mathbf{k})} d^3x \frac{d^3k}{(2\pi)^3} \\ &= \int \frac{1}{2\omega_\mathbf{k}} \left(\not{k}+m\right)_{\alpha\beta} e^{-\mathrm{i}\omega_\mathbf{k}(t-t')} \delta(\mathbf{p}-\mathbf{k}) d^3k \\ &= \frac{1}{2\omega_\mathbf{p}} \left(\not{p}+m\right)_{\alpha\beta} e^{-\mathrm{i}\omega_\mathbf{p}(t-t')}. \end{aligned} \tag{B.51}$$

The other Wightman function is derived in similar fashion

$$D^{<}_{\mathbf{p},\alpha\beta}(t,t') = -\int \frac{1}{2\omega_\mathbf{k}} \left(\not{k}-m\right)_{\alpha\beta} e^{\mathrm{i}\omega_\mathbf{k}(t-t')} \delta(\mathbf{p}+\mathbf{k}) d^3k. \tag{B.52}$$

Note that

$$\begin{aligned} \not{p} = \gamma^\alpha p_\alpha &= \gamma^0 \omega_{\mathbf{p}} + \gamma^i p_i \\ \overset{\mathbf{p}\to-\mathbf{p}}{\Rightarrow} \quad & \gamma^0 \omega_{-\mathbf{p}} - \gamma^i p_i = \gamma^0 \omega_{\mathbf{p}} + \gamma^0\gamma^i\gamma^0 p_i = \gamma^0\gamma^\alpha p_\alpha \gamma^0 = \gamma^0 \not{p} \gamma^0, \end{aligned} \tag{B.53}$$

where we used $-\gamma^i = \gamma^{i\dagger} = \gamma^0\gamma^i\gamma^0$. We finally arrive at

$$D^<_{\mathbf{p},\alpha\beta}(t,t') = -\frac{1}{2\omega_{\mathbf{p}}}\Big(\gamma^0\Big(\not{p} - m\Big)\gamma^0\Big)_{\alpha\beta} e^{\mathrm{i}\omega_{\mathbf{p}}(t-t')}. \tag{B.54}$$

B.4 Evaluating the Dirac Traces

In this appendix, we evaluate the Dirac traces of (eq. 5.28). We start with

$$\begin{aligned} &\mathrm{tr}\Big[\gamma^0\Big(\not{p} - m\Big)\gamma^0\gamma^\mu\Big(\Big(\not{p} - \not{k}\Big) + m\Big)\gamma^\nu\Big] \\ =&\mathrm{tr}\Big[\gamma^0\not{p}\gamma^0\gamma^\mu\Big(\not{p} - \not{k}\Big)\gamma^\nu - \gamma^0 m\gamma^0\gamma^\mu\Big(\not{p} - \not{k}\Big)\gamma^\nu + \gamma^0\not{p}\gamma^0\gamma^\mu m\gamma^\nu - \gamma^0 m\gamma^0\gamma^\mu m\gamma^\nu\Big] \\ =&\mathrm{tr}\Big[\gamma^0\gamma^\alpha\gamma^0\gamma^\mu\gamma^\beta\gamma^\nu\Big]p_\alpha(p-k)_\beta - m^2\mathrm{tr}\Big[\gamma^\mu\gamma^\nu\Big]. \end{aligned} \tag{B.55}$$

For the mass term we have

$$\mathrm{tr}\Big[\gamma^\mu\gamma^\nu\Big] = 4\eta^{\mu\nu}, \tag{B.56}$$

and for the other term

$$\begin{aligned} \mathrm{tr}\Big[\gamma^0\gamma^\alpha\gamma^0\gamma^\mu\gamma^\beta\gamma^\nu\Big]p_\alpha(p-k)_\beta =&\mathrm{tr}\Big[\gamma^0\gamma^0\gamma^0\gamma^\mu\gamma^\beta\gamma^\nu\Big]p_0(p-k)_\beta + \mathrm{tr}\Big[\gamma^0\gamma^i\gamma^0\gamma^\mu\gamma^\beta\gamma^\nu\Big]p_i(p-k)_\beta \\ =&\mathrm{tr}\Big[\gamma^0\gamma^\mu\gamma^\beta\gamma^\nu\Big]p_0(p-k)_\beta - \mathrm{tr}\Big[\gamma^i\gamma^\mu\gamma^\beta\gamma^\nu\Big]p_i(p-k)_\beta, \end{aligned} \tag{B.57}$$

where we used that $\{\gamma^0, \gamma^i\} = 0$. A trace of four gamma matrices is given as

$$\mathrm{tr}\Big[\gamma^\alpha\gamma^\mu\gamma^\beta\gamma^\nu\Big] = 4\Big(\eta^{\alpha\mu}\eta^{\beta\nu} - \eta^{\alpha\nu}\eta^{\mu\beta} + \eta^{\alpha\beta}\eta^{\mu\nu}\Big). \tag{B.58}$$

Inserting this result leads to

$$\begin{aligned} \mathrm{tr}\Big[\gamma^0\gamma^\alpha\gamma^0\gamma^\mu\gamma^\beta\gamma^\nu\Big]p_\alpha(p-k)_\beta =&4\Big(\eta^{0\mu}\eta^{\beta\nu} - \eta^{0\nu}\eta^{\mu\beta} + \eta^{0\beta}\eta^{\mu\nu}\Big)p_0(p-k)_\beta \\ &- 4\Big(\eta^{i\mu}\eta^{\beta\nu} - \eta^{i\nu}\eta^{\mu\beta} + \eta^{i\beta}\eta^{\mu\nu}\Big)p_i(p-k)_\beta \\ =&4\eta^{\mu\nu}\Big(\omega_{\mathbf{p}}\omega_{\mathbf{p}-\mathbf{k}} + \mathbf{p}(\mathbf{p}-\mathbf{k})\Big) \\ &+ 4(p-k)^\nu\Big(p_0\eta^{0\mu} - p_i\eta^{i\mu}\Big) - 4(p-k)^\mu\Big(p_0\eta^{0\nu} - p_i\eta^{i\nu}\Big). \end{aligned} \tag{B.59}$$

In total we have

$$\begin{aligned} \mathrm{tr}\Big[\gamma^0\Big(\not{p} - m\Big)\gamma^0\gamma^\mu\Big(\Big(\not{p} - \not{k}\Big) + m\Big)\gamma^\nu\Big] =&4\eta^{\mu\nu}\Big(\omega_{\mathbf{p}}\omega_{\mathbf{p}-\mathbf{k}} + \mathbf{p}(\mathbf{p}-\mathbf{k}) - m^2\Big) \\ &+ 4(p-k)^\nu\Big(p_0\eta^{0\mu} - p_i\eta^{i\mu}\Big) - 4(p-k)^\mu\Big(p_0\eta^{0\nu} - p_i\eta^{i\nu}\Big). \end{aligned} \tag{B.60}$$

For the other trace we have

$$\begin{aligned}\mathrm{tr}\Big[\big(\not{p}+m\big)\gamma^\mu\gamma^0\big(\big(\not{p}-\not{k}\big)-m\big)\gamma^0\gamma^\nu\Big] =&\mathrm{tr}\Big[\gamma^\alpha\gamma^\mu\gamma^0\gamma^\beta\gamma^0\gamma^\nu\Big]p_\alpha(p-k)_\beta - m^2\mathrm{tr}\Big[\gamma^\mu\gamma^\nu\Big] \\ =&\mathrm{tr}\Big[\gamma^0\gamma^\beta\gamma^0\gamma^\nu\gamma^\alpha\gamma^\mu\Big]p_\alpha(p-k)_\beta - m^2\mathrm{tr}\Big[\gamma^\mu\gamma^\nu\Big].\end{aligned} \tag{B.61}$$

The Dirac trace for the mass term is the same as found previously. For the first term we have

$$\begin{aligned}\mathrm{tr}\Big[\gamma^0\gamma^\beta\gamma^0\gamma^\nu\gamma^\alpha\gamma^\mu\Big]p_\alpha(p-k)_\beta =&\mathrm{tr}\Big[\gamma^0\gamma^0\gamma^0\gamma^\nu\gamma^\alpha\gamma^\mu\Big]p_\alpha(p-k)_0 + \mathrm{tr}\Big[\gamma^0\gamma^i\gamma^0\gamma^\nu\gamma^\alpha\gamma^\mu\Big]p_\alpha(p-k)_i \\ =&\mathrm{tr}\Big[\gamma^0\gamma^\nu\gamma^\alpha\gamma^\mu\Big]p_\alpha(p-k)_0 - \mathrm{tr}\Big[\gamma^i\gamma^\nu\gamma^\alpha\gamma^\mu\Big]p_\alpha(p-k)_i.\end{aligned} \tag{B.62}$$

Making use of the result for a trace of four gamma matrices again, we find

$$\begin{aligned}\mathrm{tr}\Big[\gamma^0\gamma^\beta\gamma^0\gamma^\nu\gamma^\alpha\gamma^\mu\Big]p_\alpha(p-k)_\beta =&4\Big(\eta^{0\nu}\eta^{\alpha\mu} - \eta^{0\mu}\eta^{\nu\alpha} + \eta^{0\alpha}\eta^{\nu\mu}\Big)p_\alpha(p-k)_0 \\ &- 4\Big(\eta^{i\nu}\eta^{\alpha\mu} - \eta^{i\mu}\eta^{\nu\alpha} + \eta^{i\alpha}\eta^{\nu\mu}\Big)p_\alpha(p-k)_i \\ =&4\eta^{\mu\nu}\Big(\omega_{\mathbf{p}}\omega_{\mathbf{p}-\mathbf{k}} + \mathbf{p}(\mathbf{p}-\mathbf{k})\Big) + 4p^\mu\Big((p-k)_0\eta^{0\nu} - (p-k)_i\eta^{i\nu}\Big) \\ &- 4p^\nu\Big((p-k)_0\eta^{0\mu} - (p-k)_i\eta^{i\mu}\Big).\end{aligned} \tag{B.63}$$

Putting everything together we find

$$\begin{aligned}\mathrm{tr}\Big[\big(\not{p}+m\big)\gamma^\mu\gamma^0\big(\big(\not{p}-\not{k}\big)-m\big)\gamma^0\gamma^\nu\Big] =& 4\eta^{\mu\nu}\Big(\omega_{\mathbf{p}}\omega_{\mathbf{p}-\mathbf{k}} + \mathbf{p}(\mathbf{p}-\mathbf{k}) - m^2\Big) \\ &+ 4p^\mu\Big((p-k)_0\eta^{0\nu} - (p-k)_i\eta^{i\nu}\Big) - 4p^\nu\Big((p-k)_0\eta^{0\mu} - (p-k)_i\eta^{i\mu}\Big).\end{aligned} \tag{B.64}$$

To shorten notation, we rewrite

$$\Big((p-k)_0\eta^{0\nu} - (p-k)_i\eta^{i\nu}\Big) = \Big((p-k)^0\eta^{0\nu} + (p-k)^i\eta^{i\nu}\Big) = \sum_\alpha (p-k)^\alpha\eta^{\alpha\nu}, \tag{B.65}$$

to avoid confusion, we will explicitly write the sum when using short notation.
We reproduce (eq. 5.28)

$$\begin{aligned}\mathrm{tr}\Big[\big(\not{p}+m\big)\gamma^\mu\gamma^0\big(\big(\not{p}-\not{k}\big)-m\big)\gamma^0\gamma^\nu\Big] =&4\eta^{\mu\nu}\Big(\omega_{\mathbf{p}}\omega_{\mathbf{p}-\mathbf{k}} + \mathbf{p}(\mathbf{p}-\mathbf{k}) - m^2\Big) \\ &+ \sum_{\alpha,\beta} 4\eta^{\mu\alpha}\eta^{\nu\beta}\Big(p_\alpha(p-k)^\beta - p_\beta(p-k)^\alpha\Big),\end{aligned} \tag{B.66}$$

$$\begin{aligned}\mathrm{tr}\Big[\gamma^0\big(\not{p}-m\big)\gamma^0\gamma^\mu\big(\big(\not{p}-\not{k}\big)+m\big)\gamma^\nu\Big] =&4\eta^{\mu\nu}\Big(\omega_{\mathbf{p}}\omega_{\mathbf{p}-\mathbf{k}} + \mathbf{p}(\mathbf{p}-\mathbf{k}) - m^2\Big) \\ &+ \sum_{\alpha,\beta} 4\eta^{\mu\alpha}\eta^{\nu\beta}\Big(p^\alpha(p-k)_\beta - p^\beta(p-k)_\alpha\Big).\end{aligned} \tag{B.67}$$

C

Appendix C - The Semi-Classical Model in the Expanding Box

C.1 Simplifying the Dirac Equation in Milne Coordinates

Starting from

$$\gamma^0\partial_0 + \gamma^3\partial_3 = \gamma^0\Big(\cosh\eta\ \partial_\tau - \frac{1}{\tau}\sinh\eta\ \partial_\eta\Big) + \gamma^3\Big(-\sinh\eta\ \partial_\tau + \frac{1}{\tau}\cosh\eta\ \partial_\eta\Big), \tag{C.1}$$

let us simplify this result, that is used to define the Dirac equation in Milne coordinates (eq. 9.11).
Explicitly inserting the matrix representation of the Dirac gamma matrices allows us to write

$$\begin{aligned}\gamma^0\partial_0 + \gamma^3\partial_3 = &\begin{pmatrix}\cosh\eta & 0 & -\sinh\eta & 0\\ 0 & \cosh\eta & 0 & \sinh\eta\\ \sinh\eta & 0 & \cosh\eta & 0\\ 0 & -\sinh\eta & 0 & -\cosh\eta\end{pmatrix}\partial_\tau \\ &+\frac{1}{\tau}\gamma^3\begin{pmatrix}\cosh\eta & 0 & -\sinh\eta & 0\\ 0 & \cosh\eta & 0 & \sinh\eta\\ \sinh\eta & 0 & \cosh\eta & 0\\ 0 & -\sinh\eta & 0 & -\cosh\eta\end{pmatrix}\partial_\eta.\end{aligned} \tag{C.2}$$

We now consider the following matrix exponential

$$e^{-\eta\gamma^0\gamma^3} = \exp\begin{pmatrix}0 & 0 & -\eta & 0\\ 0 & 0 & 0 & \eta\\ -\eta & 0 & 0 & 0\\ 0 & \eta & 0 & 0\end{pmatrix}. \tag{C.3}$$

It can be evaluated by diagonalizing the matrix

$$e^{-\eta\gamma^0\gamma^3} = Ve^DV^{-1}, \tag{C.4}$$

with D denoting the diagonal matrix, constructed from the eigenvalues of $-\eta\gamma^0\gamma^3$ and V a transformation matrix, constructed from the eigenvectors.
The eigenvectors and eigenvalues are given as

$$\lambda_1 = -\eta, \qquad v_1^T = \begin{pmatrix} 0 & -1 & 0 & 1 \end{pmatrix}, \tag{C.5}$$

$$\lambda_2 = -\eta, \qquad v_2^T = \begin{pmatrix} 1 & 0 & 1 & 0 \end{pmatrix}, \tag{C.6}$$

$$\lambda_3 = \eta, \qquad v_3^T = \begin{pmatrix} 0 & 1 & 0 & 1 \end{pmatrix}, \tag{C.7}$$

$$\lambda_4 = \eta, \qquad v_4^T = \begin{pmatrix} -1 & 0 & 1 & 0 \end{pmatrix}. \tag{C.8}$$

Now, we can construct the transformation matrices

$$V = \begin{pmatrix} 0 & 1 & 0 & -1 \\ -1 & 0 & 1 & 0 \\ 0 & 1 & 0 & 1 \\ 1 & 0 & 1 & 0 \end{pmatrix}, \qquad V^{-1} = \frac{1}{2}\begin{pmatrix} 0 & -1 & 0 & 1 \\ 1 & 0 & 1 & 0 \\ 0 & 1 & 0 & 1 \\ -1 & 0 & 1 & 0 \end{pmatrix}. \tag{C.9}$$

Evaluating the matrix exponential now leads to

$$\begin{aligned} e^{-\eta\gamma^0\gamma^3} &= \frac{1}{2}\begin{pmatrix} 0 & 1 & 0 & -1 \\ -1 & 0 & 1 & 0 \\ 0 & 1 & 0 & 1 \\ 1 & 0 & 1 & 0 \end{pmatrix}\begin{pmatrix} e^{-\lambda} & 0 & 0 & 0 \\ 0 & e^{-\lambda} & 0 & 0 \\ 0 & 0 & e^{\lambda} & 0 \\ 0 & 0 & 0 & e^{\lambda} \end{pmatrix}\begin{pmatrix} 0 & -1 & 0 & 1 \\ 1 & 0 & 1 & 0 \\ 0 & 1 & 0 & 1 \\ -1 & 0 & 1 & 0 \end{pmatrix} \\ &= \frac{1}{2}\begin{pmatrix} e^{-\lambda}+e^{\lambda} & 0 & e^{-\lambda}-e^{\lambda} & 0 \\ 0 & e^{-\lambda}+e^{\lambda} & 0 & e^{\lambda}-e^{-\lambda} \\ e^{-\lambda}-e^{\lambda} & 0 & e^{\lambda}+e^{-\lambda} & 0 \\ 0 & e^{\lambda}-e^{-\lambda} & 0 & e^{\lambda}+e^{-\lambda} \end{pmatrix} \\ &= \begin{pmatrix} \cosh\eta & 0 & -\sinh\eta & 0 \\ 0 & \cosh\eta & 0 & \sinh\eta \\ \sinh\eta & 0 & \cosh\eta & 0 \\ 0 & -\sinh\eta & 0 & -\cosh\eta \end{pmatrix}. \end{aligned} \tag{C.10}$$

Using this result, we find

$$\gamma^0\partial_0 + \gamma^3\partial_3 = \gamma^0 e^{-\eta\gamma^0\gamma^3}\partial_\tau + \frac{1}{\tau}\gamma^3 e^{-\eta\gamma^0\gamma^3}\partial_\eta. \tag{C.11}$$

This result can now directly be used to define the Dirac equation in Milne coordinates (eq. 9.11).

C.2 Deriving the Matrix Equation for Free Expanding Box Fermions

In this appendix, we want to derive the matrix equation (eq. 10.45) for the free spinor solution in an expanding geometry. Starting point is the Dirac equation for the mode functions (eq. 10.25). When inserting the solution of the mode functions (eq. 10.44), we have to calculate the time derivative

$$\partial_\tau \hat{\psi}^{\pm}_{\mathbf{k}_\perp,\nu,s,a}(\tau) = \partial_\tau\sqrt{\tau}\Big(c^{\pm}H^{(2)/(1)}_{\mathrm{i}\nu+\frac{1}{2}}\Big(M_{\mathbf{k}_\perp}\tau\Big)P^{+} + \tilde{c}^{\pm}H^{(2)/(1)}_{\mathrm{i}\nu-\frac{1}{2}}\Big(M_{\mathbf{k}_\perp}\tau\Big)P^{-}\Big)\hat{\psi}^{\pm}_{\mathbf{k}_\perp,\nu,s,a}. \tag{C.12}$$

When calculating the derivative, the following relations for Hankel functions will be of great use [164]

$$\partial_x H_\mu^{(2)/(1)}(x) = H_{\mu-1}^{(2)/(1)}(x) - \frac{\mu}{x} H_\mu^{(2)/(1)}(x), \tag{C.13}$$

$$\partial_x H_\mu^{(2)/(1)}(x) = \frac{\mu}{x} H_\mu^{(2)/(1)}(x) - H_{\mu+1}^{(2)/(1)}(x). \tag{C.14}$$

We find

$$\begin{aligned}
&\partial_\tau \sqrt{\tau} H_{\mathrm{i}\nu+\frac{1}{2}}^{(2)/(1)}\Big(M_{\mathbf{k}_\perp}\tau\Big) \qquad\qquad (C.15)\\
=&\frac{1}{2\sqrt{\tau}} H_{\mathrm{i}\nu+\frac{1}{2}}^{(2)/(1)}\Big(M_{\mathbf{k}_\perp}\tau\Big) + \sqrt{\tau} M_{\mathbf{k}_\perp} H_{\mathrm{i}\nu-\frac{1}{2}}^{(2)/(1)}\Big(M_{\mathbf{k}_\perp}\tau\Big) - \frac{\mathrm{i}}{\sqrt{\tau}}\nu H_{\mathrm{i}\nu+\frac{1}{2}}^{(2)/(1)}\Big(M_{\mathbf{k}_\perp}\tau\Big) - \frac{1}{2\sqrt{\tau}} H_{\mathrm{i}\nu+\frac{1}{2}}^{(2)/(1)}\Big(M_{\mathbf{k}_\perp}\tau\Big)\\
=&\sqrt{\tau} M_{\mathbf{k}_\perp} H_{\mathrm{i}\nu-\frac{1}{2}}^{(2)/(1)}\Big(M_{\mathbf{k}_\perp}\tau\Big) - \frac{\mathrm{i}\nu}{\sqrt{\tau}} H_{\mathrm{i}\nu+\frac{1}{2}}^{(2)/(1)}\Big(M_{\mathbf{k}_\perp}\tau\Big),
\end{aligned}$$

$$\begin{aligned}
&\partial_\tau \sqrt{\tau} H_{\mathrm{i}\nu-\frac{1}{2}}^{(2)/(1)}\Big(M_{\mathbf{k}_\perp}\tau\Big) \qquad\qquad (C.16)\\
=&\frac{1}{2\sqrt{\tau}} H_{\mathrm{i}\nu-\frac{1}{2}}^{(2)/(1)}\Big(M_{\mathbf{k}_\perp}\tau\Big) + \frac{\mathrm{i}}{\sqrt{\tau}}\nu H_{\mathrm{i}\nu-\frac{1}{2}}^{(2)/(1)}\Big(M_{\mathbf{k}_\perp}\tau\Big) - \frac{1}{2\sqrt{\tau}} H_{\mathrm{i}\nu-\frac{1}{2}}^{(2)/(1)}\Big(M_{\mathbf{k}_\perp}\tau\Big) - \sqrt{\tau} M_{\mathbf{k}_\perp} H_{\mathrm{i}\nu+\frac{1}{2}}^{(2)/(1)}\Big(M_{\mathbf{k}_\perp}\tau\Big)\\
=&\frac{\mathrm{i}\nu}{\sqrt{\tau}} H_{\mathrm{i}\nu-\frac{1}{2}}^{(2)/(1)}\Big(M_{\mathbf{k}_\perp}\tau\Big) - \sqrt{\tau} M_{\mathbf{k}_\perp} H_{\mathrm{i}\nu+\frac{1}{2}}^{(2)/(1)}\Big(M_{\mathbf{k}_\perp}\tau\Big),
\end{aligned}$$

leading to

$$\begin{aligned}
\partial_\tau \hat{\psi}^{\pm}_{\mathbf{k}_\perp,\nu,s,a}(\tau) = \sqrt{\tau}\Bigg[& c^{\pm}\left(M_{\mathbf{k}_\perp} H_{\mathrm{i}\nu-\frac{1}{2}}^{(2)/(1)}\Big(M_{\mathbf{k}_\perp}\tau\Big) - \frac{\mathrm{i}\nu}{\tau} H_{\mathrm{i}\nu+\frac{1}{2}}^{(2)/(1)}\Big(M_{\mathbf{k}_\perp}\tau\Big)\right) P^+ \\
&+ \tilde{c}^{\pm}\left(\frac{\mathrm{i}\nu}{\tau} H_{\mathrm{i}\nu-\frac{1}{2}}^{(2)/(1)}\Big(M_{\mathbf{k}_\perp}\tau\Big) - M_{\mathbf{k}_\perp} H_{\mathrm{i}\nu+\frac{1}{2}}^{(2)/(1)}\Big(M_{\mathbf{k}_\perp}\tau\Big)\right) P^-\Bigg] \hat{\psi}^{\pm}_{\mathbf{k}_\perp,\nu,s,a}.
\end{aligned} \tag{C.17}$$

Now, we can use the following identities for the projection operators

$$\gamma^0 P^+ = \frac{1}{2}\Big(\gamma^0 + \gamma^0\gamma^0\gamma^3\Big) = \frac{1}{2}\Big(\gamma^0 - \gamma^0\gamma^3\gamma^0\Big) = \frac{1}{2}\Big(1 - \gamma^0\gamma^3\Big)\gamma^0 = P^-\gamma^0, \tag{C.18}$$

$$\gamma^0 P^- = \frac{1}{2}\Big(\gamma^0 - \gamma^0\gamma^0\gamma^3\Big) = \frac{1}{2}\Big(\gamma^0 + \gamma^0\gamma^3\gamma^0\Big) = \frac{1}{2}\Big(1 + \gamma^0\gamma^3\Big)\gamma^0 = P^+\gamma^0, \tag{C.19}$$

to rewrite

$$\begin{aligned}
\mathrm{i}\gamma^0\partial_\tau \hat{\psi}^{\pm}_{\mathbf{k}_\perp,\nu,s,a}(\tau) = \Bigg[& \mathrm{i}c^{\pm}\sqrt{\tau} M_{\mathbf{k}_\perp} H_{\mathrm{i}\nu-\frac{1}{2}}^{(2)/(1)}\Big(M_{\mathbf{k}_\perp}\tau\Big) P^- - \mathrm{i}\tilde{c}^{\pm}\sqrt{\tau} M_{\mathbf{k}_\perp} H_{\mathrm{i}\nu+\frac{1}{2}}^{(2)/(1)}\Big(M_{\mathbf{k}_\perp}\tau\Big) P^+ \\
&+ c^{\pm}\frac{\nu}{\sqrt{\tau}} H_{\mathrm{i}\nu+\frac{1}{2}}^{(2)/(1)}\Big(M_{\mathbf{k}_\perp}\tau\Big) P^- - \tilde{c}^{\pm}\frac{\nu}{\sqrt{\tau}} H_{\mathrm{i}\nu-\frac{1}{2}}^{(2)/(1)}\Big(M_{\mathbf{k}_\perp}\tau\Big) P^+\Bigg] \gamma^0 \hat{\psi}^{\pm}_{\mathbf{k}_\perp,\nu,s,a}.
\end{aligned} \tag{C.20}$$

Using properties of the projection operators

$$\gamma^3 P^+ = \frac{1}{2}\Big(\gamma^3 + \gamma^3\gamma^0\gamma^3\Big) = \frac{1}{2}\Big(\gamma^3 - \gamma^0\gamma^3\gamma^3\Big) = \frac{1}{2}\Big(1 - \gamma^0\gamma^3\Big)\gamma^3 = P^-\gamma^3, \tag{C.21}$$

$$\gamma^3 P^- = \frac{1}{2}\Big(\gamma^3 - \gamma^3\gamma^0\gamma^3\Big) = \frac{1}{2}\Big(\gamma^3 + \gamma^0\gamma^3\gamma^3\Big) = \frac{1}{2}\Big(1 + \gamma^0\gamma^3\Big)\gamma^3 = P^+\gamma^3, \tag{C.22}$$

we can rewrite the γ^3-term of (eq. 10.25)

$$-\frac{1}{\tau}\nu\gamma^3\hat{\psi}^{\pm}_{\mathbf{k}_\perp,\nu,s,a}(\tau) = \Big[- c^{\pm}\frac{\nu}{\sqrt{\tau}}H^{(2)/(1)}_{\mathrm{i}\nu+\frac{1}{2}}\big(M_{\mathbf{k}_\perp}\tau\big)P^-\gamma^3 - \tilde{c}^{\pm}\frac{\nu}{\sqrt{\tau}}H^{(2)/(1)}_{\mathrm{i}\nu-\frac{1}{2}}\big(M_{\mathbf{k}_\perp}\tau\big)P^+\gamma^3\Big]\hat{\psi}^{\pm}_{\mathbf{k}_\perp,\nu,s,a}. \tag{C.23}$$

Combining both terms, we now have

$$\begin{aligned}&\Big(\mathrm{i}\gamma^0\partial_\tau - \frac{1}{\tau}\nu\gamma^3\Big)\hat{\psi}^{\pm}_{\mathbf{k}_\perp,\nu,s,a}(\tau) \\ &\quad= \Big[\mathrm{i}c^{\pm}\sqrt{\tau}M_{\mathbf{k}_\perp}H^{(2)/(1)}_{\mathrm{i}\nu-\frac{1}{2}}\big(M_{\mathbf{k}_\perp}\tau\big)P^- - \mathrm{i}\tilde{c}^{\pm}\sqrt{\tau}M_{\mathbf{k}_\perp}H^{(2)/(1)}_{\mathrm{i}\nu+\frac{1}{2}}\big(M_{\mathbf{k}_\perp}\tau\big)P^+\Big]\gamma^0\hat{\psi}^{\pm}_{\mathbf{k}_\perp,\nu,s,a} \\ &\qquad+ \Big[c^{\pm}\frac{\nu}{\sqrt{\tau}}H^{(2)/(1)}_{\mathrm{i}\nu+\frac{1}{2}}\big(M_{\mathbf{k}_\perp}\tau\big)P^-\big(\gamma^0-\gamma^3\big) - \tilde{c}^{\pm}\frac{\nu}{\sqrt{\tau}}H^{(2)/(1)}_{\mathrm{i}\nu-\frac{1}{2}}\big(M_{\mathbf{k}_\perp}\tau\big)P^+\big(\gamma^0+\gamma^3\big)\Big]\hat{\psi}^{\pm}_{\mathbf{k}_\perp,\nu,s,a}.\end{aligned} \tag{C.24}$$

For the second term, we use

$$P^-\big(\gamma^0-\gamma^3\big) = \frac{1}{2}\big(\gamma^0-\gamma^3-\gamma^0\gamma^3\big(\gamma^0-\gamma^3\big)\big) = \frac{1}{2}\big(\gamma^0-\gamma^3+\gamma^3-\gamma^0\big) = 0, \tag{C.25}$$

$$P^+\big(\gamma^0+\gamma^3\big) = \frac{1}{2}\big(\gamma^0+\gamma^3+\gamma^0\gamma^3\big(\gamma^0+\gamma^3\big)\big) = \frac{1}{2}\big(\gamma^0+\gamma^3-\gamma^3-\gamma^0\big) = 0, \tag{C.26}$$

to simplify the previous result

$$\begin{aligned}&\Big(\mathrm{i}\gamma^0\partial_\tau - \frac{1}{\tau}\nu\gamma^3\Big)\hat{\psi}^{\pm}_{\mathbf{k}_\perp,\nu,s,a}(\tau) \\ &\quad= \sqrt{\tau}\Big[\mathrm{i}c^{\pm}H^{(2)/(1)}_{\mathrm{i}\nu-\frac{1}{2}}\big(M_{\mathbf{k}_\perp}\tau\big)P^- - \mathrm{i}\tilde{c}^{\pm}H^{(2)/(1)}_{\mathrm{i}\nu+\frac{1}{2}}\big(M_{\mathbf{k}_\perp}\tau\big)P^+\Big]M_{\mathbf{k}_\perp}\gamma^0\hat{\psi}^{\pm}_{\mathbf{k}_\perp,\nu,s,a}.\end{aligned} \tag{C.27}$$

The remaining terms of (eq. 10.25) are given by

$$\begin{aligned}&\Big[\mp\gamma^i k^i_\perp - m\Big]\hat{\psi}^{\pm}_{\mathbf{k}_\perp,\nu,s,a}(\tau) \\ &\quad= \Big[\mp\gamma^i k^i_\perp - m\Big]\sqrt{\tau}\Big(cH^{(2)/(1)}_{\mathrm{i}\nu+\frac{1}{2}}\big(M_{\mathbf{k}_\perp}\tau\big)P^+ + \tilde{c}H^{(2)/(1)}_{\mathrm{i}\nu-\frac{1}{2}}\big(M_{\mathbf{k}_\perp}\tau\big)P^-\Big)\hat{\psi}^{\pm}_{\mathbf{k}_\perp,\nu,s,a}.\end{aligned} \tag{C.28}$$

We can use

$$\gamma^i P^+ = \frac{1}{2}\big(\gamma^i+\gamma^i\gamma^0\gamma^3\big) = \frac{1}{2}\big(\gamma^i-\gamma^0\gamma^i\gamma^3\big) = \frac{1}{2}\big(\gamma^i+\gamma^0\gamma^3\gamma^i\big) = \frac{1}{2}\big(1+\gamma^0\gamma^3\big)\gamma^i = P^+\gamma^i, \tag{C.29}$$

$$\gamma^i P^- = \frac{1}{2}\big(\gamma^i-\gamma^i\gamma^0\gamma^3\big) = \frac{1}{2}\big(\gamma^i+\gamma^0\gamma^i\gamma^3\big) = \frac{1}{2}\big(\gamma^i-\gamma^0\gamma^3\gamma^i\big) = \frac{1}{2}\big(1-\gamma^0\gamma^3\big)\gamma^i = P^-\gamma^i, \tag{C.30}$$

which finally leads to

$$\begin{aligned}&\Big[\mp\gamma^i k^i_\perp - m\Big]\hat{\psi}^{\pm}_{\mathbf{k}_\perp,\nu,s,a}(\tau) \\ &\quad= \sqrt{\tau}\Big(c^{\pm}H^{(2)/(1)}_{\mathrm{i}\nu+\frac{1}{2}}\big(M_{\mathbf{k}_\perp}\tau\big)P^+ + \tilde{c}^{\pm}H^{(2)/(1)}_{\mathrm{i}\nu-\frac{1}{2}}\big(M_{\mathbf{k}_\perp}\tau\big)P^-\Big)\Big[\mp\gamma^i k^i_\perp - m\Big]\hat{\psi}^{\pm}_{\mathbf{k}_\perp,\nu,s,a}.\end{aligned} \tag{C.31}$$

Combining this with (eq. C.27), we arrive at (eq. 10.45)

$$0 = \sqrt{\tau}\Big[\tilde{c}^{\pm}H^{(2)/(1)}_{\mathrm{i}\nu-\frac{1}{2}}\big(M_{\mathbf{k}_\perp}\tau\big)P^- + c^{\pm}H^{(2)/(1)}_{\mathrm{i}\nu+\frac{1}{2}}\big(M_{\mathbf{k}_\perp}\tau\big)P^+\Big]\Big[\pm M_{\mathbf{k}_\perp}\gamma^0 \mp \gamma^i k^i_\perp - m\Big]\hat{\psi}^{\pm}_{\mathbf{k}_\perp,\nu,s,a}. \tag{C.32}$$

C.3 Normalization of the Free Fermion Spinor in an Expanding Geometry

In this appendix, we want to derive the normalization condition of the expanding box spinor, given from the scalar product of spinors in Milne coordinates (eq. 9.17),

$$\begin{aligned}
&\int |\psi(x)|^2 d^3x = \int\int \hat{\psi}^\dagger(\tau,\mathbf{x}_\perp,\eta)\hat{\psi}(\tau,\mathbf{x}_\perp,\eta)d^2x_\perp d\eta \qquad \text{(C.33)}\\
&= \int\int \left[\int \sum_{r=1}^{2}\sum_{b=1}^{N_c}\left(\hat{a}^\dagger_{r,b}(\mathbf{p}_\perp,\nu')\hat{\psi}^{+,\dagger}_{\mathbf{p}_\perp,\nu',r,b}(\tau,\mathbf{x}_\perp,\eta)+\hat{b}_{r,b}(\mathbf{p}_\perp,\nu')\hat{\psi}^{-,\dagger}_{\mathbf{p}_\perp,\nu',r,b}(\tau,\mathbf{x}_\perp,\eta)\right)\frac{d^2p_\perp}{(2\pi)^2}\frac{d\nu'}{2\pi}\right]\\
&\times\left[\int \sum_{s=1}^{2}\sum_{a=1}^{N_c}\left(\hat{a}_{s,a}(\mathbf{k}_\perp,\nu)\hat{\psi}^{+}_{\mathbf{k}_\perp,\nu,s,a}(\tau,\mathbf{x}_\perp,\eta)+\hat{b}^\dagger_{s,a}(\mathbf{k}_\perp,\nu)\hat{\psi}^{-}_{\mathbf{k}_\perp,\nu,s,a}(\tau,\mathbf{x}_\perp,\eta)\right)\frac{d^2k_\perp}{(2\pi)^2}\frac{d\nu}{2\pi}\right]d^2x_\perp d\eta.
\end{aligned}$$

When inserting the solution of the free expanding box spinor, including the explicit solution for the mode functions (eq. 10.68), one can immediately eliminate the η dependence, by identifying

$$\int e^{i\eta(\nu-\nu')}d\eta = (2\pi)\delta(\nu-\nu'), \qquad \text{(C.34)}$$

in every combination of $\hat{\psi}^{\pm,\dagger}_{\mathbf{p}_\perp,\nu',r,b}(\tau,\mathbf{x}_\perp,\eta)\hat{\psi}^{\pm}_{\mathbf{k}_\perp,\nu,s,a}(\tau,\mathbf{x}_\perp,\eta)$. In a next step, we can do a similar thing for the dependence on $\mathbf{x}_\perp$, leading to

$$\begin{aligned}
&\int |\psi(x)|^2 d^3x \qquad \text{(C.35)}\\
&= \int \sum_{s,r=1}^{2}\sum_{a,b=1}^{N_c}\Bigg[\hat{a}^\dagger_{r,b}(\mathbf{p}_\perp,\nu)\hat{a}_{s,a}(\mathbf{k}_\perp,\nu)\hat{\psi}^{+,\dagger}_{\mathbf{p}_\perp,\nu,r,b}(\tau)\hat{\psi}^{+}_{\mathbf{k}_\perp,\nu,s,a}(\tau)\underbrace{\int e^{-i\mathbf{x}_\perp(\mathbf{p}_\perp-\mathbf{k}_\perp)}d^2x_\perp}_{=(2\pi)^2\delta(\mathbf{p}_\perp-\mathbf{k}_\perp)}\\
&\quad+\hat{a}^\dagger_{r,b}(\mathbf{p}_\perp,\nu)\hat{b}^\dagger_{s,a}(\mathbf{k}_\perp,\nu)\hat{\psi}^{+,\dagger}_{\mathbf{p}_\perp,\nu,r,b}(\tau)\hat{\psi}^{-}_{\mathbf{k}_\perp,\nu,s,a}(\tau)\underbrace{\int e^{-i\mathbf{x}_\perp(\mathbf{p}_\perp+\mathbf{k}_\perp)}d^2x_\perp}_{=(2\pi)^2\delta(\mathbf{p}_\perp+\mathbf{k}_\perp)}\\
&\quad+\hat{b}_{r,b}(\mathbf{p}_\perp,\nu)\hat{a}_{s,a}(\mathbf{k}_\perp,\nu)\hat{\psi}^{-,\dagger}_{\mathbf{p}_\perp,\nu,r,b}(\tau)\hat{\psi}^{+}_{\mathbf{k}_\perp,\nu,s,a}(\tau)\underbrace{\int e^{i\mathbf{x}_\perp(\mathbf{p}_\perp+\mathbf{k}_\perp)}d^2x_\perp}_{=(2\pi)^2\delta(\mathbf{p}_\perp+\mathbf{k}_\perp)}\\
&\quad+\hat{b}_{r,b}(\mathbf{p}_\perp,\nu)\hat{b}^\dagger_{s,a}(\mathbf{k}_\perp,\nu)\hat{\psi}^{-,\dagger}_{\mathbf{p}_\perp,\nu,r,b}(\tau)\hat{\psi}^{-}_{\mathbf{k}_\perp,\nu,s,a}(\tau)\underbrace{\int e^{i\mathbf{x}_\perp(\mathbf{p}_\perp-\mathbf{k}_\perp)}d^2x_\perp}_{=(2\pi)^2\delta(\mathbf{p}_\perp-\mathbf{k}_\perp)}\Bigg]\frac{d^2k_\perp}{(2\pi)^2}\frac{d^2p_\perp}{(2\pi)^2}\frac{d\nu}{2\pi}.
\end{aligned}$$

We find

$$\begin{aligned}
\int |\psi(x)|^2 d^3 = \int \sum_{s,r=1}^{2}\sum_{a,b=1}^{N_c}\Bigg[&\hat{a}^\dagger_{r,b}(\mathbf{k}_\perp,\nu)\hat{a}_{s,a}(\mathbf{k}_\perp,\nu)\hat{\psi}^{+,\dagger}_{\mathbf{k}_\perp,\nu,r,b}(\tau)\hat{\psi}^{+}_{\mathbf{k}_\perp,\nu,s,a}(\tau) \qquad \text{(C.36)}\\
&+\hat{a}^\dagger_{r,b}(-\mathbf{k}_\perp,\nu)\hat{b}^\dagger_{s,a}(\mathbf{k}_\perp,\nu)\hat{\psi}^{+,\dagger}_{-\mathbf{k}_\perp,\nu,r,b}(\tau)\hat{\psi}^{-}_{\mathbf{k}_\perp,\nu,s,a}(\tau)\\
&+\hat{b}_{r,b}(-\mathbf{k}_\perp,\nu)\hat{a}_{s,a}(\mathbf{k}_\perp,\nu)\hat{\psi}^{-,\dagger}_{-\mathbf{k}_\perp,\nu,r,b}(\tau)\hat{\psi}^{+}_{\mathbf{k}_\perp,\nu,s,a}(\tau)\\
&+\hat{b}_{r,b}(\mathbf{k}_\perp,\nu)\hat{b}^\dagger_{s,a}(\mathbf{k}_\perp,\nu)\hat{\psi}^{-,\dagger}_{\mathbf{k}_\perp,\nu,r,b}(\tau)\hat{\psi}^{-}_{\mathbf{k}_\perp,\nu,s,a}(\tau)\Bigg]\frac{d^2k_\perp}{(2\pi)^2}\frac{d\nu}{2\pi}.
\end{aligned}$$

Let us exemplary have a look at the first term of the previous equation, inserting (eq. 10.68)

$$\begin{aligned}\hat{\psi}^{+,\dagger}_{\mathbf{k}_\perp,\nu,r,b}(\tau)\hat{\psi}^{+}_{\mathbf{k}_\perp,\nu,s,a}(\tau) =&|a|^2\tau e^{\nu\pi}u^\dagger_{r,b}(\mathbf{k}_\perp,y_k=0)\Big(e^{\mathrm{i}\frac{\pi}{4}}H^{(2),\star}_{\mathrm{i}\nu+\frac{1}{2}}\Big(M_{\mathbf{k}_\perp}\tau\Big)P^+ + e^{-\mathrm{i}\frac{\pi}{4}}H^{(2),\star}_{\mathrm{i}\nu-\frac{1}{2}}\Big(M_{\mathbf{k}_\perp}\tau\Big)P^-\Big)\\ &\times\Big(e^{-\mathrm{i}\frac{\pi}{4}}H^{(2)}_{\mathrm{i}\nu+\frac{1}{2}}\Big(M_{\mathbf{k}_\perp}\tau\Big)P^+ + e^{\mathrm{i}\frac{\pi}{4}}H^{(2)}_{\mathrm{i}\nu-\frac{1}{2}}\Big(M_{\mathbf{k}_\perp}\tau\Big)P^-\Big)u_{s,a}(\mathbf{k}_\perp,y_k=0)\\ =&|a|^2\tau e^{\nu\pi}u^\dagger_{r,b,\alpha}(\mathbf{k}_\perp,y_k=0)\Big(\Big|H^{(2)}_{\mathrm{i}\nu+\frac{1}{2}}\Big(M_{\mathbf{k}_\perp}\tau\Big)\Big|^2P^+_{\alpha\beta} + \Big|H^{(2)}_{\mathrm{i}\nu-\frac{1}{2}}\Big(M_{\mathbf{k}_\perp}\tau\Big)\Big|^2P^-_{\alpha\beta}\Big)\\ &\times u_{s,a,\beta}(\mathbf{k}_\perp,y_k=0),\end{aligned}\tag{C.37}$$

where we explicitly wrote the Dirac indices in the last step and used the following properties of the projection operator

$$P^{\pm,\dagger} = \frac{1}{2}\Big(1\pm\Big(\gamma^0\gamma^3\Big)^\dagger\Big) = \frac{1}{2}\Big(1\pm\gamma^{3,\dagger}\gamma^{0,\dagger}\Big) = \frac{1}{2}\Big(1\mp\gamma^3\gamma^0\Big) = \frac{1}{2}\Big(1\pm\gamma^0\gamma^3\Big) = P^\pm,\tag{C.38}$$

$$P^\pm P^\mp = \frac{1}{4}\Big(1\pm\gamma^0\gamma^3\Big)\Big(1\mp\gamma^0\gamma^3\Big) = \frac{1}{4}\Big(1+\gamma^0\gamma^3\gamma^3\gamma^0\Big) = \frac{1}{4}\Big(1-1\Big) = 0,\tag{C.39}$$

$$P^\pm P^\pm = \frac{1}{4}\Big(1\pm\gamma^0\gamma^3\Big)\Big(1\pm\gamma^0\gamma^3\Big) = \frac{1}{4}\Big(1\pm2\gamma^0\gamma^3-\gamma^0\gamma^3\gamma^3\gamma^0\Big) = \frac{1}{4}\Big(2\pm2\gamma^0\gamma^3\Big) = P^\pm.\tag{C.40}$$

We now have to calculate the following combinations of basis spinors

$$u^\dagger_{r,b}(\mathbf{k}_\perp,y_k=0)P^\pm u_{s,a}(\mathbf{k}_\perp,y_k=0) = \frac{1}{2}u^\dagger_{r,b}(\mathbf{k}_\perp,y_k=0)\Big(1\pm\gamma^0\gamma^3\Big)u_{s,a}(\mathbf{k}_\perp,y_k=0).\tag{C.41}$$

First, we use that the basis spinors are orthogonal

$$u^\dagger_{r,b}(\mathbf{k}_\perp,y_k=0)u_{s,a}(\mathbf{k}_\perp,y_k=0) = \delta_{rs}.\tag{C.42}$$

For the remaining term we have

$$\begin{aligned}\pm u^\dagger_{r,b}(\mathbf{k}_\perp,y_k=0)\gamma^0\gamma^3u_{s,a}(\mathbf{k}_\perp,y_k=0) =&\frac{M_{\mathbf{k}_\perp}+m}{2M_{\mathbf{k}_\perp}}\begin{pmatrix}\varphi^\dagger_r & \varphi^\dagger_r\frac{k^i_\perp\sigma_i}{M_{\mathbf{k}_\perp}+m}\end{pmatrix}\begin{pmatrix}0 & \sigma_3\\ \sigma_3 & 0\end{pmatrix}\begin{pmatrix}\varphi_s\\ \frac{k^j_\perp\sigma_j}{M_{\mathbf{k}_\perp}+m}\end{pmatrix}\\ =&\frac{M_{\mathbf{k}_\perp}+m}{2M_{\mathbf{k}_\perp}}\begin{pmatrix}\varphi^\dagger_r & \varphi^\dagger_r\frac{k^i_\perp\sigma_i}{M_{\mathbf{k}_\perp}+m}\end{pmatrix}\begin{pmatrix}\sigma_3\frac{k^j_\perp\sigma_j}{M_{\mathbf{k}_\perp}+m}\\ \sigma_3\varphi_s\end{pmatrix}\\ =&\frac{1}{2M_{\mathbf{k}_\perp}}\varphi^\dagger_r\underbrace{\{\sigma_3,\sigma_i\}}_{=0}k^i_\perp\varphi_s = 0.\end{aligned}\tag{C.43}$$

We showed

$$\hat{\psi}^{+,\dagger}_{\mathbf{k}_\perp,\nu,r,b}(\tau)\hat{\psi}^{+}_{\mathbf{k}_\perp,\nu,s,a}(\tau) = \delta_{rs}\delta_{ab}|a|^2\tau e^{\nu\pi}\Big(\Big|H^{(2)}_{\mathrm{i}\nu+\frac{1}{2}}\Big(M_{\mathbf{k}_\perp}\tau\Big)\Big|^2 + \Big|H^{(2)}_{\mathrm{i}\nu-\frac{1}{2}}\Big(M_{\mathbf{k}_\perp}\tau\Big)\Big|^2\Big).\tag{C.44}$$

In the same manner, one finds

$$\hat{\psi}^{-,\dagger}_{\mathbf{k}_\perp,\nu,r,b}(\tau)\hat{\psi}^{-}_{\mathbf{k}_\perp,\nu,s,a}(\tau) = \delta_{rs}\delta_{ab}|a|^2\tau e^{-\nu\pi}\Big(\Big|H^{(1)}_{\mathrm{i}\nu+\frac{1}{2}}\Big(M_{\mathbf{k}_\perp}\tau\Big)\Big|^2 + \Big|H^{(1)}_{\mathrm{i}\nu-\frac{1}{2}}\Big(M_{\mathbf{k}_\perp}\tau\Big)\Big|^2\Big).\tag{C.45}$$

We are now left with the off-diagonal combinations. First note, that

$$v^\dagger_{r,b}(-\mathbf{k}_\perp, y_k=0)u_{s,a}(\mathbf{k}_\perp, y_k=0) = \frac{M_{\mathbf{k}_\perp}+m}{2M_{\mathbf{k}_\perp}}\begin{pmatrix}-\chi^\dagger_r\frac{k^i_\perp\sigma_i}{M_{\mathbf{k}_\perp}+m} & \chi^\dagger_r\end{pmatrix}\begin{pmatrix}\varphi_s\\ \frac{k^j_\perp\sigma_j}{M_{\mathbf{k}_\perp}+m}\varphi_s\end{pmatrix} \tag{C.46}$$
$$= \frac{1}{2M_{\mathbf{k}_\perp}}\Big(-\chi^\dagger_r k^i_\perp\sigma_i\varphi_s + \chi^\dagger_r k^i_\perp\sigma_i\varphi_s\Big) = 0,$$

$$u^\dagger_{r,b}(-\mathbf{k}_\perp, y_k=0)v_{s,a}(\mathbf{k}_\perp, y_k=0) = \frac{M_{\mathbf{k}_\perp}+m}{2M_{\mathbf{k}_\perp}}\begin{pmatrix}\varphi^\dagger_r & -\varphi^\dagger_r\frac{k^i_\perp\sigma_i}{M_{\mathbf{k}_\perp}+m}\end{pmatrix}\begin{pmatrix}\frac{k^j_\perp\sigma_j}{M_{\mathbf{k}_\perp}+m}\chi_s\\ \chi_s\end{pmatrix} \tag{C.47}$$
$$= \frac{1}{2M_{\mathbf{k}_\perp}}\Big(\varphi^\dagger_r k^i_\perp\sigma_i\chi_s - \varphi^\dagger_r k^i_\perp\sigma_i\chi_s\Big) = 0.$$

For the products including the gamma matrices, we have

$$\pm v^\dagger_{r,b}(-\mathbf{k}_\perp, y_k=0)\gamma^0\gamma^3 u_{s,a}(\mathbf{k}_\perp, y_k=0) \tag{C.48}$$
$$= \pm\frac{M_{\mathbf{k}_\perp}+m}{2M_{\mathbf{k}_\perp}}\begin{pmatrix}-\chi^\dagger_r\frac{k^i_\perp\sigma_i}{M_{\mathbf{k}_\perp}+m} & \chi^\dagger_r\end{pmatrix}\begin{pmatrix}0 & \sigma_3\\ \sigma_3 & 0\end{pmatrix}\begin{pmatrix}\varphi_s\\ \frac{k^j_\perp\sigma_j}{M_{\mathbf{k}_\perp}+m}\varphi_s\end{pmatrix}$$
$$= \pm\frac{M_{\mathbf{k}_\perp}+m}{2M_{\mathbf{k}_\perp}}\begin{pmatrix}-\chi^\dagger_r\frac{k^i_\perp\sigma_i}{M_{\mathbf{k}_\perp}+m} & \chi^\dagger_r\end{pmatrix}\begin{pmatrix}\sigma_3\frac{k^j_\perp\sigma_j}{M_{\mathbf{k}_\perp}+m}\varphi_s\\ \sigma_3\varphi_s\end{pmatrix}$$
$$= \pm\frac{1}{2M_{\mathbf{k}_\perp}}\Big(-\chi^\dagger_r\frac{k^i_\perp\sigma_i\sigma_3\sigma_j k^j_\perp}{M_{\mathbf{k}_\perp}+m}\varphi_s + \big(M_{\mathbf{k}_\perp}+m\big)\chi^\dagger_r\sigma_3\varphi_s\Big)$$
$$= \pm\frac{1}{2M_{\mathbf{k}_\perp}}\Big(\chi^\dagger_r\frac{k^i_\perp\sigma_3\sigma_i\sigma_j k^j_\perp}{M_{\mathbf{k}_\perp}+m}\varphi_s + \big(M_{\mathbf{k}_\perp}+m\big)\chi^\dagger_r\sigma_3\varphi_s\Big)$$
$$= \pm\frac{1}{2M_{\mathbf{k}_\perp}}\Big(\chi^\dagger_r\frac{\mathbf{k}^2_\perp\sigma_3}{M_{\mathbf{k}_\perp}+m}\varphi_s + \big(M_{\mathbf{k}_\perp}+m\big)\chi^\dagger_r\sigma_3\varphi_s\Big) = \pm\chi^\dagger_r\sigma_3\varphi_s,$$

$$\pm u^\dagger_{r,b}(-\mathbf{k}_\perp, y_k=0)\gamma^0\gamma^3 v_{s,a}(\mathbf{k}_\perp, y_k=0) \tag{C.49}$$
$$= \pm\frac{M_{\mathbf{k}_\perp}+m}{2M_{\mathbf{k}_\perp}}\begin{pmatrix}\varphi^\dagger_r & -\varphi^\dagger_r\frac{k^i_\perp\sigma_i}{M_{\mathbf{k}_\perp}+m}\end{pmatrix}\begin{pmatrix}0 & \sigma_3\\ \sigma_3 & 0\end{pmatrix}\begin{pmatrix}\frac{k^j_\perp\sigma_j}{M_{\mathbf{k}_\perp}+m}\chi_s\\ \chi_s\end{pmatrix}$$
$$= \pm\frac{M_{\mathbf{k}_\perp}+m}{2M_{\mathbf{k}_\perp}}\begin{pmatrix}\varphi^\dagger_r & -\varphi^\dagger_r\frac{k^i_\perp\sigma_i}{M_{\mathbf{k}_\perp}+m}\end{pmatrix}\begin{pmatrix}\sigma_3\chi_s\\ \sigma_3\frac{k^j_\perp\sigma_j}{M_{\mathbf{k}_\perp}+m}\chi_s\end{pmatrix}$$
$$= \pm\frac{1}{2M_{\mathbf{k}_\perp}}\Big(\big(M_{\mathbf{k}_\perp}+m\big)\varphi^\dagger_r\sigma_3\chi_s - \varphi^\dagger_r\frac{k^i_\perp\sigma_i\sigma_3\sigma_j k^j_\perp}{M_{\mathbf{k}_\perp}+m}\chi_s\Big)$$
$$= \pm\frac{1}{2M_{\mathbf{k}_\perp}}\Big(\big(M_{\mathbf{k}_\perp}+m\big)\varphi^\dagger_r\sigma_3\chi_s + \varphi^\dagger_r\frac{k^i_\perp\sigma_3\sigma_i\sigma_j k^j_\perp}{M_{\mathbf{k}_\perp}+m}\chi_s\Big)$$
$$= \pm\frac{1}{2M_{\mathbf{k}_\perp}}\Big(\big(M_{\mathbf{k}_\perp}+m\big)\varphi^\dagger_r\sigma_3\chi_s + \varphi^\dagger_r\frac{\mathbf{k}^2_\perp\sigma_3}{M_{\mathbf{k}_\perp}+m}\chi_s\Big) = \pm\varphi^\dagger_r\sigma_3\chi_s.$$

We start with the off-diagonal combination

$$\begin{aligned}\hat{\psi}^{+,\dagger}_{-\mathbf{k}_\perp,\nu,r,b}(\tau)\hat{\psi}^{-}_{\mathbf{k}_\perp,\nu,s,a}(\tau) =&|a|^2\tau u^\dagger_{r,b}(\mathbf{k}_\perp,y_k=0)\Big(e^{\mathrm{i}\frac{\pi}{4}}H^{(2),\star}_{\mathrm{i}\nu+\frac{1}{2}}(M_{\mathbf{k}_\perp}\tau)P^+ + e^{-\mathrm{i}\frac{\pi}{4}}H^{(2),\star}_{\mathrm{i}\nu-\frac{1}{2}}(M_{\mathbf{k}_\perp}\tau)P^-\Big)\\ &\times\Big(e^{\mathrm{i}\frac{\pi}{4}}H^{(1)}_{\mathrm{i}\nu+\frac{1}{2}}\Big(M_{\mathbf{k}_\perp}\tau\Big)P^+ + e^{-\mathrm{i}\frac{\pi}{4}}H^{(1)}_{\mathrm{i}\nu-\frac{1}{2}}\Big(M_{\mathbf{k}_\perp}\tau\Big)P^-\Big)v_{s,a}(\mathbf{k}_\perp,y_k=0)\\ =&|a|^2\tau u^\dagger_{r,b}(\mathbf{k}_\perp,y_k=0)\Big(e^{\mathrm{i}\frac{\pi}{2}}H^{(2),\star}_{\mathrm{i}\nu+\frac{1}{2}}(M_{\mathbf{k}_\perp}\tau)H^{(1)}_{\mathrm{i}\nu+\frac{1}{2}}\Big(M_{\mathbf{k}_\perp}\tau\Big)P^+\\ &+e^{-\mathrm{i}\frac{\pi}{2}}H^{(2),\star}_{\mathrm{i}\nu-\frac{1}{2}}(M_{\mathbf{k}_\perp}\tau)H^{(1)}_{\mathrm{i}\nu-\frac{1}{2}}\Big(M_{\mathbf{k}_\perp}\tau\Big)P^-\Big)v_{s,a}(\mathbf{k}_\perp,y_k=0)\\ =&|a|^2\tau\Big(e^{\mathrm{i}\frac{\pi}{2}}H^{(2),\star}_{\mathrm{i}\nu+\frac{1}{2}}(M_{\mathbf{k}_\perp}\tau)H^{(1)}_{\mathrm{i}\nu+\frac{1}{2}}\Big(M_{\mathbf{k}_\perp}\tau\Big)\varphi^\dagger_r\sigma_3\chi_s\\ &-e^{-\mathrm{i}\frac{\pi}{2}}H^{(2),\star}_{\mathrm{i}\nu-\frac{1}{2}}(M_{\mathbf{k}_\perp}\tau)H^{(1)}_{\mathrm{i}\nu-\frac{1}{2}}\Big(M_{\mathbf{k}_\perp}\tau\Big)\varphi^\dagger_r\sigma_3\chi_s\Big),\end{aligned} \tag{C.50}$$

where we insert the result for the product of basis spinors derived previously. We can now use the following property of the Hankel functions [164]

$$H^{(2),\star}_{\mathrm{i}\nu+\frac{1}{2}}(M_{\mathbf{k}_\perp}\tau) = H^{(1)}_{-\mathrm{i}\nu+\frac{1}{2}}(M_{\mathbf{k}_\perp}\tau) = e^{\pi\mathrm{i}\left(\mathrm{i}\nu-\frac{1}{2}\right)}H^{(1)}_{\mathrm{i}\nu-\frac{1}{2}}(M_{\mathbf{k}_\perp}\tau) = e^{-\pi\nu}e^{-\mathrm{i}\frac{\pi}{2}}H^{(1)}_{\mathrm{i}\nu-\frac{1}{2}}(M_{\mathbf{k}_\perp}\tau), \tag{C.51}$$

$$H^{(2),\star}_{\mathrm{i}\nu-\frac{1}{2}}(M_{\mathbf{k}_\perp}\tau) = H^{(1)}_{-\mathrm{i}\nu-\frac{1}{2}}(M_{\mathbf{k}_\perp}\tau) = e^{\pi\mathrm{i}\left(\mathrm{i}\nu+\frac{1}{2}\right)}H^{(1)}_{\mathrm{i}\nu+\frac{1}{2}}(M_{\mathbf{k}_\perp}\tau) = e^{-\pi\nu}e^{\mathrm{i}\frac{\pi}{2}}H^{(1)}_{\mathrm{i}\nu+\frac{1}{2}}(M_{\mathbf{k}_\perp}\tau). \tag{C.52}$$

Rewriting the Hankel functions by making use of the given properties, we finally find

$$\begin{aligned}\hat{\psi}^{+,\dagger}_{-\mathbf{k}_\perp,\nu,r,b}(\tau)\hat{\psi}^{-}_{\mathbf{k}_\perp,\nu,s,a}(\tau) = |a|^2\tau e^{-\pi\nu}\Big(&H^{(1)}_{\mathrm{i}\nu-\frac{1}{2}}(M_{\mathbf{k}_\perp}\tau)H^{(1)}_{\mathrm{i}\nu+\frac{1}{2}}\Big(M_{\mathbf{k}_\perp}\tau\Big)\varphi^\dagger_r\sigma_3\chi_s\\ &-H^{(1)}_{\mathrm{i}\nu+\frac{1}{2}}(M_{\mathbf{k}_\perp}\tau)H^{(1)}_{\mathrm{i}\nu-\frac{1}{2}}\Big(M_{\mathbf{k}_\perp}\tau\Big)\varphi^\dagger_r\sigma_3\chi_s\Big) = 0.\end{aligned} \tag{C.53}$$

A similar calculation leads to the result of the other off-diagonal combination

$$\begin{aligned}\hat{\psi}^{-,\dagger}_{-\mathbf{k}_\perp,\nu,r,b}(\tau)\hat{\psi}^{+}_{\mathbf{k}_\perp,\nu,s,a}(\tau) = |a|^2\tau e^{\pi\nu}\Big(&H^{(2)}_{\mathrm{i}\nu-\frac{1}{2}}\Big(M_{\mathbf{k}_\perp}\tau\Big)H^{(2)}_{\mathrm{i}\nu+\frac{1}{2}}(M_{\mathbf{k}_\perp}\tau)\chi^\dagger_r\sigma_3\varphi_s\\ &-H^{(2)}_{\mathrm{i}\nu+\frac{1}{2}}\Big(M_{\mathbf{k}_\perp}\tau\Big)H^{(2)}_{\mathrm{i}\nu-\frac{1}{2}}(M_{\mathbf{k}_\perp}\tau)\chi^\dagger_r\sigma_3\varphi_s\Big) = 0.\end{aligned} \tag{C.54}$$

Combining all of the given results, we showed that

$$\begin{aligned}\int|\psi(x)|^2d^3x =&|a|^2\tau\int\sum_{s=1}^{2}\sum_{a=1}^{N_c}\Big[\hat{a}^\dagger_{s,a}(\mathbf{k}_\perp,\nu)\hat{a}_{s,a}(\mathbf{k}_\perp,\nu)e^{\nu\pi}\Big(\Big|H^{(2)}_{\mathrm{i}\nu+\frac{1}{2}}\Big(M_{\mathbf{k}_\perp}\tau\Big)\Big|^2+\Big|H^{(2)}_{\mathrm{i}\nu-\frac{1}{2}}\Big(M_{\mathbf{k}_\perp}\tau\Big)\Big|^2\Big)\\ &+\hat{b}_{s,a}(\mathbf{k}_\perp,\nu)\hat{b}^\dagger_{s,a}(\mathbf{k}_\perp,\nu)e^{-\nu\pi}\Big(\Big|H^{(1)}_{\mathrm{i}\nu+\frac{1}{2}}\Big(M_{\mathbf{k}_\perp}\tau\Big)\Big|^2+\Big|H^{(1)}_{\mathrm{i}\nu-\frac{1}{2}}\Big(M_{\mathbf{k}_\perp}\tau\Big)\Big|^2\Big)\Big]\frac{d^2k_\perp}{(2\pi)^2}\frac{d\nu}{2\pi}.\end{aligned} \tag{C.55}$$

C.3.1 Implementation of the Free Expanding Box Spinor on the Lattice

In this appenndix we show, how to implement the free expanding box spinor on the lattice by making use of the stochastic low-cost method. As rigorously discussed in (section 2.2.2), we replace the creation and annihilation operators by complex numbers, drawn from an

appropriate Gaussian distribution (eq. 2.48). The Fourier representation of the low-cost gendered fermion spinor is then given as

$$\hat{\psi}_{M/F}(\tau,\mathbf{x}_\perp,\eta)=\frac{1}{V}\sum_{\mathbf{k}_\perp,\nu}\sum_{s=1}^{2}\sum_{a=1}^{N_c}\left(\xi_{s,a}(\mathbf{k}_\perp,\nu)\hat{\psi}^{+}_{\mathbf{k}_\perp,\nu,s,a}(\tau,\mathbf{x}_\perp,\eta)\pm\eta_{s,a}(\mathbf{k}_\perp,\nu)\hat{\psi}^{-}_{\mathbf{k}_\perp,\nu,s,a}(\tau,\mathbf{x}_\perp,\eta)\right). \tag{C.56}$$

We can now use ensemble averages of low-cost fermions to calculate the statistical fermion propagator in the expanding box. We implement the lattice solution of the free expanding box spinor (eq. 10.93) as initial condition for the fermion sector. This requires an evaluation of the Hankel functions in the simulation. We compute them using the following algorithm

- Starting point is the following relation from [164]

$$\begin{aligned}H^{(1)}_{\frac{\mathrm{i}}{a_\eta}\sin(a_\eta\nu)}(\bar{M}_{\mathbf{k}_\perp}\bar{\tau})=&\,\mathrm{i}\frac{1}{\sin\left(\left(\frac{\mathrm{i}}{a_\eta}\sin(a_\eta\nu)\pm\frac{1}{2}\right)\pi\right)}\\&\times\left[\exp\left(-\left(\frac{\mathrm{i}}{a_\eta}\sin\left(a_\eta\nu\right)\pm\frac{1}{2}\right)\pi\mathrm{i}\right)J_{\frac{\mathrm{i}}{a_\eta}\sin(a_\eta\nu)\pm\frac{1}{2}}\left(\bar{M}_{\mathbf{k}_\perp}\bar{\tau}\right)-J_{-\frac{\mathrm{i}}{a_\eta}\sin(a_\eta\nu)\mp\frac{1}{2}}\right],\end{aligned} \tag{C.57}$$

  where $J_i(x)$ is the Bessel function of the first kind. The Bessel function of the first kind is related to the generalized gamma function via

$$J_{\frac{\mathrm{i}}{a_\eta}\sin(a_\eta\nu)\pm\frac{1}{2}}(\bar{M}_{\mathbf{k}_\perp}\bar{\tau})=\left(\frac{\bar{M}^2_{\mathbf{k}_\perp}\bar{\tau}^2}{2}\right)^{\frac{\mathrm{i}}{a_\eta}\sin(a_\eta\nu)\pm\frac{1}{2}}\sum_{n=0}^{\infty}\frac{\left(-\bar{M}_{\mathbf{k}_\perp}\bar{\tau}\right)^n}{4^n\Gamma(n+1)\Gamma\left(\frac{\mathrm{i}}{a_\eta}\sin(a_\eta\nu)\pm\frac{1}{2}+n+1\right)}. \tag{C.58}$$

- Using the previous identities, we can directly represent the Hankel functions in terms of gamma functions

$$\begin{aligned}H^{(1)}_{\frac{\mathrm{i}}{a_\eta}\sin(a_\eta\nu)\pm\frac{1}{2}}(\bar{M}_{\mathbf{k}_\perp}\bar{\tau})=&\,\mathrm{i}\frac{1}{\sin\left(\left(\frac{\mathrm{i}}{a_\eta}\sin(a_\eta\nu)\pm\frac{1}{2}\right)\pi\right)}\sum_{n=0}^{\infty}\left(-\frac{\bar{M}^2_{\mathbf{k}_\perp}\bar{\tau}^2}{4}\right)^n\frac{1}{\Gamma(n+1)}\\&\times\left[\left(\frac{\bar{M}_{\mathbf{k}_\perp}\bar{\tau}}{2}\right)^{\frac{\mathrm{i}}{a_\eta}\sin(a_\eta\nu)\pm\frac{1}{2}}\frac{\exp\left(-\left(\frac{\mathrm{i}}{a_\eta}\sin(a_\eta\nu)\pm\frac{1}{2}\right)\pi\mathrm{i}\right)}{\Gamma\left(\frac{\mathrm{i}}{a_\eta}\sin(a_\eta\nu)\pm\frac{1}{2}+n+1\right)}\right.\\&\left.-\left(\frac{\bar{M}_{\mathbf{k}_\perp}\bar{\tau}}{2}\right)^{-\frac{\mathrm{i}}{a_\eta}\sin(a_\eta\nu)\mp\frac{1}{2}}\frac{1}{\Gamma\left(-\frac{\mathrm{i}}{a_\eta}\sin(a_\eta\nu)\mp\frac{1}{2}+n+1\right)}\right]\end{aligned} \tag{C.59}$$

$$\begin{aligned}H^{(2)}_{\frac{\mathrm{i}}{a_\eta}\sin(a_\eta\nu)\pm\frac{1}{2}}(\bar{M}_{\mathbf{k}_\perp}\bar{\tau})=&\,\frac{\mathrm{i}}{\sin\left(\left(\frac{\mathrm{i}}{a_\eta}\sin(a_\eta\nu)\pm\frac{1}{2}\right)\pi\right)}\sum_{n=0}^{\infty}\left(-\frac{\bar{M}^2_{\mathbf{k}_\perp}\bar{\tau}^2}{4}\right)^n\frac{1}{\Gamma(n+1)}\\&\times\left[\left(\frac{\bar{M}_{\mathbf{k}_\perp}\bar{\tau}}{2}\right)^{-\frac{\mathrm{i}}{a_\eta}\sin(a_\eta\nu)\mp\frac{1}{2}}\frac{1}{\Gamma\left(-\frac{\mathrm{i}}{a_\eta}\sin(a_\eta\nu)\mp\frac{1}{2}+n+1\right)}\right.\\&\left.-\left(\frac{\bar{M}_{\mathbf{k}_\perp}\bar{\tau}}{2}\right)^{\frac{\mathrm{i}}{a_\eta}\sin(a_\eta\nu)\pm\frac{1}{2}}\frac{\exp\left(\left(\frac{\mathrm{i}}{a_\eta}\sin(a_\eta\nu)\mp\frac{1}{2}\right)\pi\mathrm{i}\right)}{\Gamma\left(\frac{\mathrm{i}}{a_\eta}\sin(a_\eta\nu)\mp\frac{1}{2}+n+1\right)}\right).\end{aligned} \tag{C.60}$$

  In the simulation, we compute these expressions iteratively, cutting the sum as soon as a precision of 10^{-15} has been reached.

Bibliography

[1] Wolfgang Ochs. "The Status of Glueballs". In: *J. Phys. G* 40 (2013), p. 043001. DOI: 10.1088/0954-3899/40/4/043001. arXiv: 1301.5183 [hep-ph].

[2] Yan-Rui Liu, Hua-Xing Chen, Wei Chen, Xiang Liu, and Shi-Lin Zhu. "Pentaquark and Tetraquark states". In: *Prog. Part. Nucl. Phys.* 107 (2019), pp. 237–320. DOI: 10.1016/j.ppnp.2019.04.003. arXiv: 1903.11976 [hep-ph].

[3] Heng-Tong Ding, Frithjof Karsch, and Swagato Mukherjee. "Thermodynamics of strong-interaction matter from Lattice QCD". In: *Int. J. Mod. Phys. E* 24.10 (2015), p. 1530007. DOI: 10.1142/S0218301315300076. arXiv: 1504.05274 [hep-lat].

[4] Owe Philipsen. "The QCD equation of state from the lattice". In: *Prog. Part. Nucl. Phys.* 70 (2013), pp. 55–107. DOI: 10.1016/j.ppnp.2012.09.003. arXiv: 1207.5999 [hep-lat].

[5] G. Boyd, J. Engels, F. Karsch, E. Laermann, C. Legeland, M. Lutgemeier, and B. Petersson. "Thermodynamics of SU(3) lattice gauge theory". In: *Nucl. Phys. B* 469 (1996), pp. 419–444. DOI: 10.1016/0550-3213(96)00170-8. arXiv: hep-lat/9602007.

[6] Owe Philipsen. "Lattice Constraints on the QCD Chiral Phase Transition at Finite Temperature and Baryon Density". In: *Symmetry* 13.11 (2021), p. 2079. DOI: 10.3390/sym13112079. arXiv: 2111.03590 [hep-lat].

[7] Jaroslav Adam et al. "Anisotropic flow of charged particles in Pb-Pb collisions at $\sqrt{s_{\mathrm{NN}}} = 5.02$ TeV". In: *Phys. Rev. Lett.* 116.13 (2016), p. 132302. DOI: 10.1103/PhysRevLett.116.132302. arXiv: 1602.01119 [nucl-ex].

[8] Peter Senger. "Probing dense QCD matter in the laboratory—The CBM experiment at FAIR". In: *Phys. Scripta* 95.7 (2020). Ed. by Larissa Bravina, Sonia Kabana, Victoria Volkova, and Valentin Ivanovitch Zakharov, p. 074003. DOI: 10.1088/1402-4896/ab8c14. arXiv: 2005.03321 [nucl-ex].

[9] Ulrich W. Heinz and Maurice Jacob. "Evidence for a new state of matter: An Assessment of the results from the CERN lead beam program". In: (Jan. 2000). arXiv: nucl-th/0002042.

[10] Jean-Yves Ollitrault. "Anisotropy as a signature of transverse collective flow". In: *Phys. Rev. D* 46 (1992), pp. 229–245. DOI: 10.1103/PhysRevD.46.229.

[11] S. Voloshin and Y. Zhang. "Flow study in relativistic nuclear collisions by Fourier expansion of Azimuthal particle distributions". In: *Z. Phys. C* 70 (1996), pp. 665–672. DOI: 10.1007/s002880050141. arXiv: hep-ph/9407282.

[12] J. D. Bjorken. "Highly Relativistic Nucleus-Nucleus Collisions: The Central Rapidity Region". In: *Phys. Rev. D* 27 (1983), pp. 140–151. DOI: 10.1103/PhysRevD.27.140.

[13] Ulrich Heinz and Raimond Snellings. "Collective flow and viscosity in relativistic heavy-ion collisions". In: *Ann. Rev. Nucl. Part. Sci.* 63 (2013), pp. 123–151. DOI: 10.1146/annurev-nucl-102212-170540. arXiv: 1301.2826 [nucl-th].

[14] Raimond Snellings. "Elliptic Flow: A Brief Review". In: *New J. Phys.* 13 (2011), p. 055008. DOI: 10.1088/1367-2630/13/5/055008. arXiv: 1102.3010 [nucl-ex].

[15] Björn Schenke. "The smallest fluid on Earth". In: *Rept. Prog. Phys.* 84.8 (2021), p. 082301. DOI: 10.1088/1361-6633/ac14c9. arXiv: 2102.11189 [nucl-th].

[16] Wit Busza, Krishna Rajagopal, and Wilke van der Schee. "Heavy Ion Collisions: The Big Picture, and the Big Questions". In: *Ann. Rev. Nucl. Part. Sci.* 68 (2018), pp. 339–376. DOI: 10.1146/annurev-nucl-101917-020852. arXiv: 1802.04801 [hep-ph].

[17] Alfred H. Mueller and Jian-wei Qiu. "Gluon Recombination and Shadowing at Small Values of x". In: *Nucl. Phys. B* 268 (1986), pp. 427–452. DOI: 10.1016/0550-3213(86)90164-1.

[18] Larry D. McLerran and Raju Venugopalan. "Computing quark and gluon distribution functions for very large nuclei". In: *Phys. Rev. D* 49 (1994), pp. 2233–2241. DOI: 10.1103/PhysRevD.49.2233. arXiv: hep-ph/9309289.

[19] Larry D. McLerran and Raju Venugopalan. "Gluon distribution functions for very large nuclei at small transverse momentum". In: *Phys. Rev. D* 49 (1994), pp. 3352–3355. DOI: 10.1103/PhysRevD.49.3352. arXiv: hep-ph/9311205.

[20] Larry D. McLerran and Raju Venugopalan. "Green's functions in the color field of a large nucleus". In: *Phys. Rev. D* 50 (1994), pp. 2225–2233. DOI: 10.1103/PhysRevD.50.2225. arXiv: hep-ph/9402335.

[21] Edmond Iancu, Andrei Leonidov, and Larry McLerran. "The Color glass condensate: An Introduction". In: *Cargese Summer School on QCD Perspectives on Hot and Dense Matter*. Feb. 2002, pp. 73–145. arXiv: hep-ph/0202270.

[22] Edmond Iancu and Raju Venugopalan. "The Color glass condensate and high-energy scattering in QCD". In: *Quark-gluon plasma 4*. Ed. by Rudolph C. Hwa and Xin-Nian Wang. Mar. 2003, pp. 249–3363. DOI: 10.1142/9789812795533_0005. arXiv: hep-ph/0303204.

[23] Francois Gelis, Tuomas Lappi, and Raju Venugopalan. "High energy scattering in Quantum Chromodynamics". In: *Int. J. Mod. Phys. E* 16 (2007). Ed. by Debora Peres Menezes, Marcelo Chiapparini, Marcio Jose Menon, and Sidney dos Santos Avancini, pp. 2595–2637. DOI: 10.1142/S0218301307008331. arXiv: 0708.0047 [hep-ph].

[24] Francois Gelis, Edmond Iancu, Jamal Jalilian-Marian, and Raju Venugopalan. "The Color Glass Condensate". In: *Ann. Rev. Nucl. Part. Sci.* 60 (2010), pp. 463–489. DOI: 10.1146/annurev.nucl.010909.083629. arXiv: 1002.0333 [hep-ph].

[25] Anthony Duncan. *The Conceptual Framework of Quantum Field Theory*. Oxford University Press, Aug. 2012. ISBN: 978-0-19-880765-0, 978-0-19-880765-0, 978-0-19-957326-4. DOI: 10.1093/acprof:oso/9780199573264.001.0001.

[26] Dmitri Yu. Grigoriev and V. A. Rubakov. "Soliton Pair Creation at Finite Temperatures. Numerical Study in (1+1)-dimensions". In: *Nucl. Phys. B* 299 (1988), pp. 67–78. DOI: 10.1016/0550-3213(88)90466-X.

[27] Gert Aarts and Jan Smit. "Classical approximation for time dependent quantum field theory: Diagrammatic analysis for hot scalar fields". In: *Nucl. Phys. B* 511 (1998), pp. 451–478. DOI: 10.1016/S0550-3213(97)00723-2. arXiv: hep-ph/9707342.

[28] J. Berges. "Nonequilibrium quantum fields and the classical field theory limit". In: *Nucl. Phys. A* 702 (2002). Ed. by F. Karsch and H. Satz, pp. 351–355. DOI: 10.1016/S0375-9474(02)00723-6. arXiv: hep-ph/0201204.

[29] Gert Aarts and Juergen Berges. "Classical aspects of quantum fields far from equilibrium". In: *Phys. Rev. Lett.* 88 (2002), p. 041603. DOI: 10.1103/PhysRevLett.88.041603. arXiv: hep-ph/0107129.

[30] Guy D. Moore. "Real time simulations in lattice gauge theory". In: *Nucl. Phys. B Proc. Suppl.* 83 (2000). Ed. by M. Campostrini, S. Caracciolo, L. Cosmai, A. Di Giacomo, P. Rossi, and F. Rapuano, pp. 131–135. DOI: 10.1016/S0920-5632(00)91605-0. arXiv: hep-lat/9907009.

[31] Guy D. Moore. "Measuring the broken phase sphaleron rate nonperturbatively". In: *Phys. Rev. D* 59 (1999), p. 014503. DOI: 10.1103/PhysRevD.59.014503. arXiv: hep-ph/9805264.

[32] M. Mace, S. Schlichting, and R. Venugopalan. "Off-equilibrium sphaleron transitions in the Glasma". In: *Phys. Rev. D* 93.7 (2016), p. 074036. DOI: 10.1103/PhysRevD.93.074036. arXiv: 1601.07342 [hep-ph].

[33] Niklas Müller, Sören Schlichting, and Sayantan Sharma. "Chiral magnetic effect and anomalous transport from real-time lattice simulations". In: *Phys. Rev. Lett.* 117.14 (2016), p. 142301. DOI: 10.1103/PhysRevLett.117.142301. arXiv: 1606.00342 [hep-ph].

[34] Mark Mace, Niklas Mueller, Sören Schlichting, and Sayantan Sharma. "Non-equilibrium study of the Chiral Magnetic Effect from real-time simulations with dynamical fermions". In: *Phys. Rev. D* 95.3 (2017), p. 036023. DOI: 10.1103/PhysRevD.95.036023. arXiv: 1612.02477 [hep-lat].

[35] Juergen Berges and Thomas Gasenzer. "Quantum versus classical statistical dynamics of an ultracold Bose gas". In: *Phys. Rev. A* 76 (2007), p. 033604. DOI: 10.1103/PhysRevA.76.033604. arXiv: cond-mat/0703163.

[36] Mikko Laine, Guy D. Moore, Owe Philipsen, and Marcus Tassler. "Heavy Quark Thermalization in Classical Lattice Gauge Theory: Lessons for Strongly-Coupled QCD". In: *JHEP* 05 (2009), p. 014. DOI: 10.1088/1126-6708/2009/05/014. arXiv: 0902.2856 [hep-ph].

[37] T. Lappi and L. McLerran. "Some features of the glasma". In: *Nucl. Phys. A* 772 (2006), pp. 200–212. DOI: 10.1016/j.nuclphysa.2006.04.001. arXiv: hep-ph/0602189.

[38] Soeren Schlichting and Derek Teaney. "The First fm/c of Heavy-Ion Collisions". In: *Ann. Rev. Nucl. Part. Sci.* 69 (2019), pp. 447–476. DOI: 10.1146/annurev-nucl-101918-023825. arXiv: 1908.02113 [nucl-th].

[39] Alex Krasnitz and Raju Venugopalan. "Nonperturbative computation of gluon minijet production in nuclear collisions at very high-energies". In: *Nucl. Phys. B* 557 (1999), p. 237. DOI: 10.1016/S0550-3213(99)00366-1. arXiv: hep-ph/9809433.

[40] Alex Krasnitz and Raju Venugopalan. "The Initial gluon multiplicity in heavy ion collisions". In: *Phys. Rev. Lett.* 86 (2001), pp. 1717–1720. DOI: 10.1103/PhysRevLett.86.1717. arXiv: hep-ph/0007108.

[41] Alex Krasnitz, Yasushi Nara, and Raju Venugopalan. "Coherent gluon production in very high-energy heavy ion collisions". In: *Phys. Rev. Lett.* 87 (2001), p. 192302. DOI: 10.1103/PhysRevLett.87.192302. arXiv: hep-ph/0108092.

[42] Alex Krasnitz, Yasushi Nara, and Raju Venugopalan. "Gluon production in the color glass condensate model of collisions of ultrarelativistic finite nuclei". In: *Nucl. Phys. A* 717 (2003), pp. 268–290. DOI: 10.1016/S0375-9474(03)00636-5. arXiv: hep-ph/0209269.

[43] T. Lappi. "Production of gluons in the classical field model for heavy ion collisions". In: *Phys. Rev. C* 67 (2003), p. 054903. DOI: 10.1103/PhysRevC.67.054903. arXiv: hep-ph/0303076.

[44] Alex Krasnitz and Raju Venugopalan. "The Initial energy density of gluons produced in very high-energy nuclear collisions". In: *Phys. Rev. Lett.* 84 (2000), pp. 4309–4312. DOI: 10.1103/PhysRevLett.84.4309. arXiv: hep-ph/9909203.

[45] T. Lappi. "Energy density of the glasma". In: *Phys. Lett. B* 643 (2006), pp. 11–16. DOI: 10.1016/j.physletb.2006.10.017. arXiv: hep-ph/0606207.

[46] Andreas Ipp and David I. Müller. "Progress on 3+1D Glasma simulations". In: *Eur. Phys. J. A* 56.9 (2020), p. 243. DOI: 10.1140/epja/s10050-020-00241-6. arXiv: 2009.02044 [hep-ph].

[47] Bjoern Schenke and Soeren Schlichting. "3D glasma initial state for relativistic heavy ion collisions". In: *Phys. Rev. C* 94.4 (2016), p. 044907. DOI: 10.1103/PhysRevC.94.044907. arXiv: 1605.07158 [hep-ph].

[48] Bjoern Schenke, Prithwish Tribedy, and Raju Venugopalan. "Fluctuating Glasma initial conditions and flow in heavy ion collisions". In: *Phys. Rev. Lett.* 108 (2012), p. 252301. DOI: 10.1103/PhysRevLett.108.252301. arXiv: 1202.6646 [nucl-th].

[49] Bjoern Schenke, Prithwish Tribedy, and Raju Venugopalan. "Event-by-event gluon multiplicity, energy density, and eccentricities in ultrarelativistic heavy-ion collisions". In: *Phys. Rev. C* 86 (2012), p. 034908. DOI: 10.1103/PhysRevC.86.034908. arXiv: 1206.6805 [hep-ph].

[50] Aleksi Kurkela, Aleksas Mazeliauskas, Jean-François Paquet, Sören Schlichting, and Derek Teaney. "Matching the Nonequilibrium Initial Stage of Heavy Ion Collisions to Hydrodynamics with QCD Kinetic Theory". In: *Phys. Rev. Lett.* 122.12 (2019), p. 122302. DOI: 10.1103/PhysRevLett.122.122302. arXiv: 1805.01604 [hep-ph].

[51] Adam Bzdak, Bjoern Schenke, Prithwish Tribedy, and Raju Venugopalan. "Initial state geometry and the role of hydrodynamics in proton-proton, proton-nucleus and deuteron-nucleus collisions". In: *Phys. Rev. C* 87.6 (2013), p. 064906. DOI: 10.1103/PhysRevC.87.064906. arXiv: 1304.3403 [nucl-th].

[52] Charles Gale, Sangyong Jeon, Björn Schenke, Prithwish Tribedy, and Raju Venugopalan. "Event-by-event anisotropic flow in heavy-ion collisions from combined Yang-Mills and viscous fluid dynamics". In: *Phys. Rev. Lett.* 110.1 (2013), p. 012302. DOI: 10.1103/PhysRevLett.110.012302. arXiv: 1209.6330 [nucl-th].

[53] R. Baier, Alfred H. Mueller, D. Schiff, and D. T. Son. "'Bottom up' thermalization in heavy ion collisions". In: *Phys. Lett. B* 502 (2001), pp. 51–58. DOI: 10.1016/S0370-2693(01)00191-5. arXiv: hep-ph/0009237.

[54] Aleksi Kurkela and Guy D. Moore. "Thermalization in Weakly Coupled Nonabelian Plasmas". In: *JHEP* 12 (2011), p. 044. DOI: 10.1007/JHEP12(2011)044. arXiv: 1107.5050 [hep-ph].

[55] Peter Brockway Arnold, Jonathan Lenaghan, and Guy D. Moore. "QCD plasma instabilities and bottom up thermalization". In: *JHEP* 08 (2003), p. 002. DOI: 10.1088/1126-6708/2003/08/002. arXiv: hep-ph/0307325.

[56] Jean-Paul Blaizot, Francois Gelis, Jin-Feng Liao, Larry McLerran, and Raju Venugopalan. "Bose–Einstein Condensation and Thermalization of the Quark Gluon Plasma". In: *Nucl. Phys. A* 873 (2012), pp. 68–80. DOI: 10.1016/j.nuclphysa.2011.10.005. arXiv: 1107.5296 [hep-ph].

[57] Aleksi Kurkela and Egang Lu. "Approach to Equilibrium in Weakly Coupled Non-Abelian Plasmas". In: *Phys. Rev. Lett.* 113.18 (2014), p. 182301. DOI: 10.1103/PhysRevLett.113.182301. arXiv: 1405.6318 [hep-ph].

[58] Juergen Berges, Kirill Boguslavski, Soeren Schlichting, and Raju Venugopalan. "Universal attractor in a highly occupied non-Abelian plasma". In: *Phys. Rev. D* 89.11 (2014), p. 114007. DOI: 10.1103/PhysRevD.89.114007. arXiv: 1311.3005 [hep-ph].

[59] J. Berges, K. Boguslavski, S. Schlichting, and R. Venugopalan. "Turbulent thermalization process in heavy-ion collisions at ultrarelativistic energies". In: *Phys. Rev. D* 89.7 (2014), p. 074011. DOI: 10.1103/PhysRevD.89.074011. arXiv: 1303.5650 [hep-ph].

[60] Kenji Fukushima. "Turbulent pattern formation and diffusion in the early-time dynamics in relativistic heavy-ion collisions". In: *Phys. Rev. C* 89.2 (2014), p. 024907. DOI: 10.1103/PhysRevC.89.024907. arXiv: 1307.1046 [hep-ph].

[61] Paul Romatschke and Raju Venugopalan. "The Unstable Glasma". In: *Phys. Rev. D* 74 (2006), p. 045011. DOI: 10.1103/PhysRevD.74.045011. arXiv: hep-ph/0605045.

[62] Kenji Fukushima and Francois Gelis. "The evolving Glasma". In: *Nucl. Phys. A* 874 (2012), pp. 108–129. DOI: 10.1016/j.nuclphysa.2011.11.003. arXiv: 1106.1396 [hep-ph].

[63] Thomas Epelbaum and Francois Gelis. "Fluctuations of the initial color fields in high energy heavy ion collisions". In: *Phys. Rev. D* 88 (2013), p. 085015. DOI: 10.1103/PhysRevD.88.085015. arXiv: 1307.1765 [hep-ph].

[64] Thomas Epelbaum and Francois Gelis. "Pressure isotropization in high energy heavy ion collisions". In: *Phys. Rev. Lett.* 111 (2013), p. 232301. DOI: 10.1103/PhysRevLett.111.232301. arXiv: 1307.2214 [hep-ph].

[65] Daniil Gelfand, Andreas Ipp, and David Müller. "Simulating collisions of thick nuclei in the color glass condensate framework". In: *Phys. Rev. D* 94.1 (2016), p. 014020. DOI: 10.1103/PhysRevD.94.014020. arXiv: 1605.07184 [hep-ph].

[66] Andreas Ipp and David Müller. "Broken boost invariance in the Glasma via finite nuclei thickness". In: *Phys. Lett. B* 771 (2017), pp. 74–79. DOI: 10.1016/j.physletb.2017.05.032. arXiv: 1703.00017 [hep-ph].

[67] Soeren Schlichting and Pragya Singh. "3-D structure of the Glasma initial state – Breaking boost-invariance by collisions of extended shock waves in classical Yang-Mills theory". In: *Phys. Rev. D* 103.1 (2021), p. 014003. DOI: 10.1103/PhysRevD.103.014003. arXiv: 2010.11172 [hep-ph].

[68] F. D. Aaron et al. "Combined Measurement and QCD Analysis of the Inclusive e+-p Scattering Cross Sections at HERA". In: *JHEP* 01 (2010), p. 109. DOI: 10.1007/JHEP01(2010)109. arXiv: 0911.0884 [hep-ex].

[69] F. Gelis, K. Kajantie, and T. Lappi. "Quark-antiquark production from classical fields in heavy ion collisions: 1+1 dimensions". In: *Phys. Rev. C* 71 (2005), p. 024904. DOI: 10.1103/PhysRevC.71.024904. arXiv: hep-ph/0409058.

[70] F. Gelis, K. Kajantie, and T. Lappi. "Chemical thermalization in relativistic heavy ion collisions". In: *Phys. Rev. Lett.* 96 (2006), p. 032304. DOI: 10.1103/PhysRevLett.96.032304. arXiv: hep-ph/0508229.

[71] Florian Hebenstreit, Jürgen Berges, and Daniil Gelfand. "Simulating fermion production in 1+1 dimensional QED". In: *Phys. Rev. D* 87.10 (2013), p. 105006. DOI: 10.1103/PhysRevD.87.105006. arXiv: 1302.5537 [hep-ph].

[72] Valentin Kasper, Florian Hebenstreit, and Jürgen Berges. "Fermion production from real-time lattice gauge theory in the classical-statistical regime". In: *Phys. Rev. D* 90.2 (2014), p. 025016. DOI: 10.1103/PhysRevD.90.025016. arXiv: 1403.4849 [hep-ph].

[73] D. Gelfand, F. Hebenstreit, and J. Berges. "Early quark production and approach to chemical equilibrium". In: *Phys. Rev. D* 93.8 (2016), p. 085001. DOI: 10.1103/PhysRevD.93.085001. arXiv: 1601.03576 [hep-ph].

[74] Francois Gelis and Naoto Tanji. "Quark production in heavy ion collisions: formalism and boost invariant fermionic light-cone mode functions". In: *JHEP* 02 (2016), p. 126. DOI: 10.1007/JHEP02(2016)126. arXiv: 1506.03327 [hep-ph].

[75] Naoto Tanji and Juergen Berges. "Nonequilibrium quark production in the expanding QCD plasma". In: *Phys. Rev. D* 97.3 (2018), p. 034013. DOI: 10.1103/PhysRevD.97.034013. arXiv: 1711.03445 [hep-ph].

[76] Aleksi Kurkela and Yan Zhu. "Isotropization and hydrodynamization in weakly coupled heavy-ion collisions". In: *Phys. Rev. Lett.* 115.18 (2015), p. 182301. DOI: 10.1103/PhysRevLett.115.182301. arXiv: 1506.06647 [hep-ph].

[77] Liam Keegan, Aleksi Kurkela, Paul Romatschke, Wilke van der Schee, and Yan Zhu. "Weak and strong coupling equilibration in nonabelian gauge theories". In: *JHEP* 04 (2016), p. 031. DOI: 10.1007/JHEP04(2016)031. arXiv: 1512.05347 [hep-th].

[78] Liam Keegan, Aleksi Kurkela, Aleksas Mazeliauskas, and Derek Teaney. "Initial conditions for hydrodynamics from weakly coupled pre-equilibrium evolution". In: *JHEP* 08 (2016), p. 171. DOI: 10.1007/JHEP08(2016)171. arXiv: 1605.04287 [hep-ph].

[79] Chun Shen and Li Yan. "Recent development of hydrodynamic modeling in heavy-ion collisions". In: *Nucl. Sci. Tech.* 31.12 (Oct. 2020), p. 122. DOI: 10.1007/s41365-020-00829-z. arXiv: 2010.12377 [nucl-th].

[80] Mark C. Abraao York, Aleksi Kurkela, Egang Lu, and Guy D. Moore. "UV cascade in classical Yang-Mills theory via kinetic theory". In: *Phys. Rev. D* 89.7 (2014), p. 074036. DOI: 10.1103/PhysRevD.89.074036. arXiv: 1401.3751 [hep-ph].

[81] Michal P. Heller, Aleksi Kurkela, Michal Spaliński, and Viktor Svensson. "Hydrodynamization in kinetic theory: Transient modes and the gradient expansion". In: *Phys. Rev. D* 97.9 (2018), p. 091503. DOI: 10.1103/PhysRevD.97.091503. arXiv: 1609.04803 [nucl-th].

[82] Aleksi Kurkela, Aleksas Mazeliauskas, Jean-François Paquet, Sören Schlichting, and Derek Teaney. "Effective kinetic description of event-by-event pre-equilibrium dynamics in high-energy heavy-ion collisions". In: *Phys. Rev. C* 99.3 (2019), p. 034910. DOI: 10.1103/PhysRevC.99.034910. arXiv: 1805.00961 [hep-ph].

[83] Aleksi Kurkela and Aleksas Mazeliauskas. "Chemical Equilibration in Hadronic Collisions". In: *Phys. Rev. Lett.* 122 (2019), p. 142301. DOI: 10.1103/PhysRevLett.122.142301. arXiv: 1811.03040 [hep-ph].

[84] Aleksi Kurkela and Aleksas Mazeliauskas. "Chemical equilibration in weakly coupled QCD". In: *Phys. Rev. D* 99.5 (2019), p. 054018. DOI: 10.1103/PhysRevD.99.054018. arXiv: 1811.03068 [hep-ph].

[85] Xiaojian Du and Sören Schlichting. "Equilibration of weakly coupled QCD plasmas". In: *Phys. Rev. D* 104.5 (2021), p. 054011. DOI: 10.1103/PhysRevD.104.054011. arXiv: 2012.09079 [hep-ph].

[86] Jürgen Berges, Michal P. Heller, Aleksas Mazeliauskas, and Raju Venugopalan. "QCD thermalization: Ab initio approaches and interdisciplinary connections". In: *Rev. Mod. Phys.* 93.3 (2021), p. 035003. DOI: 10.1103/RevModPhys.93.035003. arXiv: 2005.12299 [hep-th].

[87] G. D. Rochester and C. C. Butler. "Evidence for the Existence of New Unstable Elementary Particles". In: *Nature* 160 (1947), pp. 855–857. DOI: 10.1038/160855a0.

[88] V. D. Hopper and S. Biswas. "Evidence Concerning the Existence of the New Unstable Elementary Neutral Particle". In: *Phys. Rev.* 80 (6 Dec. 1950), pp. 1099–1100. DOI: 10.1103/PhysRev.80.1099. URL: https://link.aps.org/doi/10.1103/PhysRev.80.1099.

[89] Murray Gell-Mann. "Symmetries of baryons and mesons". In: *Phys. Rev.* 125 (1962), pp. 1067–1084. DOI: 10.1103/PhysRev.125.1067.

[90] Yuval Ne'eman. "Derivation of strong interactions from a gauge invariance". In: *Nucl. Phys.* 26 (1961). Ed. by R. Ruffini and Y. Verbin, pp. 222–229. DOI: 10.1016/0029-5582(61)90134-1.

[91] Murray Gell-Mann. "A Schematic Model of Baryons and Mesons". In: *Phys. Lett.* 8 (1964), pp. 214–215. DOI: 10.1016/S0031-9163(64)92001-3.

[92] G. Zweig. "An SU(3) model for strong interaction symmetry and its breaking. Version 2". In: *DEVELOPMENTS IN THE QUARK THEORY OF HADRONS. VOL. 1. 1964 - 1978*. Ed. by D. B. Lichtenberg and Simon Peter Rosen. Feb. 1964, pp. 22–101.

[93] O. W. Greenberg. "Spin and Unitary Spin Independence in a Paraquark Model of Baryons and Mesons". In: *Phys. Rev. Lett.* 13 (1964), pp. 598–602. DOI: 10.1103/PhysRevLett.13.598.

[94] M. Y. Han and Yoichiro Nambu. "Three Triplet Model with Double SU(3) Symmetry". In: *Phys. Rev.* 139 (1965). Ed. by T. Eguchi, B1006–B1010. DOI: 10.1103/PhysRev.139.B1006.

[95] H. Fritzsch, Murray Gell-Mann, and H. Leutwyler. "Advantages of the Color Octet Gluon Picture". In: *Phys. Lett. B* 47 (1973), pp. 365–368. DOI: 10.1016/0370-2693(73)90625-4.

[96] Chen-Ning Yang and Robert L. Mills. "Conservation of Isotopic Spin and Isotopic Gauge Invariance". In: *Phys. Rev.* 96 (1954). Ed. by Jong-Ping Hsu and D. Fine, pp. 191–195. DOI: 10.1103/PhysRev.96.191.

[97] Michel Le Bellac. *Thermal Field Theory*. Cambridge Monographs on Mathematical Physics. Cambridge University Press, Mar. 2011. ISBN: 978-0-511-88506-8, 978-0-521-65477-7. DOI: 10.1017/CBO9780511721700.

[98] Jurgen Baacke, Katrin Heitmann, and Carsten Patzold. "Nonequilibrium dynamics of fermions in a spatially homogeneous scalar background field". In: *Phys. Rev. D* 58 (1998), p. 125013. DOI: 10.1103/PhysRevD.58.125013. arXiv: hep-ph/9806205.

[99] Jurgen Baacke and Carsten Patzold. "Renormalization of the nonequilibrium dynamics of fermions in a flat FRW universe". In: *Phys. Rev. D* 62 (2000), p. 084008. DOI: 10.1103/PhysRevD.62.084008. arXiv: hep-ph/9912505.

[100] G. F. Giudice, M. Peloso, A. Riotto, and I. Tkachev. "Production of massive fermions at preheating and leptogenesis". In: *JHEP* 08 (1999), p. 014. DOI: 10.1088/1126-6708/1999/08/014. arXiv: hep-ph/9905242.

[101] Sz. Borsanyi and M. Hindmarsh. "Low-cost fermions in classical field simulations". In: *Phys. Rev. D* 79 (2009), p. 065010. DOI: 10.1103/PhysRevD.79.065010. arXiv: 0809.4711 [hep-ph].

[102] Christof Gattringer and Christian B. Lang. *Quantum chromodynamics on the lattice*. Vol. 788. Berlin: Springer, 2010. ISBN: 978-3-642-01849-7, 978-3-642-01850-3. DOI: 10.1007/978-3-642-01850-3.

[103] I. Montvay and G. Munster. *Quantum fields on a lattice*. Cambridge Monographs on Mathematical Physics. Cambridge University Press, Mar. 1997. ISBN: 978-0-521-59917-7, 978-0-511-87919-7. DOI: 10.1017/CBO9780511470783.

[104] Kenneth G. Wilson. "Confinement of Quarks". In: *Phys. Rev. D* 10 (1974). Ed. by J. C. Taylor, pp. 2445–2459. DOI: 10.1103/PhysRevD.10.2445.

[105] David J. Gross and Frank Wilczek. "Ultraviolet Behavior of Nonabelian Gauge Theories". In: *Phys. Rev. Lett.* 30 (1973). Ed. by J. C. Taylor, pp. 1343–1346. DOI: 10.1103/PhysRevLett.30.1343.

[106] H. David Politzer. "Reliable Perturbative Results for Strong Interactions?" In: *Phys. Rev. Lett.* 30 (1973). Ed. by J. C. Taylor, pp. 1346–1349. DOI: 10.1103/PhysRevLett.30.1346.

[107] Berndt Müller. "A New Phase of Matter: Quark-Gluon Plasma Beyond the Hagedorn Critical Temperature". In: *Melting Hadrons, Boiling Quarks - From Hagedorn Temperature to Ultra-Relativistic Heavy-Ion Collisions at CERN: With a Tribute to Rolf Hagedorn*. Ed. by Johann Rafelski. 2016, pp. 107–116. DOI: 10.1007/978-3-319-17545-4_14. arXiv: 1501.06077 [nucl-th].

[108] Francois Gelis and Bjoern Schenke. "Initial State Quantum Fluctuations in the Little Bang". In: *Ann. Rev. Nucl. Part. Sci.* 66 (2016), pp. 73–94. DOI: 10.1146/annurev-nucl-102115-044651. arXiv: 1604.00335 [hep-ph].

[109] S. A. Bass et al. "Microscopic models for ultrarelativistic heavy ion collisions". In: *Prog. Part. Nucl. Phys.* 41 (1998), pp. 255–369. DOI: 10.1016/S0146-6410(98)00058-1. arXiv: nucl-th/9803035.

[110] Hannah Petersen, Jan Steinheimer, Gerhard Burau, Marcus Bleicher, and Horst Stöcker. "A Fully Integrated Transport Approach to Heavy Ion Reactions with an Intermediate Hydrodynamic Stage". In: *Phys. Rev. C* 78 (2008), p. 044901. DOI: 10.1103/PhysRevC.78.044901. arXiv: 0806.1695 [nucl-th].

[111] R. P. Feynman. "The behavior of hadron collisions at extreme energies". In: *Conf. Proc. C* 690905 (1969), pp. 237–258.

[112] Kenji Fukushima. "Evolution to the quark–gluon plasma". In: *Rept. Prog. Phys.* 80.2 (2017), p. 022301. DOI: 10.1088/1361-6633/80/2/022301. arXiv: 1603.02340 [nucl-th].

[113] L. N. Lipatov. "Small x physics in perturbative QCD". In: *Phys. Rept.* 286 (1997), pp. 131–198. DOI: 10.1016/S0370-1573(96)00045-2. arXiv: hep-ph/9610276.

[114] E. A. Kuraev, L. N. Lipatov, and Victor S. Fadin. "The Pomeranchuk Singularity in Nonabelian Gauge Theories". In: *Sov. Phys. JETP* 45 (1977), pp. 199–204.

[115] Alexandre Deur, Stanley J. Brodsky, and Guy F. de Teramond. "The QCD Running Coupling". In: *Nucl. Phys.* 90 (2016), p. 1. DOI: 10.1016/j.ppnp.2016.04.003. arXiv: 1604.08082 [hep-ph].

[116] Jamal Jalilian-Marian, Alex Kovner, Andrei Leonidov, and Heribert Weigert. "The BFKL equation from the Wilson renormalization group". In: *Nucl. Phys. B* 504 (1997), pp. 415–431. DOI: 10.1016/S0550-3213(97)00440-9. arXiv: hep-ph/9701284.

[117] Edmond Iancu, Andrei Leonidov, and Larry D. McLerran. "Nonlinear gluon evolution in the color glass condensate. 1." In: *Nucl. Phys. A* 692 (2001), pp. 583–645. DOI: 10.1016/S0375-9474(01)00642-X. arXiv: hep-ph/0011241.

[118] Elena Ferreiro, Edmond Iancu, Andrei Leonidov, and Larry McLerran. "Nonlinear gluon evolution in the color glass condensate. 2." In: *Nucl. Phys. A* 703 (2002), pp. 489–538. DOI: 10.1016/S0375-9474(01)01329-X. arXiv: hep-ph/0109115.

[119] Y. Hatta, E. Iancu, L. McLerran, A. Stasto, and D. N. Triantafyllopoulos. "Effective Hamiltonian for QCD evolution at high energy". In: *Nucl. Phys. A* 764 (2006), pp. 423–459. DOI: 10.1016/j.nuclphysa.2005.09.006. arXiv: hep-ph/0504182.

[120] Kenji Fukushima. "Deriving the Jalilian-Marian-Iancu-McLerran-Weigert-Leonidov-Kovner equation with classical and quantum source terms". In: *Nucl. Phys. A* 775 (2006), pp. 69–88. DOI: 10.1016/j.nuclphysa.2006.06.002. arXiv: hep-ph/0603044.

[121] Alfred H. Mueller. "A Simple derivation of the JIMWLK equation". In: *Phys. Lett. B* 523 (2001), pp. 243–248. DOI: 10.1016/S0370-2693(01)01343-0. arXiv: hep-ph/0110169.

[122] Francois Gelis. "Some Aspects of the Theory of Heavy Ion Collisions". In: *Rept. Prog. Phys.* 84.5 (2021), p. 056301. DOI: 10.1088/1361-6633/abec2e. arXiv: 2102.07604 [hep-ph].

[123] Alex Kovner, Larry D. McLerran, and Heribert Weigert. "Gluon production from nonAbelian Weizsacker-Williams fields in nucleus-nucleus collisions". In: *Phys. Rev. D* 52 (1995), pp. 6231–6237. DOI: 10.1103/PhysRevD.52.6231. arXiv: hep-ph/9502289.

[124] Kenji Fukushima. "Randomness in infinitesimal extent in the McLerran-Venugopalan model". In: *Phys. Rev. D* 77 (2008), p. 074005. DOI: 10.1103/PhysRevD.77.074005. arXiv: 0711.2364 [hep-ph].

[125] T. Lappi. "Wilson line correlator in the MV model: Relating the glasma to deep inelastic scattering". In: *Eur. Phys. J. C* 55 (2008), pp. 285–292. DOI: 10.1140/epjc/s10052-008-0588-4. arXiv: 0711.3039 [hep-ph].

[126] Owe Philipsen, Björn Wagenbach, and Savvas Zafeiropoulos. "From the colour glass condensate to filamentation: systematics of classical Yang–Mills theory". In: *Eur. Phys. J. C* 79.4 (2019), p. 286. DOI: 10.1140/epjc/s10052-019-6790-8. arXiv: 1810.00723 [hep-lat].

[127] Björn Fröhlich Wagenbach. "Real-time lattice simulations of classical Yang-Mills theory and fermion effects". PhD thesis. Goethe U., Frankfurt (main), Goethe U., Frankfurt (main), 2018.

[128] Edmond Iancu, Kazunori Itakura, and Larry McLerran. "A Gaussian effective theory for gluon saturation". In: *Nucl. Phys. A* 724 (2003), pp. 181–222. DOI: 10.1016/S0375-9474(03)01477-5. arXiv: hep-ph/0212123.

[129] Tuomas Lappi. "Classical chromodynamics and heavy ion collisions". PhD thesis. Helsinki U., 2004. arXiv: hep-ph/0505095.

[130] Erich S. Weibel. "Spontaneously Growing Transverse Waves in a Plasma Due to an Anisotropic Velocity Distribution". In: *Phys. Rev. Lett.* 2 (3 Feb. 1959), pp. 83–84. DOI: 10.1103/PhysRevLett.2.83. URL: https://link.aps.org/doi/10.1103/PhysRevLett.2.83.

[131] F. Gelis. "Initial state and thermalization in the Color Glass Condensate framework". In: *Int. J. Mod. Phys. E* 24.10 (2015), p. 1530008. DOI: 10.1142/S0218301315300088. arXiv: 1508.07974 [hep-ph].

[132] Nicolas Borghini, Marc Borrell, Nina Feld, Hendrik Roch, Sören Schlichting, and Clemens Werthmann. "Statistical analysis of initial-state and final-state response in heavy-ion collisions". In: *Phys. Rev. C* 107.3 (2023), p. 034905. DOI: 10.1103/PhysRevC.107.034905. arXiv: 2209.01176 [hep-ph].

[133] Tuomas Lappi and Sören Schlichting. "Linearly polarized gluons and axial charge fluctuations in the Glasma". In: *Phys. Rev. D* 97.3 (2018), p. 034034. DOI: 10.1103/PhysRevD.97.034034. arXiv: 1708.08625 [hep-ph].

[134] J. -P. Blaizot, T. Lappi, and Y. Mehtar-Tani. "On the gluon spectrum in the glasma". In: *Nucl. Phys. A* 846 (2010), pp. 63–82. DOI: 10.1016/j.nuclphysa.2010.06.009. arXiv: 1005.0955 [hep-ph].

[135] Roger D. Woods and David S. Saxon. "Diffuse Surface Optical Model for Nucleon-Nuclei Scattering". In: *Phys. Rev.* 95 (2 July 1954), pp. 577–578. DOI: 10.1103/PhysRev.95.577. URL: https://link.aps.org/doi/10.1103/PhysRev.95.577.

[136] Krzysztof J. Golec-Biernat and M. Wusthoff. "Saturation effects in deep inelastic scattering at low Q**2 and its implications on diffraction". In: *Phys. Rev. D* 59 (1998), p. 014017. DOI: 10.1103/PhysRevD.59.014017. arXiv: hep-ph/9807513.

[137] Henri Kowalski and Derek Teaney. "An Impact parameter dipole saturation model". In: *Phys. Rev. D* 68 (2003), p. 114005. DOI: 10.1103/PhysRevD.68.114005. arXiv: hep-ph/0304189.

[138] Amir H. Rezaeian, Marat Siddikov, Merijn Van de Klundert, and Raju Venugopalan. "Analysis of combined HERA data in the Impact-Parameter dependent Saturation model". In: *Phys. Rev. D* 87.3 (2013), p. 034002. DOI: 10.1103/PhysRevD.87.034002. arXiv: 1212.2974 [hep-ph].

[139] Giuliano Giacalone, Aleksas Mazeliauskas, and Sören Schlichting. "Hydrodynamic attractors, initial state energy and particle production in relativistic nuclear collisions". In: *Phys. Rev. Lett.* 123.26 (2019), p. 262301. DOI: 10.1103/PhysRevLett.123.262301. arXiv: 1908.02866 [hep-ph].

[140] Paul Romatschke. "Relativistic Fluid Dynamics Far From Local Equilibrium". In: *Phys. Rev. Lett.* 120.1 (2018), p. 012301. DOI: 10.1103/PhysRevLett.120.012301. arXiv: 1704.08699 [hep-th].

[141] Patrick Hanus, Aleksas Mazeliauskas, and Klaus Reygers. "Entropy production in pp and Pb-Pb collisions at energies available at the CERN Large Hadron Collider". In: *Phys. Rev. C* 100.6 (2019), p. 064903. DOI: 10.1103/PhysRevC.100.064903. arXiv: 1908.02792 [hep-ph].

[142] Steffen Georg Weber and Anton Andronic. "ALICE event display of a Pb-Pb collision at 5.02A TeV". General Photo. 2016. URL: https://cds.cern.ch/record/2202730.

[143] Guy D. Moore. "Motion of Chern-Simons number at high temperatures under a chemical potential". In: *Nucl. Phys. B* 480 (1996), pp. 657–688. DOI: 10.1016/S0550-3213(96)00445-2. arXiv: hep-ph/9603384.

[144] C. Itzykson and J. B. Zuber. *Quantum Field Theory*. International Series In Pure and Applied Physics. New York: McGraw-Hill, 1980. ISBN: 978-0-486-44568-7.

[145] D. Boyanovsky, M. D'Attanasio, H. J. de Vega, R. Holman, and D. -S. Lee. "Reheating and thermalization: Linear versus nonlinear relaxation". In: *Phys. Rev. D* 52 (1995), pp. 6805–6827. DOI: 10.1103/PhysRevD.52.6805. arXiv: hep-ph/9507414.

[146] Zong-Gang Mou, Paul M. Saffin, and Anders Tranberg. "Ensemble fermions for electroweak dynamics and the fermion preheating temperature". In: *JHEP* 11 (2013), p. 097. DOI: 10.1007/JHEP11(2013)097. arXiv: 1307.7924 [hep-ph].

[147] Zong-Gang Mou, Paul M. Saffin, and Anders Tranberg. "Cold Baryogenesis from first principles in the Two-Higgs Doublet model with Fermions". In: *JHEP* 06 (2015), p. 163. DOI: 10.1007/JHEP06(2015)163. arXiv: 1505.02692 [hep-ph].

[148] Xiang-Dong Ji. "Breakup of hadron masses and energy - momentum tensor of QCD". In: *Phys. Rev. D* 52 (1995), pp. 271–281. DOI: 10.1103/PhysRevD.52.271. arXiv: hep-ph/9502213.

[149] Owe Philipsen. *Quantenfeldtheorie und das Standardmodell der Teilchenphysik: Eine Einführung*. Heidelberg: Springer Spektrum Berlin, 2018. ISBN: 978-3-662-57819-3. DOI: 10.1007/978-3-662-57820-9.

[150] J. I. Kapusta and Charles Gale. *Finite-temperature field theory: Principles and applications*. Cambridge Monographs on Mathematical Physics. Cambridge University Press, 2011. ISBN: 978-0-521-17322-3, 978-0-521-82082-0, 978-0-511-22280-1. DOI: 10.1017/CBO9780511535130.

[151] Kerson Huang. *Statistical Mechanics, 2nd Edition*. John Wiley & Sons, 1988. ISBN: 978-0-471-81518-1.

[152] Richard Courant and K. Friedrichs and Hans Lewy. "Über die partiellen Differenzengleichungen der mathematischen Physik". In: *Mathematische Annalen* 100 (1928), 32–74. URL: %7Bhttps://api.semanticscholar.org/CorpusID:120760331%7D.

[153] Christian Schäfer. "Real Time Observables for the Quark-Gluon Plasma from the Lattice". PhD thesis. Frankfurt U., 2014.

[154] Wilke van der Schee, Paul Romatschke, and Scott Pratt. "Fully Dynamical Simulation of Central Nuclear Collisions". In: *Phys. Rev. Lett.* 111.22 (2013), p. 222302. DOI: 10.1103/PhysRevLett.111.222302. arXiv: 1307.2539 [nucl-th].

[155] Paul Romatschke and Ulrike Romatschke. "Viscosity Information from Relativistic Nuclear Collisions: How Perfect is the Fluid Observed at RHIC?" In: *Phys. Rev. Lett.* 99 (2007), p. 172301. DOI: 10.1103/PhysRevLett.99.172301. arXiv: 0706.1522 [nucl-th].

[156] Bjorn Schenke, Sangyong Jeon, and Charles Gale. "Elliptic and triangular flow in event-by-event (3+1)D viscous hydrodynamics". In: *Phys. Rev. Lett.* 106 (2011), p. 042301. DOI: 10.1103/PhysRevLett.106.042301. arXiv: 1009.3244 [hep-ph].

[157] Jean-François Paquet, Chun Shen, Gabriel S. Denicol, Matthew Luzum, Björn Schenke, Sangyong Jeon, and Charles Gale. "Production of photons in relativistic heavy-ion collisions". In: *Phys. Rev. C* 93.4 (2016), p. 044906. DOI: 10.1103/PhysRevC.93.044906. arXiv: 1509.06738 [hep-ph].

[158] Azwinndini Muronga. "Causal theories of dissipative relativistic fluid dynamics for nuclear collisions". In: *Phys. Rev. C* 69 (2004), p. 034903. DOI: 10.1103/PhysRevC.69.034903. arXiv: nucl-th/0309055.

[159] L. D. Landau and E. M. Lifshitz. *Statistical Physics, Part 1*. Vol. 5. Course of Theoretical Physics. Oxford: Butterworth-Heinemann, 1980. ISBN: 978-0-7506-3372-7.

[160] T. Niida and Y. Miake. "Signatures of QGP at RHIC and the LHC". In: *AAPPS Bull.* 31.1 (2021), p. 12. DOI: 10.1007/s43673-021-00014-3. arXiv: 2104.11406 [nucl-ex].

[161] H. Elfner and J. Bernhard. In: (2013). URL: https://madai.phy.duke.edu/index.html.

[162] A. Makhlin. "Scenario for ultrarelativistic nuclear collisions. 2. Geometry of quantum states at the earliest stage". In: *Phys. Rev. C* 63 (2001), p. 044902. DOI: 10.1103/PhysRevC.63.044902. arXiv: hep-ph/0007300.

[163] A. Makhlin. "Scenario for ultrarelativistic nuclear collisions. 3. Gluons in the expanding geometry". In: *Phys. Rev. C* 63 (2001), p. 044903. DOI: 10.1103/PhysRevC.63.044903. arXiv: hep-ph/0007301.

[164] Milton Abramowitz and Irene A. Stegun, eds. *Handbook of Mathematical Functions with Formulas, Graphs, and Mathematical Tables*. Tenth Printing. Washington, DC, USA: U.S. Government Printing Office, 1972.

[165] F.J. Belinfante. "On the current and the density of the electric charge, the energy, the linear momentum and the angular momentum of arbitrary fields". In: *Physica* 7.5 (1940), pp. 449–474. ISSN: 0031-8914. DOI: https://doi.org/10.1016/S0031-8914(40)90091-X. URL: https://www.sciencedirect.com/science/article/pii/S003189144090091X.

[166] F. Gelis. "Color Glass Condensate and Glasma". In: *Int. J. Mod. Phys. A* 28 (2013), p. 1330001. DOI: 10.1142/S0217751X13300019. arXiv: 1211.3327 [hep-ph].

[167] Eric Braaten and Robert D. Pisarski. "Soft Amplitudes in Hot Gauge Theories: A General Analysis". In: *Nucl. Phys. B* 337 (1990), pp. 569–634. DOI: 10.1016/0550-3213(90)90508-B.

[168] J. C. Taylor and S. M. H. Wong. "The Effective Action of Hard Thermal Loops in QCD". In: *Nucl. Phys. B* 346 (1990), pp. 115–128. DOI: 10.1016/0550-3213(90)90240-E.

[169] Jean Paul Blaizot and Edmond Iancu. "Kinetic equations for long wavelength excitations of the quark - gluon plasma". In: *Phys. Rev. Lett.* 70 (1993), pp. 3376–3379. DOI: 10.1103/PhysRevLett.70.3376. arXiv: hep-ph/9301236.

[170] Jens Braun and Hans-Jurgen Pirner. "Effects of the running of the QCD coupling on the energy loss in the quark-gluon plasma". In: *Phys. Rev. D* 75 (2007), p. 054031. DOI: 10.1103/PhysRevD.75.054031. arXiv: hep-ph/0610331.